Coherent control of entanglement with atomic ensembles

Thesis by

Kyung Soo Choi

In Partial Fulfillment of the Requirements

for the Degree of

Doctor of Philosophy

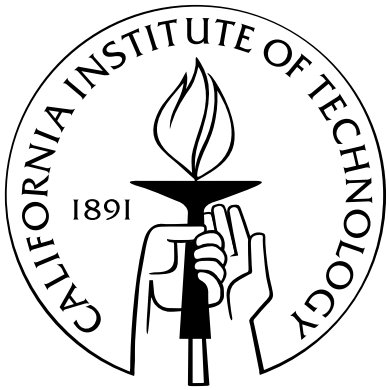

California Institute of Technology

Pasadena, California

2011

(Defended May 25, 2011)

That it will never come again is what makes life so sweet.

- *Emily Dickinson*

This dissertation is dedicated to my family and my intelligent dog, Darongee,

for lending me your happiness, love, and care.

Acknowledgements

My long tenure in the fields of atomic physics and quantum optics since 2003 as undergraduate and graduate student have been enriched by the help of many people. Here I would like to take this opportunity to thank the people who have in no small way made the research in this thesis possible.

First and foremost, I would like to thank my advisor, Prof. H. Jeff Kimble, for all the exciting moments I shared with him in his group. I have profoundly benefited from my association with him over the past 5 years. Jeff's unique taste for finding exciting research problems and generosity towards young scientists have taught me by example what it means to be a good scientist over the years. His enthusiasm for pursuing daunting problems in physics at the highest levels of scientific integrity and rigor has been a constant source of inspiration, excitement, advice, and guidance throughout my study. I deeply thank him for the unprecedented freedom he offered to explore my intellectual curiosity in our experiments, and for fostering my capacity critically as an independent researcher. His advice and encouragement were always important guiding lights towards my personal and professional development. I can only hope that during the past several years I have been able to absorb some of his magical intuition for doing interesting physics.

The strong sense of community within the quantum optics group has been an important part of my time at Caltech, and I would like to express my appreciation to all of the group members. I have worked with a brilliant set of colleagues in lab 2 for atomic ensemble experiments. In the summer of 2006, I was welcomed by Chin-Wen (James) Chou, Hui Deng, Daniel Felinto, Julien Laurat and Hugues de Riedmatten upon my arrival. During this period, James and Julien helped me a great deal to adjust into the lab, and shortly after Daniel and Hugues left the group for their positions. We had a fruitful year in the lab.

After the departure of James, we collaborated with the cQED lab in the spring of 2007. With Hui and Julien, I had the fortune to work with Andreea Boca, David Boozer, Russell Miller, and Tracy Northrup in lab 11. While this experiment has not worked out so well, many inspirations from this collaboration led to our EIT mapping experiment in the summer, which was really fun! Looking back, I realize it was during this period that I had my greatest successes in the lab with my colleagues, not because of the talent of one person but because of the collective efforts among Hui, Julien, and myself. I thank Hui for her patience and for the great colleagueship we shared over the years. I would also like to emphasize the significance of Julien's role in my development. In my first year, he helped me understand every details of the experiments through timeless discussions, and later he worked with me as a gracious colleague. His modest attitude of pursuing

science has made a positive impact on my understanding of colleagueship.

Later, the lab's legacy carried on with a new set of people. In particular, Scott Papp's arrival was instrumental to my work. He not only taught me electronics and techniques but also broadened my narrow views of science and society. The numerous discussions with him during nights, sometimes long, helped me to become a mature scientist. We shared great successes together for the two years.

In the fall of 2009, Akihisa Goban joined our lab. Simply put, he is a hardworking genius and an exceptionally talented colleague! Upon his arrival, Aki and I spent days and nights in the lab. I am very proud of the experiment that resulted from this collaboration. Apart from its significance, the 400-hour long integration time for the data presented in this experiment alone testifies to the synergy of our collective efforts. Aki pursued a number of projects with me in this thesis, and often times I was moved by his aspiring character of diligence and modesty. I thank him for his super hard work with excellence and for sharing all the excitements with me in the lab. In 2010, a talented summer intern, Lucile Veissier, joined our lab for a small project to induce a phase shift on the collective excitations. I thank her for the hard work and patience.

For the most part, theoretical advice from Prof. Steven van Enk at University of Oregon has helped the experiments in the thesis. With Pavel Lougovski, Steven has developed theoretical tools that led to the verification of multipartite entanglement. I thank Steven for the inspiring discussions and numerous collaborations, as described in the thesis.

By the fall of 2010, we started to work on a nanofiber trap project with the microtoroid lab. Ding Ding joined our lab during this time. Ding is a hard-working colleague with a bright future. With Aki, he made tireless contributions to our new fiber trap setup by way of his diligence and talent. I believe that the on-going work with Daniel Alton, Clement Lacroute, and Nate Stern in lab 1 provides new prospects in quantum optics and quantum information science that extend well beyond the free-space experiments described in this thesis. I also acknowledge the contributions by Tobias Thiele on the fiber pulling setup and the various tapered fiber characterization during the summer of 2010. With Aki and Ding, it will be interesting to explore where our work could lead to, during my stay as a postdoctoral scholar.

The quantum optics group is a home for brilliant researchers from whom I have received great advice over the years. I thank Takao Aoki, Darrick Chang, Barak Dayan, Alexey Gorshkov, Kang-Kuen Ni, Jason Petta, Cindy Regal, Elisabeth Wilcut, Dalziel Wilson, and Yi Zhao. Dal's strong commitments to research during adversities have always inspired me to work harder. I thank Aki, Dal, and Daniel for friendships outside the lab. Discussions with visiting Professors Eugene Polzik, Jun Ye, and Peter Zoller during their sabbaticals have always been illuminating. Outside of the group, I acknowledge the indirect contributions by some of our competitors (especially, the members in the groups of Vladan Vuletić and Mikhail Lukin), with whom I enjoyed intense (but friendly) competitions and invaluable discussions.

Lastly but not the least, I would like to thank Prof. Harold Metcalf at Stony Brook University for introducing me to the wonderful world of atomic physics. I learned a number of important 'finger' physics from him, which became important ingredients for my research in this thesis. In Hal's group, I worked on

Rydberg atom optics experiments as an undergraduate for 3 years. Building a complex lab from ground-up was a tremendous experience for my training as a physicist in the most positive way. Hal treated me as an important member of his group, even when I knew nothing. He has continuously supported my career and personal life over the years. I have a deep admiration for him.

I am fortunate to have been surrounded by a wonderful set of people with as much exceptional scientific calibre and grace as one could ever hope for. They have cultivated my growth in embarking on an exciting new journey, and shaped my vision of doing science. From farther distances, the unconditional love from my parents (Mansoo Choi and Youngsook Son), sister (Suzanne Choi), and grandparents (the late Changnam Choi and Myungshim Park) has been a great source of happiness and joy to me during challenging times. No matter how small, my personal treasures of triumphs have all been possible because of my parents' faith and sacrifice in my education and research. I thank them for giving me wholehearted love without return, for believing in me when I didn't, and most importantly for instilling and nurturing a childhood dream of becoming a scientist deep in my heart. It is them to whom I dedicate this thesis.

Abstract

Quantum networks are composed of quantum nodes which coherently interact by way of quantum channels. They offer powerful capabilities for quantum computation, communication, and metrology. A generic requirement for these realizations is the capability to generate and store quantum states among multiple quantum nodes, and to disseminate these resources throughout the network via the quantum channels (chapter 1). In this thesis, I describe a series of experiments whereby single excitations in atomic ensembles are strongly coupled to optical modes and provide efficient means for the coherent control of entangled states between matter and light (chapter 2).

By following the seminal proposal by Duan *et al.*, we have generated measurement-induced entanglement of an excitation between two cold atomic ensembles. Using this system, we investigated the relationship for the global bipartite entanglement and local correlations in its subsystems (chapter 3).

In addition, we achieved functional quantum nodes for entanglement distribution (chapter 4). Two pairs of remote ensembles at two quantum nodes were prepared into entangled states in a heralded and asynchronous fashion by the conditional controls of the entanglement. The quantum states of the ensembles were then distributed into polarization entangled states of photons. We also prepared an analogous quantum state and transferred the nonlocal coherence between two pairs of heralded entangled atomic ensembles, providing a step towards entanglement connection (chapter 5).

Beyond such probabilistic approaches, we demonstrated an experiment where entanglement between two quantum memories is created by the reversible and deterministic mapping of an entangled state of light via dynamic electromagnetically induced transparency (chapter 6). This experiment opens novel prospects of integrating hybrid quantum systems by way of reversible quantum interfaces between light and matter (chapter 10).

Then, we extended our work to multipartite quantum systems (chapters 7–9). We theoretically investigated the characterization of multipartite mode-entangled states by way of quantum uncertainty relations, and introduced theoretical tools to verify the entanglement orders in multipartite systems (chapter 7). In particular, we achieved entanglement for one delocalized photon among multiple optical modes ($N > 2$) (chapter 8).

Finally, we have achieved measurement-induced entanglement of spin waves among four quantum memories (chapter 9). The individual atomic components for the entangled W state of the four ensembles were

then coherently converted into four propagating entangled beams of light via superradiant emissions. We observed the statistical and dynamic transitions for the multipartite entangled spin waves. Experiments described in this thesis thereby represent significant advances of experimental and theoretical capabilities to generate, store, transfer, and characterize entanglement of matter and light over quantum networks (chapter 10).

Contents

List of Figures

List of Tables

Chapter 1

Introduction

1.1 Quantum networks

Quantum networks open a broad frontier of scientific opportunities in quantum information science, including for quantum computation, communication, metrology, and simulation[1]. For example, a quantum network can serve as a 'web' for connecting quantum processors for computation[2,3] and communication[4], as well as a 'simulator' for enabling investigations of quantum critical phenomena arising from interactions among the nodes mediated by the channels[5,6].

Apart from any algorithmic benefit, an important characteristics of a quantum network is shown by comparing the complexity of a problem to describe a quantum network, comprised of N quantum nodes (each with n qubit registers) with fully quantum connectivity, to that of a network of quantum nodes which only share classical channels (see, e.g., refs.[1,7]). The classical information required to represent a density matrix $\hat{\rho}_{\mathrm{QN}}$ of a fully quantum network is $I_{\mathrm{QN}} = 2^D = 4^{N\times n}$, where the dimensionality is $D = 2^{N\times n}$. In contrast, the size of the density matrix $\hat{\rho}_{\mathrm{N}}$ for a network that has only classical connectivity is given by $I_{\mathrm{N}} = N \times 4^n$.

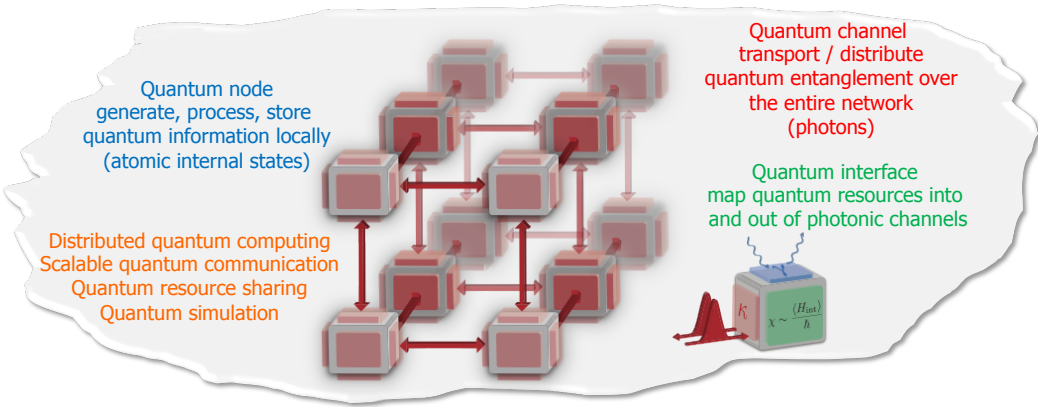

Figure 1.1: **A generic form of a quantum network composed of many quantum nodes and channels[1].** The quantum nodes (box) interact coherently each other by transporting and distributing entanglement over quantum channels (arrows). An important component for these quantum interconnects is a quantum interface for mapping the quantum resources generated from the quantum nodes into and out of the photonic channels.

Therefore, even for moderate parameters $\{N, n\} = \{10, 14\}$ for the fully quantum network, the number of classical variables $I_{\text{QN}} = 4^{140} \sim \mathcal{O}(10^{84})$ to describe $\hat{\rho}_{\text{QN}}$ can greatly exceed the number of hydrogen atoms $\mathcal{O}(10^{80})$ in the observable universe, whereas its classical counterpart $\hat{\rho}_{\text{N}}$ only yields $I_{\text{N}} = 10 \times 4^{14} \sim \mathcal{O}(10^{9})$.

While this complexity also points to the difficulty of controlling and characterizing a large-scale quantum system as $\hat{\rho}_{\text{QN}}$, quantum networks can harness physical processes to benefit from the intricacies introduced by these multipartite quantum states for quantum information processing [1–9], with rudimentary capability of the network enabled by the coherent control of quantum and entangled states of matter and light [1]. Indeed, theoretical inventions of quantum error correction and fault-tolerant quantum computing [10–16], entanglement purification and distillation [17–19], as well as privacy amplification and information reconciliation [20–23] have enabled the promising prospects for experimental implementations of distributed quantum computation [7,24], quantum resource sharing [25,26], scalable quantum communication [4,9], and quantum simulations [5,6] by way of quantum networks.

As illustrated in Fig. 1.1, the physical realization of quantum networks composed of many quantum nodes and channels [1,8,9] requires quantum dynamical systems capable of generating and storing entangled states among multiple quantum memories, and of efficiently transferring stored entanglement into quantum channels [27–33]. Such an interconnect can be achieved by utilizing the strong interactions of single photons and collective excitations in atomic ensembles for the coherent control of entanglement between matter and light [27,30,33], thereby enabling the distribution and teleportation of quantum states across the quantum network [4]. Thus, my thesis will focus on addressing specific challenges to achieve quantum networks: (1) by developing novel laboratory capabilities to generate, store, and control entangled states of matter and light [30,33–35], (2) by implementing various quantum information protocols [36,37], and (3) by devising efficient theoretical tools for multipartite entanglement characterization [33,35,38].

In a broader scope, the research for attaining quantum control over macroscopic quantum coherence and statistics represents an area of fundamental importance beyond of quantum networks, where we study and manipulate quantum states of matter and light with manifestly single quanta one-by-one. Moreover, the experimental realization of strongly correlated quantum systems of atoms and photons expands the frontiers of exquisite quantum control of entangled states with diverse applications from quantum information science, to atomic and condensed matter physics, to precision metrology, and to quantum biology. In relevance to quantum many-body physics [39,40], measurements, and controls [41], I would like to present two questions as important underlying motivations for my research, which I hope to make contact with in the remaining chapters.

1. Can quantum coherence and entanglement exist and be preserved in quantum many-body systems, either spontaneously acquired or externally induced by lasers?

2. How do we measure, manipulate, and utilize quantum entanglement in mesoscopic systems?

1.2 Ensemble-based quantum information processing and Duan-Lukin-Cirac-Zoller protocol

Historically, the investigation of collective interactions between atoms and photons began with the striking prediction[42] by Robert Dicke in 1954 that the radiative decay rate for an assembly of atoms in the excited state can be significantly modified. Under certain circumstances, the spontaneous emission of the excited state can be considerably enhanced by a 'phase-locking' of atomic dipoles with dynamic evolution of the atomic state confined within a class of symmetric collective spin states[43], a cooperative phenomena known as "superradiance" (see ref.[44] for an excellent review of theoretical descriptions of superradiant effects observed in different regimes; see also chapter 2). Since then, collective interactions have been observed in diverse systems, with a recent survey including the studies of dynamic phase transitions[45,46] and collective Lamb shifts[47], leading to the development of quantum interfaces for storing and retrieving quantum information in atomic ensembles[48].

Contemporary with these advances, various theoretical protocols have been developed for the realization of scalable quantum networks with atomic ensembles[49], including the seminal proposal by Luming Duan, Mikhail Lukin, Ignacio Cirac, and Peter Zoller (referred as the *DLCZ* protocol hereafter) in 2001 (ref.[4]). The introduction of the *DLCZ* protocol has led to a development of a remarkable worldwide community with significant achievements in the creation and distribution of entanglement. In this section, I will review recent progresses by other groups towards ensemble-based quantum memory to put the researches described in this thesis into context.

Generally, strong nonlinear interaction is required to generate nontrivial quantum resources for quantum information science. For ensemble-based quantum information processing, three important approaches to

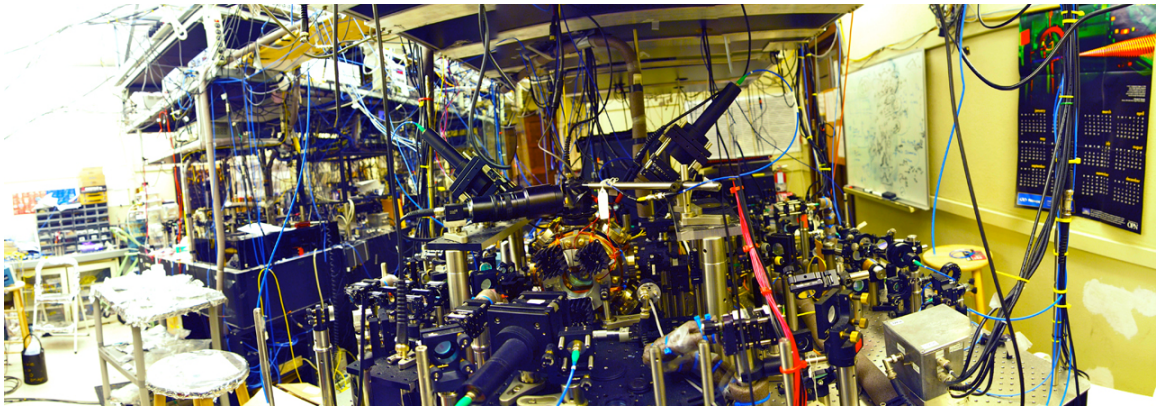

Figure 1.2: **A matter-light quantum interface in action for my experiments[30,33,34,36,37].** Cold ensembles of $\sim 10^{10}$ Cesium atoms are (i) laser cooled and trapped to $10-100$ μK, and (ii) prepared to specific ground states $|F, m_F\rangle$ via hyperfine and Zeeman pumping. In step (iii), we operate the quantum interface where the atomic quantum information (QI) is generated and stored in the ground state coherences for the hyperfine levels $|g\rangle = |F=4\rangle$, $|s\rangle = |F=3\rangle$ of the electronic ground state $6S_{1/2}$. Finally, (iv) we read out the atomic states to photonic states, and (vi) detect the photonic QI for quantum-state characterization.

matter-light interactions $\hat{H}_{\rm int}$ have been developed for continuous and discrete quantum variables[48]. In the setting of continuous variables[48,50], major achievements have been made with quantum nondemolition interactions $\hat{H}_{\rm int}^{(\rm QND)} \sim \chi_{\rm QND}\hat{P}_\gamma\hat{P}_a$ between the transverse spin components for the collection of atoms a and polarizations of light γ based on the off-resonant Faraday rotation of a probe beam[51–58]. While the atomic state in this case is not directly optically accessible, it can also be mapped to an optical field by way of teleportation. Notable advances have been the entanglement of macroscopic spin states for two atomic ensembles[59], quantum teleportation from light to matter[60], multiparticle entanglement for atoms within an ensemble[61,62], and dissipation-induced entanglement via reservoir engineering[63]. In addition, quantum measurements have been actively pursued for quantum-enhanced atom interferometry via spin squeezing (see, e.g., refs.[64–69]). Despite the spectacular advances in this field[48,50], experiments in this thesis investigate the strong interaction of single photons and collective excitations in atomic ensembles in the limit of weak excitations $\xi \ll 1$, where $\simeq |\xi|^2$ is the mean number of collective excitations.

As pioneered by *DLCZ*[4], parametric Raman interactions, $\hat{H}_{\rm int}^{(\rm par)} \sim \chi_p\hat{a}_\gamma\hat{S}_a + h.c.$, based on the weak $\chi^{(3)}$ nonlinearity of the system[70] can be applied for robust implementations of quantum communication protocols, including quantum cryptography and teleportation (chapter 2). In the regime of single excitations ($\xi \ll 1$), the required 'strong' nonlinearity is provided by projective measurements. An important aspect of this approach is that the heralded atomic state can be coherently mapped to single photons in an efficient manner via the collective matter-light interaction $\hat{H}_{\rm int}^{(\rm map)} \sim \chi_m\hat{a}_\gamma\hat{S}_a^\dagger + h.c$ (chapter 2). In particular, parallel chains of heralded entangled states can be converted into polarization entangled photons via entanglement connection (ref.[37], chapter 5) and distribution (ref.[36], chapter 6), with a built-in purification mechanism[4]. For a preamble to the original protocol, I refer to James Chou's thesis[71] and ref.[49]. In chapter 2, I will revisit the interaction Hamiltonians $\hat{H}_{\rm int}^{(\rm par)}$ and $\hat{H}_{\rm int}^{(\rm map)}$, and derive the steady-state solutions for $\hat{H}_{\rm int}^{(\rm par)}$ as well as the equation of motions for $\hat{H}_{\rm int}^{(\rm map)}$ in detail. I refer to Fig. 1.2 for a standard routine of our experiments.

In 2003, initial experiments for the *DLCZ* protocol began with the observations of quantum correlations between photon pairs emitted from an ensemble by our group (ref.[72]; see also James' thesis[71]) and by the group of Mikhail Lukin[73]. Since then, single photons were generated in a heralded fashion by reading the stored, collective excitations to propagating fields[74–80]. Conditional efficiencies 74% in free space[81] and 90% in a cavity[82] were achieved for retrieving a single excitation in the ensemble to a single photon. Off-axial phase-matching configuration for the four-wave mixing process has been pioneered by Steve Harris' group[75] and used extensively in our experiments, whereby we generate spatially separate quantum fields from the classical beams. However, as I will discuss in chapter 2, the collective spin waves generated in this fashion can have considerably shorter coherence length l_c as well as a Doppler life times τ_d than the collinear configuration.

With these capabilities for collective emissions in hand, our group generated heralded entanglement between distant ensembles in 2005 (ref.[27]; see James' thesis[71] for this remarkable piece of work). Although the degree of entanglement was small in the initial experiment[27], more recently we have been able to infer the

concurrence $C = 0.9 \pm 0.3$ for the entanglement associated with density matrix of the two ensembles (ref.[34], chapter 3). Since then, substantial progresses have been made with heralded quantum states (section 3.7), including the synchronization of indistinguishable single-photon sources[78–80] and heralded storage of polarization qubits[83]. Furthermore, Vladan Vuletić's group demonstrated that two ensembles can be entangled via the adiabatic transfer of heralded excitations in a cavity[29].

The *DLCZ* protocol is based upon a quantum repeater architecture involving independent operations on parallel chains of entangled systems, with scalability relying critically upon the conditional control of entanglement. In 2007, we took an important step towards this goal by achieving the minimal functionality required for scalable quantum networks via the asynchronous preparation and control of heralded entanglement (ref.[36], chapter 4). In this experiment[36], we distributed a pair of heralded number-state entangled states and converted them to an effective polarization entangled state, thereby violating Clauser-Horne-Shimony-Holt (*CHSH*) inequality[84] (chapter 4). Using this setup, we also established quantum coherence between ensembles that never interacted in the past by way of entanglement connection (ref.[37], chapter 5). Later, Jian-Wei Pan's group also realized elementary quantum nodes for a Briegel-Dür-Cirac-Zoller (*BDCZ*) quantum repeater[9] in 2008 (ref.[85]).

In parallel with the research on *heralded* entanglement, there has also been considerable interest in the development of *deterministic* quantum interfaces to achieve reversible mapping of quantum states of light to and from atomic ensembles via $\hat{H}_{\rm int}^{(\rm map)}$ (refs.[86,87], chapter 2). Inspired by the early pioneering experiments on ultraslow-light propagation in dense atomic medium in 1999 (refs.[88,89]), storage and retrieval of optical pulses have been demonstrated, for both classical pulses[90,91] and single-photon pulses[92,93] by way of dynamic electromagnetically induced transparency (EIT) (refs.[86,94–96], chapter 2). Similarly, quadrature squeezed states have been stored and retrieved in an ensemble in 2008 (refs.[97,98]). In 2008, we achieved an important milestone for transferring quantum entanglement over quantum networks by demonstrating the *reversible* mapping of photonic entanglement to and from two quantum memories by the EIT process (ref.[30], chapter 6). In this experiment, we prepared an entangled state of light from an "offline" source ensemble, and mapped the photonic entanglement into and out of two atomic ensembles (chapter 6). Our work on reversible quantum interfaces thereby sets the stage towards integrating hybrid quantum systems by way of photonic quantum buses (chapter 10). Recently, this approach has been extended to transfer the initial atom-photon entanglement in a cavity QED system to an entangled state of a single atom and a Bose-Einstein condensate in 2011 (ref.[99]).

Since then, a wide variety of approaches has been proposed for storing and retrieving quantum states of light in inhomogeneously broadened samples, including controlled reversible inhomogeneous broadening (CRIB) (ref.[100]), atomic frequency comb (AFC) (ref.[101]), and gradient echo storage (refs.[102,103]); see also ref.[104] for a comprehensive review. Many of these storage techniques offer unique perspectives for high-bandwidth multimode quantum memories and integrated waveguide coupling, and several groups have reported important progresses towards this goal, such as electric control of photon echos[105], coherent pulse

sequencing in atomic vapor[106] and storage of temporal modes in rare-earth solid-state ensembles[107], albeit with classical states. A vast majority of these experiments, however, do not demonstrate a *genuine* quantum memory in that they use classical states detected by postselection, and rely on the "rephasing" of the collective emissions after a uncontrollable fixed delay. More recently, time-bin entangled states have been partially stored and retrieved after a predetermined delay in 2011 (refs.[108,109]). In these experiments, however, the entangled states were detected in a *post-dicted* fashion without the possibility of mapping the *physical* state of light onto the atomic ensembles[110] (section 3.7). Nevertheless, experiments listed here represent significant advances of multimode quantum memories towards "practical" quantum repeaters[49].

Other experiments not described here are those based upon entanglement as *post-diction*, for which the physical state is not available for subsequent utilization[110] (see section 3.7 for the multiple flavors of entanglement). For example, entanglement between two remote atomic ensembles has been generated in a *post-dicted* fashion[111], and *a posteriori* teleportation has been used to transport the polarization state of light to an atomic memory[112]. In addition, ref.[113] has claimed to have generated a particular kind of a multiphoton mode-entangled state, known as a *NOON* state, and applied for measuring the collective motion of the ensemble with phase super-resolution in a "spin-wave" interferometer, although the entanglement was not verified.

The figure of merits for the collective enhancement of matter-light interaction are high retrieval efficiency[81,82] and long memory times (chapter 2). 2009 was an intense year for the 'ensemble' community to increase the storage time for collective excitations in atomic ensembles leading to a worldwide effort, with the advances ranging from millisecond quantum memories[114,115], to light storage in an atomic Mott insulator[116], and finally to the longest memory time of "1.5 seconds" for storing a coherent state in a Bose-Einstein condensate[117]. However, in most of these experiments, the retrieval efficiencies were still $\eta \lesssim 1\%$. Important experiments preceding these activities have been the demonstration of the EIT storage of coherent states in a crystal with a storage time longer than 1 second (ref.[118]), the collapse and revival of collective excitations in an atomic ensemble[119,120], and the characterization of decoherence for the heralded entanglement stored in two atomic ensembles (ref.[34], chapter 3).

Around the same time, we began to collaborate with Pavel Logouvski and Steven van Enk to develop an *efficient* theoretical protocol for verifying multipartite mode-entangled W states (ref.[38], chapter 7). We proposed to use quantum uncertainty relations[121] as a nonlinear, nonlocal entanglement witness capable of verifying *genuine* W states, and of distinguishing the 'global' N-partite entangled states from any $(N-1)$-partite entangled states as well as their mixtures[38]. By implementing this verification protocol, we generated and characterized the multipartite entanglement for one photon shared among four optical modes in 2009 (ref.[35], chapter 8).

Finally, in 2010, we made a major advance towards multipartite quantum networks by achieving measurement induced entanglement of spin waves among four quantum memories (ref.[33], chapter 9). The individual atomic components for the entangled W state of the four ensembles were coherently mapped to four entan-

gled beams of light, where we observed the statistical and dynamic transitions for the multipartite entangled spin waves (see Fig. 1.2 for the photo of the lab at the time). We also showed that our entanglement verification method is suitable for studying the entanglement order of condensed-matter systems in thermal equilibrium[33]. With regard to quantum measurements, the multipartite entangled state stored in the quantum memories can be applied for sensing an atomic phase shift beyond the limit for any unentangled state[33].

The original *DLCZ* protocol[4] has by now motivated an active field of theoretical study of quantum repeater architectures for optimizing the network scalability in view of actual laboratory capabilities[49,122–125]. Specific attentions have been made to the scaling behavior for multimode quantum repeaters[49], dynamic programming search algorithms[124], and entanglement percolation[6]. Moreover, measurement-based quantum computation has been proposed for scalable quantum computing with atomic ensembles[126]. Stationary dark-state polaritons in a standing-wave EIT medium have been proposed for strong photon-photon nonlinear interactions and quantum gates[127–130]. Single-photon entanglement purification was proposed[131] and partially demonstrated[132], but the higher-order excitations for the purified states have not been characterized[110].

By and large, significant advances of solid-state ensembles (e.g., rare-earth crystals[104]) and the achievement of *collective* strong coupling in diverse systems[133–138] have also contributed indirectly to our research program towards ensemble-based quantum information processing with neutral atoms, as described above. Collective strong coupling has been observed with Bose-Einstein condensate[133,134] and with an ensemble of trapped ions forming a Coulomb crystal[135] in the optical domain, and electron spin ensembles residing in diamonds have been coupled to a superconducting cavity in the microwave domain[136,137]. In addition, temporal modes of microwave photons have been stored and retrieved in an electron spin ensembles using a gradient echo technique[138]. Beyond the free-space experiments in this thesis, such advances are relevant to the outlook of our project (chapter 10), whereby we hope to investigate the strong interaction of heterogeneous quantum systems of atoms, photons, and phonons by way of photonic crystal nanowires[139] and atomic ensembles[a], and to distribute quantum coherence and entanglement over 'lithographically patterned' quantum networks.

1.3 My history in the group, and notable omitted results

Substantial progresses have been made in lab 2 including the heralded entanglement between two remote atomic ensembles[27], as noted above. As a result, upon my arrival in 2006, many parts of the apparatus in lab 2 were built by my predecessors, James Chou, Hugues de Riedmatten, Daniel Felinto, Alex Kuzmich, Julien Laurat, and Sergey Polyakov, since their initial work in 2003.

I acquired significant feedback and "lab lore" from James and Julien during my short overlap with them (2006–2007); see Kevin Birnbaum's thesis[142] for the definition of the term, "lab lores." I would thus like to acknowledge the early works in James' thesis[71], which formed an important basis to my experiments after 2006. Also, my training in atomic physics in Hal Metcalf's group (Stony Brook University) helped

[a] See also refs. [140,141] for new regimes of strong coupling, which may be achieved in the new system.

me to complete many tasks in this thesis in a timely fashion, including the coherent control of populations in Rydberg atomic beams by way of electromagnetically induced transparency (EIT) and stimulated Raman adiabatic passage (STIRAP).

Since 2006, we have made significant changes to the setup from experiment to experiment, and I will not be able to list the specific changes in this thesis. The details are documented throughout my lab notes, as well as those of my colleagues (James Chou, Hui Deng, Akihisa Goban, Julien Laurat, and Scott Papp). But some changes are noted in chapter 9. At the same time, I have tried, as others have in the past, to transfer as many "lab lores" and new techniques as possible to other members in lab 2.

As listed in the previous section, I have been involved in a number of experiments (chapters 3–10 in the thesis) since 2006. However, I regret that there are some results that I must omit in order to focus on experimental and theoretical results under the encompassing theme of quantum networks. I would thus like to take this opportunity to compile notable results not discussed in this thesis, to which my colleagues and I have contributed.

1.3.1 Coherent Rayleigh scattering

In 2007, I theoretically considered the possibility of using elastic Rayleigh scattering to measure the relative phase ϕ (ref.[145]) between two entangled ensembles to directly confirm the presence of the purported 'number-state' entanglement $\frac{1}{\sqrt{2}}\left(|\overline{g}_L\overline{s}_R\rangle + e^{i\phi}|\overline{s}_L\overline{g}_R\rangle\right)$ between the two ensembles in the 'cryptography' experiment (ref.[36], chapter 4). In this experiment[36], ϕ was fluctuating over the time scale of the experiment but was stable over the memory time $\tau \approx 10\ \mu s$. Because of the non-collinear geometry for the paths of the classical writing and reading pulses, and that of the non-classical fields 1 and 2, it was impossible to lock the interferometric paths to stabilize the relative phase ϕ. Nonetheless, I emphasize that the experiment[36]

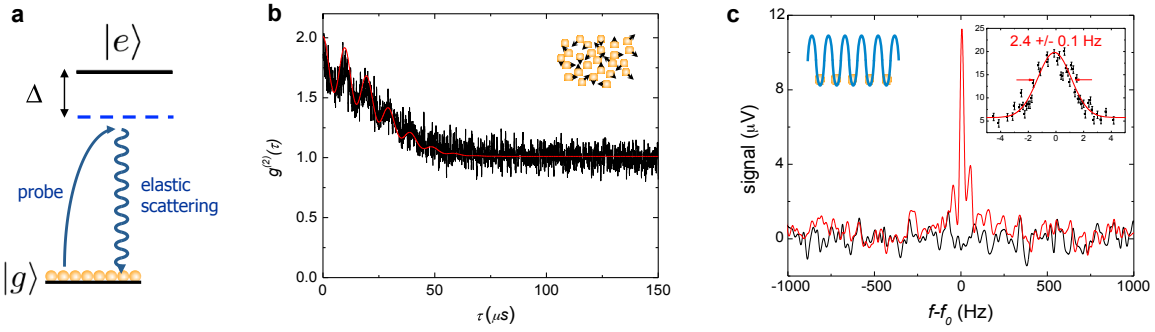

Figure 1.3: **Elastic Rayleigh scattering from atomic ensemble.** **a**, A red-detuned probe laser illuminates a cold sample of Cesium, generating elastically scattered photons[143–145]. **b**, The time-domain measurement of the photon counting statistics $g^{(2)}(\tau)$. The red solid line is a numerically simulated steady-state solution of $g^{(2)}(\tau)$, given the measured Zeeman splittings, the orientation of the magnetic field, and the temperature of the thermal atoms. **c**, Frequency-domain measurement of the linewidth of the scattered photons in the presence (absence) of atoms, as shown by the red (black) curves. The inset shows a high-resolution spectrum of the elastically scattered photons, revealing *Lamb-Dicke* narrowing.

unambiguously verified the entanglement, as we have observed polarization entanglement via the violation of *CHSH* inequality between two quantum nodes, for which we *locally* converted a pair of the purported number-state entanglement into polarization entanglement (ideally with $1/2$ of ebits).

In 2009, Scott and I made a partial measurement to show that the phases among the quadripartite entangled atomic ensembles (chapter 9) can be probed in principle (Fig. 1.3). We applied a red-detuned probe laser (detuning $\Delta = 10$ MHz from the cycling transition between ground state $|F = 4, m_F\rangle$ of $6S_{1/2}$ and excited state $|F = 5, m_F\rangle$ of $6P_{3/2}$) on an atomic sample with saturation parameter $s \ll 1$, such that the scattering process is dominantly elastic[143–145]. The time-domain measurement (Fig. 1.3b) of the photon counting statistics $g^{(2)}(\tau) \simeq 1 + |g_0^{(1)}(\tau)|^2$ (thermal atoms at $T_d \simeq 150$ μK without trapping) and the frequency-domain measurement (Fig. 1.3c) of the linewidth of the scattered photons from the trapped atoms revealed both the motional dephasing of the atoms and potentially the relative phase between the local oscillator and the scattered photons. The presence of residual magnetic field along the $\vec{k}$-vector of the probe beam induced an additional modulation on $g^{(2)}(\tau)$ for the Rayleigh scattered photons (Fig. 1.3b), due to the interferences of distinct (m_F) pathways for the $|F = 4, m_F\rangle \leftrightarrow |F = 5, m_F\rangle$ transition. The motional states of the atoms were simultaneously cooled and confined by the polarization gradient mechanism in Fig. 1.3c, thereby suppressing the motional dephasing rate down to 2.4 ± 0.1 Hz (limited by the mechanical instabilities in the measurement process). This allowed us to perform a recoil-free spectroscopy via elastic Rayleigh scattering in Fig. 1.3c (thanks to the *Lamb-Dicke* narrowing for the trapped atoms[146]).

1.3.2 Motional dephasing of spin waves

I analyzed theoretically the motional dephasing of spin waves given our phase-matching configuration, after observing an unexpected Gaussian decay of the retrieval efficiency in 2007 (see the result of ref.[34], chapter 3). Formerly, we have considered the motional dephasing only for atoms leaving the excitation region[147]. However, it turns out that the much smaller 'coherence length' for the 'timed' Dicke states[148] depends critically on the phase-matching configuration for the coherent radiation to take place, given the spatial phases encoded on the atoms (chapter 2). Independently, such a possibility was considered in the experiments by Vladan Vuletić's group[82], where they observed two time-scales for the memory time associated with the forward (long-lived) and backward (short-lived) propagating spin waves. Unfortunately, we did not pursue this idea in our experiments to improve the storage time beyond 1 ms (chapter 2).

Later, the groups of Alex Kuzmich and Jian-Wei Pan achieved millisecond quantum memories in 2008 by confining the spatial motion of the atoms[115] and by increasing the coherence length of the spin waves[114], respectively, which confirmed the validity of this idea. In our lab, the Rayleigh scattering measurements in 2009 agreed with the prediction of motional dephasing, whereby we cooled the motional state of the atoms in a near-resonant lattice formed in the process of polarization-gradient cooling[144], and inferred a motional dephasing rate $R_d = 2.4 \pm 0.1$ Hz (Fig. 1.3). In addition, we have reduced the net momentum transfer $\delta\vec{k}$ (i.e., increasing the coherence length) of the spin waves to achieve coherence times $\tau_m \simeq 60$ μs, limited at

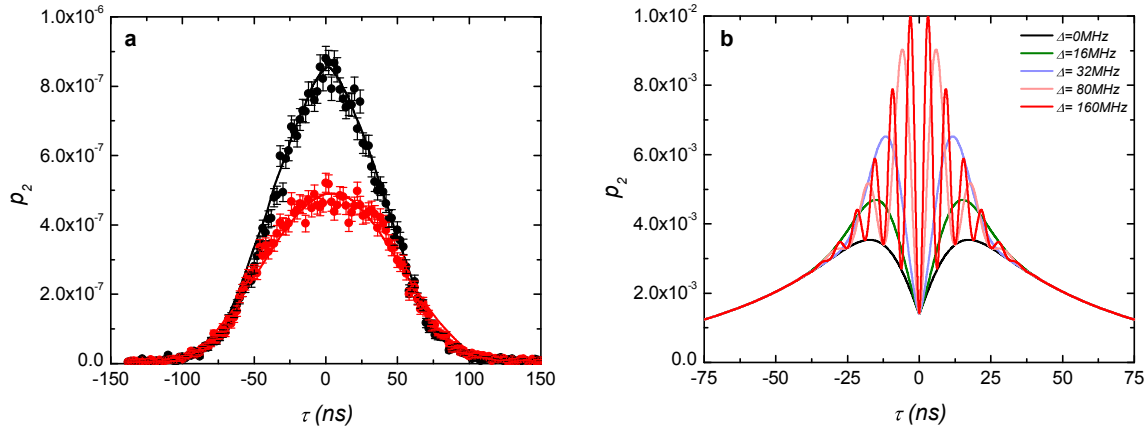

Figure 1.4: **Towards quantum interference between indistinguishable single photons emitted from an atomic ensemble and a single atom in a cavity. a**, Time-resolved Hong-Ou-Mandel (HOM) interference [149] between two coherent states. As a control experiment, we interfere two balanced coherent states emanated from each lab with orthogonal (black) and parallel (red) polarizations, where the temporal profiles of the pulses are matched close to the emission patterns of the single-photon sources. We achieve HOM visibility $V_{\mathrm{HOM}}(\tau = 0) = 0.52 \pm 0.08$ at delay $\tau = 0$ ns, similar to our expectation $V_{\mathrm{HOM}}^{\mathrm{theory}} = 0.5$ for balanced coherent states. The theoretical model (line) is based on the numerical procedure described in ref. [150], using the measured spatio-temporal modes for each beam. **b**, Simulation of the quantum interference between two indistinguishable single-photons with the ensemble cross-correlation function set at $g_{12} = 50$. We theoretically calculate the time-resolved HOM interference for various detuning Δ between the two photons, given the temporal profiles of the two transform-limited single-photon sources.

the time by the inhomogeneous Zeeman broadening in late 2007 (chapter 2, see Fig. 2.8). While these may be considered as missed opportunities, I believe that we followed the 'right' footsteps (chapters 7–9) in order to pursue more interesting ideas for my doctoral thesis.

1.3.3 Indistinguishability between heterogeneous single-photon sources

In mid-2007, we began to collaborate with the cavity QED lab (Andreea Boca, Dave Boozer, Russell Miller and Tracy Northrup in lab 11) to study the time-resolved Hong-Ou-Mandel (HOM) interference [149] between two indistinguishable single photons emitted from an ensemble and a single atom in a cavity. While we have not been able to succeed in this experiment with sufficiently large suppression for the two-fold coincidence between the two output ports of the interferometer, there were discussions regarding the non-classicality of HOM interference. During this time, I also analyzed experimentally and theoretically the temporal profile of the HOM interference for two photons emanating from each lab (see, e.g., Fig. 1.4).

1.3.4 Inducing phase shifts between collective excitations stored in atomic ensembles for quantum-enhanced phase estimation

In early 2010, Aki, Lucile, and I explored the possibility of randomly inducing a π phase shift on one of four atomic ensembles, following Steven's idea to employ a quantum-enhanced parameter estimation protocol

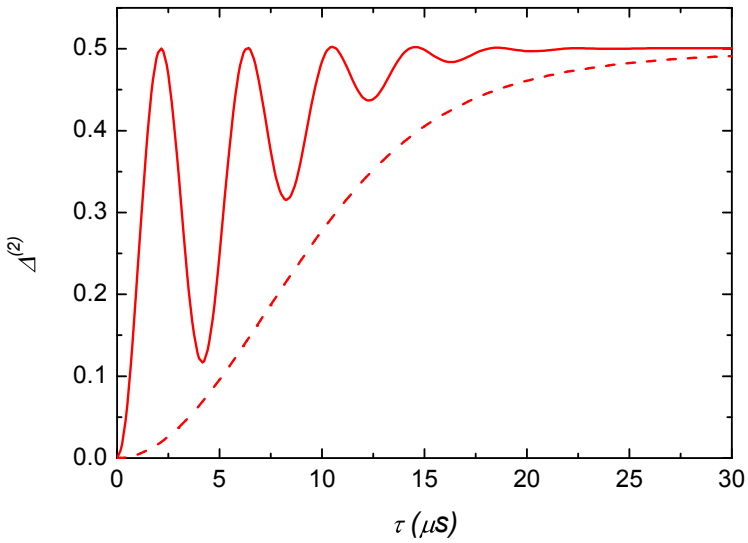

Figure 1.5: **A phase shift in the collective excitation due to an off-resonant ac-Stark shift beam.** Theoretically simulated variance $\Delta^{(2)}$ for two ensembles as a function of storage time τ, including inhomogeneous broadening from the ac-Stark shift beam. A dashed line shows the result of $\Delta^{(2)}$ without a light- shift beam, whereby $\Delta^{(2)}$ increases due to motional dephasing. We define $\Delta^{(2)} = 1 - p_{10}^2 - p_{01}^2$, where p_{10} and p_{01} are the normalized output probabilities after interfering two entangled fields (chapters 8–9).

(partially discussed in ref.[33] and chapter 9). The idea was to induce a phase shift on the ground state coherence $|F = 3\rangle - |F = 4\rangle$ by switching on an off-resonant beam. This phase-shift beam would interact with the collective excitations $|\overline{s}\rangle_k$ in a direction not phase-matched to $|\overline{s}\rangle_k$, thereby avoiding any possible collective enhancement of accidentally erasing the spin waves. In the process of this study, Lucile worked with Aki to intensity stabilize the ac-Stark shift beam I_{ac} and to lock an interference filter laser[151] to a fiber Fabry-Perot reference cavity. Aki developed a simple model for simulating the phase shifts and scattering rate for a given power I_{ac}, as shown by Fig. 1.5. However, according to our estimates, the required retrieval efficiency and the quantum efficiency to observe any quantum enhanced sensitivity (overall efficiencies of $\simeq 75\%$ for unambiguous state-discrimination protocol and $\simeq 93\%$ for minimum error discrimination protocol) proved difficult (if not impossible) with our current experimental capability.

1.3.5 Technical side-projects

1.3.5.1 Development of double-sided AR-coated UHV glass cell

In the early days, Julien and I had worked with Ron Bihler, then at Technical Glass, Inc., to prototype a ultra-high-vacuum (UHV) glass cell with double-sided anti-reflection (AR) coating on the windows. Although I will not discuss this side-project in the thesis[b], the new "frit-fusing" technique, which Ron developed in

[b]Initially, Julien and I worked with Ron Bihler (Technical Glass, Inc., now at Precision Glassblowing, Inc.) to use vacuum compatible glass epoxies (e.g., Epotek 353ND) and Vacseal to seal AR-coated cells, but it proved to be very fragile during bakes in 2006. Later, I worked with Kazuyuki Tsukamoto (Japan Cell) and Ron in 2007 to create a robust AR-coated UHV Pyrex cell by optically contacting polished glasses assisted with local heating of standard glass frits. Ron later extended this approach to develop his low-temperature frit-fusing method.

2007, combines the traditional optical contacting method with special low-temperature frits, and allows for fusion-bonding optical quality fused silica/quartz windows without damaging the AR coating. While I have considered using this cell for the next generation vacuum chamber at the time, unfortunately we have not pursued this project further because of some fear of developing fractures in the frits over time. However, I would like to note that several groups in JILA, Paris, and Stanford have by now used these cells in their BEC experiments successfully, where they have maintained pressures under 10^{-10} Torr over the last couple of years. It may be interesting to revisit this idea in the future.

1.3.5.2 Filtering quantum fields at the single-photon level from the strong classical beams

In 2008, Hui and I characterized a photo-refractive fiber Bragg grating from AOS, which Russ and Tracy have investigated before. Despite the narrow bandwidth ($\nu = 500$ MHz), the transmission was not superior to our existing setup using the Cs filter cells with paraffin coating (attached with AR-coated windows). Scott has also looked into a custom fiber cavity (Micron Optics), where the transmission was inferior to the fiber Bragg grating. I have looked into custom fiber wavelength division multiplexers (WDM) and circulators from Canadian Instruments and Research Limited (CIRL) and Oz Optics at 852 nm, which was later found to be unfavorable due to transmission loss and Brillioun scattering noise from the locking lasers in a test at CIRL. Later, Daniel in lab 1 carried on with studying the WDMs for the fiber trap in 2010.

In 2009, Aki and I characterized a custom AR-coated frit-fused Cs vapor cell with paraffin and buffer gas (Technical Glass, Inc., now part of Precision Glassblowing of Colorado) hoping for a better optical quality with the help of double-sided AR coating (section 1.3.5.1). However, the thermally redistributed paraffin contaminated the polished windows and subsequently limited the transmission as well as the wavefront distortion.

A recent reincarnation of this project has been made with my work in late 2010 with Dr. Vadim Smirnov and Dr. Igor Ciapurin at OptiGrate to produce a custom holographic grating (VBG) (Fig. 1.6a) from a photo-thermo-refractive (PTR) glass that provides an unprecedented filtering capability for the quantum fields to avoid contamination from the classical trapping beams for the fiber trap by ~ 180 dB extinction ratio and $> 95\%$ diffraction efficiency (chapter 10). Our test on the VBGs agrees well to the simulation based on coupled mode theory[152] (Fig. 1.6b). Formerly, such an attempt has been made successfully in Allan Migdall's group at NIST.

1.3.5.3 Other projects

There have been other side-projects contributing to the group in general, which I will not discuss here in detail, as Scott's work on generating pulse trains and logic gates with field programmable gating arrays (FPGA) (National Instruments) for atomic ensemble experiments[c]. While Scott and I determined that the FPGA's timing noise was insufficient for our experiments (chapters 8–9), lab 1 later used this FPGA for their

[c]Formerly, James Chou tested slower Spartan FPGAs from Xilinx.

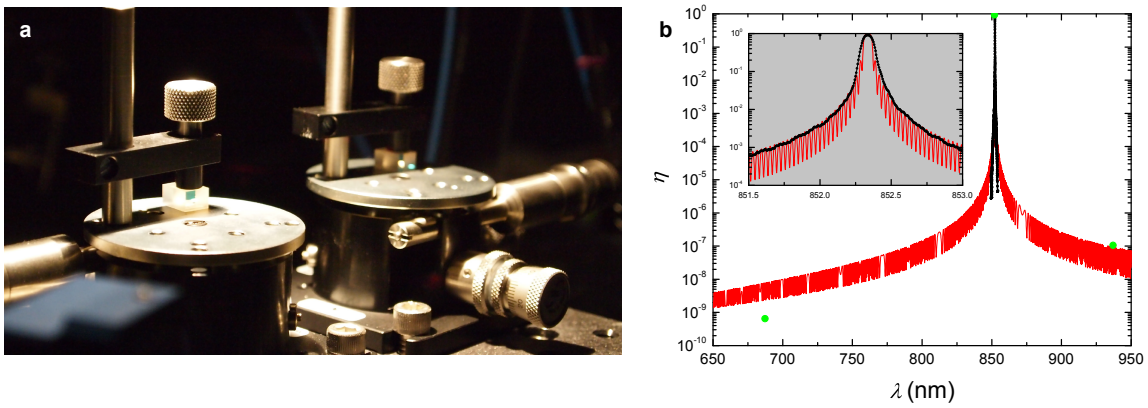

Figure 1.6: **A custom made high-performance PTR-based volume Bragg grating.** **a**, Volume Bragg grating (OptiGrate, Inc.) mounted on a high-precision 3-axis tilt-roll mount ($\sim \mu$rad sensitivity). **b**, Spectral dependence for a single volume Bragg grating. The measured extinction ratios *ER* (green circle) for the red-detuned and blue-detuned trapping beams at $\lambda = 687$ nm and 935 nm are 70 and 92 dB, respectively. The black circles are the measured diffraction efficiency around resonance. The diffraction efficiency on resonance ($\lambda_0 = 852.35$ nm) is $\eta_{\rm DE} = 93.5 \pm 0.3\%$, limited by the broadband AR coating. The red curve is a simulation based on coupled mode theory [152]. The spectral bandwidth (FWHM) is designed to be $\delta\nu = 30$ GHz and the intrinsic diffraction efficiency is $\eta_{\rm DE}^{\rm (int)} = 99.9\%$, according to my calculations for a Gaussian beam of $w_0 \simeq 1$ mm.

experiment [153]. In chapter 9, we implemented an alternative solution by way of a quantum composer and digital logic gates.

Aki and I also updated the diode laser's circuitries as well as other electronics[d]. Scott and I designed various electronic servos for locking interferometers and standard Fabry-Perot cavities, as well as for intensity stabilizations, and various logic circuits for pulse triggers, controls, and synchronizations. In appendix A, I list a few examples of the electronic circuit designs.

I characterized a variety of methods to image patches of atoms in a single collective excitation via microlens arrays ($w_0 \simeq 2$ μm with 80% filling factor) (SUSS MicroOptics and Jenoptik) and lensed fiber arrays ($w_0 \simeq 600$ nm with 5% filling factor) (Seikoh-Giken). Scott characterized ball lenses (Laseoptics) and tapered lens fibers (Nanonics) for imaging single atoms[e] ($w_0 \simeq 400$ nm). More detail on these and other projects can be found in our lab notes and written notes, and in the "lab 2 disc," which compiles all the electronic files for the printed circuit boards (PCB) in lab 2 since 2006.

1.4 List of recent advances

To summarize the advances made in this thesis, I hereby list major achievements that my colleagues and I have made over the last few years:

[d] See some examples in the 'blue book' of the electronics room and in the lab 2 disc (e.g., VCO designs, phase-sensitive detectors, high-bandwidth HV amplifiers, and piezo controllers).

[e] Later, the tapered lens fiber from Nanonics was used in lab 11a for trapping single atoms. Daniel Chao, Scott Kelber, Scott Papp, and Cindy Regal further characterized the fiber in detail.

1. Characterization of the dissipative process for heralded entanglement stored in atomic ensembles (chapter 3).

2. Realization of functional quantum nodes for entanglement distribution over a scalable quantum network (chapter 4).

3. Reversible mapping of photonic entanglement into and out of a quantum memory (chapter 6).

4. Characterization of entanglement for one photon shared among four optical modes via quantum uncertainty relations (chapter 8).

5. Coherent control of generation, storage, and transfer of multipartite entangled spin-waves to photonic multipartite entangled states (chapter 9).

In the remaining chapters, I will describe specific experimental and theoretical results of our work to substantiate the advances listed here, as well as others.

Chapter 2

Atom-light interaction

2.1 Physical system

In a classic paper in 1954, R. H. Dicke calculated the rate at which radiation is emitted spontaneously by a collection of two-level atoms[42]. By considering the entire collection of N_A atoms as a single quantum system, he found that under certain conditions the atoms in the excited state can cooperatively decay into the ground state by emitting light into a single mode at a rate $1/\tau_c \propto N_A\Gamma_0$ much faster than their incoherent emission rate $\Gamma_0 = 1/\tau_0$. The emission intensity I_{coh} is thereby collectively enhanced with $I_{\text{coh}} \propto N_A\hbar\omega_0/\tau_c \propto N_A^2$, relative to the incoherent emission intensity $I_{\text{inc}} \propto N_A\hbar\omega_0/\tau_0 \propto N_A$. Indeed, the initial investigations of non-trivial dynamics for the collective spontaneous emissions began with the studies of 'superradiance' for atoms localized in a sub-wavelength region ($|r| < \lambda_0$)[42,44].

In a subsequent paper[154], Dicke predicted that radiation into a particular mode could be enhanced (superradiance) or suppressed (subradiance) for a spatially extended sample $|r| \gg \lambda_0$, depending upon the relative spatial phases of the atoms[44,155]. In this case, superradiance is manifested by a quantum analogue of Bragg reflection of light on an atomic phase grating. Unlike the case for sub-wavelength samples $|r| < \lambda_0$, where the initial spontaneous emission of an inverted atomic system leads to a phase coherence between the atomic dipoles due to the intrinsic indistinguishability in the emission process, the superradiant emission of an extended sample is also associated with the classical constructive interference of the wavelets produced by periodically located scattering sites in the "forward" direction set by the sample geometry. Such collective spontaneous emissions over extended samples have been observed in a wide variety of physical systems, including the observations of superradiance in molecular rotational and Rydberg transitions[156,157] as well as in optical transitions[158–160]. More recently, superradiant Rayleigh emission has been observed in light scattering experiments with Bose Einstein condensates[161].

In the quest to distribute quantum coherence and entanglement over quantum networks[1,162], there has been significant interest in the Raman interaction of light with atomic ensembles consisting of a large collection of identical atoms at the single-photon level[4,48] (chapters 3–10). In this chapter, I begin with an atom-light interaction Hamiltonian in Dicke's approximation leading to a classic type of collective spontaneous

fluorescence (for $|r| < \lambda_0$) and introduce basic notations used throughout this thesis (section 2.2). Then, I discuss the steady-state solutions for spontaneous Raman interaction which creates non-classical atom-photon correlations (section 2.3), and demonstrate that the parametric interaction can be used as quantum resources (section 2.4). I also describe the equation of motions for the collective matter-light interaction via the adiabatic passage of dark-state polaritons (section 2.5). Finally, I discuss two dominant decoherence mechanisms, which result in spin-wave dissipations and finite memory time (section 2.6).

2.2 Superradiance for a collection of two-level atoms

We consider an ensemble of N_A two-level atoms at positions $\vec{r}_i$ with $i \in \{1, \cdots, N_A\}$. The sample is comprised of ground and excited states ($|g\rangle, |e\rangle$), separated by an energy of $\hbar\omega_0$. Here, we introduce the raising and lowering single-atom operators in terms of Pauli spin operators $\hat{\sigma}_i^+$ ($\hat{\sigma}_i^-$) $= |e\rangle_i\langle g|$ ($|g\rangle_i\langle e|$), and the inversion operator as $\hat{\sigma}_{z,i} = \frac{1}{2}(|e\rangle_i\langle e| - |g\rangle_i\langle g|)$. The electric dipole operator is then given by $\hat{\mathcal{D}}_i = (\hat{\sigma}_i^+ + \hat{\sigma}_i^-)d_0\vec{\epsilon}_{\rm a}$, where d_0 is the matrix element for the transition $|g\rangle \leftrightarrow |e\rangle$ and $\vec{\epsilon}_{\rm a}$ is the polarization vector for the atomic transition. We introduce the positive and negative frequency components of the electric fields

$$\vec{E}^+(\vec{r}) = \sum_{\vec{k},\epsilon} \mathcal{E}_{\vec{k},\epsilon}\hat{a}_{\vec{k},\epsilon}e^{i\vec{k}\cdot\vec{r}}\vec{\epsilon}_\gamma \tag{2.1}$$

$$\vec{E}^-(\vec{r}) = \sum_{\vec{k},\epsilon} \mathcal{E}^*_{\vec{k},\epsilon}\hat{a}^\dagger_{\vec{k},\epsilon}e^{-i\vec{k}\cdot\vec{r}}\vec{\epsilon}^*_\gamma, \tag{2.2}$$

where $\mathcal{E}_{\vec{k},\epsilon}(\vec{r})$ is the slowly-varying amplitude and $\vec{\epsilon}_\gamma$ is the optical polarization vector, for which we assumed a plane-wave expansion with $\mathcal{E}_{\vec{k},\epsilon}(\vec{r}) = -i\sqrt{\frac{\hbar ck}{2\epsilon_0\mathcal{V}}}$.

We can then write the atom-light Hamiltonian for an ensemble of N_A two-level atoms as

$$\hat{H}_{\rm ensemble} = \sum_i^{N_A} \hbar\omega_0\hat{\sigma}_{z,i} + \sum_{\vec{k}} \hbar\omega_{\vec{k}}\hat{a}^\dagger_{\vec{k}}\hat{a}_{\vec{k}} - \sum_i^{N_A}\left(\vec{E}^+(\vec{r}) + \vec{E}^-(\vec{r})\right)\cdot\hat{\mathcal{D}}_i, \tag{2.3}$$

where $\{\hat{a}_{\vec{k}}, \hat{a}^\dagger_{\vec{k}}\}$ are the mode operators for wave-vector $\vec{k}$ [a].

2.2.1 Dicke Hamiltonian

Superradiance is a transient coherent process[b] involving a collective mode of all the N_A atoms in the sample. In the collective mode, correlation and order between the dipole moments arise through spontaneous emissions in an inverted system (initial state with $|\Psi(t=0)\rangle = |e\cdots e\rangle$), due to the intrinsic indistinguishability in the emission processes of the individual atoms. After a delay t_0, the initial spontaneously emitted photons build up the coherences among the atoms, leading to a superradiant pulse. From Eq. 2.3, we write the multi-mode theory of the Dicke Hamiltonian ($|r| < \lambda_0$) (in the electric dipole and rotating wave approximations) and treat the atomic states (labeled a) as a system and electromagnetic modes (labeled γ) as a Markovian bath. The Dicke Hamiltonian is given by

$$\hat{H}_{\rm Dicke} = \underbrace{\hbar\omega_0\hat{S}_z}_{\hat{H}_{\rm a}} + \underbrace{\sum_{\vec{k}} \hbar\omega_{\vec{k}}\hat{a}^\dagger_{\vec{k}}\hat{a}_{\vec{k}}}_{\hat{H}_\gamma} + \underbrace{\sum_{\vec{k}}\left(\hbar g_{\vec{k}}\hat{S}_0^+\hat{a}_{\vec{k}} + h.c.\right)}_{\hat{H}_{\rm a\gamma}}, \tag{2.4}$$

[a] We implicitly include the polarization ϵ by absorbing the notation $(\vec{k},\epsilon) \to \vec{k}$.

[b] Other notable examples of transient cooperative effects include optical free induction decay and photon echo.

where $h.c.$ is a hermitian conjugate of the term $\hbar g_{\vec{k}} \hat{S}_0^+ \hat{a}_{\vec{k}}$, $\hbar g_{\vec{k}} = i\sqrt{\frac{\hbar c k d_0^2}{2\epsilon_0 \mathcal{V}}} \vec{\epsilon}_\gamma \cdot \vec{\epsilon}_\mathrm{a}$ is the single-atom single-photon coupling constant, $\vec{\epsilon}_{\gamma,\mathrm{a}}$ are the polarization vectors of the photon and the atomic dipole, and $\mathcal{V}$ is the coherence volume. Here, we used collective lowering and raising operators

$$\hat{S}_{\vec{k}}^- = \sum_i e^{i\vec{k}\cdot\vec{r}_i} \hat{\sigma}_i^- \simeq \hat{S}_0^- = \sum_i \hat{\sigma}_i^- \tag{2.5}$$

$$\hat{S}_{\vec{k}}^+ = \sum_i e^{-i\vec{k}\cdot\vec{r}_i} \hat{\sigma}_i^+ \simeq \hat{S}_0^+ = \sum_i \hat{\sigma}_i^+, \tag{2.6}$$

and the collective inversion operator

$$\hat{S}_z \simeq \sum_i \hat{\sigma}_i^z. \tag{2.7}$$

In addition, we define the total angular momentum operator (also known as the length of the Bloch vector $\vec{\hat{S}}_k$) as

$$\hat{S}^2 = \frac{1}{2}(\hat{S}_0^+ \hat{S}_0^- + \hat{S}_0^- \hat{S}_0^+) + \hat{S}_z. \tag{2.8}$$

In writing Eqs. 2.4–2.6, we assumed the sub-wavelength condition $e^{i\vec{k}\cdot\vec{r}_i} \simeq e^{i\vec{k}\cdot\vec{r}_0}$ for $^\forall i$ ($\hat{S}_{\vec{k}} \simeq \sum_i \hat{\sigma}_i^-$), leading to the introduction of collective symmetric states $|S, m\rangle$ of $\hat{S}_z$ and $\hat{S}_{\vec{k}}$[c].

2.2.2 Collective spin states

Collective spin states $|S, m\rangle$ for the maximum angular momentum $S = N/2$ are given by (ref.[43])

$$|S, m\rangle = \sqrt{\frac{(S+m)!}{N!(S-m)!}} (\hat{S}_0^-)^{S-m} |e \cdots e\rangle, \tag{2.9}$$

with $-S \leq m \leq S$. The collective state $|N_A/2, m\rangle$ in Eq. 2.9 represents a fully symmetric state whereby $(N_A/2 + m)$ atoms are in the excited state $|e\rangle$ and $(N_A/2 - m)$ atoms are in the ground state $|g\rangle$. The collective spin states $|S, m\rangle$ are simultaneous eigenstates of Eqs. 2.7–2.8 with the following relations

$$\hat{S}_z |S, m\rangle = m|S, m\rangle \tag{2.10}$$

$$\hat{S}^2 |S, m\rangle = S(S+1)|S, m\rangle. \tag{2.11}$$

Similarly, the collective raising and lowering operators $\hat{S}_0^\pm$ acting on $|S, m\rangle$ are

$$\hat{S}_0^\pm |S, m\rangle = \sqrt{(S \mp m)(S \pm m + 1)} |S, m \pm 1\rangle. \tag{2.12}$$

[c]For $|r| < \lambda_0$ in the optical regime, one cannot neglect the effect of van der Waals force $\sim 1/r_{ij}^3$. I refer to ref.[44] for further discussions of non-ideal superradiance in the presence of dipole-dipole coupling between the atoms.

The collective spin operators follow the commutator relations

$$\left[\hat{S}_0^+, \hat{S}_0^-\right] = 2\hat{S}_z \tag{2.13}$$

$$\left[\hat{S}_z, \hat{S}_0^\pm\right] = \pm\hat{S}_0^\pm. \tag{2.14}$$

We will use the language of collective spin algebra in the context of quantum many-body theory in chapter 9 to study the thermal behavior of entanglement in quantum spin models.

Since the Dicke Hamiltonian $\hat{H}_{\text{Dicke}}$ in Eq. 2.4 commutes with the operator $\hat{S}^2$, $\langle\hat{S}^2\rangle$ is a constant of motion. On the other hand, $[\hat{S}_z, \hat{H}_{\text{Dicke}}] \neq 0$. Thus, as we will discuss in the next section, we can expect that the inverted atomic system ($|\Psi(t=0)\rangle = |e\cdots e\rangle$) undergoes a series of cascade emissions with the atomic state confined in a ladder formed by $(2S+1)$ equidistant energy levels $E_m = m\hbar\omega_0$ of the symmetric collective states $|S, m\rangle$ shown in Fig. 2.1a, analogous to the case of spontaneous emission of a spin with angular momentum S.

2.2.3 Superradiant emission for an atomic ensemble in a sub-wavelength volume

Since the system-reservoir Hamiltonian is $\hat{H}_{\text{a}\gamma} = \sum_{\vec{k}}(\hbar g_{\vec{k}}\hat{S}_0^+\hat{a}_{\vec{k}}e^{i(\omega_0-\omega_k)t} + h.c.)$ in the interaction picture (Eq. 2.4), we can write the real part[d] of the master equation (in the Born-Markov approximation[e]) with $\frac{d}{dt}\hat{\rho}_{\text{a}}(t)|_{\text{real}} = -\frac{1}{\hbar^2}\text{Tr}_\gamma\left(\int_0^t dt'[\hat{H}_{\text{a}\gamma}(t), [\hat{H}_{\text{a}\gamma}(t'), \hat{\rho}_{\text{a}}(t)\otimes\hat{\rho}_\gamma(0)]]\right)$ following the standard procedures[164–166] as

$$\begin{aligned}\frac{d}{dt}\hat{\rho}_{\text{a}}(t)|_{\text{real}} &= -\frac{\Gamma_0}{2}\overline{n}_\gamma(\hat{S}_0^-\hat{S}_0^+\hat{\rho}_{\text{a}} - 2\hat{S}_0^+\hat{\rho}_{\text{a}}\hat{S}_0^- + \hat{\rho}_{\text{a}}\hat{S}_0^-\hat{S}_0^+) \\ &\quad -\frac{\Gamma_0}{2}(\overline{n}_\gamma+1)(\hat{S}_0^+\hat{S}_0^-\hat{\rho}_{\text{a}} - 2\hat{S}_0^-\hat{\rho}_{\text{a}}\hat{S}_0^+ + \hat{\rho}_{\text{a}}\hat{S}_0^+\hat{S}_0^-),\end{aligned} \tag{2.16}$$

where $\Gamma_0 = k^3 d_0^2/(3\pi\epsilon_0\hbar)$ is the single-atom spontaneous emission rate in the Wigner-Weisskopf theory of spontaneous decay.

To describe superradiance in the optical domain, we may approximate the reservoir modes γ as vacuum states with zero mean thermal occupation ($\overline{n}_\gamma = 0$). Then, the surviving term in this master equation (2[nd] term) describes a symmetric collective damping process for the system, cascading from the initial totally

[d]Note that the dispersive imaginary part of the master equation gives rise to collective Lamb shift and van der Waals interaction[44]. Namely, we find

$$\frac{d}{dt}\hat{\rho}_{\text{a}}(t)|_{\text{imaginary}} = -\frac{id_0^2}{4\pi\epsilon_0}\left[\sum_{i>j}\frac{1}{r_{ij}^3}\left[1-\frac{3(\vec{\epsilon}_{\text{a}}\cdot\vec{r}_{ij})^2}{r_{ij}^2}\right]\hat{\sigma}_i^+\hat{\sigma}_j^+, \hat{\rho}_{\text{a}}\right]. \tag{2.15}$$

The superradiance for Eq. 2.16 occurs because of the indistinguishability in the emission pathways among the atoms. The dispersive van der Waals interaction (Eq. 2.15) has a characteristic dipole-dipole coupling $g_{vdW} \simeq \frac{|d_0|^2}{4\pi\epsilon_0 r_{ij}^3}$, where the relative strength to Γ_0 is $\frac{g_{vdW}}{\Gamma_0} \simeq \frac{1}{10\pi}\left(\frac{\lambda_0}{r_{ij}}\right)^3$. For $|r| \ll \lambda_0$, the frequency shifts of this dipole-dipole interaction may break the symmetric behavior of superradiance as discussed here. The full analysis including van der Waals dephasing is out of scope for the current discussion, and I refer to refs.[44,163] for a detailed analysis.

[e]For sufficiently large N_A, the Markovian approximation $\hat{\rho}_\gamma(t') \simeq \hat{\rho}_\gamma(0) = \prod_{\vec{k}}|0\rangle_{\vec{k}}\langle 0|$ may break down, leading to oscillatory superradiant emissions[164,165].

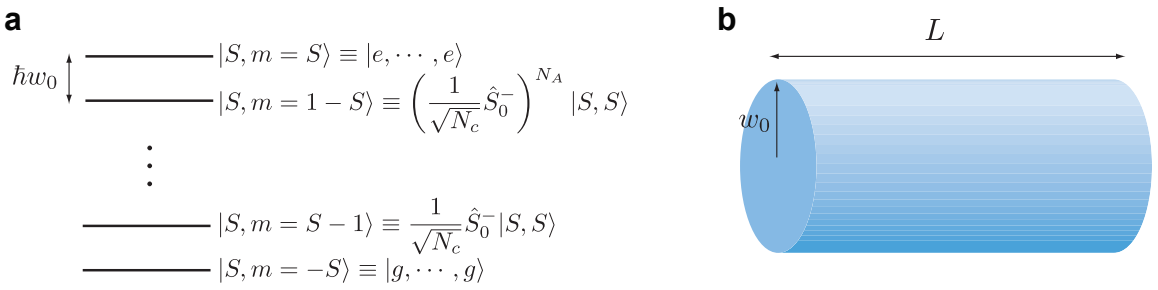

Figure 2.1: **Superradiant states and atomic Fresnel number.** **a**, Energy levels for the collective spin states. A ladder of symmetric collective spin states of maximal angular momentum $S = N_A/2$ is shown for $m \in \{-S, -S+1, \cdots, S-1, S\}$. N_c is the normalization constant. **b**, Pencil-shaped atomic ensemble. The geometric angle is given by $\theta_g = \sqrt{\pi w_0^2/L}$, whereas the diffraction angle is $\theta_d = \lambda_0/\sqrt{\pi w_0^2}$.

inverted state $|\Psi(t = 0)\rangle = |S, S\rangle$ ($|e \cdots e\rangle$) to lower symmetric collective states $|S, m\rangle$ (progressively decaying from $m = N_A/2$ to $m = -N_A/2$) in the subspace of $S = N_A/2$ (Fig. 2.1a).

Indeed, in the quantum jump picture, we can write the short-time (δt) evolution of the atomic state $\hat{\rho}_{\rm a}(t)$ as (Eq. 2.16)

$$\hat{\rho}_{\rm a}(t+\delta t) \simeq \underbrace{\left(1 - \frac{\Gamma_0 \delta t}{2}\hat{S}_0^+\hat{S}_0^-\right)\hat{\rho}_{\rm a}(t)\left(1 - \frac{\Gamma_0 \delta t}{2}\hat{S}_0^+\hat{S}_0^-\right)}_{\text{“no” photon loss}} + \underbrace{\Gamma_0 \delta t \hat{S}_0^- \hat{\rho}_{\rm a}(t)\hat{S}_0^+}_{\text{“yes” photon loss}} + \mathcal{O}(\delta t^2), \tag{2.17}$$

with the two terms corresponding to the conditional density matrices for zero and single spontaneous emitted photons, respectively. Since the collective jump operators $\hat{S}_0^{\pm}$ cannot alter the symmetry (and the total angular momentum S) of $\hat{\rho}_{\rm a}(t)$, the time-evolution of $\hat{\rho}_{\rm a}(t)$ from the initially symmetric state $|\Psi(t = 0)\rangle$ with total inversion will remain in the $S = N_A/2$ manifold with a transition probability from $|S, m\rangle$ to $|S, m-1\rangle$ given by $p(|S, m\rangle \to |S, m-1\rangle) = \Gamma_0 \delta t \langle \hat{S}_0^+ \hat{S}_0^- \rangle = \Gamma_0 \delta t (S + m)(S - m + 1)$. In particular, for $m = 0$, we find a collectively enhanced emission of $p(|S, 0\rangle \to |S, -1\rangle) \simeq \frac{\Gamma_0 \delta t N_A^2}{4}$, relative to the transition probability $\Gamma_0 \delta t N_A$ for a collection of independent atoms ($\Gamma_0 \delta t$ for single atoms).

The equation of motion for the collective spin operators $\{\hat{S}_0^{\pm}(t), \hat{S}_z(t)\}$ can be solved analytically from the master equation (Eq. 2.16) in the semi-classical approximation. Using the commutator relationships (Eqs. 2.13–2.14), we obtain the following differential equations (Eq. 2.16)

$$\frac{d}{dt}\langle \hat{S}_0^- \rangle = -\Gamma_0 \langle \hat{S}_z \hat{S}_0^+ \rangle \tag{2.18}$$

$$\frac{d}{dt}\langle \hat{S}_z \rangle = -\Gamma_0 \langle \hat{S}_0^+ \hat{S}_0^- \rangle. \tag{2.19}$$

In the semi-classical approximation (i.e., taking operators as c-numbers), we solve the equations of motions (Eqs. 2.18–2.19) and obtain $\langle \hat{S}_z(t) \rangle \simeq -S \tanh(\Gamma_0 S(t - t_d))$. This leads to a superradiant emission intensity of $I_c = -\Gamma_0 \frac{d\langle \hat{S}_z \rangle}{dt} = \frac{N_A^2 \Gamma_0}{4} \text{sech}^2\left(\frac{N_A \Gamma_0}{2}(t - t_d)\right)$.

2.2.4 Superradiance for extended atomic ensembles

The dynamics of multimode superradiance for extended samples[167,168] is more complex than the classic example of Dicke superradiance[42] in section 2.2.3, as the master equation involves various spatial phases $\vec{k}\cdot\vec{r}_i$ (thus, the geometry of the atomic sample) as well as a second-order propagation equation (i.e., Maxwell-Bloch equation, see also Eq. 2.39) through the atomic sample of length $L \gg \lambda_0$ (see Fig. 2.1b). For the current discussion, it suffices to say that if the Fresnel number $F_{\mathrm{a}} = \pi w_0^2/L\lambda_0$ is $\simeq 1$ for the atomic sample[f] ($F \simeq 1$ for our experimental parameters, see section 2.3.2.2), the propagation equations of the field for the 'pencil shaped' sample can be well approximated to a one-dimensional model[44,70,167,168]. The superradiant emission takes place along the elongated direction $\vec{k}'$ of the sample (so-called "end-fire mode")[161], for which the collective variables $\vec{S}_{\vec{k}} = \sum_i e^{i\vec{k}\cdot\vec{r}_i}\vec{\sigma}_i$ are "phase-matched." In this case, the so-called 'shape function' $f(\vec{k},\vec{k}') = \frac{1}{N_A^2}\sum_{i,j}^{N_A}\exp[i(\vec{k}-\vec{k}')(\vec{r}_j-\vec{r}_i)]$ determines the phase-matching condition from the sample geometry[167], which results from the classical interferences of the emitted photons $\vec{k}'$ from the collection of atoms excited by a pump laser with a wave-vector $\vec{k}$.

[f] As shown in Fig. 2.1b, we can express the Fresnel number $F_{\mathrm{a}} = \theta_g/\theta_d$ as the ratio between the geometric and diffraction angles ($\theta_{g,d}$) with θ_g (θ_d) $= \sqrt{\pi w_0^2}/L$ ($\lambda_0/\sqrt{\pi w_0^2}$). For $F \gg 1$, several transverse modes are necessary to describe the field propagation through the atomic ensemble, whereas $F_{\mathrm{a}} \ll 1$ gives large diffraction angle. In our experiment, L is set, by design, approximately to the Rayleigh length z_R for the Hermite-Gaussian mode of our imaging system ($L \simeq z_R$), as our atomic sample is much larger than both $\{w_0, z_R\}$. Thus $F_{\mathrm{a}} = \pi w_0^2/L\lambda_0 = z_R/L \simeq 1$. This justifies the use of the Maxwell-Bloch equation with paraxial approximation in our analysis for sections 2.3–2.5.

2.3 Parametric atom-light interaction

The weak nonlinearity of spontaneous Raman scattering can generate strong non-classical correlations between the atoms and the scattered photons[169]. As we will discuss later in section 2.4, combined with the 'strong' nonlinear response of the system by a quantum measurement, an initially independent pairs of atomic ensembles can be prepared into a heralded entangled state by a nonlocal measurement (refs.[4,27,34], see chapter 3). A critical element is the initial atom-photon correlation generated from parametric atom-light interactions $\hat{H}_{\text{int}}^{(\text{par})} \sim \chi_p \hat{a}_\gamma \hat{S}_a + h.c.$. Such quantum resources form the basis of many experiments in this thesis (chapters 3–5).

The creation of atom-photon correlations can be qualitatively understood as follows (Fig. 2.2). As shown in Fig. 2.2a, we initially prepare all the atoms in their ground state $|\overline{g}\rangle = |g, \cdots, g\rangle$. Subsequently, an off-resonant 'write' laser (red-detuned from $|g\rangle \to |e\rangle$ transition with detuning Δ_w) induces a spontaneously Raman scattered photon ($|e\rangle \to |s\rangle$), called field 1 (denoted by γ_1), in the forward direction (with probability $\xi \ll 1$), whose photon-number state $|n\rangle_{\gamma_1}$ is correlated with the number states $|n\rangle_{\text{a}}$ of the atoms being transferred from the initial state $|g\rangle$ to a metastable ground state $|s\rangle$. As it is impossible (even in principle) to discern which atom $i \in \{1 \cdots N_A\}$ has been transferred to $|s_i\rangle$ (i.e., the *which-atom* information), the number state of the atoms is associated with a collective atomic mode $\vec{\hat{S}}_{gs} = \frac{1}{N_A} \sum_i^{N_A} e^{i(\vec{k}_w - \vec{k}_1)\cdot \vec{r}_i} \vec{\hat{\sigma}}_{gs}$, corresponding to a 'spin wave' of a collective excitation. These spin-wave excitations are analogous to the symmetric superradiant states (but for *radiatively inactive* hyperfine ground state coherences $|g\rangle - |s\rangle$) in section 2.2.2. Thus, the classical writing laser drives the initial atom-field state to a two-mode squeezed state $|\Psi\rangle_{\text{a}\gamma_1} = \hat{U}_{\text{int}}^{(\text{par})} |\overline{g}\rangle = \sum_{n=0}^{\infty} c_n |n_{\text{a}}, n_{\gamma_1}\rangle$ with thermal distribution $|c_n|^2 = \frac{\overline{n}^n}{(\overline{n}+1)^{n+1}}$ through a coherent evolution of $\hat{U}_{\text{int}}^{(\text{par})} = e^{-i\int dt \hat{H}_{\text{int}}^{(\text{par})}(t)/\hbar}$, which display non-classical correlations between the two modes[72,73] (i.e., between the field 1 and the collective atomic mode). Any subsequent measurement on $|n\rangle_{\gamma_1}$ projects the spin sibling to a definite number state $|n\rangle_{\gamma_1}$ of collective excitations (section 2.4).

In this section, we describe a quantum theory for spontaneous Raman scattering in the regime of weak excitations $\xi \ll 1$ with an effective one-dimensional model. We decompose the atom-light interaction Hamiltonian for a Λ-level system by adiabatically eliminating the excited state. We also obtain the steady-state solutions for the atom-field system, which correspond to a model of non-degenerate parametric amplifier.

2.3.1 Spontaneous Raman interaction: Creating spin waves

Here, we consider an atomic ensemble consisting of N_A atoms in a Λ-level system. We assume a cylindrical atomic sample with radius w_0 and length L (Fig. 2.1b). As shown by Fig. 2.2a, the atomic ensemble interacts with a classical 'write' laser with Rabi frequency $\Omega_w(\vec{r}, t) e^{i\vec{k}_w \cdot \vec{r}}$ (where $\Omega_w(\vec{r}, t) = \tilde{\Omega}_w(t) u_w(\vec{r})$) and polarization $\vec{\epsilon}_w$, and a quantum field $\vec{\hat{E}}_1(\vec{r}, t)$, which we call field 1. Here, $u_w(\vec{r})$ is the mode function for a Hermite-Gaussian mode of the writing laser, and the positive frequency component of the quantum field

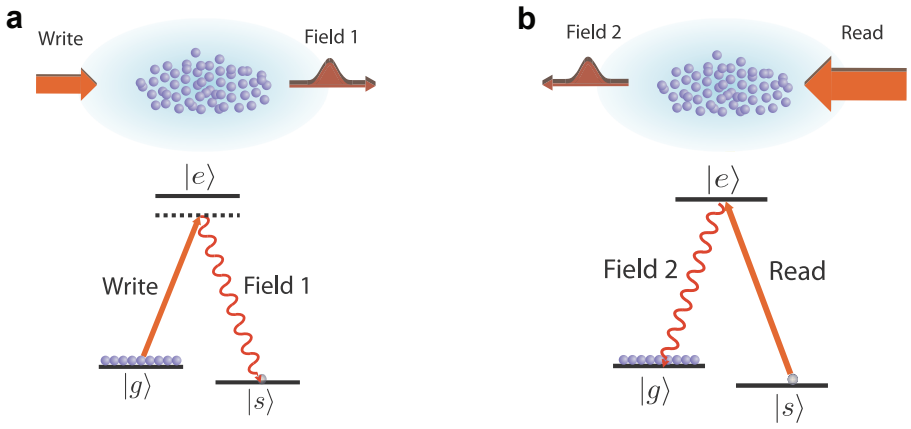

Figure 2.2: **Generating and retrieving collective excitations to photons. a**, Generating and storing single collective excitations. A weak write pulse illuminates the cold atomic sample, generating a Raman scattered photon, called field 1. The detection of a single photon in field 1 heralds the generation of a correlated single collective excitation $|\bar{s}\rangle$ in the ensemble. **b**, Retrieving single collective excitations to single photons. After a storage time τ, a strong read pulse maps the collective excitation to a single photon in field 2 via superradiant emission.

is expressed in terms of the normalized slowly-varying operator $\hat{\mathcal{E}}_1(\vec{r},t)$ with

$$\hat{\vec{E}}_1^+(\vec{r},t) = i\sqrt{\frac{\hbar w_1}{2\epsilon_0 \mathcal{V}_1}}\hat{\mathcal{E}}_1(\vec{r},t)e^{i\vec{k}_1\cdot\vec{r}}\vec{\epsilon}_1. \tag{2.20}$$

The slowly-varying operator $\hat{\mathcal{E}}_1(\vec{r},t)$ obeys the commutation relations

$$[\hat{\mathcal{E}}_1(\vec{r},t), \hat{\mathcal{E}}_1^\dagger(\vec{r}',t')] = \mathcal{V}_1\delta(\vec{r}_\perp - \vec{r}'_\perp)\delta(z - z' - c(t-t')) \tag{2.21}$$

where $\vec{r}_\perp = (x,y)$ is the transverse position vector and $\mathcal{V}_1$ is the field quantization volume.

As we described in the previous section, the writing laser is red-detuned by $\Delta_w = w_w - w_{ge}$ from the $|g\rangle \to |e\rangle$ transition, and we also include the two-photon detuning $\delta_{w1} = w_w - w_1 + w_{gs}$ for the 'field 1', where w_i with $i \in \{w,1\}$ are the respective angular frequencies for the writing laser and field 1, and w_{gs} is the hyperfine splitting for the ground states $|g\rangle - |s\rangle$. Both fields propagate approximately in the forward direction $\vec{k}_w(\vec{k}_1) \parallel \hat{z}$, and we treat the propagation of the weak quantized field in the paraxial approximation. In practice, we employ an off-axial excitation scheme pioneered by Balić *et al.*[75], with a small relative angle $\theta \leq 3^\circ$ between $\vec{k}_w$ and $\vec{k}_1$, such that $\vec{\epsilon}_1, \vec{\epsilon}_w \simeq \vec{\epsilon}_q$, where $\vec{\epsilon}_q$ is the polarization vector in the spherical basis[g].

[g] We decompose the polarization vector in the spherical tensor form,

$$\begin{aligned}\vec{\epsilon}_+ &= -\frac{1}{\sqrt{2}}(\hat{x} + i\hat{y}) \\ \vec{\epsilon}_- &= \frac{1}{\sqrt{2}}(\hat{x} - i\hat{y}) \\ \vec{\epsilon}_0 &= \hat{z}.\end{aligned}$$

2.3.1.1 Interaction Hamiltonian

In the weak depletion limit[h], where the Rabi frequency $\Omega_w(\vec{r},t)$ is constant over z, we can write the interaction Hamiltonian in the rotating wave approximation,

$$\begin{aligned}\hat{H}_s^{(\text{par})} &= \int d\vec{r} n_A(\vec{r})\{\hbar\Delta_w\hat{\sigma}_{ee}(\vec{r},t) - \hbar\delta_{w1}\hat{\sigma}_{ss}(\vec{r},t) \\ &\quad - \Big[\hbar g_p\hat{\mathcal{E}}_1(\vec{r},t)e^{i\vec{k}_1\cdot\vec{r}}\hat{\sigma}_{es}(\vec{r},t) + \hbar\Omega_w(\vec{r},t)e^{i\vec{k}_w\cdot\vec{r}}\hat{\sigma}_{eg}(\vec{r},t) + h.c.\Big]\},\end{aligned} \tag{2.22}$$

where $n_A(\vec{r})$ is the atomic density, $g_p = d_{es}\sqrt{\frac{w_{es}}{2\hbar\epsilon_0\mathcal{V}_1}}$ is the atom-photon coupling constant with dipole matrix element $d_{es} = \langle e|\hat{d}|s\rangle$. We take the quantization volume $\mathcal{V}_1$ as the sample volume. In writing the Hamiltonian $\hat{H}_s^{(\text{par})}$ in Eq. 2.22, we denoted the collective atomic variables defined *locally* at $\vec{r}$ (evaluated over a small volume[i] containing $N_{\vec{r}} \gg 1$ atoms) in the continuum limit ($\sum \to \int d\vec{r} n_A(\vec{r})$) of

$$\hat{\sigma}_{\mu\nu}(\vec{r},t) = \frac{1}{N_{\vec{r}}}\sum_i^{N_{\vec{r}}}\hat{\sigma}_{\mu\nu}^{(i)}e^{-iw_{\mu\nu}t}, \tag{2.23}$$

with single-atom operator $\hat{\sigma}_{\mu\nu}^{(i)} = |\mu\rangle_i\langle\nu|$. The collective variables follow the commutation relations,

$$[\hat{\sigma}_{\alpha\beta}(\vec{r},t),\hat{\sigma}_{\mu\nu}(\vec{r}',t)] = \frac{\mathcal{V}_1}{N_{\vec{r}}}\delta(\vec{r}-\vec{r}')(\delta_{\beta\mu}\hat{\sigma}_{\alpha\nu}(\vec{r},t) - \delta_{\nu\alpha}\hat{\sigma}_{\mu\beta}(\vec{r},t)). \tag{2.24}$$

In particular, the hyperfine ground-state coherence $\{\hat{\sigma}_{gs},\hat{\sigma}_{sg}\}$ follows the Bosonic commutator relations

$$[\hat{\sigma}_{sg}(\vec{r},t),\hat{\sigma}_{sg}^\dagger(\vec{r}',t)] \simeq \frac{\mathcal{V}_1}{N_{\vec{r}}}\delta(\vec{r}-\vec{r}')\hat{\sigma}_{gg}(\vec{r},t) + \mathcal{O}\left(\frac{1}{N_{\vec{r}}^2}\right) \tag{2.25}$$

in the weak excitation limit $\sigma_{gg} \simeq 1 \gg \sigma_{ee},\sigma_{ss}$.

2.3.1.2 Heisenberg-Lanvegin equations

In addition, the system $\hat{H}_s^{(\text{par})}$ interacts with a thermal reservoir (Markovian bath)

$$\hat{H}_r = \sum_{\vec{k},j}\hbar w_j\hat{r}_{\vec{k},j}^\dagger\hat{r}_{\vec{k},j} \tag{2.26}$$

at temperature T (mean photon number $\overline{n}_{\mu\nu}^{\text{th}}$) with reservoir mode operators $\{\hat{r}_{\vec{k},l}^\dagger,\hat{r}_{\vec{k},l}\}$ and with interaction Hamiltonian of the form

$$\hat{H}_{sr}^{(\mu\nu)} = \hbar\sum_{\vec{k},j}\left(g_{sr}(\vec{k},w_j)\hat{r}_{\vec{k},j}^\dagger\hat{\sigma}_{\mu\nu} + h.c.\right). \tag{2.27}$$

[h]This approximation is, strictly speaking, not valid for our laboratory parameters with optical depth $\tilde{d}_0(\Delta_w=0) > 10$ and small detuning $\Delta/\Gamma \simeq 2$ (chapters 3–9). In our experiments, the writing laser experience non-negligible amount of depletion as it propagates through the sample with $\Omega_w(\vec{r},t) \sim e^{-\tilde{d}_0(\Delta_w)z/L}$, where $\tilde{d}_0(\Delta_w)$ is the effective optical depth for the detuning Δ_w.

[i]The linear dimension $|\delta\vec{r}|$ of this volume must be large enough to contain macroscopic numbers of atoms, but small compared to the characteristic variation in the spin-wave amplitude: i.e., $|\delta\vec{r}| \ll \lambda_{gs} = \frac{2\pi}{|\vec{k}_w-\vec{k}_1|}$.

The total Hamiltonian including the respective reservoir modes for the atomic coherences $\sigma_{\mu\nu}$ is

$$\hat{H}_{\text{tot}} = \hat{H}_s^{(\text{par})} + \hat{H}_r + \sum_{\mu,\nu} \hat{H}_{sr}^{(\mu\nu)}. \tag{2.28}$$

In the Heisenberg-Langevin approach[143,164–166], we can describe the dynamics of the atomic operators (from Eq. 2.28) by a set of *self-consistent* equations of motions (ref.[143])

$$\partial_t \hat{\sigma}_{\mu\nu} = -\gamma_{\mu\nu}\hat{\sigma}_{\mu\nu} - \frac{i}{\hbar}[\hat{\sigma}_{\mu\nu}, \hat{H}_s^{(\text{par})}] + \hat{F}_{\mu\nu}. \tag{2.29}$$

The Langevin noise operators $\hat{F}_{\mu\nu}(\vec{r},t)$ arise from the system-reservoir interactions $\hat{H}_{sr}^{(\mu\nu)}$, and are associated with the decay term $(-\gamma_{\mu\nu}\hat{\sigma}_{\mu\nu})$ in Eq. 2.29, representing the dissipation of the atomic coherences $\hat{\sigma}_{\mu\nu}$ into the fluctuating reservoir modes (and vice versa). The exact form of $\hat{F}_{\mu\nu}(\vec{r},t)$ is not important, as they are δ-correlated ($\langle \hat{F}_{\mu\nu}^{\dagger}(t)\hat{F}_{\mu\nu}(t')\rangle_r = 2\gamma_{\mu\nu}\overline{n}_{\mu\nu}^{\text{th}}\mathcal{V}_1\delta(t-t')$ and $[\hat{F}_{\mu\nu}(t), \hat{F}_{\mu\nu}^{\dagger}(t')] = 2\gamma_{\mu\nu}\mathcal{V}_1\delta(t-t')$) and have zero reservoir average ($\langle \hat{F}_{\mu\nu}\rangle_r = 0$). In addition, the system-reservoir correlation function is given by $\langle \hat{\sigma}_{\mu\nu}^{\dagger}(t)\hat{F}_{\mu\nu}(t')\rangle = \gamma_{\mu\nu}\overline{n}_{\mu\nu}^{\text{th}}\mathcal{V}_1\delta(t-t')$. In the following discussion, we will assume vacuum states $\overline{n}_{\mu\nu}^{\text{th}} = 0$ for the reservoir modes[j].

Explicitly, the equations of motions for the optical coherences $\{\hat{\sigma}_{se}, \hat{\sigma}_{eg}\}$, and the ground-state coherence $\hat{\sigma}_{gs}$ are given by the following set of equations (with $\hat{\sigma}_{gg} \gg \hat{\sigma}_{ss}, \hat{\sigma}_{ee}$)

$$\partial_t\hat{\sigma}_{se} = -(\gamma_{se} + i(\Delta_w - w_{gs}) - i\delta_{w1})\hat{\sigma}_{se} + i\Omega_w e^{i\vec{k}_w\cdot\vec{r}}\hat{\sigma}_{sg} + \hat{F}_{se} \tag{2.30}$$

$$\partial_t\hat{\sigma}_{gs} = -(\gamma_{gs} - i\delta_{w1})\hat{\sigma}_{gs} - i\Omega_w e^{i\vec{k}_w\cdot\vec{r}}\hat{\sigma}_{es} + ig_p^*\hat{\mathcal{E}}_1 e^{-i\vec{k}_1\cdot\vec{r}}\hat{\sigma}_{ge} + \hat{F}_{gs} \tag{2.31}$$

$$\partial_t\hat{\sigma}_{eg} = -(\gamma_{eg} - i\Delta_w)\hat{\sigma}_{eg} - i\Omega_w^* e^{-i\vec{k}_w\cdot\vec{r}}\hat{\sigma}_{gg} + \hat{F}_{eg}. \tag{2.32}$$

2.3.1.3 Adiabatic elimination of excited state

In the following, we solve the steady-state solution for Heisenberg-Langevin equation of motion (Eqs. 2.30–2.32). If we assume the far off-resonant limit $\Delta_w \gg \gamma_{se}, \gamma_{eg}$ and the narrow-bandwidth $\delta w_w \ll \Delta_w$ of the write laser, we can adiabatically eliminate the excited state $|e\rangle$ and obtain the steady-state solutions for the optical coherences (i.e., $\partial_t\hat{\sigma}_{se} = \partial_t\hat{\sigma}_{eg} = 0$). Namely,

$$\hat{\sigma}_{se} \simeq -\frac{\Omega_w}{\Delta_w - w_{gs}}\left(1 + \frac{\delta_{w1} + i\gamma_{se}}{\Delta_w - w_{gs}}\right)e^{i\vec{k}_w\cdot\vec{r}}\hat{\sigma}_{sg} \tag{2.33}$$

$$\hat{\sigma}_{eg} \simeq -\frac{\Omega_w^*}{\Delta_w}\left(1 - i\left(\frac{\gamma_{eg}}{\Delta_w}\right)\right)e^{-i\vec{k}_w\cdot\vec{r}}\hat{\sigma}_{gg} - \frac{i}{\Delta_w}\left(1 - i\left(\frac{\gamma_{eg}}{\Delta_w}\right)\right)\hat{F}_{eg}. \tag{2.34}$$

By substituting these solutions (Eqs. 2.33–2.34) to Eq. 2.22, we obtain the effective interaction Hamilto-

[j]This is a reasonable approximation given that optical transitions correspond to a temperature scale $> 3,000$ K, relative to room-temperature 300 K.

nian (neglecting the noise terms and assuming constant atomic distribution $n_A(\vec{r}) = N_A/\mathcal{V}_1$)

$$\begin{aligned}\hat{H}_{\text{eff}}^{(\text{par})} &= \frac{N_A}{\mathcal{V}_1}\int d\vec{r}\left\{\hbar\Delta\hat{\sigma}_{ee}(\vec{r},t) - \hbar\delta\hat{\sigma}_{ss}(\vec{r},t) + \frac{\hbar|\Omega_w(\vec{r},t)|^2}{\Delta_w}\hat{\sigma}_{gg} - i\frac{\hbar|\Omega_w(\vec{r},t)|^2\gamma_{eg}}{\Delta_w^2}\hat{\sigma}_{gg}\right\} \\ &+\frac{1}{\mathcal{V}_1}\int d\vec{r}\left\{\hbar\chi_p(\vec{r},t;\Delta_w,\delta_{w1})\hat{\mathcal{E}}_1(\vec{r},t)\hat{\mathcal{S}}(\vec{r},t) + h.c.\right\}, \end{aligned} \tag{2.35}$$

where $\hat{\mathcal{S}}(\vec{r},t) = \sqrt{N_A}e^{-i(\vec{k}_w-\vec{k}_1)\cdot\vec{r}}\hat{\sigma}_{gs}(\vec{r},t)$ is the phase-matched slowly-varying spin-wave amplitude, and $\chi_p(\vec{r},t;\Delta_w,\delta_{w1}) \simeq g_p\sqrt{N_A}\frac{\Omega_w^*(\vec{r},t)}{\Delta_w - w_{gs}}$ is the effective parametric coupling constant. Here, the collective enhancement ($\sqrt{N_A}$) is manifested not by the increased emission rate of the Raman scattered photon, but by the increased quantum correlation between field 1 and collective excitation (section 2.4).

The first term of Eq. 2.35 includes the bare-state atomic Hamiltonian, light shift ($\sim \frac{\hbar|\Omega_w|^2}{\Delta_w}$), and the population loss of $\hat{\sigma}_{gg}$ due to optical pumping ($\sim \frac{i\hbar|\Omega_w|^2\gamma_{eg}}{\Delta_w^2}$). For our experiments, we can neglect the later two effects (optical pumping and light shift), as the intensity I_w for the write laser is well below the saturation intensity I_{sat} with a typical saturation parameter $s \equiv I_w/I_{\text{sat}} \equiv 2|\Omega_w|^2/\gamma_{eg}^2 \ll 10^{-4}$ (weak excitation limit). The second term, however, corresponds to a non-degenerate parametric amplification. This parametric matter-light interaction, denoted as

$$\hat{\mathcal{H}}_{\text{int}}^{(\text{par})}(t) = \hbar\left(\chi_p(t)\hat{\mathcal{E}}_1\hat{\mathcal{S}} + \chi_p^*(t)\hat{\mathcal{E}}_1^\dagger\hat{\mathcal{S}}^\dagger\right), \tag{2.36}$$

can generate a two-mode entangled state between the field 1 and the collective atomic mode via the squeezing operation $\hat{D} = \exp\left(-\frac{i}{\hbar}\int_0^\infty dt'\hat{\mathcal{H}}_{\text{int}}^{(\text{par})}(t')\right)$ (section 2.4).

2.3.2 Three-dimensional theory of spontaneous Raman scattering

Here, we derive a three-dimensional quantum theory of spontaneous Raman scattering by expanding the equations of motions in terms of the Hermite-Gaussian modes with mode indices (l,m). Under certain circumstance, we show that the 3D theory reduces an effective 1D model of a non-degenerate parametric amplifier between a single-mode (l,m) in field 1 and a single collective atomic mode (l,m).

2.3.2.1 Propagation equations of quantum fields and collective atomic variables

We start by deriving the equation of motion for the field $\vec{\hat{E}}_1^+(\vec{r},t)$ traveling along $\vec{k}_1 \parallel \hat{z}$ in the slowly-varying envelope approximation[143,170]. The wave equation for $\vec{\hat{E}}_1(\vec{r},t) = \vec{\hat{E}}_1^+(\vec{r},t)e^{-iw_1t} + \vec{\hat{E}}_1^-(\vec{r},t)e^{iw_1t}$ (Eq. 2.20) in a near-resonant atomic medium is given by

$$[\partial_t^2 - c^2\vec{\nabla}^2]\vec{E}_1(\vec{r},t) = -\frac{1}{\epsilon_0}\partial_t^2\vec{P}(\vec{r},t). \tag{2.37}$$

As in Eq. 2.20, we write the atomic polarization in terms of the slowly-varying atomic operator $\hat{\sigma}_{se}(\vec{r},t)$

$$\vec{\hat{P}}(\vec{r},t) = n_A(\vec{r})\left[d_{se}\vec{\epsilon}_{\rm a}\hat{\sigma}_{se}(\vec{r},t)e^{-i(\vec{k}_1\cdot\vec{r}-w_1t)} + h.c.\right]. \tag{2.38}$$

Assuming slowly-varying envelopes (i.e., $w_1\partial_t\mathcal{E}_1 \gg \partial_t^2\mathcal{E}_1$ and $w_1\hat{\sigma}_{se} \gg \partial_t\hat{\sigma}_{se}$), we then find the equation of motion for the slowly-varying amplitudes

$$\left[\partial_t - \frac{iw_1}{2}\left(1+\frac{\vec{\nabla}^2}{k_1^2}\right)\right]\mathcal{E}_1(\vec{r},t) = ig_pn_A(\vec{r})\mathcal{V}_1\hat{\sigma}_{se}(\vec{r},t)e^{-i\vec{k}_1\cdot\vec{r}}.$$

In the paraxial approximation, the quantized field propagates with the equation of motion

$$\left(\partial_t + c\partial_z - i\frac{c\vec{\nabla}_\perp^2}{2k_1}\right)\hat{\mathcal{E}}_1(\vec{r}_\perp,z,t) = ig_pn_A(\vec{r})\mathcal{V}_1\hat{\sigma}_{se}(\vec{r}_\perp,z,t)e^{-i\vec{k}_1\cdot\vec{r}}. \tag{2.39}$$

We can solve the coupled motions for the propagation of the atomic variables and the field 1 by substituting the adiabatic solutions $\hat{\sigma}_{es}, \hat{\sigma}_{ge}$ (Eq. 2.33) to the wave equation (Eq. 2.39) and to the Heisenberg-Langevin equation for the spin-wave variable $\hat{\sigma}_{gs}$ (Eq. 2.31), thereby yielding the following coupled differential equations (assuming a flat-top atomic number density $n_A(\vec{r}) = \frac{N_A}{\mathcal{V}_1}$)

$$\left(\partial_t + c\partial_z - \frac{ic\vec{\nabla}_\perp}{2k_1}\right)\hat{\mathcal{E}}_1(\vec{r},t) = i\chi_p(\vec{r},t;\Delta_w,\delta_{w1})\hat{\mathcal{S}}^\dagger(\vec{r},t) \tag{2.40}$$

$$\partial_t\hat{\mathcal{S}}(\vec{r},t) - \hat{F}_S = -\left(\frac{|\Omega_w|^2\gamma_{eg}}{\Delta_w^2} - i\delta'\right)\hat{\mathcal{S}}(\vec{r},t) + i\chi_p(\vec{r},t;\Delta_w,\delta_{w1})\hat{\mathcal{E}}_1^\dagger(\vec{r},t). \tag{2.41}$$

Here, we have assumed negligible spin-wave dephasing $\gamma_{gs} \simeq 0$ and $\delta' = \delta + \frac{|\Omega_w|^2}{\Delta_w}$, and $\hat{F}_S = \sqrt{N_A}e^{-i(\vec{k}_w-\vec{k}_1)\cdot\vec{r}}$ $\hat{F}_{gs}$ is the Langevin noise term for $\hat{\mathcal{S}}$.

2.3.2.2 Effective one-dimensional model

Here, I show that the three-dimensional Maxwell-Bloch equations (Eqs. 2.40–2.41) reduce to an effective 1D model for pencil-shaped ensembles (i.e., atomic Fresnel number $F_{\rm a} \simeq 1$) based on the formalism developed by Raymer *et al.* (ref.[70]). We assume a Gaussian write beam $\Omega_w(\vec{r},t) = \tilde{\Omega}_w(t)u_w(\vec{r}_\perp,z)$ with a mode function $u_w(\vec{r}_\perp,z)$ and $\chi_p(\vec{r},t;\Delta_w,\delta_{w1}) \simeq \chi_p'(t;\Delta_w,\delta_{w1})u_w(\vec{r}_\perp,z)$ (ref.[171]). We expand the quantum field $\hat{\mathcal{E}}_1(\vec{r},t)$ with Hermite-Gaussian modes $u_{lm}(\vec{r})$,

$$\hat{\mathcal{E}}_1(\vec{r},t) = \sum_{lm}\hat{\mathcal{E}}_{1,lm}(z,t)u_{lm}(\vec{r}) \tag{2.42}$$

$$\hat{\mathcal{S}}(\vec{r},t) = \sum_{lm}\hat{\mathcal{S}}_{lm}(z,t)u_{lm}(\vec{r}), \tag{2.43}$$

where the mode functions u_{lm} form a complete basis

$$\sum_{lm} u^*_{lm}(z,\vec{r}_\perp)u_{jk}(z,\vec{r}'_\perp) = \delta_{lj}\delta_{mk}\delta(\vec{r}_\perp - \vec{r}'_\perp), \tag{2.44}$$

and u_{lm} are the eigenfunctions for the paraxial equation $\left(\partial_z - \frac{i\vec{\nabla}_\perp}{2k_1}\right) u_{lm}(\vec{r}) = 0$ (see Eq. 2.40). Using these properties and formally integrating Eqs. 2.40–2.41 over $d\vec{r}_\perp$, we obtain the coupled equations of motions in terms of the mode functions

$$(\partial_t + c\partial_z)\hat{\mathcal{E}}_{1,lm}(z,t) = i\chi'_p \sum_{jk} \int d\vec{r}_\perp \left(u^*_{lm}(\vec{r})u_w(\vec{r})u_{jk}(\vec{r})\right) \hat{\mathcal{S}}^\dagger_{jk}(z,t) \tag{2.45}$$

$$\begin{aligned}\partial_t \hat{\mathcal{S}}_{jk}(z,t) &= -i\delta'\hat{\mathcal{S}}_{jk} - \frac{|\tilde{\Omega}_w|^2\gamma_{eg}}{\Delta_w^2} \sum_{lm} \int d\vec{r}_\perp \left(u^*_{jk}(\vec{r})|u_w(\vec{r})|^2 u_{lm}(\vec{r})\right) \hat{\mathcal{S}}_{lm} \\ &\quad + i\chi'^*_p \sum_{lm} \int d\vec{r}_\perp \left(u^*_{lm}(\vec{r})u_w(\vec{r})u_{jk}(\vec{r})\right) \hat{\mathcal{E}}^\dagger_{1,lm}.\end{aligned} \tag{2.46}$$

If we assume that the write beam ($u_w(z,\vec{r}_\perp)$) is much larger than the transverse dimension ($\vec{r}_\perp$) of the point-spread function for the imaging system of the field 1 ($u_{lm}(z,\vec{r}_\perp)$), such that $u_w(z,\vec{r}_\perp) \simeq u_w(z)$, then the integrals in Eqs. 2.45–2.46 reduce to $\int d\vec{r}_\perp \left(u^*_{lm}(\vec{r})u_w(z)u_{jk}(\vec{r})\right) \simeq \int d\vec{r}_\perp \left(u^*_{lm}(\vec{r})|u_w(z)|^2 u_{jk}(\vec{r})\right) \simeq \delta_{lj}\delta_{mk}$ (ref.[70,172]). In this case, the effective atomic density participating in the parametric interaction is defined by the field 1 mode, whose beam-waist is chosen to be much smaller than that of the write laser (pencil-shaped sample), and $F_{\rm a} = z_R/L \simeq 1$ (z_R is the Rayleigh range of field 1) in our experiment with $L \simeq z_R$. Thus, the resulting equations of motions are reduced to an effective 1D model with

$$(\partial_t + c\partial_z)\,\hat{\mathcal{E}}_{1,lm}(z,t) = i\chi_p(\vec{r},t;\Delta_w,\delta_{w1})\hat{\mathcal{S}}^\dagger_{lm}(z,t) \tag{2.47}$$

$$\partial_t \hat{\mathcal{S}}_{lm}(z,t) = -\left(\frac{|\Omega_w|^2\gamma_{eg}}{\Delta_w^2} - i\delta'\right)\hat{\mathcal{S}}_{lm}(z,t) + i\chi'^*_p(t)\hat{\mathcal{E}}^\dagger_{1,lm}(z,t) + \hat{F}_{lm}(z,t), \tag{2.48}$$

where $\hat{F}_{lm}(z,t)$ is the Langevin noise term associated with $\hat{\mathcal{S}}_{lm}$. The coupling between the creation of a single spin-wave $\hat{\mathcal{S}}^\dagger_{lm}(z,t)$ and the annihilation of a single photon $\hat{\mathcal{E}}_{1,lm}(z,t)$ in field 1 (and vice versa) in Eqs. 2.47–2.48 describes a non-degenerate parametric oscillator, which in turn generates a two-mode squeezed state between the collective atomic mode and the field 1 mode (section 2.4).

The spatio-temporal modes of $\hat{\mathcal{E}}_{1,lm}(z,t)$, $\hat{\mathcal{S}}_{lm}(z,t)$ and the normally ordered correlations such as : $\hat{\mathcal{S}}^\dagger_{lm}\hat{\mathcal{S}}_{lm}\hat{\mathcal{E}}^\dagger_{1,lm}\hat{\mathcal{E}}_{1,lm}$: can be derived from Eqs. 2.47–2.48. We will revisit some of the ideas developed here (section 2.5), whereby we solve the equation of motion for the retrieval process in the dark-state polariton picture[86,95,96]. I note that similar expressions have been derived in refs.[75,173]. More recently, optimal control theory has been applied to three-dimensional light scattering in a Λ-type ensemble[174].

2.4 Two-mode squeezed state as a quantum resource for *DLCZ* protocol

The initial atom-field state $|\overline{g}_{\rm a}, 0_{\gamma_1}\rangle$ in the Schrödinger's picture evolves to $|\Psi\rangle_{{\rm a}\gamma_1}$ via the unitary rotation $\hat{D} = \exp\left(-\frac{i}{\hbar}\int_0^\infty dt' \hat{\mathcal{H}}_{\rm int}^{\rm (par)}(t')\right)$ with the parametric interaction Hamiltonian $\hat{\mathcal{H}}_{\rm int}^{\rm (par)}$ (Eq. 2.36) derived in section 2.3.1.3. The final atom-field state ($t \to \infty$) is given by a two-mode squeezed state

$$|\Psi\rangle_{\gamma_1{\rm a}} = \sqrt{1-\xi}\sum \xi^{n/2}|n_{\gamma_1}, n_{\rm a}\rangle, \tag{2.49}$$

where $|n_{\gamma_1}\rangle$ ($|n_{\rm a}\rangle$) are the number-states for the photons $\sim (\hat{a}^\dagger)^n|0_{\gamma_1}\rangle$ (collective excitations $\sim (\hat{\mathcal{S}}^\dagger)^n|g_{\rm a}\rangle$) in field 1 (atomic ensemble), and $\xi = \tanh^2\left(i\int_0^\infty dt' \frac{1}{L}\int_0^L dz \chi_p(z,t')\right) \ll 1$ is the excitation parameter with the squeezing parameter given by $\chi_p(z,t;\Delta_w,\delta_{w1}) \simeq g_p\sqrt{N_A}\frac{\Omega_w^*(z,t)}{\Delta_w - w_{gs}}$. Additionally, we define for simplicity $\chi_p(t') = \frac{1}{L}\int_0^L dz \chi_p(z,t')$. For a rigorous treatment of dissipation and propagation effects, one needs to solve the self-consistent Heisenberg-Langevin equations in Eqs. 2.47–2.48, from which various correlation functions could be evaluated from Einstein's relations [143].

Here, we make several further remarks:

1. The mean photon number in field 1 is given by $\overline{n}_1 = {}_{\gamma_1{\rm a}}\langle\Psi|\hat{n}_1|\Psi\rangle_{\gamma_1{\rm a}} = \frac{\xi}{1-\xi}$ ($= \sinh(i\int_0^\infty dt' \chi_p(t'))$). Thus, the excitation probability $\xi = \frac{\overline{n}}{1+\overline{n}}$ follows the familiar thermal distribution. When the field 1 is traced over, the remaining atomic counterpart is equivalent to a thermal state where the ensemble exhibits super-Poissonian spin-wave statistics, $g^{(2)}(\tau) = \frac{\langle:\hat{n}_{\rm a}(t)\hat{n}_{\rm a}(t+\tau):\rangle}{|\langle\hat{n}_{\rm a}\rangle|^2} = 2$ (for $\tau = 0$).

2. For multiple ensembles and fields 1 (with the ensemble$\oplus$field 1 system labeled by $\alpha \in \{a, b, c, \cdots\}$), the overall state after the parametric Raman interaction is ideally $|\Psi\rangle_{\rm tot} = \prod_\alpha |\Psi\rangle_{\gamma_1{\rm a}}^{(\alpha)}$, where $|\Psi\rangle_{\gamma_1{\rm a}}^{(\alpha)} = \sqrt{1-\xi_\alpha}\sum \xi_\alpha^{n/2}|n_{\gamma_1}, n_{\rm a}\rangle_\alpha$.

3. In the ideal case, the conditional atomic state upon a photoelectric detection of a single field 1 photon on the mode $\hat{a}_{1,\alpha}$ is given by $\hat{\rho}_c = {\rm Tr}_1(\hat{a}_{1,\alpha}^\dagger \hat{a}_{1,\alpha}\hat{\rho}_{\gamma_1{\rm a}})$, where the initial atom-photon state prior to projection by $\hat{a}_{1,\alpha}^\dagger\hat{a}_{1,\alpha}$ is $\hat{\rho}_{\gamma_1{\rm a}} = |\Psi\rangle_{\gamma_1{\rm a}}^{(\alpha)}\langle\Psi|$.

4. The mode operators can be transformed nonlocally to $\hat{a}'_{1,\alpha} = \sum_{\alpha'} U_{\alpha,\alpha'}\hat{a}_{1,\alpha'}$ where $U_{\alpha,\alpha'}$ represents a unitary transformation of the mode operators $\hat{a}_{1,\alpha'}$. A photoelectric detection of a single photon in mode $\hat{a}'_{1,\alpha}$ leads to an effective interaction among the α' systems.

In section 2.5, we show that, after a delay τ, the collective excitation $\hat{\mathcal{S}}$ can be coherently mapped to another quantum field, called field 2 (with, ideally, unit probability) via the 'beamsplitter' transformation (Fig. 2.2b), with the dark-state polariton [86] $\hat{\Psi}_d(z,t) = \cos\theta(t)\hat{\mathcal{E}}_2(z,t) - \sin\theta(t)\hat{\mathcal{S}}(z,t)$ governing the matter-light evolution. When the atomic state is traced over, the matter-light transfer process is equivalent to replacing the collective operators $\hat{\mathcal{S}}$ and the state label, a, (indicating the atomic side of the Hilbert state) to $\hat{a}'_2 =$

$\sqrt{\eta_2}\hat{a}_2 + \sqrt{1-\eta_2}\hat{v}_2$ and a state label γ_2, respectively. Here, we account for the retrieval efficiency, the loss in the propagation and the detection of field 2 with a transmission efficiency η_2 in the beamsplitter transformation, where $\hat{v}_2$ is a vacuum mode operator[k]. Thus, ideally, we can transfer the two-mode squeezed state between an ensemble and field 1 to an equivalent state between fields 1 and 2,

$$|\Psi\rangle_{\gamma_1 \mathrm{a}} \mapsto |\Psi\rangle_{\gamma_1\gamma_2} = \sqrt{1-\xi}\sum \xi^{n/2}|n_{\gamma_1}, n_{\gamma_2}\rangle. \tag{2.50}$$

In practice, we control the excitation parameter $\xi = \tanh^2(i\int_0^\infty dt'\chi_p(t'))$ with the write intensity to modify the spin-wave statistics. For $\xi \gg 1$, the two modes contain significant *continuous-variable* entanglement, whereas in the regime of weak excitation $\xi \ll 1$, the two-mode squeezed state $|\Psi\rangle_{\gamma_1 \mathrm{a}}$ displays strong quantum correlations in the number-state basis. The field 2 and the field 1 can, indeed, exhibit strong non-classical correlations, as demonstrated experimentally in refs.[72,73], and be used as a critical resource for quantum information processing and communication[4]. Here, we calculate various intensity correlations between the fields 1 and 2, and obtain important benchmark parameters (used throughout the thesis), which characterize our experiments.

2.4.1 Two-mode squeezed state between an optical and collective atomic mode

The non-classical correlation between fields 1 and 2 can be verified by the violation of Cauchy-Schwarz inequality (refs.[170,175]),

$$R = \frac{|g_{12}|^2}{g_{11}g_{22}} \leq 1. \tag{2.51}$$

Here, we assume the initial state as the two-mode squeezed state $|\Psi\rangle_{\gamma_1\gamma_2}$ (Eq. 2.50). The normalized cross-correlation function g_{ij} between fields i, j is given by

$$g_{ij}(\tau) \equiv \frac{\langle : \hat{I}_i(t)\hat{I}_j(t+\tau) : \rangle}{\langle \hat{I}_i \rangle \langle \hat{I}_j \rangle}, \tag{2.52}$$

where $: \hat{\mathcal{O}} :$ indicates normally ordered operator for $\hat{\mathcal{O}}$. Here, $I_i = \eta_i \langle \hat{a}_i^\dagger \hat{a}_i \rangle$.

We obtain the following set of (auto- and cross-) intensity correlations,

$$\langle \Psi_{\gamma_2\gamma_1}| : \hat{I}_i : |\Psi_{\gamma_1\gamma_2}\rangle = \eta_i \frac{\xi}{1-\xi} = \overline{n}_i \tag{2.53}$$

$$\langle \Psi_{\gamma_2\gamma_1}| : \hat{I}_1\hat{I}_2 : |\Psi_{\gamma_1\gamma_2}\rangle = \eta_1\eta_2 \frac{\xi(1+\xi)}{(1-\xi)^2} \tag{2.54}$$

$$\langle \Psi_{\gamma_2\gamma_1}| : \hat{I}_i^2 : |\Psi_{\gamma_1\gamma_2}\rangle = \eta_i^2 \frac{2\xi^2}{(1-\xi)^2}, \tag{2.55}$$

[k] To include noise, we can add mixed coherent states $|v_i\rangle$ on a reservoir mode $\hat{v}_i$ entering the system $\hat{a}_i$ (see the supplementary information of ref.[33], chapter 9).

where we obtain normalized auto-correlation functions $g_{ii} = 2$ for $i \in \{1, 2\}$, and a cross-correlation

$$g_{12} = 1 + \frac{1}{\xi}. \tag{2.56}$$

Thus, we observe the presence of strong quantum correlations between the fields 1 and 2 by way of the violation of Cauchy-Schwarz inequality $R = \frac{1}{4}\left(1 + \frac{1}{\xi}\right)^2 = \frac{g_{12}^2}{4} \not\leq 1$ for $\xi < 1$ ($g_{12} > 2$). Since the initial experiments[72,73], the Cauchy-Schwarz inequality has been violated by a factor up to $R \geq 10^5$ by the group of Steve Harris in a 2D magneto-optical trap[81].

2.4.2 Heralded single-photon source

In the single-excitation regime $\xi \ll 1$, the initial two-mode squeezed state between the ensemble and field 1 can be expanded as

$$|\Psi\rangle_{\gamma_1 \mathrm{a}} \simeq |0_{\gamma_1}, 0_{\mathrm{a}}\rangle + \sqrt{\xi}|1_{\gamma_1}, 1_{\mathrm{a}}\rangle + \mathcal{O}(\xi). \tag{2.57}$$

A measurement of a single photon in field 1 ($:\hat{I}_1:$) projects the remaining ensemble counterpart to a state of (ideally) single collective excitation $\hat{\rho}_c = \mathrm{Tr}_{\gamma_1}(:\hat{I}_1: |\Psi\rangle_{\gamma_1 \mathrm{a}}\langle\Psi|)$. After a controllable delay τ, we map the single excitation to a single photon $|\Psi\rangle_{\gamma_1 \mathrm{a}} \mapsto |\Psi\rangle_{\gamma_1 \gamma_2}$ (ref.[74]). Thus, a probabilistic detection of a single photon in field 1 heralds (signals) the creation of single collective excitation, which we subsequently transfer to a single photon in a triggered fashion.

We characterize the quality of the heralded single-photon source with the conditional auto-correlation function $g_c^{(2)}$, also denoted by $w = \frac{p_{11}}{p_{10}p_{01}}$, in a Hanbury Brown-Twiss setup[176,177]. Here, the p_{ij} are the conditional probabilities to detect i, j photons in two respective detectors measuring the two modes $\hat{a}_{2,a}, \hat{a}_{2,b}$ after a beamsplitter. The transformed mode operators are given by

$$\begin{aligned} \hat{a}_{2,a} &= \frac{1}{\sqrt{2}}\left(\hat{a}_2 + \hat{v}_2\right) \\ \hat{a}_{2,b} &= \frac{1}{\sqrt{2}}\left(\hat{a}_2 - \hat{v}_2\right). \end{aligned}$$

Using these mode operators, we calculate the intensity correlations (with $i \in \{2a, 2b\}$)

$$\langle :\hat{I}_1\hat{I}_{2a}\hat{I}_{2b}: \rangle = \eta_1\eta_{2a}\eta_{2b}\frac{\xi^2(2+\xi)}{2(1-\xi)^3} \tag{2.58}$$

$$\langle :\hat{I}_1\hat{I}_i: \rangle = \eta_1\eta_i\frac{\xi(1+\xi)}{2(1-\xi)^2}, \tag{2.59}$$

for which we obtain a suppression of higher-order excitations (and non-classical photon statistics) relative to that of a coherent state

$$w = \frac{\langle :\hat{I}_1\hat{I}_{2a}\hat{I}_{2b}: \rangle\langle :\hat{I}_1: \rangle}{\langle :\hat{I}_1\hat{I}_{2a}: \rangle\langle :\hat{I}_1\hat{I}_{2b}: \rangle} = \frac{4\xi}{(1+\xi)^2} + \frac{2\xi^2}{(1+\xi^2)^2} \simeq \frac{4}{g_{12}}. \tag{2.60}$$

We compare our result of w (Eq. 2.60) to coherent states $|\alpha\rangle$, a minimum uncertainty state that defines the quantum-classical boundary[170], $w_b = \langle : \hat{n}^2 : \rangle / |\langle \hat{n} \rangle|^2 = |\alpha|^4/|\alpha|^4 = 1$ (for fields with Poissonian statistics). Thus, we obtain non-classical sub-Poissonian photon statistics $w < w_b = 1$ for $g_{12} \gtrsim 4$ (in contrast to the super-Poissonian statistics $g^{(2)}(0) = 2$ of the fields 1 and 2 when taken alone).

2.4.3 Measurement-induced entanglement

Having established the presence of quantum correlations between the number states of the field 1 and the collective excitation, we show that entanglement between two atomic ensembles can be created by a path-erasing measurement of a single photon (field 1) emitted indistinguishably from the two ensemble.

Specifically, we start from a pair of two-mode squeezed states (Eq. 2.49)

$$
\begin{aligned}
|\Psi\rangle_{\text{tot}} &= |\Psi\rangle^{(L)}_{\gamma_1 \text{a}} \otimes |\Psi\rangle^{(R)}_{\gamma_1 \text{a}} && (2.61)\\
&\simeq \sqrt{(1-\xi_L)(1-\xi_R)} \left(|0_{\gamma_1}, \overline{g}_{\text{a}}\rangle_L + \sqrt{\xi}_L e^{i\phi_L} |1_{\gamma_1}, \overline{s}_{\text{a}}\rangle_L + \mathcal{O}(\xi_L) \right) \\
&\quad \otimes \left(|0_{\gamma_1}, \overline{g}_{\text{a}}\rangle_R + \sqrt{\xi}_R e^{i\phi_R} |1_{\gamma_1}, \overline{s}_{\text{a}}\rangle_R + \mathcal{O}(\xi_R) \right) && (2.62)
\end{aligned}
$$

by illuminating the two atomic ensembles, L and R, with Ω_w. The relative phase ϕ_w between the two writing beams is given by $\phi_w = \phi_L - \phi_R$, where $\phi_{L,R}$ are the phases associated with the writing lasers illuminating ensembles L, R. A photoelectric detection $\hat{I}_{1,l} = \eta_l \hat{a}^\dagger_{1,l} \hat{a}_{1,l}$ (or $\hat{I}_{1,r} = \eta_r \hat{a}^\dagger_{1,r} \hat{a}_{1,r}$) of a single photon in field 1 after a beamsplitter projects the initial quantum state of ensemble-field system $|\Psi\rangle_{\text{tot}}$, where the mode operators for the output ports $\{l, r\}$ of the beamsplitter ($\cos(\theta_1) : \sin(\theta_1)$ ratio) are given by

$$
\begin{aligned}
\hat{a}_{1,l} &= \cos\theta_1 \hat{a}_{1,L} + e^{i\phi_1} \sin\theta_1 \hat{a}_{1,R} \\
\hat{a}_{1,r} &= -\sin\theta_1 \hat{a}_{1,L} + e^{-i\phi_1} \cos\theta_1 \hat{a}_{1,R}.
\end{aligned}
$$

The conditional atomic states upon the probabilistic photoelectric events $\hat{I}_{1,l}$ and $\hat{I}_{1,r}$ are given by

$$
\begin{aligned}
\hat{\rho}^{(l)}_{\text{ent}} &= \frac{\text{Tr}_1(\hat{I}_{1,l} \hat{\rho}_{\gamma_1 \text{a}})}{\langle \hat{I}_{1,l} \rangle} = |\Psi\rangle^{(l)}_{\text{tot}} \langle \Psi| && (2.63)\\
\hat{\rho}^{(r)}_{\text{ent}} &= \frac{\text{Tr}_1(\hat{I}_{1,r} \hat{\rho}_{\gamma_1 \text{a}})}{\langle \hat{I}_{1,r} \rangle} = |\Psi\rangle^{(r)}_{\text{tot}} \langle \Psi|. && (2.64)
\end{aligned}
$$

Thus, we obtain heralded entanglement between the two atomic ensembles,

$$
|\Psi\rangle^{(l)}_{\text{tot}} \simeq \left(\sqrt{\frac{\xi_R}{\xi_{\text{tot}}}} \sin\theta_1 |\overline{g}_{\text{a},L}, \overline{s}_{\text{a},R}\rangle + e^{i(\phi_w - \phi_1)} \sqrt{\frac{\xi_L}{\xi_{\text{tot}}}} \cos\theta_1 |\overline{s}_{\text{a},L}, \overline{g}_{\text{a},R}\rangle \right) + \mathcal{O}(\sqrt{\xi}_{L,R}) \quad (2.65)
$$

$$
|\Psi\rangle^{(r)}_{\text{tot}} \simeq \left(\sqrt{\frac{\xi_R}{\xi_{\text{tot}}}} \cos\theta_1 |\overline{g}_{\text{a},L}, \overline{s}_{\text{a},R}\rangle - e^{-i(\phi_w - \phi_1)} \sqrt{\frac{\xi_L}{\xi_{\text{tot}}}} \sin\theta_1 |\overline{s}_{\text{a},L}, \overline{g}_{\text{a},R}\rangle \right) + \mathcal{O}(\sqrt{\xi}_{L,R}), \quad (2.66)
$$

where $\xi_{\text{tot}} = \xi_L + \xi_R$ is the total excitation probability.

The degree of entanglement is characterized by concurrence [178], a monotonic function of entanglement [27],

$$C \simeq \max(Vp_1 - 2\sqrt{p_0 p_{11}}, 0) \geq \max(p_1(V - \sqrt{p_0 h_c}), 0), \tag{2.67}$$

where the two-photon contamination for the global joint state of the two ensembles and off-diagonal coherence are characterized by a normalized parameter $h_c \equiv \frac{p_{11}}{p_{10}p_{01}} \simeq 4/g_{12}$ and by $d = Vp_1/2$ (chapter 3). Here, $V = \frac{\max(\langle \hat{I}_{2,l} \rangle) - \min(\langle \hat{I}_{2,l} \rangle)}{\max(\langle \hat{I}_{2,l} \rangle) + \min(\langle \hat{I}_{2,l} \rangle)} \simeq \frac{g_{12}-1}{g_{12}+1}$ (assuming $\xi_L = \xi_R$ and $\theta_1 = \pi/4$) is the visibility for the interference between the two fields $2_L, 2_R$ retrieved from $\hat{\rho}_{\text{ent}}^{(l,r)}$ (chapter 3), with the mode operators defined as

$$\begin{aligned} \hat{a}_{2,l} &= \frac{1}{\sqrt{2}} \left(\hat{a}_{2,L} + e^{i\phi_2} \hat{a}_{2,R} \right) \\ \hat{a}_{2,r} &= \frac{1}{\sqrt{2}} \left(-\hat{a}_{2,L} + e^{-i\phi_2} \hat{a}_{2,R} \right). \end{aligned}$$

A necessary condition for entanglement is $h_c \simeq 4/g_{12} < 1$ (for independent coherent states $|\alpha_1, \alpha_2\rangle$, $h_c = 1$). A similar quantity $y_c \equiv \frac{4p_{11}p_0}{p_1^2}$ is derived in the language of quantum uncertainty (Δ) relations (chapters 7–9), where $C = \max\left(p_1\left(\sqrt{1-2\Delta} - \sqrt{y_c}\right), 0\right)$.

2.5 Collective atom-light interaction

The dynamics of N_A Λ-level atoms dressed by applied laser fields determines the optical response of the coherent atomic medium. In addition to the Dicke-like superradiant emission (section 2.2), the coherent manipulation of dark resonances[94,179–184] enables a robust and efficient method of transferring quantum states[185] between photons and spin waves in a matter-light quantum interface. Closely connected to classical coherent phenomena of coherent population trapping[179,183] (CPT) and stimulated Raman adiabatic transfer[180,181,184] (STIRAP), a dark-state polariton is a half photonic and half matter quasi-particle excitation, proposed by Michael Fleischhauer and Mikhail Lukin[86,87], which describes low-light level electromagnetically induced transparency[94,182] (EIT). Coherent preparation and control of EIT at the single-photon level are utilized in many experiments, including those in my thesis, for the coherent transfer of heralded spin-waves (section 2.3, Fig. 2.2a) to single photons (chapters 3–5 and 9, Fig. 2.2b) and for the reversible mapping of a photonic entanglement into and out of quantum memories (chapter 6, Fig. 2.3).

Stated explicitly, the dark-state polariton $\hat{\Psi}_d(z,t) = \cos\theta_d(t)\hat{\mathcal{E}}_s(z,t) - \sin\theta_d(t)\hat{\mathcal{S}}(z,t)$ is a coherent superposition state of electromagnetic and spin-wave excitations and is a quantum analogue of the classic dark state in CPT[179,183,184]. The adiabatic following of $\hat{\Psi}_d$ with respect to the rotation of mixing angle θ_d leads to a reversible and (ideally) complete transfer between quantum optical states $\hat{\mathcal{E}}_s(z,t)$ and spin-waves $\hat{\mathcal{S}}(z,t)$ without dissipation via *dynamic* EIT. Here, we theoretically analyze the operation of our quantum interface in this polaritonic picture. In chapter 6, we provide a semi-classical picture to the observations of *static* EIT and CPT, and the connections to the polaritonic picture discussed here. There, we discuss the technical considerations towards *dynamic* EIT (such as the importance of Zeeman populations in a multi-level system). In chapter 6, we also present a numerical optimization scheme for improving the storage and retrieval efficiency based on the works by Gorshkov *et al.*[186–189].

Following the method developed in section 2.3, we treat quantum mechanically the propagation and the dynamics of the coupled motions of the quantum fields (called the signal field ($\hat{\mathcal{E}}_s$), or the field 2 ($\hat{\mathcal{E}}_2$)) and the collective excitations in an EIT media. For simplicity, we call $\hat{\mathcal{E}}_s$ the quantum field of interest for storage and/or retrieval, whether it is externally provided from an offline source (signal field) or generated internally from the parametric interaction (field 2). Based on the results in section 2.3, we use an effective 1D model[86,87]. We show that the signal field's group velocity v_g can be dynamically controlled by an external control laser $\Omega_c(z,t)$ from the free-space velocity $v_g = c$ to ultraslow group velocities $v_g \ll c$ and to a complete halt $v_g = 0$ (coherent storage) for the quantum field (and vice versa). In particular, we find that dark-state polaritons $\hat{\Psi}_d$ can be dynamically decelerated and accelerated while preserving the phase-amplitude information of the quantum field $\hat{\mathcal{E}}_s$ by transferring to and from stationary collective excitations $\hat{\mathcal{S}}$.

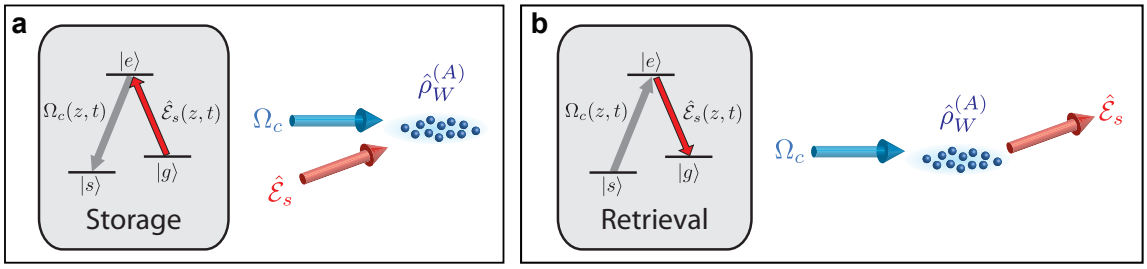

Figure 2.3: **Reversible matter-light quantum interface via dark-state polariton. a**, Mapping single photons to single collective excitations. A strong resonant control laser ($|e\rangle \rightarrow |s\rangle$ transition) with Rabi frequency $\Omega_c(z,t)$ is illuminated onto the ensemble in a counter-intuitive order[181], thereby preparing $|g\rangle$ as the dark-state. As the weak quantum field $\hat{\mathcal{E}}_s$ ($|g\rangle \rightarrow |e\rangle$ transition), called the signal field, enters the coherent atomic medium, the control laser is adiabatically turned off, thereby storing the quantum state of $\hat{\mathcal{E}}_s$ in the collective atomic excitation $\hat{\mathcal{S}}(z,t)$. **b**, Mapping single collective excitations to single photons. After a delay τ, the intensity of the control laser is adiabatically increased, thereby transferring the then dark-state $|\overline{s}\rangle$ back to the signal field $\hat{\mathcal{E}}_s$. The signal field $\hat{\mathcal{E}}_s$ propagates within the EIT window of the ensemble, provided by $\Omega_c(z,t)$.

2.5.1 Interaction Hamiltonian and formation of dark states

Here, we consider a collection of Λ-level atoms interacting with the two single-mode optical fields. The transition $|g\rangle - |e\rangle$ of each of these atoms is coupled to a slowly-varying quantized radiation mode $\hat{\mathcal{E}}_s$ (with two-photon detuning δ), called the signal field, whereas the transition $|s\rangle - |e\rangle$ is resonantly driven by a classical control field of Rabi frequency Ω_c (with detuning Δ_c). The dynamics of this system is described by the Hamiltonian $\hat{H}_s^{(\text{map})}$ in the rotating-wave approximation (following the effective one-dimensional approximation in section 2.3.2.2 and neglecting the transverse profiles), with

$$\begin{aligned}\hat{H}_s^{(\text{map})} &= \int dw \hbar w \hat{a}_w^\dagger \hat{a}_w + \sum_{i=1}^{N_A} \left(\hbar w_{es} \hat{\sigma}_{ss}^{(i)} + \hbar w_{eg} \hat{\sigma}_{gg}^{(i)} \right) \\ &\quad \underbrace{- \sum_{i=1}^{N_A} \left(\hbar \Omega_c \hat{\sigma}_{es}^{(i)} e^{i(k_c^{\parallel} z_i - w_c t)} + d_{eg} \hat{\sigma}_{eg}^{(i)} \vec{\epsilon}_{\text{a}} \cdot \vec{\hat{E}}_s^{+} e^{i(k_s z_i - w_s t)} + h.c. \right)}_{\hat{H}_{\text{int}}^{(\text{map})}}, \end{aligned} \tag{2.68}$$

where $\vec{\hat{E}}_s^{+} = i\sqrt{\frac{\hbar w_s}{2\epsilon_0 \mathcal{V}}} \int dw \hat{a}_w e^{iwz/c} \vec{\epsilon}_s$ is the positive frequency component of the signal field, and $k_c^{\parallel} = \vec{k}_c \cdot \hat{z}$ is the longitudinal projection of the wave-vector along $\hat{z}$ (also, $k_c^{\perp} = |\vec{k}_c \cdot (\hat{x}, \hat{y})| \simeq 0$). We assumed that the signal field propagates along the quantization axis $\hat{z}$ of the system (section 2.3.2.2).

A simple explanation for the formation of dark-state polariton is the existence of a family of dark eigenstates $|D, m\rangle$ for the interaction Hamiltonian $\hat{H}_{\text{int}}^{(\text{map})}$ (ref.[87]). In particular, the single-excitation state $|D, m = 1\rangle$ is (ref.[87])

$$|D, 1\rangle = \cos\theta_d(t) |\overline{g}_{\text{a}}, 1_s\rangle - \sin\theta_d(t) |\overline{s}_{\text{a}}, 0_s\rangle, \tag{2.69}$$

where $\tan\theta_d = g_d\sqrt{N_A}/\Omega_c$ defines the mixing angle, $g_d = i d_{eg}\sqrt{\frac{w_s}{2\hbar\epsilon_0 \mathcal{V}}}$ $(\vec{\epsilon}_{eg} \cdot \vec{\epsilon}_s)$ is the single atom-

photon coupling constant[1], $|n_s\rangle$ is the Fock state for the signal field, $|\overline{s}\rangle_{\rm a} = \frac{1}{\sqrt{N_A}}\sum_{i=1}^{N_A} e^{-i\Delta k_{sc} z_i}\hat{\sigma}_{gs}^{(i)\dagger}|\overline{g}\rangle_{\rm a}$ is the collective spin excitation (see section 2.3.1.1), and $\Delta k_{sc} = k_s - k_c^{\parallel}$ is the momentum transfer to the spin waves (section 2.6). Since these dark states do not contain the excited state $|e\rangle$, they are immune to spontaneous emission[185]. The collective dark states provide a robust method of mapping a weak quantum field $\hat{\mathcal{E}}_s(z,t)$ to and from collective atomic excitations $\hat{\mathcal{S}}(z,t)$ via the adiabatic rotations of $\theta_d = 0 \leftrightarrow \pi/2$ (i.e., by controlling $\Omega_c(z,t)$).

2.5.2 Heisenberg-Langevin equations

As in section 2.3.1.1, we express the system Hamiltonian $\hat{H}_s^{(\rm map)}$ with slowly-varying operators (Eqs. 2.20 and 2.23) in the limit of continuum along $\hat{z}$ (i.e., $\sum_i \rightarrow \int_0^L n_A(z)dz$) and in the rotating frame,

$$\begin{aligned}\hat{H}_s^{(\rm map)} &= \int_0^L dz n_A(z)\{\hbar\Delta_c\hat{\sigma}_{ee}(z,t) - \hbar\delta\hat{\sigma}_{ss}(z,t) \\ &\quad - \underbrace{\left[\hbar g_d\hat{\mathcal{E}}_s(z,t)e^{ik_s z}\hat{\sigma}_{eg}(z,t) + \hbar\Omega_c(z,t)e^{ik_c z}\hat{\sigma}_{es}(z,t) + h.c.\right]}_{\hat{H}_{\rm int}^{(\rm map)}}\}, \end{aligned} \tag{2.70}$$

where $n_A(z)$ is the linear atomic density ($\int dz n_A(z) = N_A$).

Following the Heisenberg-Langevin approach (Eq. 2.29), we obtain a set of differential equations governing the atomic evolutions (assuming weak signal field approximation $g_d \ll \Omega_c$ and $\overline{n}_s \ll N_A$)

$$\partial_t\hat{\sigma}_{se} = -(\gamma_{se} + i(\Delta_c - w_{gs}) - i\delta)\hat{\sigma}_{se} + i\Omega_c e^{i(k_c^{\parallel}-k_s)z}(\hat{\sigma}_{ss} - \hat{\sigma}_{ee}) + ig_d\hat{\mathcal{E}}_s\hat{\sigma}_{ge} + \hat{F}_{se} \tag{2.71}$$

$$\partial_t\hat{\sigma}_{gs} = -\gamma_{gs}\hat{\sigma}_{gs} + i\Omega_c^* e^{-i(k_c^{\parallel}-k_s)z}\hat{\sigma}_{ge} - ig_d\hat{\mathcal{E}}_s\hat{\sigma}_{es} + \hat{F}_{gs} \tag{2.72}$$

$$\partial_t\hat{\sigma}_{ge} = -(\gamma_{ge} + i\Delta_c)\hat{\sigma}_{ge} + i\Omega_c e^{i(k_c^{\parallel}-k_s)z}\hat{\sigma}_{gs} + ig_d\hat{\mathcal{E}}_s(\hat{\sigma}_{gg} - \hat{\sigma}_{ee}) + \hat{F}_{ge}, \tag{2.73}$$

and a propagation equation for the quantum field $\hat{\mathcal{E}}_s(z,t)$ in an effective one-dimension (Eq. 2.39),

$$(\partial_t + c\partial_z)\,\hat{\mathcal{E}}_s(z,t) = ig_d n_A(z)L\hat{\sigma}_{ge}(z,t). \tag{2.74}$$

Here, $\hat{F}_{\mu\nu}$ are the quantum Langevin operators for the atomic operators $\hat{\sigma}_{\mu\nu}$, as described in section 2.3.

2.5.2.1 Weak field approximation and adiabatic condition

In the weak signal field approximation with g_d ($\sigma_{gg} \simeq 1 \gg \sigma_{ee}, \sigma_{ss}, \sigma_{es} \simeq 0$) and with negligible spin-wave dephasing $\gamma_{gs} \simeq 0$ over the interaction time δt_c, we approximate $\hat{\sigma}_{ge} = -i\left(e^{i(k_c^{\parallel}-k_s)z}/\Omega_c^*\right)\partial_t\hat{\sigma}_{gs}$ (Eq.

[1] $\vec{\epsilon}_{eg}$ and $\vec{\epsilon}_s$ are the respective polarization vectors for the atomic dipole ($|g\rangle - |e\rangle$ transition) and the signal field.

2.72) and obtain the coupled equations of motions (by substituting $\hat{\sigma}_{ge}$ into Eq. 2.74, and using Eq. 2.73)

$$(\partial_t + c\partial_z)\,\hat{\mathcal{E}}_s(z,t) \simeq \frac{g_d n_A(z) L}{\Omega_c^*(z,t)} e^{i(k_c^{\parallel}-k_s)z}\partial_t\hat{\sigma}_{gs} \tag{2.75}$$

$$\hat{\sigma}_{gs} \simeq -\frac{g_d\hat{\mathcal{E}}_s}{\Omega_c}e^{-i(k_c^{\parallel}-k_s)z} \underbrace{-\frac{\gamma_0}{|\Omega_c|^2}\partial_t\hat{\sigma}_{gs} - \frac{1}{|\Omega_c|^2}\partial_t^2\hat{\sigma}_{gs}}_{\text{(Non-adiabatic terms)}} + i\frac{e^{-i(k_c^{\parallel}-k_s)z}}{\Omega_c}\hat{F}_{ge}, \tag{2.76}$$

where $\gamma_0 = \gamma_{ge} + i\Delta_c$.

In the adiabatic condition[86,190,191] ($\frac{\partial_t\Omega_c}{\Omega_c} \sim \frac{1}{\delta t_c} \ll \gamma_{ge}\tilde{d}_0(L)$ with resonant optical depth given by $\tilde{d}_0(z) = \int_0^z dz' \frac{2g_d^2 n_A(z')z}{\gamma_{ge}c}$), we perturbatively expand Eq. 2.76 to the order of $\partial_t\hat{\mathcal{O}} \sim \hat{\mathcal{O}}/\delta t_c$, and we obtain the lowest-order perturbation $\hat{\sigma}_{gs} \simeq -\frac{g_d\hat{\mathcal{E}}_s}{\Omega_c}e^{-i(k_c^{\parallel}-k_s)z}$. Thus, we obtain the adiabatic equation of motion for the quantum field $\hat{\mathcal{E}}_s(z,t)$

$$(\partial_t + c\partial_z)\,\hat{\mathcal{E}}_s(z,t) \simeq \frac{g_d^2 n_A(z) L}{\Omega_c^*(z,t)}\frac{\partial}{\partial t}\left(\frac{\hat{\mathcal{E}}_s(z,t)}{\Omega_c(z,t)}\right). \tag{2.77}$$

We note that the characteristic pulse widths $\delta t_c \simeq 10$ ns of the control laser (or the read laser) in our experiments are on the same order of magnitude as the adiabatic criteria $1/\delta t_c \simeq \gamma_{ge}\tilde{d}_0(L)$, where the resonant transmission (absent the control laser) is defined as $T_0 = e^{-\tilde{d}_0(L)}$. Thus, instead of the simplified wave equation (Eq. 2.77), we numerically solve the coupled differential equations of motions (Eqs. 2.71–2.74) in chapter 6.

2.5.2.2 Coherent atomic medium and EIT

In Eq. 2.77, we recover the usual wave equation with slow-light phenomena in *static* EIT (with static control field $\Omega_c(z,t) = \Omega_c$) with modified group velocity $v_g = c\cos^2\theta_d$. Furthermore, if there is very little population in $\hat{\sigma}_{ss}$ and $\hat{\sigma}_{se}$, the control field $\Omega_c(z,t) \simeq \Omega_c(t - z/c)$ propagates according to the free-space wave equation ($(\partial_t + c\partial_z)\,\Omega_c(z,t) = 0$). In this case, we obtain a wave equation with variable group velocity $v_g(z,t)$; namely,

$$\left(\frac{\partial}{\partial t} + v_g(z,t)\frac{\partial}{\partial z}\right)\hat{\mathcal{E}}_s(z,t) = 0, \tag{2.78}$$

where the group velocity $v_g(z,t) = c\cos^2\theta_d(z,t)$ is dynamically controlled by the Rabi frequency $\Omega_c(z,t)$ of the control laser. Here, the mixing angle is given by $\cos\theta_d = \frac{\Omega_c}{\sqrt{g_d^2 N_A + \Omega_c^2}}$ for constant density $n_A = N_A/L$.

We now briefly turn to a more classic situation encountered in EIT (see also chapter 6). For a resonant control field with $\Delta_c = 0$, the EIT medium behaves as a non-absorbing dispersive media within the transparency window given by Ω_c at the two-photon resonance $\delta = 0$ shown in Fig. 2.4. The adiabatic approximation in section 2.5.2.1 in essence compares the pulse bandwidth to the EIT window Ω_c. If the pulse bandwidth $\Delta w_s \simeq 2\pi/\delta t_c \simeq \Omega_c$, higher-order dispersion must be taken into account. Specifically, the

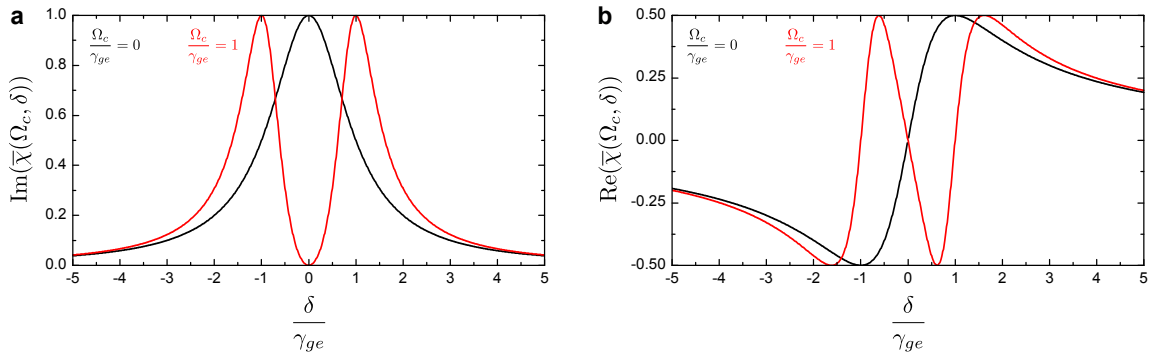

Figure 2.4: **Susceptibility $\overline{\chi}_s$ of EIT medium.** **a**, Imaginary part of the susceptibility function, $\mathrm{Im}(\overline{\chi}_s(\Omega_c,\delta))$. **b**, Real part of the susceptibility function $\mathrm{Re}(\overline{\chi}_s(\Omega_c,\delta))$. We show the dispersions of the EIT medium (red line) with a control laser Rabi frequency $\Omega_c/\gamma_{ge}=1$, as well as for the bare atomic medium (black line) with $\Omega_c=0$. Dynamic control of the group velocity (i.e., $v_g=\frac{c}{1+(w_{eg}-\delta)dn/d\delta}$ at $\delta=0$) allows shape-preserving acceleration/deceleration of the signal field in the presence of transparency $\mathrm{Im}(\overline{\chi}_s)\simeq 0$ at $\delta=0$.

susceptibility χ_s of the signal field in a homogeneous EIT medium (defined as $\mathcal{P}(z,t)=\epsilon_0\chi_s\mathcal{E}_s(z,t)$) for a resonant control field ($\Delta_c=0$) is given by (refs.[94,143])

$$\chi_s=\frac{2g_d^2N_A}{w_s}\overline{\chi}_s, \tag{2.79}$$

where $\overline{\chi}_s=\frac{\delta}{|\Omega_c|^2-\delta^2-i\gamma_{ge}\delta}$ is the normalized susceptibility function and $\mathcal{P}(z,t)=\sqrt{N_A}\hat{\sigma}_{ge}$ is the atomic polarization. $\mathrm{Im}(\overline{\chi}_s(\Omega_c,\delta))$ describes the transparency for the signal field at $\delta=0$ with the transmission given by $T(\Omega_c,\delta)=\exp\left(-k_sL\mathrm{Im}(\chi_s)\right)=\exp\left(-\tilde{d}_0\mathrm{Im}(\overline{\chi}_s)\right)$ (Fig. 2.4a), whereas $\mathrm{Re}(\overline{\chi}_s(\Omega_c,\delta))$ contributes to the refractive index $n_s(\delta)=\sqrt{1+\mathrm{Re}(\chi_s)}$ for the signal field (group velocity given by $v_g=\frac{c}{1+(w_{eg}-\delta)dn/d\delta}$) (Fig. 2.4b)[m].

Perturbatively expanding χ_s (Eq. 2.79) around $\frac{\delta}{\Omega_c}\ll 1$, we find $\chi_s\simeq\frac{2g_d^2N_A}{w_s}\left(\frac{\delta}{|\Omega_c|^2}+i\frac{\delta^2\gamma_{eg}}{|\Omega_c|^4}+\mathcal{O}(\delta^3)\right)$, where the linear dispersion gives $v_g=c\cos^2\theta_d$. In addition, we find the bandwidth of the EIT medium via $T\simeq\exp(-\delta^2/\Delta w_{\mathrm{EIT}}^2)$, where the EIT bandwidth is $\Delta w_{\mathrm{EIT}}=\frac{|\Omega_c|^2}{\gamma_{eg}\sqrt{\tilde{d}_0}}$. This leads to an adiabatic condition, where the initial signal pulse's bandwidth Δw_s must be smaller than the bandwidth of the EIT medium Δw_{EIT}: i.e., $\Delta w_s<\Delta w_{\mathrm{EIT}}$. In addition, the adiabatic passage of the dark-state polariton[192] sets a limit to the rotation speed of the mixing angle θ_d of the polariton $\hat{\Psi}_d(z,t)$[n]. Introducing a characteristic time-scale δt_c, we obtain the criteria $\delta t_c>\frac{\gamma_{eg}v_g}{g_d^2N_Ac}$ for adiabatic following[86]. Finally, I note that we have so far neglected the presence of Zeeman population and assumed an ideal Λ-level system. In fact, the distribution of Zeeman populations can inhibit the presence of EIT unless a special polarization scheme is employed (chapter 6).

[m] More generally, the "transfer" function of the signal field in the EIT medium is given by $t(\Omega,\delta,z)=\exp(ikz\chi_s/2)$, where the transmission is $T=|t|^2$.

[n] In fact, the rotation speed $\dot{\theta}_d$ of the mixing angle is proportional to the transition rate between $\hat{\Psi}_d(z,t)$ and $\hat{\Psi}_b(z,t)$.

2.5.3 Dark-state polariton

As discovered by Fleischhauer and Lukin[86], we can equivalently introduce a new set of slow-light polaritonic excitations $\{\hat{\Psi}_d(z,t), \hat{\Psi}_b(z,t)\}$ as the normal modes of the system (Eqs. 2.75–2.76) in the weak signal approximation. Namely, we have

$$\hat{\Psi}_d(z,t) = \cos\theta_d(t)\hat{\mathcal{E}}_s(z,t) - \sin\theta_d(t)\hat{\mathcal{S}}(z,t) \tag{2.80}$$

$$\hat{\Psi}_b(z,t) = \sin\theta_d(t)\hat{\mathcal{E}}_s(z,t) + \cos\theta_d(t)\hat{\mathcal{S}}(z,t), \tag{2.81}$$

where $\hat{\mathcal{S}}(z,t) = \sqrt{N_A}e^{i(k_c^{\parallel}-k_s)z}\hat{\sigma}_{gs}(z,t)$ is the slowly-varying phase-matched collective spin operator, and $\theta_d = \arctan(g_d\sqrt{N_A}/\Omega_c)$ is the mixing angle. These operators are known as the dark-state (bright-state) polaritons $\hat{\Psi}_d(z,t)$ ($\hat{\Psi}_b(z,t)$), in direct analogy with the classic dark (bright) states $|d\rangle = \cos\theta_d|g\rangle - \sin\theta_d|s\rangle$ ($|b\rangle = \sin\theta_d|g\rangle + \cos\theta_d|s\rangle$) observed in coherent population trapping (chapter 6). These polaritons follow the quasi-bosonic commutation relations[86] (with the help of Eq. 2.25),

$$\left[\hat{\Psi}_{d,k}(t), \hat{\Psi}^{\dagger}_{d,k'}(t')\right] \simeq \left[\hat{\Psi}_{b,k}(t), \hat{\Psi}^{\dagger}_{b,k'}(t')\right] \simeq \delta_{kk'}\delta(t-t'), \tag{2.82}$$

where $\hat{\Psi}_d(z,t) = \frac{2\pi}{L}\int dk\hat{\Psi}_{d,k}(t)e^{ikz}$ and $\hat{\Psi}_b(z,t) = \frac{2\pi}{L}\int dk\hat{\Psi}_{b,k}(t)e^{ikz}$.

In the adiabatic limit, where $\Omega_c\hat{\sigma}_{gs} + g_d\hat{\mathcal{E}}_s e^{-i(k_c^{\parallel}-k_s)z} \simeq 0$ (Eq. 2.76), the bright-state polariton is $\hat{\Psi}_b \simeq 0$. In this limit, we can write the equation of motions for the dark-state polariton $\hat{\Psi}_d$ with the perturbation $\hat{\mathcal{S}}(z,t) \simeq -\frac{g_d\hat{\mathcal{E}}_s}{\Omega_c}$ (Eq. 2.77) as (ref.[86]),

$$\left(\frac{\partial}{\partial t} + v_g\frac{\partial}{\partial z}\right)\hat{\Psi}_d(z,t) = 0. \tag{2.83}$$

Thus, in the adiabatic regime, the dark-state polariton $\hat{\Psi}_d(z,t)$ follows the usual wave equation as in free-space with the group velocity $v_g = c\cos^2\theta_d$ determined by the 'amount' of the photonic component (signal field $\hat{\mathcal{E}}_s$; i.e., $\cos^2\theta_d$) in the polariton $\hat{\Psi}_d(z,t)$.

2.5.4 Adiabatic following of dark-state polariton

The dark state polariton $\hat{\Psi}_d(z,t) = \cos\theta_d(t)\hat{\mathcal{E}}_s(z,t) - \sin\theta_d(t)\hat{\mathcal{S}}(z,t)$ can be considered as a beamsplitter transformation between a signal mode $\hat{\mathcal{E}}_s(z,t)$ and a spin-wave mode $\hat{\mathcal{S}}(z,t)$, with the effective matter-light interaction Hamiltonian written as (Eq. 2.70)

$$\hat{H}^{(\text{map})}_{\text{int}} = i\dot{\theta}_d(z,t)\left(\hat{\mathcal{E}}_s(z,t)\hat{\mathcal{S}}^{\dagger}(z,t) - \hat{\mathcal{E}}^{\dagger}_s(z,t)\hat{\mathcal{S}}(z,t)\right). \tag{2.84}$$

We illustrate the adiabatic evolution of dark-state polariton $\hat{\Psi}_d$ in Fig. 2.5. At the initial step (1), with $\tau = 0$, we first apply a control laser with Rabi frequency $\Omega_c(z,t)$ (resonant to the $|e\rangle \rightarrow |s\rangle$) to open the

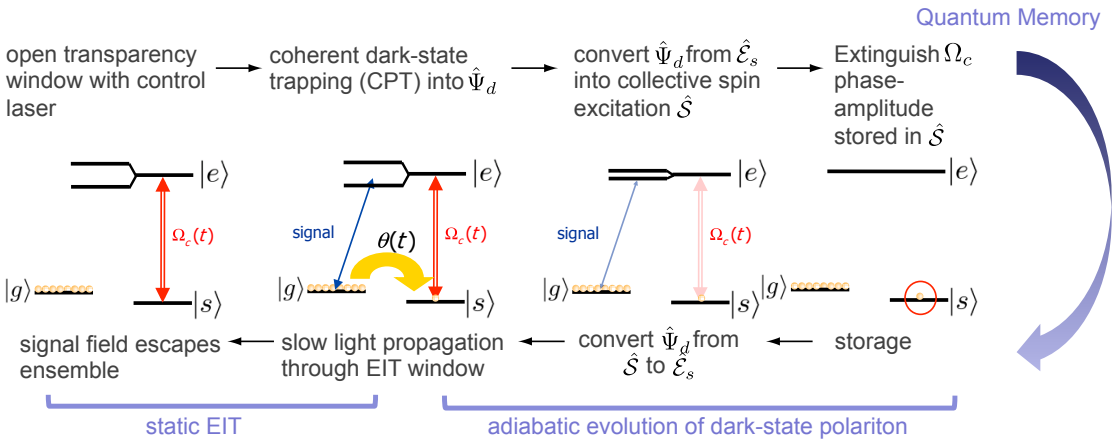

Figure 2.5: **Coherent evolution of dark state polariton.** First, we open the transparency window Ω_c with the control laser. As the signal field enters the EIT medium, it prepares the joint atom-field state in a dark state $\hat{\Psi}_d \simeq \hat{\mathcal{E}}_s(z,t)$. By adiabatically reducing the control laser's intensity to zero, we transfer the phase-amplitude information of the signal field $\hat{\mathcal{E}}_s(z,t)$ to the collective excitations $\hat{\mathcal{S}}(z,t)$. After a delay, we apply the control laser to coherently transfer the collective excitation $\hat{\mathcal{S}}(z,t)$ to the signal field $\hat{\mathcal{E}}_s(z,t)$ in a time reversal fashion. The signal field undergoes a slow-light propagation through the EIT medium, after which $\hat{\mathcal{E}}_s(z,t)$ escapes the ensemble.

transparency window in a counter-intuitive configuration[180] for the signal field $\hat{\mathcal{E}}_s(z,t)$, where the dark-state polariton $\hat{\Psi}_d = \hat{\mathcal{E}}_s$ is purely photonic (with $\Omega_c(z,t) \gg g_d\sqrt{N_A}$ and $\theta_d = 0$)[o]. In step (2), as the signal field enters the coherently dressed atomic media, the intensity for $\Omega_c(z,t)$ is adiabatically reduced to zero (thereby, $\theta_d = 0 \to \pi/2$), simultaneously decelerating the signal field[p] and transferring the phase-amplitude information of the photonic excitations $\hat{\mathcal{E}}_s$ to the collective atomic excitations $\hat{\mathcal{S}}$. In step (3), we store the spin-wave excitation for a controllable memory time τ. At the end of step (3), we apply the control laser in step (4) to reaccelerate the dark-state polariton $\hat{\Psi}_d$ back to the free-space velocity $v_g = c$, thereby coherently transferring the spin-wave amplitude $\hat{\mathcal{S}}$ back to the signal field $\hat{\mathcal{E}}_s$ (i.e., $\hat{\Psi}_d = \hat{\mathcal{S}} \to \hat{\mathcal{E}}_s$ with $\theta_d = \pi/2 \to 0$). Finally in step (5), the retrieved signal field $\hat{\mathcal{E}}_s$ propagates within the center of the transparency window with minimum absorption and escapes the EIT medium.

2.5.5 Non-adiabatic equations of motions

The dark-state polariton equation (Eq. 2.83) does not include any non-adiabatic terms, which account for the finite-bandwidth of the EIT medium and the non-adiabatic transitions between dark-state and bright-state polaritons[86,192]. More generally, we need to solve the complete equations of motions in Eqs. 2.71–2.74 with the weak signal approximation ($\sigma_{gg} \simeq 1 \gg \sigma_{ee}, \sigma_{ss}, \sigma_{es} \simeq 0$).

Here, we introduce a slowly-varying atomic polarization $\mathcal{P}(z,t) = \sqrt{N_A}\hat{\sigma}_{ge}$ induced by $\hat{\mathcal{E}}_s(z,t)$ in the

[o]For the single-excitation manifold, the dark state (Eq. 2.69) is $|\overline{g}_a, 1_s\rangle$, which is also the initial state of the system.

[p]The deceleration of the signal field is accompanied by a compression of the signal field due to the reduced group velocity v_g, where the tail of the wavepacket for the signal field catches up with the slowly propagating front part of the wavepacket. This allows us to 'fit' the signal field's wavepacket ($L_s \simeq 10$ m) within a small ensemble ($L \simeq 3$ mm).

dispersive coherent medium, and the slowly-varying phase-matched spin-wave operator $\hat{\mathcal{S}}(z,t) = \sqrt{N_A}\, e^{i(k_c^{\parallel}-k_s)z}\hat{\sigma}_{gs}$ defined in section 2.3.1.3. The dynamics of the signal field $\hat{\mathcal{E}}_s(z,t)$ and the spin-wave mode $\hat{\mathcal{S}}(z,t)$ is governed by a set of Heisenberg-Langevin equations (Eqs. 2.71–2.74),

$$
\begin{aligned}
(\partial_t + c\partial_z)\,\hat{\mathcal{E}}_s(z,t) &= ig_d n_A(z)\frac{L}{\sqrt{N_A}}\hat{\mathcal{P}}(z,t) && (2.85)\\
\partial_t\hat{\mathcal{P}}(z,t) &= -(\gamma_{ge}+i\Delta)\hat{\mathcal{P}}(z,t) + ig_d\sqrt{N_A}\hat{\mathcal{E}}_s(z,t) + i\Omega_c(z,t)\hat{\mathcal{S}} + \sqrt{2\gamma_{ge}}\hat{F}_P && (2.86)\\
\partial_t\hat{\mathcal{S}}(z,t) &= -\gamma_{gs}\hat{\mathcal{S}}(z,t) + i\Omega_c^*(z,t)\hat{\mathcal{P}} + \sqrt{2\gamma_{gs}}\hat{F}_S. && (2.87)
\end{aligned}
$$

Here, $\hat{F}_P$ and $\hat{F}_S$ are the respective δ-correlated Langevin noise operators for $\hat{\mathcal{P}}(z,t)$ and $\hat{\mathcal{S}}(z,t)$, with non-zero terms $\langle \hat{F}_P(z,t)\,\hat{F}_P^{\dagger}(z',t')\rangle = L\delta(z-z')\delta(t-t')$ and $\langle \hat{F}_S(z,t)\hat{F}_S^{\dagger}(z',t')\rangle = L\delta(z-z')\delta(t-t')$. Since the normally ordered noise operators $\langle \hat{F}_i^{\dagger}\hat{F}_i\rangle = 0$ with $i \in \{\mathcal{S},\mathcal{P}\}$ for vacuum reservoirs, we neglect them in the numerical calculation of chapter 6 (see section 2.3.1.2).

We emphasize that the collective enhancement ($\sqrt{N_A}$) of single atom-photon coupling constant g_d (Eqs. 2.85–2.87) enables a strong collective matter-light interaction with an effective coupling constant $g_{\text{eff}} = \sqrt{N_A}g_d$ between a single spin-wave of the ensemble and a single photon of the signal field. We are interested in the collectively enhanced storage (η_{s}) and retrieval (η_{r}) efficiency $\eta_{sr} = \eta_{\text{s}}\eta_{\text{r}}$ of the quantum field $\hat{\mathcal{E}}_s(z,t)$, which we define as the ratio of the number $\int dz\langle\hat{\mathcal{E}}_s^{\dagger}(z,t)\hat{\mathcal{E}}_s(z,t)\rangle$ of incoming photonic excitations in the signal field to the number of stored spin-wave excitations $\int dz\langle\hat{\mathcal{S}}^{\dagger}(z,t)\hat{\mathcal{S}}(z,t)\rangle$ (and vice versa). Specifically, for an atomic ensemble with finite optical depth $\tilde{d}_0$, there is an optimal control field $\Omega_c(z,t)$, which maximizes the transfer efficiency η_{sr}, by compromising two competing goals[186]: (1) The characteristic time variation δt_c in the control laser $\dot{\Omega}_c(z,t)$ must be slow relative to the two adiabatic criteria ($\Delta w_s \simeq \frac{2\pi}{\delta t_c} < \Delta w_{\text{EIT}}$ and $\delta t_c > \frac{\gamma_{eg}v_g}{g_d^2 N_A c}$), identified in section 2.5.2.2, to avoid dissipations of $\hat{\mathcal{P}}(z,t)$. A stronger control laser is preferable, as it provides a wider transparency window and minimizes spontaneous decay loss. On the other hand, (2) $\Omega_c(z,t)$ must small in order to localize and compress the incoming signal field's wavepacket ($L_s \simeq 10$ m) within the atomic sample ($L \simeq 3$ mm) to avoid significant leakage of the signal field.

2.5.5.1 Mapping photonic quantum states into and out of collective excitations

For a given optical depth $\tilde{d}_0$, there is an optimal Rabi frequency $\Omega_c(z,t)$ for the control field. In the experiment[30], we set $\tilde{d}_0$ and $\Omega_c(z,t)$ at 20 and 24 MHz, respectively. We show an example of our measurements of the EIT process for a single ensemble in Fig. 2.6, whereby we demonstrate the reversible mapping of a coherent state $|\alpha\rangle$ into and out the atomic memory ($|\alpha|^2 = 0.3$ per pulse). Because of finite $\tilde{d}_0$, the small length ($L = 3$ mm) of the ensemble and the turn-off time of $\Omega_c(z,t)$, we observe a considerable leakage in the storage process. The peak beyond $\tau \geq 1$ μs represents the retrieved pulse after $\tau \simeq 1$ μs of storage. Overall, we find an excellent agreement between our measurements and the numerical simulation following the coupled equations of motions in Eqs. 2.85–2.87. We use the fitted function of the input signal field as the initial state with all other parameters from independent measurements. We find an overall storage and

retrieval efficiency of $\eta_{sr} = 22 \pm 3\%$, similar to the theoretical prediction $\eta_{sr}^{\text{theory}} = 23\%$ (Fig. 2.6).

Experimentally, to avoid the dissipative absorption of the signal field $\hat{\mathcal{E}}_s(z,t)$ for our choice of polarization (σ_+ polarization), we optically pumped the atomic ensemble into a clock state $6S_{1/2}$, $|F = 4, m_F = 0\rangle$ with 90% efficiency. Initially, the strong control field $\Omega_c(z,t)$ (resonant with $6S_{1/2}, F = 3 \leftrightarrow 6P_{3/2}, F = 4$ transition with σ_+ polarization) opens the transparency window $\Omega_c(z,t) \simeq 24$ MHz for the signal mode. As the wave packet $\hat{\mathcal{E}}_s(z,t)$ of the signal field propagates through the ensemble, we extinguish the control fields $\Omega_c(z,t)$ in 20 ns, thereby coherently transforming the coherent state of the signal mode $\hat{\mathcal{E}}_{s,\text{in}}(z,t)$ to collective atomic excitation $\hat{\mathcal{S}}(z,t)$. After $\simeq 1.1$ μs, the atomic state is converted back to the signal mode $\hat{\mathcal{E}}_{s,\text{out}}(z,t)$ by switching on the control field $\Omega_c(z,t)$. We measure the normalized cross-correlation function for the input photonic state $\hat{\mathcal{E}}_{s,\text{in}}(z,t)$ with $g_{\text{in}}^{(2)} = 1.1 \pm 0.2$, as well as for the output photonic state $\hat{\mathcal{E}}_{s,\text{out}}(z,t)$ with $g_{\text{out}}^{(2)} = 1.0 \pm 0.2$, whereby we observe no degradation in the photon statistics.

In chapter 6, we discuss an experiment where we reversibly mapped a photonic entanglement into and out of quantum memories. We further examine the optimal control theory developed in ref.[188], where we theoretically apply the principle of time-reversal symmetry to optimize our reversible quantum interface.

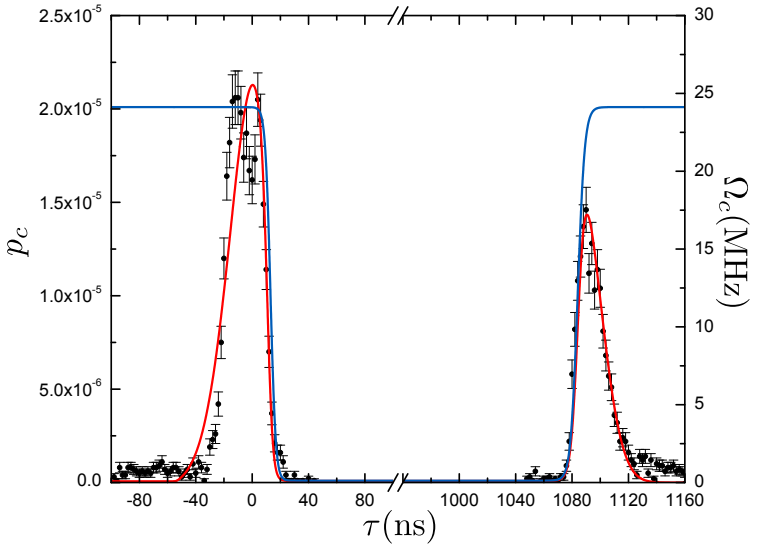

Figure 2.6: **Reversible mapping of a coherent state to and from an atomic memory.** The points around $\tau \simeq 0$ ns (i.e., -40 to 20 ns) represent the leakage of the signal field due to the finite optical depth and length of the ensemble. The points beyond $\tau \simeq 1$ μs show the retrieved signal field. The blue solid line is the estimated Rabi frequency $\Omega_c(z,t)$ of the control pulse, where we assumed $\Omega_c(t - z/c)$. The red solid curve is from a numerical calculation solving the equation of motion of the signal field in a coherently dressed medium (section 2.5.5). Error bars give the statistical error of 1 s.d for each point.

2.5.5.2 Collective enhancement: Reading spin waves

Heralded spin-waves generated from the parametric Raman interaction (section 2.3) can also be coherently transferred to photons in field 2 (with $\hat{\mathcal{E}}_s(z,t)$ replaced by $\hat{\mathcal{E}}_2(z,t)$). In particular, the initial states are $\hat{\mathcal{E}}_2(z,0) = 0$ and $\hat{\mathcal{S}}(z,0)$ with the spin-wave spatio-temporal mode $\hat{\mathcal{S}}(z,0)$ taken from the solution of Eqs. 2.47–2.48, evolved from the parametric interaction. We can then rigorously solve the non-adiabatic equations of motions (Eqs. 2.85–2.87) in the polaritonic picture. In practice, neglecting the spatio-temporal modes and self-consistent treatments of fluctuation and dissipation from first principles, we may model the mapping process as a beamsplitter transformation (a pseudo-model) from the spin-wave mode to the field 2 mode, where the readout noise is simulated by adding coherent-state reservoirs [193] (see chapter 9).

2.6 Decoherence

We have so far neglected the presence of spin-wave decoherence for $\hat{\sigma}_{gs}$ by setting $\gamma_{gs} = 0$ (e.g., neglecting spin-exchange collisions). Practically, this is a good approximation, given that the interaction times $\delta t_{w,r}$ for the writing and reading processes are fast compared to the relevant coherence times. However, if the delay τ between the storage and retrieval processes is longer than the coherence time τ_m of the spin waves, we must also include various spin-wave dynamics induced by the decoherence mechanisms. Here, we will review two major dissipative contributions[q] to spin-wave coherence in our experiment: (1) Inhomogeneous broadening and (2) motional dephasing.

2.6.1 Inhomogeneous broadening of spin waves

In our experiment, inhomogeneous broadenings of spin waves are dominated by two factors: (1) Inhomogeneous light shifts between $|g\rangle - |s\rangle$ (in the case of a nano-fiber trap in chapter 10), and from (2) inhomogeneous Zeeman broadening (see, e.g., chapters 4–5). Here, we describe a one-dimensional model[r] for the second type of decoherence mechanism. This model, however, should also be applicable to the first type of decoherence. The Zeeman decoherence model described in this section is similar to the one developed by Daniel Felinto [147].

We assume an initial atom-field state $\hat{\rho}_{\mathrm{a}\gamma_1} = \hat{\rho}_{\mathrm{a}}(0) \otimes \hat{\rho}_{\gamma_1}(0)$, where $\hat{\rho}_{\mathrm{a}}(0) = p_{m_{F_g}} |F_g, m_F\rangle\langle F_g, m_F|$ is the initial atomic state with Zeeman populations p_{m_F}, and $\hat{\rho}_{\gamma_1}(0) = |0_{\vec{k}_1}\rangle\langle 0_{\vec{k}_1}|$ is the initial vacuum state for field 1 (with all other modes traced over). In the single-excitation limit, a photoelectric event in field 1 (with unit detection efficiency) heralds an atomic state $\hat{\rho}_{\mathrm{a}}(t_w) = |\psi(t_w)\rangle_{\mathrm{a}}\langle\psi(t_w)|$ containing a single spin-wave excitation, with

$$|\psi(t_w)\rangle_{\mathrm{a}} = \frac{1}{\sqrt{N_A}} \left(\sum_i e^{i(\vec{k}_w \cdot \vec{r}_i - k_1 z_i)} |g_1, \cdots, g_{i-1}, \tilde{s}_i(t_w), g_{i+1}, \cdots, g_{N_A}\rangle \right), \tag{2.88}$$

where $e^{i(\vec{k}_w \cdot \vec{r}_i - k_1 z_i)}$ gives the phase-matching condition $(\vec{k}_w - \vec{k}_r) \cdot \vec{r}_i - (k_1 - k_2) z_i = 0$ during the reading process (section 2.6.2) and t_w is the time at the end of the write pulse. Here, given the initial atomic state $\hat{\rho}_{\mathrm{a}}(0)$ populated with multiple Zeeman sublevels, the single-atom spin flip $\tilde{s}_i(t_w)$ corresponds to a superposition of Zeeman-dependent hyperfine spin flips given by

$$|\tilde{s}_i(t_w)\rangle = \frac{1}{\sqrt{N_c}} \sum_{m_{F_g}, m_{F_s}} \sqrt{p_{m_{F_g}}} \sqrt{\xi^{q_w, q_1}_{m_{F_g}, m_{F_s}}} e^{i\mu_B \left(g_g m_{F_g} - g_s m_{F_s}\right) B_z(\vec{r}_i) t_w / \hbar} |s_{m_{F_s}}\rangle, \tag{2.89}$$

---

[q] Dispersive van der Waals interaction between the atomic dipoles $g_{vdW} \sim \frac{d_0^2}{4\pi\epsilon_0 r_{ij}^3}$ lead to a van der Waals dephasing for sufficiently high density. Generally, for high phase-space density, one may additionally consider elaborate collisional processes and radiation trapping [194] (due to imperfect optical pumping). Alternatively, the atoms can be trapped in an optical lattice to reduce collisional dephasing [116].

[r] The spatial variation of the magnetic field across the transverse directions can be neglected, given the aspect ratio of the atomic sample ($2w_0/L \simeq 2 \times 50\ \mu\mathrm{m}/3\ \mathrm{mm} \ll 1$). The inhomogeneous Zeeman broadening is thus dominated by the longitudinal inhomogeneity $B_z(z)$ of magnetic field.

where $N_c = \sum_{m_{F_g},m_{F_s}} \xi^{q_w,q_1}_{m_{F_g},m_{F_s}}$ is the normalization constant, $g_{g,s}$ are the respective g-factors for the ground states $\{|g\rangle,|s\rangle\}$, μ_B is the Bohr's magneton, $B_z(\vec{r}_i) = \vec{B}(\vec{r}_i)\cdot\hat{z}$ is the magnetic field projected along $\hat{z}$ at position $\vec{r}_i$, and $\xi^{q_w,q_1}_{m_{F_g},m_{F_s}}$ is the generalized effective coupling constant for the specific excitation pathway (see Eq. 2.49). Here, $q_{w,1}$ are the polarization helicities for the writing laser and the field 1.

This expression can be easily derived from $\xi = \tanh^2(i\int_0^\infty dt' \int_0^L dz \chi_p(z,t'))$ (Eq. 2.35) by generalizing the parametric coupling constant χ_p to accommodate Zeeman-dependent transition constants (which depends on the parameters $\{F_g, F_s, m_{F_g}, m_{F_s}, q_w, q_1\}$ via the various Cleabsh-Gordan coefficients). Alternatively, Eq. 2.89 can be derived from the mapping Hamiltonian $\hat{H}^{(\text{map})}_{\text{tot}}$. In writing Eqs. 2.88–2.89, I assumed the effective single-mode model for parametric interaction $\xi^{q_w,q_1}_{m_{F_g},m_{F_s}}$ in section 2.3.2.2, where the beam-waist of the writing laser is substantially larger than that of the quantum field. The Larmor precession of a single-atom spin-flip after a delay τ is then described by

$$\langle \tilde{s}_i(t_w+\tau)|\tilde{s}_i(t_w)\rangle = \frac{1}{N_c}\sum_{m_{F_g},m_{F_s}} p_{m_{F_g}} \xi^{q_w,q_1}_{m_{F_g},m_{F_s}} e^{i\mu_B\left(g_g m_{F_g} - g_s m_{F_s}\right)B_z(\vec{r}_i)\tau/\hbar}. \tag{2.90}$$

To understand the collective dynamics of $\hat{\rho}_{\text{a}}(\tau)$, we now calculate the overlap function ${}_{\text{a}}\langle\psi(t_w+\tau)|\psi(t_w)\rangle_{\text{a}}$ between the initial collective state and the final collective state, where the retrieval efficiency η_r is ideally proportional to $|{}_{\text{a}}\langle\psi(t_w+\tau)|\psi(t_w)\rangle_{\text{a}}|^2$ (section 2.5). If we assume that the atoms are stationary so that the phase-matching condition is preserved, using Eqs. 2.88–2.90, we obtain the following overlap,

$$\begin{aligned} {}_{\text{a}}\langle\psi(t_w+\tau)|\psi(t_w)\rangle_{\text{a}} &= \frac{1}{N_A N_c}\sum_{m_{F_g}} p_{m_{F_g}} \xi^{q_w,q_1}_{m_{F_g},m_{F_g}+q_w-q_1} \\ &\quad\times \int_0^L dz n(z) e^{i\mu_B\left((g_g-g_s)m_{F_g} - g_s(q_w-q_1)\right)B_z(z)\tau/\hbar}, \end{aligned} \tag{2.91}$$

where we made the continuum approximation for the summation $\sum_i \to \int dz n(z)$ and assumed pure polarization states ($q_{w,1}$) for the writing laser and the field 1 (i.e., $m_{F_s} = m_{F_g} + q_w - q_1$).

Assuming a flat-top atomic distribution $n(z) = N_A/L$ and a quadratically inhomogeneous Zeeman shift $B_z(z) = (4\delta B_z/L^2)(z-L/2)^2$, we obtain

$${}_{\text{a}}\langle\psi(t_w+\tau)|\psi(t_w)\rangle_{\text{a}} = \frac{1}{N_c\sqrt{L}}\sum_{m_{F_g}} p_{m_{F_g}} \xi^{q_w,q_1}_{m_{F_g},m_{F_g}+q_w-q_1} f_d(\tau), \tag{2.92}$$

where the decay amplitude $f_d(\tau)$ for the Raman transition $m_{F_g} \to m_{F_s} = m_{F_g} + q_w - q_1$ is given by

$$f_d(\tau) = -\frac{\sqrt{i\pi}\,\text{erf}\left(\sqrt{-i\alpha_{m_{F_g}}\tau}\right)}{2\sqrt{\alpha_{m_{F_g}}\tau}}, \tag{2.93}$$

with a Zeeman-dependent decay constant $\alpha_{m_{F_g}} = \mu_B((g_g-g_s)m_{F_g} - g_s(q_w-q_1))\delta B_z/\hbar$. The function $\text{erf}(x) = \frac{2}{\sqrt{\pi}}\int_0^x dx' e^{-x'^2}$ is the error function. In Fig. 2.7, we show the result of our calculation

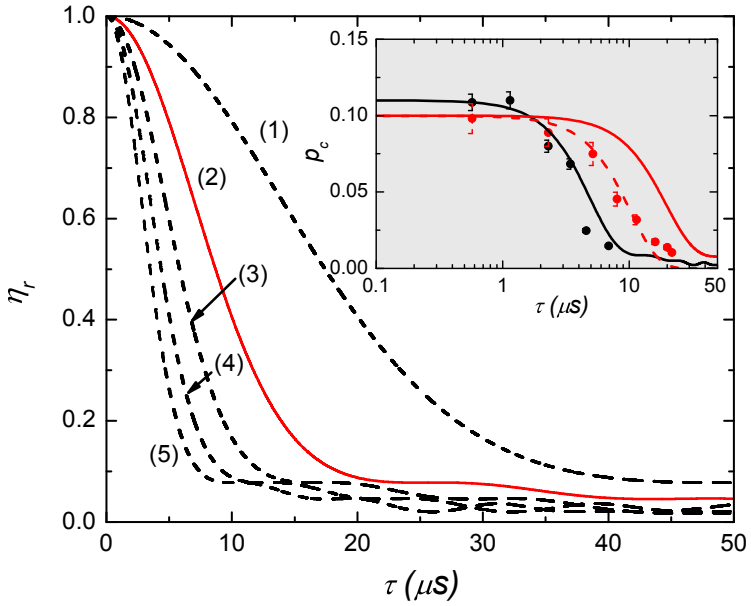

Figure 2.7: **Spin-wave decoherence due to inhomogeneous Zeeman broadening.** We show the normalized retrieval efficiency based on the theoretical expression $\eta_r \sim |_{\rm a}\langle\psi(t_w+\tau)|\psi(t_w)\rangle_{\rm a}|^2$ (Eq. 2.93) as a function of storage time τ, for (1) $\delta B_z = 10$, (2) 20, (3) 30, (4) 40, and (5) 50 mG. A typical experimental value for the inhomogeneous Zeeman broadening is $\delta B_z = 20$ mG (red line), after nulling the magnetic fields with bias coils (based on our measurement of off-resonant Raman spectroscopy [195]). We assumed the length of the ensemble to be $L = 3$ mm. The atomic cloud is initially prepared in the ground state $|g\rangle$ with uniform Zeeman distribution $p_{m_{F_g}} = 1/F_g$. In this calculation, $\{|g\rangle, |s\rangle, |e\rangle\}$ denote the levels $\{|6S_{1/2}, F = 4\rangle, |6S_{1/2}, F = 3\rangle, |6P_{3/2}, F = 4\rangle\}$. (inset) We measure the conditional probability p_c to detect a single-photon in field 2 as a function of τ. The expected Zeeman dephasing is $\tau_d \simeq 30$ μs (red line) at $\delta B_z \simeq 10$ mG (based on Raman spectroscopy), whereas the measured coherence time is only $\tau_d \simeq 12$ μs (red points). This result is consistent with the theoretical prediction for motional dephasing (red dashed line) in Fig. 2.8. For reference, we also plot the spin-wave coherence measurements at $\delta B_z \simeq 30$ mG (black points), which are consistent with Zeeman dephasing (black line). The vertical axes of the theory (black, red) lines for η_r are scaled to fit the experimental data for the photoelectric detection probability p_c of the field 2.

of the retrieval efficiency η_r after storage time τ. Note that the second-order approximation $B_z(z) = (4\delta B_z/L^2)(z - L/2)^2$ is reasonable for our experiment, since the Helmholtz bias coils can in principle cancel inhomogeneous Zeeman broadening only up to the first-order. Collective Larmor rephasing (oscillation in η_r at long τ), also known as dark-state polariton collapse and revival [119,120], is suppressed in our case of inhomogeneous Zeeman broadening by the additional factor of $2\sqrt{\alpha_{m_{F_g}}\tau}$ in the denominator.

Generally, the temporal profile of the spin-wave dephasing $\eta_r(\tau)$ due to Zeeman broadening depends on both the number density $n(z)$ and the inhomogeneous magnetic field $B_z(z)$ across the sample. Practically, the atomic density is approximately a Gaussian distribution $n(z) \sim e^{-4z^2/L^2}$ in our experiment. If we assume that the first-order (linear) Zeeman shift is dominant, with $B_z(z) = (\delta B_z/L)z$, the equivalent expression for $\langle\tilde{s}(t_w+\tau)|\tilde{s}(t_w)\rangle$ (see, e.g., Eq. 2.91) simply depicts a Fourier transform of $n(z)$, which results in a Gaussian decay of η_r. Thus, the temporal profile of $\eta_r(\tau)$ may provide some information about the spatial inhomogeneity of the Zeeman levels, given the measured atomic density $n(z)$.

2.6.2 Motional dephasing of spin waves

As seen in Eq. 2.88, the spin-wave dynamics is also dictated by the spatial coherence $\vec{k}_w \cdot \vec{r}_i - k_1 z_1$ of the spin-wave, which preserves the phase-matching condition required for collective enhancement. Here, we provide a simple model for motional dephasing

We first assume a linear atomic motion by $\vec{r}_i(t_w + \tau) = \vec{r}_i(t_w) + \vec{v}_i \tau$ during the storage time τ for the i^{th} atom. The final collective state after motional dephasing can thus be written as

$$|\psi(t_w + \tau)\rangle_{\text{a}} = \frac{1}{\sqrt{N_A}} \left(\sum_i e^{i\delta k (y_i(t_w) + v_{y,i}\tau)} |g_1, \cdots, g_{i-1}, \tilde{s}_i, g_{i+1}, \cdots, g_{N_A}\rangle \right), \tag{2.94}$$

where $\delta k = |\vec{k}_w - \vec{k}_1| \simeq k_w \sin\theta_{w1}$ is the net momentum transfer to the spin-wave (with a small angle approximation $\theta_{w1} \ll 1$ between the k-vectors of the writing laser and field 1 on the $y - z$ plane) and $v_{y,i} = \vec{v}_i \cdot \hat{y}$ is the atomic velocity projected along $\hat{y}$.

As we discussed in section 2.6.1, the retrieval efficiency is proportional to the overlap $|_{\text{a}}\langle\psi(t_w+\tau)|\psi(t_w)\rangle_{\text{a}}|^2$. If we assume a continuum limit for the momentum distribution $g(v)$ of the thermal atoms, the overlap is given by

$$_{\text{a}}\langle\psi(t_w + \tau)|\psi(t_w)\rangle_{\text{a}} \quad = \quad \int dv g(v) e^{i\delta k v \tau}. \tag{2.95}$$

For thermal atoms at T_d, as in our case of laser-cooled Cesium atoms $T_d \simeq 100\ \mu$K, the atomic motion follows the Maxwell-Boltzmann distribution $g(v) = e^{-mv^2/2k_B T_d}$. The retrieval efficiency $\eta_r(\tau) \sim |_{\text{a}}\langle\psi(t_w + \tau)|\psi(t_w)\rangle_{\text{a}}|^2$ is then (Fourier-transforming $g(v)$)

$$\eta_r = e^{-\tau^2/\tau_d^2}, \tag{2.96}$$

where $\tau_d = \lambda_s/2\pi v_s$ with $v_s = \sqrt{2k_B T_d/m}$. Here, we defined the spatial coherence length $\lambda_s = 2\pi/\delta k$ for the spin-wave with momentum transfer δk.

In Fig. 2.8, we show the temporal profile of the normalized retrieval efficiency η_r as a function of storage time τ (Eq. 2.96) for various temperatures T_d and for two different angles $\theta_{w1} \simeq 3^\circ$ ($\theta_{cs} \simeq 2^\circ$) between the two fields (thereby, varying the coherence length λ_s of the spin-wave). I note that there are two relevant factors which fully characterize the motional dephasing τ_d: (1) Atomic motion v_s and (2) spin-wave coherence length λ_s. By decreasing the temperature T_d of the atomic sample, we can reduce the mean velocity $v_s = \sqrt{2k_B T_d/m}$, and thereby increase the coherence time, as shown in Fig. 2.8. By placing an optical lattice along the momentum transfer $\delta\vec{k} \parallel \hat{y}$[s], the atomic motion can also be dramatically reduced[115–117,196] (see also Fig. 1.3 in chapter 1). On the other hand, to improve τ_c, it is also possible to increase the spin-wave coherence length $\lambda_s = 2\pi/\delta k$ for a given v_s (Fig. 2.8) by moving to a collinear geometry ($\vec{k}_w \parallel \vec{k}_1$) with

[s] In this case, it is important to also consider the inhomogeneous light shifts between $|g\rangle - |s\rangle$ from the optical lattice, as discussed in the previous section.

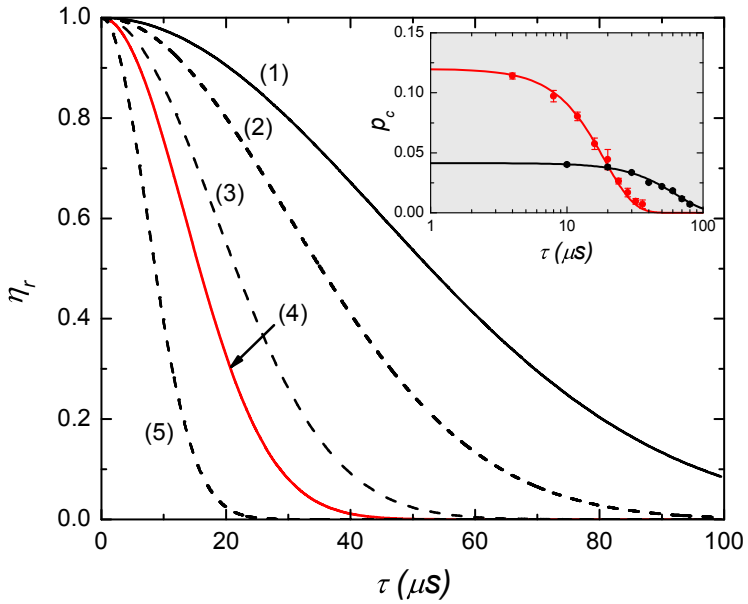

Figure 2.8: **Spin-wave dephasing due to atomic motion.** We show the normalized retrieval efficiency based on the theoretical expression $\eta_r \sim |_{\rm a}\langle\psi(t_w+\tau)|\psi(t_w)\rangle_{\rm a}|^2$ (Eq. 2.96) as a function of storage time τ, for (1) $T_d = 30$ μK (with $\theta_{w1} = 2°$), and for (2) $T_d = 80$ μK (with $\theta_{w1} = 3°$), (3) $T_d = 150$ μK (with $\theta_{w1} = 3°$), (4) $T_d = 250$ μK (with $\theta_{w1} = 3°$), (5) $T_d = 550$ μK (with $\theta_{w1} = 3°$). (inset) A typical experimental value for the motional dephasing is $\tau_d \simeq 20$ μs ($T_d \simeq 150$ μK, $\theta_{w1} \simeq 3°$), as shown in the inset with experimental data (red points) and theory line (3) (red line). After optimizing polarization gradient cooling ($T_d \simeq 30$ μK) and optical pumping to clock state $|F = 4, m_F = 0\rangle$ (along with the increase in the spin-wave coherence length via $\theta_{cs} \simeq 2°$), we further achieve a memory time of ~ 65 μs (black points) for storing and retrieving a coherent state. The vertical axes of the theory (black, red) lines for η_r are scaled to fit the experimental data for the photoelectric detection probability p_c of the fields (signal field, field 2).

Zeeman storage (at the magic magnetic field), thereby to $\delta\vec{k} = \vec{k}_w - \vec{k}_1 \simeq 0$ (with coherence length $\lambda_s \simeq 3$ cm $\gg L, w_0$ eventually extending beyond the size of the atomic sample). In this case, the storage time τ due to atomic motion will be limited by the collisional dephasing[116,117] and by the loss of atoms from the excitation volume[78].

In the inset of Fig. 2.8, we show our measurement for the decay of the (conditional) photoelectric detection probability p_c of a signal (field 2) pulse after a storage time τ for a coherent state $|\alpha\rangle$ with $|\alpha|^2 \simeq 0.9$ per pulse (for a heralded collective excitation), shown by black (red) points. In particular, after cooling the atoms to $T_d \simeq 30$ μK, optical pumping to the clock state, and increasing the spin-wave coherence length by reducing $\theta_{cs} = 3° \to 2°$, we achieve a memory time of ~ 65 μs for storing and retrieving a coherent state, a substantial improvement relative to the result in chapter 6.

Chapter 3

Characterization of heralded entanglement between two atomic ensembles

This chapter is largely based on ref. [34]. Reference [34] refers to the then current literature in 2007 at the time of publication.

3.1 Introduction

Beyond a fundamental significance, quantum control of entanglement between material systems is an essential capability for quantum networks and scalable quantum communication architectures (refs. [9,162], see also chapter 1). In recent years, significant advances have been achieved in the control of the quantum states of atomic systems, including entanglement of trapped ions [197,198] and between macroscopic spins [59]. By following the seminal paper of Duan, Lukin, Cirac, and Zoller (*DLCZ*) (ref. [4], chapter 2), entanglement between single collective excitations stored in two remote atomic ensembles has also been demonstrated [27]. In the *DLCZ* protocol, entanglement is created in a probabilistic but heralded way from quantum interference in the measurement process [199–201]. The detection of a photon from one or the other atomic ensemble in an indistinguishable fashion results in an entangled state with one collective spin excitation shared coherently between the ensembles[a]. Such entanglement has been critical for the initial implementation of functional quantum nodes for entanglement distribution (ref. [36], chapter 4), for the investigation of entanglement swapping (ref. [37], chapter 5) and for light-matter teleportation [112].

Because of the relevance to quantum networking tasks, it is important to obtain detailed characterizations of the physical processes related to the creation, storage, and utilization of heralded entanglement. Towards this end, significant advances have been demonstrated in the generation of photon-pairs [74,75] and the efficient retrieval of collective excitation [76,77]. Moreover, decoherence processes for a single atomic ensemble in the

[a] See also chapter 9 for an initial demonstration of measurement-induced entanglement of spin waves among multiple quantum memories.

regime of collective excitation have been investigated theoretically (ref. [147], chapter 2) and a direct measurement of decoherence for one stored component of a Bell state recently was performed [202]. However, to date no direct study has been reported for the decoherence of an entangled system involving two distinct atomic ensembles, which is a critical aspect for the implementation of elaborate protocols [122,123,203]. The decoherence of entanglement between ensembles has been shown in recent setups (chapter 2), through the decay of the violation of a Bell inequality (ref. [36], chapter 4) and the decay of the fidelity of a teleported state [112]. However, a quantitative analysis was not provided since these setups involved many other parameters, such as phase stability over long distances.

In this chapter, I discuss measurements that provide a detailed and quantitative characterization of entanglement between collective atomic excitations. Specifically, we determine the concurrence C (ref. [178]) as a function of the normalized degree of correlation g_{12} (ref. [76]) for the ensembles, including the threshold $g_{12}^{(0)}$ for entanglement ($C > 0$). We also map the decay of the concurrence $C(\tau)$ as a function of storage time for the entangled state, and interpret this decay by measuring the local decoherence on both ensembles taken independently. Compared to ref. [27], these observations are made possible by a new system that requires no active phase stability and that implements conditional control for the generation, storage, and readout of entangled atomic states.

3.2 Experimental setup

Our experiment is illustrated in Fig. 3.1. A single cloud of cesium atoms in a magneto-optical trap is used; two ensembles are defined by different optical paths 1 mm apart [36,204]. This separation is obtained by the use of birefringent crystals close to the cloud, which separate orthogonal polarizations [71]. At 40 Hz, the trap magnetic field is switched off for 7 ms. After waiting 3 ms for the magnetic field to decay, the two samples are simultaneously illuminated with 30-ns-long and 10 MHz red-detuned write pulses, at a rate of 1.7 MHz. Given the duty cycle of the experiment, the effective rate is 180 kHz. Spontaneous Raman scattered fields induced by the write beams are collected into single-mode fibers, defining for each ensemble optical modes that we designate as fields $1_{U,D}$ with 50 μm waist and a 3° angle relative to the direction of the write beams [75,76]. The fields $1_{U,D}$ are frequency filtered to block spontaneous emission from atomic transitions $|e\rangle \rightarrow |g\rangle$, which do not herald the creation of a collective excitation. After this stage, and before detection, fields $1_{U,D}$ are brought to interfere on a polarizing beam-splitter. A detection event at $D_{1a,1b}$ that arises indistinguishably from either of the fields $1_{U,D}$ projects the atomic ensembles into an entangled state where, in the ideal case, one collective excitation is coherently shared between the U, D ensembles [4,27].

3.3 Entanglement generation and storage

In the ideal case of small excitation probability, the atom-field 1 joint state can be written for each ensemble:

$$|\Psi\rangle = |0_a\rangle|0_1\rangle + \sqrt{\xi}|1_a\rangle|1_1\rangle + O(\xi) \ , \tag{3.1}$$

with $|n_1\rangle$ the state of the field 1 with n photons and $|n_a\rangle$ the state of the ensemble with n collective excitations (chapter 2). Upon a detection event at $D_{1a,1b}$, in the ideal case, the atomic state is projected into

$$|\Psi_{U,D}\rangle = \frac{1}{\sqrt{2}}(|0_a\rangle_U|1_a\rangle_D \pm e^{i\phi}|1_a\rangle_U|0_a\rangle_D) + O(\sqrt{\xi}), \tag{3.2}$$

where $|0_a\rangle_{U,D}, |1_a\rangle_{U,D}$ refers to the two ensembles U, D with $0, 1$ collective excitations, respectively[4]. The $\pm$ sign is set by the detector that records the heralding event. The overall phase ϕ is the sum of the phase difference of the write beams at the U and D ensembles and the phase difference acquired by fields 1 in propagation from the ensembles to the beamsplitter. To achieve entanglement, this phase must be constant from trial to trial[110]. In order to meet this requirement, the initial demonstration reported in ref.[27] employed

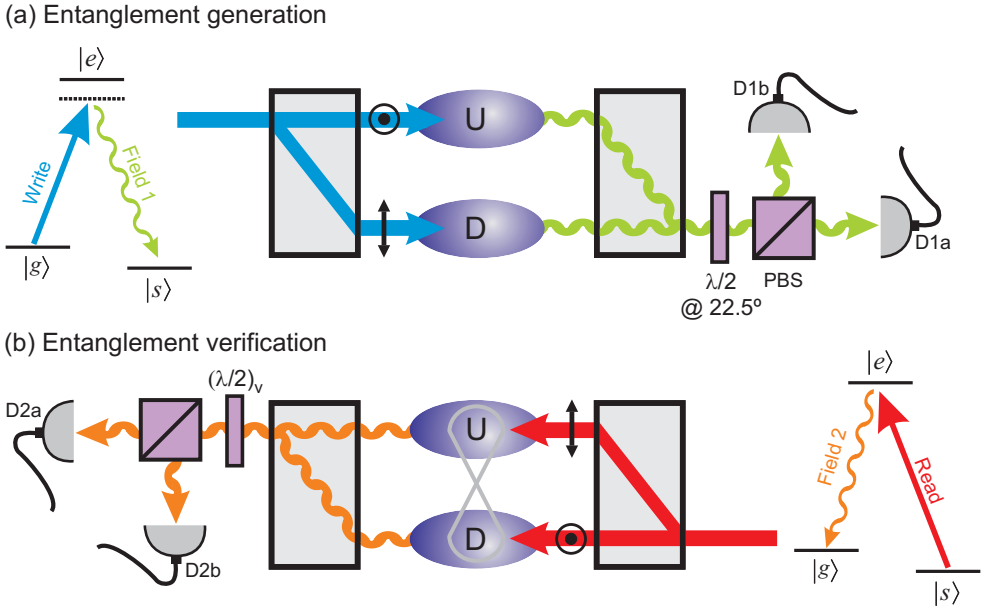

Figure 3.1: **Entanglement generation and verification.** **a**, Entanglement generation and storage. A weak write pulse is split into two paths separated by 1 mm and excites simultaneously two atomic samples, U, D. The resulting fields $1_{U,D}$ are combined at the polarizing beamsplitter (PBS) and sent to the single-photon detectors $D_{1a,1b}$. A detection event at D_{1a} or D_{1b} heralds the creation of entanglement. **b**, Entanglement verification. After a storage time τ, entanglement is verified by mapping the atomic state to propagating fields $2_{U,D}$ by way of read pulses. Tomography is then achieved in two steps, as described in the text. The atomic cloud is initially prepared in the ground state $|g\rangle$. $\{|g\rangle, |s\rangle, |e\rangle\}$ denote the levels $\{|6S_{1/2}, F = 4\rangle, |6S_{1/2}, F = 3\rangle, |6P_{3/2}, F = 4\rangle\}$. Note that the fields $1_{U,D}$ and $2_{U,D}$ are detected with a small angle relative to the classical beams, which is not represented here for the sake of simplicity.

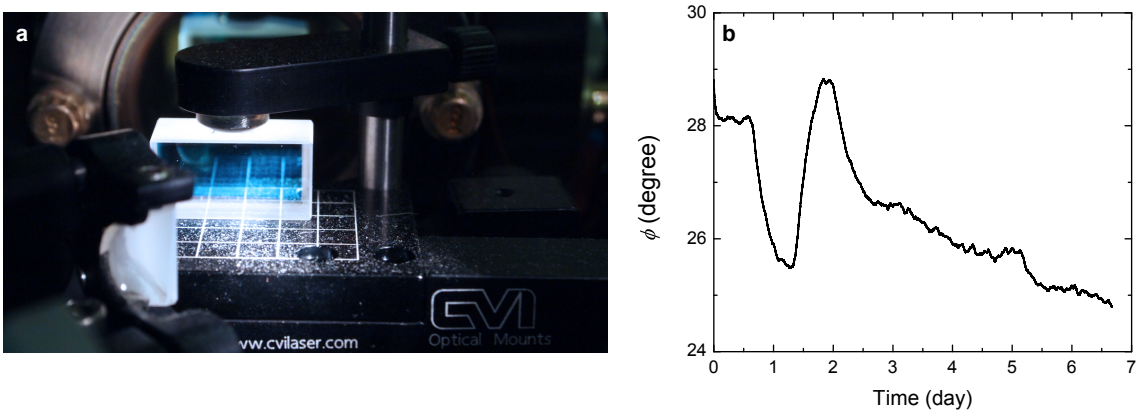

Figure 3.2: **Passive stability of a Mach-Zehnder interferometer formed by a pair of beam displacers. a**, A calcite beam displacer mounted on a stable prism mount. **b**, Long-term phase instability of an interferometer formed by two beam displacers. By mounting the two crystals in an anti-symmetric configuration (Fig. 3.1), the phase drifts are passively compensated to the first order for thermal expansions of the crystals as well as for mechanical instabilities along all translational degrees of freedom (except for tilting). The relative phase ϕ does not change by more than a few degrees over several days.

auxiliary fields to achieve active stabilization for various phases for two ensembles located in distinct vacuum apparatuses. By contrast, in our current setup (Fig. 3.1a), ϕ is determined only by the differential phase for the two paths with orthogonal polarizations defined by the birefringent crystals (Fig. 3.2a); our small setup has sufficient passive stability without the need of adjustment or compensation. The relative phase ϕ does not change by more than a few degrees over 24 hours (Fig. 3.2b).

3.4 Entanglement verification

To operationally verify entanglement between the U, D ensembles, the respective atomic states are mapped into photonic states by applying simultaneously read pulses in the configuration introduced in ref.[75], as depicted in Figure 3.1b (see also chapter 5.3.3). The delocalized atomic excitation is retrieved with high efficiency thanks to collective enhancement[4,76] and, in the ideal case, $|\Psi_{U,D}\rangle$ would be mapped directly to the photonic state of fields $2_{U,D}$ with unity efficiency and no additional components. Stability for the phase difference of the read beams and of fields $2_{U,D}$ is also required in this process; it is again achieved by the passive stability of our current scheme[71]. Since entanglement cannot be increased by local operations[205], the entanglement for the atomic state will always be greater than or equal to that measured for the light fields.

A model-independent determination of entanglement based upon quantum tomography of the fields $2_{U,D}$ has been developed in ref.[27]. The model consists of reconstructing a density matrix, $\tilde{\rho}_{2_U,2_D}$, obtained from the full density matrix by restriction to the subspace with no more than one photon per mode. We also assume that all off-diagonal elements between states with different numbers of photons vanish. The model thus leads to a lower bound for entanglement. As detailed in ref.[27], $\tilde{\rho}_{2_U,2_D}$ can be written in the photon-number basis

$|n\rangle|m\rangle$ with $\{n,m\}=\{0,1\}$ as follows:

$$\tilde{\rho}_{2_U,2_D}=\frac{1}{P}\begin{pmatrix} p_{00} & 0 & 0 & 0 \\ 0 & p_{01} & d & 0 \\ 0 & d^* & p_{10} & 0 \\ 0 & 0 & 0 & p_{11} \end{pmatrix}. \tag{3.3}$$

Here, p_{ij} is the probability to find i photons in mode 2_U and j in mode 2_D; d is the coherence term between the $|1\rangle|0\rangle$ and $|0\rangle|1\rangle$ states; and $P=p_{00}+p_{01}+p_{10}+p_{11}$. From $\tilde{\rho}_{2_U,2_D}$, one can calculate the concurrence C, which is a convenient monotone measurement of entanglement ranging from 0 for a separable state to 1 for a maximally entangled state[178]:

$$C=\max(0,C_0) \text{ with } C_0=\frac{1}{P}(2|d|-2\sqrt{p_{00}p_{11}}). \tag{3.4}$$

In the regime of low excitation and detection probabilities in which the experiment is performed, the vacuum p_{00} can be approximated by $p_{00}\sim 1-p_c$, while the terms p_{01} and p_{10} are given by $p_{10}=p_{01}=p_c/2$. p_c is the conditional probability of detecting a photon in field 2 from one ensemble following a detection event for field 1.

Experimentally, we reconstruct $\tilde{\rho}_{2_U,2_D}$ and then calculate C by using two configurations for the detection of fields $2_{U,D}$, corresponding to two settings of the $(\lambda/2)_v$ waveplate shown in Fig. 3.1b. The diagonal elements of $\tilde{\rho}_{2_U,2_D}$ are determined from measurements of the photon statistics for the separated fields $2_U, 2_D$, i.e., by detecting independently each field. To access the coherence term d, fields $2_{U,D}$ are coherently superimposed and the count rates from the resulting interference are recorded as a function of the relative phase between the $2_{U,D}$ fields. It can be shown that $d\simeq V(p_{10}+p_{01})/2\sim Vp_c/2$ (ref.[27]), where V is the visibility of the interference fringe.

3.5 Main results

3.5.1 Scaling behavior of heralded entanglement to excitation probability

To investigate the scaling of entanglement with excitation probability ξ, we determine the concurrence C for various values of ξ for fixed memory time $\tau=200$ ns. As ξ increases, higher-order terms in the expansion of Eq. (3.2) cannot be neglected, precisely as in parametric down-conversion. A convenient parameter to assess the excitation regime of each ensemble is the normalized intensity cross-correlation function g_{12} between field 1 and field 2 (ref.[76]), defined as $g_{12}=p_{12}/(p_1p_2)$ with p_{12} the joint probability for detection events from field 1 and 2 in a given trial and p_i the probability for unconditional detections in field i. In the ideal case, this function is related to the excitation probability ξ by $g_{12}=1+1/\xi$, where $g_{12}>2$ defines the

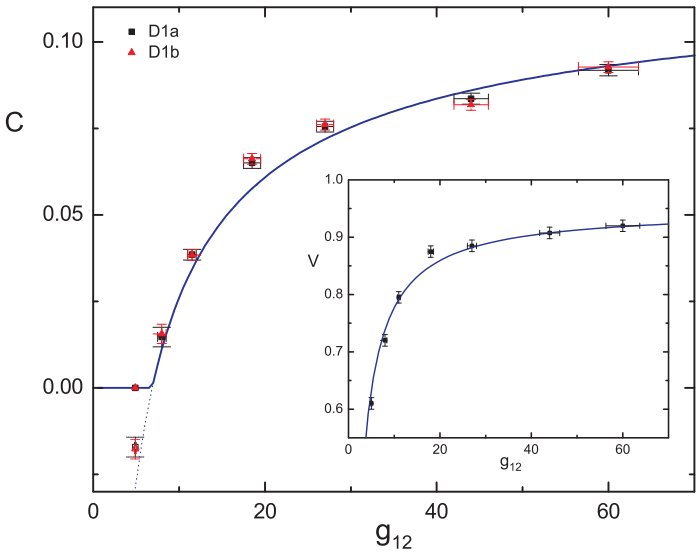

Figure 3.3: **Concurrence C as a function of the normalized cross-correlation function g_{12}, for the two possible heralding events (detection at D_{1a} or D_{1b}).** The solid line is obtained from Eq. (3.5) with the fitted overlap (see inset) and taking an independently-measured retrieval efficiency at 13.5%. The dotted line corresponds to C_0. Inset: Average visibility of the interference fringe between the two field-2 modes. The solid line is a fit using the expression given by Eq. (3.6), with the overlap $\overline{\lambda}$ fitted to 0.95 ± 0.01.

nonclassical border in the ideal case[72] and $g_{12} \gg 2$ being the single-excitation regime for the ensembles[74].

Expressing the two-photon component for the two ensembles as $p_{11} = \xi p_c^2 \sim p_c^2/g_{12}$, we rewrite the concurrence as:

$$C \simeq \max[0, p_c(V - 2\sqrt{(1-p_c)/g_{12}})] \,, \tag{3.5}$$

where g_{12} is for either ensemble alone, with $g_{12}^{(U)} = g_{12}^{(D)} \equiv g_{12}$ assumed. The visibility V can be expressed in terms of g_{12} as the higher-order terms act as a background noise. With $(1/2)p_1p_2$ a good estimation for the background, the visibility can be written as

$$V \simeq \overline{\lambda}\,\frac{p_{12} - p_1p_2}{p_{12} + p_1p_2} = \overline{\lambda}\,\frac{g_{12}-1}{g_{12}+1} \,, \tag{3.6}$$

where $\overline{\lambda}$ is the overlap between fields $2_{U,D}$ (ref.[78]). In the limit of near zero excitation, as g_{12} goes to infinity, the concurrence reaches its asymptotic value given by the retrieval efficiency $\overline{\lambda}p_c$[b].

Fig. 3.3 presents our measurements of the concurrence C as a function of g_{12}. As the excitation probability is decreased, g_{12} increases as does the entanglement. The threshold to achieve $C > 0$ is found to be $g_{12}^{(0)} \simeq 7$, corresponding to a probability $p_h \simeq 1.2 \times 10^{-2}$ per trial for the creation of the heralded atomic entangled state and to a preparation rate ~ 2 kHz. Note that $C = 0$ (or C not greater than zero) does not imply that there is no entanglement, only that any possible entanglement is not detected by our protocol,

[b] An alternative approach is to determine the suppression of two-photon events relative to the square of the probability of single-photon events for the fields 2, $h \equiv \frac{p_{11}}{p_{10}p_{01}}$. $h < 1$ is a necessary condition for entanglement[27,34,36]. Here, for $g_{12} = 60$, $h = 0.060 \pm 0.005$.

which provides a lower bound for the entanglement. More importantly, in an infinite dimensional Hilbert space, entangled states are dense in the set of all states[206], so that zero entanglement is not provable for an actual experiment by way of the concurrence.

To confirm the model leading to Eq. (3.6), the inset gives the measured visibility V as a function of g_{12}. The solid line is a fit according to Eq. (3.6) with free parameter $\overline{\lambda}$, leading to an overlap $\overline{\lambda} = 0.95 \pm 0.01$, in agreement with the value $\overline{\lambda} = 0.98 \pm 0.03$ obtained from an independent two-photon interference measurement. With the fitted value of $\overline{\lambda}$ and with the independently determined value of the conditional probability $p_c = 0.135 \pm 0.005$ from measurements performed on each ensemble separately, we compare our measurements of C with the prediction of Eq. 3.5 (solid line in Fig. 3.3) and find good agreement.

Table 3.1 provides the diagonal elements of the density matrix $\tilde{\rho}_{2_U,2_D}$ and the concurrence for the case $g_{12} = 60 \pm 4$ corresponding to a probability to create atomic entanglement $p_h = 9 \times 10^{-4}$ per trial (160 Hz). A value $C = 0.092 \pm 0.002$ is directly measured at detectors D_{2a}, D_{2b} without correction. By way of the independently determined propagation and detection efficiencies, we infer the density matrix $\tilde{\rho}^{output}_{2_U,2_D}$ for fields $2_U, 2_D$ at the output of the ensembles, from which we obtain a concurrence $C^{output}_{2_U,2_D} = 0.35 \pm 0.1$. This value exceeds the then published state of the art by two orders of magnitude[27]. This leap underlines the progress obtained in terms of suppression of the two-photon component and achievable retrieval efficiency over the past year[76,77]. Finally, by way of the conditional readout efficiency $\eta = 45 \pm 10\%$ for mapping of quantum states of the U, D ensembles to the fields $2_U, 2_D$, we estimate the density matrix $\tilde{\rho}_{U,D}$ and the concurrence $C_{U,D} = 0.9 \pm 0.3$ for the collective atomic state. We emphasize that $C_{U,D}$ is an estimate determined from the model developed in ref.[74] where the fields at the output of the MOT consist of a two-mode squeezed state plus background fields in coherent states.

3.5.2 Characterization of decoherence for heralded entanglement stored in two atomic ensembles

Turning then to a characterization of the decay of entanglement with storage time τ, we present in Fig. 3.4 measurements of concurrence $C(\tau)$ for fixed excitation probability $p_h = 1.6 \times 10^{-3}$ corresponding to $g_{12} = 30$ at $\tau = 200$ ns. $C > 0$ for $\tau \lesssim 20\ \mu s$, providing a lower bound for the lifetime of entanglement of the ensembles corresponding to 4 km propagation delay in an optical fiber.

Table 3.1: **Diagonal elements and concurrence of the density matrices for fields $2_{U,D}$, without and with correction for propagation losses and detection efficiencies.** The last column provides the estimated elements and concurrence for the atomic state by considering the readout efficiency η. $g_{12} = 60 \pm 4$.

	$\tilde{\rho}_{2_U,2_D}$	$\tilde{\rho}^{output}_{2_U,2_D}$	$\tilde{\rho}_{U,D}$
p_{00}	0.864 ± 0.001	0.54 ± 0.08	0 ± 0.3
p_{10}	$(6.47 \pm 0.02) \times 10^{-2}$	$(22 \pm 4) \times 10^{-2}$	0.5 ± 0.15
p_{01}	$(7.07 \pm 0.02) \times 10^{-2}$	$(24 \pm 4) \times 10^{-2}$	0.5 ± 0.15
p_{11}	$(2.8 \pm 0.2) \times 10^{-4}$	$(3 \pm 2) \times 10^{-3}$	0.015 ± 0.025
C	0.092 ± 0.002	0.35 ± 0.1	0.9 ± 0.3

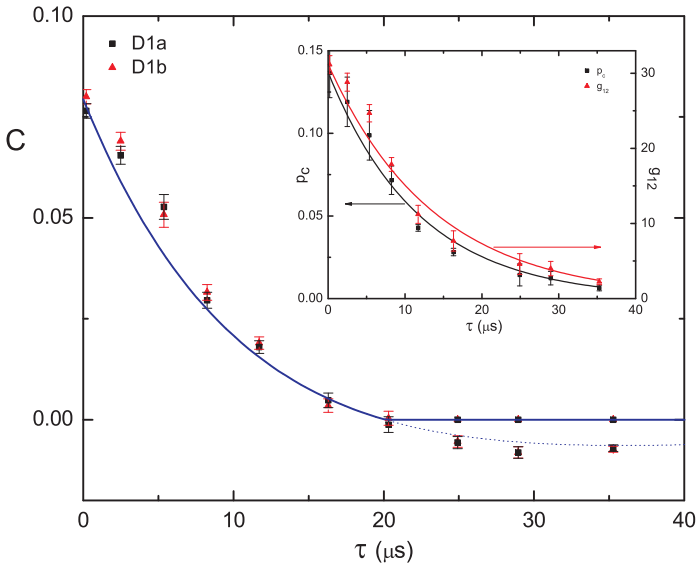

Figure 3.4: **Concurrence C as a function of the storage time τ.** The solid line is obtained from Eq. (3.5) assuming the fitted exponential decays, given in the inset, of the individual parameters p_c and g_{12} measured independently. The dotted line corresponds to C_0.

To investigate the dynamics in Fig. 3.4, the inset shows the decay of the average g_{12} and conditional probability p_c for the ensembles taken independently. Such local decoherence has been investigated as the result of inhomogeneous broadening of the Zeeman ground states due to residual magnetic fields [120,147,202]. Our current measurement shows the effect of this local decoherence on the entanglement of the joint system of the ensembles. For this purpose, our measurements of C are superposed with a line $C(\tau)$ given by Eq. 3.5, where the fitted exponential decay for $p_c(\tau), g_{12}(\tau)$ (with similar decay $\simeq$ 13 μs) and the overlap $\overline{\lambda}$ determined in Fig. 3.3 are employed. The agreement evidenced in Fig. 3.4 confirms the principal role of local dephasing in the entanglement decay.

3.6 Conclusion

In conclusion, we have reported a detailed study of the behavior of entanglement between collective excitations stored in atomic ensembles, including the dependence of the concurrence on the degree of excitation and the quantitative relationship of local decoherence to entanglement decay. The temporal dynamics reveal a finite-time decay, with separability onset for storage time $\tau_m \sim 20\ \mu s$. From a more general perspective, the inferred concurrence for the collective atomic state, $C_{U,D} = 0.9 \pm 0.3$, is comparable to then current values obtained for entanglement in the continuous variable regime [207] and for entanglement of the discrete internal states of trapped ions [197,198].

3.7 Multiple "flavors" of entanglement

While progress in traditional physics has been historically made by confirming the *consistency* of experimental data with theoretical models, it is essential to employ *robust*, *model-independent* procedures in quantum optics and quantum information science, in order to unambiguously characterize and verify the entanglement for the purported state created in one's experiment[110,208]. Diverse approaches to entanglement verification and quantification have been developed so far, including entanglement monotones and witnesses[40,110,208]. For excellent accounts of recent results, I refer to the reviews by refs.[40,208]. Also, I refer to chapters 7–9, where we have developed a particular form of an entanglement witness for verifying multipartite mode-entangled W states[38].

In this section, I would like to provide a brief overview on the different categories of entanglement[c] one could generate in an experiment, largely based on the description in ref.[110]. By this, I hope to distinguish the 'flavors' of entanglement for the *heralded* and *deterministic* quantum states described in this thesis, and those based on *post-dicted* states largely reported elsewhere in the literature (chapter 1) which are not directly applicable for scalable quantum networks[1].

1. *Deterministic* (*a priori*) entanglement

   For *deterministic* entanglement, one has a source that generates multiple copies (i.e., in de Finetti representation[211], $\hat{\rho}^{(N_c)} = \int d\hat{\rho} P(\hat{\rho}) \hat{\rho}^{\otimes N_c}$) of a state, $\hat{\rho} = \hat{\rho}_{\text{det}}$, where

   $$\hat{\rho}_{\text{det}} = \hat{\rho}_{\text{ent}}. \tag{3.7}$$

   By performing measurements on a subset of $\hat{\rho}^{(N_c)}$ (e.g., via quantum-state tomography), one concludes in principle that the physical state $\hat{\rho}_{\text{det}}$ contains an entangled state $\hat{\rho}_{\text{ent}}$ every instant of its creation. The entangled component $\hat{\rho}_{\text{ent}}$ is identical to the physical state $\hat{\rho}_{\text{det}}$ generated in an experiment. Thus, the entangled state $\hat{\rho}_{\text{ent}}$ is created on demand "at the push of the button." Importantly, the purported entanglement is unambiguously verified directly from measurements on the physical state $\hat{\rho}_{\text{det}}$ without destructively filtering a small fictitious (entangled) component $\hat{\rho}'_{\text{ent}}$ of $\hat{\rho}_{\text{det}}$ and subsequently measuring $\hat{\rho}'_{\text{ent}}$ by *post-selection* (i.e., *a posteriori* entanglement). Depending on the amount of entanglement, *deterministic* entanglement may be employed for a wide variety of large-scale quantum information tasks (section 1.1), including scalable quantum computation and entanglement distribution. For example, we demonstrated a reversible quantum interface, whereby deterministic entanglement can be mapped into and out of two quantum memories (chapter 6). Prominent examples of this type of entanglement

[c] Note that while there is only one class of entanglement (Bell states) for bipartite qubits ($N = 2$), there are different *classes* of entanglement for $N > 2$, associated with the equivalency under stochastic local operation and classical communication (SLOCC)[209,210]. My goal, however, is not to discuss about the *classes* of entanglement, which is an active research problem on its own, but rather to differentiate the various types of entanglement generated in an experiment, in terms of the amount of entanglement for the actual *physical* state.

include the various entangled states for continuous variable beams of light and atomic ensembles, and between trapped ions, Rydberg atoms, and superconducting qubits (section 1.2).

2. *Heralded* entanglement

Here, one refers to the state in the de Finetti representation $\hat{\rho}^{(N_c)} = \int d\hat{\rho} P(\hat{\rho}) \hat{\rho}^{\otimes N_c}$, where $\hat{\rho} = \hat{\rho}_{\text{her}}$ with,

$$\hat{\rho}_{\text{her}} = (1 - p_{\text{yes}}) \hat{\rho}_{\text{no}} \otimes \hat{\rho}_{\text{unent}} + p_{\text{yes}} \hat{\rho}_{\text{yes}} \otimes \hat{\rho}_{\text{ent}}. \tag{3.8}$$

This is an entangled state subject to an ensemble measurement of the subset of $\hat{\rho}^{(N_c)}$, for which one could reliably estimate the amount of entanglement $E(\hat{\rho}_{\text{ent}})$. For heralded states, we have orthogonal states $\{\hat{\rho}_{\text{no}}, \hat{\rho}_{\text{yes}}\}$ for the heralding system (*lhs* of the direct products in Eq. 3.8) with probabilities $\{1 - p_{\text{yes}}, p_{\text{yes}}\}$, for which one could subject the auxiliary states $\{\hat{\rho}_{\text{no}}, \hat{\rho}_{\text{yes}}\}$ in a test to distinguish probabilistically whether the state $\hat{\rho}_{\text{her}}$ is prepared in the entangled $\hat{\rho}_{\text{ent}}$ or unentangled states $\hat{\rho}_{\text{unent}}$. Albeit with possibly low success probability p_{yes}, we can indeed create a physical state with the desired maximally entangled $\hat{\rho}_{\text{ent}}$ with a high fidelity by projecting the ancilla states. Thus, *heralded* entanglement can be as powerful as *a priori* entanglement, except that one may have to generate many copies before obtaining $\hat{\rho}_{\text{ent}}$ if p_{yes} is small. This type of entanglement may be employed for diverse large-scale quantum information protocols, including universal quantum computations[2,212,213] and scalable quantum communications[4,9] (section 1.1).

In chapters 3–5, 8, and 9, we initially entangled the number-states between the (heralding) fields 1 and the atomic state via the two-mode squeezing operation described in chapter 2. By projecting the fields onto an entangled state $\frac{1}{2}(|10\rangle + |01\rangle)$, we prepared a high-fidelity entanglement (ideally, 1-ebit of entanglement) for the heralded state $\hat{\rho}_{\text{ent}}$ *physically stored* in the atomic ensembles. For example, in this chapter, we have achieved $C_{U,D} = 0.9 \pm 0.3$ for the physical state with $p_h \simeq 10^{-3}$ without post-selecting $\hat{\rho}_{\text{ent}}$. But as the scheme is probabilistic, the heralding process requires us to generate on average $\sim 1/p_h$ copies of the state $\hat{\rho}_{\text{her}}$ to obtain $\hat{\rho}_{\text{ent}}$. This type of entanglement can be used for conditional enhancement of entanglement distribution and connection[36,37] (chapters 4–5) and even promoted to a deterministic quantum state[79,80] via the conditional control of heralded quantum states[78], with a sufficient memory time τ_m (see ref.[115]).

3. *A posteriori* entanglement

Here, one generates $\hat{\rho}^{(N_c)} = \int d\hat{\rho} P(\hat{\rho}) \hat{\rho}^{\otimes N_c}$, where $\hat{\rho} = \hat{\rho}_{\text{post}}$ with,

$$\hat{\rho}_{\text{post}} = (1 - p_{\text{yes}}) \hat{\rho}_{\text{unent}} + p_{\text{yes}} \hat{\rho}_{\text{ent}}, \tag{3.9}$$

where $p_{\text{yes}} \ll 1$, in many cases of practical importance. Here, one devises the measurement strategy such that it is only sensitive to the desired entangled state $\hat{\rho}_{\text{ent}}$ with *post-selection*, thereby destructively

measuring the quantum state. While such a measurement strategy may display classical recording of significant non-classical correlations (e.g., by way of the violation of Bell's inequality), the actual amount of entanglement for the physical state $\hat{\rho}_{\text{post}}$ is very small: i.e., $E(\hat{\rho}_{\text{post}}) \sim p_{\text{yes}} E(\hat{\rho}_{\text{ent}})$. If the post-selection procedures can be simulated by local filters, one can in principle conclude the presence of entanglement. But, entanglement $E(\hat{\rho}_{\text{ent}})$ via post-diction greatly overestimates the amount of entanglement $E(\hat{\rho}_{\text{post}})$ in $\hat{\rho}_{\text{post}}$ (i.e., referring instead to the fictitious component $\hat{\rho}_{\text{ent}}$).

Because of the destructive nature in the measurement process, the entanglement in $\hat{\rho}_{\text{ent}}$ cannot exist independent of the null (unentangled) events $\hat{\rho}_{\text{unent}}$. Indeed, in typical downconverter experiments, with $p_{\text{yes}} \ll 1$, the quantum state one needs to assign for the two purportedly entangled optical modes is not that of a maximally entangled state $|\Psi_+\rangle = \frac{1}{\sqrt{2}}(|HV\rangle + |VH\rangle)$ of two photons, but that of a state of the form:

$$\hat{\rho}_{\text{PDC}} \simeq p_0 \hat{\rho}_0 + p_{\text{yes}} |\Psi_+\rangle\langle\Psi_+| + \hat{\rho}_{\geq 2}. \tag{3.10}$$

Thus, based on a positive detection event, one succeeds in implementing the desired protocol *a posteriori*.

Such an entangled state is not desirable for realizing most scalable quantum architectures, including quantum networks, as the amount of entanglement is extremely small for the physical state (typically, $p_{\text{yes}} \ll 10^{-3}$). Furthermore, given a density matrix $\hat{\rho}_{\text{PDC}}$, the pure-state decompositions of Eq. 3.10 may be written in a form in different pure-state decomposition, for which the pure states in the decomposition are all unentangled[178]. Unfortunately, a wide range of literature has been reported, whereby entanglement in the state of Eq. 3.10 is claimed to exist in the form of $|\Psi_+\rangle$ instead of $\hat{\rho}_{\text{PDC}}$. I refer to reference[110] for prominent examples, for which entanglement verifications were not carried out correctly.

3.8 Technical details

3.8.1 Some notes on the magic of beam displacers

The passive stability of the beam displacers has attracted us to use these components throughout our experiments (chapters 3–9). We ordered the displacers from Novaphase, for which they used laser-grade calcite crystals with exceptionally low striae and optical inhomogeneity for reducing the scattering noise of the classical beams, and polished the calcite surface with $\lambda/10$ flatness over the entire aperture and $S/D = 20/10$. However, I'd like to note that since 2009 there has been a global shortage of calcite crystals, which made them compromise the quality of calcite crystals. For example, the new batch purchased in 2010 had higher densities of scattering centers for the experiment in chapter 9, with the fluorescence clearly visible under an IR scope. As of 2011, it is unclear when we will be able to obtain high-quality calcite crystals with low scatter density as in the pre-2009 batches. Currently, for any serious quantum optics experiments involving

strong classical beam, the only practical alternative is to use synthetically grown YVO_4 beam displacers, despite the lower transmission at our wavelengths. The residual broadband fluorescence from the crystal can be overcome by employing a narrow-band high-efficiency volume Bragg grating (see Fig. 1.6 in chapter 1).

Chapter 4

Functional quantum nodes for entanglement distribution

This chapter is largely based on ref. [36]. Reference [36] refers to the then current literature in 2007 at the time of publication.

4.1 Introduction

In quantum information science [162], distribution of entanglement over quantum networks is a critical requirement for quantum metrology [41], quantum computation [8,214], and communication [8,9]. Quantum networks are composed of quantum nodes for processing and storing quantum states, and quantum channels that link the nodes (chapter 1). Substantial advances have been made with diverse systems towards the realization of such networks, including ions [215], single trapped atoms in free space [216,217] and in cavities [218], and atomic ensembles in the regime of continuous variables [60].

An approach of particular importance has been the seminal work of Duan, Lukin, Cirac, and Zoller (*DLCZ*) for the realization of quantum networks based on entanglement between single photons and collective excitations in atomic ensembles [4]. Critical experimental capabilities have been achieved, beginning with the generation of non-classical fields [72,73] with controlled waveforms [75] and extending to the creation and retrieval of single collective excitations [74,92,93] with high efficiency [76,77]. Heralded entanglement with quantum memory, which is the cornerstone of networks with efficient scaling, was achieved between two ensembles [27]. More recently, conditional control of the quantum states of a single ensemble [79,80,202] and of two distant ensembles [78] has also been implemented, such quantum states are likewise required for the scalability of quantum networks based on probabilistic protocols.

Our goal is to develop the physical resources that enable quantum repeaters [9], thereby allowing entanglement based quantum communication tasks over quantum networks on distance scales much larger than set by the attenuation length of optical fibers, including quantum cryptography [21]. For this purpose, heralded number-state entanglement [27] between two remote atomic ensembles is not directly applicable. Instead,

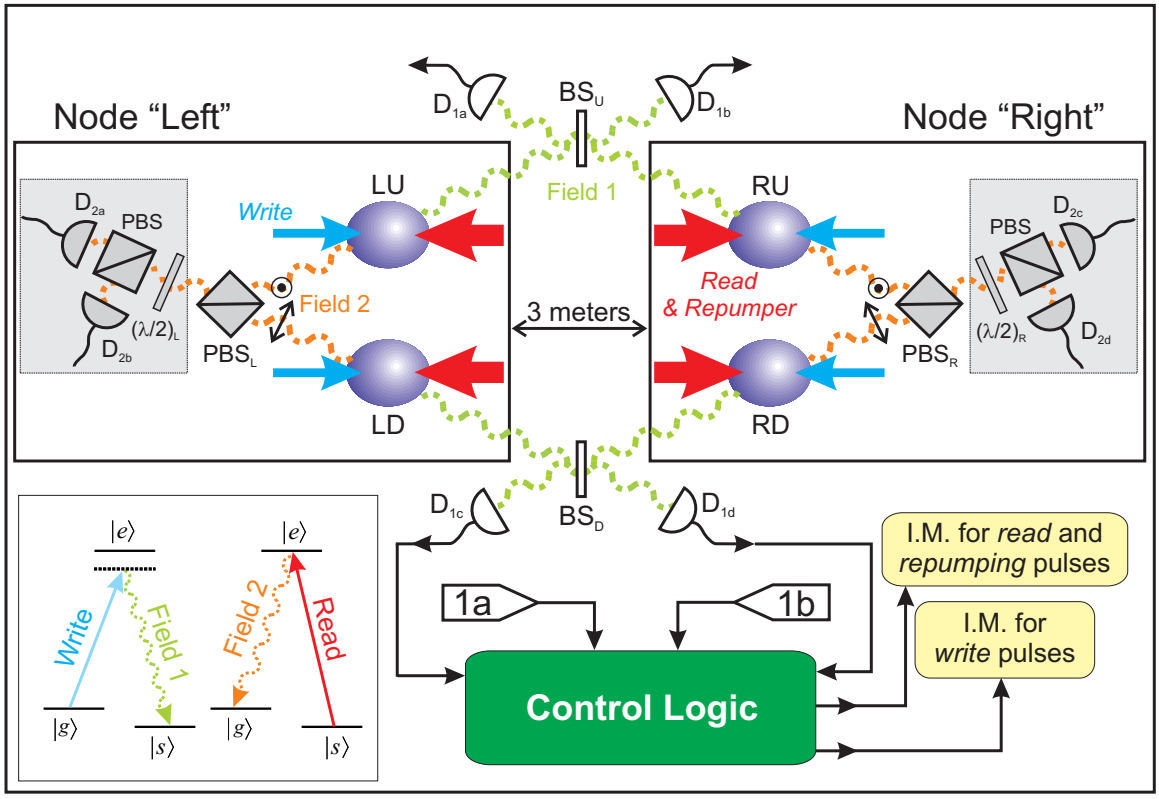

Figure 4.1: **Setup for distributing entanglement between two quantum nodes (L, R) separated by 3 meters.** The inset shows the relevant atomic levels for the $6S_{1/2} \rightarrow 6P_{3/2}$ transition in atomic Cesium, as well as the associated light fields. The ensembles are initially prepared in $|g\rangle$. Weak write pulses then induce spontaneous Raman transitions $|g\rangle \rightarrow |e\rangle \rightarrow |s\rangle$, resulting in the emission of anti-Stokes fields (fields 1) near the $|e\rangle \rightarrow |s\rangle$ transition along with the storage of collective excitations in the form of spin-flips shared among the atoms[4]. With this setup, a photodetection event at either detector D_{1a} or D_{1b} (D_{1c} or D_{1d}) heralds entanglement between the collective excitation in LU and RU (LD and RD)[27]. BS_U and BS_D are implemented using two orthogonal polarizations in one fiber beam splitter, yielding excellent relative path stability. A heralding detection event triggers the control logic to gate off the light pulses going to the corresponding ensemble pair (U or D) by controlling the intensity modulators (*IM*). The atomic state is thus stored while waiting for the second ensemble pair to be prepared. After both pairs of ensembles U, D are entangled, the control logic releases strong read pulses to map the states of the atoms to Stokes fields 2 via $|s\rangle \rightarrow |e\rangle \rightarrow |g\rangle$. Fields 2_{LU} and 2_{LD} (2_{RU} and 2_{RD}) are combined with orthogonal polarizations on the polarizing beam splitter PBS_L (PBS_R) to yield field 2_L (2_R). If only coincidences between fields 2_L and 2_R are registered, the state is effectively equivalent to a polarization maximally entangled state. $(\lambda/2)_{L,R}$ are rotatable half-wave plates.

DLCZ proposed the use of pairs of ensembles (U_i, D_i) at each quantum node i, with the sets of ensembles $\{U_i\}, \{D_i\}$ separately linked in parallel chains across the network[4]. Relative to the state of the art in ref.[27], the *DLCZ* protocol requires the capability for the independent control of pairs of entangled ensembles between two nodes.

In this chapter, we have created, addressed, and controlled pairs of atomic ensembles at each of two quantum nodes, thereby demonstrating entanglement distribution in a form suitable both for quantum network architectures and for entanglement-based quantum communication schemes. Specifically, two pairs of remote

ensembles at two nodes were each prepared in an entangled state[27], in a heralded and asynchronous fashion[78], thanks to the conditional control of the quantum memories. After a signal heralding that the two chains are prepared in the desired state, the states of the ensembles were coherently transferred to propagating fields locally at the two nodes. The fields were arranged such that they effectively contained two photons, one at each node, whose polarizations were entangled. The entanglement between the two nodes was verified by the violation of a Bell inequality. The effective polarization-entangled state, created with favorable scaling behavior, was thereby compatible with entanglement-based quantum communication protocols[4].

4.2 Conditional control of heralded entanglement and entanglement distribution

The architecture for our experiment is shown in Fig. 4.1. Each quantum node, L (left) and R (right), consists of two atomic ensembles, U (up) and D (down), or four ensembles altogether, namely (LU, LD) and (RU, RD), respectively. We first prepared each pair in an entangled state (chapter 3), in which one excitation is shared coherently, by using a pair of coherent weak write pulses to induce spontaneous Raman transitions $|g\rangle \rightarrow |e\rangle \rightarrow |s\rangle$ (bottom left, Fig. 4.1). The Raman fields (1_{LU},1_{RU}) from (LU, RU) were combined at the 50-50 beamsplitter BS_U, and the resulting fields were directed to single-photon detectors. A photoelectric detection event in either detector indicated that the two ensembles were prepared. The remote pair of D ensembles, (LD, RD), was prepared in an analogous fashion.

Conditioned upon the preparation of both ensemble pairs (LU, LD) and (RU, RD), a set of read pulses was triggered to map the stored atomic excitations into propagating Stokes fields in well-defined spatial modes through $|s\rangle \rightarrow |e\rangle \rightarrow |g\rangle$ with the use of a collective enhancement[4] (bottom left, Fig. 4.1; see also chapter 2). This generated a set of four fields denoted by (2_{LU},2_{RU}) for ensembles (LU, RU) and by (2_{LD},2_{RD}) for ensembles (LD, RD). In the ideal case and neglecting higher-order terms, this mapping results in a quantum state for the fields 2 given by

$$\begin{aligned} |\psi_{2_{LU},2_{RU},2_{LD},2_{RD}}\rangle &= \frac{1}{2}(|0\rangle_{2_{LU}}|1\rangle_{2_{RU}} \pm e^{i\eta_U}|1\rangle_{2_{LU}}|0\rangle_{2_{RU}})_U \\ &\quad \otimes(|0\rangle_{2_{LD}}|1\rangle_{2_{RD}} \pm e^{i\eta_D}|1\rangle_{2_{LD}}|0\rangle_{2_{RD}})_D \, . \end{aligned} \tag{4.1}$$

Here, $|n\rangle_x$ is the n-photon state for mode x, where $x \in \{2_{LU}, 2_{RU}, 2_{LD}, 2_{RD}\}$, and η_U (η_D) is the relative phase resulting from the writing and reading processes for the U (D) pair of ensembles[27]. The $\pm$ signs for the conditional states U, D result from the unitarity of the transformation by the beamsplitters (BS_U, BS_D). The extension of Eq. 4.1 to incorporate various imperfections is given in sections 4.8–4.11.

Apart from an overall phase, the state $|\psi_{2_{LU},2_{RU},2_{LD},2_{RD}}\rangle$ can be rewritten as follows

$$\begin{aligned}|\psi_{2_{LU},2_{RU},2_{LD},2_{RD}}\rangle \quad = \quad & \frac{1}{2}[e^{-i\eta_D}|1\rangle_{2_{RU}}|1\rangle_{2_{RD}}|\text{vac}\rangle_{2_L} \pm e^{i\eta_U}|1\rangle_{2_{LU}}|1\rangle_{2_{LD}}|\text{vac}\rangle_{2_R} \\ & \pm(|0\rangle_{2_{LU}}|1\rangle_{2_{LD}}|0\rangle_{2_{RD}}|1\rangle_{2_{RU}} \pm e^{i(\eta_U-\eta_D)}|1\rangle_{2_{LU}}|0\rangle_{2_{LD}}|1\rangle_{2_{RD}}|0\rangle_{2_{RU}})],\end{aligned} \tag{4.2}$$

where $|\text{vac}\rangle_{2_i}$ denotes $|0\rangle_{2_{iU}}|0\rangle_{2_{iD}}$. If only coincidences between both nodes L, R are registered, the first two terms (i.e., with $e^{-i\eta_D}, e^{i\eta_U}$) do not contribute. Hence, as noted by *DLCZ*, excluding such cases leads to an effective density matrix equivalent to the one for a maximally entangled state of the form of the last term in Eq. 4.2. Notably, the absolute phases η_U and η_D do not need to be independently stabilized. Only the relative phase $\eta = \eta_U - \eta_D$ must be kept constant, leading to $1/2$ unit of entanglement for two quantum bits (i.e., 1/2 ebit).

4.2.1 Real-time control of entanglement, phase stability, and polarization encoding

The experimental demonstration of this architecture for implementing the *DLCZ* protocol relies critically on the ability to carry out efficient parallel preparation of the (LU, RU) and (LD, RD) ensemble pairs, as well as the ability to stabilize the relative phase η. The first requirement is achieved by the use of real-time control, as described in ref.[78] in a simpler case. As shown in Fig. 4.1, here we implemented a control logic that monitors the outputs of field 1 detectors [a]. A detection event at either pair triggers electro-optic intensity modulators (*IM*) that gate off all laser pulses traveling toward the corresponding pair of ensembles, thereby storing the associated state. Upon receipt of signals heralding that the two pairs of ensembles (LU, RU) and (LD, RD) have both been independently prepared, the control logic triggers the retrieval of the stored states by simultaneously sending a strong read pulse into each of the four ensembles. Relative to the case where no logic is implemented, this process resulted in a 19-fold enhancement in the probability of generating this overall state from the four ensembles.

The second requirement, for stability of the relative phase η, could be accomplished by active stabilization of each individual phase η_U, η_D, as in ref.[27]. Instead of implementing this challenging technical task (which ultimately would have to be extended across longer chains of ensembles), our setup exploits the passive stability between two independent polarizations propagating in a single interferometer to prepare the two ensemble pairs. No active phase stabilization is thus required. In practice, we found that the passive stability of our system was sufficient for operation overnight without adjustment. Additionally, we implemented a procedure that deterministically sets the relative phase η to zero.

We also extend the original *DLCZ* protocol (Fig. 4.1) by combining fields (2_{LU}, 2_{LD}) and (2_{RU}, 2_{RD}) with orthogonal polarizations on polarizing beamsplitters *PBS*$_L$ and *PBS*$_R$ to yield fields 2_L and 2_R, respectively. The polarization encoding opens the possibility of performing additional entanglement purification and thus leads to superior scalability[122,203]. In the ideal case, the resulting state would now be effectively

[a] See the appendix of James Chou's thesis for the circuit design[71].

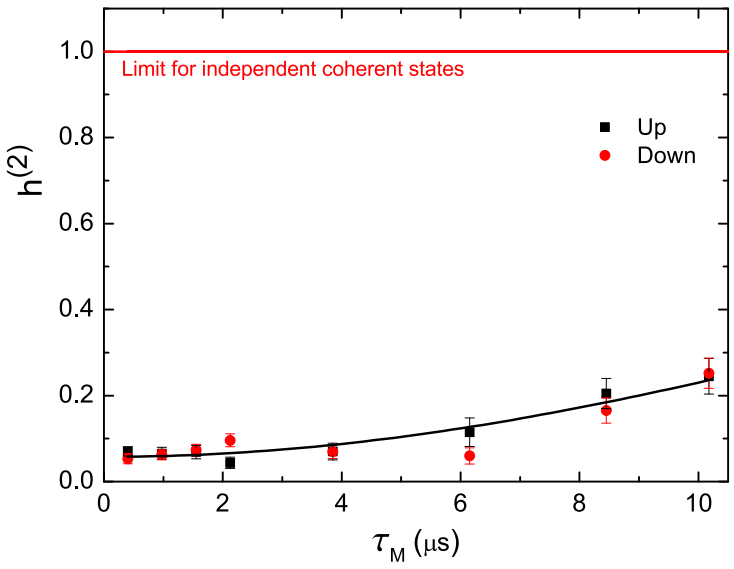

Figure 4.2: **Temporal growth of the suppression $h_X^{(2)}$.** Suppression $h_X^{(2)}$ of the probabilities for each ensemble to emit two photons compared to the product of the probabilities that only one photon is emitted, as a function of the duration τ_M that the state is stored before retrieval. The solid line gives a fit for the U pair. Error bars indicate statistical errors.

equivalent to a maximally entangled state for the polarization of two photons

$$|\psi^{\pm}_{2_L,2_R}\rangle_{\text{eff}} \propto |H_{2_L}\rangle|V_{2_R}\rangle \pm e^{i\eta}|V_{2_L}\rangle|H_{2_R}\rangle\,, \tag{4.3}$$

where $|H\rangle$ ($|V\rangle$) stands for the state of a single photon with horizontal (vertical) polarization. The sign $\pm$ of the superposition in Eq. 4.3 is inherited from Eq. 4.1 and is determined by the particular pair of heralding signals recorded by (D_{1a},D_{1b}) and (D_{1c},D_{1d}). The entanglement in the polarization basis is well-suited for entanglement-based quantum cryptography[4,21], including the security verification by way of the violation of a Bell inequality, as well as for quantum teleportation[4].

4.3 Characterization of $h^{(2)}$

As a first step to investigate the joint states of the atomic ensembles, we recorded photoelectric counting events for the ensemble pairs (LU, RU) and (LD, RD) by setting the angles for the half-wave plates $(\lambda/2)_{L,R}$ shown in Fig. 4.1 to 0°, such that photons reaching detectors D_{2b} and D_{2d} (D_{2a} and D_{2c}) come only from the ensemble pair U (D). Conditioned upon detection events at D_{1a} or D_{1b} (D_{1c} or D_{1d}), we estimated the probability that each ensemble pair U, D contains only a single, shared excitation as compared to the probability for two excitations by way of the associated photoelectric statistics. In quantitative terms, we determine the ratio[27]

$$h_X^{(2)} \equiv \frac{p_{X,11}}{p_{X,10}p_{X,01}}\,, \tag{4.4}$$

where $p_{X,mn}$ are the probabilities to register m photodetection events in mode 2_{LX} and n events in mode 2_{RX} ($X = \{U, D\}$), conditioned on a detection event at D_1.

A necessary condition for the two ensembles (LX, RX) to be entangled is that $h_X^{(2)} < 1$, where $h_X^{(2)} = 1$ corresponds to the case of independent (unentangled) coherent states for the two fields[27]. Fig. 4.2 shows the measured $h_X^{(2)}$ versus the duration τ_M (where M stands for memory) that the state is stored before retrieval. For both U and D pairs, $h^{(2)}$ remains well below unity for storage times $\tau_M \lesssim 10\ \mu s$. For the U pair, the solid line in Fig. 4.2 provides a fit by the simple expression $h^{(2)} = 1 - A \exp\left(-(\tau_M/\tau_0)^2\right)$. The fit gives $A = 0.94 \pm 0.01$ and $\tau_0 = 22 \pm 2\ \mu s$, providing an estimate of a coherence time for our system. A principal cause for decoherence is an inhomogeneous broadening of the ground state levels by residual magnetic fields (ref.[147], chapter 2). The characterization of the time dependence of $h^{(2)}$ constitutes an important benchmark of our system.

4.4 Measurement of correlation function

We next measure the correlation function $E(\theta_L, \theta_R)$, defined by

$$E(\theta_L, \theta_R) = \frac{C_{ac} + C_{bd} - C_{ad} - C_{bc}}{C_{ac} + C_{bd} + C_{ad} + C_{bc}}\,. \tag{4.5}$$

Here, C_{jk} gives the rates of coincidences between detectors D_{2j} and D_{2k} for fields 2, where $j, k \in \{a, b, c, d\}$, conditioned upon heralding events at detectors D_{1a}, D_{1b} and D_{1c}, D_{1d} from fields 1. The angles of the two half-wave plates $(\lambda/2)_{L,R}$ are set at $\theta_L/2$ and $\theta_R/2$, respectively. As stated before, the capability to store the state heralded in one pair of ensembles and then to wait for the other pair to be prepared significantly improves the various coincidence rates C_{jk} by a factor that increases with the duration τ_M that a state can be preserved[78] (section 4.11).

Fig. 4.3 displays the correlation function E as a function of θ_R, for **a**, $\theta_L = 0°$ and for **b**, $45°$. Relative to Fig. 4.2, these data are taken with increased excitation probability (higher write power) to validate the phase stability of the system, which is evidently good. Moreover, these four-fold coincidence fringes in Fig. 4.3a provide a further verification that predominantly one excitation is shared between a pair of ensembles. The analysis provided in section 4.8 with the measured cumulative $h^{(2)}$ parameter for this set of data, $h^{(2)} = 0.12 \pm 0.02$, predicts a visibility of $V = 78 \pm 3\%$ in good agreement with the experimentally determined $V \cong 75\%$. Finally, the fact that one of the fringes is inverted with respect to the other in Fig. 4.2b corresponds to the two possible signs in Eq. 4.3. As for $\theta_L = 45°$ the measurement is sensitive to the square of the overlap $\overline{\lambda}$ of photon wavepackets for fields $2_{U,D}$, we infer $\overline{\lambda}_{U,D} \simeq 0.85$ from the reduced fringe visibility ($V \cong 55\%$) in Fig. 4.3b relative to Fig. 4.3a , if all the reduction is attributed to a non-ideal overlap. An independent experiment for two-photon Hong-Ou-Mandel interference[149] in this setup has shown an overlap of $\overline{\lambda} \simeq 0.90$, confirming that the reduction can be principally attributed to the non-ideal overlap (section

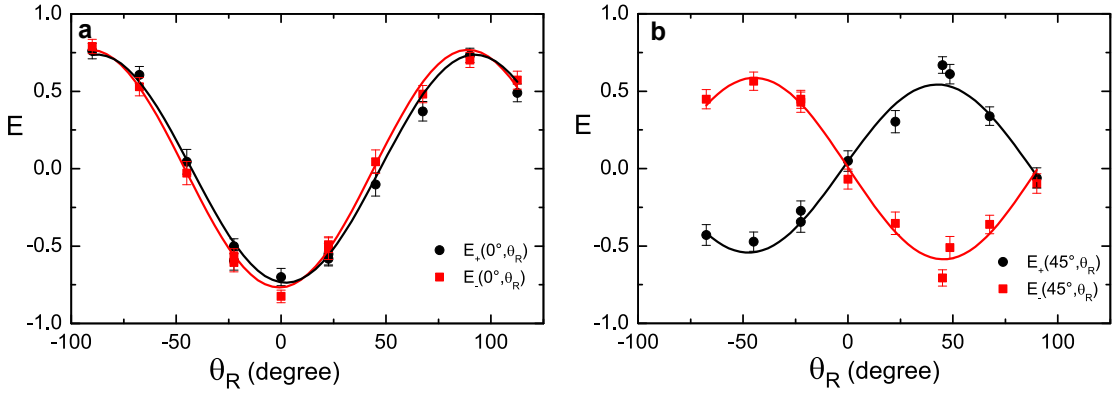

Figure 4.3: **Measured correlation function $E(\theta_L, \theta_R)$ as a function of θ_R with θ_L fixed at a, 0° and b, 45°.** The excitation probabilities for the ensembles are increased by ~ 1.5 times relative to Fig. 4.2, with each point taken for 30 minutes at typically 400/hour coincidence rate for each fringe. Error bars indicate statistical errors.

4.9). Other possible causes include imperfect phase alignment $\eta \neq 0$ and imbalance of the effective state coefficients.

4.5 Violation of Bell inequality

With the measurements from Figs. 4.2 and 4.3 in hand, we verify entanglement unambiguously by way of the violation of a Bell inequality[219]. For this purpose, we choose the canonical values, $\theta_L = \{0^\circ, 45^\circ\}$ and $\theta_R = \{22.5^\circ, -22.5^\circ\}$, and construct the *CHSH* parameters

$$\begin{aligned} S_+ &\equiv |E(0^\circ, 22.5^\circ) + E(0^\circ, -22.5^\circ) \\ &\quad + E(45^\circ, -22.5^\circ) - E(45^\circ, 22.5^\circ)| \qquad (4.6) \\ S_- &\equiv |E(0^\circ, 22.5^\circ) + E(0^\circ, -22.5^\circ) \\ &\quad + E(45^\circ, 22.5^\circ) - E(45^\circ, -22.5^\circ)| \qquad (4.7) \end{aligned}$$

for the two effective states $|\psi^{\pm}_{2_L,2_R}\rangle_{\text{eff}}$ in Eq. 4.3. For local, realistic hidden variable theories, $S_\pm \leq 2$[219]. Fig. 4.4 shows the *CHSH* parameters $S_\pm$ as functions of the duration τ_M up to which one pair of ensembles holds the prepared state, in the excitation regime of Fig. 4.2. As shown in section 4.8, the requirements for minimization of higher-order terms are much more stringent in this experiment with four ensembles than with simpler configurations[202].

Fig. 4.4a and b give the results for our measurements of $S_\pm$ with binned data. Each point corresponds to the violation obtained for states generated at $\tau_M \pm \Delta\tau_M/2$ (with the bin size $\Delta\tau_M$ marked by the thick horizontal lines). Strong violations of the inequality $S_\pm \leq 2$ are obtained for short memory times, with for instance $S_+ = 2.55 \pm 0.14 > 2$ and $S_- = 2.61 \pm 0.13 > 2$ for the second bin, demonstrating the

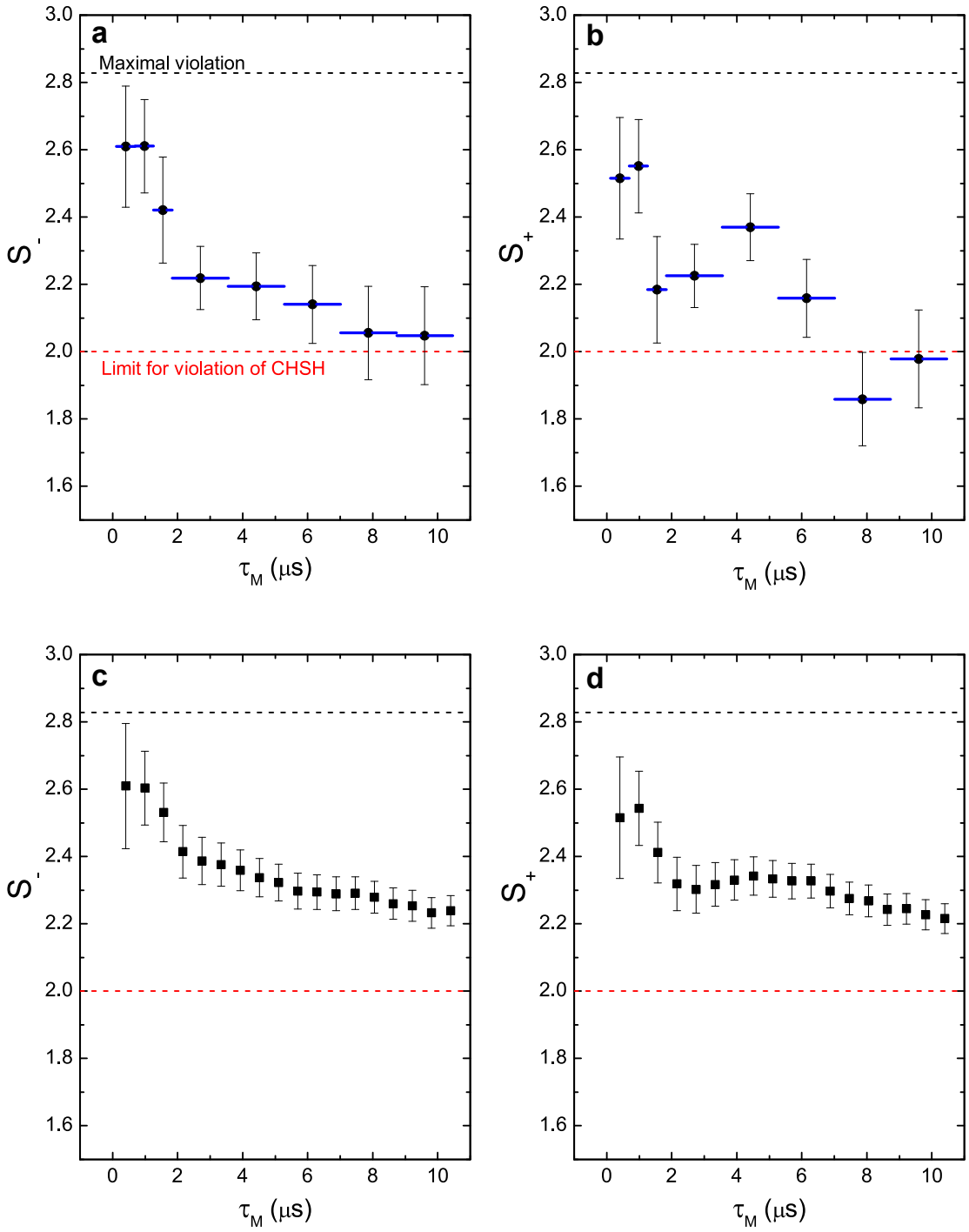

Figure 4.4: **Measured *CHSH* parameters and the violation of Bell inequality.** We measured the *CHSH* parameters $S_{\pm}$, for the two possible effective states in Eq. 4.3, as functions of duration τ_M for which the first ensemble pair holds the prepared state. The excitation probabilities are kept low for high correlation (as in Fig. 4.2). Panels **a** and **b** are the binned data. The horizontal thick lines indicate the size of the bins used. Panels **c** and **d** are the cumulative data. The coincidence rate for these measurements is about 150/hour for each effective state. Error bars indicate statistical errors.

presence of entanglement between the fields 2_L and 2_R, as well as between the two quantum nodes L and R. Therefore, these fields can be exploited to perform entanglement-based quantum communication protocols, such as quantum key distribution with, at minimum, security against individual attacks[4,220].

As it can be seen in Fig. 4.4, the violation decreases with increasing τ_M. The decay is largely due to the time-varying behavior of $h^{(2)}$ in Fig. 4.2. In addition to this decay, the S_+ parameter exhibits modulation with τ_M. We have explored different models to understand the time dependence of the *CHSH* parameters, but so far we have not found satisfactory agreement between model calculations and measurements. Nevertheless, the density matrix for the ensemble over the full memory time is potentially useful for tasks such as entanglement connection, as shown by panels Fig. 4.4c and d where cumulative data are given. Each point at memory time τ_M gives the violation obtained by taking into account all the states generated from 0 to τ_M. Overall significant violations are obtained, namely $S_+ = 2.21 \pm 0.04 > 2$ and $S_- = 2.24 \pm 0.04 > 2$ at $\tau_M \sim 10$ μs.

4.6 Conclusion

In our experiment, we are able to generate excitation-number entangled states between remote locations, which are well suited for scaling purposes, and, with real-time control, to operate them as if they were effectively polarization entangled states, which are appropriate for quantum communication applications, such as quantum cryptography. Measurements of the suppression $h^{(2)}$ of two-excitation components versus storage time demonstrates explicitly the major source that causes the extracted polarization entanglement to decay, emphasizing the critical role of multi-excitation events in the experiments aiming for a scalable quantum network. The present scheme, which constitutes a functional segment of a quantum repeater in terms of quantum state encoding and channel control, allows the distribution of entanglement between two quantum nodes. But the extension of our work to longer chains involving many segments becomes more complicated, and out of reach for any current system. For long-distance communication, the first quantity to improve is the coherence time of the memory. Better cancellation of the residual magnetic fields and switching to new trap schemes should improve this parameter to ~ 0.1 sec by employing an optical trap[147], thereby increasing the rate of preparing the ensembles in the state of Eq. 4.1 to ~ 100 Hz. The second challenge which would immediately appear in an extended chain would be the increase of the multi-excitation probability with the connection stages. Recently, ref.[122] has theoretically demonstrated the prevention of such growth in a similar setup, but its full scalability still requires very high retrieval and detection efficiency, and photon-number resolving detectors. These two points clearly show that the quest of scalable quantum networks is still a theoretical and experimental challenge. The availability of our first functional segment opens the way for fruitful investigations.

4.7 Experimental details

Ensembles (LU, LD) are pencil-shaped groups of cold Cesium atoms released from a magneto-optical trap (MOT), while ensembles (RU, RD) are prepared from another MOT, 3 meters away. $\{|g\rangle, |s\rangle, |e\rangle\}$ correspond to the hyperfine levels $\{|6S_{1/2}, F = 4\rangle, |6S_{1/2}, F = 3\rangle, |6P_{3/2}, F' = 4\rangle\}$, respectively. In each MOT, the ensembles U, D are separated by 1 mm by way of birefringent beam displacers (chapter 3). The MOT is formed at a repetition rate of 40 Hz in a steady-state regime (with MOT loading time of ~ 6 s.). In each cycle, the MOT is loaded for 18 ms, after which the magnetic field is quickly switched off. The trapping beams are turned off 3 ms after the magnetic field, while the repumping beam stays on for another 100 μs before being switched off in order to prepare the atoms in the $F = 4$ ground state $|g\rangle$. 3.4 ms after the magnetic field is turned off, trials of the protocol (each consisting of successive write, read, and repumping pulses) are repeated with 575 ns period for 3.4 ms. In each trial, the write pulse is ≈ 30 ns in duration and 10 MHz red-detuned from the $|g\rangle \rightarrow |e\rangle$ transition. The read and the repumping pulses are both derived from the read beam (resonant with the $|s\rangle \rightarrow |e\rangle$ transition) with 30 ns and 75 ns duration, respectively. The read pulse is closely followed by the repumping pulse. The read pulse is delayed ≈ 400 ns after the write pulse, leaving time for the control logic to gate it off, along with the subsequent pulses. Independent phase stability measurements show that the phase η between the two ensembles drifts in a negligible way, $(\pi/30)$ over 500 μs corresponding to 870 trials. Some other parameters of the experiments are calibrated and listed in Table 4.1.

Table 4.1: **Noise and efficiencies.** The intrinsic retrieval efficiency for mapping single collective excitations to single photons is $\eta_U = 18 \pm 3\%$ ($\eta_D = 23 \pm 3\%$) for the U (D) ensembles.

	U	D
Field 1 dark count rate	~ 10 Hz	~ 10 Hz
Field 2 dark count rate	~ 100 Hz	~ 100 Hz
Conditional detection efficiency p_c	$6.4\% \pm 0.5\%$	$8.0\% \pm 0.5\%$
Field 2 propagation efficiency	$68 \pm 5\%$	$68 \pm 5\%$
Field 2 detector quantum efficiency	$50 \pm 5\%$	$50 \pm 5\%$

4.8 Fringe visibility as a function of $h^{(2)}$

Let us consider that the two pairs of ensembles, *U* and *D*, have been prepared by heralded detections at D_{1a}, D_{1b} and D_{1c}, D_{1d}. Denote by p_{10}, p_{01}, and p_{11} the probability p_{ij} to register i photodetection events in field 2_{LU} and j in field 2_{RU} after firing the read pulses. We will assume, for simplicity, the various p_{ij} are the same for both pairs of ensembles. For each of them, the suppression of the two-photon events relative to the square of the probability for single-photon events is characterized by the parameter $h^{(2)}$ (ref.[27]),

$$h^{(2)} = \frac{p_{11}}{p_{10}p_{01}}. \tag{4.8}$$

We next relate $h^{(2)}$ to the maximal C_{max} and minimal C_{min} coincidence probabilities between various output ports of the detection polarizing beamsplitters (*PBS*) for the left and right nodes at detectors D_{2a}, D_{2b} and D_{2c}, D_{2d} (see Fig. 4.1). Consider, for example, the transmitted ports of the *PBS* at the L, R detectors for the case that the left node has the half-wave plate $(\lambda/2)_L$ set to $0°$. In this case, fields 2_{LU} and 2_{LD} are detected independently, with field 2_{LD} transmitted at the *PBS*. On one hand, C_{max} is obtained for crossed polarizers (i.e., $(\lambda/2)_R$ set to $45°$ at the right node, with then field 2_{RU} transmitted) and is given to lowest order by

$$C_{\text{max}} = p_{10}p_{01}. \tag{4.9}$$

This term corresponds to the case where only a single excitation is distributed in each pair, and each retrieved photon is detected from a transmitted port on each side L, R.

On the other hand, the minimum coincidence probability C_{min} is obtained for parallel polarizers (i.e., $(\frac{\lambda}{2})_R = 0°$ at the right node, with then field 2_{RD} transmitted) and can be written as

$$C_{\text{min}} = p_{11}. \tag{4.10}$$

This term corresponds to coincidences due to photons coming from the same pair of ensembles. The smaller is the excitation probability, the smaller is this background term.

Taking Eqs. 4.9 and 4.10 into account, we find that the visibility V for the number of coincidences as a function of the right polarizer angle (i.e., the angle for $(\frac{\lambda}{2})_R$) is given by

$$V = \frac{C_{\text{max}} - C_{\text{min}}}{C_{\text{max}} + C_{\text{min}}} = \frac{1 - h^{(2)}}{1 + h^{(2)}}. \tag{4.11}$$

Assuming that the visibility is the same in each basis, we then find a *CHSH* parameter S (ref.[221]) equal to

$$S = 2\sqrt{2}\,V = 2\sqrt{2}\,\frac{1 - h^{(2)}}{1 + h^{(2)}}. \tag{4.12}$$

A minimal value $h^{(2)}_{\text{min}} = 0.17$ is thus required to violate the *CHSH* inequality $S < 2$ in the absence of any imperfections except the intrinsic two-photon component. This value underlines that this experiment is much more stringent in terms of minimization of high-order terms than previously reported setups. For example, in ref.[202], where entanglement between a photon and a stored excitation is reported, a value of $h^{(2)}$ equal to 0.68 was sufficient to violate the inequality. The dramatic improvement reported recently by different groups for the quality of the photon pairs emitted by an atomic ensemble was thus an enabling step for the practical realization of such a more elaborate procedure involving a total of 4 ensembles reported in section 4.5.

4.9 Two-photon interference and inferred overlaps

For a non-unity overlap $\overline{\lambda}$ of the field-2 photon wavepackets, the visibility of the fringes in the 45° basis is decreased by a factor $\overline{\lambda}^2$. This overlap can be determined by the two-photon interference, which is implemented by mixing the fields 2_U and 2_D on each side (R and L) by rotating the half-wave plates $(\lambda/2)_L, (\lambda/2)_R$ by 22.5°. If the single photon wavepackets are indistinguishable, no coincidences should be observed. However, the two-photon component can lead to coincidences, which reduce the visibility. Let us determine the expected visibility as a function of the two-photon component by way of a simple model.

Consider P_n the probability of finding n photons in field 2, and assume the various P_n are the same for both ensembles involved. In the ideal case where all ensembles have the same properties, the two-photon suppression for each field 2 can also be characterized by the same $h^{(2)}$ parameter used before, which can be written here as

$$h^{(2)} = \frac{2P_2}{P_1^2}. \tag{4.13}$$

When the half-wave plates $(\lambda/2)_L, (\lambda/2)_R$ are at 0°, the fields 2 are detected independently and the probability p_{max} to register coincidences is given by

$$p_{\text{max}} = P_1^2. \tag{4.14}$$

When the half-wave plates $(\lambda/2)_L, (\lambda/2)_R$ are rotated to 22.5°, if the two fields overlap perfectly, the term with one photon in each input does not lead to coincidences. If we denote by $\overline{\lambda}$ the overlap, the probability p_{min} to have one photon in each output is then

$$p_{\text{min}} = \frac{(1-\overline{\lambda}^2)}{2}P_1^2 + \frac{P_2}{2} + \frac{P_2}{2} = [1 - \overline{\lambda}^2 + h^{(2)}]\frac{P_1^2}{2}. \tag{4.15}$$

From these two probabilities, we find that the visibility of the dip in coincidences can be written as

$$V_{\text{dip}} = \frac{p_{\text{max}} - p_{\text{min}}}{p_{\text{max}}} = \frac{1 + \overline{\lambda}^2 - h^{(2)}}{2}. \tag{4.16}$$

In our case, the measured Hong-Ou-Mandel visibility V_{dip} is $85 \pm 2\%$ for the left node and $89 \pm 2\%$ for the right one. The measured average $h^{(2)}$ parameter for this set of data is 0.09 ± 0.01, which leads to visibilities $V_{\text{model}} = 95.5 \pm 0.5\%$ in the case of perfect overlap ($\overline{\lambda} = 1$). From the measured visibilities and this simple model, we then estimate the overlaps, $\overline{\lambda} = 0.89 \pm 0.03$ for the left node and $\overline{\lambda} = 0.93 \pm 0.03$ for the right node.

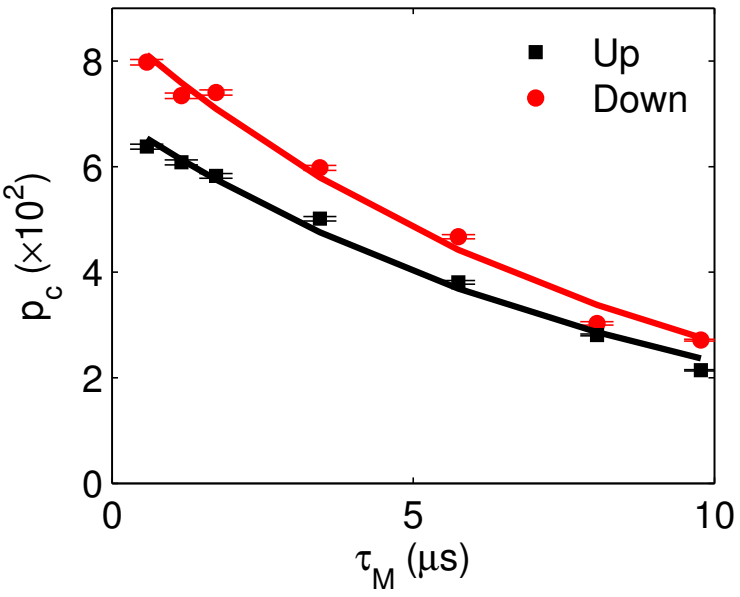

Figure 4.5: **Conditional probability as a function of the storage time.** Conditional probability p_c of detecting one photon in a field 2 for the U (black squares) and D (red circles) pairs, as a function of the storage time τ_M. The error bars indicate statistical errors. The solid lines are fits using Eq. 4.17.

4.10 Decoherence time of the stored excitation

Residual magnetic fields, which lead to inhomogeneous broadening of the ground states levels, is the major limiting factor of the coherence time τ_c of the stored excitation (refs.[147,202], chapter 3). Consequently, if we neglect dark counts, the conditional retrieval efficiency $p_c = p_{01} + p_{10}$ is expected to decay exponentially with the storage time τ_M

$$p_c = p_c^{(0)} \exp(-\frac{\tau_M}{\tau_c}). \tag{4.17}$$

Fig. 4.5 shows an independent measurement of p_c vs. τ_M, with the U and D pairs separated. Fitting the data with Eq. 4.17 gives, for the U and D pairs, respectively, we obtain $p_c^{(0)} = 7.0\% \pm 0.1\%$ and $8.7\% \pm 0.2\%$, and $\tau_c = 9.1 \pm 0.6\mu$s and $8.5 \pm 0.5\mu$s.

The decay of p_c leads to a similar exponential decay of C_{ij}. C_{ij} $(i, j = a, b, c, d)$ are the coincidence count rates of two field 2 photons conditioned on the two heralding field 1 photons defined before. Summing over all C_{ij} used in calculating $S_\pm$, we obtain the total coincidence count rates $C_{S\pm}$ for the measurement of the Bell parameters S_+ and S_-. $C_{S\pm}(\tau_M)$ corresponds to the probability distribution of the $S_\pm(\tau_M)$, and is reflected in the statistical error bars $\Delta S_\pm(\tau_M)$. The decay of $C_{S\pm}$ with τ_M is shown in Fig. 4.6. Fitting the data with exponential functions,

$$C_{S\pm} = C_{S\pm}^{(0)} \exp(-\tau_M/\tau_\pm), \quad \tau_M > 0, \tag{4.18}$$

gives $\tau_+ = 9.1 \pm 0.4\mu$s and $\tau_- = 8.1 \pm 0.3\mu$s, in good agreement with τ_c. Note that $C^{(0)}_{S\pm} = 2C_{S\pm}(\tau_M = 0)$, since $C_{S\pm}(\tau = 0)$ is conditioned on two excitation in a same trial, while $C_{S\pm}(\tau > 0)$ is conditioned on two excitations created in two different trials: the factor of 2 accounts for the two possible orders of excitations ('U' then 'D,' or 'D' then 'U').

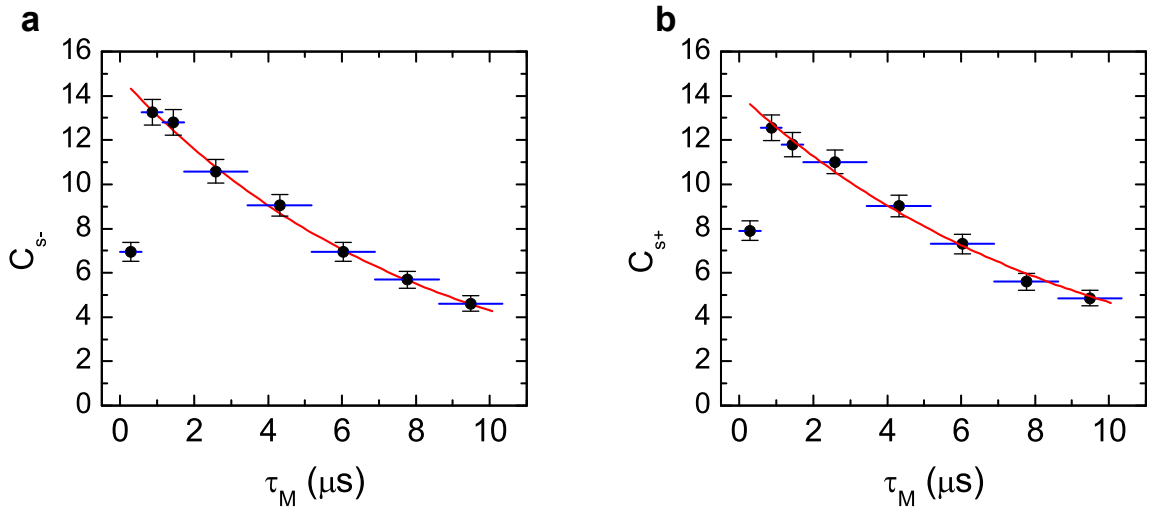

Figure 4.6: τ_M**-dependence of the total conditional count rates** $C_{S\pm}$ **in the measurement of a,** S_+ **and b,** S_-**.** The horizontal thick lines indicate the size of the memory bin. The error bars indicate statistical errors. The solid lines are fits using Eq. 4.18.

4.11 Conditional control and increase in generation rate

As demonstrated in ref.[78], the conditional control of remote quantum memories enables a large enhancement of coincidence rates relative to the case where no control logic is implemented. I refer to James' thesis[71] for the details of the logic circuit implemented in this and former experiments. If the state prepared in one pair of ensembles is held up to N trials, the rate for preparing both pairs is increased by a factor $(2N + 1)$ for very low excitation probability[78]. Fig. 4.7a gives the probability p_{11} of simultaneously preparing the two pairs. After 17 trials, an increase by a factor 34 is obtained experimentally, close to the expected value of 35. The gain in the probability p_{1122} of generating the effective entangled state is expected to be the same if the coherence time τ_c is long enough. However, our finite coherence time results in a smaller increase of the probability to detect field 2 coincidences. This increase is given in Fig. 4.7b, with a comparison to the ideal case of very long coherence time. A 19-fold enhancement is finally obtained. Let us note that the different experimental rates can be obtained from these probabilities times the number of trials per second ($\sim 2.36 \times 10^5$/s).

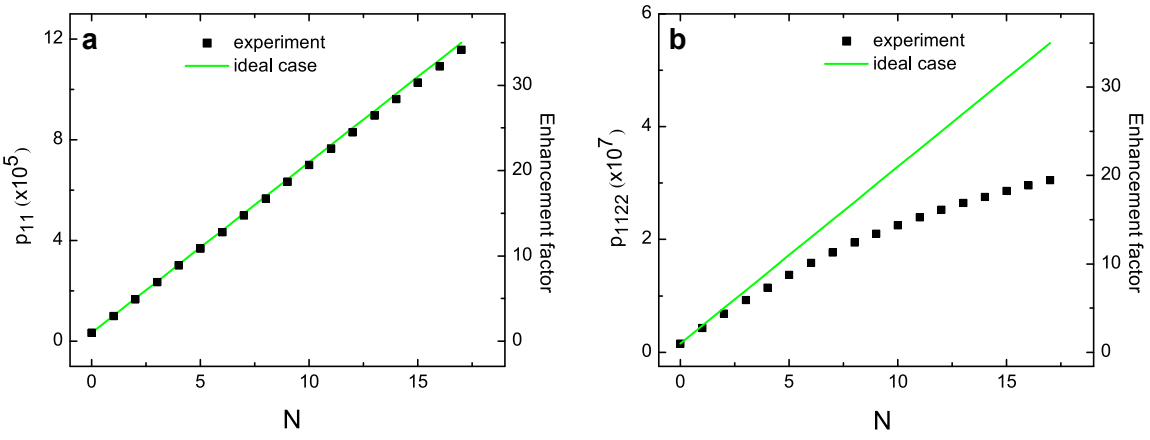

Figure 4.7: **Conditional enhancement.** Probabilities of coincidence detection as functions of the number of trials N for which the first prepared pair holds the entangled state. **a**, Measured probability p_{11} of preparing the two pairs. **b**, Measured probability p_{1122} of detecting field 2 coincidences. The green solid line corresponds to the ideal case of very long coherence time. Both panels give in addition to these probabilities the enhancement factor obtained relative to the case without conditional control.

4.12 Correlation functions $E(0°, \theta_R)$, $E(45°, \theta_R)$ for the ideal effective state

In practice, various imperfections lead to deviations from the ideal effective state in Eq. 4.2. We have developed a detailed model relevant to our experiment based on the two-mode squeezed states in chapter 2, but here we will consider only a generic form. Collective excitations are not shared with equal amplitudes between a pair of ensembles because of imperfections in the writing and heralding processes. Likewise, the mapping of atomic states to states of field 2 by the read pulses is not ideal. Overall, these various imperfections lead to a state $|\psi_{2_{LU},2_{RU},2_{LD},2_{RD}}\rangle$ for field 2 given by (neglecting multi-photon processes),

$$\begin{aligned}
|\psi_{2_{LU},2_{RU},2_{LD},2_{RD}}\rangle &= \Big(\epsilon_{RU}|0_{2_{LU}}\rangle|1_{2_{RU}}\rangle \pm e^{i\eta_U}\epsilon_{LU}|1_{2_{LU}}\rangle|0_{2_{RU}}\rangle\Big) \\
&\quad \otimes\Big(\epsilon_{RD}|0_{2_{LD}}\rangle|1_{2_{RD}}\rangle \pm e^{i\eta_D}\epsilon_{LD}|1_{2_{LD}}\rangle|0_{2_{RD}}\rangle\Big) \\
&= \epsilon_{RU}\epsilon_{RD}|0_{2_{LU}}\rangle|0_{2_{LD}}\rangle|1_{2_{RU}}\rangle|1_{2_{RD}}\rangle \\
&\quad \pm e^{i\eta_U}e^{i\eta_D}\epsilon_{LU}\epsilon_{LD}|1_{2_{LU}}\rangle|1_{2_{LD}}\rangle|0_{2_{RU}}\rangle|0_{2_{RD}}\rangle \\
&\quad \pm e^{i\eta_U}\epsilon_{RD}\epsilon_{LU}|1_{2_{LU}}\rangle|0_{2_{LD}}\rangle|0_{2_{RU}}\rangle|1_{2_{RD}}\rangle \\
&\quad \pm e^{i\eta_D}\epsilon_{RU}\epsilon_{LD}|0_{2_{LU}}\rangle|1_{2_{LD}}\rangle|1_{2_{RU}}\rangle|0_{2_{RD}}\rangle\,, \qquad (4.19)
\end{aligned}$$

where ϵ_X is the probability amplitude that a photon is created in field 2_X. The first and second terms in the expansion correspond to the cases that the two excitations are both retrieved at node 'right' and 'left', respectively. Thus, the effective state that yields one detection event at node 'left' and the other at node 'right' consists of the last two terms. After the fields are combined by PBS_L and PBS_R, we get the (unnormalized)

effective state of fields 2_L and 2_R

$$|\psi_{2_L,2_R}\rangle_{\text{eff}} = \alpha|H_{2_L}V_{2_R}\rangle \pm \beta|V_{2_L}H_{2_R}\rangle\ , \tag{4.20}$$

where $\alpha \propto e^{i\eta_D}\epsilon_{RU}\epsilon_{LD}$ and $\beta \propto e^{i\eta_U}\epsilon_{RD}\epsilon_{LU}$.

From the effective state $|\psi_{2_L,2_R}\rangle_{\text{eff}}$, we can derive the various coincidence probabilities P_{ij}, $i,j \in \{a,b,c,d\}$, where $\{a,b,c,d\}$ refers to the detectors $D_{2\{a,b,c,d\}}$ for field 2 in Fig. 4.1. When θ_L is fixed at 0°, we find (assuming unity detection efficiency)

$$\begin{aligned} P_{ac} &= |\alpha|^2\text{sin}^2\theta_R \\ P_{bd} &= |\beta|^2\text{sin}^2\theta_R \\ P_{ad} &= |\alpha|^2\text{cos}^2\theta_R \\ P_{bc} &= |\beta|^2\text{cos}^2\theta_R \\ E(0^\circ,\theta_R) &\propto P_{ac} + P_{bd} - P_{ad} - P_{bc} = -\text{cos}(2\theta_R) \end{aligned} \tag{4.21}$$

irrespective of the $\pm$ sign.

By contrast, when θ_L is fixed at 45°, we obtain

$$\begin{aligned} P_{ac} &= \frac{1}{4}[1 \pm 2|\alpha||\beta|\ \text{cos}\phi\ \text{cos}(90^\circ - 2\theta_R) \\ &+ (|\beta|^2 - |\alpha|^2)\ \text{sin}(90^\circ - 2\theta_R)], \end{aligned}$$

where $\phi = \text{arg}(\beta) - \text{arg}(\alpha)$. Let $\alpha = \text{cos}\varphi$, and $\beta = \text{sin}\varphi$. Denoting $\delta = 45^\circ - \theta_R$, we have

$$\begin{aligned} P_{ac} &= \frac{1}{4}[1 \pm |\text{sin}2\varphi|\ \text{cos}\phi\ \text{cos}2\delta - \text{cos}2\varphi\ \text{sin}2\delta] \\ P_{bd} &= \frac{1}{4}[1 \pm |\text{sin}2\varphi|\ \text{cos}\phi\ \text{cos}2\delta + \text{cos}2\varphi\ \text{sin}2\delta] \\ P_{ad} &= \frac{1}{4}[1 \mp |\text{sin}2\varphi|\ \text{cos}\phi\ \text{cos}2\delta + \text{cos}2\varphi\ \text{sin}2\delta] \\ P_{bc} &= \frac{1}{4}[1 \mp |\text{sin}2\varphi|\ \text{cos}\phi\ \text{cos}2\delta - \text{cos}2\varphi\ \text{sin}2\delta] \\ E(45^\circ,\theta_R) &\propto P_{ac} + P_{bd} - P_{ad} - P_{bc} = \pm|\text{sin}2\varphi|\ \text{cos}\phi\ \text{cos}2\delta. \end{aligned} \tag{4.22}$$

From the expression for $E(45^\circ,\theta_R)$, we see that the deviation of $|\alpha|$ and $|\beta|$ from the balanced value, $1/\sqrt{2}$, will lead to reduction in the visibility of $E(45^\circ,\theta_R)$ fringes and thus the magnitudes of the *CHSH* parameters $S_{(\pm)}$. We believe that such an imbalance is responsible for the results displayed in Fig. 4.3b for $E(45^\circ,\theta_R)$ and Fig. 4.4 for $S_{(\pm)}$ at $\tau_M = 0$, with measurements underway to quantify this association.

Note that an alternative combination of P_{ij} gives

$$\begin{aligned} F(45^\circ, \theta_R) &\equiv -P_{ac} + P_{bd} + P_{ad} - P_{bc} \\ &= \cos 2\varphi \sin 2\delta. \end{aligned} \tag{4.23}$$

In particular, $F(45^\circ, \theta_R)$ allows us to determine φ and thus the magnitude of the coefficients α and β, independent of ϕ. Specifically, the visibility of the $F(45^\circ, \theta_R)$ fringes normalized to that of $E(0^\circ, \theta_R)$'s fringes yields $\cos 2\varphi$.

Chapter 5

Experimental transfer of 'coherence': Towards entanglement connection

This chapter is largely based on ref.[37]. Reference[37] refers to the then current literature in 2007 at the time of publication.

5.1 Introduction

The distribution of entanglement between different parties enables the realization of various quantum communication protocols, such as quantum cryptography, dense coding, and teleportation (refs.[3,162], see also chapter 1). Such distribution relies on entanglement swapping, namely the teleportation of entanglement, which aims at entangling two distant systems which never interacted in the past. Important aspects of this striking feature have already been demonstrated with independent sources of entangled light. In the discrete variable regime, one can generate two independent pairs of polarization entangled beams and subject a superposition of two of the beams to a Bell-state analyzer[a]. The two remaining beams are then projected into an entangled state[222]. More recently, unconditional entanglement swapping has been achieved for continuous quantum variables of light[223,224].

However, to enable quantum communication over arbitrary long distances, entanglement needs to be stored in matter systems. In the quantum repeater architecture[9], entanglement is distributed by swapping through a chain of spatially separated entangled pairs of memories, leading to the possibility of scalable long-distance communication (see Fig. 5.1). Connecting entangled matter systems is thus a critical requirement for the practical realization of quantum networks (chapter 1). Along this line, generation of entanglement between atomic systems has been reported, including entanglement of the discrete internal states of two trapped ions[225], long-lived entanglement of macroscopic quantum spins[59] and, heralded entanglement between atomic ensembles in the single excitation regime (refs.[27,34], chapter 3). However, no entanglement

[a]Note that an entanglement swapping scheme with linear optics is inherently probabilistic (with success probability 50%), because it cannot distinguish the two among the four Bell states[222] (except for the case of continuous variable entangled states[223,224]). Strong nonlinearity is physically required to achieve a quantum gate, which allows for distinguishing all four possible Bell-state projections.

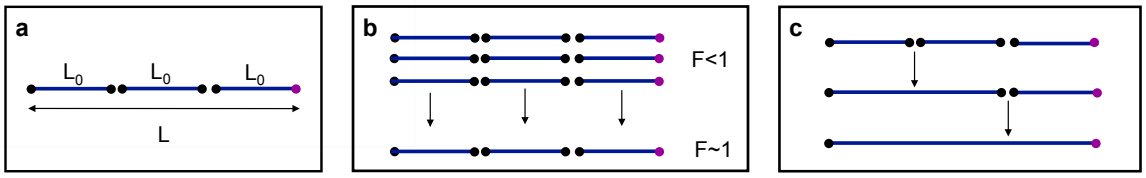

Figure 5.1: **A generic scheme for a bipartite quantum repeater architecture[9]. a**, Entanglement generation and storage. To link two quantum nodes with distance L, we first divide the (long-distance) communication channel into shorter segments (each with length of L_0 and negligible optical attenuation), and generate a linear chain of entangled states in quantum memories (dots). **b**, Entanglement purification. By preparing parallel chains of entangled states in **a**, we probabilistically purify the entangled states with low fidelity $F < 1$ into a single chain comprised of high-fidelity ($F \sim 1$) entangled states. **c**, Entanglement connection. Finally, we sequentially connect the entangled state by entanglement swapping, and eventually prepare a high-fidelity entanglement between the two quantum nodes over a long distance L.

connection has been demonstrated so far with such matter systems. In this chapter, I describe our work towards entanglement connection of atomic ensembles and demonstrate for the first time the transfer of coherence between two atomic ensembles which never interacted[37].

This chapter is organized as follows. In section 5.2, I will give a brief overview of our matter building block, namely an atomic ensemble in the regime of single collective excitation. In section 5.3, I discuss the principles of measurement-induced entanglement between excitation from two remote atomic ensembles, and connection of two pairs. The theoretical model developed in chapter 3 to verify experimentally entanglement is summarized[27,34], and used to give insights into the connection process. The experimental setup is finally presented in section 5.4, together with the experimental results. Finally, I will conclude with our perspectives on realizing entanglement connection experimentally in section 5.5.

5.2 Atomic ensemble in the single-excitation regime

In 2001, Duan, Lukin, Cirac and Zoller (*DLCZ*) proposed an original approach to perform scalable long-distance quantum communications, involving atomic ensembles, linear optics and single photon detectors[4]. The building block is a large ensemble of N identical atoms with a Λ-type level configuration, as shown in Fig. 5.2. A weak light pulse, called write pulse, with frequency close to the $|g\rangle \rightarrow |e\rangle$ transition, illuminates the atoms and induces spontaneous Raman scattering into a photonic mode called field 1. For a low enough write power, such that two excitations are unlikely to occur, the detection of a field 1 photon heralds the storage of a single collective excitation distributed among the whole ensemble. As discussed in chapter 2, the joint state of the atoms and field 1 is a two-mode squeezed state,

$$|\Psi\rangle = |0_a\rangle|0_1\rangle + \sqrt{\chi}|1_a\rangle|1_1\rangle + \mathcal{O}(\chi), \tag{5.1}$$

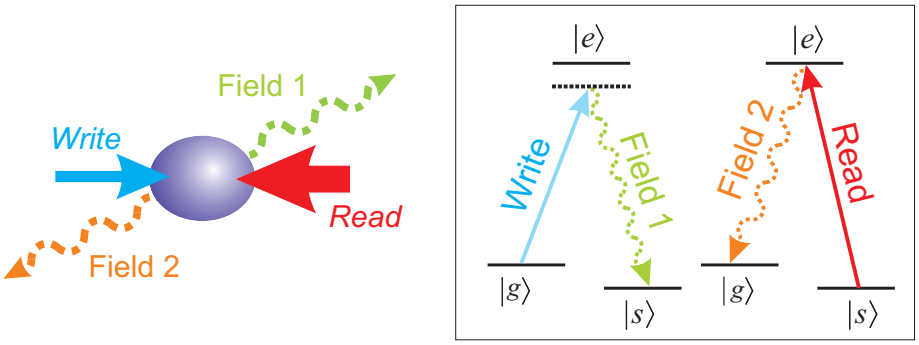

Figure 5.2: ***DLCZ* building block in a counter-propagating and off-axis configuration.** The inset shows the relevant atomic levels for the $6S_{1/2} \rightarrow 6P_{3/2}$ transition in cesium, as well as the associated light fields. The ensemble is initially prepared in $|g\rangle$. A weak write pulse then induces spontaneous Raman transitions $|g\rangle \rightarrow |e\rangle \rightarrow |s\rangle$, resulting with small probability in the emission of a photon (field 1, detected inside a single mode fiber with at a small angle to the write beam) along with the storage of a collective excitation. After a programmable delay, a strong read pulse then maps the state of the atoms to another photonic mode, field 2, via $|s\rangle \rightarrow |e\rangle \rightarrow |g\rangle$.

where $|n_1\rangle$ stands for the state of the field 1 with n photons and χ corresponds to the small probability of a single photon scattered into field 1 by the atoms illuminated by the write pulse. We define $|0_a\rangle \equiv \bigotimes_i^N |g\rangle_i$ and $|1_a\rangle$ denotes a symmetric collective excitation, with

$$|1_a\rangle = \frac{1}{\sqrt{N}} \sum_{i=1}^{N} |g\rangle_1 \cdots |s\rangle_i \cdots |g\rangle_N. \tag{5.2}$$

A read pulse, on resonance with the $|s\rangle \rightarrow |e\rangle$ transition, can later, after a programmable delay, transfer this atomic excitation into another photonic mode, field 2, with collective enhancement (refs. [147,226], chapter 2). After the readout, the resultant state of the fields 1 and 2 is ideally

$$|\Phi\rangle = |0_1\rangle|0_2\rangle + \sqrt{\chi}|1_1\rangle|1_2\rangle + \mathcal{O}(\chi).$$

The two photonic modes, fields 1 and 2, contain quantum correlations [72], precisely as in the case of parametric down-conversion (chapter 2). The lower is the excitation probability $\chi \rightarrow 0$, the better is the approximation of the non-vacuum part by a photon pair, at the price of reduced count rates.

The optically thick atomic ensemble is obtained from cold cesium atoms in a magneto-optical trap (MOT). At a frequency of 40 Hz, the magnetic field is switched off for 7 ms. After waiting about 3 ms for the magnetic field to decay, sequences of writing, reading, and repumping processes are carried out for about 4 ms, with a period of 575 ns. The weak write pulses, with a 200 μm beam waist and linear polarization, are detuned 10 MHz below resonance. The read pulse is orthogonally polarized to the write pulse and mode-matched to it in a counter-propagating configuration. Both write and read pulses are 30 ns long. Fields 1 and 2 are collected into mode-matched fibers with a 3° angle relative to the common direction defined by write and read beams [75], and with a waist of 50 μm defined by the backward projection of our imaging system into the

sample (chapter 2). Before detection, field 1 passes through a filtering stage in order to filter out the photons that are spontaneously emitted when the atoms in the sample go back to $|g\rangle$, without creating the desired collective excitation.

Three parameters well characterize the system experimentally: (i) how well the system is in the single excitation regime, (ii) how efficient is the retrieval of a single excitation, and (iii) how long the excitation can be stored before retrieval while preserving its coherence. The first parameter is determined by a measurement of the suppression of the two-photon component of the field 2 obtained from the retrieval of the excitation[b]. Suppression below 1% of the value for a coherent state has been reported in our system[76]. The ability to efficiently retrieve the excitation is also critical. The probability to have a photon in field 2 in a single spatial mode at the output of the atomic ensemble once an event has been recorded for field 1 can be as high as 50%, leading to a probability around 12.5 % for having a detection event[76]. Last but not least, the writing and retrieval processes can be separated by a programmable delay. As this delay is increased, the above two quantities (two-photon suppression and retrieval efficiency) decay in a typical time scale around 10 to 20 μs. The principal causes for this finite coherence time are the residual magnetic field that inhomogeneously broadens the ground state levels of the atomic samples, as well as the motional decoherence (chapter 2). Detailed theoretical and experimental studies of the decoherence have been reported in refs.[36,78,147,202] (see chapters 3–4).

5.3 Measurement-induced entanglement and connection of atomic ensembles

Starting from this building block, *DLCZ* proposed in their seminal paper to generate and store entanglement for excitation in two remote ensembles and then to connect two pairs. This section presents these measurement-induced schemes, which rely on quantum interference in the detection of a photon emitted by one of the ensembles. After establishing entanglement, directly or via connection, a difficult experimental task is to prove the entanglement[110]. A robust model developed in ref.[27] (see also chapter 3) is then presented.

5.3.1 Entanglement between two ensembles

Let us consider now two atomic ensembles, for which fields 1 are superposed on a $50/50$ beamsplitter, in an indistinguishable way, with the outputs directed towards two single-photon detectors (Fig. 5.3). The detection of a field 1 photon from either of the two ensembles results in an entangled state with one excitation shared coherently between the two ensembles. In more details, after two write pulses are sent into the two ensembles

[b] In chapters 3–4, we have used the parameter $h = \frac{p_{11}}{p_{10}p_{01}}$ to quantify the higher-order excitation for the joint state of the two ensembles. Note that there is analogous parameter, $w = \frac{2p_2}{p_1^2}$ (sometimes, denoted by $g^{(2)}(\tau)$), which quantifies the suppression of higher-order excitation for a single ensemble (or a single beam of light) relative to that of a coherent state ($w = 1$).

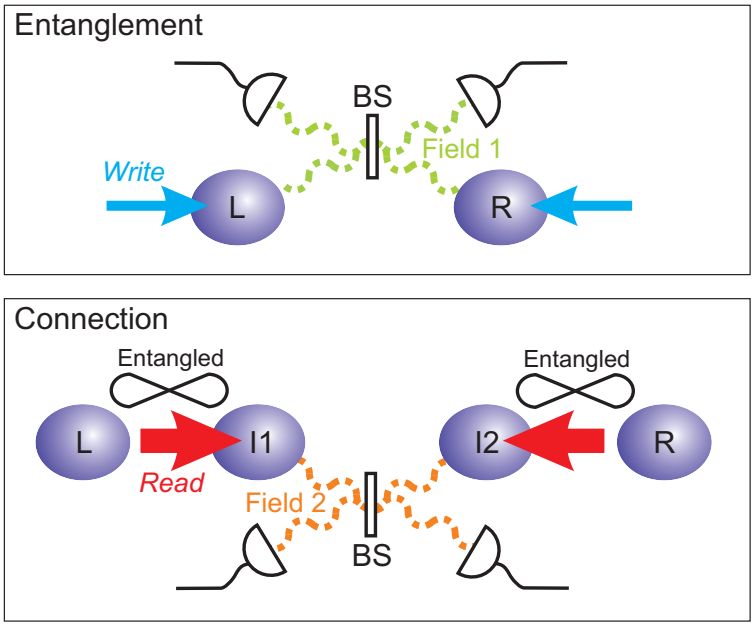

Figure 5.3: **Setups for entanglement generation between two atomic ensembles and entanglement connection between two pairs.** In both cases, the entanglement results from the interference of photonic modes at a 50/50 beamsplitter, with outputs directed towards single-photon detectors. The photonic modes consist in **a**, field 1 modes from both ensembles or **b**, field 2 modes after reading of one ensemble of each pair.

simultaneously, the scattered fields 1 and ensembles are in the product state,

$$\begin{aligned} |\Psi_{LR}\rangle \quad &\propto \quad [|0_a\rangle|0_1\rangle + e^{i\beta_L}\sqrt{\chi}|1_a\rangle|1_1\rangle + \mathcal{O}(\chi)]_L \\ &\otimes[|0_a\rangle|0_1\rangle + e^{i\beta_R}\sqrt{\chi}|1_a\rangle|1_1\rangle + \mathcal{O}(\chi)]_R. \end{aligned} \tag{5.3}$$

Here, β_R and β_L correspond to overall propagation phases determined by the write pulses. Detection of a photon in either detector then projects the state of the ensembles as follows, in the ideal case where higher-order terms are neglected,

$$\begin{aligned} \rho^{'}_{LR} \quad &= \quad \mathrm{Tr}_{1_L 1_R}[\rho(\frac{1}{\sqrt{2}}(a_{1_L} \pm e^{i\theta}a_{1_R})|\Psi_{LR}\rangle)] \\ &= \quad |\Psi^{'}_{LR}\rangle\langle\Psi^{'}_{LR}| \\ \text{with} \quad &\quad |\Psi^{'}_{LR}\rangle = \frac{1}{\sqrt{2}}(|0_a\rangle_L|1_a\rangle_R \pm e^{i\eta}|1_a\rangle_L|0_a\rangle_R). \end{aligned} \tag{5.4}$$

Here, $\rho(|\Psi\rangle) \equiv |\Psi\rangle\langle\Psi|$, $\mathrm{Tr}_{1_L 1_R}$ stands for tracing over the states of fields 1_L and 1_R, a_{1_L} and a_{1_R} are the annihilation operators associated with fields 1_L and 1_R, $\theta = \theta_R - \theta_L$ the difference phase shift between the two field 1 paths from the ensemble to the beamsplitter, and finally the overall phase $\eta = (\beta_L - \beta_R) + (\theta_L - \theta_R)$. This phase η is the sum of the phase difference of the write beams at the L and R ensembles and the phase difference acquired by fields 1 in propagation from the ensembles to the beamsplitter. To achieve entanglement, this phase has to be kept constant (ref. [110], chapter 9). In order to meet this stringent and challenging require-

ment in the initial demonstration reported in[27], the different phases have been independently controlled and actively stabilized by using auxiliary fields. Finally, the $\pm$ sign in Eq. 5.4 comes from the π phase difference between the two outputs of a beamsplitter: depending on which detector records the heralding event, two different entangled states are generated, and stored for subsequent utilization.

5.3.2 Entanglement connection

When two pairs of atomic ensembles are prepared in such an entangled state (Fig. 5.3), one can connect the pairs by sending strong read pulses into one ensemble of each pair. The fields 2 resulting from this readout are then brought to interference at a $50/50$ beamsplitter. Again, a single click on either detector prepares the remaining ensembles in an entangled state[4].

After independent preparation of entanglement for the pairs $\{L, I1\}$ and $\{R, I2\}$ and perfect reading of the states of the ensembles $I1$ and $I2$, the joint state of the fields 2 and the ensembles can be written, neglecting higher-order terms,

$$\begin{aligned} |\Psi_{L,R,2_{I1},2_{I2}}\rangle &= \frac{1}{2}[|0\rangle_{2_{I2}}|1_a\rangle_R \pm e^{i\zeta_{R,I2}}|1\rangle_{2_{I2}}|0_a\rangle_R)] \\ &\quad \otimes[|0\rangle_{2_{I1}}|1_a\rangle_L \pm e^{i\zeta_{L,I1}}|1\rangle_{2_{I1}}|0_a\rangle_L)] \end{aligned} \tag{5.5}$$

where the phases resulting from the entanglement generation and the readout process are given by $\zeta_{i,Ij} = (\beta_{Ij} - \beta_i) + (\theta_{Ij} - \theta_i) + \delta_{Ij}$, with δ_{Ij} the phase of the read beam at the Ij ensemble. Fields 2_{I1} and 2_{I2} are then mixed on a 50/50 beamsplitter, and detection of a photon in either detector projects the remaining two ensembles L and R into

$$\rho_{LR}^{(\pm)} = \mathrm{Tr}_{2_{I1}2_{I2}}[\rho(\frac{1}{\sqrt{2}}(a_{2_{I1}} \pm e^{i\gamma}a_{2_{I2}})|\Psi_{L,R,2_{I1},2_{I2}}\rangle)] \tag{5.6}$$

which can be written as

$$\begin{aligned} \rho_{LR}^{(\pm)} &= \frac{1}{2}|0\rangle\langle 0| + \frac{1}{2}|\Phi_{L,R}^{(\pm)}\rangle\langle\Phi_{L,R}^{(\pm)}| \\ \text{with} \quad & |\Phi_{L,R}^{(\pm)}\rangle = |0\rangle_L|1\rangle_R \pm e^{i\xi}|1\rangle_L|0\rangle_R \end{aligned} \tag{5.7}$$

where $\xi = \zeta_{R,I2} - \zeta_{L,I1} + \gamma$. This overall phase is the sum of the phase difference for entanglement generation for each pair, the phase difference between the two read beams up to the two ensembles and the phase difference of the generated fields 2 from the ensembles to the beamsplitter.

The vacuum part comes from the probability of reading the two excitations at the same time, leaving no remaining excitation in the system. In the ideal case, the connection succeeds 50% of the time. Let us underline also that, significantly, the absolute phases do not necessarily need to be stabilized to succeed in

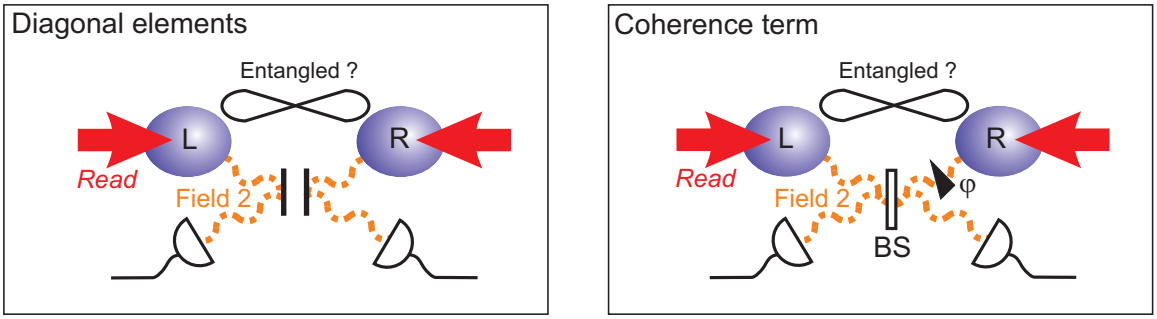

Figure 5.4: **Procedure for verifying entanglement between two atomic ensembles.** The atomic state is mapped to photonic modes via simultaneous strong read pulses and quantum tomography of the generated fields 2 is performed. For this purpose, fields 2 are detected independently (diagonal elements) or in a $50/50$ beamsplitter configuration where the phase of one of the paths is scanned (coherence term).

the connection. Only the overall phase ξ must be kept constant. This feature is exploited in the proposed experimental setup, where passive stability is found to be enough to meet this requirement.

The generated state given by Eq. 5.7 is what *DLCZ* called an "effective maximally-entangled state" (EME) as any state of this form would be purified to a maximally entangled state in the proposed entanglement-based communication scheme[4]. The vacuum coefficient only influences the success probability, but not the overall fidelity of the long-distance communication. This important feature is known as "built-in purification."

5.3.3 Experimental verification of entanglement

To experimentally verify the entanglement between the two atomic ensembles, L and R as sketched in Fig. 5.4, a solution is to map the delocalized atomic excitation into a field state by applying simultaneous strong read pulses. For perfect state transfer, the entangled state of the atoms would be mapped to an ideal entangled state of the two photonic modes (chapter 2).

However, the presence of various noises, the vacuum contribution (coming from a finite retrieval efficiency or also a finite success probability in the case of the swapping), as well as higher-order terms, has to be taken into account. In order to prove experimentally the generation of entanglement at the atomic level, our group has developed in ref.[27] a robust, model-independent determination of entanglement based upon quantum tomography of the fields 2 (chapter 3). As entanglement cannot be increased by local operations on either of the two ensembles, the entanglement for the state of the ensembles will always be greater than or equal to that measured for the light fields. The model consists of reconstructing a reduced density matrix, ρ, obtained from the full density matrix by restricting it to the subspace where no more than one photon populates each mode. It can be shown that this reduced density matrix exhibits less or equal entanglement than does the full one. The model will thus lead to a lower bound of the entanglement, enabling an unambiguous determination of the presence of entanglement, at the price of eventually underestimating its actual magnitude.

The reduced density matrix can be written as

$$\rho = \frac{1}{P}\begin{pmatrix} p_{00} & 0 & 0 & 0 \\ 0 & p_{01} & d & 0 \\ 0 & d^* & p_{10} & 0 \\ 0 & 0 & 0 & p_{11} \end{pmatrix} \tag{5.8}$$

in the photon-number basis $|n\rangle|m\rangle$, with $\{n, m\} = \{0, 1\}$. p_{ij} is the probability of finding i photons in mode 2_L and j in mode 2_R, d is the coherence term between the $|1\rangle|0\rangle$ and $|0\rangle|1\rangle$ states, and $P = p_{00} + p_{01} + p_{10} + p_{11}$. From this density matrix, one can calculate the concurrence C, which is a monotone measurement of entanglement[178]:

$$C = \max(2|d| - 2\sqrt{p_{00}p_{11}}, 0). \tag{5.9}$$

Let us underline, as $d^2 \leq p_{10}p_{01}$, a necessary requirement for $C > 0$ is that there is a suppression of two-photon events relative to the square of the probability of single-photon events for the fields 2, $h \equiv p_{11}/(p_{10}p_{01}) < 1$.

Experimentally, the density matrix is reconstructed by using two different configurations, as sketched in Fig. 5.4. The diagonal elements are determined by measuring individual statistics, i.e., by detecting independently each field. The coherence term can be measured by combining the fields 2 on a $50/50$ beamsplitter and recording the count rate as a function of the phase difference between them. This results in an interference fringe with a visibility V. It can been shown that $d \simeq V(p_{10} + p_{01})/2$. Together, this two-stage measurement gives access to the concurrence C.

5.3.4 Entanglement connection revisited

The principle of entanglement connection has been explained previously in the ideal case where higher-order terms and vacuum contributions are neglected. Let us consider now the more general case, which can be described by the previous approach. We consider two pairs of entangled ensembles and consider that the fields 2 after reading can be described by the same density matrix ρ' with diagonal elements p'_{ij}. The relevant question is now what will be the expression of ρ, the reduced density matrix for the fields 2 of the two remaining ensembles after the connection.

Let us assume that $p'_{10} = p'_{01}$. To later normalize the events conditioned on swapping, one needs to first determine the probability to have a click heralding the connection at one output of the beamsplitter. To the first order, this quantity can be written as

$$p' = 2 \times \frac{1}{2}p'_{10} = p'_{10}. \tag{5.10}$$

The factor $1/2$ corresponds to the 50% chance that the photon be reflected or transmitted at the beamsplitter (i.e., with each detection event uniquely associated with the entangled states $\Phi_{LR}^{(\pm)}$), while the factor 2 results from the symmetry of the scheme where the photon can come from either ensemble.

One can then evaluate, after the reading of the two remaining ensembles, the probability of having one photon for one mode and zero for the other, when a swap event has been detected

$$p_{10} \quad = \quad p_{01} = \frac{1}{2}(p_{10}'^2 + p_{11}' p_{00}' + p_{11}' p_{10}')/p' \sim \frac{1}{2} p_{10}'. \tag{5.11}$$

The terms inside the parenthesis correspond to one photon in mode 2_L and zero in 2_R (or the other way around), and all the other combinations for 2_{I1} and 2_{I2} which can give a swapping event. The final factor $1/2$ comes from the fact, already established before in the ideal case, that the swapping succeeds, to the first order, 50% of the time.

Finally, in a similar way, the probability to have one photon in each mode is given by:

$$p_{11} \quad = \quad \frac{1}{2} p_{11}' (p_{11}' + 2p_{10}')/p' \sim p_{11}'. \tag{5.12}$$

The main feature which appears here is that the weight of the two-photon component stays the same, while the single-photon component is divided by two. As a result, if one calculates for the connected pairs the new suppression h of two-photon events relative to the square of the probability for single-photon events as a function of the initial h' for each entangled pair: $h \sim 4h'$. This result points out the difficulty which could arise in the experimental demonstration of entanglement connection: one needs to start with atomic ensembles entangled with a very low two-photon component, at the price of low count rates and statistics.

5.4 Experimental setup and measurement results

In this section, we present a scheme that permits us to investigate entanglement connection between two pairs of atomic ensembles, without the requirement of any active phase stabilization (see also chapter 4 for a similar setup). Experimental results are finally given.

5.4.1 Experimental setup

The experimental setup is depicted in Fig. 5.5. Two parallel pairs of atomic ensembles are first prepared independently, following the measurement-induced method detailed in section 5.3. This preparation stage is speeded up by real-time conditional control (refs.[36,78], chapter 4): a detection event at either pair triggers intensity modulators that gate off all laser pulses going to the corresponding pair of ensembles, thereby storing the associated state. After successfully preparing both pairs, strong read pulses are sent into the ensembles. The fields 2_{I1} and 2_{I2} are brought to interfere and a detection event on either detector heralds the connection

process. Thanks to the conditional control, a 20-fold enhancement is obtained in the probability to establish the connection (chapter 4), leading to a rate of connection around 4 Hz. Depending on the combinations of field 1 and field 2 detector clicks, two different entangled states $|\Phi_{L,R}^{(\pm)}\rangle$ are generated for the two remaining ensembles, denoted by $+$ and $-$, with a π phase-shift between them.

As pointed out before, the process of connection between the two remaining ensembles, which never interacted in the past, only requires the stability of the relative phase ξ over trials. This overall phase is defined as the phase difference between the absolute phase of all the paths (write beams, field 1, read pulses, and field 2 on the connection side) for the upper pair and the ones for the lower pair. Instead of actively stabilizing all individual phases as it was performed in ref.[27] where two ensembles were involved, this requirement is

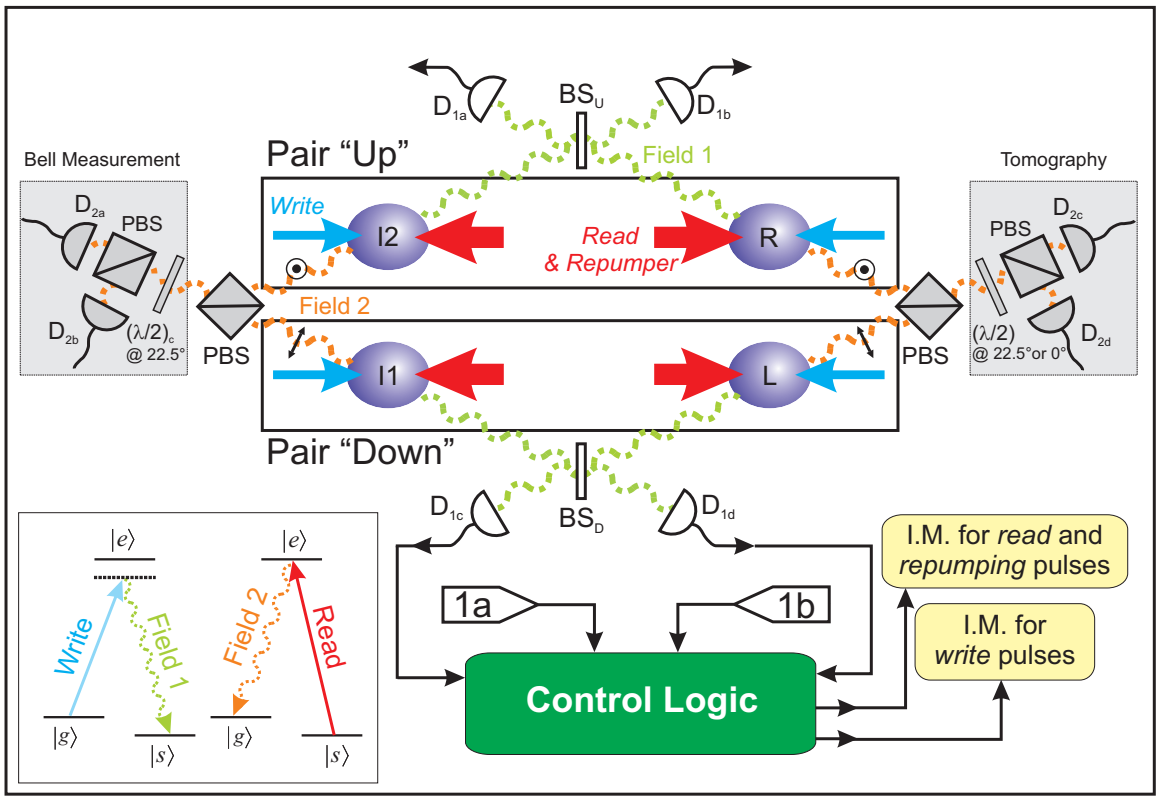

Figure 5.5: **Experimental setup for entanglement connection.** For each pair, "Up" and "Down," the ensembles are separated by 3 meters. Fields 1_{I2} and 1_R from pair "Up" are brought to interference at a 50-50 beamsplitter (BS_U). A photo-detection event at either detector D_{1a} or D_{1b} heralds entanglement between the collective excitation in $I2$ and R. The "Down" pair is prepared in a similar fashion via events at D_{1c}, D_{1d}. A heralding detection event triggers the control logic to gate off the light pulses going to the corresponding ensemble pair by controlling intensity modulators (*IM*). The atomic state is thus stored while waiting for the second ensemble pair to be prepared. After both pairs of ensembles have been prepared, the control logic releases strong read pulses. Fields 2_{I2} and 2_{I1} (2_R and 2_L) are combined with orthogonal polarizations on polarizing beamsplitters. Fields 2_{I2} and 2_{I1} are detected with the half-wave plate $(\lambda/2)_c$ at 22.5°, which is equivalent to a $50/50$ beamsplitter configuration. The fields 2 from the remaining ensembles are characterized conditionally on a detection event heralding the connection. The two configurations of Fig. 5.4 correspond to two different angles, 0° and 22.5°, of the half-wave plate $(\lambda/2)$.

Table 5.1: **Diagonal elements of the density matrix ρ deduced from the records of photoelectric counts, for the two different states after connection, denoted $+$ and $-$.** These values are obtained by considering unit detection efficiency. Errors bars correspond to statistical errors.

Probability	+	-
p_{00}	0.949 ± 0.003	0.948 ± 0.003
p_{10}	$(1.97 \pm 0.05) \times 10^{-2}$	$(1.99 \pm 0.05) \times 10^{-2}$
p_{01}	$(3.06 \pm 0.06) \times 10^{-2}$	$(3.16 \pm 0.06) \times 10^{-2}$
p_{11}	$(4.1 \pm 0.7) \times 10^{-4}$	$(4.9 \pm 0.8) \times 10^{-4}$

fulfilled in our setup by exploiting the passive stability between two independent polarizations propagating in a single interferometer (ref.[36], chapter 4). All the paths for the upper and lower pairs are common, except inside a small interferometer where orthogonal polarizations are separated to define the two ensembles on each side (chapter 3). Operation over more than 24 hours is possible without any adjustment as the phase does not change by more than a few degrees (chapter 3). As a result, no active phase stabilization is required, simplifying significantly the experimental investigation of the connection process. Note that although the present configuration is sufficient to demonstrate the principle of the connection, an experiment where the final pair of ensembles L and R are distant, as in Fig. 5.3b, would require active stabilization of the various phases, since in that case all the paths would be distinct[c]. Our configuration for passive stability is better suited to the case of parallel chains of ensembles, as in the original proposal of *DLCZ*.

5.4.2 Characterization of the states generated upon connection

The generated state is analyzed by using the tomography technique explained in section 5.3.3. Conditioned upon a connection event, the density matrix ρ of the fields 2 is reconstructed following the two required steps: the measurement of the diagonal elements and the determination of the coherence terms.

Table 5.1 gives the measured diagonal elements deduced from the records of photoelectric counts, for both generated states, after a connection event. Unit detection efficiency is assumed, which can only lead to a smaller value for the concurrence than the actual field concurrence for finite detection efficiency. From these values, one can deduce the suppression h of the two-photon events relative to the square of the probability for single-photon events. We find $h_+ = 0.7 \pm 0.1 < 1$ and $h_- = 0.8 \pm 0.1 < 1$. From independent measurements, we inferred the h' parameter for each pair before connection to be $h' = 0.20 \pm 0.05$. The experimentally determined values of h are thus consistent with the expression $h = 4h'$ established previously. As pointed out before, this relation arises from the intrinsic property that the connection succeeds only 50% of the time. This can be seen in the quantities $2p_{01} \sim 4\%$ and $2p_{10} \sim 6\%$, which should be equal to half the retrieval efficiency. The retrieval efficiencies (including detection) independently measured for each ensemble were both around 10%.

In order to access the coherence term, Fig. 5.6 shows the probability of having a detection event on either

[c]The relative phase ζ between the entangled ensembles can in principle be probed, given that ζ is sufficiently stable over the memory time. See section 1.3.1 for more information.

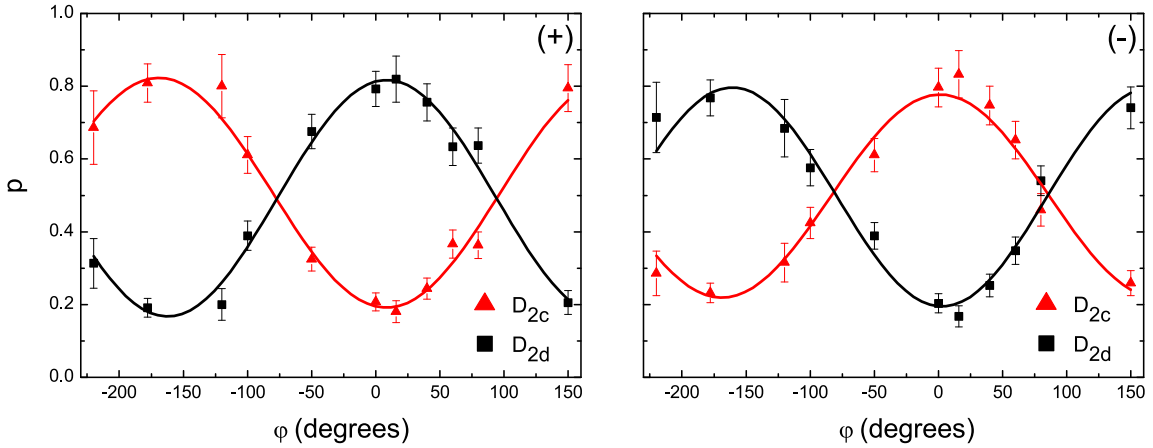

Figure 5.6: **Coherence between the two atomic ensembles L and R induced by the connection event.** p is the probability after connection to have a detection event on either detectors $D2c$ and $D2d$ when the fields 2_L and 2_R interfere, as a function of the phase φ. For each phase setting, data are acquired for 30 minutes, each atomic state being generated overall at about 2 Hz. Errors bars correspond to statistical errors.

output of the beamsplitter, normalized to the sum of these events, as a function of the phase-shift between the fields 2_L and 2_R. Practically, the relative phase is scanned by adjusting the phases of the two classical read beams via birefringent waveplates. The visibilities are found to be $V_+ = 64 \pm 3\%$ and $V_- = 59 \pm 3\%$. A simple model[36] predicts for our excitation probability a visibility equal to $65 \pm 10\%$. By taking into account the measured overlap of the photon wavepacket for fields 2 deduced from a two-photon interference[36], 0.90 ± 0.05, the expected visibility can be roughly estimated to be $55 \pm 10\%$ if all the reduction is attributed to a non-perfect overlap. In the absence of conditioning, the visibility drops to near zero, the residual visibility (below 3%) being explained by finite polarization extinction ratio in our setup. This result demonstrates for the first time the creation of coherence between two atomic ensembles which never interacted in the past. The reconstructed density matrices are shown in Fig. 5.7.

With these data in hand, the concurrences C can be estimated for both states,

$$C_+ = \max\left(-(7 \pm 4) \times 10^{-3}, 0\right) = 0 \tag{5.13}$$

$$C_- = \max\left(-(1.3 \pm 0.4) \times 10^{-2}, 0\right) = 0. \tag{5.14}$$

These values show finally the absence of entanglement, or at least, that our entanglement measurement, which provides a lower bound of the atomic entanglement, cannot detect entanglement in this particular case. One can correct from detection efficiencies and propagation losses[27], but any zero concurrence will stay zero by this correction. The h values confirm anyway that the connected systems are barely in the regime where the two-photon events are suppressed relative to single-photon events. One needs to start with smaller h' for the initial pairs. h' as low as 0.05 can be obtained routinely for each pair in our lab but the count rate to characterize the connection would be prohibitively low.

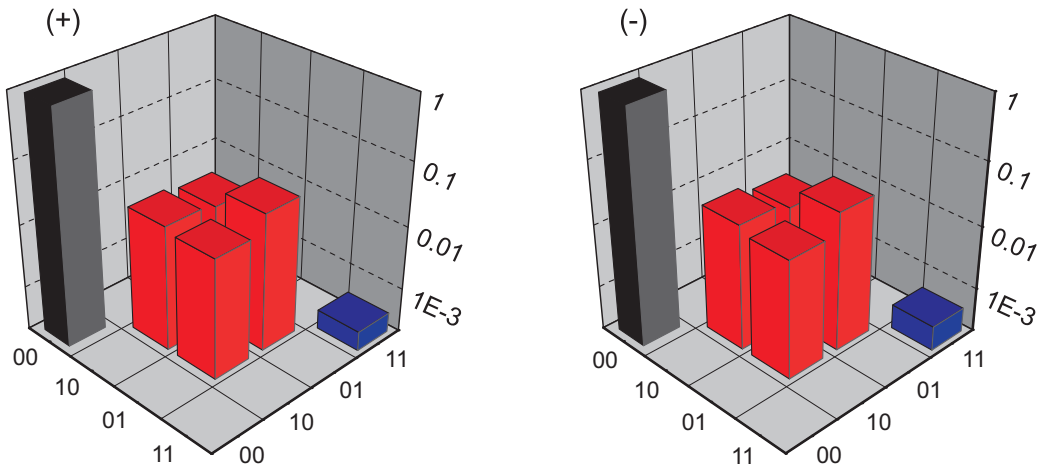

Figure 5.7: **Density matrix for the fields after entanglement connection.** We reconstructed density matrix for both generated states, at the detector location.

5.5 Discussion and prospects towards entanglement connection

In summary, in this chapter, we have presented a possible scheme to demonstrate entanglement connection between atomic ensembles which never interacted in the past. Such striking capability is a critical requirement for the future development of elaborate quantum networks. Our investigation has shown for the first time the creation of coherence upon the connection process. This result validates the proposed setup, in particular its passive phase stability, and constitutes a significant step towards the entanglement connection of matter systems.

To finally generate and prove entanglement connection between the remaining ensembles, very stringent condition on the suppression of the two-photon component needs to be satisfied, at the sacrifice of the count rate in our current setup (chapter 4). Overall, the figure of merit of any elaborate experiment is the product of the probability to prepare the entangled state at each write pulse and the coherence time. Improvements in these two directions have to be explored. The first one can be addressed by, for instance, multiplexing the atomic ensembles. One can imagine to use spatially-resolving detectors, namely array of single-photon detectors, and adaptive optical systems to reconfigure the optical interconnects. Improving the coherence time is a second critical direction as more elaborate protocols are involved. It would require better nulling of the residuals magnetic fields and also the use of improved trapping techniques[147] like a large dipole-trap, as a magneto-optical trap will be rapidly limited by the diffusion of the atoms outside the excitation region (chapter 2). An increase by two orders of magnitude, from tens of μs to ms, would enable, for instance, an experimental demonstration of entanglement connection in our current setup in a few hours of data taking (Fig. 5.8). All together, these improvements would enable deeper investigation of experimental quantum networking, and will definitely lead to fruitful insights into the distribution and processing of quantum information.

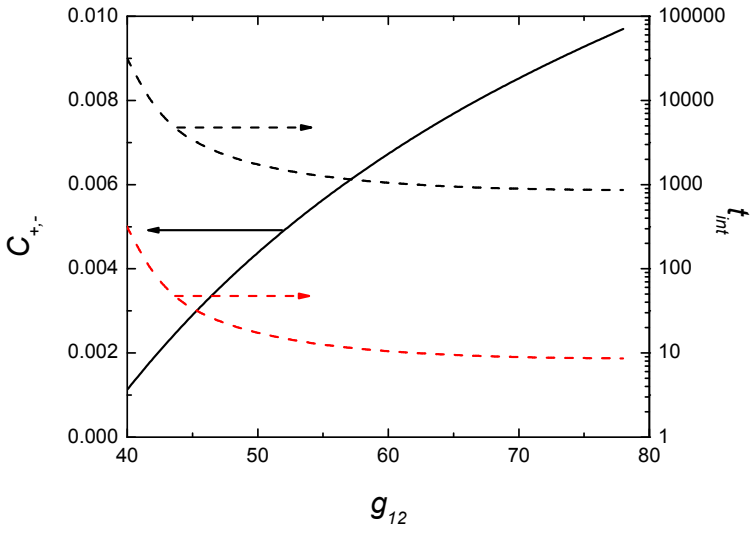

Figure 5.8: **Theoretical concurrence $C_{\pm}$ (black line) after a swapping event as a function of the correlation function g_{12} between fields 1 and 2.** The total integration time to achieve 4 standard deviation statistics for $C_{\pm} > 0$ is given in units of hours with the current memory time of ~ 15 μs (black dashed line) and with the improved coherence time of ~ 1.5 ms (red dashed line).

Chapter 6

Mapping photonic entanglement into and out of quantum memories

This chapter is largely based on ref. [30]. Reference [30] refers to the then current literature in 2008 at the time of publication.

6.1 Introduction

In the quest to achieve quantum networks over long distances [1,227], an area of considerable activity has been the interaction of light with atomic ensembles comprised of a large collection of identical atoms (ref. [4], see also chapter 1). In the regime of continuous variables, a particularly notable advance has been the teleportation of quantum states between light and matter [60]. For discrete variables with photons taken one by one, important achievements include the efficient mapping of collective atomic excitations to single photons (refs. [76,77,79,80], chapter 2), the realization of entanglement between distant ensembles (refs. [27,34], chapter 3) and, recently, entanglement distribution involving two pairs of ensembles (ref. [36], chapter 4). The first step toward entanglement swapping has been made (ref. [37], chapter 5), and light-matter teleportation has been demonstrated with post-diction [112].

In all these cases, progress with single photons has relied upon probabilistic schemes following the measurement-induced approach developed in the seminal paper by Duan, Lukin, Cirac and Zoller (*DLCZ*) [4] and subsequent extensions [49]. For the *DLCZ* protocol, heralded entanglement is generated by detecting a single photon emitted indistinguishably by one of two ensembles. Intrinsically, the probability p to prepare entanglement with only 1 excitation shared between two ensembles is related to the quality of entanglement, since the likelihood for contamination of the entangled state by processes involving 2 excitations likewise scales as p (ref. [34], chapter 3), and results in low success probability. Although the degree of stored entanglement can approach unity for the (rare) successful trials (ref. [34], chapter 3), the condition $p \ll 1$ dictates reductions in the count rate and compromises in the quality of the resulting entangled state (e.g., as $p \to 0$, processes such as stray light scattering and detector dark counts become increasingly important). Further-

more, for finite memory time, subsequent connection of entanglement becomes increasingly challenging (ref.[37], chapter 5).

The separation of processes for the generation of entanglement and for its storage enables this drawback to be overcome. In this chapter, we demonstrate such a division by way of reversible mapping of an entangled state into a quantum memory. The mapping is obtained by using adiabatic passage based upon dynamic electromagnetically induced transparency (EIT) (refs.[86,88,89,94], see also sections 2.5 and 6.9 for details). Storage and retrieval of optical pulses have been demonstrated previously, for both classical pulses[90,91] and single-photon pulses[92,93]. Adiabatic transfer of a collective excitation has been demonstrated between two ensembles coupled by a cavity mode[29], which can provide a suitable approach for generating on-demand entanglement over short distances. However, for efficient distribution of entanglement over quantum networks, reversible mapping of an entangled state between matter and light, as illustrated in Fig. 6.1a, has not been addressed until now.

In our experiment, entanglement between two atomic ensembles $L_{\rm a}, R_{\rm a}$ is created by first splitting a single photon into two modes $L_{\rm in}, R_{\rm in}$ to generate an entangled state of light[228–230]. This entangled field state is then coherently mapped to an entangled matter state for $L_{\rm a}, R_{\rm a}$. On demand, the stored atomic entanglement for $L_{\rm a}, R_{\rm a}$ is converted back into entangled photonic modes $L_{\rm out}, R_{\rm out}$. As opposed to the original *DLCZ* scheme, our approach is inherently deterministic, suffering principally from the finite efficiency of mapping single excitations to and from an atomic memory, with efficiency $\simeq 50\ \%$ having been achieved. Moreover, the contamination of entanglement for $L_{\rm a}, R_{\rm a}$ from processes involving 2 excitations can be arbitrarily suppressed (independent of the mapping probabilities) with continuing advances in on-demand single-photon sources[231]. Our experiment thereby provides a promising avenue to distribute and store quantum entanglement deterministically over remote atomic ensembles for scalable quantum networks[232] (see also chapter 10 for a potential application of this scheme for hybrid quantum networks).

6.2 Deterministic quantum interface between matter and light

The experimental setup is depicted in Fig. 6.1. Our single-photon source is based on Raman transitions in an optically thick cesium ensemble[4,76], called a source ensemble (see section 6.8). This system generates 28-ns-long single photons (resonant with $6S_{1/2}, F = 4 \leftrightarrow 6P_{3/2}, F' = 4$ transition) in a heralded fashion[76]. The single photons are polarized at 45° from the eigen-polarizations of the beam displacer BD_1 (Fig. 1b) which splits them into entangled optical modes $L_{\rm in}, R_{\rm in}$ (called the signal modes) to produce, in the ideal case, the following state

$$\frac{1}{\sqrt{2}}(|0_{L_{\rm in}}\rangle|1_{R_{\rm in}}\rangle + e^{i\phi_{\rm in}}|1_{L_{\rm in}}\rangle|0_{R_{\rm in}}\rangle). \tag{6.1}$$

The next stage consists of coherently mapping the photonic entanglement for $L_{\rm in}, R_{\rm in}$ into atomic ensembles $L_{\rm a}, R_{\rm a}$ (called the memory ensembles) within a single cloud of cold cesium atoms in a magneto-optical

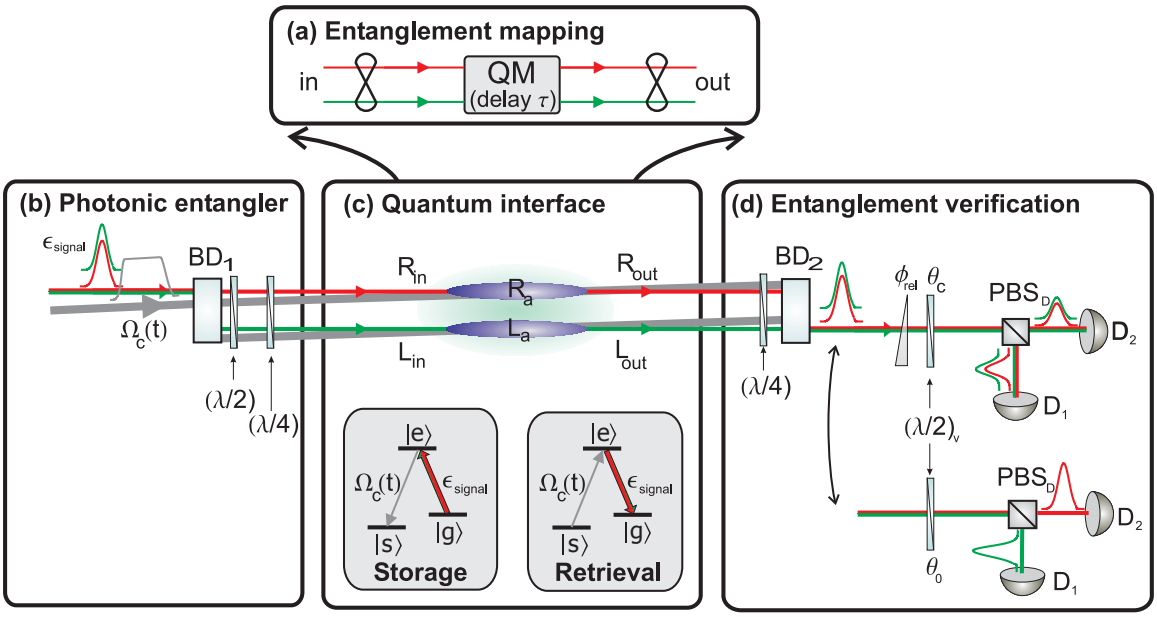

Figure 6.1: **Overview of the experiment. a,** Reversible mapping. Illustration of the mapping of an entangled state of light into and out of a quantum memory (QM) with controllable storage time τ. **b,** Photonic "entangler." A beam displacer BD_1 splits an input single photon into two orthogonally polarized, entangled modes $L_{\mathrm{in}}, R_{\mathrm{in}}$, which are spatially separated by 1 mm. With waveplates $\lambda/2$ and $\lambda/4$, the signal fields $\epsilon_{\mathrm{signal}}$ for $L_{\mathrm{in}}, R_{\mathrm{in}}$ and control fields $\Omega_{\mathrm{c}}^{(L,R)}(t)$ are transformed to circular polarizations with the same helicity along each path L, R, and copropagate with an angle of $3°$. **c,** Quantum interface for reversible mapping. Photonic entanglement between $L_{\mathrm{in}}, R_{\mathrm{in}}$ is coherently mapped into the memory ensembles $L_{\mathrm{a}}, R_{\mathrm{a}}$ by switching $\Omega_{\mathrm{c}}^{(L,R)}(t)$ off adiabatically. After a programmable storage time, the atomic entanglement is reversibly mapped back into optical modes $L_{\mathrm{out}}, R_{\mathrm{out}}$ by switching $\Omega_{\mathrm{c}}^{(L,R)}(t)$ on. Relevant energy diagrams for the storage and retrieval processes are shown in the insets. States $|g\rangle$, $|s\rangle$ are the hyperfine ground states $F = 4$, $F = 3$ of $6S_{1/2}$ in atomic cesium; state $|e\rangle$ is the hyperfine level $F' = 4$ of the electronic excited state $6P_{3/2}$. **d,** Entanglement verification. After a $\lambda/4$ plate, the beam displacer BD_2 combines modes $L_{\mathrm{out}}, R_{\mathrm{out}}$ into one beam with orthogonal polarizations. With $(\lambda/2)_{\mathrm{v}}$ at $\theta_{\mathrm{c}} = 22.5°$ before the polarization beamsplitter ($\mathrm{PBS}_{\mathrm{D}}$), single photon interference is recorded at detectors D_1, D_2 by varying the relative phase ϕ_{rel} by a Berek compensator. With $(\lambda/2)_{\mathrm{v}}$ at $\theta_0 = 0°$, photon statistics for each mode $L_{\mathrm{out}}, R_{\mathrm{out}}$ are measured independently.

trap (MOT) (Fig. 6.1c). Ensembles $L_{\mathrm{a}}, R_{\mathrm{a}}$ are defined by the well-separated optical paths of the entangled photonic modes $L_{\mathrm{in}}, R_{\mathrm{in}}$ (section 6.6). To avoid dissipative absorption for the fields in modes $L_{\mathrm{in}}, R_{\mathrm{in}}$ for our choice of polarization[93], we spin-polarize the atomic ensemble into a clock state $|F = 4, m_F = 0\rangle$ (section 6.6). Initially, the strong control fields $\Omega_{\mathrm{c}}^{(L,R)}$ (resonant with $6S_{1/2}, F = 3 \leftrightarrow 6P_{3/2}, F' = 4$ transition) open transparency windows $\Omega_{\mathrm{c}}^{(L,R)}(0)$ in $L_{\mathrm{a}}, R_{\mathrm{a}}$ for the signal modes. As the wavepacket of the signal field propagates through each ensemble, the control fields $\Omega_{\mathrm{c}}^{(L,R)}(t)$ are turned off in 20 ns by an electro-optical intensity modulator, thereby coherently transforming the fields of the respective signal modes to collective atomic excitations within $L_{\mathrm{a}}, R_{\mathrm{a}}$. This mapping leads to an entanglement between quantum memories $L_{\mathrm{a}}, R_{\mathrm{a}}$, with atomic state $\frac{1}{\sqrt{2}}(|\overline{g}_{L_{\mathrm{a}}}\rangle|\overline{s}_{R_{\mathrm{a}}}\rangle + e^{i\phi_{\mathrm{a}}}|\overline{s}_{L_{\mathrm{a}}}\rangle|\overline{g}_{R_{\mathrm{a}}}\rangle)$. After a user-defined delay, chosen here to be 1.1 μs, the atomic entanglement is converted back into entangled photonic modes by switching on the control fields $\Omega_{\mathrm{c}}^{(L,R)}(t)$ (section 6.9), with a photon state $\frac{1}{\sqrt{2}}(|0_{L_{\mathrm{out}}}\rangle|1_{R_{\mathrm{out}}}\rangle + e^{i\phi_{\mathrm{out}}}|1_{L_{\mathrm{out}}}\rangle|0_{R_{\mathrm{out}}}\rangle)$. The con-

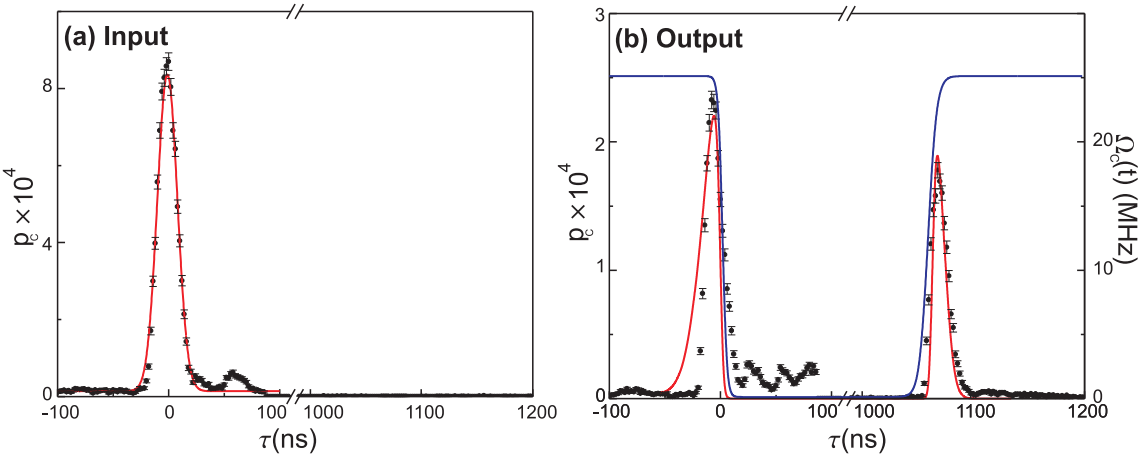

Figure 6.2: **Single-photon storage and retrieval for a single ensemble. a,** Input. The data points are the measured probability p_c for the signal field, a single photon generated from a separate "offline" source atomic ensemble[76]. The red solid line represents a Gaussian fit of $1/e$ width of 28 ns. **b,** Storage and retrieval. The points around $\tau = 0$ μs represent "leakage" of the signal field due to the finite optical depth and length of the ensemble. The points beyond $\tau = 1$ μs show the retrieved signal field. The overall storage and retrieval efficiency is 17 ± 1 %. The blue solid line is the estimated Rabi frequency $\Omega_c(t)$ of the control pulse. The red solid curve is from a numerical calculation solving the equation of motion of the signal field in a dressed medium (ref.[86], chapter 2). Error bars give the statistical error for each point.

trolled readout allows the extensions to quantum controls for entanglement connection and distribution by way of asynchronous preparation (refs.[36,37], chapters 4 and 5).

6.2.1 Single-photon storage and retrieval

For a given optical depth $\tilde{d}_0$, there is an optimal Rabi frequency $\Omega_c(t)$ for the control field. In our experiment, $\tilde{d}_0$ and $\Omega_c(0)$ are 15 and 24 MHz, respectively. An example of our measurements of the EIT process for a single ensemble is presented in Fig. 6.2, which shows the input single-photon pulse (Fig. 6.2a) and its storage and retrieval (Fig. 6.2b); see also chapter 2. Due to finite $\tilde{d}_0$, small length (≈ 3 mm) of the ensemble and the turn-off time of the intensity modulator, there is considerable loss in the storage process, as evidenced by the counts around $\tau = 0$ μs in Fig. 6.2b. The peak beyond $\tau = 1$ μs represents the retrieved pulse after 1.1 μs of storage. Overall, we find good agreement between our measurements and the numerical calculation following the methods of ref.[86], using the fitted function of the input signal field (Fig. 6.2a) as the initial condition, with all other parameters from independent measurements (section 6.9). We find the overall storage and retrieval efficiency of $\eta_{\rm sr} = 17 \pm 1$ %, also in agreement with the simulation of $\eta_{\rm sr}^{\rm theory} = 18$ %.

6.2.2 Entanglement verification

With these results in hand for the individual L_a, R_a ensembles, we next turn to the question of verification of entanglement for the optical modes of $L_{\rm in}, R_{\rm in}$ and $L_{\rm out}, R_{\rm out}$. We follow the protocol introduced in ref.[27]

by (1) reconstructing a reduced density matrix $\hat{\rho}$ constrained to a subspace containing no more than one excitation in each mode, and (2) assuming that all off-diagonal elements between states with different numbers of photons vanish, thereby obtaining a lower bound for any purported entanglement. In the photon-number basis $|n_L, m_R\rangle$ with $\{n, m\} = \{0, 1\}$, the reduced density matrix $\hat{\rho}$ is written as (ref.[27], chapter 3)

$$\hat{\rho} = \frac{1}{P}\begin{pmatrix} p_{00} & 0 & 0 & 0 \\ 0 & p_{10} & d & 0 \\ 0 & d^* & p_{01} & 0 \\ 0 & 0 & 0 & p_{11} \end{pmatrix}. \tag{6.2}$$

Here, p_{ij} is the probability to find i photons in mode L_k and j in mode R_k, $d \simeq \frac{V(p_{10}+p_{01})}{2}$ is the coherence between $|1_L 0_R\rangle_k$ and $|0_L 1_R\rangle_k$, $P = p_{00} + p_{10} + p_{01} + p_{11}$, and V is the visibility for interference between modes L_k, R_k, with $k \in \{\text{in}, \text{out}\}$. The degree of entanglement of $\hat{\rho}$ can be quantified in terms of concurrence, $C = \frac{1}{P}\text{max}(0, 2|d| - 2\sqrt{p_{00}p_{11}})$, which is a monotone function of entanglement, ranging from 0 for a separable state to 1 for a maximally entangled state[178].

6.3 Coherent and reversible quantum interface for photonic entanglement

6.3.1 Quantum-state tomography on the input photonic state

We first perform tomography on the input modes $L_{\text{in}}, R_{\text{in}}$ to verify that they are indeed entangled. To this end, we remove the memory ensembles to transmit directly the signal fields into the verification stage, following our protocol of complementary measurements as described in Fig. 6.1d (See section 6.7). The interference fringes between the two input modes are shown in Fig. 6.3a. From the independently determined propagation and detection efficiencies, we use the measurements at D_1, D_2 to infer the quantum state for the input modes $L_{\text{in}}, R_{\text{in}}$ entering the faces of $L_{\text{a}}, R_{\text{a}}$, with the reconstructed density matrix $\hat{\rho}_{\text{in}}$ given in Fig. 6.3a. The concurrence derived from $\hat{\rho}_{\text{in}}$ is $C_{\text{in}} = 0.10 \pm 0.02$, so that the fields for $L_{\text{in}}, R_{\text{in}}$ are indeed entangled. The value of the concurrence is in good agreement with the independently derived expectation of $C_{\text{in}}^{\text{theory}} = 0.10 \pm 0.01$, which depends on the quality of the single photon and the vacuum component (i.e., the overall efficiency) (ref.[34], chapter 3). Given a heralding click from our single-photon source, the probability to have a single photon at the face of either memory ensemble is $15\ \%$, leading to a vacuum component of $85\ \%$. We also independently characterize the suppression w of the two-photon component relative to a coherent state (for which $w = 1$) and find $w = 0.09 \pm 0.03$. Our input entanglement is only limited by the current properties of our single-photon source, which will be improved with the rapid advances in sources of single photons[231].

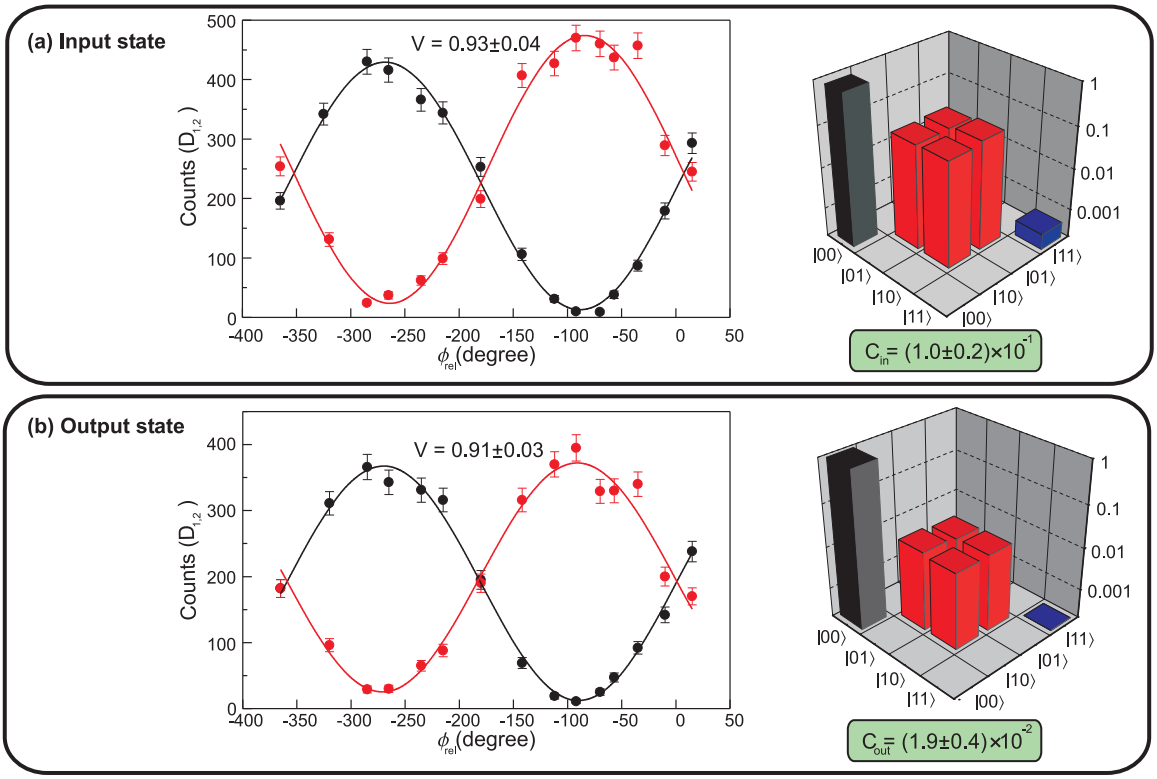

Figure 6.3: **Entanglement for the input and output optical modes.** To verify entanglement, complementary measurements are performed : interference leading to a fringe when the relative phase ϕ_{rel} is scanned and independent photon statistics for each light mode. The figure shows the interference fringes and the reconstructed density matrices (in log scale) for the photonic modes **a,** at the input of the memory and **b,** the output after storage and retrieval. The estimated concurrence is given in each case. Each point of the fringe is taken for $20,000$ $(100,000)$ heralding events for the input (output) state. Error bars indicate statistical errors.

6.3.2 Quantum-state tomography on the output photonic state

Having verified the entanglement for the input modes $L_{\text{in}}, R_{\text{in}}$, we next map this photonic entanglement into $L_{\text{a}}, R_{\text{a}}$, which serve as a quantum memory (Fig. 6.1c). After storing the entanglement for 1.1 μs, we transfer the resulting atomic excitation on demand from the memory to the output modes $L_{\text{out}}, R_{\text{out}}$ and perform quantum-state tomography to determine $\hat{\rho}_{\text{out}}$ as for $\hat{\rho}_{\text{in}}$. As shown in Fig. 6.3, the visibility for interference of the fields after storage and retrieval shows no appreciable degradation (from $V_{\text{in}} = 0.93 \pm 0.04$ to $V_{\text{out}} = 0.91 \pm 0.03$). From the measurements at D_1, D_2, we infer the quantum state $\hat{\rho}_{\text{out}}$ at the output faces of $L_{\text{a}}, R_{\text{a}}$, as displayed in Fig. 6.3b. The associated concurrence $C_{\text{out}} = (1.9 \pm 0.4) \times 10^{-2}$ is in agreement with $C_{\text{out}}^{\text{theory}} = (1.7 \pm 0.1) \times 10^{-2}$. Since mapping of atomic states from $L_{\text{a}}, R_{\text{a}}$ into field modes $L_{\text{out}}, R_{\text{out}}$ is a local operation, this measurement provides a lower bound for the entanglement between the $L_{\text{a}}, R_{\text{a}}$ ensembles. Thus, we demonstrate the reversible mapping of an entangled state of the electromagnetic field to and from a material system. For completeness, Table 6.1 gives the diagonal elements and concurrences of $\bar{\hat{\rho}}_{\text{in}}$, $\bar{\hat{\rho}}_{\text{out}}$ determined directly at D_1, D_2 without correction for propagation and detection efficiencies.

6.4 Discussion and analysis

We emphasize that although the entanglement associated with $\hat{\rho}_{\text{out}}$ is heralded (because of the nature of our single-photon source), our protocol for generation and storage of entanglement is intrinsically deterministic. The transfer efficiency of entanglement from input modes to output modes of the quantum memory is limited by the storage and retrieval efficiency η_{sr} of the EIT process. This transfer can be quantified by the ratio $\tilde{\lambda}$ of the concurrence C_{out} for the output state $\hat{\rho}_{\text{out}}$ to C_{in} for the input state $\hat{\rho}_{\text{in}}$. For an ideal source of single photons on-demand (with no vacuum component), the input concurrence is approximated by $C_{\text{in}} \simeq \alpha V$, where α denotes the transmission efficiency of the single photon from the source to the entangler in Fig. 6.1b (ref.[34], chapter 3). Similarly, for the output, $C_{\text{out}} \simeq \alpha \eta_{\text{sr}} V$, where we assume that the visibility V is preserved by the mapping processes. Thus, $\tilde{\lambda} = \frac{C_{\text{out}}}{C_{\text{in}}} \simeq \eta_{\text{sr}}$, which therefore estimates the maximum amount of entanglement in modes $L_{\text{out}}, R_{\text{out}}$ for the case of an (ideal) single photon generated deterministically. In our experiment, the entanglement transfer reaches $\tilde{\lambda} = (20 \pm 5)$ %. By way of optimal pulse shaping and improved optical depth, the entanglement transfer can be greatly improved (section 6.10.2).

The performance of our quantum interface depends also on the memory time τ_{m} over which one can faithfully retrieve a stored quantum state. For our system, independent measurements of η_{r} made by varying the storage duration τ allow us to determine $\tau_{\text{m}} = 8 \pm 1$ μs, as limited by inhomogeneous Zeeman broadening and motional dephasing (section 6.6 and chapter 2). Active and passive compensations of the residual magnetic field would improve τ_{m}, along with improved optical trapping techniques (chapter 2).

6.5 Conclusion

In conclusion, our work provides the first realization of mapping an entangled state into and out of a quantum memory. Our protocol alleviates the significant drawback of probabilistic protocols[4], where low preparation probabilities prevent its potential scalability[37], and thus our strategy leads to efficient scaling for high-fidelity quantum communication[232]. Our current results are limited by the large vacuum component of our available single-photon source, which principally reduces the degree of entanglement in the input, and by the limited retrieval efficiency of the EIT process, which bounds the entanglement transfer to $\tilde{\lambda} = (20 \pm 5)$ %. With improved retrieval efficiency and memory time, along with the rapid development of on-demand

Table 6.1: **Experimentally determined diagonal elements and concurrences.** We directly measure the diagonal elements $\bar{p}_{ij}$ and concurrences $\bar{C}_{\text{in}}, \bar{C}_{\text{out}}$ for the density matrices $\bar{\hat{\rho}}_{\text{in}}, \bar{\hat{\rho}}_{\text{out}}$ derived directly from detectors D_1, D_2 without correction for losses and detection efficiencies. Statistical errors are also given.

	$\bar{\hat{\rho}}_{\text{in}}$	$\bar{\hat{\rho}}_{\text{out}}$
$\bar{p}_{00}$	0.9800 ± 0.0001	0.99625 ± 0.00003
$\bar{p}_{10}$	$(1.043 \pm 0.008) \times 10^{-2}$	$(2.09 \pm 0.02) \times 10^{-3}$
$\bar{p}_{01}$	$(0.957 \pm 0.008) \times 10^{-2}$	$(1.67 \pm 0.02) \times 10^{-3}$
$\bar{p}_{11}$	$(8 \pm 2) \times 10^{-6}$	$(2 \pm 2) \times 10^{-7}$
$\bar{C}$	$(1.28 \pm 0.09) \times 10^{-2}$	$(2.5 \pm 0.5) \times 10^{-3}$

single-photon sources[231], our protocol enables the deterministic generation, storage, and distribution of entanglement among remote quantum memories for scalable quantum networks. Such networks have diverse applications in quantum information science, including for quantum metrology, where quantum sensing is provided by the atomic entanglement and readout by coherent mapping to the photonic modes (chapter 9).

In the broader context of quantum information theory, our experiment provides an important contribution to the lively debate about "*single-particle*" entanglement[228,229,233]. One resolution of these discussions is a gedanken experiment in which an entangled state for a single-particle is mapped into a two-particle system by local operations, thereby verifying the presence of entanglement for the original "*single-particle*" state[233]. Our experiment demonstrates that an entangled state with one photonic excitation shared between two optical modes (see Eq. 6.1) can be converted into an entangled state for two atomic ensembles by way of coherent mapping. The presence of entanglement between the two atomic ensembles is explicitly quantified by the lower bound $C_{\text{out}} = (1.9 \pm 0.4) \times 10^{-2}$, thereby realizing the proposal of ref.[233] for "*single-particle*" entanglement.

6.6 Experimental details

A 22 ms preparation stage and 3 ms experiment run are conducted every 25 ms period. During the preparation stage, atomic ensembles are loaded in a MOT for 18 ms and further cooled by optical molasses for 3 ms where the MOT magnetic field is turned off. For 800 μs, we optically pump the atomic ensembles to the $6S_{1/2}\,|F = 4, m_F = 0\rangle$ state in atomic cesium. During this stage, the trapping beam is turned off while the intensity of the repumping beam is reduced to $0.1 I_{\text{sat}}$ where I_{sat} is the saturation intensity. The quantization axis is chosen along the k-vector of the signal modes and defined by a pulsed magnetic field of 0.2 G. A pair of counter-propagating Zeeman pumping beams (10 MHz red-detuned from $4 \leftrightarrow 4'$ transition and linearly polarized along the quantization axis) illuminate the ensembles in a direction perpendicular to modes $L_{\text{in}}, R_{\text{in}}$. The MOT repumping beam serves as a hyperfine pumping beam. The experiment is conducted at a repetition rate of 1.7 MHz during a 3 ms interval before the next MOT loading cycle. A small bias field of 10 mG is left on to define the quantization axis for the experiment. The various photon statistics throughout the experiment are detected by single-photon Si-avalanche Photodetectors (Perkin-Elmer SPCM-AQR-13) where the pulse signals are stamped with 2 ns resolution into a file by a 4-channel event time digitizer (FAST ComTec P7888) for data-acquisition. The overall transmission efficiencies (including the detector and propagation efficiencies) are 12 ± 2 % and 14 ± 2 % for the ensembles $L_{\text{a}}, R_{\text{a}}$.

The limitations to our experiment imposed by inhomogeneous Zeeman broadening are described in ref.[34] (chapters 2–3). Possible misalignment between the quantization axis and the bias magnetic field is estimated to be below 5 degrees. Following ref.[195], we are investigating active compensation of the residual magnetic field to improve τ_{m}. In our experiment, the memory time τ_{m} was also plagued by the residual control laser during storage due to finite extinction ratio 50 dB of the modulator (waveguide electro-optical modulator and

two sets of acousto-optical modulators), which set $\tau_{\rm m} \simeq 1$ ms. In addition, thermal motion of the atoms (at $T_d = 150$ μK) sets the memory time of $\tau_{\rm m} \simeq 15$ μs due to the motional dephasing, where optical trapping may dramatically improve the coherence time for the collective excitations (chapter 2).

6.7 Operational verification of entanglement

Operationally, the various elements of $\hat{\rho}$ are obtained by recombining the L_k, R_k fields with a second beam displacer, BD_2, as illustrated in Fig. 6.1d, to obtain a single spatial mode with orthogonal polarizations for the L_k, R_k fields (refs.[34,36], chapters 3 and 4), with $k \in \{\text{in,out}\}$. The diagonal elements of $\hat{\rho}$ are measured with $(\lambda/2)_{\rm v}$ set at 0° so that detection events at D_1, D_2 are recorded directly for the L_k, R_k fields. To determine the off-diagonal components of $\hat{\rho}$, the modes L_k, R_k are brought into interference with $(\lambda/2)_{\rm v}$ set at 22.5°, as shown in Fig. 6.1d. By varying the relative phase $\phi_{\rm rel}$ between the modes, we determine the visibility for single-photon interference and thereby deduce d.

6.8 Single-photon generation

The single-photon source is based upon the protocol[4,76] composed of time-delayed photon pairs, called fields 1,2 emitted from a cesium ensemble in a MOT called the source ensemble. The source ensemble is located 3 m from the memory ensembles, both of which are synchronized by a 80 MHz clock signal. For photon-pair production, a sequence of write and read pulses illuminates the source ensemble. The single photon generation is heralded by probabilistic detection of a Raman scattered field 1 from a write pulse (10 MHz red-detuned from $4 \leftrightarrow 4'$ transition). Conditioned on the heralding signal, a strong read pulse (resonant to $3 \leftrightarrow 4'$ transition) maps the excitation into a photonic mode, field 2, with probability of 50 %, which then propagates to the setup described in Fig. 6.1. The resulting conditional probability to have a single photon, field 2, at the face of memory ensemble is 15 %. The separation between the entangled optical modes $L_{\rm in}, R_{\rm in}$ after the entangler is 1 mm and each of the modes is focused down to a $1/e$ full width of 50 μm at $L_{\rm a}, R_{\rm a}$. The heralding signal triggers a control logic which disables the single-photon source and all associated laser beams for the programmable duration of the storage process for the quantum interface (ref.[36], chapter 4). As the retrieval process is in the slow-light regime, the temporal shape of the single photon is controlled by the intensity of the read laser, thereby changing the group velocity of the field 2 in the source ensemble[75,234].

6.9 EIT storage and retrieval

The coherent interface between the signal modes and collective spin waves is achieved by dynamically controlling the EIT window $\Omega_{\rm c}(t)$, defined by the atom-light interaction of a resonant control field. A quantum field propagating through an externally controlled dressed state medium is best described as a slow-light,

dark-state polariton (DSP), $\hat{\Psi}(z,t)$ [86], a coherent mixture of matter-like and photonic excitations, expressed as (chapter 2)

$$\hat{\Psi}(z,t) = \cos\theta(t)\hat{\varepsilon}_{\text{signal}} - \sin\theta(t)\sqrt{N_A}\hat{\sigma}_{\text{gs}} \tag{6.3}$$

where $\cos^2\theta(t) = \frac{\Omega_c^2(t)}{\Omega_c^2(t)+g_d^2 N_A} = \frac{v_g(t)}{c}$, g_d is the atom-photon coupling constant for the signal field, N_A is the number of atoms, $\hat{\sigma}_{\text{gs}}$ is the atomic coherence operator for ground states $|g\rangle$ and $|s\rangle$, and $\Omega_c(t)$ is the Rabi frequency of control field. As the signal field propagates through the medium, the group velocity v_g of the DSP is adiabatically reduced to zero as $\Omega_c(t)$ decreases to zero, thereby rotating the mixing angle $\theta(t)$ from a purely photonic state to a matter-like collective spin coherence (chapter 2). When the control field is re-activated, the collective spin excitation is coherently converted into a photonic mode in a time-reversal fashion. In the experiment, under the assumption of perfect state preparation, the relevant energy diagrams for the storage and retrieval processes are ground states $|g\rangle = |F = 4, m_F = 0\rangle$, $|s\rangle = |F = 3, m_F = 0\rangle$, and the excited state $|e\rangle = |F^{'} = 4, m_{F'} = \pm 1\rangle$ as shown in the insets of Fig. 6.1.

The overall efficiency η_{sr} of the EIT process and the temporal shape of the output fields are predicted by numerically solving the equations of motion in ref. [86] (see chapter 2 for detailed description, see also section 6.10). Under experimental conditions, the projected storage and retrieval efficiency is $\eta_{\text{sr}}^{\text{theory}} = 18$ % as shown in Fig. 6.2. We consider two strategies that could improve η_{sr}: increasing the optical depth and appropriate pulse-shaping. By following the same calculation as above, we find that the EIT efficiency reaches its asymptotic value of $\eta_{\text{sr}} \simeq 30$ % when the optical depth is increased to $\tilde{d}_0 \simeq 50$ with all other parameters corresponding to the current experiment (section 6.10.2.1). On the other hand, as demonstrated in ref. [235], by iterating time-reversed version of the output signal field into the input, one achieves an optimal pulse-shape for the signal field which balances the transmission loss due to finite bandwidth of the pulse and the leakage due to the imperfect compression of the signal field within the atomic ensembles to reach maximum η_{sr} for a given control field $\Omega_c(t)$. This maximum η_{sr} for a given control field is in principle only dependent on the optical depth $\tilde{d}_0$ (section 6.10.2.2). Equivalently, the control field $\Omega_c(t)$ can be optimized for a given signal field as investigated theoretically in ref. [236]. Note that efficiencies approaching 50 % have been achieved in ref. [235].

6.10 Theoretical discussions

The dynamics of laser-induced coherence of atomic states can dramatically modify the optical response of an atomic medium, leading to destructive quantum interferences between the excitation pathways[95,96]. In this way, resonant absorption and refraction can be eliminated by way of electromagnetically induced transparency (EIT)[94]. In this section, we describe a semi-classical theory of EIT. For a complete quantum theory of *dynamic* EIT, I refer to chapter 2, whereby the equations of motions for the fields and atomic variables are derived in a *self-consistent* manner. We also present our theoretical result of time-reversal optimization[188] for η_{sr} using our experimental parameters[30].

6.10.1 Static electromagnetically induced transparency

Here, we present a semi-classical theory for *static* EIT[94,182,237,238]. While the situation for *dynamic* EIT is somewhat different, *static* EIT describes the phenomena of ultra-slow propagation of the signal field in a coherent atomic medium[88,239]. We also examine the equivalence between the semi-classical model and the full quantum model.

6.10.1.1 Semi-classical model of EIT

Electromagnetically induced transparency can be explained semi-classically in terms of (1) Fano-like quantum interferences between the decay pathways of Autler-Townes resonances[237,238], and (2) "adiabatic preparation" or "optical pumping" to a dark state in the dressed state picture[86,179–181,183,184], as employed traditionally in coherent population trapping (CPT) and stimulated Raman adiabatic passage (STIRAP), respectively. In particular, I will adapt the latter approach (2), as the polaritonic quantum dynamics[86] described in chapter 2 can be mapped to a semi-classical adiabatic passage in the setting of dark and bright states[181].

As in chapter 2, we consider an effective (*non-hermitian*) Hamiltonian $\hat{H}_{\text{EIT}}$ for an atomic ensemble interacting with a weak classical signal field $\mathcal{E}_s$ (Rabi frequency Ω_s) and a strong control laser (Rabi frequency Ω_c) in the rotating frame (following the notations introduced in section 2.5), with

$$\hat{H}_{\text{eff}} = \hat{H}_{\text{EIT}} - i\hbar\gamma_{ge}\hat{\sigma}_{ee} - i\hbar\gamma_{gs}\hat{\sigma}_{ss}, \tag{6.4}$$

where the system Hamiltonian $\hat{H}_{\text{EIT}}$ for the EIT interaction is given by

$$\hat{H}_{\text{EIT}}/\hbar = \Delta_c\hat{\sigma}_{ee} - \delta\hat{\sigma}_{ss} - \left(\Omega_s\hat{\sigma}_{eg} + \Omega_c\hat{\sigma}_{es} + h.c.\right). \tag{6.5}$$

Δ_c is the single-photon detuning for the control laser, and δ is the two-photon detuning between the signal field and the control laser. Here, the decay channels ($-i\hbar\gamma_{ge}\hat{\sigma}_{ee}$, $-i\hbar\gamma_{gs}\hat{\sigma}_{ss}$) result in losses of atomic coherences at rates γ_{ge} and γ_{gs}. In the following discussions, I will assume a negligible ground-state dissipation $\gamma_{gs} \simeq 0$ and resonant excitation by the control laser with $\Delta_c = 0$.

For open quantum systems, quantum-state evolution by a master equation in the Lindblad form (e.g., for Eq. 6.5) is equivalent to that of a stochastic wave-function method (quantum-trajectory method) accompanied by quantum jumps[a] (refs. [164–166,240,241]). Assuming a wave-function of the form $|\psi(t)\rangle = c_g(t)|g\rangle + c_s(t)|s\rangle + c_e(t)|e\rangle$, the *non-hermitian* effective Hamiltonian $\hat{H}_{\text{eff}}$ (Eq. 6.4) yields the following equations of motions (from the Schrödinger's equation),

$$\dot{c}_g = i\Omega_s^* c_e \tag{6.6}$$

$$\dot{c}_s = -(\gamma_{gs} - i\delta)c_s + i\Omega_c^* c_e \tag{6.7}$$

$$\dot{c}_e = -(\gamma_{ge} - i\delta)c_e + i\Omega_s c_g + i\Omega_c c_s. \tag{6.8}$$

Since $\Omega_s \ll \Omega_c$ and the initial state is $|\psi(0)\rangle = |g\rangle$, we assume that the probability amplitude remains in $c_g(t) \simeq 1$ for all time t. Fourier transforming Eqs. 6.7–6.8 (with $\partial_t \mapsto iw$) and solving for $\{c_s, c_e\}$, we obtain

$$c_s(w) = \frac{\Omega_s \Omega_c^*}{(w - i\gamma_{ge} - \delta)(w - \delta) - |\Omega_c|^2}$$

$$c_e(w) = \frac{\Omega_s (w - \delta)}{(w - i\gamma_{ge} - \delta)(w - \delta) - |\Omega_c|^2}.$$

The off-diagonal atomic polarization ρ_{eg} can thus be expressed as $\rho_{eg} = c_g^* c_e \simeq c_e$, while the normalized linear susceptibility function is $\overline{\chi}_s = \frac{\rho_{eg}}{\Omega_s}$ (see chapter 2). Redefining $(\delta - w) \rightarrow \nu$, we arrive at the expression for the normalized linear susceptibility $\overline{\chi}_s$ in Eq. 2.79 with

$$\overline{\chi}_s = \frac{\nu}{|\Omega_c|^2 - \nu^2 - i\gamma_{ge}\nu}. \tag{6.9}$$

The relationship between $\overline{\chi}_s$ and group velocity v_g (and transparency window) is explained in chapter 2 for an ideal Λ-level system. In section 6.10.1.3, we further illustrate the importance of optical pumping and polarization orientations of the control laser and the signal field for observing EIT in a Λ-level system comprised of multiple Zeeman sublevels.

6.10.1.2 The emergence of dark and bright states

The underlying principle for the cancellation of absorption in EIT is directly related to the phenomena of dark-state and coherent population trapping [183]. Let us examine the effective Hamiltonian $\hat{H}_{\text{eff}}$ with $\delta = 0$. In

[a] We note that the effective Hamiltonian $\hat{H}_{\text{eff}}$ (Eq. 6.4) does not capture the repopulations of $\hat{\sigma}_{gg}$ and $\hat{\sigma}_{ss}$ due to spontaneous emissions ($-i\hbar\gamma_{ge}\hat{\sigma}_{ee}$). As a semi-classical analysis, we neglect the quantum jump processes [164,165] and only consider the evolution of the stochastic wave-function $|\psi(t)\rangle$ under the effective Hamiltonian over time $\tilde{t}$. This approximation is valid in the quantum trajectory method for our initial condition $c_{gg} + c_{ss} \simeq 1$, as long as the jump probability is $p_{\text{jump}} = \langle\psi| \exp\left(\frac{i}{\hbar}\int_0^{\tilde{t}} dt(\hat{H}_{\text{eff}} - \hat{H}_{\text{eff}}^\dagger)\right)|\psi\rangle \simeq \int_0^{\tilde{t}} dt\left(\gamma_{ge}|c_{ee}|^2 + \gamma_{gs}|c_{ss}|^2\right) \ll 1$ for $\gamma_{gs} \simeq 0$.

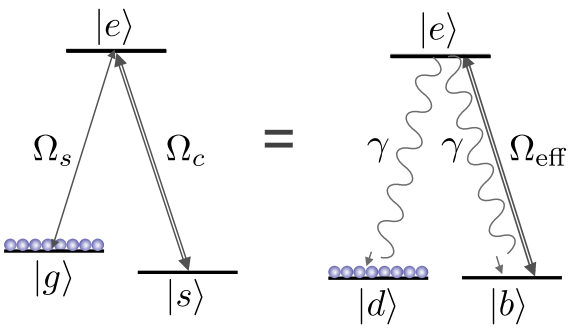

Figure 6.4: **Qualitative equivalence between electromagnetically induced transparency and coherent population trapping.** As shown by Eq. 6.10, the phenomena of EIT in the atomic bare-state basis can be equivalently described as a dark-state pumping process (CPT) in the dark- and bright-state basis for two-photon detuning $\delta = 0$.

the dark- and bright-state picture, we may equivalently write $\hat{H}_{\text{eff}}$ (Eq. 6.4) in the following way,

$$\hat{H}_{\text{eff}}/\hbar = -i\gamma_{ge}\hat{\sigma}_{ee} - \Omega_{\text{eff}}\underbrace{(\sin^*\theta_d|g\rangle + \cos^*\theta_d|s\rangle)}_{|b\rangle}\langle e| - \Omega_{\text{eff}}|e\rangle\underbrace{(\sin\theta_d\langle g| + \cos\theta_d\langle s|)}_{\langle b|}, \tag{6.10}$$

where $\theta_d = \arctan(\Omega_s/\Omega_c)$ is the mixing angle, and $\Omega_{\text{eff}} = \sqrt{|\Omega_c|^2 + |\Omega_s|^2}$ is the effective Rabi frequency which couples the bright state $|b\rangle = \sin^*\theta_d|g\rangle + \cos^*\theta_d|s\rangle$ to the excited state $|e\rangle$. Similarly, we introduce a sibling, a dark state $|d\rangle = \cos^*\theta_d|g\rangle - \sin^*\theta_d|s\rangle$ (one of the three eigenstates of $\hat{H}_{\text{eff}}$) orthonormal to the bright state $|b\rangle$, which does not couple to the excited state $|e\rangle$ via $\hat{H}_{\text{eff}}$ (thus, immune to spontaneous emission). Here, I used the notations, $\{\sin^*\theta_d, \cos^*\theta_d\}$, to define the complex conjugates of $\{\sin\theta_d, \cos\theta_d\}$.

In the picture of dark- and bright-state basis (Eq. 6.10), the atomic level diagram in the bare-state picture is transformed to a diagram akin to the case of optical pumping, as shown in Fig. 6.4. Here, the bright-state $|b\rangle$ couples dissipatively to the excited state $|e\rangle$ with an effective Rabi frequency Ω_{eff}, while the dark-state $|d\rangle$ is decoupled from the signal field $\mathcal{E}_s$ and the control laser Ω_c. Thus, if the initial atomic state is prepared in an admixture of both ground states ($|g\rangle$ and $|s\rangle$), the coherently dressing Ω_{eff} will "optically pump" the atoms in the bright state $|b\rangle$ to the dark state $|d\rangle$ through the spontaneous emission from the excited state $|e\rangle$. As there are little atoms left in $|b\rangle$ after dark-state pumping (with negligible optical thickness for the $|b\rangle \leftrightarrow |e\rangle$ transition), the atoms will be trapped in the dark state via coherent population trapping (CPT) and the signal field will exhibit full spectroscopic transparency on resonance $\delta = 0$.

In the case of EIT, the initial atomic state can further be prepared to the dark state $|d\rangle \simeq |g\rangle$ (with $\Omega_s \ll \Omega_c$) prior to the EIT dressing (by means of optical pumping), from which excitations cannot occur. Therefore, by rotating the mixing angle $\theta_d = 0 \rightarrow \pi/4$, we can adiabatically transfer the initial state to a superposition state $|d\rangle = \frac{1}{2}(|g\rangle - |s\rangle)$ of maximum atomic coherence $\hat{\sigma}_{gs}$, as in stimulated Raman adiabatic transfer[181,184] (STIRAP). There is a qualitative similarity between the adiabatic following of $|d\rangle$ and the dynamics of the dark-state polariton $\hat{\Psi}_d$. Heuristically considering the Fock state of the signal field, we can

write the dark state in a familiar form $|d\rangle = \cos^* \theta_d |\overline{g}_a, 1_s\rangle - \sin^* \theta_d |\overline{s}_a, 0_s\rangle$, identical to the single-excitation dark-state $|D, 1\rangle = \hat{\Psi}_d^\dagger |\overline{g}_a, 0_s\rangle$ (Eq. 2.69) in chapter 2. Hence, the quantum theory of dark-state polaritons[86] (chapter 2) is associated with the classical picture of dark- and bright-states in CPT and STIRAP.

6.10.1.3 Importance of the Zeeman sublevels

In the presence of multiple Zeeman sublevels, the susceptibility function $\chi_s = \frac{2g_d^2 N_A}{w_s}\overline{\chi}_s$ in Eq. 2.79 of chapter 2 and Eq. 6.9 generalizes to a normalized form $\overline{\chi}_s$ of

$$\overline{\chi}_s(\delta) = \frac{1}{N_c}\sum_{m_F} \frac{p_{m_F}|C^{F_g,1,F_e}_{m_F,\epsilon_s,m_F+\epsilon_s}|^2\delta}{|\Omega_c|^2|C^{F_s,1,F_e}_{m_F+\epsilon_s-\epsilon_c,\epsilon_c,m_F+\epsilon_s}|^2 - \delta^2 - i\gamma_{ge}\delta}, \tag{6.11}$$

where $N_c = \sum_{m_F} p_{m_F}|C^{F_g,1,F_e}_{m_F,\epsilon_s,m_F+\epsilon_s}|^2$ is the normalization constant, $\{\epsilon_s, \epsilon_c\}$ are the respective helicities for the signal field and the control lasers, and $C^{f_1,f_2,f_3}_{m_1,m_2,m_3} \equiv \langle f_1 m_1 f_2 m_2 | f_3 m_3\rangle$ are the Clebsch-Gordan coefficients. In deriving Eq. 6.11, we assumed that the initial atomic state is $\hat{\rho}_a = \sum_{m_F} p_{m_F}|F_g, m_F\rangle\langle F_g, m_F|$.

For the ideal susceptibility function in Fig. 2.4 of chapter 2, the imaginary part of the susceptibility is $\mathrm{Im}(\chi_s) = 0$ on resonance $\delta = 0$, thereby providing a transparency window for the signal field. At the same time, the real part of the linear susceptibility function $\mathrm{Re}(\chi_s)$ provides a strong dispersion on resonance for slow-light propagation. In the presence of Zeeman populations p_{m_F}, however, the coherent atomic medium exhibits EIT only for specific polarization orientations $\{\epsilon_s, \epsilon_c\}$ of the signal field and the control lasers. Particularly, if the one of the Clebsch-Gordan coefficients $C^{F_g,1,F_s}_{m_F+\epsilon_s-\epsilon_c,\epsilon_c,m_F+\epsilon_s}$ vanishes, the uncoupled Zeeman populations may have sufficient optical depths to cause dissipative absorption of the signal field and the absence of transparency.

As shown in Fig. 6.5, the EIT spectroscopy with lin//lin configuration (for the signal field and the control

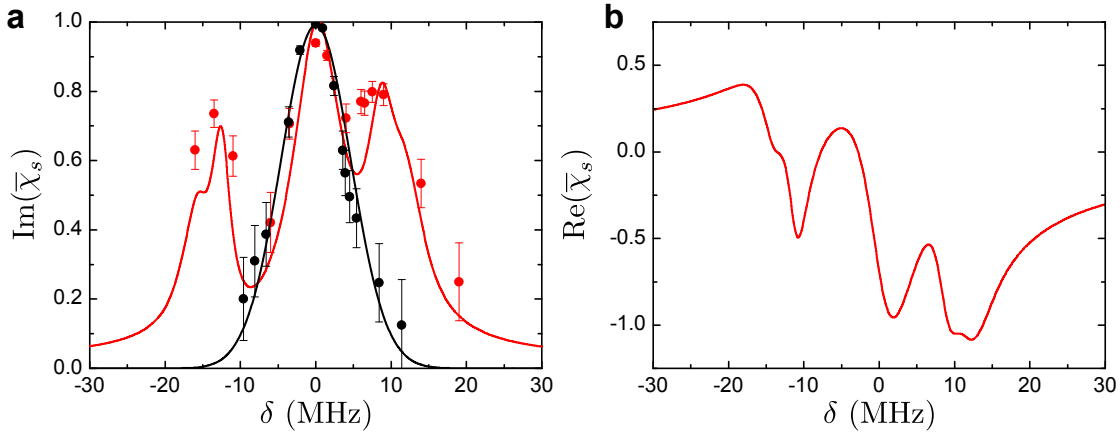

Figure 6.5: **EIT spectroscopy with lin//lin configuration. a,** Measurement of imaginary part of the susceptibility function $\mathrm{Im}(\overline{\chi}_s)$. We show the measured $\mathrm{Im}(\overline{\chi}_s)$ as red (black) points in the presence (absence) of control laser Ω_c with the polarization orientations given by $\epsilon_c = \epsilon_s = \hat{y}$. The data agrees well to the theoretically predicted spectra (lines). **b**, Theoretically predicted real part of the susceptibility function $\mathrm{Re}(\overline{\chi}_s)$.

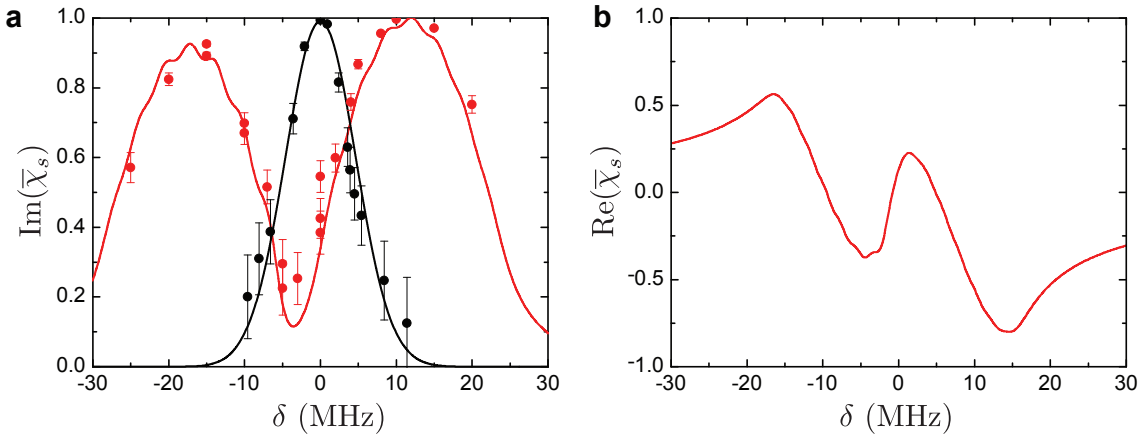

Figure 6.6: **EIT spectroscopy with $\sigma_\pm$//$\sigma_\pm$ configuration. a,** Measurement of imaginary part of the susceptibility function Im($\overline{\chi}_s$). We show the measured Im($\overline{\chi}_s$) as red (black) points in the presence (absence) of control lasers Ω_c with the polarization orientations given by $\epsilon_c = \epsilon_s = \sigma_+$. The data agrees well to the theoretically predicted spectra (lines). **b**, Theoretically predicted real part of the susceptibility function Re($\overline{\chi}_s$).

laser) does not show a transparency window on resonance. Since the two edge states ($|F' = 4, m_{F'} = \pm 4\rangle$) of the Zeeman sublevels in the electronically excited state $|e\rangle$ of $6P_{3/2}$ cannot couple to the hyperfine ground state $|s\rangle = |F = 3, m_F\rangle$ with the control laser Ω_c due to selection rule, the signal field experiences a strong resonant absorption by the optical depths for the residual atoms residing in the Zeeman sublevels $|F = 4, m_F = \pm 4\rangle$ of the hyperfine ground state $6S_{1/2}$ ($|g\rangle$) as represented by the peak in Im($\overline{\chi}_s$) around $\delta = 0$. The asymmetry in the two side peaks (Autler-Townes splitting for the Zeeman states coupled to the control laser) of Fig. 6.5 is due to the uncalibrated detuning Δ_c of the control laser respect to the $|s\rangle \leftrightarrow |e\rangle$

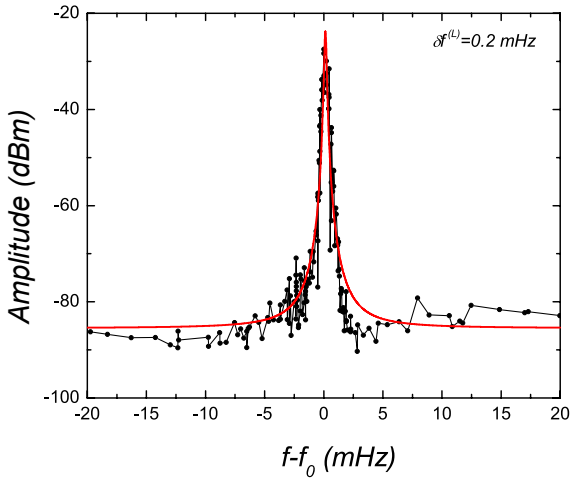

Figure 6.7: **Phase locked lasers for EIT spectroscopy.** We show the beat note spectrum between two lasers, responsible for the signal field and the control laser, in EIT spectroscopy. Assuming a Lorentzian spectrum, we deduce a beat-note linewidth of ~ 0.2 mHz, limited by the phase noise in the detection.

transition (which use as a fitting parameter in Fig. 6.5). The solid lines are the theoretical predictions based on Eq. 6.11, with the assumption of the initial state $p_{m_F} = 1/(2F_g + 1)$

Instead, we now apply a signal field and a control laser with helicities $\{\epsilon_s, \epsilon_c\} = \sigma_\pm$ in Fig. 6.6. As shown in Fig. 6.6a, the measured susceptibility function clearly demonstrates electromagnetically induced transparency around $\delta = 0$. Here, the red-detuned offset of the transparency window is due to the presence of the detuning Δ_c of the control laser. In Fig. 6.5b, we also show the real part of the linear susceptibility, similar to the result obtained for the ideal Λ-level system (Fig. 2.4). Furthermore, in our experiment[30] (Fig. 6.1), we initialize the atoms to a clock state $|g\rangle = |F = 4, m_F = 0\rangle$. With $\epsilon_{c,s} = \sigma_\pm$, the coherent dressings by the control and signal fields allow clock-state preserving transitions (section 6.6), which form a Λ-level with $|g\rangle = |F = 4, m_F = 0\rangle$, $|s\rangle = |F = 4, m_F = 0\rangle$, and $|e\rangle = |F' = 4, m_{F'} = \pm 1\rangle$. By optically pumping the ensemble to $|g\rangle = |F = 4, m_F = 0\rangle$ with efficiency ~ 90 %, we achieve a maximum transparency $T = 95$ % on resonance.

6.10.2 Dynamic electromagnetically induced transparency

In chapter 2, we derived the Heisenberg-Langevin equations of motions in the polaritonic picture. In this section, we numerically solve the equations of motions and compare the theoretically simulated spatio-temporal modes $\mathcal{E}_s$ to the experiment, where we store and retrieve a coherent state $|\alpha\rangle$ for various optical depths. We also show a theoretical simulation of time-reversal optimization of the storage and retrieval efficiency η_{sr} based on ref.[188] for our experimental parameters[30].

6.10.2.1 Scaling behavior to optical depth and pitfalls via dissipative absorption

As we discussed in chapter 2, the dynamics of the signal field $\hat{\mathcal{E}}_s(z,t)$ and the collective atomic excitation $\hat{\mathcal{S}}(z,t)$ in the one-dimensional approximation is governed by the following coupled equations of motions (Eqs. 2.85–2.87),

$$\left(\partial_t + c\partial_z\right)\hat{\mathcal{E}}_s(z,t) = ig_d n_A(z)\frac{L}{\sqrt{N_A}}\hat{\mathcal{P}}(z,t) \tag{6.12}$$

$$\partial_t\hat{\mathcal{P}}(z,t) = -(\gamma_{ge} + i\Delta)\hat{\mathcal{P}}(z,t) + ig_d\sqrt{N_A}\hat{\mathcal{E}}_s(z,t) + i\Omega_c(z,t)\hat{\mathcal{S}} + \sqrt{2\gamma_{ge}}\hat{F}_P \tag{6.13}$$

$$\partial_t\hat{\mathcal{S}}(z,t) = -\gamma_{gs}\hat{\mathcal{S}}(z,t) + i\Omega_c^*(z,t)\hat{\mathcal{P}} + \sqrt{2\gamma_{gs}}\hat{F}_S, \tag{6.14}$$

where $\hat{\mathcal{P}}(z,t)$ is the atomic polarization $|g\rangle - |e\rangle$ induced by the quantum field $\hat{\mathcal{E}}_s(z,t)$ in the presence of coherent dressing $\Omega_c(z,t)$. Assuming a coherent-state input, we numerically solve the complex-value equations of motions (Eqs. 6.12–6.14) by neglecting the Langevin terms $\hat{F}_S = \hat{F}_P = 0$, which do not contribute to normally-ordered expectation values. Here, we fit the atomic ensemble with a Gaussian spatial profile to infer the atomic density $n_A(z) = \frac{2N_A}{\sqrt{\pi}L}\exp\left(-4z^2/L^2\right)$ from the fluorescence measurement, and

the spatio-temporal mode of the control laser $\Omega_c(t - z/c)$ approximated by

$$\Omega_c(x) = \Omega_c \times \frac{\tanh[c_1 x] + \tanh[-c_2(x-\tau)]}{2}, \tag{6.15}$$

with the parameters $\{\Omega_c, c_1, c_2\}$ determined from independent measurements on the intensity of the control laser. N_A is determined from the measured value of the optical depth $\tilde{d}_0$ for the $|g\rangle - |e\rangle$ transition (optical depth is defined as the transmission $T = e^{-\tilde{d}_0}$ of the signal field absent the control laser). For the details of the derivations for Eqs. 6.12–6.14, I refer to the discussions in chapter 2.

Experimentally, we apply a control laser with $\Omega_c \simeq 24$ MHz (rise and fall times $\delta t_c = 1/c_1 = 1/c_2 \simeq 7$ ns, defined as the time-scales resulting in an intensity changes of $10\% - 90\%$) and a phase-locked signal laser $\mathcal{E}_s$ (Fig. 6.7) resonant to $|g\rangle - |e\rangle$ transition (with two-photon detuning $\delta = 0$) in a counter-intuitive order[181]. The signal field $\mathcal{E}_s$ is assumed to be in a coherent state $|\alpha\rangle$ with $|\alpha|^2 \simeq 0.3$ per pulse (Gaussian pulse width 30 ns for the incoming signal pulse). The relative delay between Ω_c and $\mathcal{E}_s$ is tuned to maximize the storage and retrieval efficiency η_{sr}. As in the main experiment[30] (sections 6.1–6.9), we prepare the atomic ensemble into the clock state $|g\rangle = |F = 4, m_F = 0\rangle$ by optical pumping. We reduce the repetition rate of the laser cooling and trapping cycle from 40 Hz to 0.2 Hz in order to increase the atomic density[242,243] via compressed MOT (CMOT)[243] for 200 ms after the normal MOT loading and cooling (4 s). We then further cool the atoms with polarization gradient cooling for 50 ms, followed by optical pumping (1 ms) to the clock state. With

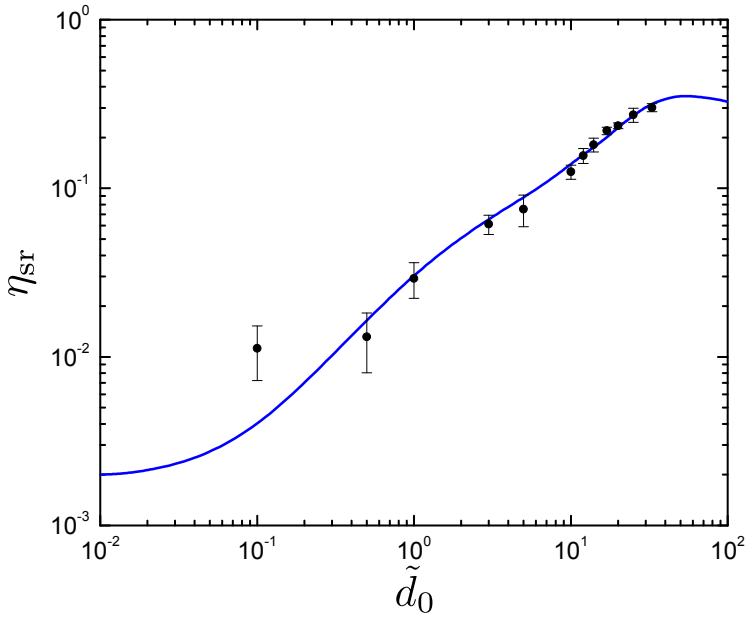

Figure 6.8: **Investigation of reversible transfer of a coherent state to and from an atomic memory.** We study the dependence of storage and retrieval efficiency η_{sr} to the optical depth $\tilde{d}_0$, with the measurements shown by black points. We achieve a maximum efficiency of $\eta_{\text{sr}} \simeq 30\ \%$ at $\tilde{d}_0 \simeq 33$. The theoretical simulation (blue line) based on Eqs. 6.12–6.14 shows excellent agreement with our measurement. The error bars indicate the statistical uncertainty of 1 s.d.

the improved setup, we achieve a maximum resonant optical depth of $\tilde{d}_0 \gtrsim 50$, albeit with reduced optical pumping efficiency $\sim 70\%$ due to radiation trapping, compared to the main experiment[30] (sections 6.1–6.9). The optical depth $\tilde{d}_0$ is varied by tuning the value of the magnetic field to the desired value during the normal MOT phase (before compression).

In Fig. 6.8, we show the overall transfer efficiency η_{sr} for storing and retrieving a coherent state $|\alpha\rangle$ in an atomic ensemble (with storage time $\tau = 1$ μs) as a function of optical depth $\tilde{d}_0$ (see e.g., Fig. 2.6 for a time-domain measurement at $\tilde{d}_0 = 20$). In particular, we achieve a maximum storage and retrieval efficiency of $\eta_{\text{sr}} = 30 \pm 2$ % at optical depth $\tilde{d}_0 \simeq 33$. We also find excellent agreement between the theoretical predicted EIT efficiency $\eta_{\text{sr}}^{\text{theory}}(\tilde{d}_0)$ and the experimentally measured η_{sr}. We emphasize that for higher optical depth $\tilde{d}_0 \gtrsim 60$ (a region beyond the capability at the time), the storage and retrieval efficiency η_{sr} is expected to decrease, due to the reduced bandwidth of the EIT medium at high $\tilde{d}_0$ (chapter 2, see also Fig. 6.10). For further improvement in η_{sr}, it is thus important to increase the intensity of the control laser[b] for higher $\tilde{d}_0$.

In order to optimize η_{sr} for a finite $\tilde{d}_0$, we need to compromise the control laser's intensity between two competing regimes. On the one hand, (1) a large Rabi frequency Ω_c is preferred to increase bandwidth of the EIT medium and to avoid dissipative absorption of $\mathcal{E}_s$. On the other hand, (2) a sufficiently small Ω_c is required to compress the signal field's wavepacket inside the ensemble for avoiding significant leakage. In analogy, these two competing effects[c] at finite $\tilde{d}_0$ can be cast in terms of the proper shaping of the spatio-temporal mode of the signal field $\mathcal{E}_s$ for a fixed Ω_c. In the next section, we discuss an iterative optimization strategy based on the works by Gorshkov *et al.*[187–189], which leads to global maximization of η_{sr} in the fully adiabatic regime, as demonstrated experimentally by Novikova *et al.*[235].

6.10.2.2 Iterative optimization strategy based on time-reversal symmetry

In the fully adiabatic regime, the mapping process is well described by the dynamics of dark-state polariton $\hat{\Psi}_d(z,t) = \cos\theta_d(t)\hat{\mathcal{E}}_s(z,t) - \sin\theta_d(t)\hat{\mathcal{S}}(z,t)$ with a beamsplitter-like Hamiltonian $\hat{H}_{\text{int}}^{(\text{map})}$ (Eq. 2.84) in chapter 2, given by

$$\hat{H}_{\text{int}}^{(\text{map})} = i\dot{\theta}_d(z,t)\left(\hat{\mathcal{E}}_s(z,t)\hat{\mathcal{S}}^\dagger(z,t) - \hat{\mathcal{E}}_s^\dagger(z,t)\hat{\mathcal{S}}(z,t)\right). \tag{6.16}$$

$\dot{\theta}_d(z,t)$ gives the rate of change in the mixing angle $\theta_d(z,t)$, which we assume to be small in order for adiabatic passage (chapter 2). The unitary transformation $\hat{U}_{\text{int}}^{(\text{map})}(t) = \exp(-\frac{i}{L\hbar}\int_0^t dt' \int_0^L dz \hat{H}_{\text{int}}^{(\text{map})}(z,t'))$

[b] With a large Rabi frequency Ω_c for the control laser, there may be a non-negligible contribution from a competing four-wave mixing process[244], where the atoms initially at $|g\rangle$ is off-resonantly driven to $|s\rangle$ by Ω_c generating an anti-Stokes photon, followed by a resonant scattering back to $|g\rangle$ with Ω_c seeded by the signal field (Stokes photon). We do not consider this four-wave mixing process in our calculation, as it is suppressed by the large ground-state splitting ~ 9 GHz.

[c] For a given Ω_c, we need to keep the signal pulse $\mathcal{E}_s$ as short as possible to compress $\mathcal{E}_s$ within the atomic sample and to avoid leakage. On the other hand, we need to broaden the spatial extent of $\mathcal{E}_s$ as much as possible to reduce its pulse bandwidth well below the EIT bandwidth of the coherent atomic medium.

describes the mapping process, where we individually define the storage ($\eta_{\rm s}$) and retrieval ($\eta_{\rm r}$) efficiencies as

$$\eta_{\rm s} = \frac{\int dz \langle \hat{\mathcal{S}}^\dagger(z,t_s)\hat{\mathcal{S}}(z,t_s)\rangle}{\int dz \langle \hat{\mathcal{E}}_s^\dagger(z,t_0)\hat{\mathcal{E}}_s(z,t_0)\rangle} \tag{6.17}$$

$$\eta_{\rm r} = \frac{\int dz \langle \hat{\mathcal{E}}_s^\dagger(z,t_f)\hat{\mathcal{E}}_s(z,t_f)\rangle}{\int dz \langle \hat{\mathcal{S}}^\dagger(z,t_r)\hat{\mathcal{S}}(z,t_r)\rangle}, \tag{6.18}$$

evaluated at the respective times t_s (falling edge) and t_r (rising edge) with delay $\tau = t_r - t_s$. $\hat{\mathcal{E}}_s(z,t_0)$ and $\hat{\mathcal{E}}_s(z,t_f)$ give the initial (incoming) and final (outgoing) states of the signal field.

Qualitatively, it is easier to understand the optimal retrieval strategy for $\eta_{\rm r}$ than to understand the optimal storage $\eta_{\rm s}$, as we assume a pre-existing collective spin-wave with a profile $\langle \hat{\mathcal{S}}^\dagger(z,t_r)\hat{\mathcal{S}}(z,t_r)\rangle$ at time t_r. In this case, unlike the storage, we are not restrained by the control laser due to the leakage of the signal field. In practice, however, an abrupt activation of $\Omega_c(z,t)$ can reduce the retrieval efficiency by the non-adiabatic transition of $\Psi_d(z,t)$ to the bright-state polariton $\Psi_b(z,t)$. Here, we give a heuristic argument for the optimal $\eta_{\rm r}^{\rm opt}$ (ref.[188]), where we assume a fully adiabatic regime for $\Omega_c(z,t)$ and an optimally shaped $\langle \hat{\mathcal{S}}^\dagger(z,t_r)\hat{\mathcal{S}}(z,t_r)\rangle$. For a rigorous proof in the adiabatic regime, I refer to the original works in refs.[187–189]. We then show that the time-reversed version of the optimal retrieval process leads to an optimal storage with efficiency $\eta_{\rm s}^{\rm opt} = \eta_{\rm r}^{\rm opt}$.

We first consider the forward retrieval in a Gaussian signal mode with beam-waist w_0 (section 2.3.2.2). Beyond the Rayleigh range, the solid-angle $\Omega_{\rm solid}$ of this mode is given by $\Omega_{\rm solid} \simeq \frac{\lambda^2}{4\pi w_0^2 \ln 2}$. The collectively enhanced scattering rate into this mode is then simply $\Gamma_c = \Omega_{\rm solid} N_A^2 \Gamma_0 = \frac{\lambda^2}{4\pi w_0^2 \ln 2} N_A^2 \Gamma_0$, whereas the scattering rate into all other modes is given approximately by $\Gamma_n \simeq N_A \Gamma_0$. Here, $\Gamma_0 = 2\pi\gamma_{ge}$ is the single-atom scattering rate. The optimal retrieval efficiency $\eta_{\rm r}^{\rm opt}$ is then given by

$$\eta_{\rm r}^{\rm opt} = \frac{\Gamma_c}{\Gamma_c + \Gamma_n} \simeq \frac{3\tilde{d}_0}{3\tilde{d}_0 + 8} \simeq 1 - \frac{8}{3\tilde{d}_0}, \tag{6.19}$$

where we used the relations for resonant absorption cross-section $\sigma_0 = 3\lambda^2/2\pi$ and optical depth $\tilde{d}_0 \simeq N_A\sigma_0/(\pi w_0^2)$. Thus, we find that the optimal retrieval efficiency for $\eta_{\rm r}^{\rm opt}$ depends only on the optical depth $\tilde{d}_0 = \frac{g_d^2 N_A}{\gamma_{ge}\kappa_{\rm eff}}$ (where $\kappa_{\rm eff} = c/L$), which plays the role of a cooperativity parameter (chapter 2).

From the qualitative argument given above for achieving the optimal $\eta_{\rm r}^{\rm opt}$, we now discuss the principle of time-reversal as an optimization tool for storage $\eta_{\rm s}$. We consider the storage map $\hat{U}_{\rm int}^{\rm (map)}(t)$ on the initial state $|\overline{g}_{\rm a}, 1_s\rangle$ given by $|D,1\rangle = \hat{\Psi}_d^\dagger |\overline{g}_{\rm a}, 0_s\rangle$ in the Schrödinger picture. The storage probability $\eta_{\rm s}$ is then given by

$$\eta_{\rm s}^{\rm opt} = |\langle \overline{s}_{\rm a}, 0_s | \hat{U}_{\rm int}^{\rm (map)}(t) | \overline{g}_{\rm a}, 1_s\rangle|^2. \tag{6.20}$$

Using the unitarity relation for $\hat{U}_{\rm int}^{\rm (map)\dagger}(t) = \hat{U}_{\rm int}^{\rm (map)}(-t)$, we find that the storage efficiency is identical to the retrieval efficiency,

$$\eta_{\rm s}^{\rm opt} = |\langle \overline{g}_{\rm a}, 1_s | \hat{U}_{\rm int}^{\rm (map)}(-t) | \overline{s}_{\rm a}, 0_s\rangle|^2 = \eta_{\rm r}^{\rm opt}, \tag{6.21}$$

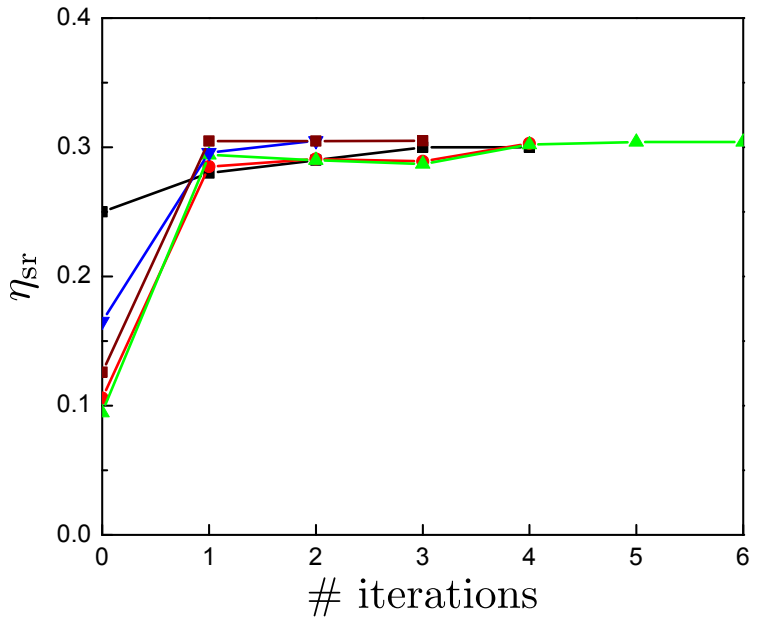

Figure 6.9: **Iterative optimization scheme for maximizing storage and retrieval efficiency.** We apply theoretically the time-reversal symmetry[186] for optimizing the EIT efficiency $\eta_{\rm sr}$ at optical depth $\tilde{d}_0 = 17$, where $\eta_{\rm sr}$ converges to $\simeq 30\ \%$ after $2-3$ steps. The various colors indicate different initial conditions for the signal fields $\mathcal{E}^{(1)}_{s,\rm in}(z,t)$.

if the time-reversed version $\hat{U}^{(\rm map)}_{\rm int}(t)$ of the retrieval map $\hat{U}^{(\rm map)}_{\rm int}(-t)$ is used for storage.

This means that if the retrieval map $\hat{U}^{(\rm map)}_{\rm int}(-t)$ yields an optimal retrieval $\eta_{\rm r}^{\rm opt}$ of some spin-wave mode $\tilde{\hat{\mathcal{S}}}(z,t)$ to an output signal mode $\tilde{\hat{\mathcal{E}}}_s(z,t)$, we can realize an inverse evolution by time-reversing $\hat{U}^{(\rm map)}_{\rm int}(t)$ (time-reversing the control $\Omega_c(-z,t)$ and the signal fields $\tilde{\hat{\mathcal{E}}}_s(-z,t)$ in Eq. 6.16) to achieve optimal efficiency $\eta_{\rm s}^{\rm opt} = \eta_{\rm r}^{\rm opt}$, where the incoming field $\tilde{\hat{\mathcal{E}}}_s(-z,t)$ is mapped onto the stationary excitation $\tilde{\hat{\mathcal{S}}}(z,t)$. Here, we note that the negative sign in z implies a backward propagation, corresponding to the situation of backward storage $(\tilde{\hat{\mathcal{E}}}_s(-z,t), \Omega_c(-z,t))$ followed by forward retrieval $(\tilde{\hat{\mathcal{E}}}_s(-z,t), \Omega_c(-z,t))$. The time-reversal symmetry also applies to forward storage followed by forward retrieval, as in our experimental setup[30], albeit with reduced optimal efficiency $\eta_{\rm r}^{\rm opt} = \eta_{\rm s}^{\rm opt} \sim 1 - \frac{1}{\sqrt{\tilde{d}_0}}$ (ref.[186]). For a rigorous proof of time-reversal symmetry as an optimization tool, I refer to ref.[188] where Eqs. 6.12–6.14 are analytically solved in the fully adiabatic regime.

In the non-adiabatic regime, as in our case, the time-reversal optimization generally does not converge to the global maximum of $\eta_{\rm sr}$. Such a 'fast' storage regime has been considered in ref.[245] using gradient ascent methods. Nonetheless, we numerically apply the method of time-reversal symmetry to theoretically maximize $\eta_{\rm sr}^{\rm opt}$ for a given optical depth $\tilde{d}_0$. We start by storing an initial signal field $\mathcal{E}^{(1)}_{s,\rm in}(z,t)$ and retrieving to $\mathcal{E}^{(1)}_{s,\rm out}(z,t)$ in step $i = 1$. We then apply the time-reversed version of the output $\mathcal{E}^{(1)}_{s,\rm out}(z,t)$ in step $i = 1$ into the input signal field $\mathcal{E}^{(2)}_{s,\rm in}(z,t) = \mathcal{E}^{(1)}_{s,\rm out}(-z,t)$ in step $i = 2$. By iterating this process $i \to n$ until $\mathcal{E}^{(n)}_{s,\rm in}(z,t) = \mathcal{E}^{(n)}_{s,\rm in}(-z,t)$, we optimize the storage and retrieval efficiency $\eta_{\rm sr}^{\rm opt}$. Fig. 6.9 shows such a

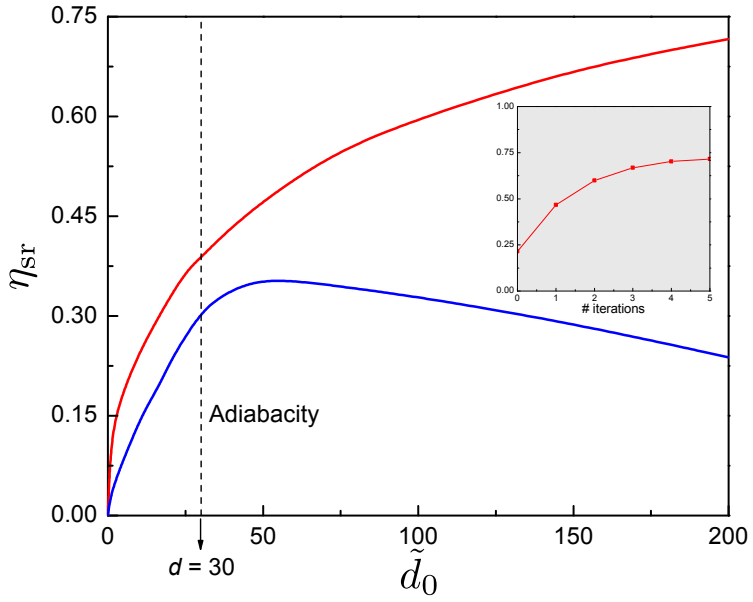

Figure 6.10: **Time-reversal optimization of EIT transfer efficiency.** We show the transfer efficiency $\eta_{\rm sr}$ as a function of optical depth $\tilde{d}_0$. We also compare the result of the optimal $\eta_{\rm sr}^{\rm opt}$ (red line) to $\eta_{\rm sr}$ (blue line) given for our experimental parameters in Fig. 6.8.

numerical process for optical depth $\tilde{d}_0 = 17$ (with same parameters $\{c_1, c_2, \Omega_c\}$ used in section 6.10.2.1) starting from various initial conditions $\mathcal{E}_{s,\rm in}^{(1)}(z,t)$, where we converge to the same maximum EIT efficiency $\eta_{\rm sr}^{\rm opt} \simeq 30\ \%$ after $2-3$ iterations.

In addition, this numerical optimization scheme allows us to benchmark the maximum transfer efficiency $\tilde{\lambda} \simeq \eta_{\rm sr}^{\rm opt}$ of entanglement as a function $\tilde{d}_0$. In Fig. 6.10, we apply the time-reversal optimization as a function of optical depth $\tilde{d}_0$, shown as red line. We demonstrate that $\eta_{\rm sr}^{\rm opt}$ (red line) can be further improved relative to the EIT efficiency $\eta_{\rm sr}$ of our experiment parameters (blue line) (see also Fig. 6.8) beyond $\tilde{d}_0 \gtrsim 50$. In particular, unlike Fig. 6.8, we find a monotonic improvement in the transfer efficiency $\eta_{\rm sr}$ as a function of optical depth $\tilde{d}_0$. For reference, we indicate the boundary at which the adiabatic condition $\tilde{d}_0 \gamma_{ge} \delta t_c \gg 1$ is met[87].

Chapter 7

Characterization of entanglement for multiple optical modes via quantum uncertainty relations

This chapter is largely based on ref.[38]. Reference[38] refers to the then current literature in 2009 at the time of publication.

7.1 Introduction

Detecting and classifying entanglement is an important challenge in the field of quantum information science (chapter 1). One problem is of a theoretical nature, to decide whether a given density matrix $\hat{\rho}$ of multiple quantum systems is entangled or separable. Even for bipartite systems, this is a hard problem for which no efficient general solution is known for higher-dimensional Hilbert spaces, although a simple test based on the negativity of the partial transpose of the density matrix leads to a sufficient criterion for entanglement[246,247]. If $\hat{\rho}$ is entangled, the next issue is how to classify the type of entanglement. For more than two subsystems, the full classification of all entanglement classes is as yet an unsolved problem (e.g., refs.[209,210,248,249]).

In an experiment, the practical task of detecting entanglement is even harder. If one would perform a full tomographic measurement, then in the limit of infinitely many data one would end up with an arbitrarily accurate estimate of a density matrix $\hat{\rho}$, and thus reduce the experimental problem to the theoretical problem mentioned above. In all other cases, one needs different tests that make use of less than full knowledge of the density matrix. The main practical disadvantage of full tomography is the rapidly growing number (with the number of quantum systems and with the dimension of the Hilbert spaces involved) of measurements needed to find all elements of a density matrix. The other challenge is obtaining a physical density matrix from a *finite* set of measured data[250,251].

Thus, there is an ever-growing demand for simpler experimental tests revealing entanglement. Fortunately, for bipartite systems there exists a handful of different experimental techniques for entanglement

detection[40,110]. In this chapter, we will focus on a particular type of multipartite entangled states (namely, W states[209]) that can be produced in systems with variable numbers of excitations. We think in particular of experiments with atomic ensembles (e.g., refs.[27,30,73,93], chapters 3–6) based on the *DLCZ* protocol[4] in which information can be stored in the number of atomic excitations of each ensemble (chapter 9), as well as of experiments on photonic systems (e.g., refs.[229,252–255]), where the number of photons in a given mode can be used as a quantum variable (chapter 8). In the following, we will use the words "excitation" and "photon" interchangeably.

7.2 Verifying multipartite mode-entangled W states

We define the state $|W\rangle$ as a mode-entangled analogue of standard N-partite W states of qubits. It is a pure state where a single excitation is shared symmetrically among N modes[a]

$$|W\rangle = \frac{1}{\sqrt{N}} \sum_{i=1}^{N} |0, \cdots, 0_{i-1}, 1_i, 0_{i+1}, \cdots, 0\rangle, \tag{7.1}$$

where $|0\rangle$ denotes a state of a mode with no excitations and $|1\rangle$ is a state with a single excitation. The subscripts $i \in \{1 \ldots N\}$ refer to modes that are in *spatially distinct locations*, so that the concepts of "local operations" and hence entanglement are unambiguously defined[256–258].

In this chapter, we solve the problem of detecting the entanglement of a W state (and its noisy cousins) in two steps. In section 7.3, we will focus on detecting and classifying entanglement within the subspace of a fixed *total* number of excitations (in all modes together), namely one. In section 7.4, we complete the analysis by including the remaining parts of the Hilbert space, the subspace with no excitations and the subspace with more than a single excitation in total. Including both subspaces is crucial in the analysis. Earlier detection schemes[259,260] for W states in the context of photons were incomplete due to the neglect of states with multiple photons. Moreover, I will discuss how to include imperfections such as losses, most relevant for the actual implementation of our method (refs.[33,35], chapters 8, 9).

7.3 Genuine N-mode one-photon entanglement

N parties can be entangled in many different ways. In some papers, "genuine" N-party entangled states include states that are mixtures of M-party entangled states with $M < N$, as long as such mixtures are not biseparable along any particular splitting of the N parties into two groups (for instance, ref.[261]). Here, however, we will classify such mixtures as M-party entangled states, and the name "genuine N-party entanglement" in our case is reserved for states that can only be written as a mixture of pure states that all possess N-party entanglement. Thus, our criterion for genuine N-party entanglement is more severe.

[a]Following convention, we set all phase factors equal to unity; our entanglement detection method, however, will not make any assumption about the phase factors of the state actually generated in one's experiment, see Eq. 7.14.

Recently it has been suggested that uncertainty relations can be used as an entanglement criterion for finite-dimensional systems (refs.[57,121], see also ref.[262] for an experimental implementation using local observables on two qubits). The uncertainty principle sets up a fundamental limit on how accurately observables of a quantum system can be simultaneously determined. For instance, if $\{\hat{M}_i\}, i = 1 \dots K$ is some set of observables, then the measurement uncertainty in a given state $\hat{\rho}$ is the sum of variances of all observables $\hat{M}_i$ (i.e., $\sum_i \delta M_i(\hat{\rho})^2$). This sum is equal to zero, if and only if the state for which measurements of all $\{\hat{M}_i\}$ are performed on is a simultaneous eigenstate of all $\{\hat{M}_i\}$. If there is no such state (when the observables are not all mutually commuting), then there is a positive number C such that

$$\sum_{i=1}^{K} \delta M_i(\hat{\rho})^2 \geq C. \tag{7.2}$$

In particular, Hofmann and Takeuchi pointed out in 2003 that the existence of the lower uncertainty bound C can be employed as a separability criterion[121]. Indeed, if for some fixed set of observables an inequality of the form (Eq. 7.2) holds for *all* separable states, then its violation is a signature of entanglement.

The uncertainty bound has another obvious but important property. Namely, one can never decrease the average uncertainty by mixing different states. In other words, for any state $\hat{\rho} = \sum_m p_m \hat{\rho}_m$ and any observable A, the following inequality holds true,

$$\delta A(\hat{\rho})^2 \geq \sum_m p_m \delta A(\hat{\rho}_m)^2. \tag{7.3}$$

The proof is rather straightforward and can be found in ref.[121].

With the uncertainty criterion at hand, we still have some flexibility over the types of observables to choose. In principle, all observables can be divided into two groups — local and nonlocal. Whereas local observables can be measured separately for each and every party and therefore tend to be easier to access in an experiment, they often cannot reliably detect genuine multipartite entanglement. Nonlocal observables, on the other hand, require a simultaneous nonlocal measurement of several parties at a time, which often is experimentally challenging. Here, we show how experimentally accessible nonlocal observables can be constructed to unambiguously detect genuine multipartite entanglement of the W-type.

The basic idea behind the construction of nonlocal observables is to choose them as projectors onto a basis of N-partite entangled states. Simultaneous eigenstates of these projectors are necessarily entangled states, and the variance in the projectors is minimized for N-party entangled states. A sufficiently small variance is then a sufficient criterion for genuine N-party entanglement. In order to illustrate this idea, we will consider a system of four modes ($K = 4$) sharing a single photon[b]. The problem at hand is then to find a set of nonlocal observables which allows to separate all four-mode separable and biseparable states from the genuinely four-mode entangled states such as the W state of Eq. 7.1. We note that the general construction

[b] See chapter 8 for an example of $K = 2$, whereby we studied the correspondence between the conventional entanglement measure (concurrence) and the uncertainty relations.

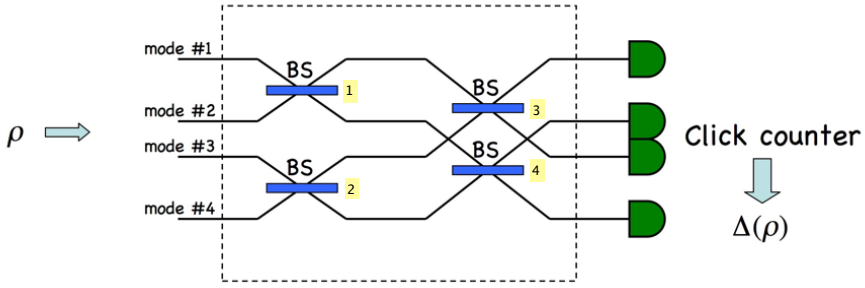

Figure 7.1: **Verification interferometer for measuring sum uncertainty.** Beamsplitter setup to project $\hat{\rho}$ onto the four W states (Eqs. 7.4–7.7): four input modes are converted into four output modes by a set of four 50/50 lossless beamsplitters, numbered 1–4. From the count statistics of (ideal) detectors placed at the four output modes one obtains the quantity $\Delta(\hat{\rho})$ defined in Eq. 7.8. The effects of losses and asymmetries in the beamsplitters, and non-ideal detectors are discussed in section 7.6.1.

for an arbitrary N can be done in a similar fashion. Moreover, the nonlocal observables for single photons we use can be measured just using linear optics (beamsplitters) and non-number resolving photodetectors.

The Hilbert space of a system of four modes sharing exactly one photon is spanned by four basis product vectors $\{|1000\rangle, |0100\rangle, |0010\rangle, |0001\rangle\}$. This basis can always be rotated to a basis constituted by four W-like states,

$$|W_1\rangle = \frac{1}{2}(|1000\rangle + |0100\rangle + |0010\rangle + |0001\rangle), \tag{7.4}$$

$$|W_2\rangle = \frac{1}{2}(|1000\rangle - |0100\rangle - |0010\rangle + |0001\rangle), \tag{7.5}$$

$$|W_3\rangle = \frac{1}{2}(|1000\rangle + |0100\rangle - |0010\rangle - |0001\rangle), \tag{7.6}$$

$$|W_4\rangle = \frac{1}{2}(|1000\rangle - |0100\rangle + |0010\rangle - |0001\rangle). \tag{7.7}$$

The mode transformation from the four product states to these four W-like states can be decomposed in terms of unitary operations that can be implemented with beamsplitters and phase-shifters (see Fig. 7.1).

The next step is to choose four projectors onto the basis Eqs. 7.4–7.7 as nonlocal observables $\hat{M}_i = |W_i\rangle\langle W_i|$, with $i \in \{1, \ldots, 4\}$. Clearly, the only simultaneous eigenstates of all four operators $\hat{M}_i$ are the four states $|W_i\rangle$. The total variance of all $\hat{M}_i$'s vanishes for any one of the four states $|W_i\rangle$. In contrast, for product states, the total variance is bounded from below, since there is no simultaneous product eigenstate of all the $\hat{M}_i$. Therefore, we can write down an uncertainty-based entanglement criterion using nonlocal observables for any state $\hat{\rho}_1$ within the subspace of a single excitation, in terms of the sum of variances of

$\hat{M}_i$,

$$\begin{aligned}\Delta(\hat{\rho}_1) &= \sum_{i=1}^{4} \mathrm{Tr}(\hat{\rho}_1 [|W_i\rangle\langle W_i|]^2) - [\mathrm{Tr}(\hat{\rho}_1 |W_i\rangle\langle W_i)]^2 \\ &= \sum_{i=1}^{4} \left[\langle W_i|\hat{\rho}_1|W_i\rangle - \langle W_i|\hat{\rho}_1|W_i\rangle^2\right] \\ &= 1 - \sum_{i=1}^{4} \langle W_i|\hat{\rho}_1|W_i\rangle^2, \end{aligned} \tag{7.8}$$

where the subscript 1 is there to remind us the state $\hat{\rho}_1$ contains exactly 1 excitation.

To find the lower bound on Δ for unentangled states, it is sufficient to consider pure states, thanks to Eq. 7.3. For a pure state $\hat{\rho}_1 = |\alpha\rangle\langle\alpha|$, we have

$$\Delta(\hat{\rho}_1) = 1 - \sum_{i=1}^{4} |\langle W_i|\alpha\rangle|^4. \tag{7.9}$$

The next step is to find the minimum of $\Delta(\hat{\rho}_1)$ by maximizing $\sum_i |\langle W_i|\alpha\rangle|^4$ over all separable states $|\alpha\rangle$ containing a single excitation. There are three types of pure four-mode states that are *not* four-mode entangled [c].

1. Fully separable pure states, which are products of four single-mode states. There are only four such states within the subspace of interest, namely $|1000\rangle$, $|0100\rangle$, $\ldots$, $|0001\rangle$.

2. Biseparable states with at most two-mode entanglement. Here, the two modes must be in the vacuum state, and the most general pure state in this class is of the form $|00\rangle \otimes (a|01\rangle + b|10\rangle)$, or similar states by permuting the different modes.

3. Biseparable states with at most three-mode entanglement. Here, at least one mode is in the vacuum state, and the most general pure state, up to permutations of the modes, is of the form $|0\rangle \otimes (a|001\rangle + b|010\rangle + c|100\rangle)$.

Given the most general pure state within each class, it is straightforward to calculate the 3 corresponding minimum values of $\Delta(\hat{\rho}_1)$, and the results are depicted in Fig. 7.2. For example, for any pure fully separable state $|\alpha\rangle$, the overlap $|\langle W_i|\alpha\rangle|^2 = 1/4$ for any i, and so $\Delta(\hat{\rho}_1) = 3/4$. For general mixtures of fully separable states, this number gives the best possible lower bound on the variance. We note that the numerical results from the next section confirms the results of Fig. 7.2.

As an example, consider the Werner-like mixture of a W state [263] and the maximally mixed state of four

[c] Note that there is only one class of four-mode entangled states with one excitation: i.e., states of the W-type $a|0001\rangle + b|0010\rangle + c|0100\rangle + d|1000\rangle$. Our method can be used to detect *any* four-mode entangled state within the subspace of a single excitation, by modifying the projectors appropriately.

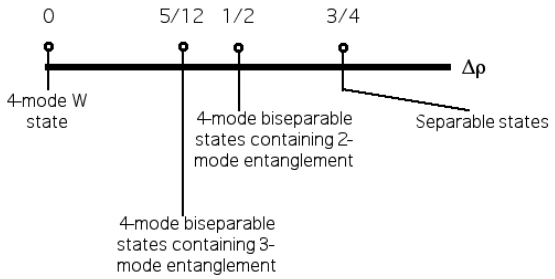

Figure 7.2: **Minimum variances Δ for various types of four-mode pure states containing exactly one excitation (photon).** We find minimum variances $\Delta_b^{(4)} = 0$ for four-mode entangled states, $\Delta_b^{(3)} = 5/12$ for three-mode entangled states, $\Delta_b^{(2)} = 1/2$ for two-mode entangled states, and $\Delta_b^{(1)} = 3/4$ for fully separable states.

modes with a single excitation, $\hat{\rho}_{\rm mm} = \frac{1}{4}(|0001\rangle\langle 0001| + |0010\rangle\langle 0010| + |0100\rangle\langle 0100| + |1000\rangle\langle 1000|)$,

$$\hat{\rho}_1(p) = p|W_1\rangle\langle W_1| + (1-p)\hat{\rho}_{\rm mm}. \tag{7.10}$$

Using the above criterion for $\Delta(\hat{\rho}_1(p)) = 3/4 - 3p^2/4$, we find that for $p > 2/3$ we can detect genuine four-mode entanglement, and for $p > \sqrt{3}/3 \simeq 0.577$ we detect at least three-mode entanglement. Moreover, for any $p < 1$, the state $\hat{\rho}_1(p)$ is entangled, even if just two-mode entangled.

If the number of modes N is arbitrary, then the minimum uncertainty $\Delta(\hat{\rho}_1)$ for biseparable $(N-1)$-mode entangled states can be shown, after some algebra, to be given by $(2N-3)/N(N-1)$. In the limit of large N, this bound rapidly approaches zero, hence making it practically impossible to distinguish in this way genuine N-partite entanglement from mere $(N-1)$-partite entanglement.

Finally, we note that similar uncertainty-based entanglement criteria can in principle be applied to all types of N-mode states with fixed total number of excitations. If the total photon number is larger than 1, however, the unitary transformation from the product states to a basis consisting of entangled states can in general not be performed with linear optical operations only. Therefore, measurements in such a basis would no longer be necessarily deterministic in that case.

7.4 Detecting W states in an experiment

Due to experimental imperfections, an actual state, produced in a laboratory, is never a pure state with a fixed number of excitations, such as, say, Eq. 7.4. In experiments with atomic ensembles (chapter 9), a state $\hat{\rho}_W$ is routinely generated whose single-excitation part $\hat{\rho}_1$ has a large overlap with a W state, but contains a significant contribution from the vacuum $\hat{\rho}_0$ and from states with more than one excitation $\hat{\rho}_{\geq 2}$. As a conservative estimate, we can ignore coherent superpositions of states with different numbers of excitations[d],

[d] One can get rid of such coherences by local operations [27].

and hence we can write down $\hat{\rho}_W$ in a generic form

$$\hat{\rho}_W = p\hat{\rho}_0 + q\hat{\rho}_1 + (1-p-q)\hat{\rho}_{\geq 2}, \tag{7.11}$$

where the subscripts $\{0, 1, \geq 2\}$ indicate the numbers of excitations. Typically, the magnitude of $1-p-q$ is of the order of 1% or even less. The main source of contamination to the desired single-excitation part is the vacuum. Moreover, $\hat{\rho}_1$ is not necessarily a pure state, and is not necessarily a state of N *single* modes either.

Even if the uncertainty measure from the preceding section would identify the presence of four-mode entanglement in the state $\hat{\rho}_1$, this does not guarantee that $\hat{\rho}_W$ itself carries any entanglement. The standard counterexample[264] is a four-mode state of the (unnormalized) form

$$|+\rangle \propto (|0\rangle + \epsilon|1\rangle)^{\otimes 4}, \tag{7.12}$$

for which the one-excitation part $\hat{\rho}_1$ is genuinely four-party entangled, although the state $\hat{\rho}_W$ itself is fully separable[e]. Therefore, in order to justify the presence of entanglement in an experiment, it is not sufficient to measure only the variance $\Delta(\hat{\rho}_1)$ of the single-excitation part of the density matrix, but it is crucial to measure the numbers $\{p, q\}$. Once p, q, and $\Delta(\hat{\rho}_1)$ are determined, one can check if there exists a completely separable or biseparable state $\hat{\rho}_{\text{test}}$ with the same values of p, q, and $\Delta(\hat{\rho}_1)$. If no such state exists, then one can conclude unambiguously that $\hat{\rho}_W$ is entangled.

More precisely, for fixed values of p and q, we would like to find the minimum possible value for the variance, Δ_{min}, consistent with the various sorts of biseparable or fully separable states. In the following, we will plot the results for the case where $q = 0.1$, which is the relevant case for the experiment (ref.[35], chapter 8). We will find Δ_{min} in that case as a function of $r := 1-p-q$.

Before discussing in turn the various classes of separable and biseparable states, we make several remarks: We note that Δ_{min} within each class cannot increase with decreasing q. The reason is that given any state $\hat{\rho}$, we can always mix in the vacuum $\hat{\rho}_0$ without changing the variance Δ, and without increasing the entanglement. But this mixing operation clearly does decrease q. Hence, Δ_{min} cannot increase with decreasing q.

Similarly, we could mix in a fully separable state containing more than a single photon in some given mode, e.g., a tensor product of the vacuum and one mode with 2 or more photons. This again does not affect Δ, and does not increase entanglement, but does decrease q. For this reason, in our attempts to find the minimum variance, we do not need to consider states with more than a single photon in any given mode, as those states will have a larger value of Δ than the minimum possible for given q.

Moreover, we could take a state of N single modes and convert it into a state of multiple modes in N locations, by locally applying a random unitary operation. This local operation does not move a state up the entanglement hierarchy and does not affect any of the quantities Δ, q, and r. Thus, excluding fully separable

[e]To resolve this conundrum, we note that postselecting one photon in total constitutes a nonlocal filter. Thus, projecting $\hat{\rho}_1$ out of $\hat{\rho}_W$ can increase the amount of entanglement[264] and lead to a spurious detection of entanglement when there was none.

states and biseparable states of N single modes is sufficient for detecting entanglement.

Because $\hat{\rho}_1$ is subnormalized to q, we have, instead of the inequality (7.3), the inequality

$$q\Delta(\hat{\rho}_1) \geq \sum_{m=1} p_m q_m \Delta(\hat{\rho}_{m,1}), \tag{7.13}$$

where $q = \sum_m p_m q_m$ and $\hat{\rho} = \sum_m p_m \hat{\rho}_m$. The subscript 1 means the single-excitation component $\hat{\rho}_1$ ($\hat{\rho}_{m,1}$) of $\hat{\rho}$ ($\hat{\rho}_m$).

Finally, instead of projecting $\hat{\rho}_W$ onto the four states (Eqs. 7.4–7.7), in an experiment one would really project $\hat{\rho}_W$ onto four states of the form,

$$\begin{aligned}
|W_1'\rangle &= \frac{1}{2}(|1000\rangle + e^{i\phi_1}|0100\rangle + e^{i\phi_2}|0010\rangle + e^{i\phi_3}|0001\rangle), \\
|W_2'\rangle &= \frac{1}{2}(|1000\rangle - e^{i\phi_1}|0100\rangle - e^{i\phi_2}|0010\rangle + e^{i\phi_3}|0001\rangle), \\
|W_3'\rangle &= \frac{1}{2}(|1000\rangle + e^{i\phi_1}|0100\rangle - e^{i\phi_2}|0010\rangle - e^{i\phi_3}|0001\rangle), \\
|W_4'\rangle &= \frac{1}{2}(|1000\rangle - e^{i\phi_1}|0100\rangle + e^{i\phi_2}|0010\rangle - e^{i\phi_3}|0001\rangle),
\end{aligned} \tag{7.14}$$

and vary over all three phases ϕ_k, $k \in \{1, 2, 3\}$ (by inserting phase-shifters in the appropriate modes) to find the minimum variance Δ_{min}, thus optimizing the entanglement test. Our method is otherwise independent of which values of ϕ_k attain that minimum.

7.4.1 Fully separable four-mode states

It is relatively easy to account for all separable and biseparable states in the case of four modes. Let us first calculate p, q, $\Delta(\hat{\rho}_1)$ for fully separable states. We first consider pure states $|\psi_s\rangle$ of the form

$$|\psi_s\rangle = \bigotimes_{i=1}^{4} \frac{(|0\rangle + \epsilon_i|1\rangle)}{\sqrt{1 + |\epsilon_i|^2}}, \tag{7.15}$$

for complex parameters ϵ_i. As argued above, we do not have to consider states with more than a single excitation in any one mode. For the pure state $|\psi_s\rangle$, a corresponding density matrix can be constructed from $\hat{\rho}_s = |\psi_s\rangle\langle\psi_s|$:

$$\hat{\rho}_s = p\hat{\rho}_{s,0} + q\hat{\rho}_{s,1} + r\hat{\rho}_{s,\geq 2}, \tag{7.16}$$

where

$$p = \prod_{i=1}^{4} \frac{1}{1 + |\epsilon_i|^2}$$

and

$$q = p \sum_{i=1}^{4} |\epsilon_i|^2.$$

We can visualize a set of pure completely separable states, and in particular its border, by plotting values of $\Delta(\hat{\rho}_{s,1})$ versus r for a fixed value of the single-excitation probability q, by randomly varying over all values of ϵ_i consistent with that value of q. By symmetry, it is clear the minimum variance will be obtained for real parameters. The result is shown in Fig. 7.3, and we can clearly identify the region of full separability, the lightly shaded area (colored in yellow). The minimum value of $\Delta(\hat{\rho}_{s,1})$ at $r = 0$ is $3/4$ in agreement with our previous discussion (see Fig. 7.2). Even though $\Delta(\hat{\rho}_{s,1})$ approaches zero for sufficiently large values of r [f], the density matrix $\hat{\rho}_s$ remains *fully separable* [g].

Moreover, we manage to find the pure states which reside on the pure-state boundary, indicated as black dots in Fig. 7.3. The boundary can be parameterized by two parameters, either q and r, or, more simply, by ϵ and $\tilde{\epsilon}$. Namely, the extremum values of the variance for pure fully separable states are attained for states of the form

$$|\psi_{\epsilon,\tilde{\epsilon}}\rangle \propto (|0\rangle + \epsilon|1\rangle)(|0\rangle + \tilde{\epsilon}|1\rangle)^{\otimes 3}. \tag{7.17}$$

One may notice the lower border for pure states in Fig. 7.3 is not convex as plotted. This indicates that points corresponding to certain mixed states may fall below the pure-state boundary. Thus, we have also tested randomly chosen mixtures of random pure states, as well as mixtures of states on that boundary. And some mixed states (plotted in green) indeed have a smaller variance. Thus, the minimum variance is attained by mixed states in this case, and the correct lower bound is indicated in red. This lower bound coincides with the convex hull of the graph for pure states (i.e., $\hat{\rho}_{s,\text{convex}} = a_1|\alpha_1\rangle\langle\alpha_1| + a_2|\alpha_2\rangle\langle\alpha_2|$, where $|\alpha_{1,2}\rangle \in \{|\psi_{\epsilon,\tilde{\epsilon}}\rangle\}$ are the minimum uncertainty states in the pure-state boundary).

7.4.2 Biseparable states with at most two-mode entanglement

The next class of states to consider is biseparable states: i.e., states that can be described by a density matrix $\hat{\rho}_{\text{bis}} = \sum_{i=1}^{M} \hat{\rho}_i^A \otimes \hat{\rho}_i^B$. The division into subsystems A and B in the case of four modes has two distinct possibilities—either system A represents *one* of the modes and system B consists of the remaining *three* modes (e.g., bipartition $(1|234)$) or both systems A and B represent *two* modes each (e.g., bipartition $12|34$). We will study the latter case first. We represent a pure biseparable state with at most two-mode entanglement by

$$|\psi\rangle_{AB} = |\psi\rangle_A \otimes |\psi\rangle_B, \tag{7.18}$$

[f] See also the last subsection of this section.
[g] See the example mentioned above.

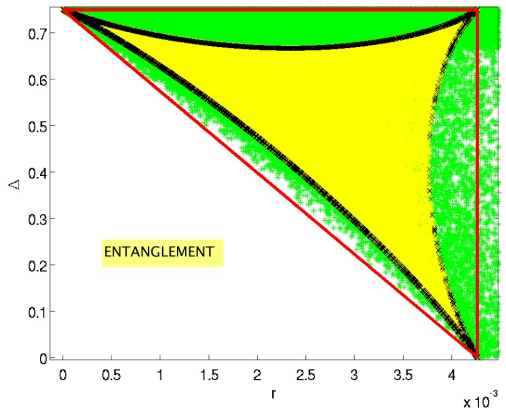

Figure 7.3: **Scatter plot (in yellow) of the variance $\Delta(\hat{\rho}_{s,1})$ of the single-photon part for randomly chosen, pure, fully separable states versus the probability of finding multiple excitations, r for a fixed single-photon probability $q = 0.1$.** The black crosses are data points for a particular subset of pure states, attaining the extremum values of the variance for the set of pure states. Also plotted is the variance for randomly chosen *mixed* states (in green). For this particular value of q those values for the variance fall within the convex hull of the graph for pure states (the red line is the convex hull of the black curve). The region below the lowest red line then corresponds to entangled states (as indicated by the word "ENTANGLEMENT"): but this includes two-mode, three-mode, and four-mode entanglement.

with both two-mode states $|\psi\rangle_k$ for $k \in \{A, B\}$ of the form

$$|\psi\rangle_k \propto |00\rangle + \epsilon_k|01\rangle + \epsilon'_k|10\rangle, \tag{7.19}$$

where we included phase factors into the parameters ϵ_k and ϵ'_k.

For the same reason given in the preceding subsection, we do not have to consider contributions from the terms with more than a single excitation in any one mode. The expression for the variance Δ is symmetric under the interchange of any two modes, and so it is immaterial which two modes constitute system A. We again vary over the complex parameters $\{\epsilon_k, \epsilon'_k\}$ for fixed value of the single-photon probability $q = 0.1$ to find the set of all pure biseparable states with at most two-mode entanglement, as a function of the multiple-excitation probability r. By symmetry, the minimum variance is attained for real coefficients.

The lightly-shaded (yellow) area in Fig. 7.4 then depicts the set containing all biseparable states with at most two-mode entanglement. Indeed, we have checked explicitly that points corresponding to mixed states fall within the shaded region, unlike in the preceding case of fully separable states. The shaded region of Fig. 7.4 includes that of Fig. 7.3, simply because the set of fully separable states is a subset of the set of states with at most two-mode entanglement. The minimum value of Δ at $r = 0$ is $1/2$, confirming the result from Fig. 7.2.

Just as in the preceding subsection, we find the pure states living on the boundary. The boundary is again parameterized by two parameters, ϵ and $\tilde{\epsilon}$. Namely, the minimum variance is attained for biseparable states

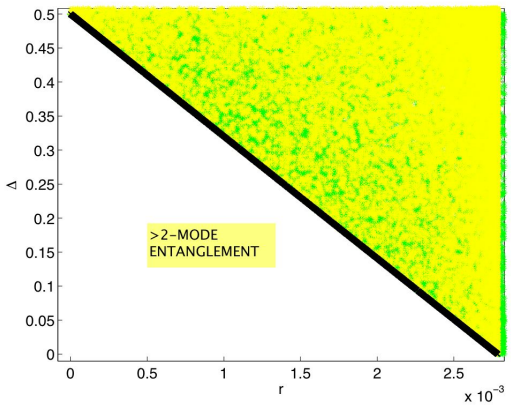

Figure 7.4: **Scatter plots of the variance of the single-photon part for randomly chosen biseparable states with at most two-mode entanglement.** The graph is convex, and points corresponding to mixed states (plotted in green) fall within the yellow region. The region below the black curve corresponds to at least three-mode entanglement.

of the form

$$|\psi_{\epsilon,\tilde{\epsilon}}\rangle_{AB} \propto (|00\rangle + \epsilon|10\rangle + \epsilon|01\rangle)(|00\rangle + \tilde{\epsilon}|10\rangle + \tilde{\epsilon}|01\rangle).$$

In this case, it is straightforward to extract the minimum variance as a function of q and r:

$$\Delta_{\text{min}} = 1/2 - 2r(1-q)/q^2 + 2r^2/q^2, \tag{7.20}$$

which is indeed almost linear in r when $r \ll 1$. Moreover, this boundary is convex. We can rewrite the minimum variance more compactly as

$$\Delta_{\text{min}} = 1/2 - 2rp/q^2. \tag{7.21}$$

7.4.3 Biseparable states with three-mode entanglement

A pure state of the entire four-mode system (with up to two excitations) that has at most three-mode entanglement can be described by the following biseparable vector,

$$|\psi\rangle_{AB} \propto (|0\rangle + \epsilon_1|1\rangle) \otimes (|000\rangle + \epsilon_2|100\rangle + \epsilon_3|010\rangle + \epsilon_4|001\rangle), \tag{7.22}$$

where we have arbitrarily chosen the first mode to be the system A (bipartition $(1|234)$, with single mode $A = 1$ and composite mode $B = \{234\}$). The analysis, however, is symmetric with respect to our choice for the system A. In the second term, we do not have to consider states with more than a single photon in system B. Although the measurement determining whether there are multiple excitations in the three modes comprising system B is not a local filtering operation in the usual sense, it is local with respect to the bipartite

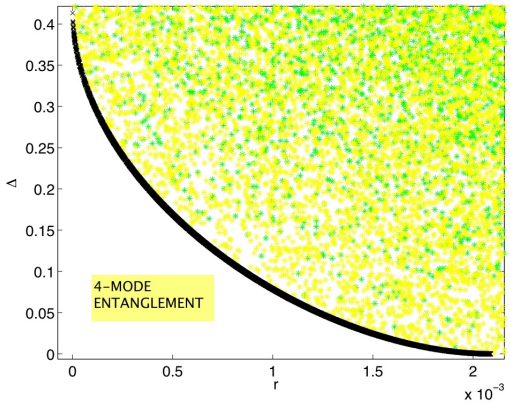

Figure 7.5: **Scatter plots of the variance of the single-photon part for randomly chosen biseparable states with at most three-mode entanglement for $q = 0.1$.** Points corresponding to mixed states fall within the lightly shaded (yellow) region, and are plotted in green. The region below the black curve corresponds to states with genuine four-mode entanglement.

cut $A|B$, which is the relevant cut in this case.

The result for $q = 0.1$ is plotted in Fig. 7.5. Like in the case for fully separable states, we observe the existence of points whereby the values of $\Delta(\hat{\rho}_1)$ are close to zero. Again, we should not misjudge the presence of entanglement in these states, since the states we are operating with are biseparable by construction. The region for r larger than $\approx 2 \times 10^{-3}$, where the minimum variance no longer is a decreasing function of r, contains no physical states with smaller variance.

The lightly-shaded (yellow) region depicts the convex set of biseparable states with at most three-mode entanglement, and includes the set of fully separable states, although (interestingly) not necessarily the set of states with *two* two-mode entangled states (it does for $q = 0.1$). We have explicitly verified that points corresponding to mixed states (plotted in green) fall within the yellow region. The minimum value of Δ at $r = 0$ is perhaps a little hard to discern, but is indeed equal to $5/12$, the value obtained analytically in the preceding section (Fig. 7.2). The lower boundary (plotted in black) corresponds to states of the form

$$|\psi\rangle_{AB} \propto (|0\rangle + \tilde{\epsilon}|1\rangle) \otimes (|000\rangle + \epsilon|100\rangle + \epsilon|010\rangle + \epsilon|001\rangle), \tag{7.23}$$

with real and positive $\epsilon > \tilde{\epsilon}$.

Since the boundary of minimum variance is the lowest for this type of biseparable states, it is the relevant boundary for the purpose of detecting genuine four-mode entanglement. For this reason, we plot these boundaries for several values of q.

For increasing values of q, the minimum possible variance for 3-mode entangled states increases and reaches the limit of $\max(\Delta_{\text{min}}) = 5/12$ for $q \to 1$. Figs. 7.6–7.8 approach this limit for values $q = 0.4$ through $q = 0.7$ to $q = 0.9$.

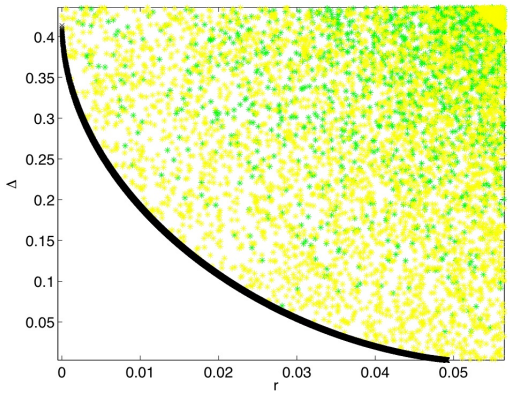

Figure 7.6: **Scatter plots of the variance of the single-photon part for randomly chosen biseparable states with at most three-mode entanglement for** $q = 0.4$**.** Points corresponding to mixed states fall within the lightly shaded (yellow) region, and are plotted in green. The region below the black curve corresponds to states with genuine four-mode entanglement.

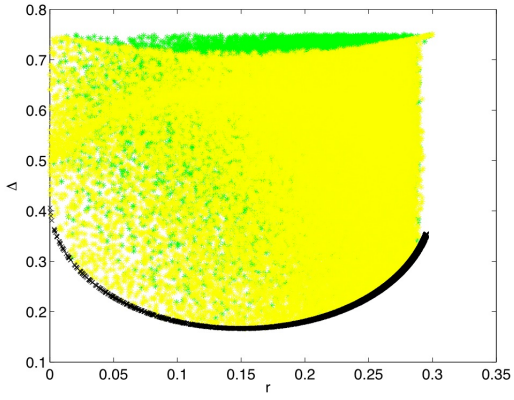

Figure 7.7: **Scatter plots of the variance of the single-photon part for randomly chosen biseparable states with at most three-mode entanglement** $q = 0.7$**.** Points corresponding to mixed states fall within the lightly shaded (yellow) region, and are plotted in green. The region below the black curve corresponds to states with genuine four-mode entanglement.

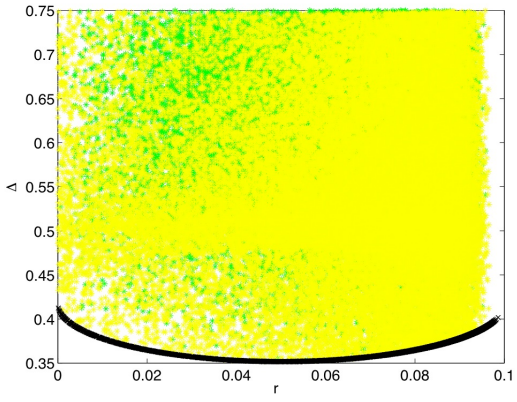

Figure 7.8: **Scatter plots of the variance of the single-photon part for randomly chosen biseparable states with at most three-mode entanglement** $q = 0.9$**.** Points corresponding to mixed states fall within the lightly shaded (yellow) region, and are plotted in green. The region below the black curve corresponds to states with genuine four-mode entanglement.

7.4.4 Full analysis

Based on an exclusion analysis, a practical inseparability criterion can be formulated. In an experiment aimed at detecting a genuinely four-mode entanglement, (i) one measures the diagonal elements r, q, and (ii) the off-diagonal elements for Δ. Then one plots, according to the previous considerations, values of Δ versus r for all separable and biseparable models, feeding in the value of q attained from the experiment. The measured values of p, q, and Δ are represented by a single point in that plot. If that point lies *outside* all three shaded regions of the model plots, the state produced in the experiment must carry genuine four-mode entanglement. Partial conclusions about entanglement can be reached when the point falls outside some and inside other regions.

In particular, if the measurement point lies outside the shaded region of Fig. 7.3, but inside the shaded regions of Figs. 7.4 and 7.5, one can only conclude that one has an entangled state, but it could be merely two-mode entangled. If the point falls outside the shaded regions of both Figs. 7.3 and 7.4, but inside the shaded region of Fig. 7.5, one has at least three-mode entanglement. Of course, if the point falls inside the shaded region of Fig. 7.3, no firm conclusion can be reached about entanglement, as there is a fully separable state consistent with one's values for p, q, Δ. In addition, for the case of two modes, there is an analytical analogue of the current scheme of uncertainty relations by way of p, q, Δ and bipartite concurrence (chapter 8).

We plot the three minimum variance boundaries for different small values of q as a function of a scaled variable $y_c := 8rp/3q^2$ (see the next subsection for an explanation for this choice of variable) in Fig. 7.9. One sees the boundaries depend only weakly on that parameter.

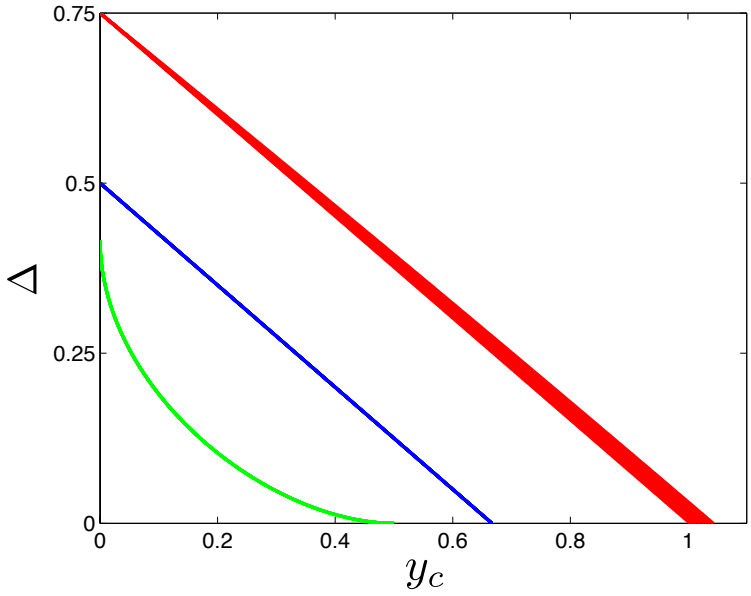

Figure 7.9: **Boundaries for the minimum variance for the three types of biseparable states as functions of $y_c := 8rp/3q^2$ for 10 values of $q = 0.02, 0.04, \ldots 0.2$.** The reason for choosing this particular variable y_c is given in section 7.5. The lowest-lying (green) curves correspond to 3-party entangled states, the highest-lying (red) curves correspond to fully separable states, the middle (blue) curves correspond to biseparable states with 2-mode entanglement. The variance depends only weakly on q for the red curves, and is independent of q for the green and blue curves.

7.5 Some necessary conditions for entanglement

Let us finally consider the conditions on entanglement in the simple situation where the variance $\Delta(\hat{\rho}_1)$ vanishes and where q is not too large. We consider the same three classes of unentangled states as before.

1. Fully separable states with $\Delta(\hat{\rho}_1) = 0$ must be of the form $(|0\rangle + \epsilon|1\rangle)^{\otimes 4}$. For such states, the point at which the variance is zero is characterized by

$$\frac{8}{3}\frac{rp}{q^2} = 1 + \frac{q}{6p} + \frac{q^2}{96p}. \tag{7.24}$$

   For small values of q, we can give the approximate relation, which is valid for fully separable states,

$$y_c \geq 1,$$

   with $y_c = 8rp/3q^2$ being the quantity appearing on the left-hand side of Eq. 7.24. A necessary (although not sufficient) condition for any type of entanglement is then simply

$$y_c < 1.$$

   For Fig. 7.3, in which we took $q = 0.1$, this places a strict upper limit on r of $r < 4.125 \times 10^{-3}$ for

entanglement to be detectable through Δ.

2. Biseparable states with $\Delta(\hat{\rho}_1) = 0$ and at most two-mode entanglement must be of the form $(|00\rangle + \epsilon|01\rangle + \epsilon|10\rangle)^{\otimes 2}$. For such states, the boundary of zero variance is at $y_c = 2/3$, and hence all biseparable states satisfy

$$y_c \geq \frac{2}{3}.$$

For Fig. 7.4, in which $q = 0.1$, this places a strict upper limit on r of $r < 2.75 \times 10^{-3}$ for entanglement involving at least three modes to be detectable through Δ.

3. Biseparable states with $\Delta(\hat{\rho}_1) = 0$ and at most three-mode entanglement must be of the form $(|0\rangle + \epsilon|1\rangle) \otimes (|000\rangle + \epsilon|001\rangle + \epsilon|010\rangle + \epsilon|100\rangle$. For such states, we similarly derive

$$y_c \geq \frac{1}{2}.$$

For Fig. 7.5, in which $q = 0.1$, this places an upper limit on r of $r < 2.06 \times 10^{-3}$ for entanglement to be detectable through Δ.

In order to demonstrate genuine four-mode entanglement one must violate all of these conditions. That is, one must violate the strongest of these conditions, and hence one must have

$$y_c < \frac{1}{2}. \tag{7.25}$$

This condition for four-mode entanglement is necessary but not sufficient for nonzero values of $\Delta(\hat{\rho}_1)$. The form of the conditions also indicates why the scaled variable y_c, used in Fig. 7.9, is a useful quantity for small q for fully separable states, and for biseparable states irrespective of the value of q.

7.6 Experimental verification of mode entanglement

7.6.1 Losses and asymmetries

So far we have assumed that the variance measurement device is ideal: beamsplitters (see Fig. 7.1) were assumed lossless and perfectly balanced, and detectors were perfect. In this subsection, we relax those conditions and describe the modifications necessary to include these imperfections. First, we consider the effect of imbalanced beamsplitters.

7.6.1.1 Imbalanced beamsplitters

Suppose, then, we have the same setup as depicted in Fig. 7.1, but with the four beamsplitters having reflection and transmission probabilities $|t_k|^2$ and $|r_k|^2$ not necessarily equal to $1/2$. Consider one output mode,

say the top one (mode $\#1$). There is one path a photon can take from the input mode $\#1$ to reach the top output mode: it has to reflect off of beamsplitter $\#1$ and it has to reflect off of beamsplitter $\#3$. The amplitude for that path is then $r_1 r_3$, in terms of the reflection amplitudes of beamsplitters $\#1$ and $\#3$. Here we ignore phase factors due to propagation (they can be trivially inserted in the end). Similarly, a photon from input mode $\#2$ can reach the top output mode along just one path, with amplitude $t_1 r_3$. Writing down the amplitudes for photons starting in input modes $\#3$ and $\#4$ shows that a photo-detection at the top output mode projects onto the (input) state

$$|\tilde{W}_1\rangle = r_1 r_3 |1000\rangle + t_1 r_3 |0100\rangle + r_2 t_3 |0010\rangle + t_2 t_3 |0001\rangle. \tag{7.26}$$

This is a properly normalized state, even if the beamsplitters are not balanced. The normalization follows from the relation $|r_k|^2 + |t_k|^2 = 1$ for lossless beamsplitters.

We can similarly write down the states onto which one projects if detecting a photon in one of the remaining output modes:

$$|\tilde{W}_2\rangle = t_1 r_4 |1000\rangle + r_1 r_4 |0100\rangle + t_2 t_4 |0010\rangle + r_2 t_4 |0001\rangle, \tag{7.27}$$

$$|\tilde{W}_3\rangle = r_1 t_3 |1000\rangle + t_1 t_3 |0100\rangle + r_2 r_3 |0010\rangle + t_2 r_3 |0001\rangle, \tag{7.28}$$

$$|\tilde{W}_4\rangle = t_1 t_4 |1000\rangle + r_1 t_4 |0100\rangle + t_2 r_4 |0010\rangle + r_2 r_4 |0001\rangle. \tag{7.29}$$

These states, too, are normalized. Moreover, the four states are all orthogonal, as follows from the unitarity relation $t_k^* r_k + t_k r_k^* = 0$. One can still calculate the variance of photodetector counts (albeit with reduced sensitivity to detect $|W\rangle$), using the modified projectors onto the $\tilde{W}$ states, but that variance will not give as much information as in the balanced case about four-mode entanglement. For example, consider the extreme case of a mirror replacing beamsplitter $\#4$: that is, assume now that $r_4 = 1$ and $t_4 = 0$. Then states $|\tilde{W}_2\rangle$ and $|\tilde{W}_4\rangle$ are no longer four-mode entangled states, but only two-mode entangled states. Thus, certain two-mode entangled states would give rise to a zero variance in this extreme case.

This implies that even if one's experiment cannot use perfect $50/50$ beamsplitters, one should at least try to make them as balanced as possible. In such cases, one needs in general a lower variance Δ than in the ideal balanced case to conclude one has four-mode entanglement due to the reduced sensitivity of the projectors.

7.6.1.2 Losses

Now let us consider losses. We can model linear losses (both propagation losses, and inefficiencies of the photodetectors) by imagining lossless paths but with additional beamsplitters reflecting away some portion of the light in the lossy paths. The output of those additional beamsplitters does not lead to the output detectors, but to other (unmonitored) output modes which are traced out. The overall transformation from input to output is still unitary, which implies there must also be additional input modes (just as many as there

are unmonitored output modes). A photodetection in one of the desired output modes projects onto a set of orthonormal states on the larger Hilbert space of all input modes. If we write down the projections of those states onto the four input modes of interest, we will end up with sub-normalized states. For example, considering for the moment (see the next subsection where we take into account multiple excitations) only states with exactly one photon, a detection in the top output mode projects $\hat{\rho}_W$ onto the state

$$|\tilde{W}_1'\rangle = T_{11}r_1r_3|1000\rangle + T_{21}t_1r_3|0100\rangle + T_{31}r_2t_3|0010\rangle + T_{41}t_2t_3|0001\rangle, \tag{7.30}$$

where the transmission amplitude T_{k1} for $k \in \{1,2,3,4\}$ is the product of all loss amplitudes encountered by a photon propagating from input k to the top output detector (including the inefficiency of the detector).

The variance we are interested in is conditioned on detecting (at least) one photon in the desired output modes. Once we detect a photon in the top mode, we renormalize the state $|\tilde{W}_1'\rangle$ and project onto:

$$|\tilde{W}_1''\rangle = \frac{|\tilde{W}_1'\rangle}{\sqrt{\langle\tilde{W}_1'|\tilde{W}_1'\rangle}}. \tag{7.31}$$

The four states onto which we project conditionally, $|\tilde{W}_k''\rangle$ for $k = 1\ldots4$ are, therefore, properly normalized, but they are not orthogonal, unless all losses are balanced (i.e., if $T_{lk} =$ const. for all $l, k \in \{1\ldots4\}$).

Again, we can still use a variance based on the modified nonorthogonal projectors, but that variance will give less information than in the ideal lossless balanced case. For instance, if all photodetectors but one are completely inefficient and never detect any photon, the variance would be zero for any input state. Thus, in an actual experiment, one would have to make the losses as balanced as possible in order for the variance to contain as much information about four-mode entanglement as possible. Of course, one would also like to limit the size of the losses for various different reasons.

With the new projectors onto the nonorthogonal states $|\tilde{W}_k''\rangle$ in hand, we can perform the same calculations as we did in the ideal case: find the minimum variance consistent with unentangled input states, input states with two-mode entanglement, and input states with three-mode entanglement, respectively, for fixed values of q and r. We display three illustrative examples (for $q = 0.1$): (i) in Fig. 7.10, we assume no losses but unbalanced beamsplitters, (ii) in Fig. 7.11, we assume losses, but balanced beamsplitters, and (iii) in Fig. 7.12, we show the net effects of both losses and imbalances. All figures show the tendency of the minimum variance to decrease compared to the ideal lossless and balanced case, thereby resulting in reduced sensitivity.

7.6.2 Measured variance vs $\Delta(\hat{\rho}_1)$

In the presence of losses, the measured variance, Δ_m, is not just due to the single-excitation part, but from the multi-excitation part of the input state as well. Thus, the measured variance has to be corrected (upwards in fact) in order to find an estimate for the variance $\Delta(\hat{\rho}_1)$ due to the single-excitation part, because that is the quantity we used above to detect entanglement.

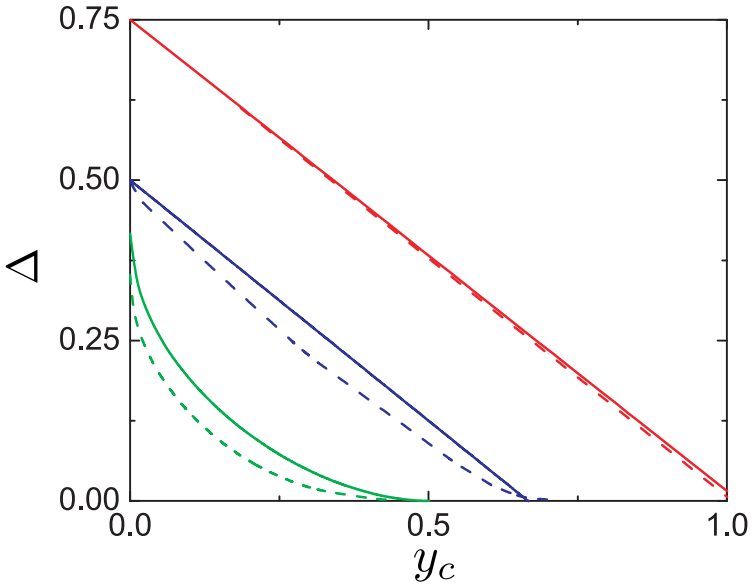

Figure 7.10: **Minimum variance for imbalanced beamsplitters.** We find the minimum variance curves for the case where all beamsplitter ratios are $55/45$ (dashed lines) rather than $50/50$ (solid lines).

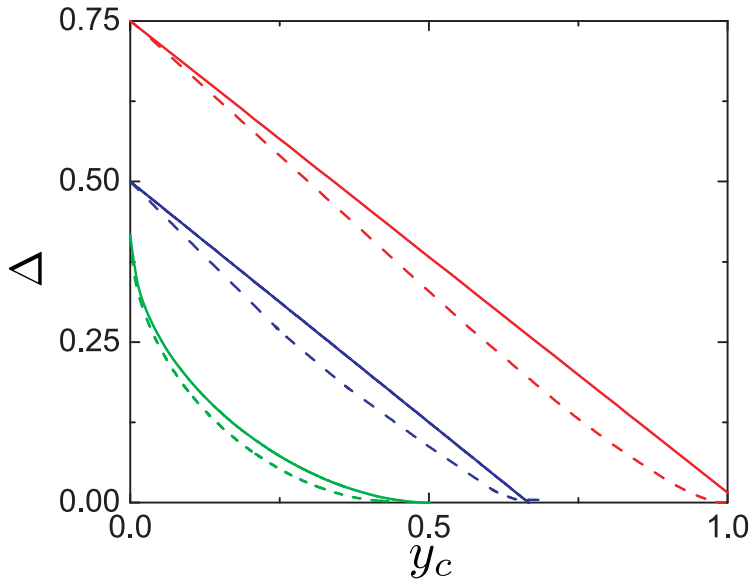

Figure 7.11: **Minimum variance for imbalanced losses.** We show the minimum variance curves for the case where there is one lossy path with transmission probability of 60% (a typical parameter) (dashed lines), compared to the ideal lossless case (solid lines).

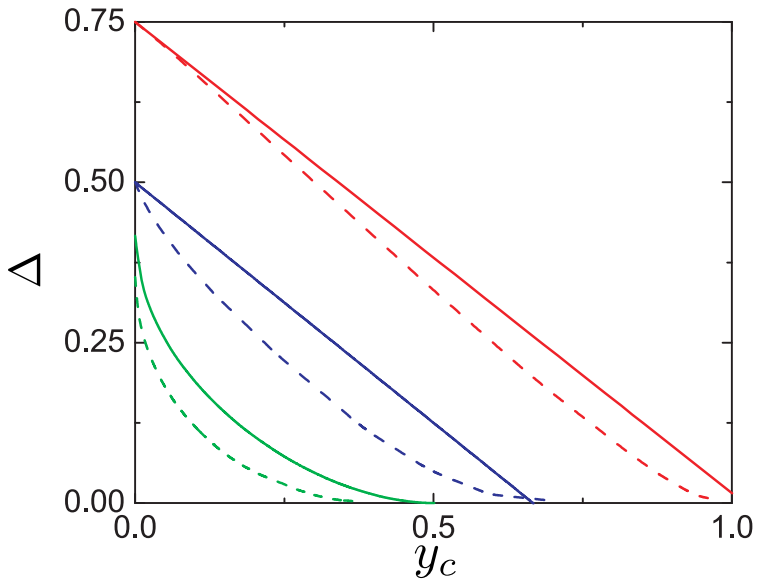

Figure 7.12: **Minimum variance for imbalanced beamsplitters and losses.** We show the minimum variance curves for the case where there is one lossy path with a transmission probability of 60% and unbalanced $55/45$ beamsplitters (dashed lines), compared to the ideal lossless and balanced case.

We discuss a simple case (balanced losses throughout the system and the use of non-number resolving threshold detectors[h]), where we find that we simply have to multiply the measured variance algebraically with a factor $c > 1$ to obtain an upper bound on Δ (see chapter 9 for a more efficient numerical method to conservatively correct for the measured variance). That is, the variance Δ is upper-bounded by $c\Delta_m$. Let us now evaluate the correction factor c.

Consider the propagation of the purported experimental state[i],

$$\hat{\rho}_W = p_0\hat{\rho}_0 + p_1\hat{\rho}_1 + p_{\geq 2}\hat{\rho}_{\geq 2}. \tag{7.32}$$

Under balanced losses (which can be characterized by a single transmission efficiency $|T|^2$), this state transforms to $\hat{\rho}_T$ where

$$\hat{\rho}_T = p'_0\hat{\rho}_0 + p'_1(q'_1\hat{\rho}_1^{(1)} + (1-q'_1)\hat{\rho}_1^{(2)}) + p'_{\geq 2}\hat{\rho}_{\geq 2}^{(2)}. \tag{7.33}$$

Here, $\hat{\rho}_1^{(i)}$ is the 1-photon subspace of $\hat{\rho}_{|T|^2}^{(r)}$ originating from the i-photon $\hat{\rho}_i$ subspace of $\hat{\rho}_W^{(r)}$ for $i \in \{1,2\}$, and $\hat{\rho}_{\geq 2}^{(2)}$ is the 2-photon subspace after the transmission. To the leading order of $\hat{\rho}_{\geq 2}^{(2)}$ (neglecting 3-photon and 4-photon subspaces[j]), $\{p'_0, p'_1, p'_2\}$ are

$$p'_0 = p_0 + (1-|T|^2)p_1 + (1-|T|^2)^2 p_2 \tag{7.34}$$

[h]The effect of imbalanced beamsplitters in the presence of balanced losses is easily included in this calculation. The final bound, including imbalanced losses and imbalanced beamsplitters, has the same form Eq. 7.43 with the same expression for $q_1 = p'_1 q'_1/Q$.

[i]Here we have changed the notation to make it easier to keep track of the meaning of all symbols

[j]In chapters 8–9, we include the higher-order terms up to one photon (excitation) per mode (ensemble) into our analysis.

$$p_1' = |T|^2 p_1 + 2|T|^2(1-|T|^2)p_2 \tag{7.35}$$

$$p_2' = |T|^4 p_2, \tag{7.36}$$

and q_1' is given as

$$q_1' = \frac{|T|^2 p_1}{|T|^2 p_1 + 2|T|^2(1-|T|^2)p_2}. \tag{7.37}$$

Thus, if we denote the normalized probability of the detector (assumed to be non-number resolving) in mode k finding (at least) one photon by P_k, then we have

$$P_k = \frac{p_1' q_1'}{Q} P_{1,k}^{(1)} + \frac{p_1'(1-q_1')}{Q} P_{2,k}^{(1)} + \frac{p_2'}{Q} P_{2,k}^{(2)}, \tag{7.38}$$

where $Q = p_1' + p_2'$. Here, $P_{1,k}^{(1)}$ ($P_{2,k}^{(1)}$) is the probability of a 1-photon in output mode k originating from the $1(2)$-photon subspace $\hat{\rho}_1$ ($\hat{\rho}_2$), and $P_{2,k}^{(2)}$ is the probability of 2-photon in output mode k. To be conservative (for our purposes of finding a *sufficient* condition for entanglement), we assume that the two photons are directed towards *one* detector at a time so that we cannot distinguish $P_{1,k}^{(1)}$ from $P_{2,k}^{(2)}$. By denoting $q_1 = p_1' q_1'/Q$ as the probability of detecting desired events and X_k as the normalized probability of detecting undesired events (that is, $P_{2,k}^{(1)}$ and $P_{2,k}^{(2)}$), we obtain

$$P_k = q_1 P_{1,k}^{(1)} + (1-q_1) X_k. \tag{7.39}$$

The measured variance Δ_m is given as

$$\Delta_m = 1 - \sum_k P_k^2. \tag{7.40}$$

On the other hand, the 1-photon variance Δ is defined as

$$\Delta(\hat{\rho}_1) = 1 - \sum_k (P_{1,k}^{(1)})^2. \tag{7.41}$$

As a conservative correction to Δ_m, we assume that the unwanted events (X_k) are all directed towards the output mode j which contains the maximum 1-photon probability $P_{1,j}^{(1)}$ (i.e., $X_j = 1$ and $X_k = 0$ for $k \neq j$). This way, the measured variance is *lower* than the variance Δ. Thus, our conservative bound gives then

$$\Delta_m = 1 - (q_1 P_{1,j}^{(1)} + (1-q_1))^2 - q_1^2 \sum_{k \neq j} (P_{1,k}^{(1)})^2. \tag{7.42}$$

Using the inequality $2(1 - P_{1,j}^{(1)}) \geq (1 + P_{1,j}^{(1)})(1 - P_{1,j}^{(1)}) = 1 - (P_{1,j}^{(1)})^2$, we obtain

$$\Delta_m \geq q_1[\Delta + (1-q_1) \sum_{k \neq j} (P_{1,k}^{(1)})^2] \geq q_1 \Delta. \tag{7.43}$$

Therefore, we obtain a correction factor of

$$c = \frac{1}{q_1}, \tag{7.44}$$

where

$$q_1 = \frac{p_1' q_1'}{Q} = \frac{p_1}{p_1 + (2 - |T|^2) p_{\geq 2}}. \tag{7.45}$$

Note that in the limit of $p_0 \approx 1$ the correction factor asymptotically converges to

$$c \approx 1 + \frac{3}{8}(2 - |T|^2) p_1 R. \tag{7.46}$$

7.7 Summary and Discussion

We theoretically demonstrated how to verify N-party entanglement of W states or states lying close to W states, in the case quantum information is encoded in the number of excitations per mode. Our method takes into account the presence of the vacuum state, as well as multiple excitations; moreover, it takes into account losses during the verification measurements, as well as imperfect beamsplitters. The method applies to any number of modes, but we focused on four modes for illustrative purposes, as the method was applied in actual experiments (refs.[33,35], chapters 8–9) to four modes (atomic ensembles). A relatively straightforward set of measurements allows one, in that case, to distinguish genuine four-party entanglement from three-party entanglement, which in turn can be distinguished from two-party entanglement and fully separable states. One must obtain estimates of three parameters: a variance Δ determined from the single-excitation component of the state, the single-photon probability q, as well as the multi-photon probability r. For example, the simple condition of Eq. 7.25 is a necessary condition for genuine four-party entanglement (where our definition of genuine multipartite entanglement is more severe than usual), which involves only r and q. To obtain sufficient conditions for multipartite entanglement, one must also include the value of Δ in the analysis, forming the parameter space for the nonlinear, nonlocal entanglement witness $\{\Delta, y_c\}$ (ref.[33], chapter 9).

The measurement of Δ combines the various modes by simple beamsplitters, and is thus nonlocal. In this way, one does *not* need local oscillators, which one would need if the entanglement verification method used local measurements only[228,233,265–272]. In our case, the modes interfere with each other, rather than with external reference beams. Thus, our method cannot be applied to eliminate local hidden variable models (through Bell inequalities, for example, in the bipartite case), but it can be applied to verifying entanglement, which is a very different beast indeed[110].

Chapter 8

Multipartite entanglement for one photon among four optical modes

This chapter is largely based on ref.[35]. Reference[35] refers to the then current literature in 2009 at the time of publication.

8.1 Introduction

Investigations of entanglement for two quantum systems have answered many fundamental questions in quantum physics[219,273] and revealed powerful new capabilities of quantum mechanics within the field of quantum information science (refs.[1,3,162], see also chapter 1). Many of these advances have used well-tested methods for the characterization of quantum entanglement in bipartite (i.e., two-component) systems[40,110]. Entangled states of more than two systems enhance our knowledge of quantum theory, as new classes of states are available[40,209,210]. Beyond applications to conventional quantum computation[3], exotic multipartite states have emerged as crucial resources for new directions in quantum information processing such as measurement-based quantum computation[212,213], quantum secret sharing[274], and quantum simulation[5]. Despite the extraordinary promise that they offer, unambiguously detecting multipartite entangled states is still a major challenge from both an experimental and a theoretical standpoint.

Genuine N-partite entanglement is realized only with the simultaneous participation of all N of the constituent systems. The exponential increase with N in the amount of information required to describe the overall quantum system, while exceedingly beneficial for large-scale quantum information protocols[3], makes the task of classifying[209,210] and detecting such entangled states extremely difficult[40]. Still, there are prescribed methods to detect entanglement in select classes of multipartite states that generally rely on reconstructing the density matrix $\hat{\rho}$. Linear entanglement witnesses supplemented by tomography of $\hat{\rho}$ have been used to detect entanglement in six[275] and eight[276] atomic ions, as well as for hyper-entangled photons[277]. A serious drawback of quantum-state tomography is the prohibitive number of measurements and their accuracies that are required with increasing N.

In this chapter, I will focus on a specific class of quantum states in which exactly one photon is coherently shared among N distinct optical modes in the form of

$$|W\rangle = \frac{1}{2}[(|1000\rangle + e^{i\phi_1}|0100\rangle) + e^{i\phi}(|0010\rangle + e^{i\phi_2}|0001\rangle)], \tag{8.1}$$

shown here for $N = 4$, and with the relative phases ϕ, ϕ_1, ϕ_2 of the modes. This is a so-called W state, which plays an important role in quantum information protocols with photonic and matter qubits, as its entanglement is known to be robust against losses (e.g., tracing over a set of modes $K \leqslant N - 2$).

To detect entanglement for pure states in the form of Eq. 8.1 and their mixed state counterparts $\hat{\rho}_W$, we introduce the use of fundamental quantum uncertainty relations (see chapter 7). It has long been known for continuous variable systems that the uncertainty principle for non-commuting observables defines a boundary of measurement precision that can only be crossed by entangled states[278,279]. This observation has formed the basis of numerous Einstein-Podolsky-Rosen type experiments[280], including the unconditional teleportation[281]. For discrete variable systems as in Eq. 8.1, the uncertainty principle can be recast as a sum of uncertainties in certain physical observables that must always be greater than some minimum bound Δ_b for all unentangled states, whether pure or mixed (refs.[38,121], chapter 7).

As a first test of this novel concept, we created a bipartite entangled state analogous to $|W\rangle$. We verified the entanglement both by violation of an uncertainty relation[38] and by the well-established method of concurrence (refs.[27,34,37,178], see also chapters 2 and 4). The precise agreement of these two measurements over a wide range of parameter space attests to the reliability of uncertainty-based verification for entanglement of discrete variables (Figs. 8.1b and 8.2). We then extended our setup to create multipartite entangled states that coherently share a single photon among four optical modes and applied our verification protocol to them. Varying the phase coherence and the photon statistics of a candidate state $\hat{\rho}_W$ allowed us to explore the boundary between separable and entangled states, including those that separate four-fold, three-fold, and two-fold entanglement.

8.2 Nonlinear, nonlocal entanglement witness by way of quantum uncertainty relations

Our verification protocol is based on an exclusion principle for which N-mode entanglement can be unambiguously detected by simultaneously measuring physical observables $\{\hat{M}_i\}$ (projectors) with $i \in \{1, \ldots, N\}$ more precisely than is possible with only $(N-1)$-mode entangled states and their mixtures[38,121]. Specifically, we consider a sum uncertainty relation $\Delta = \sum_{i=1}^{N} \langle \hat{M}_i^2 \rangle - \langle \hat{M}_i \rangle^2 = 1 - \sum_{i=1}^{N} \langle \hat{M}_i \rangle^2$, and its lower bound $\Delta_b^{(K)}$, which is obtained for the one photon subspace of all states with at most $K < N$ mode entanglement. For any K-mode entangled state the inequality $\Delta \geq \Delta_b^{(K)}$ holds; therefore a violation of this inequality serves

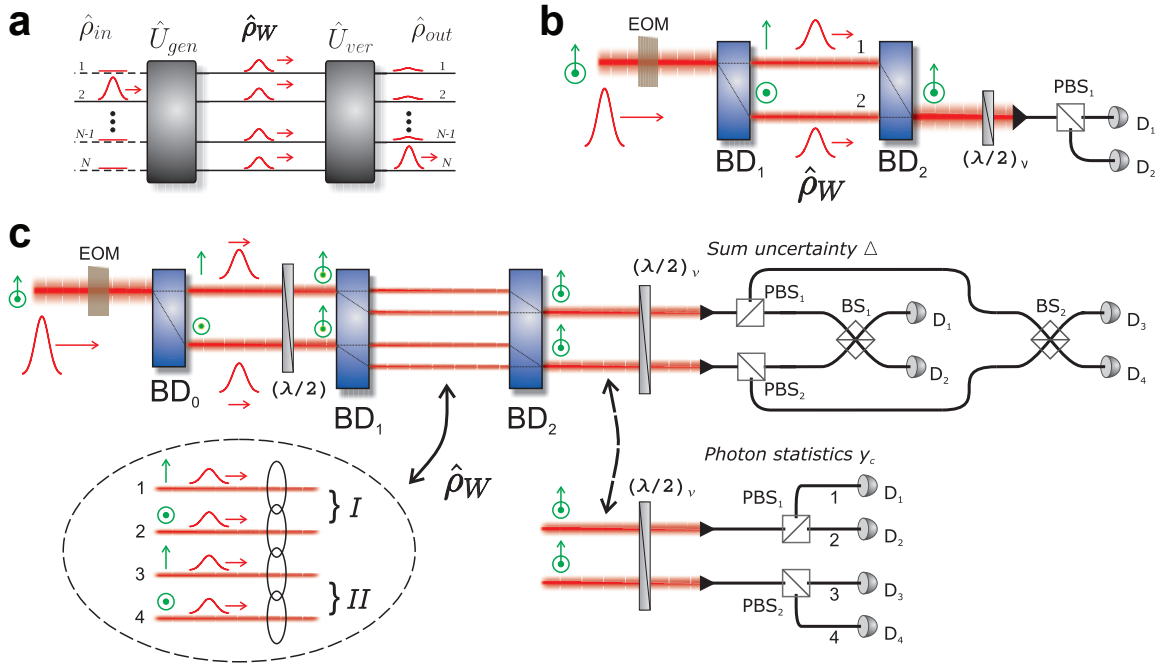

Figure 8.1: **Diagram of our entanglement generation and verification setups. a**, A single-photon pulse is transformed from a single input into an N-mode entangled state by $\hat{U}_{\text{gen}}$, and entanglement is verified with the operation $\hat{U}_{\text{ver}}$. **b**, Details of the setup for bipartite entanglement. Single photons are coherently split to occupy the two modes defined by the interferometer BD_1–BD_2 with the relative phase ϕ of $\hat{\rho}_W$ controlled by the EOM. By setting the waveplate $(\lambda/2)_{\text{v}}$ at 0°, the occupation of the individual modes is detected at D_1 and D_2, and we obtain the two-photon components of $\hat{\rho}_W$. With a setting of $(\lambda/2)_{\text{v}}$ at 22.5° single photon interference occurs at PBS_1, from which we obtain Δ; see also Fig. 8.2A. **c**, Details of the setup to create and verify quadripartite entanglement. The sequence of beamsplitters BD_0 and BD_1 generate the optical modes 1–4 which share a single photon. To measure Δ, we jointly optimize the relative phases in the verification interferometers for interferences at $\text{PBS}_{1,2}$ ($(\lambda/2)_{\text{v}}$ at 22.5°) and $\text{BS}_{1,2}$ to minimize the photon probability of all but one output mode. Here switching between measurements of Δ and y_c requires the indicated reconfiguration of fiber-optic components.

as a sufficient condition for genuine N-mode entanglement (see section 7.3). The projective operators are $\{\hat{M}_i\} = \{|W_i\rangle\langle W_i|\}$ with

$$
\begin{aligned}
|W_1\rangle &= \tfrac{1}{2}(|1000\rangle + e^{i\beta_1}|0100\rangle + e^{i\beta_2}|0010\rangle + e^{i\beta_3}|0001\rangle) \\
|W_2\rangle &= \tfrac{1}{2}(|1000\rangle - e^{i\beta_1}|0100\rangle - e^{i\beta_2}|0010\rangle + e^{i\beta_3}|0001\rangle) \\
|W_3\rangle &= \tfrac{1}{2}(|1000\rangle - e^{i\beta_1}|0100\rangle + e^{i\beta_2}|0010\rangle - e^{i\beta_3}|0001\rangle) \\
|W_4\rangle &= \tfrac{1}{2}(|1000\rangle + e^{i\beta_1}|0100\rangle - e^{i\beta_2}|0010\rangle - e^{i\beta_3}|0001\rangle)
\end{aligned}
\tag{8.2}
$$

for the case of $N = 4$, and with phases $\{\beta_j\}$ where $j \in \{1, 2, 3\}$. They are optimally sensitive to entanglement, for particular settings of β_j, since the entangled state $|W\rangle$ in Eq. 8.1 is the only simultaneous eigenstate of all projective operators $\hat{M}_i$ (ref.[38], chapter 7).

In our work, the purported N-mode entangled state ($\hat{\rho}_W$) analogous to $|W\rangle$ is generated via the operation $\hat{\rho}_{\text{in}} \xrightarrow{\hat{U}_{\text{gen}}} \hat{\rho}_W$ (Fig. 8.1a) on an input state $\hat{\rho}_{\text{in}}$. Similarly entanglement is verified with $\hat{\rho}_W \xrightarrow{\hat{U}_{\text{ver}}} \hat{\rho}_{\text{out}}$. We

implement $\hat{M}_i$ for the case of two (Fig. 8.1b) and four (Fig. 8.1c) optical modes using beamsplitters[282] and photodetectors. The limit $\Delta \rightarrow 0$ indicates a significant overlap of the state $\hat{\rho}_W$ with only one of the projectors $\hat{M}_i$. In particular, for any choices of ϕ, ϕ_1, ϕ_2 that define Eq. 8.1 and the three corresponding orthonormal states, our measurements of $\hat{M}_i$ would yield $\Delta = 0$ for optimal settings of the phases β_j. A small Δ corresponds to a large statistical imbalance in the event distribution of the output optical modes, with one mode strongly preferred over the others. Conversely, if the generated state contains a photon which occupies one mode, e.g. $|1000\rangle$, our measurements would yield $\Delta = 0.75$. Due to the presence of transmission losses and beamsplitter imbalances in our setups, the projectors $|W_i\rangle\langle W_i|$ evolve into mixed states with significant vacuum components, but genuine multipartite entanglement can still be robustly detected for $\hat{\rho}_W$ (ref.[38], see section 8.11).

To determine theoretically the boundaries $\Delta_b^{(K)}$ for N-mode entanglement, we calculate Δ for all possible admixtures of states containing at most $K = N - 1$ mode entanglement. The presence of more than one excitation in $\hat{\rho}_W$ may allow significant overlap of its one-photon subspace with $|W\rangle$ (chapter 7), leading to a spurious detection of entanglement. Therefore, it is necessary to determine the contamination of the state $\hat{\rho}_W$ due to multiple excitations. By invoking local filtering operations, we are justified in confining our analysis to the reduced density matrix $\hat{\rho}_W^{(r)} = p_0\hat{\rho}_0 + p_1\hat{\rho}_1 + p_{\geq 2}\hat{\rho}_{\geq 2}$ which contains no more than one photon per mode, while still being guaranteed a lower bound of entanglement[27,110]. In our experiments, we measure the photon probabilities p_0, p_1, and $p_{\geq 2}$ that characterize the occupation of the vacuum subspace $\hat{\rho}_0$, the single-photon subspace $\hat{\rho}_1$, and the subspace containing multiple excitations $\hat{\rho}_{\geq 2}$. The degree of contamination due to more than one excitation is quantified by the parameter $y_c = 2(\frac{N}{N-1})\frac{p_2 p_0}{p_1^2}$, which is normalized to the case of independent and balanced coherent states for which $y_c = 1$. The observation of measurement uncertainty Δ below the threshold $\Delta_b^{(K)}$ together with a determination of y_c, then, manifestly confirms the presence of genuine $(K+1)$-mode entanglement.

8.3 Experimental procedure

Our experimental starting point is the generation of heralded single photons via Raman transitions in an optically dense atomic ensemble of cesium atoms[4] (section 8.8). Two-mode entangled states are created by coherently splitting a single photon into parallel modes with beamdisplacer BD_1 (Fig. 8.1b); the modes' relative phase, analogous to ϕ in Eq. 8.1, is controlled by an electro-optic modulator (EOM). The spatially separated modes are recombined at BD_2 and coupled into a single-mode optical fiber, with each mode encoded in the polarization bases $|H\rangle$ and $|V\rangle$. Achieving entanglement requires a constant relative phase of the optical modes. Absent any fluctuating drive voltage on the EOM, the beamdisplacer pair BD_1–BD_2 forms a passively stable interferometer (refs.[34,36], chapter 3). By driving the EOM with a randomly oscillating voltage, the phase coherence of the modes is destroyed, and any entanglement between them is lost. This setup provides a calibrated tool to explore the boundary between separable and entangled states.

8.4 Characterization of bipartite entanglement by concurrence and uncertainty relations

Following the generation of bipartite states, we search for the signatures of entanglement using our verification protocol. To measure Δ, we rotate the polarizations of both modes by 45° and interfere them with a polarizing beamsplitter (PBS_1). We record the photoelectric detection events at single-photon counters D_1 and D_2, and convert them to the normalized joint photon probabilities P_{ij} (i.e., i photons for mode 1 and j for mode 2). Varying the relative phase of the modes after they exit BD_2 produces the interference fringes shown in the inset to Fig. 8.2a (corresponding to P_{10} and P_{01}), which allow us to identify the minimum value of Δ supported by the modes for a given y_c. In particular, the sum uncertainty Δ is related to the fringe visibility V by $\Delta = \frac{1}{2}(1 - V^2)$. When the relative phase β between modes $1, 2$ is either 0° or 180°, we obtain a value of Δ as small as 0.006, which corresponds to a visibility of 99.4% (section 8.10). To measure the two-photon suppression of $\hat{\rho}_W$, we detect the individual modes and record the time series of all relevant coincidence events (i.e., P_{ij} with $i + j = 0, 1,$ or 2). Based on a calibration of the transmission from the face of BD_2 to the detectors, we infer the photon probabilities that determine y_c (section 8.9). We control y_c via the pump intensity for Raman transitions in the source ensemble (section 8.8, chapter 2).

8.4.1 Scaling behavior of concurrence and uncertainty relations for bipartite entanglement

We have explored bipartite entanglement verification in our system by varying both the phase coherence and the two-photon suppression of $\hat{\rho}_W$. Fig. 8.2a shows the dependence of Δ on the amplitude $\delta\phi$ of phase noise produced by the EOM. These results were obtained with two-photon contamination $y_c = 0.063 \pm 0.011$ such that entanglement is detected when $\Delta \lesssim 0.46$. With $\delta\phi = 360^\circ$, we expect the fringe visibility to be minimized, and therefore $\Delta = 0.5$. As $\delta\phi$ decreases below 270°, the statistics of our measurements become sufficiently imbalanced that the presence of entanglement is manifest. Absent any phase noise in the state generated at BD_1 (i.e., $\delta\phi = 0$), we obtain $\Delta \leq 0.03$ over a wide range of y_c as shown in Fig. 8.2b. The first-order coherence of our single-photon source and the phase stability of our apparatus guarantee $\Delta \approx 0$. The boundary in Δ between fully separable states and those that contain entanglement, $\Delta_b^{(1)}$, depends primarily on y_c through the relationship $\Delta_b^{(1)} = \frac{1}{2}(1 - y_c)$. Given the uncertainty of our measurements, of which the largest contribution is counting fluctuations in y_c, all of the states created with $y_c \leq 0.86$ verifiably contain bipartite entanglement.

A rigorous correspondence exists between our uncertainty verification protocol (for two modes) and concurrence, a measure of bipartite entanglement[178] (section 8.10). As a tool to understand the dependencies of the sum uncertainty and as a secondary confirmation of two-mode entanglement, we inferred the normalized concurrence $C_N = V - \sqrt{y_c}$ from our measurements of Δ (section 8.10). Using previously introduced rela-

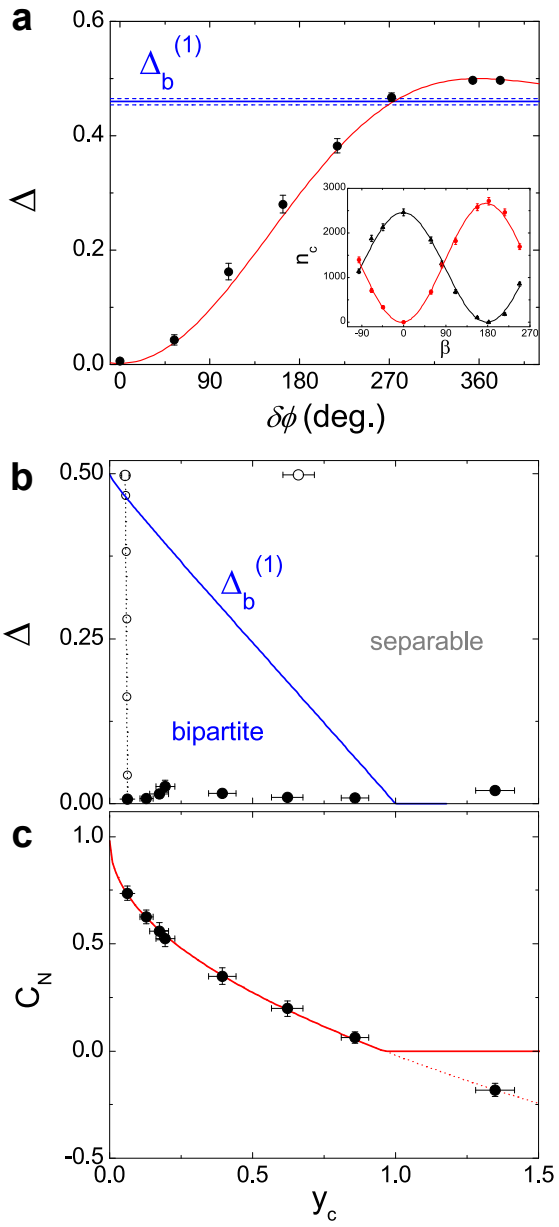

Figure 8.2: **Detection of entanglement between two optical modes using uncertainty relations. a**, The sum uncertainty Δ as a function of peak-to-peak phase noise $\delta\phi$ in the generated state $\hat{\rho}_W$. The solid blue line gives the boundary, $\Delta_b^{(1)}$, between entangled and separable states. The dotted lines indicate the range of $\Delta_b^{(1)}$ values that result from the uncertainty in our measurements of y_c. The red line is a fit to the data based upon a uniform distribution of phase noise. (Inset) Number of photons detected n_c in the output modes for a measurement time of 250 s as the relative phase β of the verification interferometer is varied. At minima and maxima of n_c we obtain $\Delta = 0.01$. **b**, Measured sum uncertainty with $\delta\phi = 0$ (filled circles) and boundary $\Delta_b^{(1)}$ (blue line) as a function of two-photon suppression. Data with $y_c < 1.0$ demonstrate entanglement of the two modes. By varying $\delta\phi$ from 0° to 360° (open circles), the modes' phase coherence is reduced, resulting in a loss of entanglement for $\delta\phi \gtrsim 270°$. **c**, Concurrence C_N (filled circles) inferred from measurements of Δ and the boundary $\Delta_b^{(1)}$. The solid line shows a theoretical prediction of concurrence $(\max(C_N, 0))$ based on an independent measurement of V and $p_1 = 0.22 \pm 0.02$. All the error bars in this figure represent standard deviations.

tionships, we can reformulate it as $C_N = \sqrt{1-2\,\Delta} - \sqrt{1-2\,\Delta_b^{(1)}}$. The inferred concurrence data shown in Fig. 8.2c demonstrate an increasing C_N, therefore a larger degree of entanglement, as we decrease y_c. Importantly, this behavior is in excellent quantitative agreement with our theoretical expectation for concurrence based upon quantum-state tomography[27,34]; this validates the use of uncertainty relations for entanglement verification (see Fig. 8.8 in section 8.10).

8.5 Experimental realization of multipartite entangled state for one photon

We now describe our investigation of multipartite entanglement with a single photon shared among four optical modes (Figs. 8.3 and 8.4). To generate four-mode entangled states we use the setup shown in Fig. 8.1c. A third beamdisplacer (BD_0) is added to the two-mode setup immediately before BD_1; it coherently splits a single photon polarized at 45° into two modes. In this case, the space between BD_1 and BD_2 supports four independent modes of $\hat{\rho}_W$ (composed of pairs I and II) that share a single photon. The EOM influences only the relative phase of the two pairs I, II, labeled ϕ in Eq. 8.1, leaving intact their individual phase coherence, and it provides a means to induce dephasing between the I, II pairs. The four spatially separated modes in the state $\hat{\rho}_W$ are combined into two separated spatial modes (each carrying the two modes encoded via the polarizations $|H\rangle$ and $|V\rangle$) that exit BD_2 and are coupled into single-mode fibers.

Measurements of Δ are performed by rotating the polarizations of all the modes by 45°, and pairwise interfering them with the network of four cascaded beamsplitters shown in Fig. 8.1c. We record all photoelectric events from detectors $\{D_1, ..., D_4\}$, but employ only events with a single photodetection for the determination of Δ (section 8.9). In this case, Δ depends jointly on the fringe visibilities of all four interferometric outputs. While BD_1 and BD_2 still guarantee long-term interferometric stability for the two pairs of modes I and II, the relative phases between other pairs are actively stabilized with respect to a laser that shares the same path. With the stabilization laser off, we apply calibrated feed-forward signals to the servo electronics, which transiently optimize the setup for measurements of various phase dependencies of Δ, including its global minimum (section 8.8). To extract y_c for the separated modes $1-4$, we insert the "photon statistics" setup at the location indicated in Fig. 8.1c, and we ensure that no interference occurs at PBS_1 and PBS_2 by setting the polarizations to the eigenaxes of the respective PBS. We obtain a record of the sixteen photon probabilities P_{ijkl} that determine y_c, with indices $i, j, k, l \in \{0, 1\}$ (section 8.9).

8.5.1 Scaling behavior of uncertainty relations for multipartite entanglement

8.5.1.1 Decoherence of multipartite entanglement induced by phase noise

Using sum uncertainty relations (refs.[38,121], chapter 7), we have unambiguously detected the presence of full four-mode entanglement in a photonic W state. Naturally, since $N > 2$, entanglement may be found amongst

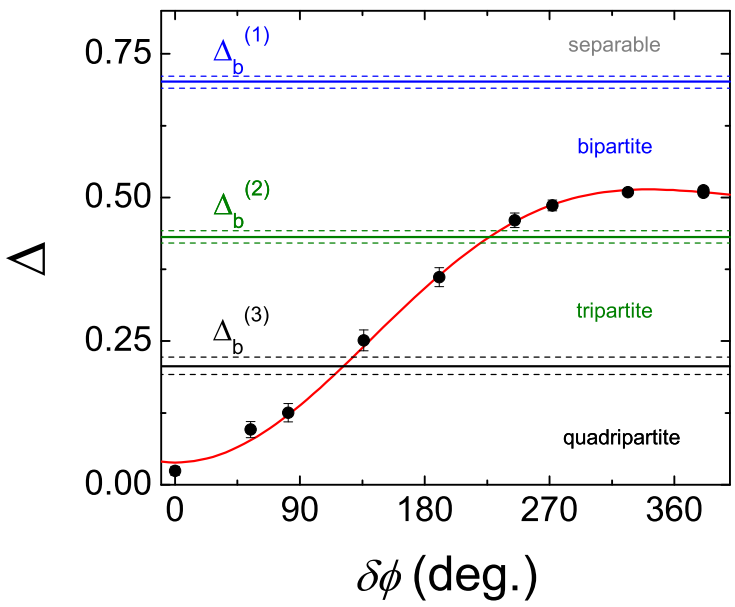

Figure 8.3: **Dependence of sum uncertainty Δ on the amplitude of phase noise $\delta\phi$ in the state $\hat{\rho}_W$.** These data were acquired with an approximately constant y_c in the range $0.06 - 0.08$; under these conditions $\Delta \lesssim 0.2$ demonstrates genuine four-mode entanglement. The horizontal lines indicate the boundaries $\Delta_b^{(K)}$ for entanglement. Here, the uncertainty of each boundary $\Delta_b^{(K)}$ (dashed lines) corresponds to the observed fluctuations in y_c. The red line is a fit to the data based on a model including a uniform distribution of phase noise.

not only the full set of modes, but bipartite and tripartite entangled states exist within a subset of them. A crucial feature of our verification protocol is that it clearly defines boundaries that distinguish between states with $\{N, N-1, \cdots, 2\}$ mode entanglement. As in the case with $N = 2$, the boundaries for $N = 4$ exist within the parameter space defined by Δ and y_c. To understand how the multipartite entanglement is affected by the phase coherence of $\hat{\rho}_W$, we introduce phase noise $\delta\phi$ over the range $0^\circ - 360^\circ$ between the two pairs of modes. Fig. 8.3 shows Δ as a function of $\delta\phi$ and the theoretical boundaries for two-, three-, and four-mode entanglement. For $\delta\phi \leqslant 225^\circ$, our verification protocol confirms the presence of genuine multipartite entanglement for three and four modes. Owing to the fact that dephasing is induced among only two pairs, the measured sum uncertainties do not exceed the threshold ($\Delta_b^{(1)} = 0.7$) defined by fully separable states[a]. A primary feature of multipartite W states is their resilience against phase noise, evidenced by the fact that the state which results from tracing over two modes in Eq. 8.1 still remains two-mode entangled[283]. This property of $|W\rangle$ explains our observation of entanglement even in the face of complete dephasing between the pairs I and II with 360° of phase noise.

[a]While there is a bipartite split between the pairs I and II (due to complete dephasing ϕ), we cannot unambiguously locate the bipartite split from the measurements presented in Fig. 8.3, as our verification protocol involves collective measurements on all four modes (section 7.3). In addition, note that we reserve the term, *genuine* N-partite entanglement, for states which can only be written in a pure-state decomposition of N-partite entangled states, thereby excluding the weaker condition of "N-partite entanglement" for mixtures of $M < N$ partite states along all possible bipartitions (i.e., a N-partite entangled state which does not have a physical split).

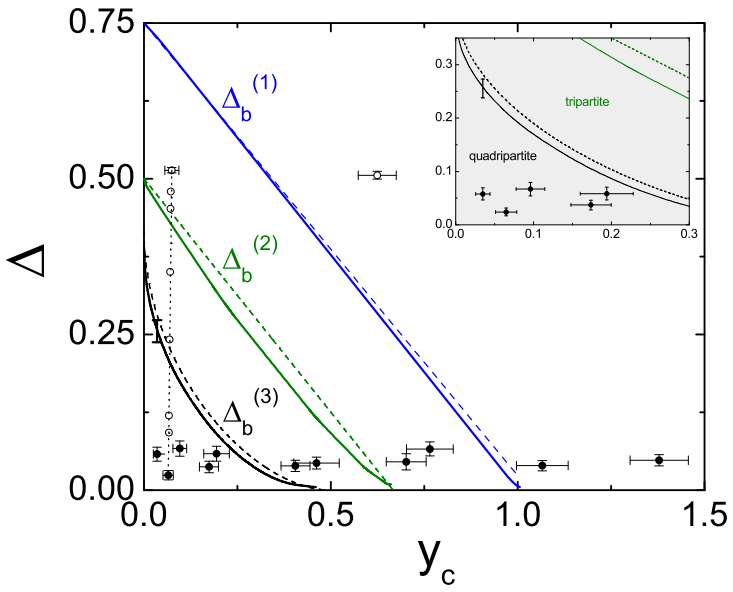

Figure 8.4: **Statistical transition of multipartite entanglement.** Sum uncertainty Δ as a function of two-photon suppression for $\delta\phi = 0°$ (closed circles) and $\delta\phi = 0°$–$360°$ (open circles). Solid lines indicate the boundaries between separable, bipartite, and tripartite entangled states for the parameters of our experiment. To understand the sizes of boundary corrections from the ideal case, the dashed lines show $\Delta_b^{(K)}$ for the ideal balanced and lossless case. The error bar on $\Delta_b^{(3)}$ indicates the statistical uncertainty in the boundary (section 8.11). (Inset) An expanded view of the quadripartite sector.

8.5.1.2 Statistical transition of multipartite entanglement

We have also explored the transitions from fully separable to bipartite ($K = 1$), tripartite ($K = 2$), and quadripartite ($K = 3$) entangled W states by measuring the sum uncertainty as a function of two-photon suppression y_c, with our results presented in Fig. 8.4. With $\delta\phi = 0$, we obtain a uniformly low $\Delta \leq 0.08$ over a range in y_c from $0.035 - 1.37$. These values of Δ are larger than in the two-mode case (Fig. 8.2b), and are explained by a small imbalance in $\hat{\rho}_W$ and by imperfections in the entanglement verification interferometers. Furthermore, these imperfections play an important role in the determination of the boundaries $\Delta_b^{(K)}$ for entanglement. As detailed in section 8.11, small imbalances in the beamsplitter ratios of PBS_1, PBS_2 and BS_1, BS_2 in Fig. 8.1c, and non-balanced transmission losses lead to displacements of the boundaries toward smaller $\{\Delta, y_c\}$. To reduce these boundary corrections, the beamsplitter ratios were all matched to $50\%/50\%$ to less than 3%, and the difference in losses of corresponding free-space and in-fiber optical paths were always held to less than 4%. Fig. 8.4 shows the sizes of the corrections by displaying the boundaries $\Delta_b^{(K)}$ for the ideal lossless and balanced case as dashed lines.

8.6 Advantage of multipartite entanglement verification via uncertainty relations

In comparison to quantum-state tomography, our multipartite verification protocol features an exponential reduction in the number of measurements required to unambiguously detect entanglement. Specifically, our protocol requires us to determine 2^4 elements of $\hat{\rho}_W^{(r)}$ for y_c and 4 elements of $\hat{U}_{\text{ver}}^{\dagger}\,\hat{\rho}_W^{(r)}\,\hat{U}_{\text{ver}}$ for Δ, a total of 20 elements out of the $4^4 = 256$ that comprise the reduced density matrix $\hat{\rho}_W^{(r)}$. Our protocol inherently features the use of nonlocal measurements $\hat{M}_i$, thereby requiring only two unique experimental steps to measure all necessary elements and unambiguously detect entanglement in $\hat{\rho}_W$. Furthermore, the nonlinear structure of Δ allows the simultaneous detection of all possible realizations of Eq. 8.1 (refs.[38,40]). These features alleviate the need for any complicated mechanism to control the measurement basis, which can be a challenge in tomography experiments[277] and other local-measurement-based verification protocols for $\hat{\rho}_W$. Although linear witnesses might also enable entanglement detection with less than full knowledge of $\hat{\rho}_W$ obtained from a few experimental steps[260], the unambiguous verification of entanglement requires robustness in the face of experimental imperfections, including multiple excitations and losses (section 8.11).

8.7 Conclusion

Our study has introduced a new technique for the unambiguous verification of multipartite W states. Specifically we examined entanglement in heralded quantum states specified by $\hat{\rho}_W$ with $N = 2, 4$. Entanglement detected with our protocol refers to that of the complete density matrix $\hat{\rho}_W$ presented to our verification system, and not to fictitious components deduced via post selection[110]. An extension of our protocol to different mode entangled states (requiring increased experimental resources) is discussed in chapter 7 (ref.[38]). Photonic entanglement, such as generated here, can be coherently mapped into atomic memories by way of electromagnetically induced transparency[30] for scalable quantum networks (chapter 6).

8.8 Experimental details

8.8.1 Ensemble-based single-photon source

The first step in our experiment is the conditional generation of single photons based on the proposal by Duan, Lukin, Cirac, and Zoller (*DLCZ*) (refs.[4,226]). In this protocol, heralded single photons are generated from excitations stored within an atomic ensemble. Single photon sources based upon atomic ensembles have been studied extensively; see refs.[74–76,79,82] for in-depth information. Here, we briefly present the experimental details relevant to our investigations.

We implement the *DLCZ* protocol with a cloud of $\sim 10^6$ cesium atoms that are collected using a magneto-

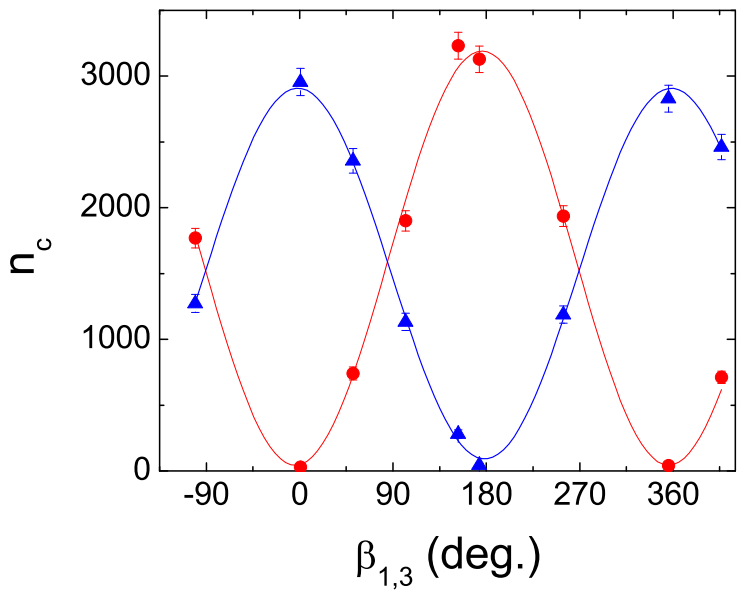

Figure 8.5: **Interference fringe in the four-mode sum uncertainty setup.** Number of detected photons n_c in output mode 1 (blue triangles) and output mode 2 (red circles) are plotted as a function of the phase $\beta_{1,3}$. Here a fringe visibility in excess of 99% and wide tunability of $\beta_{1,3}$ demonstrate the experimental capabilities necessary for measurements of Δ.

optical trap (MOT). Periodically, at a rate of 40 Hz, we switch off the trapping lasers and the magnetic field for the MOT, and we prepare all the atoms into the $F = 4$ hyperfine manifold ($6^2S_{1/2}$) of Cs. After waiting 3 ms for the MOT fields to decay, we begin a series of ≈ 6400 trials, each with a period of 625 ns. To begin each trial, we illuminate the cloud with a weak near-resonant "write" laser pulse which excites a Raman transition with low probability for a collective mode of the ensemble. The success of this process is heralded by a Raman scattered single photon that is correlated with the presence of an atomic excitation. By way of a many-atom cooperative enhancement [70,226], the atomic excitation can be efficiently converted into a single photon in a well-defined spatial mode with the application of an intense "read" pulse. This heralded single photon forms the basis of this experiment described in this chapter.

We have studied the characteristics of our single photon source in detail [75,76]. Importantly, the two-photon suppression, $y_c = 2(\frac{N}{N-1})\frac{p_2 p_0}{p_1^2}$, where N is the number of optical modes, of the purportedly entangled state $\hat{\rho}_W$ depends critically on the presence of multiple collective excitations within the ensemble (i.e., the single-photon source). The relative probability of a trial that has multiple ensemble excitations to a trial that has a single excitation can be suppressed by reducing the write laser intensity. Therefore, we can exercise full control over y_c of the quantum state $\hat{\rho}_W$ by way of a tunable write laser intensity. Furthermore, we can understand the efficiency of heralded single-photon generation. After accounting for detector and transmission losses, we estimate that the efficiency of the read-out process in our experiments is $\approx 50\%$. This leads to a single-photon probability of $p_1 \approx 20\%$ ($p_1 \approx 10\%$) in our two-mode (four-mode) experiments for the entangled state $\hat{\rho}_W$ in Fig. 8.1.

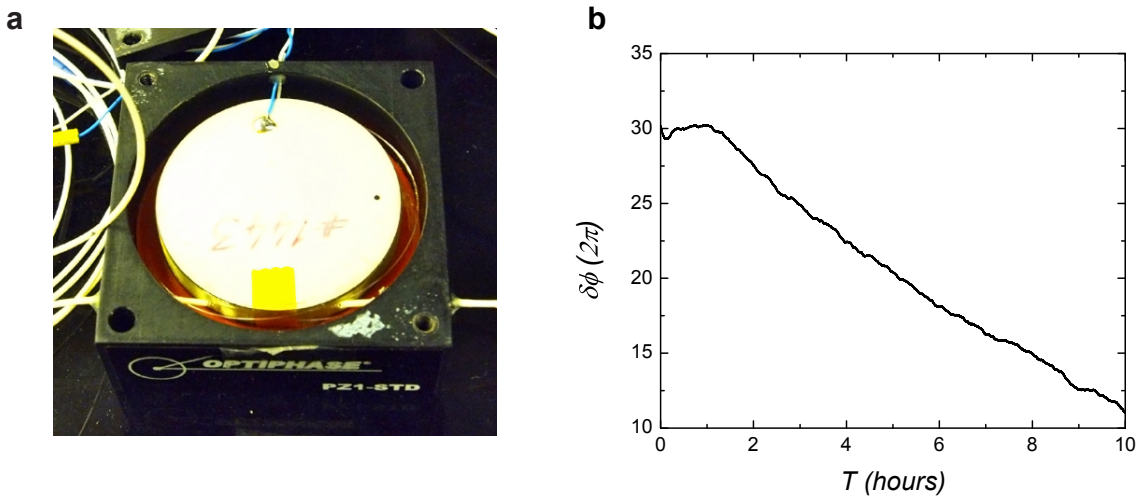

Figure 8.6: **A high-bandwidth fiber stretching module. a**, Inside the fiber stretching module (Optiphase), PM fiber is mounted on a circular disc piezoelectric transducer (PZT), which has a sharp mechanical resonance around $\simeq$ 55 kHz. The breathing mode of the PZT element is used to phase-modulate the fiber at $\sim$ 100 kHz (above the first resonance). Two lock-in amplifiers (DSP lock-in amplifiers, SRS 830 and 510) are used to generate an error signal by modulation spectroscopy on the interferometers in Fig. 8.1. The output of the locking servo described in Appendix A is fed into a high-voltage amplifier (Burleigh, PZ-70) to drive the fiber stretcher. At 1 kV, we estimated the reduction of polarization extinction ratio for the PM fiber from 30 dB to 20 dB, due to spurious stress-induced birefringence. **b**, Dynamic range of the active phase stabilization scheme via fiber stretchers. Thanks to the high dynamic range (up to $\delta\phi \sim 50 \times 2\pi$ at 852 nm) of the fiber stretchers, we can set the interferometer to a certain value of phase over several days without needing to re-lock the interferometer (mainly limited by the stability of the reference laser).

8.8.2 Phase stabilization

The generation and verification of entanglement in our experiments require that the relative phases of the purportedly entangled optical modes in Fig. 8.2 be stable (the various phase factors that describe the state $|W\rangle$ are shown in Eq. 8.1). As described in section 8.3, our experiments with two-mode entanglement (Fig. 8.2a) feature passive stability of the modes' relative phase $\beta_{1,2}$, guaranteed by the Mach-Zehnder interferometer formed with a pair of beamdisplacers BD_1–BD_2 (ref.[34], chapter 3). These beamdisplacers are birefringent crystals which separate an input state into two parallel modes based on its polarization. Therefore, the two displacers support a pair of interferometrically stable modes, which are encoded in $|H\rangle$ and $|V\rangle$.

However, for our quadripartite entanglement experiments (Fig. 8.1c), the beamdisplacer pairs alone cannot define four spatially resolved stable optical modes. Therefore, we have devised a convenient method that combines passive stability and active stabilization. The beamdisplacers BD_1–BD_2 support four modes of which the relative phases of modes $\{1, 2\}$ ($\beta_{1,2}$) and $\{3, 4\}$ ($\beta_{3,4}$) are inherently stable. However, as is clearly visible in Fig. 8.1c, the relative phases of modes $\{1, 3\}$ ($\beta_{1,3}$) and $\{2, 4\}$ ($\beta_{2,4}$) depend on the independent paths through, for example, fiber-optic PBS_1 and PBS_2 (Fiber PBS from Oz Optics). By incorporating an auxiliary reference laser, E_{aux}, we can actively control the relative path lengths of the modes $\{1, 3\}$ and $\{2, 4\}$. Prior to BD_0 in Fig. 8.1c, we overlap the orthogonally polarized E_{aux} and the input mode ($\hat{\rho}_{\text{in}}$); the

frequency of E_{aux} is the same as the single photon's. To stabilize $\beta_{1,3}$ and $\beta_{2,4}$, we set $(\lambda/2)_{\text{v}}$ at 0° and create interference fringes at the outputs of BS_1 and BS_2. Phase-modulation spectroscopy allows us to lock the relative phases so that a high contrast interference ($V > 0.99$) is achieved for quantum fields (Fig. 8.5). The control of the relative path lengths for the modes, as well as their modulation, is afforded by piezoelectric fiber stretcher modules (Fig. 8.6a, see also Appendix A for the locking servo) located between PBS_1 and BS_1, and PBS_2 and BS_2, in Fig. 8.1c. These devices provide up to $50 \times 2\pi$ of dynamic range enabling the interferometers to remain continuously locked for several days (Fig. 8.6b).

Importantly, to avoid noise associated with the auxiliary laser in the single-photon detectors $\{D_1, \cdots, D_4\}$, E_{aux} must be filtered out. In our work, phase stabilization is performed asynchronously with entanglement generation and its verification in the fiber-based network of interferometers (Appendix A). This eliminates the need to wavelength filter E_{aux} as was necessary in previous experiments[27]. During the 21 ms of our 40 Hz experimental cycle that the MOT is activated, E_{aux} is switched on, the output modes of the sum uncertainty setup are directed toward an auxiliary set of detectors with MEMS fiber multiplexers (Sercalo), and our servo electronics stabilize $\beta_{1,3}$ and $\beta_{2,4}$. To prepare for measurements of Δ, we switch off E_{aux} and reroute the output modes to the single-photon detectors with the MEMS multiplexers, and we use dynamic polarization rotators (nematic liquid-crystal waveplates from Meadowlark[b]) to set $(\lambda/2)_{\text{v}}$ at 22.5°. Further, we apply calibrated feedforward signals to the servo electronics that can precisely scan the relative phases of modes $\{1, 3\}$ and $\{2, 4\}$ to explore the dependencies of our Δ measurements. Fig. 8.5 shows the number of photons (n_c) detected at D_1 and D_2 as a function of $\beta_{1,3}$. Here, all other relevant optical phases in our setup were optimized to achieve minimum Δ. Therefore, at the minima and maxima of n_c corresponding to $\beta_{1,3} = 0,\ 180^\circ,\ 360^\circ$, we find that Δ is 0.06 ± 0.01.

8.9 Inference of the photon probabilities for obtaining y_c and Δ

Our entanglement verification protocol requires that we characterize the photon probabilities of the sum uncertainty output modes and those of modes 1–4 that comprise the state $\hat{\rho}_W$. We infer these photon probabilities from a time record of photodetection events obtained with single photon counters placed at the outputs of the relevant modes. Based upon independent measurements of the transmission losses to the photodetectors, we determine the photon probabilities[193]. Specifically, for measurements of y_c we obtain a set of sixteen probabilities that characterize the diagonal elements of the reduced density matrix $\hat{\rho}_W^{(r)} = p_0\hat{\rho}_0 + p_1\hat{\rho}_1 + p_{\geq 2}\hat{\rho}_{\geq 2}$. The diagonal elements are P_{ijkl} where the index $i = \{0, 1\}$ is for finding zero or one photon in mode 1 of $\hat{\rho}_W$, $j = \{0, 1\}$ in mode 2, and so on for k, l in modes 3 and 4 (Fig. 8.1c). The vacuum subspace of $\hat{\rho}_W^{(r)}$ is characterized by the term $p_0 = P_{0000}$. Four elements comprise the one-photon subspace, $\hat{\rho}_1$, via

[b]Bandwidth of the liquid-crystal (LC) waveplates is slow (only $\sim$ 1 kHz) compared to that of Pockels cells, which was still suitable for our purpose. In addition, since these are biaxial nematic devices, there are only two stable positions whereby the eigenaxes of the crystal could align[284]. However, one advantage is that the LC only requires a modest amount of voltage (< 5 V) to set the fast axis of the crystal to the predetermined direction.

$p_1 = P_{1000}+P_{0100}+P_{0010}+P_{0001}$. Likewise, 11 elements comprise the subspace with two or more photons, $\hat{\rho}_{\geq 2}$, subject to the restriction of one photon per mode, with $p_{\geq 2} = P_{1100}+P_{1010}+\cdots+P_{1110}+\cdots+P_{1111}$. In the case of y_c measurements, the typical detection efficiency including the photodetector quantum efficiency is $\approx 20\%$. To infer the photon probabilities at the outputs of the verification interferometers (Fig. 8.1c) for our measurements of Δ, we follow a similar procedure, but we confine our analysis to the subspaces $\hat{\rho}_0$ and $\hat{\rho}_1$. In this case, the typical photon detection efficiency is $\approx 30\%$.

Similarly, due to the uses of photon non-resolving photodetectors and lossy paths for our projectors (Eq. 8.2), the measured sum uncertainty Δ_{m} includes spurious contributions from multiple photons $p_{\geq 2}$. To account for this, we follow the procedure described in section 7.6.2 (ref.[38], chapter 7), which leads to a conservative estimation of the photon sum uncertainty Δ arising only from $\hat{\rho}_1$. In the case of balanced losses, the correction factor c is expressed in terms of two-photon suppression y_c and transmission efficiency η with

$$c \approx (1 + \frac{3}{8}(2-\eta)p_1 y_c), \tag{8.3}$$

where we apply $c\Delta_m > \Delta$ to obtain a conservative estimate of the 1-photon Δ (section 7.6.2; see also chapter 9 for a more efficient method for obtaining the upper bound of Δ). For our experimental parameters, the correction factor $(c-1) \approx 6\%$ is obtained for $y_c = 1$, as depicted in black line of Fig. 8.7. This is significantly smaller than the fractional uncertainties $\frac{\delta(\Delta_m)}{\Delta_m} \approx 25\%$ of our data. Furthermore, since the correction factor scales as y_c, the correction factor gives $(c-1) < 1\%$ for the relevant data sets of $y_c < 0.2$ for four-mode entanglement (Fig. 8.4). Following the standard procedures for loss propagations[193], we also account for the effect of differential losses and imbalanced beamsplitter ratios (red line in Fig. 8.7).

8.9.1 Imbalances and threshold detectors

In chapter 7, we developed a method to account for losses and imbalances. Here, we obtain an explicit formulas of q_1 in the case of differential losses and imbalanced beamsplitter ratios. In order to propagate $\hat{\rho}_W^{(r)}$ through the imbalanced verification interferometers, we rewrite $\hat{\rho}_W^{(r)}$,

$$\hat{\rho}_W^{(r)} = p_0\hat{\rho}_0 + \hat{\rho}_1' + \hat{\rho}_2', \tag{8.4}$$

in terms of mode operators $\hat{a}_i$ where

$$\hat{\rho}_1' = \sum_{i,j} \frac{P_i + P_j}{2} V(i,j)\hat{a}_i^\dagger|\overline{0}\rangle\langle\overline{0}|\hat{a}_j \tag{8.5}$$

$$\hat{\rho}_2' = \sum_{j>i}^{4}\sum_{l>k}^{4} \frac{P_{ij} + P_{kl}}{2} V(ij,kl)\hat{a}_i^\dagger\hat{a}_j^\dagger|\overline{0}\rangle\langle\overline{0}|\hat{a}_k\hat{a}_l. \tag{8.6}$$

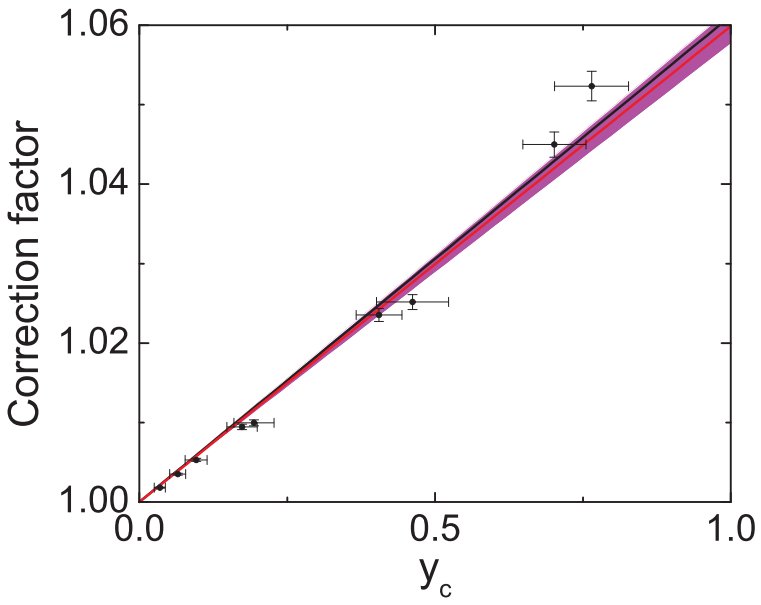

Figure 8.7: **Correction factor c as a function of two-photon contamination y_c.** The black line corresponds to the calculation of c for balanced losses $\eta = 36\%$ and fixed $p_1 = 9\%$. The red line is a calculation of c including differential losses $\{\eta\}$ and imbalanced beamsplitter ratios $\{\alpha\}$ (Table 8.1). The uncertainty of c due to the systematic uncertainties in $\{\eta, \alpha\}$ is shown as purple bands. The filled circles show c using the data points in the experiment (i.e., using the parameters P_{ijkl} of each points). The uncertainty in the vertical direction includes the systematic uncertainties in $\{\eta, \alpha\}$ as well as the statistical uncertainties in P_{ijkl}.

Here, $V(i,j) = V(j,i)$ and $V(i,i) = 1$. Through the lossy and imbalanced setup in Fig. 8.1, the mode operators $\hat{a}_i$ are transformed into following forms,

$$\hat{a}_i \mapsto \sum_{i'} e^{i\phi_{i'}^{(i)}} \sqrt{\alpha_{i'}^{(i)}} (\sqrt{\eta_{i'}^{(i)}} \hat{a}_{i'} + \sqrt{1-\eta_{i'}^{(i)}} \hat{v}_{i'}). \tag{8.7}$$

Here, $\hat{v}_{i'}$ is the vacuum mode operator. The precise correspondences between the imbalances $\{\alpha_{i'}^{(i)}, \eta_{i'}^{(i)}, \phi_{i'}^{(i)}\}$ and experimental parameters (Table 8.1 and Fig. 8.1) are not shown for clarity.

The state $\hat{\rho}_W^{(r)}$, then, is transformed to a state (see section 7.6.2 for the balanced case),

$$\hat{\rho}_\eta^{(r)} = p_0' \hat{\rho}_0 + p_1' (q_1' \hat{\rho}_1^{(1)} + (1-q_1') \hat{\rho}_1^{(2)}) + p_{\geq 2}' \hat{\rho}_{\geq 2}^{(2)}, \tag{8.8}$$

where the relevant parameters $\{p_1' q_1', p_1'(1-q_1'), p_2'\}$ are given as[c]

$$p_1' q_1' = \sum_{i,j} \frac{P_i + P_j}{2} V(i,j) \sum_\kappa e^{-i(\phi_\kappa^{(i)} - \phi_\kappa^{(j)})} \sqrt{\eta_\kappa^{(i)} \eta_\kappa^{(j)}} \sqrt{\alpha_\kappa^{(i)} \alpha_\kappa^{(j)}} \tag{8.9}$$

[c]Here, we have assumed that the two-photon subspace is fully coherent, $V(ij,kl) = 1$, thereby leading to $\Delta(\hat{\rho}_1^{(2)}) = \Delta(\hat{\rho}_2^{(2)}) = 0$ and a conservative estimate of Δ.

$$p_1'(1-q_1') = \sum_{i>j}\sum_{k>l}\frac{P_{ij}+P_{kl}}{2}\frac{1}{2}\sum_{\kappa_1,\kappa_2}\sqrt{\alpha_{\kappa_1}^{(i)}\alpha_{\kappa_2}^{(j)}\alpha_{\kappa_1}^{(k)}\alpha_{\kappa_2}^{(l)}}e^{-i(\phi_{\kappa_1}^{(k)}+\phi_{\kappa_2}^{(l)}-\phi_{\kappa_1}^{(i)}-\phi_{\kappa_2}^{(j)})}\times \\ (\sqrt{\eta_{\kappa_1}^{(i)}(1-\eta_{\kappa_2}^{(j)})}+\sqrt{\eta_{\kappa_2}^{(j)}(1-\eta_{\kappa_1}^{(i)})})(\sqrt{\eta_{\kappa_1}^{(k)}(1-\eta_{\kappa_2}^{(l)})}+\sqrt{\eta_{\kappa_2}^{(l)}(1-\eta_{\kappa_1}^{(k)})}) \tag{8.10}$$

$$p_{\geq 2}' = \sum_{i>j}\sum_{k>l}\frac{P_{ij}+P_{kl}}{2}\sum_{\kappa_1,\kappa_2}\sqrt{\alpha_{\kappa_1}^{(i)}\alpha_{\kappa_2}^{(j)}\alpha_{\kappa_1}^{(k)}\alpha_{\kappa_2}^{(l)}}e^{-i(\phi_{\kappa_1}^{(k)}+\phi_{\kappa_2}^{(l)}-\phi_{\kappa_1}^{(i)}-\phi_{\kappa_2}^{(j)})}\sqrt{\eta_{\kappa_1}^{(i)}\eta_{\kappa_2}^{(j)}\eta_{\kappa_1}^{(k)}\eta_{\kappa_2}^{(l)}}. \tag{8.11}$$

Therefore, correction factor $c = 1/q_1$ is given as (chapter 7)

$$q_1 = \frac{p_1'q_1'}{p_1'+p_{\geq 2}'}. \tag{8.12}$$

In the case of balanced losses η, it can be confirmed that Eqs. 8.3 and 8.12 are equivalent.

Here, we give the definitions of $\{\alpha_{i'}^{(i)}, \eta_{i'}^{(i)}, \phi_{i'}^{(i)}\}$ following the notations in Fig. 8.9.

$$\alpha_{i'}^{(i)} = \begin{pmatrix} \alpha_{14}'\alpha_{12} & \alpha_{14}'(1-\alpha_{12}) & (1-\alpha_{14}')\alpha_{34} & (1-\alpha_{14}')(1-\alpha_{34}) \\ \alpha_{23}'(1-\alpha_{12}) & \alpha_{23}'\alpha_{12} & (1-\alpha_{23}')(1-\alpha_{34}) & (1-\alpha_{23}')\alpha_{34} \\ (1-\alpha_{23}')(1-\alpha_{12}) & (1-\alpha_{23}')\alpha_{12} & \alpha_{23}'(1-\alpha_{34}) & \alpha_{23}'\alpha_{34} \\ (1-\alpha_{14}')\alpha_{12} & (1-\alpha_{14}')(1-\alpha_{12}) & \alpha_{14}'\alpha_{34} & \alpha_{14}'(1-\alpha_{34}) \end{pmatrix} \tag{8.13}$$

$$e^{i\phi_{i'}^{(i)}} = \begin{pmatrix} e^{i\phi_{i_1}} & e^{i\phi_{i_2}} & -e^{i\phi_{i_3}} & -e^{i\phi_{i_4}} \\ e^{i\phi_{i_1}} & -e^{i\phi_{i_2}} & -e^{i\phi_{i_3}} & e^{i\phi_{i_4}} \\ e^{i\phi_{i_1}} & -e^{i\phi_{i_2}} & e^{i\phi_{i_3}} & -e^{i\phi_{i_4}} \\ e^{i\phi_{i_1}} & e^{i\phi_{i_2}} & e^{i\phi_{i_3}} & e^{i\phi_{i_4}} \end{pmatrix} \tag{8.14}$$

$$\eta_{i'}^{(i)} = \begin{pmatrix} \eta_1\eta_1' & \eta_2\eta_1' & \eta_3\eta_4' & \eta_4\eta_4' \\ \eta_1\eta_2' & \eta_2\eta_2' & \eta_3\eta_3' & \eta_4\eta_3' \\ \eta_1\eta_2' & \eta_2\eta_2' & \eta_3\eta_3' & \eta_4\eta_3' \\ \eta_1\eta_1' & \eta_2\eta_1' & \eta_3\eta_4' & \eta_4\eta_4' \end{pmatrix} \tag{8.15}$$

8.10 Concurrence and bipartite uncertainty relations

For bipartite systems, there exist entanglement measures such as concurrence (*C*) and entanglement of formation (*EOF*) (ref.[178]), which range from 0 for a fully separable state to 1 for a maximally entangled state[110]. In Fig. 8.2, we quantitatively compared our method of entanglement verification with uncertainty relations to a theoretical calculation of concurrence based on a model in chapter 3 (ref.[34]). Here, we derive a relationship between concurrence and the degree that a measurement of the sum uncertainty violates the entanglement boundary, specified by the measured Δ and the uncertainty bound $\Delta_b^{(1)}$.

Following ref.[27], we find that the concurrence is given by $C = Vp_1 - 2\sqrt{p_0p_2}$ (chapter 3), where V corresponds to the fringe visibility when the two modes are interfered[27]. If we normalize the concurrence by the 1-photon probability p_1, we obtain

$$C_N \equiv \frac{C}{p_1} = V - \sqrt{y_c} \tag{8.16}$$

where $y_c = \frac{4p_2p_0}{p_1^2}$.

Let us first define the visibility V in terms of the measured Δ. We denote P_{10} (P_{01}) as the normalized probability of finding only 1 photon in the output mode 1 (2) (Fig. 8.2a) such that $P_{10} + P_{01} = 1$. The visibility is given as $V = |P_{10} - P_{01}|$. Similarly, the sum uncertainty is defined as $\Delta = 1 - (P_{10})^2 - (P_{01})^2$, which then yields,

$$V = \sqrt{1 - 2\Delta}. \tag{8.17}$$

We relate the two-photon contamination y_c to the uncertainty bound $\Delta_b^{(1)}$. In this way, we can understand the dependence of C_N on the degree for which the inequality $\Delta \geq \Delta_b^{(1)}$ is violated. In order to derive the uncertainty bound $\Delta_b^{(1)}$, we consider a separable state of the form,

$$|\Psi_{sep}\rangle = \frac{(|0_1\rangle + e^{i\phi_1}\sqrt{\varepsilon_1}|1_1\rangle)(|0_2\rangle + e^{i\phi_2}\sqrt{\varepsilon_2}|1_2\rangle)}{\sqrt{(1+\varepsilon_1)(1+\varepsilon_2)}} \tag{8.18}$$

with $p_0 = 1 - p_1 - p_2$, $p_1 = \frac{\varepsilon_1 + \varepsilon_2}{(1+\varepsilon_1)(1+\varepsilon_2)}$, $p_2 = \frac{\varepsilon_1\varepsilon_2}{(1+\varepsilon_1)(1+\varepsilon_2)}$, and the phases ϕ_1, ϕ_2. This state parameterizes all possible pure separable states, and mixed states can be accounted by arbitrarily mixing different pure states. For bipartite systems, however, the uncertainty bound for pure states is convex (Fig. 8.2b), and any mixing of the pure states increases the sum uncertainty [121]. Therefore, we only consider the cases for pure states, and we find

$$\Delta_b^{(1)} = \frac{1 - y_c}{2}. \tag{8.19}$$

By substituting Eq. 8.17 and 8.19 into Eq. 8.16, we obtain the relationship between concurrence and the violation of uncertainty bounds for a biseparable system, namely

$$C_N = \sqrt{1 - 2\Delta} - \sqrt{1 - 2\Delta_b^{(1)}}. \tag{8.20}$$

We emphasize the equivalence of the two verification protocols based on the violation of the uncertainty bound and the concurrence. The operational differences between the two entanglement verification protocols are the measurements of visibility (by varying the relative phase $\beta_{1,2}$) and the sum uncertainty Δ (with a fixed relative phase $\beta_{1,2}$). In Fig. 8.8, we compare the concurrence $C_N^{(\hat{\rho}_W)}$ directly measured via quantum state tomography [27] and the concurrence C_N inferred from violation of the uncertainty bound $\Delta_b^{(1)}$ (Fig. 8.2c). The precise correspondence of the two experimental results suggest that the underlying relationship between the two entanglement verification methods, as derived here (Eq. 8.20), is correct.

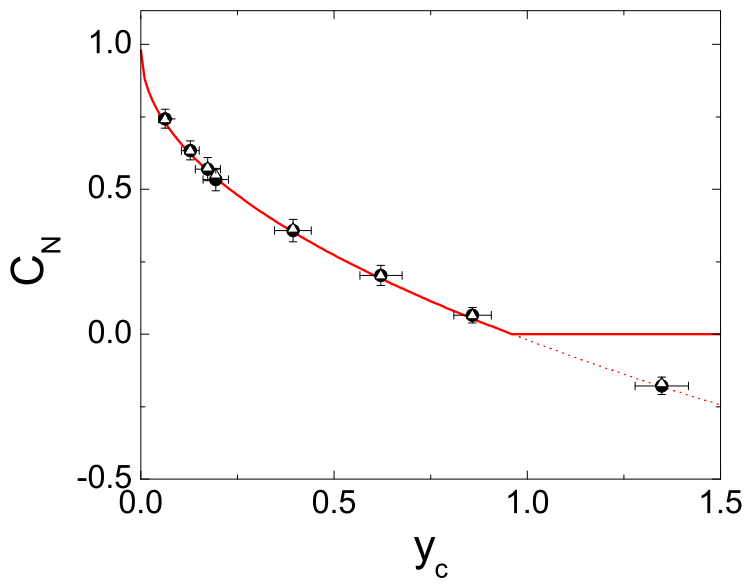

Figure 8.8: **Comparison between the directly measured concurrence and the inferred concurrence.** We compare the directly measured concurrence $C_N^{(\hat{\rho}_W)}$ (open triangles) based on quantum state tomography [27] and the concurrence C_N (filled circles) inferred from the measured degree of violation of the uncertainty bound specified with parameters $\{\Delta, \Delta_b^{(1)}\}$ (Fig. 8.2, Eq. 8.20). The red curve shows the theoretical prediction of concurrence as a function of the two-photon component y_c based on a model in ref. [34]. The errors in C_N reflect the 1σ-statistical uncertainties and the error bars for the measured concurrence $C_N^{(\hat{\rho}_W)}$ are not shown for clarity. The precise correspondence between $C_N^{(\hat{\rho}_W)}$ and C_N validates the use of Eq. 8.20.

8.11 Constructing the projective operators for the uncertainty relations

In the presence of transmission losses $\{\eta, \eta'\}$ and imbalanced beamsplitter ratios $\{\alpha, \alpha'\}$ in the verification interferometers shown in Fig. 8.9, the projectors no longer correspond to the pure state descriptions $\hat{M}_i = |W_i\rangle\langle W_i|$ in Eq. 8.2 (ref. [38], chapter 7). Using the standard technique for loss propagations and beamsplitter transformations [193], the original projectors $|W_i\rangle\langle W_i|$ become mixed states of the following form,

$$|W_i\rangle\langle W_i| \mapsto (1 - q_1^{(i)})|0000\rangle\langle 0000| + q_1^{(i)}|\Pi_i\rangle\langle\Pi_i|, \tag{8.21}$$

where $q_1^{(i)}$ gives the probability of a successful projective measurement in mode i for an entangled state $|\Pi_i\rangle$, $|0000\rangle\langle 0000|$ is the vacuum state, and $|\Pi_i\rangle\langle\Pi_i|$ is a pure state containing a single-photon shared among four optical modes (ref. [38], chapter 7). In the case of a conditional measurement (i.e., post-selecting the cases where we find a single-excitation among the four outputs of the cascaded beamsplitters in Fig. 8.1c), $|\Pi_i\rangle\langle\Pi_i|$ describes the projective measurement for the output mode i, $\hat{M}_i = |\Pi_i\rangle\langle\Pi_i|$. Unlike the original projectors $|W_i\rangle$ in Eq. 8.2, these projectors $|\Pi_i\rangle$ may not be orthogonal, but they span the single-photon subspace $\hat{\rho}_1$ of the physical state $\hat{\rho}_W$.

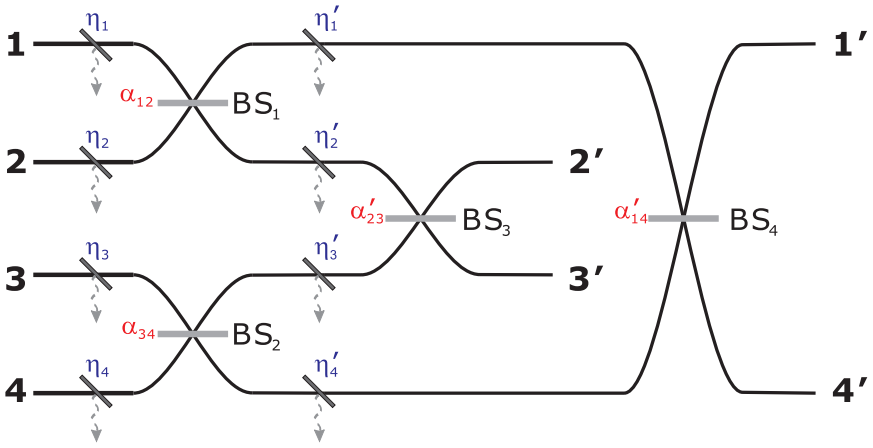

Figure 8.9: **A simplified setup for the verification protocol (sum uncertainty).** The setup includes differential transmission efficiencies $\{\eta, \eta'\}$ (blue) and imbalanced beam-splitter ratios $\{\alpha, \alpha'\}$ (red). The wiggly dashed arrows correspond to the auxiliary output modes which are traced over for loss propagation.

Generally, any imbalances (whether they are due to differential losses or beamsplitter ratios) in the verification interferometers cause reductions of the overlaps $|\langle W_i|\Pi_i\rangle|^2$ between projectors $|W_i\rangle$ and $|\Pi_i\rangle$, thereby making the protocol less sensitive to entanglement in $\hat{\rho}_W$ (ref.[38], section 7.6.1). In practice, the corrected bounds $\Delta_b^{(K)}$ always decrease towards smaller two-photon component y_c from the ideal lossless and balanced case, as shown for our experimental parameters $\{\eta, \eta'\}$ and $\{\alpha, \alpha'\}$ in Fig. 8.4. Furthermore, the uncertainties in the measurement of $\{\eta, \eta'\}$ and $\{\alpha, \alpha'\}$ cause an uncertainty in the determination of the bounds $\Delta_b^{(K)}$.

Fig. 8.9 depicts the setup for our verification protocol indicating the losses $\{\eta, \eta'\}$ and beamsplitter ratios $\{\alpha, \alpha'\}$ of the interferometers. Experimental parameters and their uncertainties for $\{\eta, \eta'\}$ and $\{\alpha, \alpha'\}$ are shown in Table 8.1. In our data analysis, we infer the photon statistics of modes $\{1', \cdots, 4'\}$ in $\hat{\rho}_{\text{out}}$ at the outputs of the verification interferometers from the measured photodetection statistics at detectors $\{D_1, \cdots, D_4\}$. Thus, we exclude the losses corresponding to the output paths of the verification interferometers from our analysis. The small imbalances between the terms $\{\alpha, \alpha'\}$ and $\{\eta, \eta'\}$ in Table 8.1 contribute to the small correction of the theoretical bounds $\Delta_b^{(K)}$ from the ideal projectors $|W_i\rangle$ to non-ideal projectors $|\Pi_i\rangle$. To understand the small corrections of $\Delta_b^{(K)}$ from $|W_i\rangle$ to $|\Pi_i\rangle$ for our parameters, we investigate the effect of $\{\eta, \eta'\}$ and $\{\alpha, \alpha'\}$ on the bound $\Delta_b^{(3)}$ for states containing at most tripartite entanglement for a fixed two-photon contamination $y_c = 0.035$, corresponding to the lowest measured y_c in our experiment.

Table 8.1: **Experimental parameters and their uncertainties for beamsplitter ratios $\{\alpha, \alpha'\}$ and transmission efficiencies $\{\eta, \eta'\}$ of the verification interferometers.** The systematic uncertainties $(\delta\kappa)$ of $\{\kappa\}$ are fractionally $(\delta\kappa/\kappa) = 5\%$ for $\kappa \in \{\alpha, \alpha', \eta, \eta'\}$. Note that $\alpha_{12} \simeq \alpha_{34} \simeq \alpha'_{14} \simeq \alpha'_{23}$. The absolute differences in the pairs of transmission efficiencies ($\{\eta_1, \eta_2\}$,$\{\eta_3, \eta_4\}$,$\{\eta'_1, \eta'_4\}$, $\{\eta'_2, \eta'_3\}$) influence the correction to $\Delta_b^{(K)}$.

α_{12}	α_{34}	α'_{23}	α'_{14}	η_1	η_2	η_3	η_4	η'_1	η'_4	η'_2	η'_3
0.5	0.53	0.52	0.53	0.57	0.57	0.52	0.56	0.67	0.66	0.62	0.66

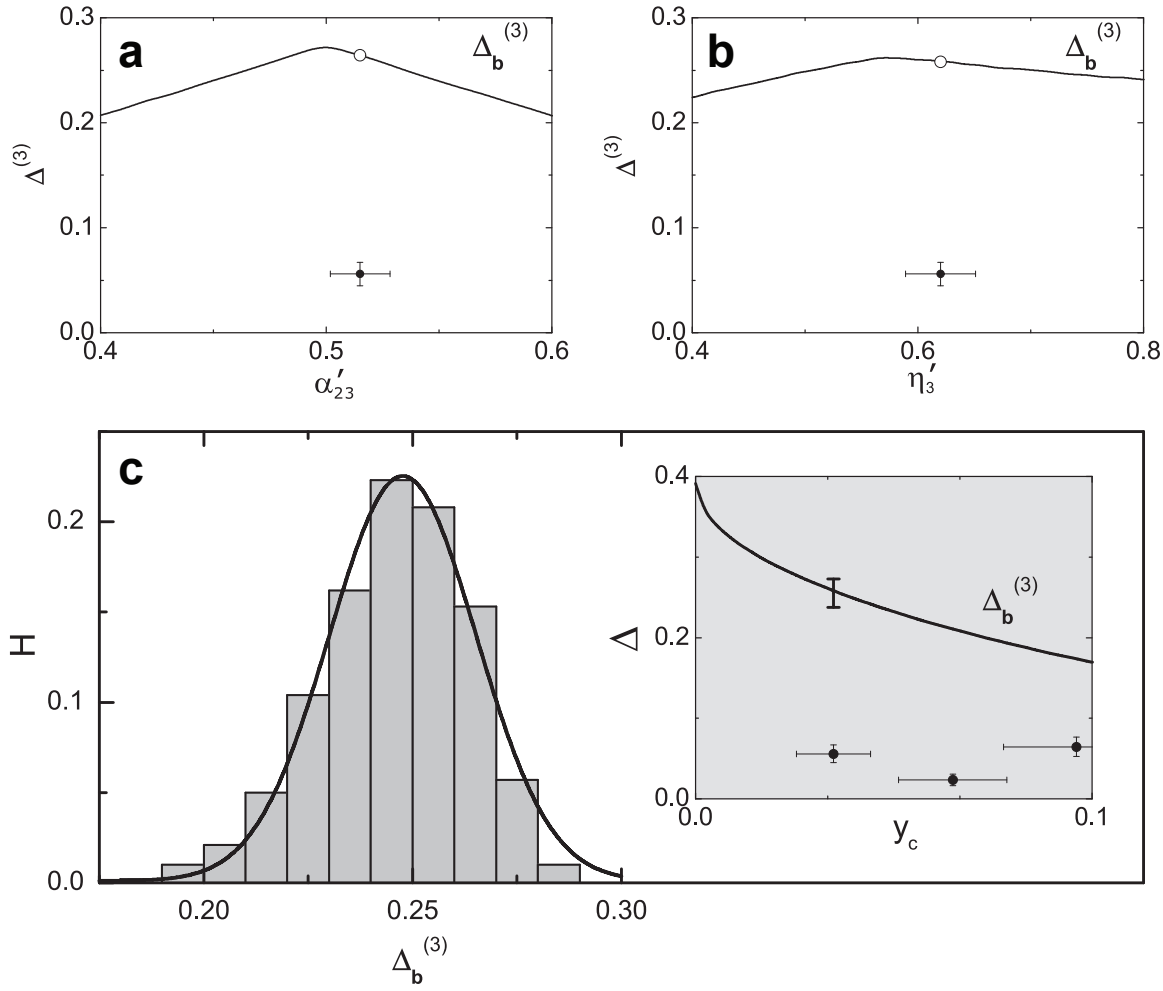

Figure 8.10: **The effect of imbalances and losses to the determination of $\Delta_b^{(3)}$.** Scanning the boundary $\Delta_b^{(3)}$ for states containing at most three-mode entanglement as a function of **a**, the beamsplitter ratio α'_{23} (shown as a black line), and **b**, the transmission efficiency η'_3 (shown as a black line) at $y_c = 0.035$, which corresponds to the lowest two-photon contamination measured in Fig. 8.4. The measured Δ at $y_c = (3.5 \pm 0.9) \times 10^{-2}$ is shown as a filled circle, with a horizontal error indicating the systematic uncertainty in estimating **a**, α'_{23} and **b**, η'_3, respectively. The vertical error is the statistical uncertainty for the measured Δ. **c**, Histogram $H(\Delta_b^{(3)})$ of the three-mode boundary $\Delta_b^{(3)}$ by repeating the calculations from randomly drawn sets of the transmission efficiencies $\{\eta, \eta'\}$ and beamsplitter ratios $\{\alpha, \alpha'\}$ at $y_c = 0.035$. The histogram is fitted to a Gaussian function (shown as a black line) with $(1/e)$ half-width $\delta\Delta_b^{(3)} = 0.018$. The uncertainty $\delta\Delta^{(3)}$ is determined by the joint distribution of $\{\alpha, \alpha'\}$ and $\{\eta, \eta'\}$. Here, we assume independent normal distributions for the individual parameters in $\{\alpha, \alpha'\}$ and $\{\eta, \eta'\}$. (Inset) Confidence level in the violation of the inequality $\Delta \geq \Delta_b^{(3)}$ for the three-mode bound $\Delta_b^{(3)}$. Experimentally measured Δ are shown as filled circles, and the black line indicates the the three-mode bound $\Delta_b^{(3)}$, along with its uncertainty for $y_c = 0.035$. The large suppression of Δ from $\Delta_b^{(3)}$ compared to the uncertainty $\delta\Delta_b^{(3)}$ for the bound affirms the unambiguous detection of genuine four mode entanglement.

Figs. 8.10a and 8.10b illustrate the processes of reductions in the three-mode boundary $\Delta_b^{(3)}$ at $y_c = 0.035$, due to **a**, imbalanced beamsplitter ratio (α'_{23}) and **b**, differential loss (η'_3), while leaving all other parameters in $\{\alpha, \alpha'\}$ and $\{\eta, \eta'\}$ fixed (Table 8.1). In particular, the correction ranges of $\Delta_b^{(3)}$ due to the

individual uncertainties of α'_{23} and η'_3 are small compared to the measured $\sim 20\,\sigma$ (standard deviation) suppression of the sum uncertainty Δ at $y_c = 0.035$ relative to $\Delta_b^{(3)}$ (shown as a filled circle in Fig. 8.10).

Finally, we discuss our analysis of the uncertainty $\delta\Delta_b^{(3)}$ in the bound $\Delta_b^{(3)}$ (Fig. 8.10c) due to the systematic uncertainties of all the parameters in $\{\alpha, \alpha'\}$ and $\{\eta, \eta'\}$. We construct the histogram H of $\Delta_b^{(3)}$ by iterating the calculation of $\Delta_b^{(3)}$ with randomly drawn sets of $\{\alpha, \alpha', \eta, \eta'\}$. Here, the parameters $\{\alpha, \alpha'\}$ and $\{\eta, \eta'\}$ are assumed to follow independent normal distributions, with their means and systematic uncertainties shown in Table 8.1. By fitting the histogram with a Gaussian distribution, we infer an uncertainty $\delta\Delta_b^{(3)} = 0.018$ and the center $\langle\Delta_b^{(3)}\rangle = 0.25$ for the boundary $\Delta_b^{(3)}$. These values should be compared to the measured $\Delta = (5.6 \pm 1.1) \times 10^{-2}$ at $y_c = (3.5 \pm 0.9) \times 10^{-2}$. As depicted in the inset of Fig. 8.10c, our measurement yields $\sim 9\,\sigma$ suppression of the uncertainty bound, reflecting the high confidence level in the violation of the bound $\Delta_b^{(3)}$. Our experiment, therefore, unambiguously verifies the presence of four-mode entanglement with the imbalances $(\{\alpha, \alpha'\}, \{\eta, \eta'\})$ in the verification interferometers.

Chapter 9

Entanglement of spin waves among four quantum memories

This chapter is largely based on ref. [33]. Reference [33] refers to the then current literature in 2010 at the time of publication.

9.1 Introduction

Diverse applications in quantum information science require coherent control of the generation, storage, and transfer of entanglement among spatially separated physical systems (refs. [1–6], see also chapter 1). Despite its inherently multipartite nature, entanglement has been studied primarily for bipartite systems [3], where remarkable progress has been made in harnessing physical processes to generate 'push-button' and 'heralded' entanglement (refs. [27–29,32,285,286], chapters 3–5), as well as to map entangled states to and from atoms, photons, and phonons (refs. [30,31], chapter 6).

For multipartite systems, the 'size' of a physical state, described by the system's density matrix $\hat{\rho}_N$, grows exponentially with the number of subsystems N and makes the entangled states exceedingly difficult to represent with classical information. Importantly, this complexity for $\hat{\rho}_N$ increases the potential utility of multipartite entanglement in quantum information science, including for quantum algorithms [2,3] and simulation [5]. Redundant encoding of quantum information into multipartite entangled states enables quantum error correction and fault-tolerant computation [2,3]. Intricate long-range correlation of many-body systems is intimately intertwined with the behavior of multipartite entanglement [39,40]. In addition, mobilizing multipartite entanglement across quantum networks could lead to novel quantum phase transitions for the network [6].

Counterposed to these opportunities, the complex structure of multipartite entanglement presents serious challenges both for its formal characterization and physical realization [3,40,110,208]. Indeed, there are relatively few examples of laboratory systems that have successfully generated multipartite entanglement [35,275–277,287,288]. Most works have considered the entanglement for spin systems, notably trapped ions [275,276], which are applicable to the matter nodes of quantum networks. But the methodologies for verifying multipartite entangle-

ment are problematic for the infinite-dimensional bosonic systems of the quantum channels (e.g., multipartite quadrature[287,288] and number-state[35] entanglement for optical modes (chapter 8)). *A posteriori* multipartite entanglement has been inferred from a small subset of preferred detection events of photons from parametric down-conversion[277].

In addition to the characterization of multipartite entanglement, an important capability for quantum networks is provided by quantum interfaces capable of generating, storing, and dynamically allocating the entanglement of matter nodes into photonic channels (see ref.[104] and references therein). In this chapter, as illustrated in Fig. 9.1a, we introduce such a quantum interface for quadripartite entangled states based upon coherent, collective emission from matter to light. We present a systematic study of the generation and storage of quadripartite entangled states of spin-waves in a set of four nodes of atomic memories, as well as of the coherent transfer of the entangled components of the material state into individual photonic channels. We observe transitions of M to $(M-1)$-partite entangled states via controlled spin-wave statistics of the atomic memories, as well as the dynamic evolution of multipartite entanglement in a dissipative environment, from fully quadripartite entangled to unentangled.

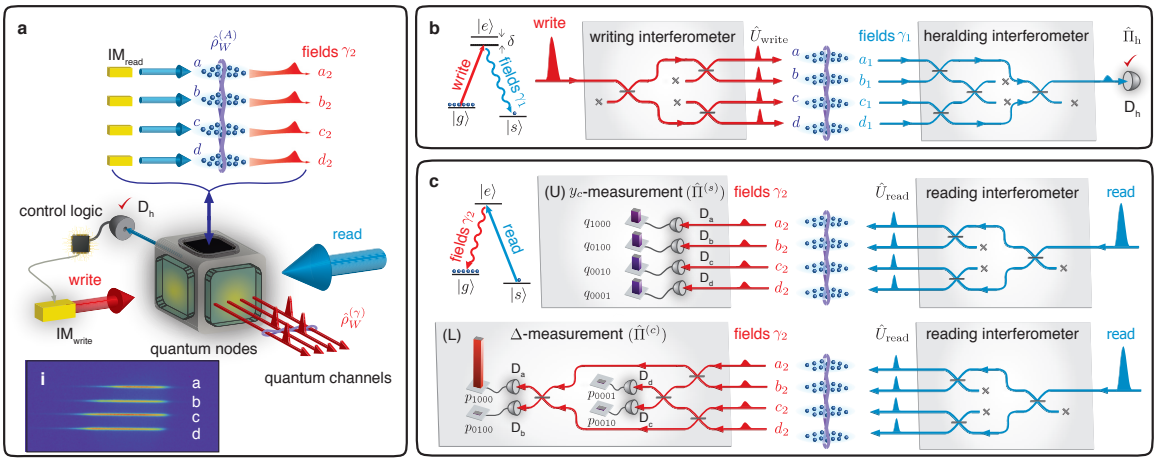

Figure 9.1: **Overview of the experiment. a,** Quantum interfaces for multipartite quantum networks. Inset **i**, a fluorescence image of the laser-cooled atomic ensembles $\{a, b, c, d\}$ that become entangled (section 9.9). **b,** Entanglement generation. A weak write laser is split into four components to excite the atomic ensembles via parametric interactions $\hat{U}_{\text{write}}$ (chapter 2), leading to Raman scattered fields $\gamma_1 = \{a_1, b_1, c_1, d_1\}$ emitted by the ensembles. Entangled state $\hat{\rho}_W^{(A)}$ for four atomic ensembles $\epsilon = \{a, b, c, d\}$ (Eq. 9.1) is heralded by a projective measurement $\hat{\Pi}_h$ at detector D_h, derived from quantum interference of four fields γ_1 in the heralding interferometer. **c,** Quantum-state exchange and entanglement verification. Read lasers are applied to the ensembles to coherently transform the atomic entangled state $\hat{\rho}_W^{(A)}$ into quadripartite entangled beams of light $\hat{\rho}_W^{(\gamma)}$ (Eq. 9.2) via quantum-state transfers, $\hat{U}_{\text{read}}$ (chapter 2), with each beam propagating through quantum channels $\gamma_2 = \{a_2, b_2, c_2, d_2\}$. (U) Upper panel for y_c-measurement—The quantum statistics $\{q_{ijkl}\}$ for the individual modes of $\hat{\rho}_W^{(\gamma)}$ with $i, j, k, l \in \{0, 1\}$ photons are measured with projectors $\{\hat{\Pi}_i^{(s)}\}$ at detectors $D_{a,b,c,d}$. (L) Lower panel for Δ-measurement—Mutual coherences for $\hat{\rho}_W^{(A)}$ are accessed with projectors $\{\hat{\Pi}_i^{(c)}\}$ from detection statistics $\{p_{ijkl}\}$ at $D_{a,b,c,d}$. Further details are given in section 9.12.

9.2 Quantum interface between light and matter for quadripartite entangled states

Our experiment proceeds in four steps (see section 9.10). First, in step (1) an entangled state $\hat{\rho}_W^{(A)}$ of four atomic ensembles is generated by quantum interference in a quantum measurement[4,27] (Fig. 9.1b). Given a photoelectric detection event at D_h, the conditional atomic state is ideally a quadripartite entangled state $\hat{\rho}_W^{(A)} = |W\rangle_A\langle W|$ with

$$|W\rangle_A = \tfrac{1}{2}[(|\overline{s}_a, \overline{g}_b, \overline{g}_c, \overline{g}_d\rangle + e^{i\phi_1}|\overline{g}_a, \overline{s}_b, \overline{g}_c, \overline{g}_d\rangle) + e^{i\phi_2}(|\overline{g}_a, \overline{g}_b, \overline{s}_c, \overline{g}_d\rangle + e^{i\phi_3}|\overline{g}_a, \overline{g}_b, \overline{g}_c, \overline{s}_d\rangle)], \tag{9.1}$$

whose single quantum spin-wave $|\overline{s}_\epsilon\rangle$ is coherently shared among four ensembles $\epsilon = \{a, b, c, d\}$. These entangled states are known as W-states, comprised of atomic ground states $|\overline{g}_\epsilon\rangle = |g\cdots g\rangle_\epsilon$ and single collective excitations $|\overline{s}_\epsilon\rangle = \frac{1}{\sqrt{N_{A,\epsilon}}}\sum_{i=1}^{N_{A,\epsilon}}|g\cdots s_i\cdots g\rangle_\epsilon$, where $N_{A,\epsilon}$ is the number of atoms in ensemble ϵ.

After the heralding event, step (2) consists of storage of $\hat{\rho}_W^{(A)}$ in the ensembles for a user-controlled time τ. At the end of this interval, step (3) is initiated with read beams to coherently transfer the entangled atomic components of $\hat{\rho}_W^{(A)}$ into a quadripartite entangled state of light $\hat{\rho}_W^{(\gamma)} = |W\rangle_\gamma\langle W|$ via cooperative emissions[4] (Fig. 9.1c), where

$$|W\rangle_\gamma = \frac{1}{2}[(|1000\rangle + e^{i\phi_1'}|0100\rangle) + e^{i\phi_2'}(|0010\rangle + e^{i\phi_3'}|0001\rangle)]. \tag{9.2}$$

This photonic state is a mode-entangled W-state (refs.[35,38], chapters 7–8), which shares a single delocalized photon among four spatially separated optical modes $\gamma_2 = \{a_2, b_2, c_2, d_2\}$.

9.3 Characterization of quadripartite entangled states via quantum uncertainty relations

Finally, in step (4) we characterize the heralded entanglement for $\hat{\rho}_W^{(\gamma)}$ from complementary measurements of photon statistics and coherence[35,38] (Fig. 9.1c) via the techniques developed in chapters 7–8. In particular, we consider a reduced density matrix $\hat{\rho}_r = p_0\hat{\rho}_0 + p_1\hat{\rho}_1 + p_{\geq 2}\hat{\rho}_{\geq 2}$ containing up to one photon per mode, which leads to a lower bound for the entanglement of the actual physical states $\{\hat{\rho}_W^{(A)}, \hat{\rho}_W^{(\gamma)}\}$. Here, $\{p_0, p_1, p_{\geq 2}\}$ are the probabilities for 0 and 1-photon $\hat{\rho}_{0,1}$, and higher-order subspaces $\hat{\rho}_{\geq 2}$, which can be populated for any realistic system. As illustrated in the upper panel of Fig. 9.1c, we characterize the statistical contamination for $\hat{\rho}_W^{(\gamma)}$ due to $\{\hat{\rho}_0, \hat{\rho}_{\geq 2}\}$ with a normalized measure[38], namely $y_c \equiv \frac{8}{3}\frac{p_{\geq 2}p_0}{p_1^2}$, ranging from $y_c = 0$ for a

single excitation to $y_c = 1$ for balanced coherent states, by detecting the photon statistics q_{ijkl} of γ_2 at the output faces of the ensembles.

We also quantify the mutual coherences for $\hat{\rho}_W^{(\gamma)}$ by measuring photon probabilities $\{p_{1000}, p_{0100}, p_{0010}, p_{0001}\}$ at the outputs of the verification (v) interferometer. We determine the sum uncertainty $\Delta \equiv \sum_{i=1}^{N=4} \langle(\hat{\Pi}_i^{(c)})^2 - \langle\hat{\Pi}_i^{(c)}\rangle^2\rangle$ for the variables $\{\hat{\Pi}_i^{(c)}\} = \{|W_i\rangle_v\langle W_i|\}$, which project $\hat{\rho}_r$ onto a set of four orthonormal W-states $\{|W_i\rangle_v\}$ with phases $\{\beta_1, \beta_2, \beta_3\}_v$ selected by the actively stabilized paths in the verification interferometer (section 9.12.2). Hence, for the ideal W-state (Eq. 9.2) with $\beta_i = \phi_i'$, we have $\Delta = 0$ associated with $p_{1000} = 1$ and $p_{0100} = p_{0010} = p_{0001} = 0$, as observed in the bar plots of the lower panel of Fig. 9.1c for $y_c = 0.04 \pm 0.01$. In contrast, mixed states with no phase coherences would result in balanced probabilities ($p_{1000} = p_{0100} = p_{0010} = p_{0001} = 1/4$) and $\Delta = 0.75$.

The pair $\{\Delta, y_c\}$ thereby defines the parameter space for the multipartite entanglement employed in our experiment, with the entanglement parameters $\{\Delta, y_c\}$ serving as a nonlocal, nonlinear entanglement witness (ref.[38], chapter 7). Our criterion for 'genuine' M-partite entanglement takes the most stringent form of nonseparability[208] and excludes all weaker forms of entanglement (section 9.13). Specifically, for a given value of y_c, we determine the boundary $\Delta_b^{(M-1)}$ for the minimal uncertainty possible for all states containing at most $(M-1)$-mode entanglement and their mixtures (section 9.13.3). For our quadripartite states $N = 4$, we derive $\{\Delta_b^{(3)}, \Delta_b^{(2)}, \Delta_b^{(1)}\}$ for tripartite, bipartite entangled, and fully separable states, as functions of y_c. Thus, a measurement of quantum statistics y_c and the associated coherence Δ with $\Delta < \Delta_b^{(1,2,3)}$ manifestly confirms the presence of genuine $M = 4$ partite entanglement (refs.[35,38], chapters 7–8). Furthermore, we can unambiguously distinguish genuine M and $(M-1)$-partite entangled states for any $M \leq N$ by observing Δ below $\Delta_b^{(M-1)}$.

9.4 Quadripartite entanglement among four atomic ensembles

Fig. 9.2 presents our results for quadripartite entanglement for storage time $\tau_0 = 0.2$ μs. We first investigate off-diagonal coherence for the purportedly entangled atomic and photonic states, $\{\hat{\rho}_W^{(A)}, \hat{\rho}_W^{(\gamma)}\}$, in Fig. 9.2a. As the bipartite phase β_2 is varied, we observe interferences in $\{p_{1000}, p_{0100}, p_{0010}, p_{0001}\}$, and hence a variation in Δ, that results from the coherence between the bipartite entangled components of $\hat{\rho}_W^{(\gamma)}$ for the modes $\{a_2, b_2\}$ and $\{c_2, d_2\}$. Furthermore, for optimal settings of β_2, the observed values of Δ (black points) fall below the bounds $\{\Delta_b^{(3)}, \Delta_b^{(2)}, \Delta_b^{(1)}\}$ (red, green, purple bands) for $y_c = 0.06 \pm 0.02$, and signal the generation of a fully quadripartite entangled state. The observed quadripartite entanglement arises from the intrinsic indistinguishability of probability amplitudes for one collective excitation $|\overline{s}_\epsilon\rangle$ among the four ensembles. We also present results from a control experiment with a 'crossed' state $\hat{\rho}_\times^{(A)}$ (orange points) that consists of an incoherent mixture of entangled pairs $\{a, b\}$ and $\{c, d\}$ (see section 9.5.1).

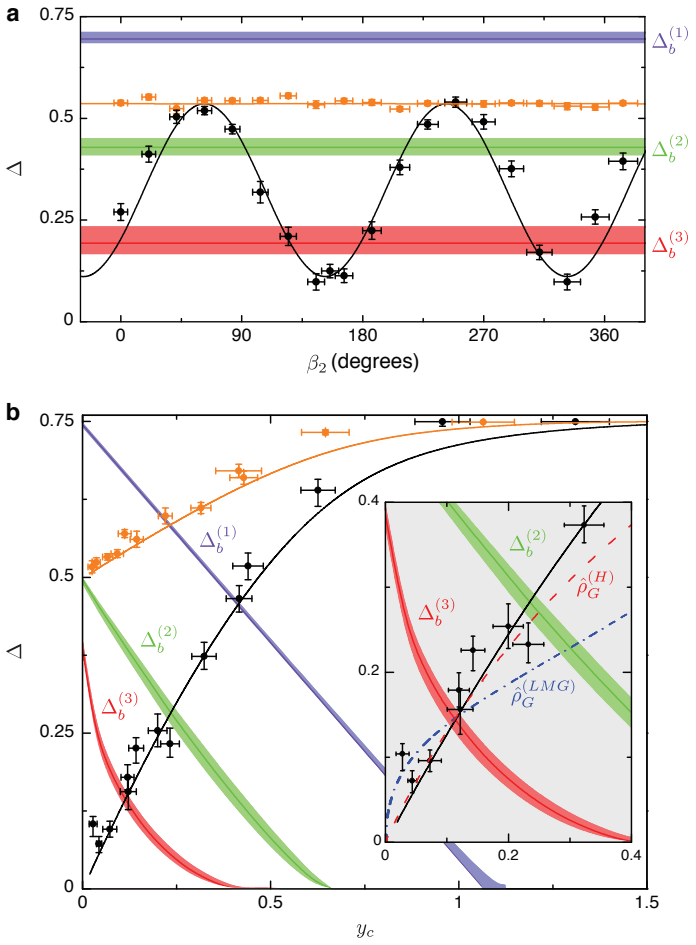

Figure 9.2: **Quadripartite entanglement among four atomic ensembles. a,** Quantum interference between the bipartite entangled pairs of the full quadripartite state (black points) as a function of bipartite phase β_2. **b,** Exploring the entanglement space $\{\Delta, y_c\}$ for quadripartite states. By controlling the spin-wave statistics, we observe transitions from quadripartite, to tripartite, to bipartite entangled states, and to fully separable states (black points). We also display our results for the 'crossed' quantum state $\hat{\rho}_{\times}^{(A)}$ (orange points), as further discussed in section 9.5.1. Inset, expanded view of entanglement parameters $\{\Delta, y_c\}$. Results for entanglement thermalization $\{\Delta^{(T)}, y_c^{(T)}\}$ of the spin systems $\hat{\rho}_G^{(\mathrm{H})}$ ($\hat{\rho}_G^{(\mathrm{LMG})}$) are shown by the red dashed (blue dash-dotted) line. The red, green, and purple bands represent the minimum uncertainties for 3-mode ($\Delta_b^{(3)}$) and 2-mode entanglement ($\Delta_b^{(2)}$), and for fully separable states ($\Delta_b^{(1)}$), with thicknesses of the bands from the central lines corresponding to ± 1 s.d. of the bounds $\{\Delta_b^{(3)}, \Delta_b^{(2)}, \Delta_b^{(1)}\}$ (section 9.13.3). In all cases, error bars for the data reflect the statistical and systematic uncertainties, as further detailed in section 9.13.4.

9.5 Statistical transitions for multipartite entangled spin waves

Next, we characterize $\hat{\rho}_W^{(\gamma)}$ (and $\hat{\rho}_W^{(A)}$) over the full parameter space $\{\Delta, y_c\}$. In a regime of weak excitation ($\xi \ll 1$) for the ensemble-field pairs $\{\epsilon, \gamma_1\}$, the heralded state $\hat{\rho}_W^{(A)}$ is approximately

$$\hat{\rho}_W^{(A)}(\tau = 0) \simeq (1 - 3\xi)|W\rangle_A\langle W| + 3\xi\hat{\rho}_{\geq 2}^{(A)} + \mathcal{O}(\xi^2), \tag{9.3}$$

where $\hat{\rho}_{\geq 2}^{(A)}$ includes uncorrelated spin-waves with two or more quanta in the set of four ensembles due to atomic noise. For $\xi \to 0$, a heralding event at D_h leads to a state with high fidelity to $|W\rangle_A$ stored in the four ensembles. However, for increasing ξ, $\hat{\rho}_{\geq 2}^{(A)}$ becomes important, leading to modifications of the spin-wave statistics for $\hat{\rho}_W^{(A)}$ and thereby to the entanglement parameters $\{\Delta^{\text{th}}, y_c^{\text{th}}\}$. Hence, by varying ξ via the overall intensity for the write beam, we adjust the quantum statistics y_c and coherence Δ of the entangled states $\{\hat{\rho}_W^{(A)}, \hat{\rho}_W^{(\gamma)}\}$.

This procedure is employed in Fig. 9.2b to parametrically increase $\{\Delta, y_c\}$ in tandem. As y_c is raised from $y_c \simeq 0$ in the quantum domain to the classical regime with $y_c \simeq 1$, we observe transitions of the directly measured photonic states $\hat{\rho}_W^{(\gamma)}$ (black points) from fully quadripartite entangled ($\Delta < \Delta_b^{(3)}$) to tripartite entangled ($\Delta_b^{(3)} < \Delta < \Delta_b^{(2)}$), to bipartite entangled ($\Delta_b^{(2)} < \Delta < \Delta_b^{(1)}$), and finally to fully separable states ($\Delta_b^{(1)} < \Delta$). As shown by the curves, our observations correspond well to a theoretical model for entanglement generation, transfer, and verification (see section 9.14). In comparison to our former work on coherent splitting of a photon[35] in chapter 8, the heralded atomic and photonic W-states $\{\hat{\rho}_W^{(A)}, \hat{\rho}_W^{(\gamma)}\}$ offer qualitatively richer statistical passages through the entanglement spaces delineated by $\{\Delta, y_c\}$. Here, the quantum coherence Δ is intrinsically linked to the statistical character y_c due to quantum correlations between the heralding fields γ_1 and the excitation statistics of the ensembles.

For $\xi \ll 1$, the coherent contribution $\hat{\rho}_c^{(A)}$ of the delocalized single quantum strongly dominates over any other processes for the full quadripartite state $\hat{\rho}_W^{(A)}$ in Eq. 9.3. With a heralding probability $p_h \simeq 3 \times 10^{-4}$ ($\xi \simeq 5 \times 10^{-3}$), we achieve the smallest entanglement parameters $\Delta^{\text{min}} = 0.07^{+0.01}_{-0.02}$ and $y_c^{\text{min}} = 0.038 \pm 0.006$ for the generated quadripartite entangled states. These parameters are suppressed below the closest 3-mode boundary $\Delta_b^{(3)}$ by ten standard deviations. Furthermore, because the local mapping of quantum states from matter to light cannot increase entanglement[27], our measurements of $\hat{\rho}_W^{(\gamma)}$ unambiguously provide a lower bound of the quadripartite entanglement stored in $\hat{\rho}_W^{(A)}$. Therefore, the observed strong violation of the uncertainty relations for $\{\Delta^{\text{min}}, y_c^{\text{min}}\}$ categorically certifies for the creation of measurement-induced entanglement of spin-waves among four quantum memories, as well as for the coherent transfer of the stored quadripartite entangled states to an entangled state of four propagating electromagnetic fields.

In terms of state fidelity, our approach for heralded multipartite entanglement generation compares favorably to matter systems utilizing local interactions (e.g., trapped ions[275,276]). Despite the intrinsically low preparation probability, the resulting quadripartite entangled state $\hat{\rho}_W^{(A)}$ stored in the four ensembles has high fidelity with the ideal W-state, namely $F^{(A)} = {}_A\langle W|\hat{\rho}_W^{(A)}|W\rangle_A$. As discussed in section 9.13.2, we estimate a lower bound for the unconditional entanglement fidelity $F^{(A)} \geq 0.9 \pm 0.1$, as compared to the theoretical fidelity $F_{\text{th}}^{(A)} = 0.98$ derived for the parameters in our experiment.

Apart from the creation of novel multipartite entangled spin-waves, an important benchmark of a quantum interface is the transfer efficiency λ of multipartite entanglement from matter to light[30]. Since no known measure applies to our case, we tentatively define the entanglement transfer $\lambda = F^{(\gamma)}/F^{(A)}$, with physical fidelity $F^{(\gamma)} = {}_\gamma\langle W|\hat{\rho}_W^{(\gamma)}|W\rangle_\gamma$ for the photonic state $\hat{\rho}_W^{(\gamma)}$. In particular for $\xi \ll 1$, we obtain $F_{\text{th}}^{(\gamma)} \simeq$

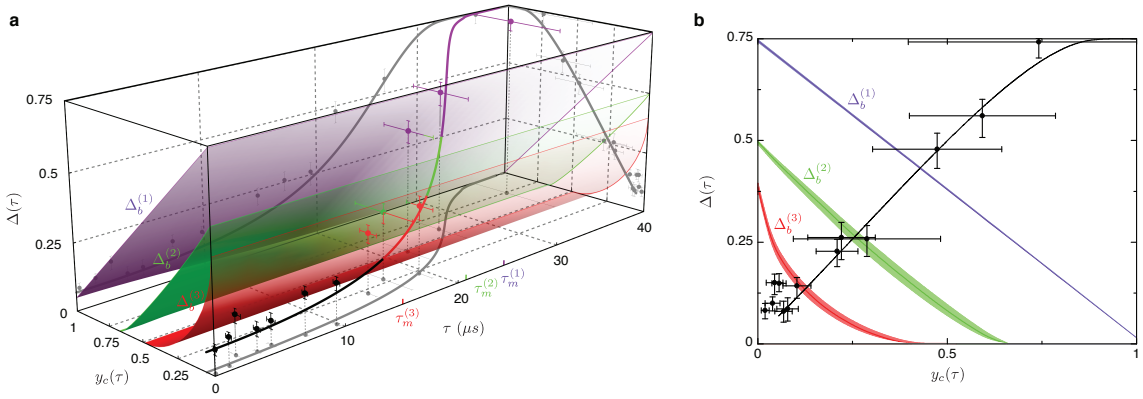

Figure 9.3: **Dissipative dynamics of atomic entanglement. a,** Dynamic evolution of entanglement parameters $\{\Delta(\tau), y_c(\tau)\}$ for the multipartite quantum state. We observe crossing of the boundaries defined by 3-mode (red surface, $\Delta_b^{(3)}$), 2-mode (green surface, $\Delta_b^{(2)}$) entangled states, and separable states (purple surface, $\Delta_b^{(1)}$). We indicate various entanglement orders for quadripartite (black), tripartite (red), bipartite entangled (green) states, and fully separable states (purple) for the data points and the curve. The projections of the data points into the planes (y_c, τ) and (Δ, τ) display the individual passages of $\{\Delta(\tau), y_c(\tau)\}$ (section 9.14.5). **b,** Projection of entanglement dynamics onto the (Δ, y_c) plane. The curves in **a** and **b** are from a theoretical model including motional dephasing. Error bars for the data represent the statistical and systematic uncertainties.

$\eta_{\text{read}} F_{\text{th}}^{(A)}$, which thereby gives $\lambda_{\text{th}} \simeq \eta_{\text{read}} = 38 \pm 4\%$ dictated by the retrieval efficiency η_{read}. While fidelity is an often used measure, we emphasize that $F^{(\gamma)}$ cannot be used to set a threshold for entanglement, since $\hat{\rho}_W^{(\gamma)}$ can exhibit multipartite entanglement for any $F^{(\gamma)} > 0$.

9.5.1 Generation and characterization of a 'crossed' quantum state

As a control experiment, we reconfigured the heralding interferometer such that path-information could in principle be revealed up to the bipartite split of the ensemble pairs $\{a, b\}$ and $\{c, d\}$ by analyzing the polarization state of the heralding photon γ_1. In this case, the heralding measurement $\hat{\Pi}_\times$ prepares a 'crossed' atomic state $\hat{\rho}_\times^{(A)}$ with no coherence shared between $\{a, b\}$ and $\{c, d\}$. Thus, we observe an absence of interference in Fig. 9.2a (orange points). However, this modified $\hat{\Pi}_\times$ preserves the bipartite entanglement within $\{a, b\}$ and $\{c, d\}$, which explains our observation of the uncertainty Δ reduced below the 1-mode bound $\Delta_b^{(1)}$ for $y_c = 0.07 \pm 0.01$. Similarly, we also detect the statistical transition of the bipartite entanglement to fully separable states for the 'crossed' state in Fig. 9.2b, despite the disentanglement for the physical bipartition (|) of $\{a, b\}|\{c, d\}$.

9.6 Dissipative dynamics of atomic entanglement

To investigate the dynamical behavior of the observed quadripartite entangled states, we study the temporal evolution of multipartite entanglement stored in the atomic ensembles as a function of a storage time τ.

Decoherence for the atomic W-state is governed by motional dephasing of spin-waves (ref.[82], chapter 2), in which the imprinted atomic phases in $|\overline{s}_\epsilon\rangle$ evolve independently due to thermal motion, thereby transforming the initial collective state into a subradiant state uncorrelated with the heralding fields γ_1 (section 9.14.5). The net effect is an increase of both entanglement parameters $\{\Delta, y_c\}$ with a time-scale $\tau_m \simeq 17\ \mu s$ (see section 9.9). Eventually, the growth in $\{\Delta(\tau), y_c(\tau)\}$ leads to time-dependent losses of entanglement, marked by successive crossings of the boundaries set by $\{\Delta_b^{(3)}, \Delta_b^{(2)}, \Delta_b^{(1)}\}$.

We examine the dissipative dynamics of multipartite entanglement for the quantum memories of four ensembles via the evolution of both $\{\Delta, y_c\}$ in Fig. 9.3a. We observe the passage of the initial quadripartite entangled state $\hat{\rho}_W^{(A)}(\tau_0)$ at $\tau_0 = 0.2\ \mu s$ through various domains, progressively evolving from M-partite entanglement to $(M-1)$-partite entanglement at memory times $\tau = \tau_m^{(M-1)}$, with the final state $\hat{\rho}_W^{(A)}(\tau_f)$ measured at $\tau_f = 36.2\ \mu$s. The crossings of the bounds $\{\Delta_b^{(3)}, \Delta_b^{(2)}, \Delta_b^{(1)}\}$ occur at $\tau_m^{(3)} = 15\ \mu s$, $\tau_m^{(2)} = 21\ \mu s$, and $\tau_m^{(1)} = 24\ \mu s$, respectively. In addition, the measured entanglement parameters evolve in qualitative agreement to the simulated dynamics derived for $\hat{\rho}_W^{(A)}(\tau)$ from our theoretical model (solid line), with deviations (especially for Δ_{th}) discussed in section 9.14.5. Fig. 9.3b displays the parametric losses of entanglement via $\{\Delta(\tau), y_c(\tau)\}$.

9.7 Thermalization of multipartite entanglement in quantum magnets

Finally, an interesting extension is to relate the characterization of multipartite entanglement via $\{\Delta, y_c\}$ to the relaxations of entanglement in quantum many-body systems[39,40]. We consider two ferromagnetic spin models (Heisenberg-like and Lipkin-Meshkov-Glick Hamiltonians $\hat{H}_{\text{H}}$, $\hat{H}_{\text{LMG}}$) as well as their thermal entanglement $\{\Delta^{(T)}, y_c^{(T)}\}$ (see section 9.15). Results of our analysis are shown in the inset of Fig. 9.2b by the red dashed (blue dash-dotted) lines for the Gibbs thermal equilibrium states $\hat{\rho}_G^{(\text{H})}$ ($\hat{\rho}_G^{(\text{LMG})}$) of $\hat{H}_{\text{H}}$ ($\hat{H}_{\text{LMG}}$). The statistical character of $\hat{\rho}_W^{(A)}$ for our system of four ensembles follows the thermalization of $\hat{\rho}_G^{(\text{H})}$ ($\hat{\rho}_G^{(\text{LMG})}$) for $y_c \lesssim 0.2$, whereby $\hat{\rho}_{\geq 2}^{(A)}$ is thermally populated. This comparison suggests that our method for entanglement characterization could be applied to access the link between off-diagonal long-range order and multipartite entangled spin-waves in thermalized quantum magnets[39,40].

9.8 Conclusion

In conclusion, our measurements explicitly demonstrate a coherent matter-light quantum interface for multipartite entanglement by way of the operational metric of quantum uncertainty relations (refs.[35,38,121], chapters 7–8). High-fidelity entangled spin-waves are generated in four spatially separated atomic ensembles and coherently transferred to quadripartite entangled beams of light. The quantum memories are individually addressable and can be readily read-out at different times for conditional control of entanglement[4], as applied in chapters 3–6. With recent advances by other groups, the short memory times obtained in Fig. 9.3 could be

improved beyond 1 s (section 9.11.1).

Further possibilities include the creation of yet larger multipartite entangled states with efficient scaling[4] for the realization of multipartite quantum networks. For example, quadripartite entangled states of ensemble sets $\{a, b, c, d\}$ and $\{a', b', c', d'\}$ could be extended by swapping between $\{a, a'\}$ to prepare a hexapartite entangled state for $\{b, b', c, c', d, d'\}$ (see section 9.11.1). Generalization of such processes will prepare a single macroscopic entangled state for observing entanglement percolation[6] and extreme non-locality of W-states[289,290], as well as for studying quantum phase transitions in strongly-correlated systems[39,40]. Finally, the entangled spin-waves can be applied for quantum metrology to detect a phase shift of π on an unknown component of $\hat{\rho}_W^{(A)}$ with efficiency beyond any separable state (see section 9.11.2).

9.9 Spin-wave quantum memory

The quantum information of the entangled state for Eq. 9.1 is encoded in the quantum numbers of spin-waves (collective excitations) for the pseudo-spin of the hyperfine ground electronic levels $6S_{1/2}$ ($F = 3, F = 4$) in atomic cesium. The fluorescence images shown in the inset of Fig. 9.1a depict the collective atomic modes of ensembles $\epsilon = \{a, b, c, d\}$ for exciting the entangled spin-waves $\hat{\rho}_W^{(A)}$ with 1 mm separations and 60 μm waists. The geometry of the collective excitations for the four ensembles $\{a, b, c, d\}$ is defined by the point-spread functions of the imaging systems for the fields $\{\gamma_1, \gamma_2\}$, within a cold cloud of $N_{A,\epsilon} \approx 10^6$ cesium atoms (chapter 2). We use an off-axial configuration[75] for individually addressing each ensemble ϵ with an angle $\theta = 2.5^\circ$ between the classical and nonclassical beams (section 9.12.1), that creates spin-waves $|\overline{s}_\epsilon\rangle$ associated with wave-numbers $\delta\vec{k} = \vec{k}_{\text{write}} - \vec{k}_{\gamma_1}$ for each ϵ. These spin-waves are analogous to other types of collective excitations in many-body systems, such as magnons and plasmons, and the spin-waves can be converted to dark-state polaritons for the coherent transfer $\hat{U}_{\text{read}}$ of entanglement (chapter 2). For the phase-matching configuration and temperature of our ensembles, the memory times $\{\tau_m^{(3)}, \tau_m^{(2)}, \tau_m^{(1)}\}$ in Fig. 9.3 are dominantly determined by the motional dephasing of the spin-waves $|\overline{s}_\epsilon\rangle$ (ref.[82], chapter 2). With thermal velocity of $v_t \simeq 14$ cm/s, we estimate a memory time $\tau_m \simeq \frac{0.85\,\mu m}{4\pi \sin(\theta/2) v_t} = 17\ \mu s$. On the other hand, the ground-state dephasing due to inhomogeneous broadening is expected to be $> 50\ \mu s$ in our experiment, inferred from two-photon Raman spectroscopy (chapter 2).

9.10 Operating the quantum interface

For the quantum interface to function during the 3 ms window, in step (1) 20-ns writing (red-detuned $\delta = 10$ MHz from $|g\rangle - |e\rangle$ transition) and 100-ns repumping (resonant with $|s\rangle - |e\rangle$) pulses are applied sequentially to the ensembles ϵ, synchronized to a clock running at $R_c \simeq 2$ MHz. This process creates pairwise correlated excitations[4] between the collective atomic modes $|\overline{s}_\epsilon\rangle$ of the ensembles ϵ and the optical fields γ_1 ($\delta = 10$ MHz below $|s\rangle - |e\rangle$). Photodetection of a single photon for the combined fields γ_1 at the output

of the heralding interferometer effectively erases the which-path information for γ_1, and imprints the entangled spin-wave $\hat{\rho}_W^{(A)}$ (Eq. 9.3) onto the ensembles $\{a, b, c, d\}$ via $\mathrm{Tr}_h(\hat{\Pi}_h \hat{U}_{\text{write}}^{\dagger} \hat{\rho}_g^{(A)} \hat{U}_{\text{write}})$. The heralding event at D_h triggers control logic in Fig. 9.1a which deactivates intensity modulators of the writing (IM_{write}), repumping and reading lasers (IM_{read}) for the quantum storage of $\hat{\rho}_W^{(A)}$ in step (2). After a user-controlled delay τ, step (3) is initiated with 20-ns-strong read pulses (Rabi frequency 24 MHz, resonant with $|s\rangle - |e\rangle$) that address the ensembles in Fig. 9.1c and coherently transfer the entangled atomic components $\{a, b, c, d\}$ of $\hat{\rho}_W^{(A)}(\tau)$ one-by-one to propagating beams $\gamma_2 = \{a_2, b_2, c_2, d_2\}$, comprising the entangled photonic state $\hat{\rho}_W^{(\gamma)}(\tau)$, via the operation $\hat{\rho}_W^{(\gamma)} = \mathrm{Tr}_A(\hat{U}_{\text{read}}^{\dagger} \hat{\rho}_W^{(A)} \hat{U}_{\text{read}})$. Here, Tr_A traces over the atomic systems which are later shelved into the ground states $|\overline{g}_\epsilon\rangle$. The retrieval efficiency η_{read} is collectively enhanced for large N_A (ref.[4]), leading to $\eta_{\text{read}} = 0.38 \pm 0.06$ in our experiment. The average production rate for the atomic quadripartite entanglement with $\{\Delta^{\min}, y_c^{\min}\}$ is $r_p = R_c D_c p_h \simeq 60$ Hz, while the actual rate during the 3 ms operating window is $r_q = R_c p_h \simeq 500$ Hz. The atomic level diagrams for entanglement generation and quantum-state exchanges are shown as insets to Figs. 9.1b and 9.1c. States $|g\rangle$, $|s\rangle$ are hyperfine ground states $F = 4$, $F = 3$ of $6S_{1/2}$ in atomic cesium; state $|e\rangle$ is the hyperfine level $F' = 4$ of the electronic excited state $6P_{3/2}$.

9.11 Prospects and discussion

9.11.1 Improving memory time and matter-light transfer efficiency

By operating the clock speed at $R_c \to 10$ MHz and $\tau_m^{(3)} \approx 20\ \mu s$, we could prepare hexapartite ($M = 6$) entanglement with probability $3z\eta_{\text{read}} p_h^2/8 \approx 10^{-5}$ by connecting two quadripartite states $\hat{\rho}_W^{(A)}$ for $\{\Delta^{\min}, y_c^{\min}\}$, with enhancement factor $z = 400$ (ref.[36]), thereby giving a local production rate of $r_q \approx 50 - 100$ Hz, or an average rate $r_p \approx 5 - 10$ Hz with our current duty cycle D_c. The most challenging aspect of verifying the hexapartite entangled states is the quantification of the higher-order contamination $\hat{\rho}_{\geq 2}$, which we estimate ~ 1 event per 10 hr. This integration rate is feasible with our current system. More generally, M_1 and M_2-partite entangled states can be fused together by entanglement connection to create a $M = (M_1 + M_2 - 2)$-partite entangled state. However, the memory times $\{\tau_m^{(3)}, \tau_m^{(2)}, \tau_m^{(1)}\}$ in Fig. 9.3 and the entanglement transfer λ from matter to light limit our capability to scale the multipartite entanglement beyond $M > 6$ by way of conditional control and connection of entanglement[36,37] with our current experimental parameters (chapters 4–5).

The prerequisite storage techniques for suppressing both the internal and motional spin-wave dephasings can be extended for τ_m with advances in ensemble-based quantum memories[48,114,115]. Recent experiments with single ensembles have achieved coherence times up to $\tau_m \simeq 1.5$ seconds in quantum degenerate gases[116,117] albeit with efficiencies $\lesssim 1\%$. The transfer efficiency can also be increased to $\lambda_{\text{th}} \simeq 0.9$ by enclosing the ensembles with high finesse cavities[82]. System integrations by way of atom-chip technology

and waveguide coupling [133,291] hold great potential for scalability given the strong cooperativity and the long coherence [292]. At this level, two or more heralded processes of multipartite entanglement generations can be made 'on-demand' on time scales of $\tau_{\text{det}} \sim \frac{1}{R_c p_h} = 1$ ms, with $\tau_m \gg \tau_{\text{det}}$ (refs. [36,37], chapters 4–5).

Realistically, the expansion of multipartite entangled states $\hat{\rho}_W^{(A)}$ will be limited by the intrinsic degradations of the entanglement parameters $\{\Delta, y_c\}$, that inevitably increase with each step of entanglement connection (ref. [37], chapter 5), and by the specific quantum repeater architecture implemented on $\hat{\rho}_W^{(A)}$. The latter is an extremely rich area of research in view of the large classes of methods for connecting multipartite entangled states, making it premature to specify a particular architecture for multipartite entanglement expansion. However, our experiment will hopefully stimulate theoretical studies of complex repeater architectures for multipartite systems, beyond traditional one-to-one networks [49].

9.11.2 Quantum-enhanced parameter estimation with entangled spin-waves

We describe a quantum-enhanced parameter estimation protocol whereby a phase shift on a single ensemble ϵ_i of the quadripartite state $\epsilon_i \in \{a, b, c, d\}$ can be detected with efficiency beyond that for any separable state. Specifically, we consider a π-phase shift $\hat{U}_{\pi,\epsilon_i} = \exp(i\pi\hat{n}_{\epsilon_i})$ applied on an unknown spin-wave component $\epsilon_i \in \{a, b, c, d\}$ ($\hat{n}_{\epsilon_i} = \hat{S}_{\epsilon_i}^{\dagger}\hat{S}_{\epsilon_i}$) of the atomic state $\hat{\rho}_W^{(A)}$, or on a spatial field mode $\gamma_{2i} \in \{a_2, b_2, c_2, d_2\}$ of the photonic state $\hat{\rho}_W^{(\gamma)}$ ($\hat{n}_{\gamma_{2i}} = \hat{a}_{\gamma_{2i}}^{\dagger}\hat{a}_{\gamma_{2i}}$). Our goal is to find the π-phase shifted ensemble ϵ_i (optical mode γ_{2i}), in a *single-measurement* under the condition that an average of one spin-wave is populated in total; i.e., $\sum_i \text{Tr}(\hat{n}_{\epsilon_i}\hat{\rho}_W^{(A)}) = 1$ (or $\sum_i \text{Tr}(\hat{n}_{\gamma_{2i}}\hat{\rho}_W^{(\gamma)}) = 1$ for optical modes). As a quantum benchmark, we consider an average success probability $P_s = \frac{1}{4}\sum_{\epsilon_i} \text{Tr}(\hat{\Pi}_{\epsilon_i}^{(u)}\hat{U}_{\pi,\epsilon_i}^{\dagger}\hat{\rho}_W^{(A)}\hat{U}_{\pi,\epsilon_i})$ (failure probability $P_f = 1 - P_s$) for distinguishing the phase-shifted ensemble ϵ_i (mode γ_{2i}) among the four possibilities $\{a, b, c, d\}$ ($\{a_2, b_2, c_2, d_2\}$) by way of *unambiguous quantum-state discrimination* $\{\hat{\Pi}_{\epsilon_i}^{(u)}\}$ (refs. [293–296]).

First, we consider an ideal W-state $|W\rangle_o = |W\rangle_A$ (or $|W\rangle_{\gamma_2}$) with atomic phases $\phi_i \in \{\phi_1, \phi_2, \phi_3\}$ (photonic phases $\phi_i' \in \{\phi_1', \phi_2', \phi_3'\}$). In this case, the π-phase shifted entangled W-states

$$|W_{\epsilon_i}\rangle_f \in \{|W_a^{(\pi)}\rangle_f, |W_b^{(\pi)}\rangle_f, |W_c^{(\pi)}\rangle_f, |W_d^{(\pi)}\rangle_f\}$$

can be detected deterministically, because $|W_{\epsilon_i}^{(\pi)}\rangle_f = \hat{U}_{\pi,\epsilon_i}|W\rangle_o$ forms an orthonormal complete set that spans the state-space $\hat{\rho}_1$, resulting from the underlying symmetry of $|W\rangle_o$ with respect to any rotation $\hat{U}_{\pi,\epsilon_i}$ on a generalized Bloch sphere. Operationally, we set the verification phases $\beta_{1,2} - \phi_{1,2}' = 0$ and $\beta_3 - \phi_3' = \pi$. Then, the π-phase shifted ensemble ϵ_i can be unambiguously discriminated because the otherwise balanced output photon probabilities $\vec{p}_v = \{p_{1000}, p_{0100}, p_{0010}, p_{0001}\} = \{0.25, 0.25, 0.25, 0.25\}$ of the verification interferometer will be transformed to $\vec{p}_v = \{1, 0, 0, 0\}$ for a π-phase induced on ensemble a, to $\vec{p}_v = \{0, 1, 0, 0\}$ on ensemble b, to $\vec{p}_v = \{0, 0, 1, 0\}$ on ensemble c, and to $\vec{p}_v = \{0, 0, 0, 1\}$ on ensemble d, each with success probability $P_s^{(\text{ent})} = 1$.

For fully separable states $|\Psi\rangle_o = |\psi_a\rangle_a|\psi_b\rangle_b|\psi_c\rangle_c|\psi_d\rangle_d$ with $|\psi_{\epsilon_i}\rangle_{\epsilon_i} = \sum_{n=0}^{\infty} c_{\epsilon_i}^{(n)}|n\rangle_{\epsilon_i}$, we displace

the resulting π-phase shifted state $|\Psi_{\epsilon_i}^{(\pi)}\rangle_f = \hat{U}_{\pi,\epsilon_i}|\Psi\rangle_o$ with a local unitary transformation $\hat{V}_{\epsilon_i}|\psi_{\epsilon_i}\rangle_{\epsilon_i} = |0\rangle_{\epsilon_i}$. The overall process $\hat{V}_a\hat{V}_b\hat{V}_c\hat{V}_d\hat{U}_{\pi,\epsilon_i}$ maps the initial product state $|\Psi\rangle_o$ into $\hat{V}_a\hat{U}_{\pi,a}|\psi_a\rangle_a|0\rangle_b|0\rangle_c|0\rangle_d$ (a phase shift on ensemble a), $|0\rangle_a\hat{V}_b\hat{U}_{\pi,b}|\psi_b\rangle_b|0\rangle_c|0\rangle_d$ (ensemble b), $|0\rangle_a|0\rangle_b\hat{V}_c\hat{U}_{\pi,c}|\psi_c\rangle_c|0\rangle_d$ (ensemble c), and $|0\rangle_a|0\rangle_b|0\rangle_c\hat{V}_d\hat{U}_{\pi,d}|\psi_d\rangle_d$ (ensemble d), with only one ϵ_i containing $\langle\hat{n}_{\epsilon_i}\rangle > 0$ excitations. Thus, we can *unambiguously* identify the phase-shifted ensemble ϵ_i given a photodetection, albeit with a failure probability $P_f = \frac{1}{4}\sum_{\epsilon_i}|_{\epsilon_i}\langle 0|\hat{V}_{\epsilon_i}\hat{U}_{\pi,\epsilon_i}|\psi_{\epsilon_i}\rangle_{\epsilon_i}|^2 = \frac{1}{4}\sum_{\epsilon_i}|_{\epsilon_i}\langle\psi_{\epsilon_i}|\hat{U}_{\pi,\epsilon_i}|\psi_{\epsilon_i}\rangle_{\epsilon_i}|^2$ arising from *inconclusive* null events (i.e., $|0000\rangle\langle 0000|$). We derive the maximum success probability $P_s^{(\max)} = 1 - P_f^{(\min)}$ and the optimal state $|\Psi\rangle_o = |\Psi\rangle_{\text{opt}}$ by minimizing $P_f^{(\min)}$ over all possible realizations of $c_{\epsilon_i}^{(n)}$ satisfying $\sum_{\epsilon_i}\langle\psi_{\epsilon_i}|\hat{n}_{\epsilon_i}|\psi_{\epsilon_i}\rangle_{\epsilon_i} = 1$. Specifically, we find that an optimal (pure) separable state $|\Psi\rangle_{\text{opt}} = \prod_{\epsilon_i}(\sqrt{3/4}|0\rangle_{\epsilon_i} + \sqrt{1/4}|1\rangle_{\epsilon_i})$ can be used for the parameter estimation protocol to infer ϵ_i with $P_s^{(\max)} = 0.75$. Similarly, maximum success probability $P_s^{(\text{coh})}$ can be derived for multimode coherent states $\prod_{\epsilon_i}|\alpha_{\epsilon_i}\rangle_{\epsilon_i}$, giving a classical bound of $P_s^{(\text{coh})} = 1 - 1/e$.

Finally, we consider the upper bound $P_s^{(\max)}$ for mixed separable states $\hat{\rho}_o^{(\text{sep})}$ with pure state decompositions $\hat{\rho}_o^{(\text{sep})} = \sum_m p_m|\Psi_m\rangle_o\langle\Psi_m|$. Generally, the transformations $\hat{V}_{\epsilon_i}$, as discussed above, do not exist for $\hat{\rho}_o^{(\text{sep})}$, excluding the possibility of an unambiguous state discrimination. Thus, the success probability $P_s(\hat{\rho}_o^{(\text{sep})})$ is upper bounded by the convex combinations of $\{|\Psi_m\rangle\}$, thereby

$$P_s(\hat{\rho}_o^{(\text{sep})}) \leq \sum_m p_m P_s(|\Psi_m\rangle_o\langle\Psi_m|) \leq P_s^{(\max)} = 0.75. \tag{9.4}$$

Importantly, the maximum success probability $P_s^{(\max)} = 0.75$, attainable for any $\hat{\rho}_o^{(\text{sep})}$, is less than $P_s^{(\text{ent})} = 1$ for entangled states $|W\rangle_o$. Thus, the entangled spin-waves in the experiment can be applied for sensing an atomic phase shift beyond the limit for any unentangled state.

9.12 Experimental details

The experiment consists of a 22 ms preparation stage and a 3 ms period for operating the quantum interface in Fig. 9.1 with a repetition rate 40 Hz and a duty cycle $D_c = 3/25$. For the preparation, we load and laser-cool cesium atoms (peak optical depth ≈ 30) in a magneto-optical trap for 18 ms, after which the atoms are released from the trap with dynamically compensated eddy-currents. The atoms are further cooled in an optical molasses ($T_t \simeq 150\ \mu K$) for 3.8 ms, and optically pumped to $|g\rangle$ for 0.2 ms. During this time, a phase-reference laser ($F = 3 \leftrightarrow F' = 4'$ transition) also propagates through the atomic ensembles for the active stabilization of the verification interferometer in Fig. 9.1c via *ex-situ* phase-modulation spectroscopy[35], which does not affect the operation of the quantum interface (section 9.12.2). Concurrently, dense cesium atoms in paraffin coated vapor cells located at the heralding and verification ports are prepared to the respective ground states $|g\rangle$ ($|s\rangle$) for filtering the coherent-state lasers scattered into the quantum fields γ_1 (γ_2).

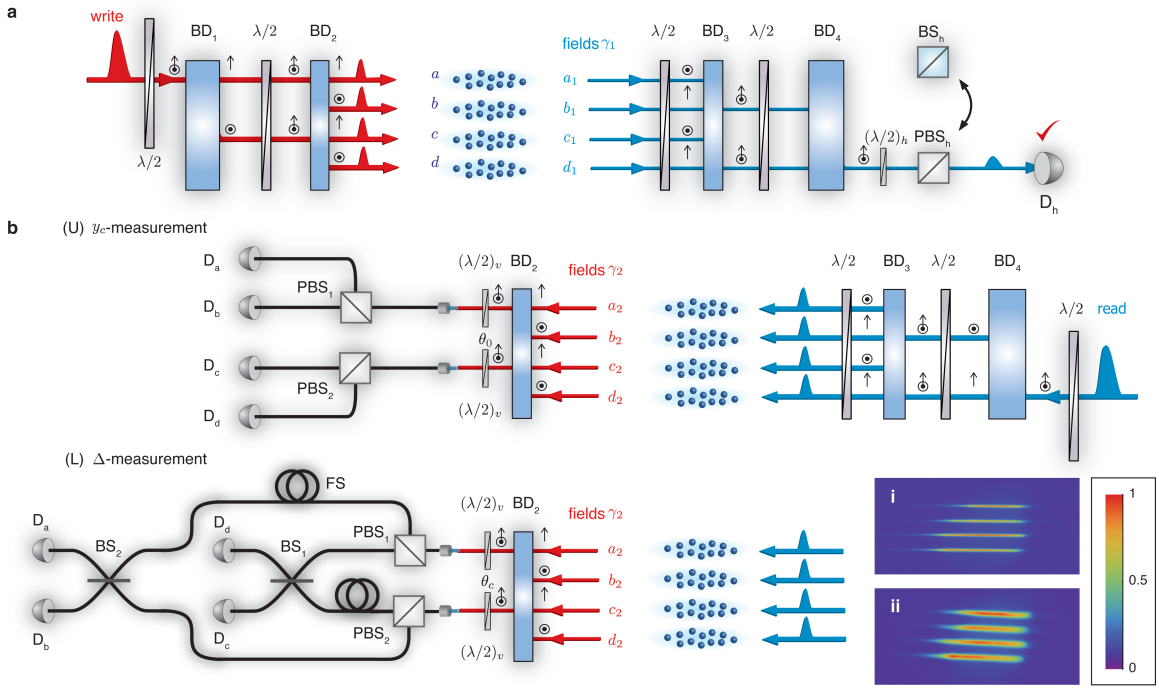

Figure 9.4: **Experimental schematics for entanglement generation, transfer, and verification. a,** Entanglement generation. A weak write laser is sequentially split into four components by displacers $\{\mathrm{BD}_1, \mathrm{BD}_2\}$ to excite atomic ensembles $\epsilon = \{a, b, c, d\}$. The resulting fields $\gamma_1 = \{a_1, b_1, c_1, d_1\}$ are brought into interferences with displacer BD_4 and polarizing beamsplitter PBS_h, and sent to a single-photon detector D_h. A detection event at D_h heralds the creation of a quadripartite entangled state. **b,** Quantum-state transfer and entanglement verification. After a storage time τ, we convert the atomic state of the ensembles $\epsilon = \{a, b, c, d\}$ to an entangled state for fields $\gamma_2 = \{a_2, b_2, c_2, d_2\}$ by way of strong read pulses. (U) y_c-measurement—By setting the waveplates $(\lambda/2)_v$ to $\theta_0 = 0°$, we measure the occupation statistics of the individual modes with detectors $D_{a,b,c,d}$. (L) Δ-measurement—With $(\lambda/2)_v$ at $\theta_c = 22.5°$, we optimize the verification phases $\{\beta_1, \beta_2, \beta_3\}_v$ for constructive interferences of the fields γ_2 at $\mathrm{PBS}_{1,2}$ and $\mathrm{BS}_{1,2}$. Piezoelectric fiber stretching modules (FS) are used in the verification interferometer for active stabilizations of $\{\beta_1, \beta_2, \beta_3\}_v$. The quadripartite atomic entanglement is generated for four collective atomic modes of the ensembles $\epsilon = \{a, b, c, d\}$ in inset (i), which are individually controlled by the classical writing, repumping, and reading lasers, whose fluorescence is shown in inset (ii). Both images in the insets (i), (ii) result from background-subtracted fluorescences of the four atomic ensembles. The quantum fields $\{\gamma_1, \gamma_2\}$ are generated in a non-collinear geometry[75] with a crossing angle of 2.5° (not shown) relative to the classical beams (chapter 2).

9.12.1 Experimental procedures for matter-light quantum interface

As shown in Fig. 9.4a, we split a write pulse into four beams with two calcite beam-displacers $\{\mathrm{BD}_1, \mathrm{BD}_2\}$, with output fields of the form $\vec{E}_{\mathrm{write}} = (\vec{E}_a + e^{i\phi_1^{(w)}}\vec{E}_b) + e^{i\phi_2^{(w)}}(\vec{E}_c + e^{i\phi_3^{(w)}}\vec{E}_d)$. We control their relative intensities using the two waveplates $(\lambda/2)$ near $\{\mathrm{BD}_1, \mathrm{BD}_2\}$, with writing phases $\phi_i^{(w)} \in \{\phi_1^{(w)}, \phi_2^{(w)}, \phi_3^{(w)}\}$ set by the tilting angles of $\{\mathrm{BD}_1, \mathrm{BD}_2\}$. In turn, the heralding fields $\gamma_1 = \{a_1, b_1, c_1, d_1\}$ emitted from the writing process are combined into two spatial modes at BD_3, with each mode carrying polarizations $\{|H\rangle, |V\rangle\}$ to accommodate the fields $\gamma_1^{(ab)} = \{a_1, b_1\}$ and $\gamma_1^{(cd)} = \{c_1, d_1\}$. We then interfere the polarization components of the spatial modes $\{\gamma_1^{(ab)}, \gamma_1^{(cd)}\}$ by way of BD_4, whose output modes experience

polarization interference at the polarizing beamsplitter PBS_h, with one output monitored by the heralding detector D_h. Here, the relative phases acquired by the propagation of fields γ_1 before the detection at D_h are given by $\phi_i^{(h)} \in \{\phi_1^{(h)}, \phi_2^{(h)}, \phi_3^{(h)}\}$. We control $\phi_i^{(h)}$ with a set of Berek compensators.

A photoelectric detection of a single photon γ_1 emitted indistinguishably by one of four ensembles $\epsilon = \{a, b, c, d\}$ prepares an atomic entangled state $\hat{\rho}_W^{(A)}$, whose mutual phases $\phi_i \in \{\phi_1, \phi_2, \phi_3\}$ between ensembles $\{a, b\}$, $\{a, c\}$, and $\{c, d\}$ are $\phi_i = \phi_i^{(w)} - \phi_i^{(h)}$ for $i \in \{1, 2, 3\}$. To generate a 'crossed' quantum state $\hat{\rho}_\times^{(A)}$, we replace PBS_h with a non-polarizing beamsplitter BS_h in the heralding interferometer (Fig. 9.4a), such that the fields $\gamma_1^{(ab)}$ and $\gamma_1^{(cd)}$ are mixed with orthogonal polarizations. While in practice we do not discriminate events arising from the fields $\gamma_1^{(ab)}$ and $\gamma_1^{(cd)}$, the intrinsic possibility of analyzing the polarization state of the heralding photon to infer the two distinct events completely destroys the bipartite coherence (and entanglement) for the split between $\{a, b\}$ and $\{c, d\}$.

Finally, after a variable delay, a strong counter-propagating read pulse, with reading phases $\phi_i^{(r)} \in \{\phi_1^{(r)}, \phi_2^{(r)}, \phi_3^{(r)}\}$ set by $\{\mathrm{BD}_3, \mathrm{BD}_4\}$, transforms the entangled atomic components $\{a, b, c, d\}$ of $\hat{\rho}_W^{(A)}$ to entangled beams $\gamma_2 = \{a_2, b_2, c_2, d_2\}$ comprising the photonic state $\hat{\rho}_W^{(\gamma)}$. The photonic phases $\{\phi_1', \phi_2', \phi_3'\}$ of $\hat{\rho}_W^{(\gamma)}$ depend on the overall accumulation of atomic phases ϕ_i via $\phi_i' = \phi_i^{(r)} - \phi_i$. Importantly, the set of calcite displacers $\{\mathrm{BD}_1, \mathrm{BD}_2, \mathrm{BD}_3, \mathrm{BD}_4\}$ forms an interferometrically stable four-mode Mach-Zehnder device, in which any common-mode phase drift of $\{\phi_i^{(w)}, \phi_i^{(r)}, \phi_i^{(h)}, \phi_i'\}$ is passively counter-balanced over several days. Thus, the entangled state $\hat{\rho}_W^{(A)}$ ($\hat{\rho}_W^{(\gamma)}$) in our experiment is generated with stable phases $\{\phi_1, \phi_2, \phi_3\}$ ($\{\phi_1', \phi_2', \phi_3'\}$) from trial to trial, which can be transferred to independent reference frames for entanglement verification without exploiting additional quantum channels [110].

9.12.2 Operational procedures for entanglement verification

To verify the entanglement of the photonic state $\hat{\rho}_W^{(\gamma)}$, we use a nonlocal, nonlinear uncertainty relation (ref. [38], chapter 7), in which mode-entangled states for $M > 2$ can be efficiently detected with a significantly smaller number of measurements than conventional techniques [35,38], as discussed in chapters 7–8. Specifically, our protocol requires measurements of (U) the photon statistics y_c and (L) the mutual coherences Δ of the multipartite entangled optical modes, as shown in Fig. 9.4b.

Operationally, we measure the entanglement parameters by first combining the four optical modes $\gamma_2 = \{a_2, b_2, c_2, d_2\}$ with BD_2 into two spatial modes $\gamma_2^{(ab)} = \{a_2, b_2\}$ and $\gamma_2^{(cd)} = \{c_2, d_2\}$, with each mode $\{a_2, b_2\}$ ($\{c_2, d_2\}$) of γ_2 encoded in the respective polarizations $\{|H\rangle, |V\rangle\}$ of $\gamma_2^{(ab)}$ ($\gamma_2^{(cd)}$). By rotating two waveplates $(\lambda/2)_v$ before $\mathrm{PBS}_{1,2}$ between $\theta_0 = 0°$ and $\theta_c = 22.5°$, and by reconfiguring the fiber-optical connections, we switch between the measurement setups for accessing y_c and Δ.

In particular, measuring the sum uncertainty Δ involves pairwise interference of the optical channels $\gamma_2 = \{a_2, b_2, c_2, d_2\}$. The coherence properties of the photonic state are characterized by the stable photonic phases of $\{\phi_1', \phi_2', \phi_3'\}$, and by the off-diagonal elements $d_{\alpha\beta}$ of $\hat{\rho}_W^{(\gamma)}$ (section 9.13.1). This requires high phase stability of $\{\beta_1, \beta_2, \beta_3\}_v$ for the relative optical paths of the verification interferometer shown in Fig.

9.4b. Here, $\{\beta_1, \beta_2, \beta_3\}_v$ denote to the relative phases between the modes $\{a_2, b_2\}$, $\{a_2, c_2\}$, and $\{c_2, d_2\}$, respectively. Additionally, $\{\beta_1, \beta_2, \beta_3\}_v$ of each optical path leading from the output faces of the ensembles must be tuned to $\{\phi_1', \phi_2', \phi_3'\}$ such that maximum constructive interferences for the fields $\{a_2, b_2, c_2, d_2\}$ occur in a pairwise and sequential fashion (ref.[35], see a similar setup in section 8.8.2). We achieve the optimal settings of these phases by varying $\{\beta_1, \beta_2, \beta_3\}_v$ and recording the sum uncertainty. Fig. 9.2a shows such a measurement for β_2.

To stabilize the verification phases $\{\beta_1, \beta_2, \beta_3\}_v$, we incorporated an auxiliary reference laser $\vec{E}_{\text{aux}}$ to probe the interferometer during the laser cooling and trapping stage of our experiment via an *ex-situ* phase modulation spectroscopy. The active stabilizations of $\{\beta_1, \beta_2, \beta_3\}_v$ rely upon the passively stable paths of the eight quantum fields $\{\gamma_1, \gamma_2\}$.

During the phase stabilization stage, the outputs of the verification interferometer are routed to a set of auxiliary photodetectors by micro-electro-mechanical switches (MEMS) to monitor $\{\beta_1, \beta_2, \beta_3\}_v$. We also use another set of MEMS for switching $\vec{E}_{\text{aux}}$, which can extinguish the intensity of the reference laser with an overall extinction of $\gtrsim 200$ dB during the operation of the quantum interface. Additionally, by setting the frequency of $\vec{E}_{\text{aux}}$ to the $|s\rangle - |e\rangle$ transition of cesium, $\vec{E}_{\text{aux}}$ initializes the ensembles $\epsilon = \{a, b, c, d\}$ to the ground state $|g\rangle$ of the quantum interface. Based on the interference signal of $\vec{E}_{\text{aux}}$, we apply a feedback signal to the two piezoelectric fiber stretching modules (FS) in Fig. 9.4 that control the relative path lengths (β_2) leading from the ensembles. The remaining phases $\{\beta_1, \beta_3\}_v$ are passively stabilized by stable interferometers (over several days), and controlled independently with a set of calcite Berek compensators.

To operate the quantum interface (3 ms), (i) we set the control signals for the fiber stretchers to values $V_0 + V_c$, with set-point V_0 corresponding to a fixed phase β_2 of the interferometer during stabilization, (ii) switch off the laser $\vec{E}_{\text{aux}}$, and (iii) reroute the interferometer outputs to the single-photon counters $D_{a,b,c,d}$ via the MEMS for 3 ms. This system allows to set the phase β_2 to an arbitrary value by incrementing V_0 by V_c to $V_0 + V_c$, with no degradation for the quantum statistics and coherence of $\hat{\rho}_W^{(\gamma)}$. Moreover, the verification phases remain stable for the 3-ms operating duration of the quantum interface. Thus, the asynchronous (*'ex-situ'*) sequences for acquiring and stabilizing $\{\beta_1, \beta_2, \beta_3\}_v$ of the verification interferometer do not affect the sensitive operation of the quantum interface. In addition, the asynchronous timings allow the generation process of the atomic (photonic) entanglement with atomic (photonic) phases $\{\phi_1, \phi_2, \phi_3\}$ ($\{\phi_1', \phi_2', \phi_3'\}$) to be independent of the procedures for stabilizing the verification phases $\{\beta_1, \beta_2, \beta_3\}_v$, thereby satisfying the entanglement verification criteria of ref.[110].

9.13 Quantum uncertainty relations and genuine multipartite entanglement

In order to verify the entanglement by way of $\{\Delta, y_c\}$, we first evaluate the photon statistics $\{p_0, p_1, p_{\geq 2}\}$ for the y_c-measurement. Operationally, this is accomplished by measuring the individual probabilities q_{ijkl} for $i,j,k,l \in \{0,1\}$ photons to occupy the respective optical modes $\gamma_2 = \{a_2, b_2, c_2, d_2\}$ at the output faces of the ensembles via photoelectric detections $\{\hat{\Pi}_i^{(s)}\}$. For the Δ-measurement, we quantify the off-diagonal coherence $\overline{d}$ of $\hat{\rho}_W^{(\gamma)}$ by pairwise interferences of all possible sets of modes $\alpha, \beta \in \{a_2, b_2, c_2, d_2\}$ with the verification interferometer. The photon probabilities $\{p_{1000}, p_{0100}, p_{0010}, p_{0001}\}$ at the output modes of the verification interferometer thereby result from the coherent interferences of the four purportedly entangled fields γ_2 that depend on the phase orientations $\{\beta_1, \beta_2, \beta_3\}_v$ of $\{\hat{\Pi}_i^{(c)}\}$ (section 9.12.2).

Our conclusion of genuine multipartite entanglement for the atomic and photonic states $\{\hat{\rho}_W^{(A)}, \hat{\rho}_W^{(\gamma)}\}$ does not rely on weaker conditions based on the non-separability along any fixed bipartition of $\{\hat{\rho}_W^{(A)}, \hat{\rho}_W^{(\gamma)}\}$. The genuine M-partite entangled states created from our experiment can only be represented as mixtures of pure states that *all* possess M-partite entanglement, as for the case of genuine 'k-producibility' in multipartite spin models[39,40]. We take caution that our entanglement verification protocol cannot be applied for verifying the *absence* of entanglement for the physical state $\hat{\rho}_W^{(\gamma)}$ in an infinite dimension[206]. Finally, we emphasize that our analysis makes use of the full physical state $\{\hat{\rho}_W^{(A)}, \hat{\rho}_W^{(\gamma)}\}$ including the vacuum component $\hat{\rho}_0$ and higher-order terms $\hat{\rho}_{\geq 2}$, and does not rely on a spurious *post-diction* based upon a preferred set of detection events (see sections 9.13.3–9.13.4).

In the following, I will derive useful relationships between the entanglement witness by way of quantum uncertainty relations and other measures.

9.13.1 Relationship between quantum uncertainty and off-diagonal coherences

We derive here the general expression for the upper bound of the sum uncertainty Δ as a function of the coherence $\overline{d}$. First, we note that Δ is only sensitive to the 1-excitation subspace $\hat{\rho}_1$ of $\hat{\rho}_r$ with

$$\hat{\rho}_1 = \begin{pmatrix} s_{1000} & d_{ab} & d_{ac} & d_{ad} \\ d_{ba}^* & s_{0100} & d_{bc} & d_{bd} \\ d_{ca}^* & d_{cb}^* & s_{0010} & d_{cd} \\ d_{da}^* & d_{db}^* & d_{dc}^* & s_{0001} \end{pmatrix},$$

normalized such that $\mathrm{Tr}(\hat{\rho}_1) = s_{1000} + s_{0100} + s_{0010} + s_{0001} = 1$. Here, the diagonal elements $\vec{s}_1 = \{s_{1000}, s_{0100}, s_{0010}, s_{0001}\}$ of $\hat{\rho}_1$ are related to the 1-photon probabilities $\vec{q}_1 = \{q_{1000}, q_{0100}, q_{0010}, q_{0001}\}$ at the faces of the ensembles via $p_1 \vec{s}_1 = \vec{q}_1$. By transforming $\hat{\rho}_1$ into the basis spanned by $\{|W_i\rangle_v\}$, we find the expressions for the normalized output photon probabilities $\{p_{1000}, p_{0100}, p_{0010}, p_{0001}\}$ of the verification

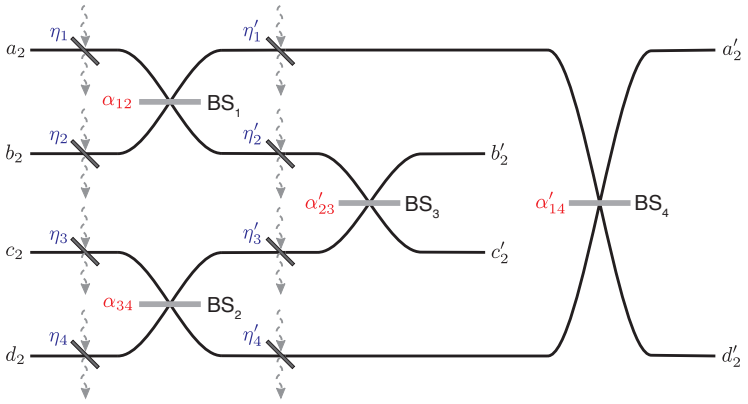

Figure 9.5: **Various imperfections in verification interferometer.** The verification interferometer transforms the input photonic modes $\gamma_2 = \{a_2, b_2, c_2, d_2\}$ to the output modes $\gamma'_2 = \{a'_2, b'_2, c'_2, d'_2\}$. The projectors $\hat{\Pi}_i^{(c)}$ are transformed into imbalanced states $\hat{\pi}_i^{(c)}$ due to losses and imbalances in the verification protocol. The transmission efficiencies $\{\eta, \eta'\}$ (blue) and beamsplitting ratios $\{\alpha, \alpha'\}$ (red) are shown. Dashed arrows are the auxiliary modes for loss propagations of the input state $\hat{\rho}_W^{(\gamma)}$.

interferometer as functions of $\vec{s}_1$ and $d_{\alpha\beta}$. The sum uncertainty Δ is then expressed as $\Delta = \frac{3}{4} - \{(|d_{ab}| + |d_{cd}|)^2 + (|d_{ac}| + |d_{bd}|)^2 + (|d_{ad}| + |d_{bc}|)^2\}$. Thus, we obtain $\Delta \lesssim \frac{3}{4}(1 - 16\overline{d}^2)$. The average value of the six unique off-diagonal elements is $\overline{d} = \frac{1}{6}\sum_{\alpha,\beta} |d_{\alpha\beta}|$ with $0 \leq \overline{d} \leq 1/4$, and the effective interference visibility is given by $V_{\text{eff}} = 4\overline{d}$.

9.13.2 Derivation of entanglement fidelity

We obtain here the expression for the lower bound unconditional entanglement fidelity $F^{(A)} = \tilde{p}_1 F_1$, where $\tilde{p}_1$ is the probability for a single spin-wave $\hat{\rho}_1^{(A)}$ in the heralded state $\hat{\rho}_W^{(A)}$, and $F_1 = \langle W_1|\hat{\rho}_1^{(A)}|W_1\rangle$ is the conditional fidelity for $\hat{\rho}_1^{(A)}$. We start by noting that the projective measurement $\hat{\Pi}_i^{(c)}$ for Δ gives the conditional fidelity F_1 of $\hat{\rho}_r$ onto one of four orthonormal W-states, $|W_i\rangle_v = |W_1\rangle_v$, for example, $|1000\rangle + e^{i\beta_1}|0100\rangle + e^{i\beta_2}(|0010\rangle + e^{i\beta_3}|0001\rangle)$. Hence, we can define $\Delta = 1 - F_1^2 - \sum_{i=2}^4 F_i^2$ in terms of the respective overlaps F_i. Because of the orthonormality $\sum_{i=1}^4 F_i = 1$, the sum uncertainty is bounded by $\Delta \geq 1 - F_1^2 - (1 - F_1)^2$, whereby we obtain $F_1 \geq \sqrt{\frac{1}{2}(\frac{1}{2} - \Delta)} + \frac{1}{2}$. Finally, by combining the probability $\tilde{p}_1$ for exciting one spin-wave distributed among the four ensembles, we access the lower bound fidelity $F^{(A)} \geq \tilde{p}_1(\sqrt{\frac{1}{2}(\frac{1}{2} - \Delta)} + \frac{1}{2})$ obtained unconditionally for the heralded atomic state $\hat{\rho}_W^{(A)}$. In principle, the imbalances in the interferometer can rotate the projectors into non-orthonormal sets (ref.[38], chapter 7). However, the measured losses and the beam-splitter ratios are sufficiently balanced such that any changes in $F^{(A)}$ due to modified projectors are well within the uncertainties of the data, as evidenced by the close-to-unity projection fidelity $F^{(\pi)} = 99.9^{+0.1}_{-0.2}\%$ (section 9.13.3). In the experiment, $\tilde{p}_1$ and F_1 are determined from the inferences of the spin-wave statistics (via y_c), and of the coherences (via Δ), respectively.

9.13.3 Numerical optimizations of the uncertainty bounds and their errors

In the presence of technical imperfections in the verification interferometer arising from imbalances in transmission losses $\{\eta, \eta'\}$ and beamsplitting ratios $\{\alpha, \alpha'\}$ of Fig. 9.5, the ideal projectors $\hat{\Pi}_i^{(c)} = |W_i\rangle_v\langle W_i|$ evolve into modified sets $\hat{\pi}_i^{(c)} = |W_i'\rangle_v\langle W_i'|$, which project the input $\hat{\rho}_r$ onto imbalanced W-states $|W_i'\rangle_v$, with chapters 7–8 providing further details. Generally, these projectors $\hat{\pi}_i^{(c)}$ are non-orthonormal due to the differential losses, but still span the single-excitation subspace $\hat{\rho}_1$ of $\hat{\rho}_r$. Importantly, the reductions of projection fidelities $F_i^{(\pi)} = {}_v\langle W_i|\hat{\pi}_i^{(c)}|W_i\rangle_v \leq 1$ of $\hat{\pi}_i^{(c)}$ can only decrease the *efficacy* of the verification protocol for detecting larger sets of states that belong to the state space of genuine W-states. Therefore, the observation of Δ below the bounds $\Delta_b^{(M-1)}$ using the modified projectors is still a sufficient condition for genuine M-partite entanglement (ref.[38], chapter 7). In the experiment, the losses and beamsplitter ratios for the interferometer are matched within 5%, as shown in Table 9.1.

To quantify the accuracies of our projectors $\pi_i^{(c)}$ to those of an ideal Δ-measurement, we numerically simulate the projection fidelities $F_i^{(\pi)}$ of the modified $\hat{\pi}_i^{(c)}$, as implemented by the measurement apparatus in Fig. 9.4b, to the ideal $\hat{\Pi}_i^{(c)}$. For this, we assume normal distributions for the parameters in Table 9.1 due to their systematic uncertainties, and build histograms of $F_i^{(\pi)}$ in Fig. 9.6, which give the probability densities $p_d(F_i^{(\pi)})$ for $F_i^{(\pi)}$ such that $\int_0^1 p_d dF_i^{(\pi)} = 1$. Due to the quadratic structure of the projection fidelities, $F_i^{(\pi)}$ is insensitive to small variations in the parameters of Table 9.1 when the verification interferometer is close to balanced (i.e., $\alpha_{12} \simeq \alpha_{34} \simeq \alpha_{14}' \simeq \alpha_{23}' \simeq 1/2$, $\eta_1 \simeq \eta_2 \simeq \eta_3 \simeq \eta_4$, and $\eta_1' \simeq \eta_2' \simeq \eta_3' \simeq \eta_4'$). Thus, we find a mean value $F^{(\pi)}$ of the four projection fidelities with $F^{(\pi)} = \frac{1}{4}(F_a^{(\pi)} + F_b^{(\pi)} + F_c^{(\pi)} + F_d^{(\pi)}) = 99.9^{+0.1}_{-0.2}\ \%$ by fitting the resulting probability densities $p_d^{(i)}$ to asymmetric Gaussian distributions $G(F_i^{(\pi)})$. The close-to-unity $\{F_i^{(\pi)}\}$ justify our analysis of the entanglement fidelities $\{F^{(A)}, F^{(\gamma)}\}$ for the atomic and photonic states.

In addition, we extend this model to numerically minimize the uncertainty bounds $\{\Delta_b^{(3)}, \Delta_b^{(2)}, \Delta_b^{(1)}\}$ over the full range of y_c for tripartite, bipartite entangled states, and for fully separable states, respectively (refs.[35,38], chapters 7–8). The calibration errors in the parameters of Table 9.1 give rise to the bands in the uncertainty bounds of Figs. 9.2 and 9.3, which depict the ± 1 s.d. uncertainties of the respective boundaries. In Fig. 9.7, we show the probability distributions of the bounds $\{\Delta_b^{(3)}, \Delta_b^{(2)}, \Delta_b^{(1)}\}$ for the minimal entanglement parameters $\{\Delta^{\min}, y_c^{\min}\}$ achieved in section 9.5.

Table 9.1: **Experimental imperfections in verification interferometer.** Measured beamsplitter values $\{\alpha, \alpha'\}$ and transmission efficiencies $\{\eta, \eta'\}$ for the verification interferometer in Fig. 9.5 are shown. The systematic uncertainties $(\delta\kappa)$ of $\{\kappa\}$ are fractionally $(\delta\kappa/\kappa) = 0.05$ for $\kappa \in \{\alpha, \alpha', \eta, \eta'\}$. Note that $\alpha_{12} \simeq \alpha_{34} \simeq \alpha_{14}' \simeq \alpha_{23}' \simeq 1/2$, $\eta_1 \simeq \eta_2 \simeq \eta_3 \simeq \eta_4$, and $\eta_1' \simeq \eta_2' \simeq \eta_3' \simeq \eta_4'$.

α_{12}	α_{34}	α_{23}'	α_{14}'	η_1	η_2	η_3	η_4	η_1'	η_4'	η_2'	η_3'
0.51	0.49	0.50	0.48	0.52	0.54	0.52	0.50	0.95	0.96	0.91	0.93

9.13.4 Data and error analysis

The calibration errors in Table 9.1 and the finite quantum efficiencies η_d for the non-number resolving (threshold) detectors D_i may cause the actual entanglement parameters $\{\Delta, y_c\}$ of the physical states $\{\hat{\rho}_W^{(A)}, \hat{\rho}_W^{(\gamma)}\}$, that result from the ideal POVM values of $\{\hat{\Pi}_i^{(c)}, \hat{\Pi}_i^{(s)}\}$, to be inferred incorrectly from our measurements. We describe here how $\{\Delta, y_c\}$ can be conservatively estimated from the photoelectron statistics of the detectors D_i.

First, we confine our analysis to the reduced subspace $\hat{\rho}_r = p_0\hat{\rho}_0 + p_1\hat{\rho}_1 + p_{\geq 2}\hat{\rho}_{\geq 2}$ of the physical density matrices $\{\hat{\rho}_W^{(A)}, \hat{\rho}_W^{(\gamma)}\}$ up to one excitation per mode and ensemble. Importantly, this truncation process can be simulated by local filters on the individual modes of $\{\hat{\rho}_W^{(A)}, \hat{\rho}_W^{(\gamma)}\}$ and leads to a *model-independent*

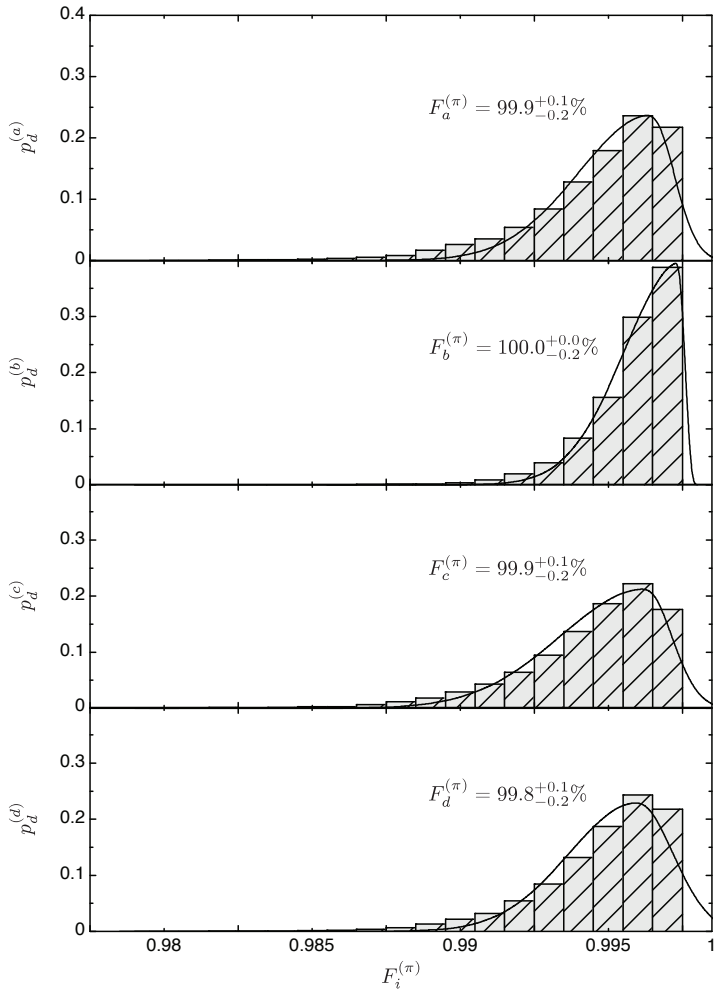

Figure 9.6: **Projection fidelities for quantum uncertainty relations.** We show histograms for the projection fidelities $F_i^{(\pi)}$ of the modified operator $\hat{\pi}_i^{(c)}$ to the ideal $\hat{\Pi}_i^{(c)}$ associated with detector D_i for $i \in \{a, b, c, d\}$. The mean value of the projection fidelities of $99.9^{+0.1}_{-0.2}$ % is deduced by fitting the respective probability densities $p_d^{(i)}$ with asymmetric Gaussian distributions $G(F_i^{(\pi)})$ (see the main text).

inference of the lower-bound entanglement of the full physical state $\{\hat{\rho}_W^{(A)}, \hat{\rho}_W^{(\gamma)}\}$ (ref.[27,34,110], chapter 3). The truncations of $\{\hat{\rho}_W^{(A)}, \hat{\rho}_W^{(\gamma)}\}$ into $\hat{\rho}_r$ also justify the use of single-photon avalanche photodetectors for the (local) y_c-measurement, since threshold detectors with finite efficiencies can be simulated by local filters[110]. We extract the photon statistics for the diagonal elements $\{p_0, p_1, p_{\geq 2}\}$ of $\hat{\rho}_r$ by a Bernoulli inversion[170] of the photoelectron statistics at D_i to the photon statistics q_{ijkl} at the faces of the ensembles (ref.[35], chapter 8). The spin-wave statistics can then be deduced by back-propagating the field statistics at the face of the ensembles to the spin-wave statistics $\{\tilde{p}_0, \tilde{p}_1, \tilde{p}_{\geq 2}\}$ for the reduced subspace of the ensembles, assuming linear mapping from matter to light (refs.[30,34], chapters 3 and 6).

For the sum uncertainty Δ, we additionally employ a numerical algorithm that estimates the upper bound of Δ for the one-excitation subspace $\hat{\rho}_1$. By defining the success probability $q_i^{(s)}$ for a single-photoelectric detection event $\overline{p}_i$ to arise from $\hat{\rho}_1$, the single-photoelectron probability $\overline{p}_i$ is given by (ref.[38], chapter 7),

$$\overline{p}_i = q_i^{(s)} p_i^{(s)} + (1 - q_i^{(s)}) p_i^{(f)}. \tag{9.5}$$

Here, $p_i^{(s)} = \mathrm{Tr}(\hat{\pi}_i^{(c)} \hat{\rho}_1)$ is the conditional probability for one photon at D_i originating from $\hat{\rho}_1$, normalized with $\sum_i p_i^{(s)} = 1$. On the other hand, $p_i^{(f)}$ is the normalized probability for a false single-photon event based on a spurious detection of a single photoelectron. Such an event can occur with a failure probability $1 - q_i^{(s)}$ if multiple photons are transmitted and registered at the same detector as a single photoelectron, or if the higher-order terms $\hat{\rho}_{\geq 2}$ at the faces of the ensembles are transformed into a single photon before the detectors by the lossy propagations (Table 9.1). Eq. 8.12 of chapter 8 (refs.[35,38]) provides the explicit expression for $q_i^{(s)}$. We do not subtract spurious backgrounds from atomic fluorescence, scattering noise, and detector dark counts.

Then, our goal is to unambiguously determine an upper bound of $\Delta = 1 - \sum_i (p_i^{(s)})^2$ for all possible realizations of $p_i^{(f)}$. We constrain this optimization problem with a set of data for the measured single-photoelectron probabilities $\overline{p}_i$ (Δ-measurement) and the photon statistics y_c (thereby, $\{p_0, p_1, p_{\geq 2}\}$ of $\hat{\rho}_r$), as well as the transmission efficiencies in Table 9.1 and the detection efficiencies for D_i. With these parameters, we assign the success probability $q_i^{(s)}$ of projecting the purported state $\hat{\rho}_r$ onto $\hat{\pi}_i^{(c)}$. Instead of algebraically upper bounding Δ (ref.[38], see chapters 7–8), which can yield an unphysically large result $\Delta > 0.75$, we perform a Monte-Carlo analysis to numerically determine a set of $p_i^{(s)}$ that maximizes Δ within the physical limit $\sum_i p_i^{(f)} = 1$ over the distributions of $q_i^{(s)}$. Here, the errors of $q_i^{(s)}$ occur from the systematic uncertainties of $\{\eta, \eta'\}$ and of the detection efficiencies, as well as of the statistical uncertainties of y_c of $\hat{\rho}_r$.

This procedure was employed for all the data sets of Figs. 9.2 and 9.3 (as well as of Figs. 9.8–9.10) to obtain conservative estimates of the entanglement parameters $\{\Delta, y_c\}$. The numerical errors for the Monte-Carlo simulations of all the data and the boundaries are well within $< 0.1\%$ of their overall uncertainties. In Fig. 9.7, we display a histogram for the minimal entanglement parameters $\{\Delta^{\min}, y_c^{\min}\} = \{0.07^{+0.01}_{-0.02}, 0.038 \pm 0.006\}$ (section 9.5). We find that $\Delta^{\min}$ (black bars) is suppressed below $\Delta_b^{(3)} =$

$0.261^{+0.010}_{-0.015}$ (red bars) by 10 s.d. We emphasize that we do not subtract any noise in the detection statistics nor do we post-select our data in the analysis, and thereby characterize the quantum state $\{\hat{\rho}_W^{(A)}, \hat{\rho}_W^{(\gamma)}\}$ that is physically available to the user.

9.14 Details on the theoretical model for the quantum interface

We describe theoretical models for the generation, storage, and transfer of the multipartite atomic state $\hat{\rho}_W^{(A)} = \mathrm{Tr}_h(\hat{\Pi}_h \hat{U}_{\text{write}}^\dagger \hat{\rho}_g^{(A)} \hat{U}_{\text{write}})$ to the photonic state of $\hat{\rho}_W^{(\gamma)} = \mathrm{Tr}_A(\hat{U}_{\text{read}}^\dagger \hat{\rho}_W^{(A)} \hat{U}_{\text{read}})$.

9.14.1 Entanglement generation

As we discussed in chapter 2, we begin our model with an interaction Hamiltonian (ref.[4])

$$\hat{H}_{\text{write}}^{(\epsilon)}/\hbar = \frac{g_0 \Omega_{\text{write}}^{(\epsilon)}}{\delta} (\hat{a}_{\gamma_1} \hat{S}_\epsilon + \hat{a}_{\gamma_1}^\dagger \hat{S}_\epsilon^\dagger) \tag{9.6}$$

for the parametric writing process of ensemble ϵ with excitation parameter $\xi = \tanh(g_0 \int \Omega_{\text{write}}^{(\epsilon)}(t) dt/\delta)$. Here, $\Omega_{\text{write}}^{(\epsilon)}$ (δ) is the Rabi frequency (detuning) of the writing laser, and $\hat{a}_{\gamma_1}$ ($\hat{S}_\epsilon$) is the annihilation operator for the fields γ_1 (collective excitations in ensemble ϵ). The writing process transforms the initial atomic state $|\overline{g}_\epsilon\rangle$ into individual products of two-mode squeezed states between the fields γ_1 and ensembles ϵ via $\hat{U}_{\text{write}} = \prod_\epsilon \exp(i \Delta t_w \hat{H}_{\text{write}}^{(\epsilon)}/\hbar)$, with the writing phases $\{\phi_1^{(w)}, \phi_2^{(w)}, \phi_3^{(w)}\}$ included in $\Omega_{\text{write}}^{(\epsilon)}$.

Upon the transformation of the fields γ_1 by our heralding interferometer, we find that the output mode operator for γ_1 is given by (up to an overall normalization) $\hat{a}_h \mapsto \hat{a}_{a_1} + e^{i\phi_1^{(h)}} \hat{a}_{b_1} + e^{i\phi_2^{(h)}} (\hat{a}_{c_1} + e^{i\phi_3^{(h)}} \hat{a}_{d_1})$, where $\hat{a}_{i_1}$ is the mode operator for the field $i_1 \in \gamma_1$. Here, we omit the vacuum terms because we make

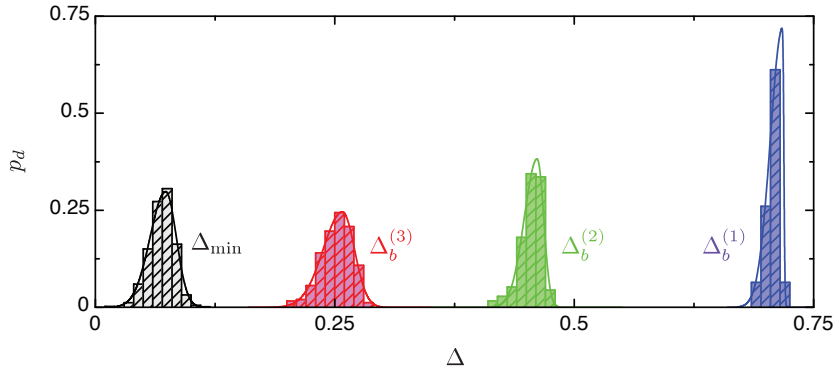

Figure 9.7: **Numerical optimizations for the minimal entanglement parameters and the uncertainty bounds.** Histograms of a Monte-Carlo analysis for minimizing 1-mode bound $\Delta_b^{(1)}$ (purple bars), 2-mode bound $\Delta_b^{(2)}$ (green bars), and 3-mode bound $\Delta_b^{(3)}$ (red bars) are shown for the smallest measured values of the entanglement parameters $\{\Delta^{\min}, y_c^{\min}\}$ (black bars) in section 9.5. The vertical axis is the probability density p_d corresponding to the respective value of Δ. The lines are fits to Gaussian distributions $p_d(\Delta) = G(\Delta)$ with asymmetric widths for ± 1 s.d.

use of normally ordered expectation values. Additionally, the heralding measurement $\hat{\Pi}_h$ with the threshold detector D_h is modeled with η_h, describing the overall efficiency for detecting γ_1 (including losses in the heralding channels, quantum efficiency of D_h and mode-matching efficiency to the collective state[74]), where

$$\hat{\Pi}_h = 1 - \sum_{n=0}^{\infty} \frac{:(-\eta_h \hat{a}_h^\dagger \hat{a}_h)^n:}{n!}. \tag{9.7}$$

Therefore, by calculating $\hat{\rho}_W^{(A)} = \mathrm{Tr}_h(\hat{\Pi}_h \hat{U}_{\text{write}}^\dagger \hat{\rho}_g^{(A)} \hat{U}_{\text{write}})$ for $\hat{\rho}_g^{(A)} = |\overline{g}_\epsilon\rangle\langle\overline{g}_\epsilon|$ and $\eta_h \ll 1$, we obtain the analytic expression of the atomic state $\hat{\rho}_W^{(A)}$ in Eq. 9.3 in the ideal case without additional noise (see section 9.14.4 for our noise model). The atomic entangled state $\hat{\rho}_W^{(A)}$ is thereby obtained non-destructively from a quantum measurement $\hat{\Pi}_h$ on the heralding systems γ_1, whereby the higher-order contamination $\hat{\rho}_{\geq 2}^{(A)}$ scales with ξ instead of ξ^2. The creation of $\hat{\rho}_W^{(A)}$ is then heralded by the photoelectric detection $\hat{\Pi}_h$ of the fields γ_1 with probability $p_h = \mathrm{Tr}(\hat{\Pi}_h \hat{U}_{\text{write}}^\dagger \hat{\rho}_g^{(A)} \hat{U}_{\text{write}})$.

9.14.2 Entanglement transfer

The transfer of the stored quadripartite entanglement to the photonic entanglement is described by a linear mapping process $\hat{U}_{\text{read}}$ (ref.[86], chapter 2), which transfers the delocalized collective state $|\overline{s}_\epsilon\rangle$ of the ensembles ϵ to the individual fields γ_2 with retrieval efficiency η_{read}. The reading process then generates a photonic state $\hat{\rho}_W^{(\gamma)} = \mathrm{Tr}_A(\hat{U}_{\text{read}}^\dagger \hat{\rho}_W^{(A)} \hat{U}_{\text{read}})$ via a 'beamsplitter' rotation $\hat{U}_{\text{read}}$ of $\hat{\rho}_W^{(A)}$ into $\hat{\rho}_W^{(\gamma)}$ with a ratio given by η_{read} (and reading phases $\{\phi_1^{(r)}, \phi_2^{(r)}, \phi_3^{(r)}\}$), after which the atomic states are traced over.

9.14.3 Entanglement verification

Finally, we model the photoelectric detection statistics of the photonic state $\hat{\rho}_W^{(\gamma)}$ at $D_{a,b,c,d}$. The detection probabilities for the output channels $\gamma_2' = \{a_2', b_2', c_2', d_2'\}$ of the entanglement verification setups in Figs. 9.4b and 9.5 can be modeled with projectors

$$\hat{\Pi}_0^{(\gamma_2')} = \sum_{n=0}^{\infty} \frac{:(-\eta_{\gamma_2'} \hat{a}_{\gamma_2'}^\dagger \hat{a}_{\gamma_2'})^n:}{n!} \tag{9.8}$$

for null events, and

$$\hat{\Pi}_1^{(\gamma_2')} = 1 - \hat{\Pi}_0^{(\gamma_2')} \tag{9.9}$$

for events that register one or more photons. Here, $\eta_{\gamma_2'}$ is the overall efficiency for detecting a photon in field γ_2' at $D_{a,b,c,d}$.

The photoelectric detection probabilities $\overline{p}_{ijkl}^{(c,s)}$ for counting i,j,k,l photoelectrons at $D_{a,b,c,d}$ can be calculated from the projectors $\hat{\Pi}_{ijkl}^{(c,s)} = \hat{\Pi}_i^{(a_2')} \hat{\Pi}_j^{(b_2')} \hat{\Pi}_k^{(c_2')} \hat{\Pi}_l^{(d_2')}$, via $\overline{p}_{ijkl}^{(c,s)} = \mathrm{Tr}(\hat{\Pi}_{ijkl}^{(c,s)} \hat{\rho}_W^{(\gamma)})$, for the respective configurations $\{c,s\}$ of Δ and y_c setups in Fig. 9.4b. Finally, the mode operator $\hat{a}_{\gamma_2'}$ for the output channel γ_2' is given by $(\hat{a}_{a_2'}, \hat{a}_{b_2'}, \hat{a}_{c_2'}, \hat{a}_{d_2'})^T = \hat{U}^{(c,s)} \cdot (\hat{a}_{a_2}, \hat{a}_{b_2}, \hat{a}_{c_2}, \hat{a}_{d_2})^T$. Here, the transfer matrix $\hat{U}^{(c,s)}$ is (i) a

unity matrix $\hat{U}^{(s)} = \mathbf{I}$ for the y_c-measurement, and (ii)

$$\hat{U}^{(c)} = \frac{1}{2}\begin{pmatrix} 1 & e^{i\beta_1} & e^{i\beta_2} & e^{i(\beta_2+\beta_3)} \\ 1 & -e^{i\beta_1} & -e^{i\beta_2} & e^{i(\beta_2+\beta_3)} \\ 1 & -e^{i\beta_1} & e^{i\beta_2} & -e^{i(\beta_2+\beta_3)} \\ 1 & e^{i\beta_1} & -e^{i\beta_2} & -e^{i(\beta_2+\beta_3)} \end{pmatrix} \tag{9.10}$$

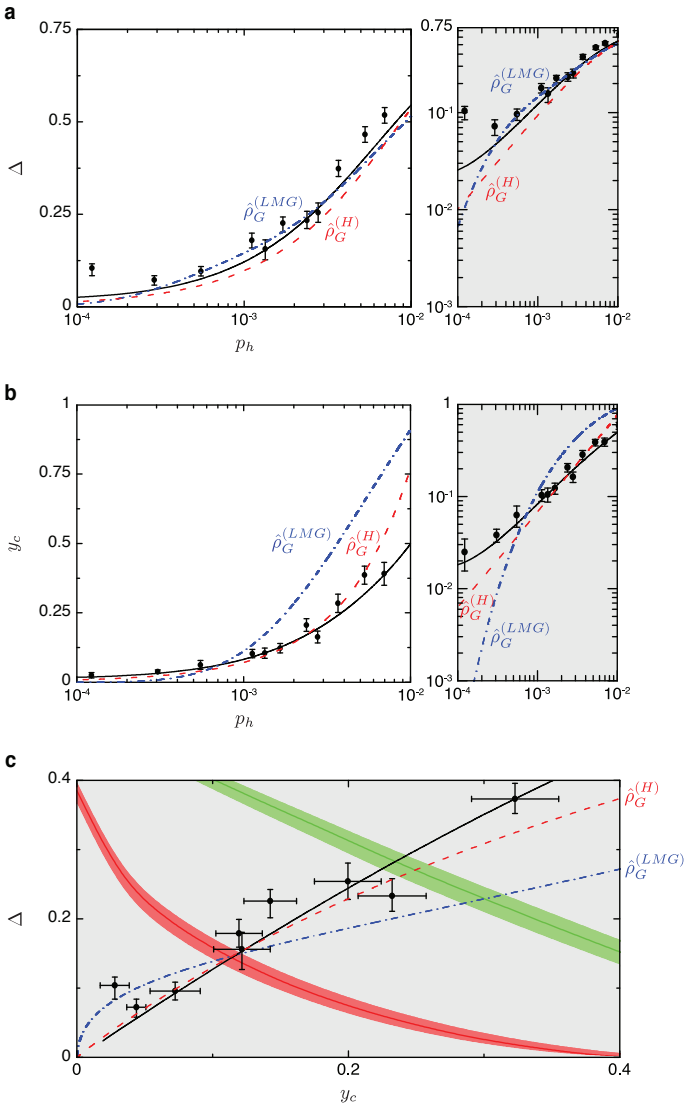

Figure 9.8: **Statistical evolutions of the individual entanglement parameters.** The data points and black line depict the statistical dependences of **a,** Δ and **b,** y_c to the heralding probability $p_h(\xi)$ for Fig. 9.2b. **c,** We also display the expanded view of the entanglement parameters $\{\Delta, y_c\}$ depicting the statistical transitions of multipartite atomic entanglement (inset of Fig. 9.2b). The thermal behaviors $\{\Delta^{(T)}, y_c^{(T)}\}$ of the thermal equilibrium states $\hat{\rho}_G^{(\mathrm{H})}$ and $\hat{\rho}_G^{(\mathrm{LMG})}$ of the Heisenberg-like and the Lipkin-Meshkov-Glick models are shown as red dashed and blue dash-dotted lines, respectively. Here, the horizontal axis is the heralding probability $p_h(\xi)$, with thermal excitation given by $\xi = e^{-\beta_T J}$ for the spin models.

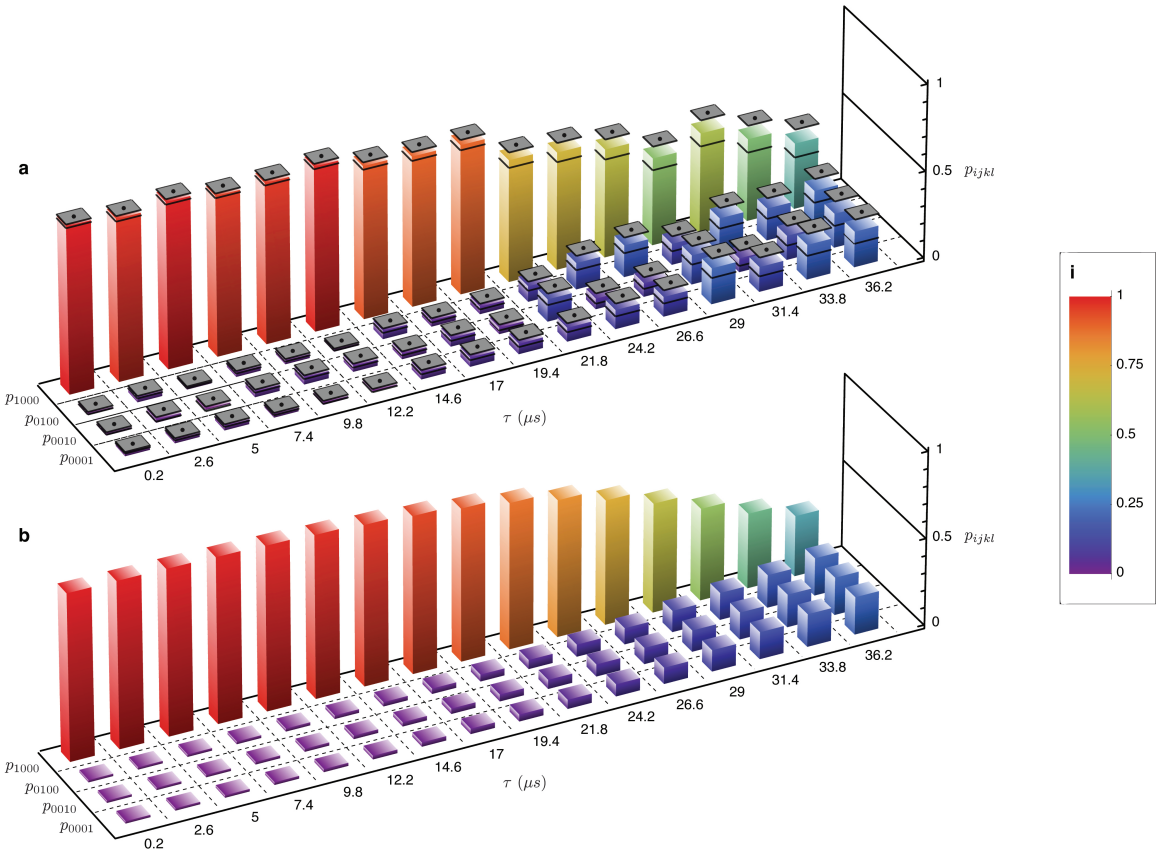

Figure 9.9: **Temporal decay of coherences stored in four atomic ensembles. a,** Evolution of the photon probabilities $\{p_{1000}, p_{0100}, p_{0010}, p_{0001}\}$ for occupying the output modes of the verification interferometer (Δ-measurement) versus storage time τ. For readability, the heights of the bars are shown in accord to the color convention of the inset **i**. Error bars, shown as grey squares, reflect the statistical uncertainties for each point. **b,** Photon probabilities $\{p_{1000}, p_{0100}, p_{0010}, p_{0001}\}$ from our theoretical model, which assumes a memory time determined from the temperature of the cold atomic samples and the net momentum transfer to the atomic spin-waves (chapter 2).

for the Δ-measurement (Fig. 9.5), where we assume balanced loss in writing Eq. 9.10, but not for our general analysis.

9.14.4 Incorporating noise into the model

To include the effects of atomic fluorescence and laser scattering noise emanating from the writing and reading processes, as well as of the background contamination including dark counts in the detectors, we mix dephased coherent states $\hat{\rho}_{r_B,q} = \int ||r_B|e^{i\phi_q}\rangle_q\langle|r_B|e^{i\phi_q}|d\phi_q$ and $\hat{\rho}_{r_I,q} = \int ||r_I|e^{i\phi_q}\rangle_q\langle|r_I|e^{i\phi_q}|d\phi_q$ into quantum channels $q \in \{\gamma_1, \gamma_2\}$ of the initial state, and find that

$$\hat{\rho}_g^{(A)} = \prod_{\epsilon} |\overline{g}_\epsilon\rangle\langle\overline{g}_\epsilon| \prod_{\gamma_1} (\hat{\rho}_{r_B,\gamma_1} \otimes \hat{\rho}_{r_I,\gamma_1}) \prod_{\gamma_2} (\hat{\rho}_{r_B,\gamma_2} \otimes \hat{\rho}_{r_I,\gamma_2}), \tag{9.11}$$

with quantum fields $\gamma_1 = \{a_1, b_1, c_1, d_1\}, \gamma_2 = \{a_2, b_2, c_2, d_2\}$. Here, $\{r_B, r_I\}$ are the respective probability amplitudes for the background and intensity-dependent noises (atomic fluorescence and scattering noise). In the experiment, we directly measure the noises $|r_{B,\gamma_1}|^2$, $|r_{B,\gamma_2}|^2$, and $|r_{I,\gamma_2}|^2$. We also infer the heralding and retrieval efficiencies $\{\eta_h, \eta_{\text{read}}\}$, as well as the scattering noise $|r_{I,\gamma_1}|^2 \propto |\Omega^{(\epsilon)}_{\text{write}}|^2$ for the writing laser by independently measuring the individual quantum correlation functions g_{γ_1,γ_2} for the fields $\{\gamma_1, \gamma_2\}$, following the methods in refs.[30,34,74] and chapters 3, 6.

Finally, using the initial state of $\hat{\rho}_g^{(A)}$ in Eq. 9.11, we approximate the physical state of $\hat{\rho}_W^{(A)} = \text{Tr}_h(\hat{\Pi}_h \hat{U}^\dagger_{\text{write}} \hat{\rho}_g^{(A)} \hat{U}_{\text{write}})$. We then simulate $\hat{\rho}_W^{(\gamma)} = \text{Tr}_A(\hat{U}^\dagger_{\text{read}} \hat{\rho}_W^{(A)} \hat{U}_{\text{read}})$ as well as the various expectation values of $\langle \hat{\Pi}^{(c,s)}_{ijkl} \rangle$ associated with the photoelectron statistics $\overline{p}^{(c,s)}_{ijkl}$ of $\{\Delta, y_c\}$. Finally, we perform the numerical algorithm described in section 9.13.4 and obtain the theoretical expectations of $\{\Delta_{\text{th}}, (y_c)_{\text{th}}\}$ as functions of heralding probability p_h, shown in Fig. 9.8. The theoretical curves in Fig. 9.2 are given by the parametric dependences of the entanglement parameters $\{\Delta_{\text{th}}, (y_c)_{\text{th}}\}$ to the heralding probability p_h.

9.14.5 Temporal dynamics of atomic multipartite entanglement

As described in section 9.9, the decoherence mechanism for the atomic W-state $\hat{\rho}_W^{(A)}(\tau)$ is dictated primarily by the motional dephasings of spin-waves (ref.[82], chapter 2). Qualitatively, the dephasings of the ensembles $\epsilon = \{a, b, c, d\}$ arise from independent evolutions of the spatial phases $\phi_j^{(sw)}(\tau) = \delta\vec{k} \cdot \vec{r}_j(\tau) + \phi_i$ imprinted on the spin-waves $|\overline{s}_\epsilon(\tau)\rangle = \sum_j e^{i\phi_j^{(sw)}(\tau)} |g \cdots s_j \cdots g\rangle_\epsilon$ due to thermal motions, where $\delta\vec{k} = \vec{k}_w - \vec{k}_1$ and $\phi_i = \phi_i^{(w)} - \phi_i^{(h)}$. Specifically, by assuming a Boltzmann velocity distribution with a mean velocity v_t for each ensemble ϵ, we find analytically that the probability p_c for the coherent atomic component $\hat{\rho}_c^{(A)}$ of $\hat{\rho}_W^{(A)}(\tau)$ decays over time τ, following $p_c \propto |\langle \overline{s}_\epsilon(0) | \overline{s}_\epsilon(\tau) \rangle|^2 \simeq e^{-\tau^2/\tau_m^2} + \mathcal{O}(1/N_{A,\epsilon})$ (refs.[82,114], chapter 2).

We follow a procedure similar to section 9.14 to simulate the dynamics of the atomic W-state $\hat{\rho}_W^{(A)}(\tau)$. In particular, absent any noise (i.e., $\hat{\rho}_g^{(A)} = |\overline{g}_\epsilon\rangle\langle\overline{g}_\epsilon|$) and for $\eta_h \ll 1$, we obtain the atomic dynamics

$$\begin{aligned} \hat{\rho}_W^{(A)}(\tau) \quad &\simeq \quad (1 - 3\xi)(\cos^2\theta(\tau)\hat{\rho}_c^{(A)} + \sin^2\theta(\tau)\hat{\rho}_n^{(A)}) \\ &\quad +3\xi\hat{\rho}_{\geq 2}^{(A)} + \mathcal{O}(\xi^2), \end{aligned} \tag{9.12}$$

where the mixing angles are $\cos^2\theta(\tau) = e^{-\tau^2/\tau_m^2}$ and $\sin^2\theta(\tau) = 1 - e^{-\tau^2/\tau_m^2}$. Thus, the decoherence for the atomic W-state results from the incoherent mixing of the initial superradiant state $\hat{\rho}_c^{(A)} \simeq |W\rangle_A\langle W|$ at $\tau = 0$ to mixtures of subradiant states $\hat{\rho}_n^{(A)}$ at $\tau > 0$, which increase the vacuum component $\hat{\rho}_0$ for the photonic state $\hat{\rho}_W^{(\gamma)}$. In turn, the increase of the subradiant states $\hat{\rho}_n^{(A)}$ contributes to a reduction in the coherent component $\hat{\rho}_c^{(A)}$ of $\hat{\rho}_W^{(A)}(\tau)$, as well as to a build-up of uncorrelated atomic noise $\hat{\rho}_{\geq 2}^{(A)}$ relative to $\hat{\rho}_c^{(A)}$. The net effect is a simultaneous degradation of the entanglement parameters $\{\Delta, y_c\}$ with a time-scale $\tau_m = 1/(|\delta\vec{k}|v_t) \simeq 17\ \mu s$. For the actual simulations in Fig. 9.2, we perform the full calculations including

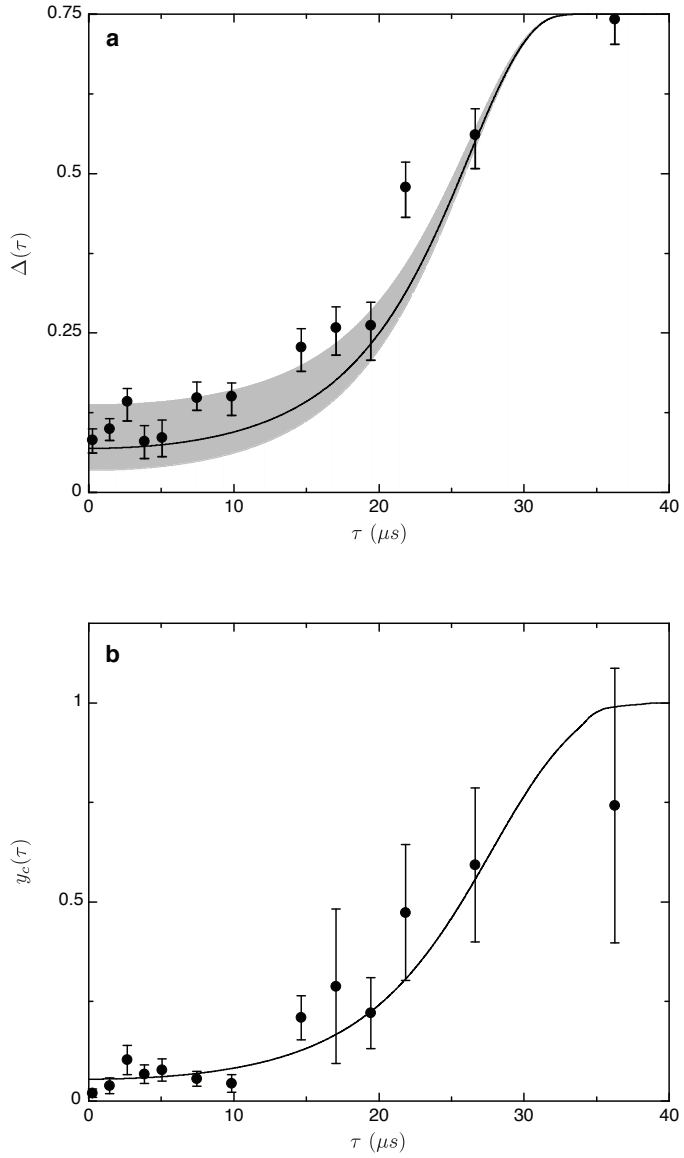

Figure 9.10: **Temporal evolutions of the individual entanglement parameters.** Due to the motional dephasings of the spin-waves, the experimentally measured entanglement parameters (black points), for **a,** $\Delta(\tau)$, and for **b,** $y_c(\tau)$, increase with a time-scale $\tau_m \simeq 17\mu s$. The theoretical simulation for the temporal behavior of $\{\Delta, y_c\}$ is displayed as a black solid line. The gray band around the theoretical curve $\delta(\tau)$ represents the $1/e$ uncertainty of the simulation due to the systematic error of the measured overlap $\overline{\lambda}$.

section 9.14 to incorporate the atomic fluorescence, laser scattering, and background noise.

Fig. 9.9 illustrates the temporal reduction in the overall coherence $\overline{d}$ of the full quadripartite state in our experiment (see section 9.6). Operationally, the loss of coherence is observed in terms of the decrease in imbalances among $\{p_{1000}, p_{0100}, p_{0010}, p_{0001}\}$ as a function of storage time τ, and hence to an increase in Δ. The behavior of the experimentally observed photon probabilities in Fig. 9.9a results from the progressive decay of the initial coherence for $\hat{\rho}_W^{(A)}(\tau_0)$ at $\tau_0 = 0.2\ \mu s$ for which $V_{\text{eff}}(\tau_0) = 4\overline{d} = 0.95 \pm 0.02$, evolving

then to $V_{\text{eff}}(\tau_f) = 0.10^{+0.25}_{-0.10}$ for the final state $\hat{\rho}_W^{(A)}(\tau_f)$ measured at $\tau_f = 36.2$ μs. The observed evolution is qualitatively in good agreement with our theoretical model of the photon probabilities shown in Fig. 9.9b. The spin-wave statistics are similarly modified by phase decoherence leading to an increase of y_c, from $y_c(\tau_0) = 0.03 \pm 0.01$ to $y_c(\tau_f) = 0.74 \pm 0.34$.

Finally, in Fig. 9.10, we show the dissipative dynamics of the atomic W-state (section 9.6), displayed independently for $\Delta(\tau)$ (Fig. 9.10a) and $y_c(\tau)$ (Fig. 9.10b). The complete 3-dimensional dynamics of the atomic W-states is displayed in Fig. 9.3. The temporal behaviors of $\{\Delta(\tau), y_c(\tau)\}$ in our experiment of the quadripartite atomic state (black points) are in qualitatively good agreement with the simulated dynamics for $\hat{\rho}_W^{(A)}(\tau)$ (black line). However, for Δ, we find that our data points consistently lie above the theoretical dynamics for $\hat{\rho}_W^{(A)}(\tau)$.

One possible explanation is that for the Δ-measurement, stringent interferometric stabilities and excellent overlaps $\overline{\lambda}$, close to unity, are required for all the 16 spatio-temporal modes $\{\vec{k}, s\}$, composed of the 8 quantum fields $\gamma_1 = \{a_1, b_1, c_1, d_1\}$ and $\gamma_2 = \{a_2, b_2, c_2, d_2\}$, as well as of the 8 classical writing and reading pulses, with s corresponding to the polarization state of each field. Ultimately, the wavepacket overlap for the entangled fields $\gamma_2 = \{a_2, b_2, c_2, d_2\}$ is limited by the differential optical depths of the cold samples $\{a, b, c, d\}$, which in turn yield differential group velocities during the slow light process of coherent transfer from $\hat{\rho}_W^{(A)}$ to $\hat{\rho}_W^{(\gamma)}$ by way of dynamic electromagnetically induced transparency (ref.[86], chapter 2).

We include this effect in the model via a field overlap $\overline{\lambda}$ (ref.[150]), where a fit corresponding to Fig. 9.8 gives $\overline{\lambda} = 0.98$ ($\overline{\lambda} = 0.95$ for Fig. 9.10a), with similar results obtained from the calculation of overlap for the measured temporal shapes of the wave-packets $\gamma_2 = \{a_2, b_2, c_2, d_2\}$. For the simulated dynamics of Fig. 9.3a (section 9.6), we use the field overlaps $\overline{\lambda}$ obtained independently from classical measurements of the interferometric visibility for both 'classical' (write, read) and 'quantum' interferometers (quantum fields γ_1, γ_2). Thus, the discrepancy in $\Delta(\tau)$ can be largely attributed to the systematic uncertainty in the inference of $\overline{\lambda} = 0.97 \pm 0.03$, with the uncertainty corresponding to the dynamics of $\Delta(\tau)$ shown as a gray band in Fig. 9.10a.

9.15 Entanglement thermalization

Here, we formulate the thermal equilibrium state $\hat{\rho}_G$ (refs.[39,297]) of a Heisenberg-like model $\hat{H}_{\rm H}$ and a Lipkin-Meshkov-Glick model $\hat{H}_{\rm LMG}$, as presented in Fig. 9.2b of section 9.5 (see also Fig. 9.8c). We compare the entanglement parameters $\{\Delta^{(T)}, y_c^{(T)}\}$ obtained from $\hat{H}_{\rm H}$ and $\hat{H}_{\rm LMG}$ to the observed statistical behavior of the quadripartite states of the ensembles.

9.15.1 Heisenberg-like model

We begin with a Heisenberg-like Hamiltonian $\hat{H}_{\rm H}$ of four ($N_s = 4$) spins $\{i, j\}$ of spin vectors $\vec{S}^{(i)} = \{\hat{S}_x^{(i)}, \hat{S}_y^{(i)}, \hat{S}_z^{(i)}\}$ with isotropic infinite-ranged ferromagnetic interaction ($J_{ij} = J > 0$ for all $\{i, j\}$), where

$$\hat{H}_{\rm H} = -\frac{J}{N_s}\sum_{\langle i,j\rangle}\vec{S}^{(i)}\cdot\vec{S}^{(j)} + h_z\sum_i \hat{S}_z^{(i)} + \hat{H}_p.$$

Here, $\hat{H}_{\rm H}$ includes a standard Heisenberg interaction $-\frac{J}{N_s}\sum_{\langle i,j\rangle}\vec{S}^{(i)}\cdot\vec{S}^{(j)} + h_z\sum_i \hat{S}_z^{(i)}$, as well as a spin-projection term $\hat{H}_p = 2h_z|S,-S\rangle\langle S,-S|$ which selects out the collective spin state $|S,-S\rangle$ with bias energy $2h_z$ and suppresses the thermal equilibrium population of $|S,-S\rangle$.

Since the Hamiltonian $\hat{H}_{\rm H}$ commutes with the collective spin operators $\{\vec{S}^2, \hat{S}_z\} \equiv \{(\sum_i \vec{S}^{(i)})^2, \sum_i \hat{S}_z^{(i)}\}$, $\hat{H}_{\rm H}$ is diagonal in the basis of collective spin states $|S, M\rangle$ for $0 \le S \le N_s/2$ and $-S \le M \le S$. The eigenenergies are

$$\mathcal{E}_{S,M} = \begin{cases} -\frac{J}{4}S(S+1) + h_z M + \frac{3J}{4}, & \text{if } |S,M\rangle \neq |2,-2\rangle \\ -\frac{3J}{4}, & \text{if } |S,M\rangle = |2,-2\rangle. \end{cases}$$

The degeneracy for $|S, M\rangle$ is given by $D_S = \frac{(2S+1)N_s!}{(N_s/2+S+1)!(N_s/2-S)!}$ (ref.[170]). Importantly, for any value of $h_z > 0$, the ground state is $|2,-1\rangle \equiv |W_1\rangle = \frac{1}{2}(|1000\rangle + |0100\rangle + |0010\rangle + |0001\rangle)$ with energy $\mathcal{E}_{2,-1} = -\frac{3J}{4} - h_z$. In the following sections, we will set the magnetic field to $h_z = J/2$.

9.15.2 Thermal equilibrium state

We solve for the Gibbs state, $\hat{\rho}_G^{(\rm H)} = \frac{1}{Z}e^{-\beta_T \hat{H}_{\rm H}}$, where $Z = {\rm Tr}(e^{-\beta_T \hat{H}_{\rm H}})$ is the partition function and beta parameter $\beta_T = 1/k_B T$ for thermal energy $k_B T$ at temperature T. Explicitly, we obtain $\hat{\rho}_G^{(\rm H)} = \frac{1}{Z}\sum_{S,M} D_S e^{-\beta_T \mathcal{E}_{S,M}}\hat{\rho}_{S,M}$. Here, the component $\hat{\rho}_{S,M}$ is a mixed state that contains all possible $|S, M\rangle$ for the degeneracy of D_S; e.g., $\hat{\rho}_{1,-1} = \frac{1}{3}(|W_2\rangle\langle W_2| + |W_3\rangle\langle W_3| + |W_4\rangle\langle W_4|)$ is a mixture of three non-symmetrized single-excitation W-states, $\{|W_2\rangle, |W_3\rangle, |W_4\rangle\}$.

By mapping the spin-states to number-states ($|\downarrow,\uparrow\rangle \mapsto |0,1\rangle$) [a], we obtain a Gibbs number-state $\hat{\rho}_G^{(n)}$ in the form of

$$\hat{\rho}_G^{(n)}(T) = p_0\hat{\rho}_0 + p_1\hat{\rho}_1 + p_{\ge 2}\hat{\rho}_{\ge 2}, \tag{9.13}$$

[a] Physically, the transfer of the spin-states to number-states can be accomplished by coherent mapping to photons.

as in the reduced density matrices $\hat{\rho}_r$ of $\{\hat{\rho}_W^{(A)}, \hat{\rho}_W^{(\gamma)}\}$. Our goal is to calculate the thermal (T) behavior of multipartite entanglement[39,297] for $\hat{\rho}_G^{(n)}$ via the entanglement parameters $\{\Delta^{(T)}, y_c^{(T)}\}$.

Because the vacuum component $\hat{\rho}_0$ and the higher-order terms $\hat{\rho}_{\geq 2}$, as well as the non-symmetric single-excitation states $\hat{\rho}_{1,-1}$ of $\hat{\rho}_1$ are more energetic than the ground state $|W_1\rangle$, the Gibbs state $\hat{\rho}_G^{(n)}(T=0)$ is the symmetric W-state $|W_1\rangle\langle W_1|$ at zero temperature. For low temperature ($\beta_T \gg 1$), we approximate $\hat{\rho}_G^{(n)}$ by

$$\hat{\rho}_G^{(n)}(T) \simeq Z_0\hat{\rho}_0 + Z_1\hat{\rho}_1 + (1 - Z_1 - Z_0)\hat{\rho}_{\geq 2}, \tag{9.14}$$

with $Z_0 = e^{\frac{3\beta_T J}{4}}$ and $Z_1 = Z_W + 3Z_X$. The single-excitation subspace $\hat{\rho}_1$ is

$$\hat{\rho}_1(T) \simeq \frac{1}{Z_1}(Z_W|W_1\rangle\langle W_1| + 3Z_X\hat{\rho}_{1,-1}), \tag{9.15}$$

with $Z_W = e^{\frac{\beta_T(4h_z+3J)}{4}}$, $Z_X = e^{\frac{\beta_T(4h_z-J)}{4}}$. Here, the thermal excitations from the ground state $|W_1\rangle\langle W_1|$ to one of $\hat{\rho}_{1,-1}$ occur with probability $\xi = Z_X/Z_W = e^{-\beta_T J}$.

9.15.3 Entanglement parameters

For the sum uncertainty $\Delta^{(T)}$, we only consider the single-excitation subspace $\hat{\rho}_1$ (Eq. 9.15). The probability to find $|W_1\rangle$ is $p_{1000} = \langle W_1|\hat{\rho}_1|W_1\rangle = \frac{1}{1+3e^{-\beta_T J}}$, whereas the probabilities to find the non-symmetric states are $p_{0100} = p_{0010} = p_{0001} = \frac{e^{-\beta_T J}}{1+3e^{-\beta_T J}}$. For $\beta_T \gg 1$, we deduce the sum uncertainty $\Delta^{(T)} \simeq 6e^{-\beta_T J} = 6\xi$. Similarly, we find the quantum statistics $y_c^{(T)} \simeq \frac{16}{3}e^{-\beta_T J} = \frac{16}{3}\xi$. Thus, the parametric relation

$$\Delta^{(T)} \simeq 6 \times \frac{3}{16}y_c^{(T)} = \frac{9}{8}y_c^{(T)} \tag{9.16}$$

replicates the statistical behavior of $\Delta_{\text{th}} \simeq \frac{9}{8}(y_c)_{\text{th}}$ for the ensembles (section 9.14) in the low-excitation regime (equivalent to $\beta_T \gg 1$).

By performing the full calculation of $\{\Delta^{(T)}, y_c^{(T)}\}$ for $\hat{\rho}_G^{(n)}$ without any approximations and by inserting the excitation probability $\xi = e^{-\beta_T J}$ into the expression of heralding probability $p_h(\xi)$ for $\hat{\rho}_W^{(A)}$ (section 9.14), we compare the theoretical expectations $\{\Delta^{(T)}, y_c^{(T)}\}$ of the thermal state $\hat{\rho}_G^{(\text{H})}$ to the experimental data, presented in Fig. 9.2b as a red dashed line (section 9.5; see also Fig. 9.8c). In Fig. 9.8, we plot the dependences of the individual parameters $\Delta^{(T)}$ and $y_c^{(T)}$ to p_h as red dashed lines. The panels on the right-hand side show the log-log scale plots of the figures for small values of ξ.

9.15.4 Lipkin-Meshkov-Glick model

We simulate the entanglement parameters $\{\Delta^{(T)}, y_c^{(T)}\}$ of a thermal equilibrium state $\hat{\rho}_G^{(\mathrm{LMG})}$ for an isotropic Lipkin-Meshkov-Glick (LMG) Hamiltonian $\hat{H}_{\mathrm{LMG}}$ (refs.[298–300]), where

$$\hat{H}_{\mathrm{LMG}} = -\frac{J}{4}\sum_{\langle i,j\rangle}(\hat{S}_x^{(i)}\hat{S}_x^{(j)} + \hat{S}_y^{(i)}\hat{S}_y^{(j)}) + h_z\sum_i \hat{S}_z^{(i)},$$

with infinite-range interactions $J > 0$. The energy states are the collective spin states $|S, M\rangle$ with the eigenenergy $\mathcal{E}_{S,M} = -\frac{J}{4}(S(S+1) - M^2) + \frac{J}{2} + h_z M$. By setting $h_z = J/2$, the ground state can be made $|W_1\rangle$. Proceeding with the methods in sections 9.15.2–9.15.3, we calculate $\{\Delta^{(T)}, y_c^{(T)}\}$ for the Gibbs state $\hat{\rho}_G^{(\mathrm{LMG})}$ of $\hat{H}_{\mathrm{LMG}}$, as depicted in the blue dash-dotted lines of Fig. 9.8 and Fig. 9.2b.

Chapter 10

Conclusion and outlook

10.1 Conclusion

So here I am at the very last chapter of my doctoral thesis. I find it difficult not to feel nostalgic about my experience in the Caltech quantum optics group over the past 5 years. I am fortunate to have led and undertaken a 'collective' endeavor of an 'ensemble' of many brilliant scientists. Looking back, my stay at Caltech was a tremendous journey of excitement, passion, trust, and fulfillment shared collectively among my peers and myself, as we faced and solved challenges in the lab. Indeed, this thesis is a result of many people's hard work and collaboration, and I acknowledge their tireless contributions to the body of work for my doctoral thesis, as further summarized in the acknowledgement section. Personally, developing keen fellowship with these people has been by far one of the most meaningful achievements I have made during my time here. I hope that by writing this thesis I have adequately summarized the scientific advances of our experiments in the unifying theme of quantum networks, which we have contributed to a field that has been growing at an explosive pace (chapters 1–2).

In this thesis, I presented a series of experimental and theoretical studies (chapters 3–9), which, I believe, have made important contributions to the field (chapter 1). Following the Duan-Lukin-Cirac-Zoller protocol[4], we have studied in detail the decoherence mechanism for the entanglement stored in two atomic ensembles (ref.[34], chapter 3), demonstrated the first functional quantum nodes for the *DLCZ* quantum network (ref.[36], chapter 4), and made the initial step towards entanglement connection (ref.[37], chapter 5). We have demonstrated the first reversible mapping of photonic entanglement into and out of quantum memories (ref.[30], chapter 6). We have theoretically developed a nonlocal, nonlinear entanglement witness based on quantum uncertainty relations to efficiently characterize multipartite entanglement (ref.[38], chapter 7), and applied the entanglement verification protocol to verify multipartite mode-entanglement for one photon (ref.[35], chapter 8). Finally, we have achieved measurement-induced entanglement of spin waves among multiple quantum memories and opened new prospects towards multipartite quantum networks (ref.[33], chapter 9).

10.2 Outlook

In less than a decade since the initial demonstrations of a quantum interface between light and matter[90,91], light-matter quantum interface has become one of the pillars in the field of quantum information processing and communication, and one of the most active areas of research at the present time. A number of the experiments has made fundamental discoveries of new physical processes of controlling quantum coherence and entanglement, with promising results revealing various paths towards the realization of scalable quantum networks, including those in chapters 3–9.

Despite the remarkable advances, the current state of the art is still primitive relative to that required for the robust and scalable implementation of sophisticated network protocols (see chapter 9). One of the long-standing issues in achieving a large-scale quantum network is the unfavorable laboratory scalability for free-space ensemble-based approaches. Indeed, an important drawback of the current experiments in my thesis is the tremendous technical complexities required to implement even the rudimentary quantum information operations with sufficient fidelities for quantum error-corrections, as vividly illustrated in Fig. 10.1. I believe that this brings a very pragmatic opportunity for us to transit from the present free-space quantum optical laboratory to nano-integrated systems comprised of ultracold atomic ensembles and solid-state spin ensembles interacting on a photonic waveguide circuit.

An initial step towards such a hybrid quantum system was made in 2008 with our proof-in-principle experiment, whereby an entangled state between two cold atomic ensembles was created by the reversible and deterministic mapping of an entangled state of light (ref.[30], chapter 6). More recently, we achieved the coherent transfer of the quantum information stored in multipartite entangled spin waves of four quantum nodes of a network to multipartite entangled beams of light, each propagating through individual photonic quantum channels (ref.[33], chapter 9). Importantly, these recent experiments are natural precursors for creating a 'hybrid' entangled state for many solid-state and spin-wave qubits via the coherent mapping of a photonic entangled quantum bus over a 'lithographically patterned' quantum network.

In addition, I am particularly interested in studying the behavior of quantum entanglement in quantum many-body systems[39,40]. For example, in chapter 9, we investigated the thermal entanglement for the 'spin waves' in quantum magnets and related such thermal spin relaxation processes to the statistical behavior of our system of four atomic ensembles[33]. Creating such theoretical and experimental tools to probe quantum critical phenomena would contribute to the study of quantum entanglement in condensed matter systems and the creation of nonlocal quantum phases that have not heretofore existed[33]. Theoretical investigations of entanglement verification are crucial in this area of research[33,57,121,208], in conjunction with developing experimental tools for quantum information processing (refs.[30,33], chapter 6 and 9).

In line with a broader scope of the program towards a hybrid quantum network, such a lithographic optical network may provide an attractive platform to create and control exotic quantum phases associated with novel 'classes' of entanglement. I am intrigued by the aspect that these quantum phases may be 'induced'

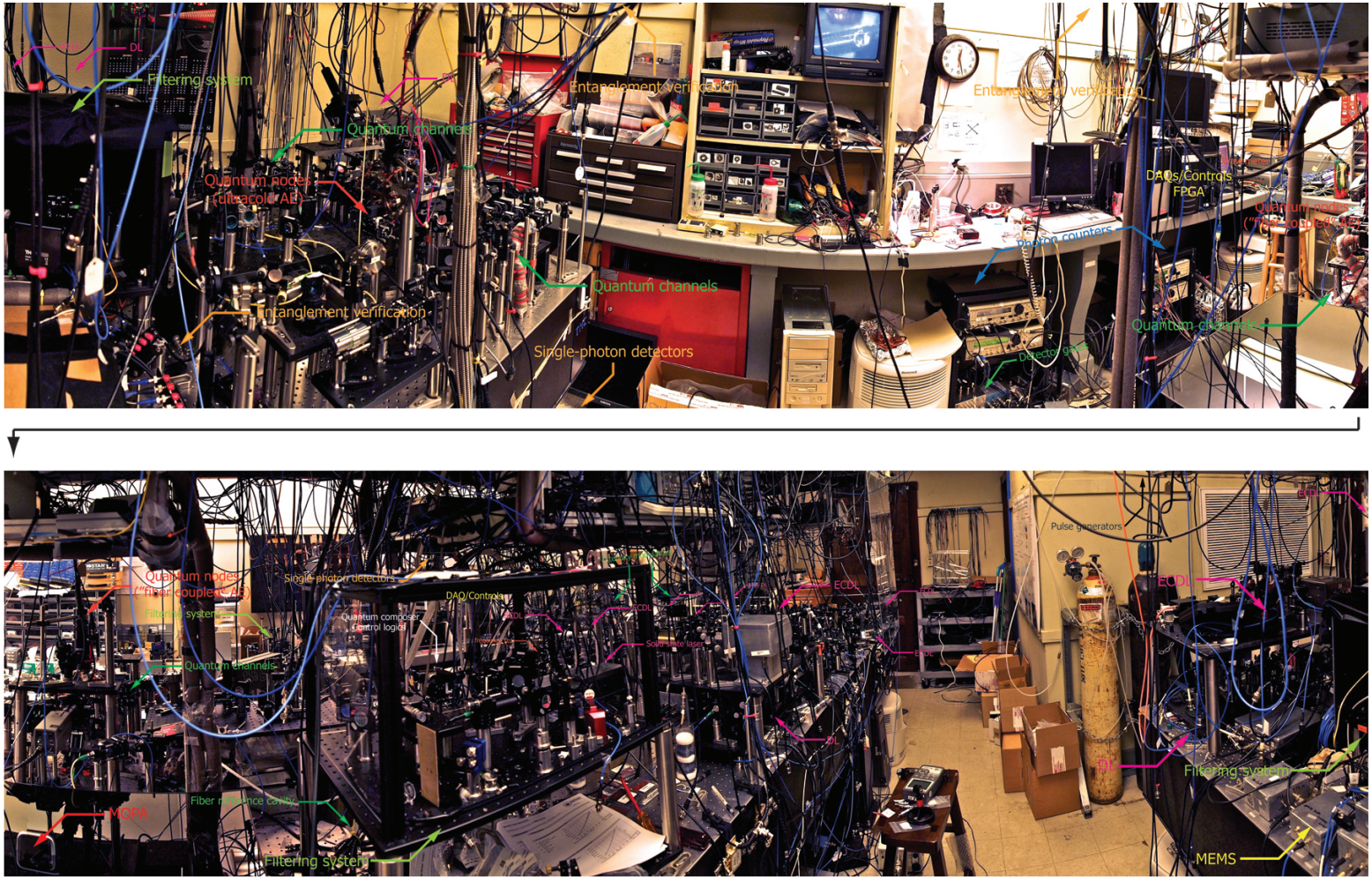

Figure 10.1: **Scaling behavior of laboratory complexity.** A panorama photo of our lab in early 2011. Dazzling complexity is required for laser cooling and trapping, as well as for state-initialization and for generating the classical beams for writing and reading spin waves. A significant portion of the setup is dedicated for laser stabilizations (with a total of 18 lasers operating at the moment), filtering the quantum fields at the single-photon level with high efficiency, and data acquisition. AE: Atomic ensembles, DAQ: Data acquisition system, DL: Diode laser, ECDL: External cavity diode laser, FPGA: Field-programmable gate array, MEMS: Micro-electro-mechanical systems, and MOPA: Master oscillator power amplifier (tapered amplifier).

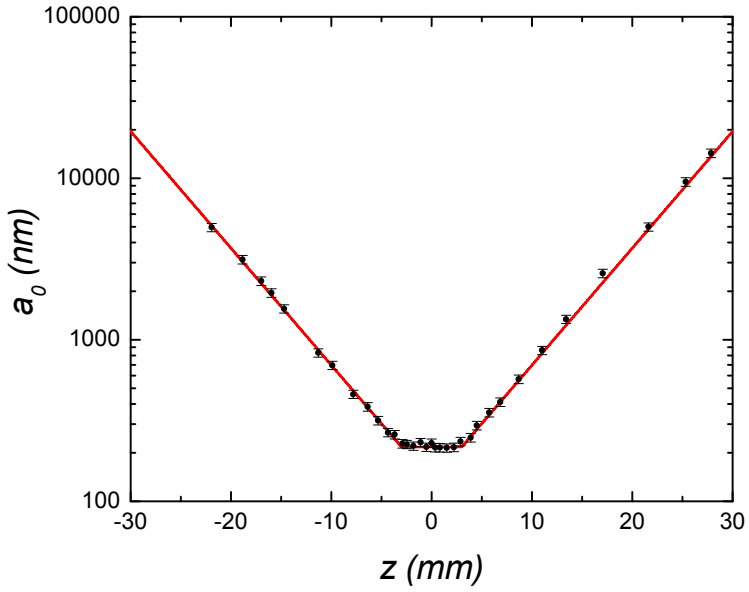

Figure 10.2: **Tapered fiber profile measured by a scanning electron microscope (SEM).** We show the tapered fiber profile based on SEM images taken by Daniel Alton and Clement Lacroute for a pulled SiO_2 fiber. The theoretical line (red line) is based on a simple model of volumetric conservation of the initial cylindrical fiber for a given hot-spot region, which results in an exponential tapering of the fiber radius[301]. The fiber radius at the center is $a_0 \simeq 250$ nm over a flat region of $z_0 \sim 6$ mm.

with nonlocal interactions of atomic pseudo spins and electronic spins by quantum-state exchanges and teleportation over quantum networks[8]. The research performed towards this end is both of fundamental interest for enhancing our understanding of quantum physics and of potential technological importance. Its highly interdisciplinary character encompasses a broad spectrum of fields in physics as well as in computer science and information theory.

10.3 Trapping atomic ensembles with evanescent waves of a nanofiber

Along this line, my colleagues and I are now involved in a long-term program of integrating 'quantum transistors' of atom-like qubits and 'quantum interfaces' to achieve connectivity for the quantum information stored in spin-wave quantum memories[1] to single photons and phonons, with the 'quantum wiring' provided by the quantum circuits imprinted on nanophotonic structures[139,302]. Recent advance includes the observations of electromagnetically induced transparency for trapped ultracold atoms in hollow core fibers[303–306], as well as the trapping and probing of atomic ensembles via the evanescent fields surrounding tapered nanofibers[291,307–309].

While prominent examples of off-resonant interaction between evanescent waves and matter have used planar dielectric geometry for atom optics and interferometry[310–312] as well as for surface traps of quantum degenerate gases[313–315], recent progresses of atom-light interactions with optical waveguides[291,305–309] set the stages for the fiber integrations of free-space quantum systems in a quantum network (chapters 3–9)

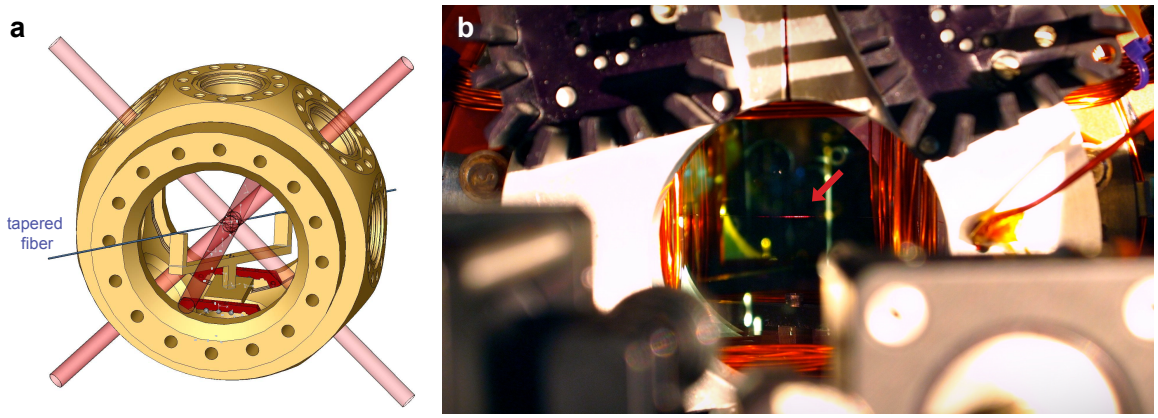

Figure 10.3: **A nanofiber trap for atomic ensembles. a**, CAD drawing (Solidworks) of the fiber trap setup. **b**, A photo of the nanofiber probing laser-cooled cesium atoms in a UHV chamber. The red glow of the tapered nanofiber is due to the Rayleigh scattering of blue-detuned evanescent fields ($\lambda_b = 687$ nm).

via quantum-state transfer between matter and light[30,33] and for the localization and strong coupling of single atoms and photons near microcavities[153,316]. Furthermore, these effective 1-dimensional systems may be applied for investigating quantum many-body phenomena with long-range interactions mediated by the waveguide[317].

As a first step, my colleagues and I have been investigating a nanofiber atom trap ($a_0 = 200 \sim 250$ nm radius), for which single atoms can be trapped within the small mode-volume of the evanescent fields. Inspired by the initial experiments[133,291,292,318], we have theoretically developed a novel state-insensitive two-color fiber trap to increase coherent times τ_c and trap life time τ_t (Fig. 10.5). As illustrated in Fig. 10.5, the engineered potential U_{trap} provides 3-dimensional confinement for trapping single atoms 150 nm away from the nanofiber with trap depths up to $U_{\text{trap}} \simeq 0.5$ mK (ref.[319]).

Recently, we have fabricated such a nano-thin tapered optical fiber from a flame-brushing technique with hydrogen torch in lab 1 (for a nice review of diverse techniques used for tapered fiber fabrication, I refer to ref.[320]). While Daniel Alton, Clement Lacroute, and Tobias Thielle in lab 1 led the responsibility for the fiber fabrication and the pulling setup[321], Aki and I have also contributed to the characterization of the polarization properties of the fabricated nanofibers and to the theoretical understanding of the fiber pulling process[301,320,322–325]. In particular, Daniel Alton and Clement Lacroute can now pull fibers quite consistent with the theoretically simulated fiber profile[301], as shown by Fig. 10.2.

We have placed such a nanofiber in our vacuum chamber shown in Fig. 10.3 and we are currently working towards trapping an atomic ensemble around the fiber. We have observed the transmission spectrum T with thermal cesium atoms released from a magneto-optical trap by the near field of the optical nanofiber in Fig. 10.4a and determined a resonant optical depth of $d_0 = (5.8 \pm 0.3) \times 10^{-3}$ by a probe laser E_p at the $6S_{1/2}, F = 4 \leftrightarrow 6P_{3/2}, F = 5$ transition. From the measured phase space density, we extrapolate that only ~ 1 atom is present on average within the interaction volume. We also measured the saturation effect of the atomic dipole via the evanescent field E_p, and studied preliminary results for the mechanical effects of

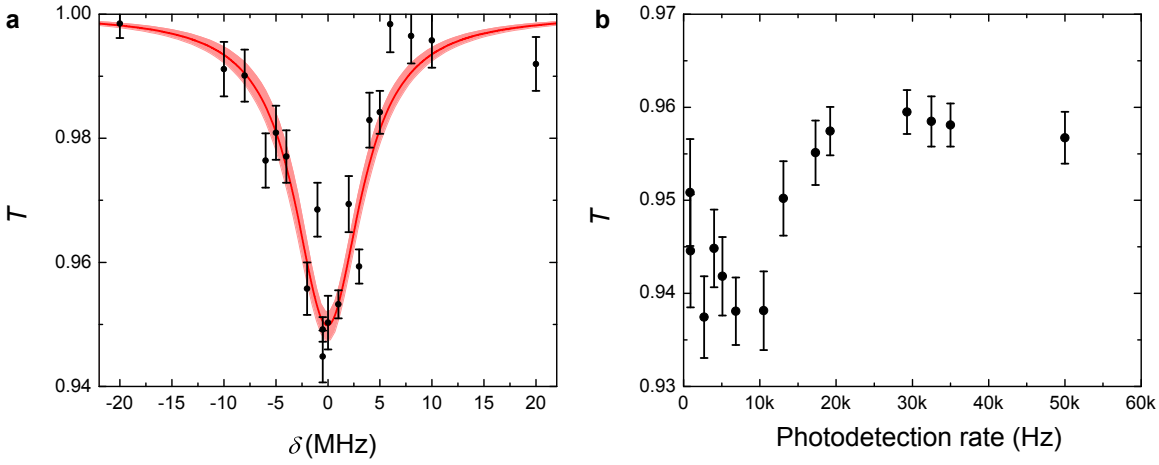

Figure 10.4: **Probing cold atoms with a tapered nanofiber. a**, The evanescent field of the tapered nanofiber is used to probe the transmission T of the nanofiber near the cycling transition $F = 4\ (6S_{1/2}) \leftrightarrow F = 5\ (6P_{3/2})$ of atomic cesium, as a function of detuning δ. The measured linewidth of the transition is $\Gamma = 7.7 \pm 0.9$ MHz, with a small optical depth $d_0 = (5.8 \pm 0.3) \times 10^{-2}$ on resonance, due to the limited phase space density of the magneto-optical trap at the time. The red band is the $1/e$ confidence level of a Lorentzian fit. **b**, Observation of saturation effects for thermal atoms nearby a nanofiber.

the atoms by the probe laser. Theoretically, we are further exploring novel state-insensitive trapping geometries with the adiabatic trapping potential predicted in Fig. 10.5. The details of the theoretical calculations, however, will be discussed elsewhere.

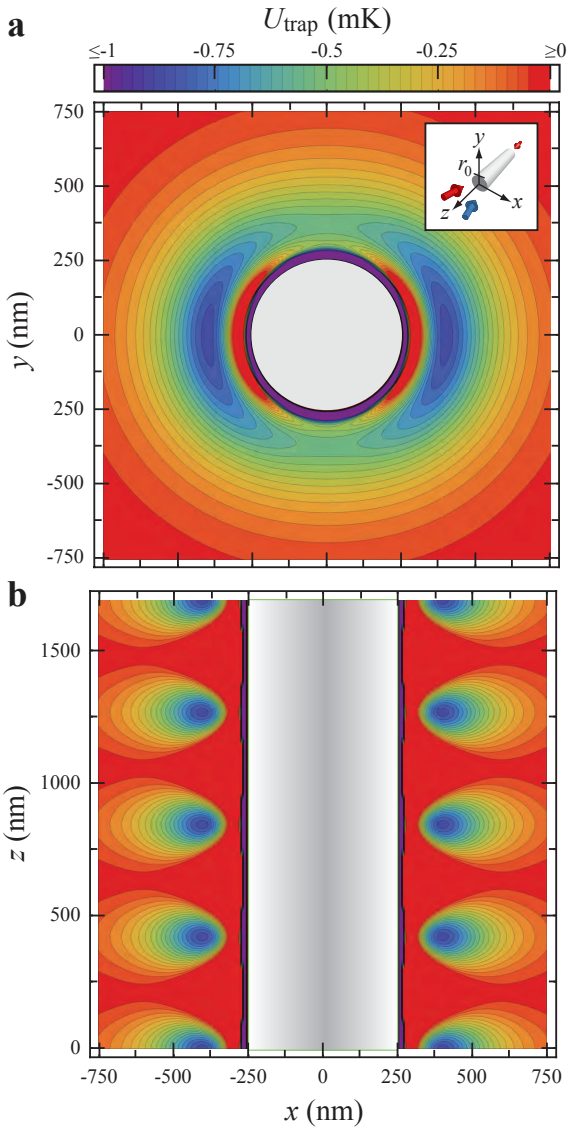

Figure 10.5: **Trapping single atoms with nanofibers.** A two-color optical trap around a nanofiber[319]. The trapping potential U_{trap} is generated by two evanescent fields that provide a 3D confinement for the trapped atoms outside the 500 nm diameter optical fiber, shown in **a**, the x-y plane, and in **b**, x-z plane. Specifically, U_{trap} results from two counter-propagating red-detuned beams (935 nm, red arrows), and a blue-detuned beam (687 nm, blue arrow) in a 'magic' configuration, as shown in the inset. The standing wave structure of the attractive red-detuned field and the repulsive force from the blue-detuned beam enable trapping of single atoms at each node of U_{trap} near the dielectric waveguide despite the strong surface potential $U_{surface}$, thereby reducing collisional and motional dephasing of spin waves.

Appendix A

Electronic circuitry

A.1 Designing printed circuit boards

Printed circuit boards provide a convenient platform for assembling electronic circuits. Comprised of sandwiches of alternating insulating and conducting layers (including signal traces and reference planes), proper PCB designs can be a challenging task. Nonetheless, PCB design is one of the most important tasks in achieving optimal performance of the final system. For example, the track length of the PCBs can be shortened to reduce the overall delay[a], and the tracks can be patterned for controlled line impedance in the high-frequency domain by way of transmission lines. In this appendix, I discuss basic technical considerations for designing electronic circuits and for producing PCBs[326,327] with a few examples of digital and analog circuits I have used in the lab. In the 'lab 2 disc', you can find more electronic files for the PCB boards (e.g., high-voltage amplifier, bias coil controller, and phase-sensitive detectors) designed since 2006. For an in-depth treatment of PCB designs and instructions, I refer to ref.[327].

Printed circuit board technology has made great improvements in manufacturing tolerance and board density over the years, but the basic construction layout has not changed significantly. PCB are made out of patterned copper sheets (with etching) on a dielectric insulator such as FR-4 epoxy fiberglass. A simple multilayer PCB consists of (from top to bottom): A silkscreen, top solder mask, top copper plane, inner ground plane, inner power plane, bottom copper plane, bottom solder mask. The silkscreen layer outlines the components and texts (yellow ink). The front and back planes form the component footprints, whereby the vias and traces are etched away. This allows to interconnect components on the same plane (traces) and components from the top to the bottom planes (vias). It is a good practice to order the board with solder masks to prevent solder bridges from forming between adjacent pads and traces.

Also, it may be useful to begin with a multilayer (e.g., 4-plane) board if you have high-power or high-frequency components which may cause electromagnetic interference (EMI) radiation. The two additional copper planes serve as the power and ground planes. This may be useful for high-speed digital circuits, where

[a]For modern digital circuits, it is common to find clock speeds greater than 1 GHz. For high-frequency analog components, the servo bandwidth may be limited simply by the propagation distance of the signals.

one can reduce the power wiring inductance and impedance to the high-speed components. By placing the tracks on the inner planes (i.e., creating a stripline), the outer conducting planes can shield high-frequency radiation and improve the noise immunity of the circuit. Since any through-hole pad on a four-layer board can be connected to or isolated from either of these planes, the ground and power planes can also be used to reroute the signals.

Here is a standard workflow for developing a simple PCB board:

1. Capture the schematics and circuit diagrams.
2. Design component footprints.
3. Establish PCB outline.
4. Set up design rules.
5. Place components.
6. Manually route traces and auto-router.
7. Export into Gerber format.

While there are excellent programs available at low cost, I have used a free CAD program (also a PCB manufacturer), called 'ExpressPCB', for drawing the schematics and the PCB layouts and for ordering the boards.

A.2 Multilayer board design

A.2.1 Vias

A via connects (top and bottom) layers on the PCB using plated through holes (PTH) technology. The PCB board is drilled and the inner surface (of the cylinder) is plated with silver. For connecting to high-power planes, the via's size should be chosen with care (see section A.2.3). For multilayer design, vias can also be formed between the inner layers (buried vias), and between the outer layer and one of the internal layers (blind vias). For smaller sizes < 6 mil, microvias can be formed to achieve higher component density by deforming the copper plane with a high-power laser. Note that vias cause discontinuity in the line impedance for $\nu > 10$ MHz, and surface mount components are preferable for connecting the pins to traces (or a patterned transmission line for microwave frequency, section A.2.3).

A.2.2 Pads

A pad is a small conducting surface made out of copper used for a component pin. As a standard, it is useful to identify the ground pin (or pin #1) of the component with a square pad, and the signals with round pads.

An anti-pad can be used to isolate the pin to the copper plan. A thermal pad can be used to restrict the heat flow when the pin is connected to one of the copper planes. For PTH vias, as a general rule of thumb, it is good to keep a pad-to-hole ratio of 2:1.

A.2.3 Traces

A trace connects two points on the PCB by etching away the copper plane. The trace on the PCB is a copper stripline (rectangular cross-section) not a wirebound (circular cross-section), and the depth is set by the PCB manufacturer (typically, $d \simeq 1.5$ mil). A tricky problem is to set the width w of the trace for a given length l. This requires several considerations including power and heat management (for high-current traces), breakdown voltage in atmosphere and dielectric constant of FR4 (for high-voltage traces), and wire impedances (for high-frequency signal traces and digital logic), as further described in section A.3. When placing a trace, it is usually good to keep a space of > 7 mil between the traces and between any adjacent conducting pads. Otherwise, the etching process may develop hairline shorts or openings. I also refer to the concepts of 'electric clearance' and 'creepage distance' in section A.3.2. For narrow traces below $w < 12$ mil, it is good to put a chamfer for a 90° bend, formed with two short 45° angle bends. To avoid crosstalk between two traces above a ground plane, it is good to decrease the distance between the plane and trace as much as possible, and increase the distances between traces. The crosstalk coupling between two traces scales as $\propto \frac{l}{(1+(\Delta d/\Delta h)^2)}$, where Δd is the shortest distance between the two traces, Δh is the distance from the ground place to the traces, and l is the length of the traces. With most CAD programs, one can write a design rule to specify the minimum trace widths and maximum bending angles at the fabrication tolerances of the PCB manufacturer.

A.2.4 Planes

A plane is an uninterrupted conductive area of the entire PCB layer. Traces are formed by etching out a plane and by isolating from the power planes to distribute power and signals to the PCB components. It is very important to have at least one dedicated power and ground planes as low-impedance reference planes. If the system is composed of mixed analog and digital circuits, it is important to separate analog and digital ground and power planes. The analog ground plane should be placed below the analog power plane, and the digital ground plane underneath the digital power plane, with no overlap among the four planes (check the vias!). The analog and digital traces will run on the surface of the PCB board, while the inner planes will shield the analog components from the high-frequency radiation and noise of the digital ground. For high-frequency application, it is good to avoid the signal traces on the ground plane, as the discontinuity in the ac current flow can lead to EMI. While an uninterrupted ground plane can be thought as a reasonably good low-impedance reference, for traces running with high-frequency (> 1 MHz) current, the inductive coupling sets a specific path for the return loop current, which tends to minimize the loop area. The return current, thus, flows on the

ground plane underneath the signal traces[b]. For high-current application, it may be good to consider putting a star ground or a split ground plane to the main power filter.

A.2.5 Components

There are many types of packaging available today, some of which include PTH components, surface mount, and wirebound components. Metallic components such as heat sinks, crystals, switches, connectors may cause shorts if placed over traces on the top layer. If one must be placed above the trace of the top layer, it may be important to consider the dielectric constant of the surface mask (i.e., the green insulating layer on the surface planes). Wirebound components, which usually have a nice integrated heat sink, are useful for high-power applications. Both the PTH and wirebound components may be detrimental for high-frequency applications as the discontinuity in the solder joint may cause EMI radiation or significant voltage attenuation from the high-contact impedance (see section A.3.3). In this case, it may be a good idea to find an alternative surface mount component.

A.3 Technical considerations

A.3.1 Leakage resistance

Leakage resistance is a static circuit board effect, where contaminants on the PCB surface (e.g., flux residues) cause leakage currents across the circuit nodes. Ref.[327] suggests a simple cleaning method: (1) wipe the PCB with isopropanol, (2) wash with deionized water, and (3) bake at $85°C$ for a few hours. Another method to prevent leakage currents is to "guard" the sensitive signal tracks and power lines by surrounding with the ground planes exposed above the coating in order to sink the leakage current.

A.3.2 Electrical clearance and creepage distance for high-voltage applications

The electrical clearance is the minimum distance between two conductive high-voltage traces, where a dielectric breakdown occurs between the traces by air ionization (depending on humidity, altitude, and temperature). According to ref.[327], it is good to restrict the minimum distance between tracks to 315 mil. Similarly, a creepage distance is the shortest distance between two conductive traces, whereby the dielectric breakdown occurs along the insulation (FR4, relative dielectric permittivity $\epsilon_{\text{FR4}} \simeq 4.5$ and dielectric breakdown $\simeq 40$ kV/mm). It is important to keep the tracks separated with distances larger than the creepage distance to avoid localized conduction on the insulating surface by electric discharges.

A.3.3 High-frequency electrical transmission lines

The induction of a copper trace plays an important role for high-frequency analog devices and for high-speed digital logic. A wire inductance (for wirebound components) is given by $L_{\text{wire}} = 0.2$ (nH/mm) $\times l[\ln(2l/r) - 0.75]$, where r is the radius of the wirebound. A strip inductance (e.g., for copper trace) is $L_{\text{strip}} = 0.2$ (nH/mm) $\times l[\ln(2l/(w+h)) + 0.22(w+h)/l + 0.5]$. For optimal EMI reduction, high-frequency signal traces should be embedded in the internal layers between power or ground planes, forming a stripline transmission line, where the power planes shield the high-frequency radiation.

First, it is important to determine whether or not a transmission line is needed. For a high-speed logic with rise/fall time t_r, the trace needs to be terminated with their characteristic impedance if the track length l is greater than the characteristic length $l_c = v_s t_r$, where the signal travels conservatively at a speed of $v_s \simeq 2$ in/ns. Similarly, in the analog domain, an active non-inverting amplifier with a maximum bandwidth of f_m has an equivalent rise time $t_r = 0.35/f_m$. Thus, one should consider transmission line techniques when placing signal tracks with $l > l_c = v_s t_r$. There are two typical high-frequency transmission lines (i.e., microstrip and stripline transmission lines), which are relatively simple to fabricate on a PCB. The determination of the parameters to obtain a good transmission line depends on the thickness of the dielectric layer to the reference plane, dielectric permittivity of the insulating layer, the routing copper thickness, and the trace width. Note that vias cause discontinuities in the characteristic impedance of a transmission line.

A.3.3.1 Microstrip transmission line

A simple method for a two-layer PCB is to use the ground plane and a signal trace for controlled impedance, as shown in Fig. A.1a. This geometry is known as a microstrip transmission line[326]. The characteristic impedance of a microstrip is given by

$$Z_{\text{micro}} \simeq \frac{87}{\sqrt{1.41 + \epsilon_{\text{FR4}}}} \ln[6h/\pi(0.8w + t)]. \tag{A.1}$$

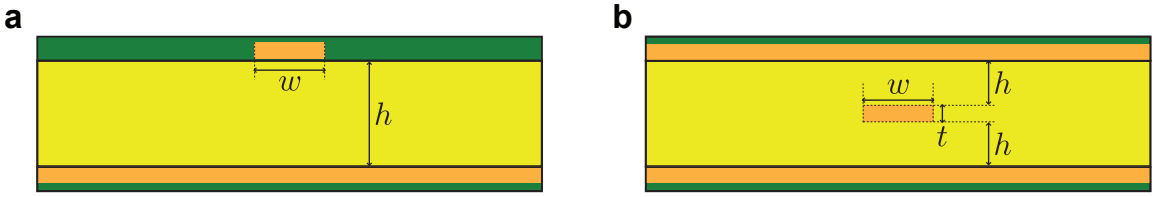

Figure A.1: **Controlled impedance transmission lines. a**, Microstrip transmission line. **b**, Stripline transmission line. The layer thickness t and depth h are usually set by the manufacturer. By choosing the width w of the track, one can control the impedance of the transmission line. The green layer is the insulating silk screen, the yellow layer is the dielectric FR-4 glass epoxy, and the gold layer is the copper which forms a conductive layer.

[b] In reality, the finite conductivity of the copper plane sets a finite area of the return loop, where the return loop flows 'close' to the signal trace.

In addition to the characteristic impedance Z_{micro}, the microstrip has a characteristic line capacitance of C_{micro} (pF/in) $\simeq \frac{0.67(\epsilon_{\text{FR4}}+1.41)}{\ln[6h/\pi(0.8w+t)]}$. In most cases, the thickness h of the insulating FR4 layer is set by the manufacturer, and the only controlled parameter is the width w of the track. By setting the value of w, the impedance Z_{micro} can be set to typical values of 50 Ω or 75 Ω for impedance matching. For typical value of $\epsilon_{\text{FR4}} = 4$ with $h \gg t$, $w/h \simeq 2$ gives 50 Ω impedance. The signal propagates in the microstrip transmission line at a velocity of v_{micro} (in/ps) $= \frac{1}{85\sqrt{0.475\epsilon_{\text{FR4}}+0.67}}$.

A.3.3.2 Stripline transmission line

For a multilayer PCB, a preferred choice is to pattern a stripline transmission line for the signal track, by embedding the signal trace between the power and ground plane, as shown in Fig. A.1b. A sandwich of the two low-impedance ground planes and the embedded signal trace forms a symmetric stripline. Because of the inductive coupling, the return current paths for the high-frequency signal trace are located on the planes directly above and below the signal trace (see section A.2.4). Thus, the high-frequency signal is tightly confined within the signal trace (see also section A.3.4), thereby minimizing emissions and shielding the tracks from the environment.

The characteristic impedance of a stripline transmission line is given by

$$Z_{\text{strip}} = \frac{60}{\sqrt{\epsilon_{\text{FR4}}}} \ln[6(t+2h)/\pi(0.8w+t)]. \tag{A.2}$$

In addition, a symmetric stripline has a characteristic capacitance of C_{strip} (pF/in) $\simeq \frac{1.41\epsilon_{\text{FR4}}}{\ln[3.81h/(0.8w+t)]}$. The signal propagates in the stripline transmission line at v_{strip} (in/ps) $= \frac{1}{85\sqrt{\epsilon_{\text{FR4}}}}$.

A.3.4 High-frequency skin effect

Signal currents at high frequencies tends to flow through the perimeter of the conductive trace due to inductive coupling. The skin depth causes an effective conduction area of ac-current flow smaller than the cross-section of the trace. In addition to the effects of impedance at higher frequencies, the skin effect results in an increase of resistance at higher frequency. The skin depth d_{skin} for copper is approximately given by $d_{\text{skin}} \sim 2$ (μm $\sqrt{\text{GHz}}$) $/\sqrt{f}$. Assuming an effective cross-section for the current flow by a flat-top profile $A = w \times d_{\text{skin}}$, the resistance for copper is then $R_{\text{skin}} \sim 8 \times 10^{-3}$ ($\Omega/\sqrt{\text{GHz}}$) $\sqrt{f}(l/w)$ (see Eq. A.3). For dc-currents, see section A.3.6.

A.3.5 Stray capacitance

The capacitance between two conducting layers with a distance d and area A is $C_{\text{plate}} = 8.9\epsilon_{\text{FR4}}$ (aF/mm) $\times A/d$ (see Fig. A.1), where $d = h$ (Fig. A.1a) or $d = 2h + t$ (Fig. A.1b). A voltage noise V_n on one plane can capacitively couple to another plane with a coupling voltage of $\delta V_c = V_n Z_1/(Z_1 + Z_2)$ where Z_1 is the

circuit impedance and $Z_2 = -i/wC_{\text{plate}}$. To prevent capacitive coupling between two signal traces and two planes, one may insert a ground plane, acting as a Faraday shield between the noise source and the affected circuit.

A.3.6 High-current thermal management

A general rule of thumb is to keep the temperature increase to $\Delta T \lesssim 10^{\circ}C$. The sheet resistance of a trace is given by

$$R_{\text{trace}} = \rho_{\text{electric}} l/wd, \tag{A.3}$$

where $\rho_{\text{electric}} = 1.7 \times 10^{-6}$ Ω cm is the electric resistivity for copper at $T = 300$ K and l is the length of the track[c]. The temperature rise is then $\Delta T = \theta P_{\text{trace}}$, where $P_{\text{trace}} = I^2 R_{\text{trace}}$ is the power dissipation across the trace and $\theta = \rho_{\text{thermal}} l/wd$ is the thermal resistance of copper. The thermal resistivity of copper is $\rho_{\text{thermal}} \simeq 0.25$ cm $^{\circ}C/W$. For reference, the currents required to have $\sim 10^{\circ}C$ increase in temperature for standard track widths are shown in Table A.1. By connecting the signals to an active component (e.g., operational amplifier) in a Kelvin configuration, one can mitigate for the errors arising from the voltage drop across the signal trace, but it requires a negative feedback. Instead of using traces to ground the pins, star-grounding[326] to the main power filter or the usage of split ground planes (causing an effective star grounding) helps to obtain a good ground with low impedance[d].

Table A.1: **Thermal management of a copper trace.** We show the current I_{trace} required for a $10^{\circ}C$ increase in temperature for a sheet copper of depth $d = 1.5$ mil with various width w.

w (mil)	I_{trace} (A)
10	0.3
15	0.4
20	0.7
25	1
50	2
100	4

[c]For low-impedance circuits, one may need to also consider the temperature of coefficient for copper $\sim 0.5\%$ per $^{\circ}C$ at 300 K. Also note that the manufacturer often quotes the trace thickness d in the units of ounces of copper per ft^2, with common thicknesses 0.5 oz, 1 oz, 2 oz. For power traces, it is good to use 2 oz.

[d]Instead of using a ground trace, it is generally a good idea to have a ground plane, as the plane can be used as a low-impedance reference.

A.4 Control logic and buffer circuits

For the experiments in chapters 6–9, the slow cycling rate 40 Hz for the laser cooling and trapping stages is derived from a time base of the digital pulse generator (SRS DG535), which in turn triggers two phase-locked 16-output digital delay generators (SRS DG645). The overall system provides robustness compared to the previous generation (chapters 3–5) by integrating with proper buffer and line drivers (SN74ABTH25245) for better impedance matching and for sinking the large amount of current when "power gating" multiple single-photon avalanche photodiodes[e] (Perkin Elmer SPCM SQRH-16). The experimental repetition rate (2 MHz) is synchronized to a master clock running at 100 MHz (time base, 25 ppm 100 MHz crystal oscillator, with rms jitter of < 400 ps) via downconversion. A multiplexed pulse generator (quantum composer 9518^{+}) is controlled by Labview through USB interface. The TTL pulses generated from the quantum composer in burst mode are fed into a control logic, which relay or inhibit the signals conditioned on the photoelectric event at the SPCMs, with the rising edges of the pulses corresponding to the instants of detection.

As shown in Fig. A.2, the logic circuit consists of (i) dozens of control logic and gate pulse circuits, (ii) a memory gate pulse generator, and (iii) a field 1 sync circuit. Here, I describe the functions of each of the components: (i) The control logic relays the signal if the memory pulse (mem) is high. (ii) For the memory gate pulse generator, a field 1 pulse (red line) is split into multiple paths by a high-speed 1-8 clock distributor (CDC341), with one arm triggering a monostable multivibrator (74LS123ND) on the rising edge for a maximum wait time of τ_w (ns) $= 6 + 0.05C_m$ (pF) $+ 0.45R_m$ (kΩ)$C_m + 11.6R_m$, thereby relaying a logical 0 up to τ_w regardless of the input. If the monostable multivibrator detects a falling edge in the clear signal (CLR, black line) at $\tau_m < \tau_w$, the output (memory pulse) is raised to a logical 1-state (green line). Otherwise, the output is raised to t_w regardless of the state of CLR. In turn, the clear signal (CLR, black line) is generated from a triggered delay generator with programmable delay τ_m. (iii) The photoelectric detection event of field 1 can arrive randomly within the detection window. Field 1 sync circuit relays a pulse synchronized to the external master clock if a field 1 is registered.

In Fig. A.3, I show the printed circuit board for the control logic and the line drivers. All outputs of the logic circuit undergo a set of line drivers to provide proper impedance matching. The track lengths are significantly shorter than the characteristic length $l_c = v_s t_r$ given the typical rise-time of the logic ~ 1 ns (section A.3.3). Long tracks are optimized by employing microstrip transmission lines and line drivers.

[e] The bias voltage in the APD is abruptly turned off in $\ll 1\mu s$ by sinking ~ 380 mA at the gate voltage input of SPCM SQRH-16. When the bias voltage is zero, we can send significant amount of light onto the APD for acquiring the lock of interferometers without modifying the noise characteristics and quantum efficiency of the detector.

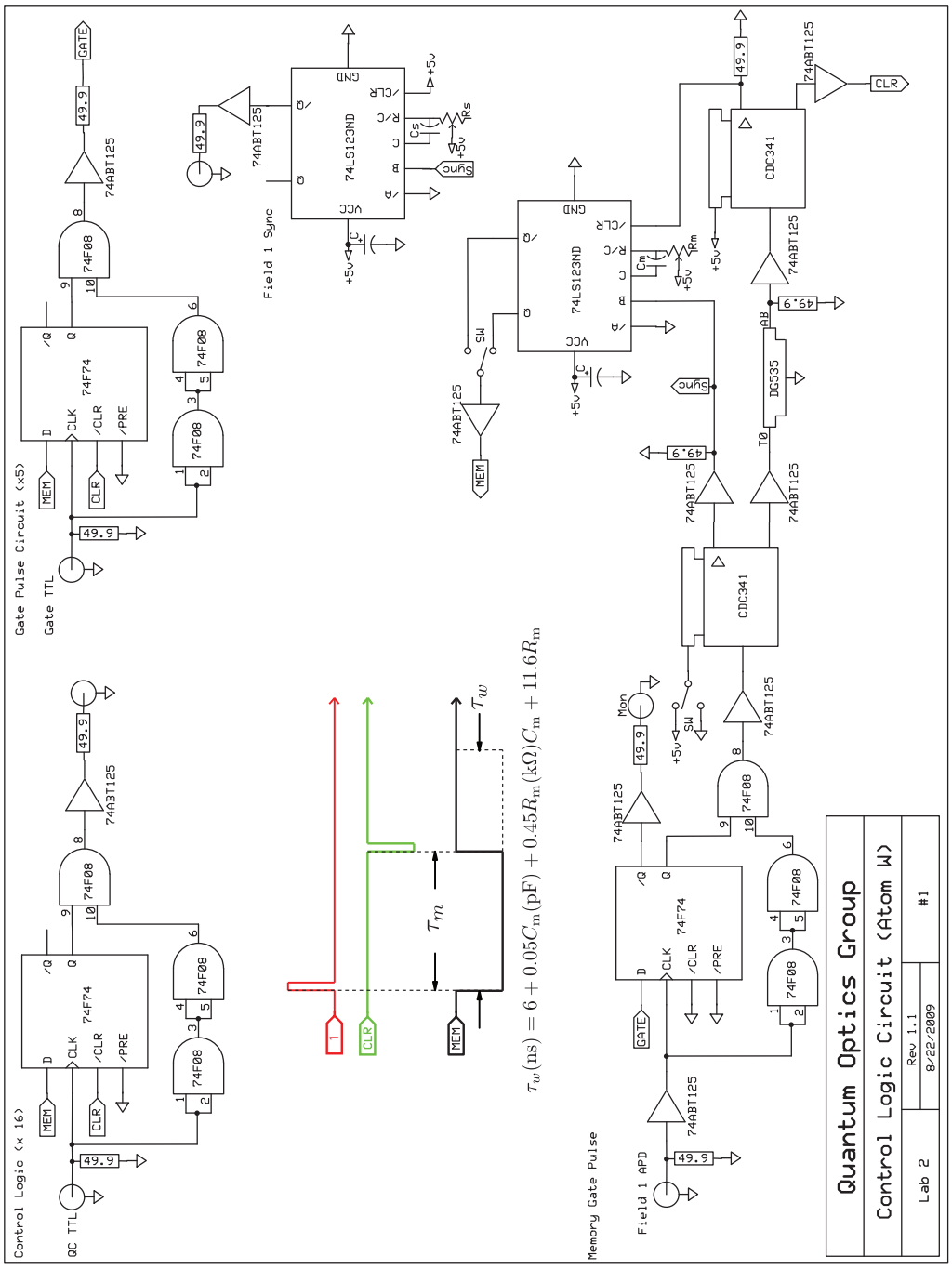

Figure A.2: **Circuit diagram for conditional control logic for triggering and relaying various signals.** The logic circuit consists of (i) control logic and gate pulse circuits, (ii) a memory gate pulse generator, and (iii) a field 1 sync circuit.

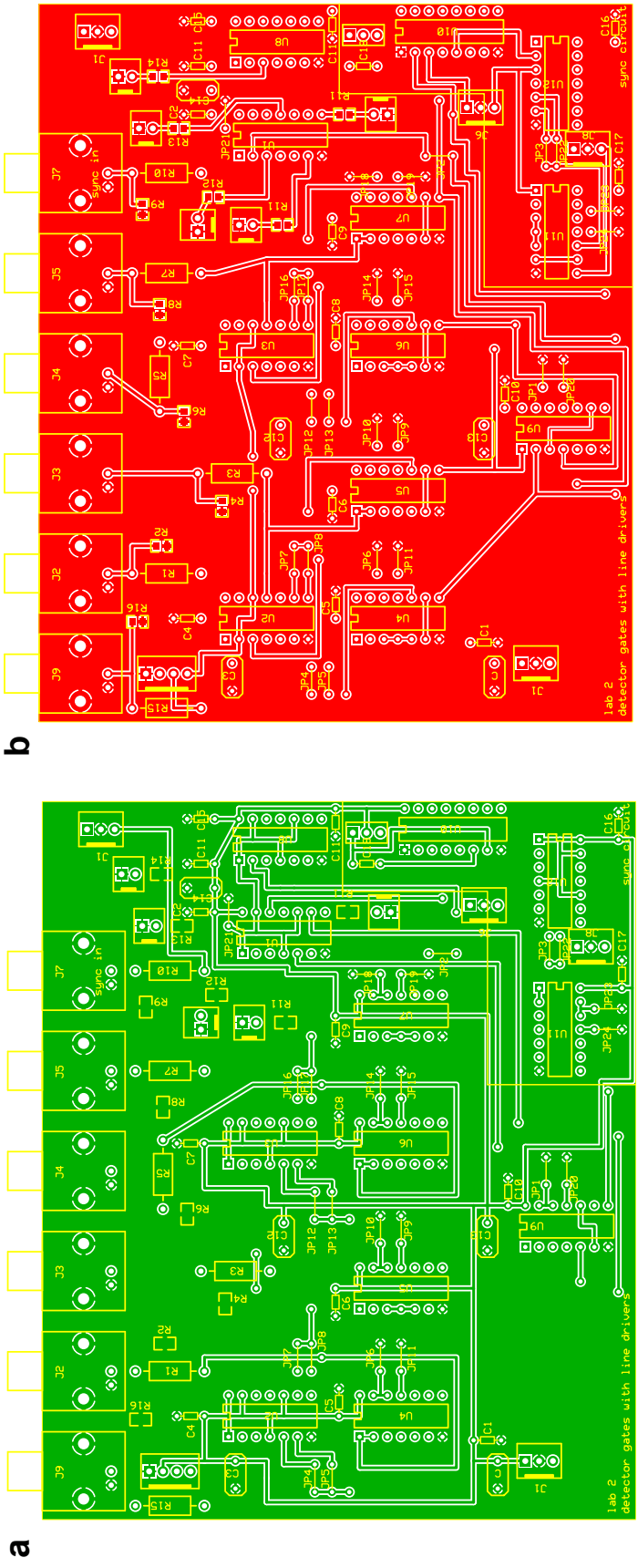

Figure A.3: **PCB board for conditional control logic for triggering and relaying various signals.** The logic circuit consists of (i) control logic and gate pulse circuits, (ii) a memory gate pulse generator, and (iii) a field 1 sync circuit.

A.5 Laser diode current controller

The diode laser systems in our group have evolved over time. While the mechanical aspects of the laser systems remain largely the same, new types of lasers have been introduced to lab 2, including an external cavity interference filter laser[f] [151,328]. Because of obsolete parts in the previous design of our group (by Joseph Buck), Aki and I redesigned the laser diode controllers, including the current controller, temperature controller, and FET modulation board. The current controller is still based on the original design [329] by K. G. Libbrecht and J. L. Hall, but I made some improvements to the circuit in a source/sink configuration in terms of temperature stability and noise characteristics of the circuit. Also, an override function was added. The temperature controller [330] and the FET modulation board remain the same, where we replaced the obsolete voltage reference.

I show the circuit design for the laser current controller in Fig. A.4 and the PCB layout in Fig. A.5. A negative (positive) voltage regulator, LM337 (LM317), provides the stable supply voltage with slow turn-on and current limit to the diode laser in the sink (source) mode. The precision voltage reference, LM399 (or LTZ1000 for better thermal stability 0.05 ppm$/^{\circ}C$) is heavily filtered to reduce noise, and the RC network in the LT1028 circuit provides stable operation with low noise. The Vishay sense resistor (VHP-4) is wired in a Kelvin configuration for dc-current stability. Low-level current modulation (Mod) is used for driving the error signal from dc to ~ 10 MHz, and an ac-coupled input (RF in) is used for RF-sideband modulation.

[f] More details on the interference filter laser, which Julien and I built during his visit in the summer of 2008, can be found in my lab notes.

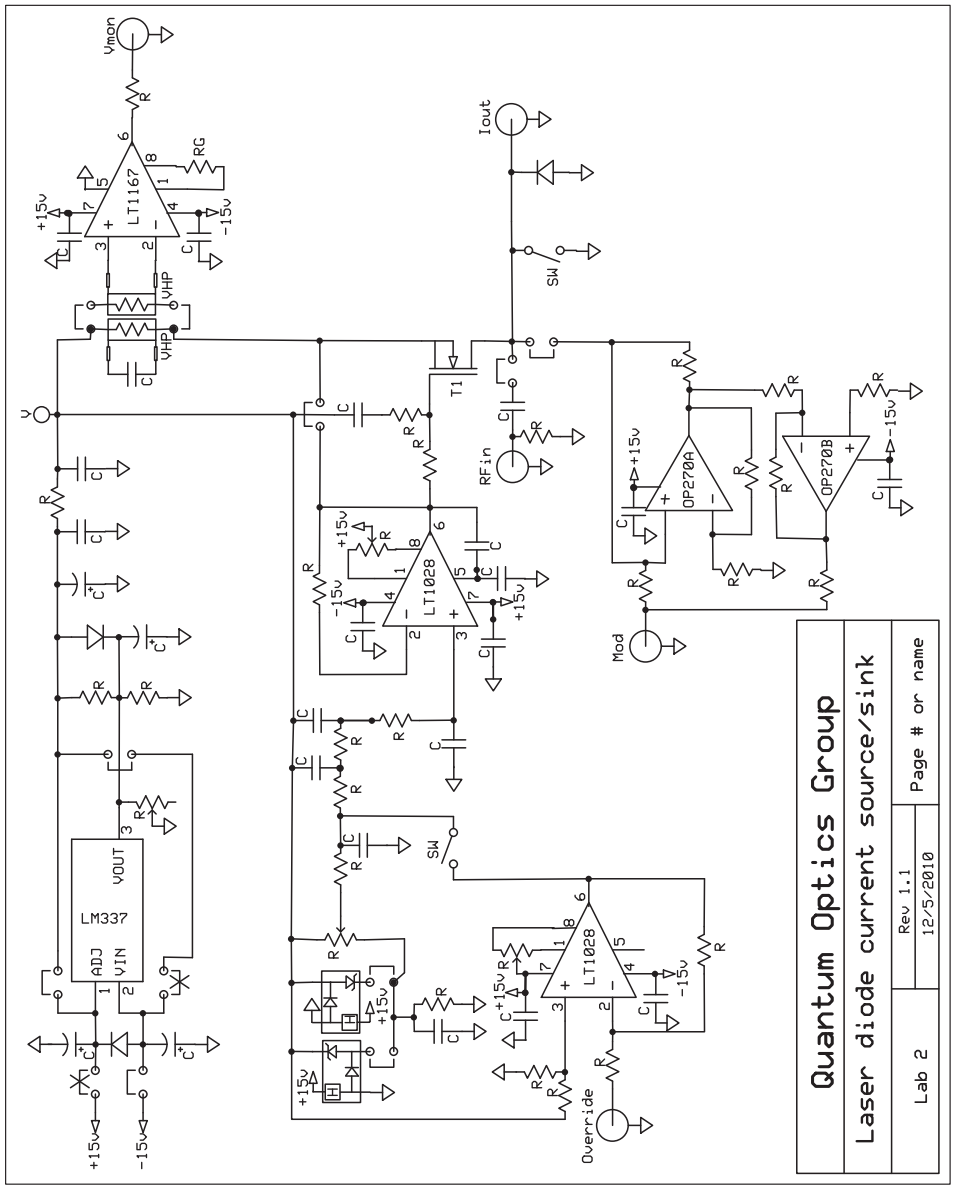

Figure A.4: **Circuit diagram for diode laser current controller.** The circuit diagram is shown for a current sink. For an analogous current source circuit, one needs to replace the negative voltage regulator LM337 with a positive one LM317, and connect the voltage reference LTZ1000 in a opposite manner.

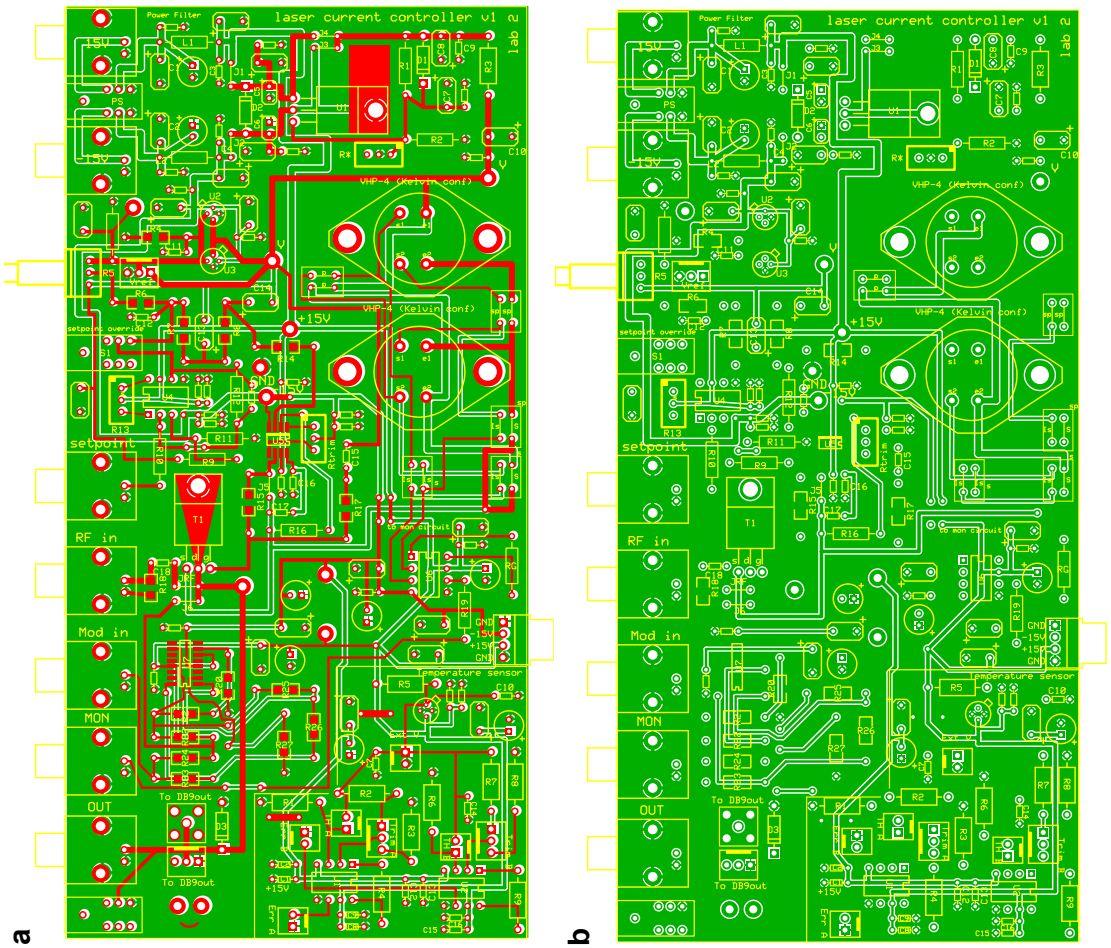

Figure A.5: **PCB board for laser diode current controller.** The circuit diagram is shown for a current sink. For an analogous current source circuit, one needs to replace the negative voltage regulator LM337 with a positive one LM317, and connect the voltage reference LTZ1000 in a opposite manner. The PCB also includes a small area dedicated for the temperature sensor with a bridge circuit.

A.6 Locking circuits for interferometers and intensity stabilization

For the experiments in chapters 8–9, we locked the verification interferometer via an *ex-situ* phase modulation spectroscopy. An important part of this technique is the capability to acquire and stabilize the interferometric phase to ϕ_0, to sample and hold (S&H) the phase ϕ_0 value over the experimental duration t_d, and to feed-forward an offset phase $\phi_{\text{exp}} = \phi_0 + \delta\phi$ during t_d. The power gating and the MEMS switches protects the single photon APDs from the strong reference laser. During the experimental phase, the reference laser is extinguished to > 180 dB, and the MEMS switches reroute the fiber optical channels to the single-photon detectors.

The active component of our interferometric stabilization scheme is a fiber stretching module (PZ1, Optiphase) with modulation constant $\beta = 0.4$ rad/V over dc $-$ 20 kHz (see Fig. 8.6). The phase is modulated at ~ 88 kHz (generated from SRS SR830) above the first resonance at $\nu_m \simeq 55$ kHz. The phase modulation is switched off by rf-switches (Minicircuit ZASWA-2-50DR) during t_w. The reference laser is monitored by a photodetector (or by a custom inline evanescent power tap PIN Si-detector, Oz optics OPM-11), resulting in the signal V_{pd}. Two lock-in amplifiers (SRS SR830 and SR510) demodulate the signals V_{pd} to generate error signals V_{der}. The error signal V_{der} and the photodiode signal V_{pd} are fed into the phase stabilization servo, as shown by Fig. A.6. Depending on the application, the two signals are summed or subtracted (i.e., $V_{\text{err}} = \alpha V_{\text{der}} \pm (1-\alpha)V_{\text{pd}}$). The P gain is controlled either by the proportional non-inverting amplifier or by changing the modulation depth, and the I gain is controlled by the integrator (with the variable capacitor). The phase stabilization servo bandwidth is limited to ~ 10 kHz by a Sallen-Key type low pass filter to avoid exciting ν_m of the stretching modules. A set of TTLs (S&H TTL and jump TTL) controls the sample and hold (S&H, LF398), and the jump operations (low-noise switch, MAX319) in the servo. The output of the servo is amplified by a high-voltage ($0-1$ kV) amplifier (Burleigh PZ70), which drives the fiber stretching modules (PZ1, Optiphase). This circuit was modified to stabilize the intensity of a diode laser. The set-point of the lock (i.e., phase set value ϕ_0 or intensity set value I_0) can be monitored at the set-point output and controlled by the error-signal bias point. The jump potentiometer controls the feedforward voltage for $\delta\phi$. For reference, I show the PCB layout for the phase stabilization and intensity stabilization servo in Fig. A.7.

A.7 Other electronics

In the "lab 2 disc", I compile more electronic circuitries in lab 2: Low-noise bias coil controller and servo, buffer circuits, laser current controller and temperature controller, high-voltage amplifier, digital clock distribution circuit, photodiode trans-impedance amplifier, phase-sensitive detector, phase stabilizer, laser diode protection board, piezo servo, dc high-voltage source, temperature sensor, controller for voltage-controlled oscillator (VCO), and high-Q phase reference with a phase-locked dielectric resonator oscillator (PDRO, Herley-CTI).

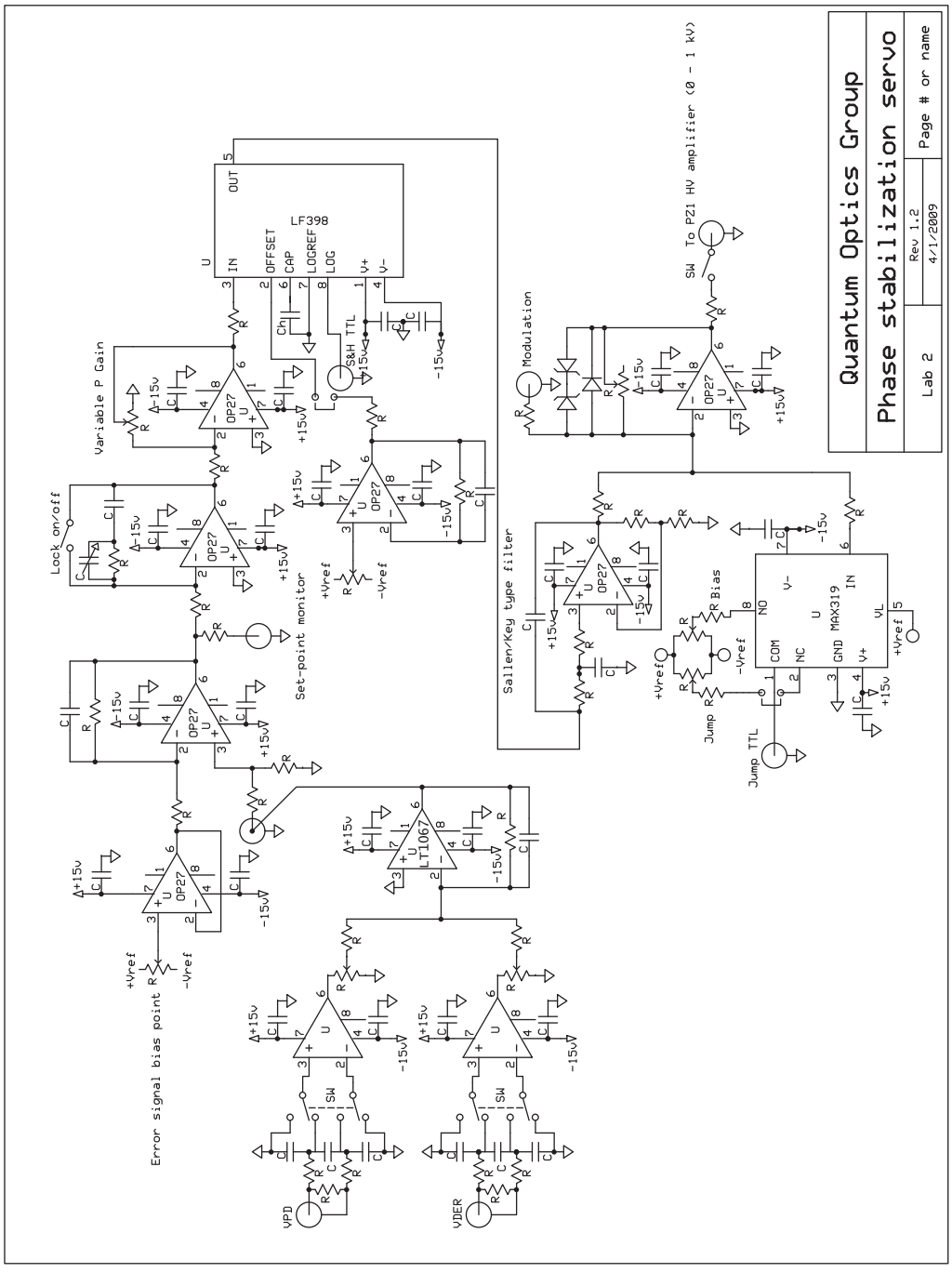

Figure A.6: **Circuit diagram for phase stabilization and intensity stabilization servo.** After acquiring the lock during the laser cooling and trapping period, LF398 samples and holds the output value of the servo during t_d, where the phase of the interferometer is set to ϕ_0. The jump TTL is initiated 3 ms afterwards to trigger a ultra-low noise switch MAX319 to offset the phase to $\phi_{\text{exp}} = \phi_0 + \delta\phi$ of the interferometer. The output of the servo is amplified by Burleigh PZ70.

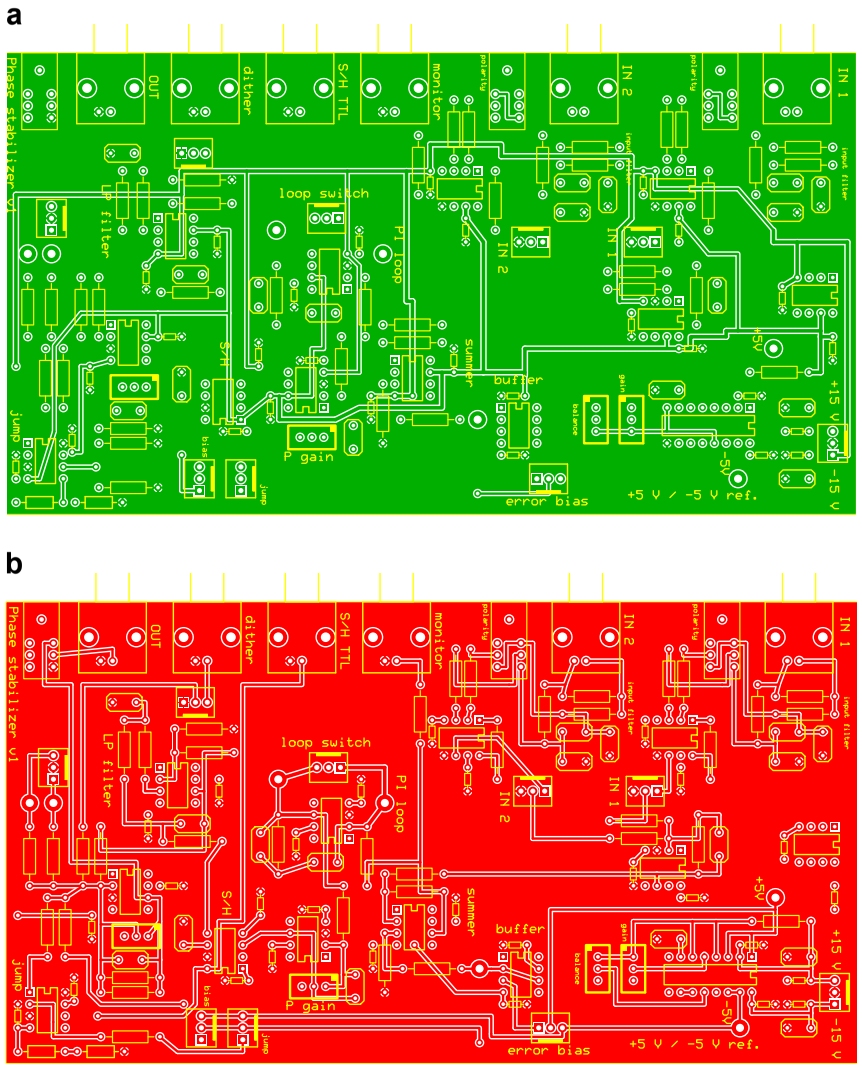

Figure A.7: **PCB board for locking interferometers and intensity stabilization.** After acquiring the lock during the laser cooling and trapping period, LF398 samples and holds the output value of the servo during t_d, where the phase of the interferometer is set to ϕ_0. The jump TTL is initiated 3 ms afterwards to trigger a ultra-low noise switch MAX319 to offset the phase to $\phi_{\text{exp}} = \phi_0 + \delta\phi$ of the interferometer. The output of the servo is amplified by Burleigh PZ70.

Appendix B

Simulating boundaries for multipartite entangled states

In this appendix, I describe our numerical method of generating the boundaries $\Delta_b^{(3,2,1)}$ for biseparable states containing at most tripartite entanglement, bipartite entanglement and for fully separable states, as discussed in chapters 7–9.

B.1 Numerical GPU computing with NVIDIA's CUDA

Thermal (simulated) annealing[331–334] is one of the most successful *sequential* methods for global optimization of some function $f(\vec{\lambda})$ over parameters $\vec{\lambda}$. The specific problem we have in hand is a minimization problem of finding the boundaries $\Delta_b^{(M)}$ for states $\hat{\rho}^{(M)}$ which contain at most *genuine* M-partite entanglement. Violation of this bound $\Delta < \Delta_b^{(M)}$ *unambiguously* signals the presence of genuine $(M+1)$-partite entanglement. Thus, we have $f = \tilde{\Delta}_b^{(M)}$ and $\vec{\lambda} = \hat{\rho}^{(M)}$, where $\tilde{\Delta}_b^{(M)}$ is evaluated for some non-optimal state $\hat{\rho}^{(M)}$; see the next section for a concrete example of fully separable state ($M = 1$).

The initial attempt to obtain the boundaries $\Delta_b^{(M)}$ in a robust fashion was done by thermal annealing, as shown by Fig. B.1. Interestingly, the inspiration of thermal annealing comes from crystallography, where a sequence of heating and controlled cooling is used to grow the size of the crystal and minimize the defects[334]. For a given step n in the annealing procedure, heating allows thermal excitations[a] (with 'energy' $\tilde{k}_B T_n$) to avoid the state s_n getting stuck at some local minimum (in our case, $\tilde{\Delta}_b^{(M)}$) with transition probability $p_{n,n+1}$ from s_n to s_{n+1} (in our case, we choose a Boltzmann-like factor $p_{n,n+1} \sim \exp\left(-\frac{\tilde{\Delta}_b^{(M)}(s_{n+1}) - \tilde{\Delta}_b^{(M)}(s_n)}{\tilde{k}_B T_n}\right)$)[b], while the controlled cooling of $\tilde{k}_B T$ allows to find the configurations (in our case, $s_n = \hat{\rho}_n^{(M)}$ to $s_{n+1} = \hat{\rho}_{n+1}^{(M)}$) with lower internal energy than the initial one (in our case, from $\tilde{\Delta}_b^{(M)}(s_n)$ to $\tilde{\Delta}_b^{(M)}(s_{n+1})$).

By analogy, in each step of the annealing algorithm, we replace the current state s_n by a random neigh-

[a] Here, the tilde '$\sim$' in $\tilde{k}_B$ is used to signify that $\tilde{k}_B$ is not the Boltzmann constant k_B but a scaling factor to make an analogy to energy.

[b] Note that because the transition probability $p_{n,n+1}$ is still higher for states with lower variance than the initial one, the annealing at a given temperature T_n tends to seek for solutions s_{n+1} with lower $\tilde{\Delta}_b^{(M)}(s_{n+1})$ than $\tilde{\Delta}_b^{(M)}(s_n)$.

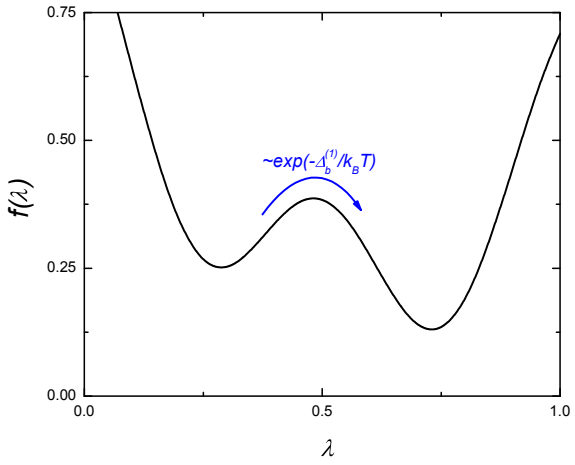

Figure B.1: **Global minimization of a multivariate function $f(\vec{\lambda})$ via simulated annealing.** For simulated annealing, thermal excitations can be used to overcome the local minima on the left with transition probability $p_{n,n+1} = \exp(-\frac{f(\vec{\lambda}_{n+1})-f(\vec{\lambda}_n)}{\tilde{k}_B T_n})$ as the step n progresses. In this scheme, one requires an annealing schedule to reduce the 'temperature' T_n as a function of the step size n, eventually cooling the system $\vec{\lambda}_n$ to the ground state with 'energy' f.

boring state s_{n+1}, chosen with probability $p_{n,n+1}$ depending on the "thermal" energy $\tilde{k}_B T_n$ that is gradually decreased during the process. Thus, in order to obtain the global minimum $\Delta_b^{(M)}$, the thermal annealing requires a dedicated method to manage the 'cooling' rate for $\tilde{k}_B T_n$, known as the annealing schedule, which decreases the thermal excitations of the parameters in $\hat{\rho}_n^{(M)}$ as n is increased (eventually, reaching to the optimal state, $\lim_{n\to\infty} \hat{\rho}_n^{(M)} = \hat{\rho}_{\text{opt}}^{(M)}$, where $\tilde{\Delta}_b^{(M)}(\hat{\rho}_{\text{opt}}^{(M)}) = \Delta_b^{(M)}$). While I was able to get a numerical agreement between the analytical result and the optimal solution obtained by thermal annealing for balanced verification interferometer, I found it difficult to find an efficient annealing schedule robust to the changes in parameters $\{\alpha, \beta, \eta\}$ describing the interferometer and the constraints $\{p_1, y_c\}$ on the quantum state $\hat{\rho}_n^{(M)}$ being considered, which resulted in either getting stuck in a local minimum (quenching), or taking a vast amount of time to converge on the global minimum. In addition, as thermal annealing is necessarily *sequential* (in that the new solution s_{n+1} depends on the older one s_n), I found it tricky to program the thermal annealing to take advantages of parallel computations.

As an alternative, I decided to implement a more comprehensive and exhaustive random search algorithm, which generated all possible $\hat{\rho}^{(M)}$ for a given set of parameters $\{\alpha, \beta, \eta\}$ and constraints $\{p_1, y_c\}$, and found the minimum variance $\Delta_b^{(M)}$ among them. As each step in the search algorithm is completely random and independent, the optimization problem is inherently parallel (*concurrent*), and importantly very simple to program. In chapter 8, I have used the built-in parallel computing toolbox in Matlab, where I found ~ 4 times the convergence time compared to that of using a single core[c].

Around the same time, I learned that NVIDIA had developed a parallel computing architecture, known as compute unified device architecture (CUDA), which use graphical processing unit (GPU) instead of the

[c]To generate the boundaries in Fig. 8.4 of chapter 8, it took ~ 1 week of running time.

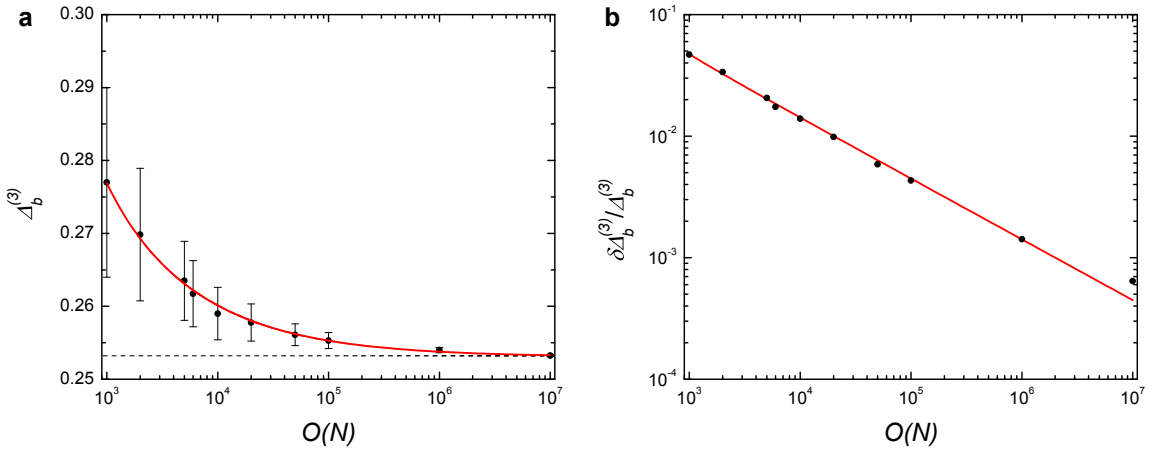

Figure B.2: **Accuracy and precision of the random search algorithm. a**, We show the convergence behavior (*accuracy*) of the Monte-Carlo method to obtain $\Delta_b^{(3)}$ by randomly searching for quantum states $\hat{\rho}^{(M)}$ (data points) to the analytical solution of $\Delta_b^{(3)}$ (dashed line) for balanced verification interferometer (section 7.4.3) as a function of numbers of quantum states $\mathcal{O}(N)$. **b**, We show the reduction in the fractional uncertainty $\frac{\delta\Delta_b^{(3)}}{\Delta_b^{(3)}}$ (*precision*) for numerically obtaining the solutions $\Delta_b^{(3)}$ (data points) as a function of numbers of quantum states $\mathcal{O}(N)$.

traditional CPU. From a computing perspective, GPUs are heavily multithreaded many-core chips, comprised of hundreds of cores, with each core capable of running multiple concurrent threads[d]. Since the introduction of CUDA, the so-called general purpose GPU (GPGPU) computing has become a major trend in scientific computing, thanks to the prospects of building a 'personal' supercomputers (exceeding 1 Teraflops) to solve certain (massively parallel) scientific problems. Important features of CUDA include shared memory, which can greatly improve the performance of bandwidth-limited applications; double precision floating point arithmetic; and an arbitrary load/store memory model, which enables many new algorithms which were previously difficult or impossible to implement on the GPU.

As of 2011, these GPU accelerations are now built into Mathematica 8 and Matlab 2011a. But at the time of the experiment in chapter 9, these features were not readily available. Thus, we implemented the GPU computing for the Monte-Carlo simulation with an open source development project for Matlab, called "GPUmat". As described in section B.2, even with my limited experience on parallel computing models, I found that the GPU-accelerated code (GPUmat) employed in chapter 9 out-performed a similar parallel code using 4 CPU cores with Intel Xeon processor in chapter 8 by a factor of ~ 12. The enhancement in GPGPU computing due to increased data parallelism allowed us to perform error analysis of the boundaries $\Delta_b^{(1,2,3)}$ in Figs. 9.2–9.3 arising from the systematic uncertainties of the verification interferometers (section 9.13.3). For reference, in Fig. B.2, I show the convergence behavior of the numerical random search algorithm (data points) for $\Delta_b^{(3)}$ to the analytically predicted value of $\Delta_b^{(3)}$ (dashed line) for balanced verification interferometers (see chapter 7) as a function of $\mathcal{O}(N)$ numbers of quantum states with $\{p_1, y_c\} = \{0.1, 0.035\}$. In

[d]In my case, I just used NVIDIA GeForce GT 330M, comprised of 48 parallel processing units, each running at 1.26 GHz with multi-threading, yielding theoretically a total processing power ~ 180 Gigaflops.

section B.2, I will describe our method of the Monte-Carlo simulation using GPUmat.

B.2 Monte-Carlo simulation for realistic verification interferometers

To generate the boundaries, we need to consider all possible (mixed) states containing bipartite and tripartite entanglement, as well as fully separable states for a given p_1. I refer to chapter 7 for a more detailed theoretical formalism. Here, we will review the case for a fully separable state. A pure separable state $|\psi\rangle_{\text{sep}}^{(a)}$ is given by the form:

$$|\psi\rangle_{\text{sep}}^{(a)} = \prod_k |\varphi\rangle_k^{(a)}, \tag{B.1}$$

where $|\varphi\rangle_k^{(a)} = \frac{1}{\sqrt{1+|\epsilon_k^{(a)}|^2}}(|0\rangle + e^{i\phi_k^{(a)}}\epsilon_k^{(a)}|1\rangle)$. Based on Eq. B.1, we can further consider a mixed state of the form:

$$\hat{\rho}_{\text{sep}}^{(ab)} = |A_{ab}|^2 |\psi\rangle_{\text{sep}}^{(a)}\langle\psi| + (1-|A_{ab}|^2)|\psi\rangle_{\text{sep}}^{(b)}\langle\psi|, \tag{B.2}$$

which corresponds to the mixing of two pure separable states $|\psi\rangle_{\text{sep}}^{(a)}$ and $|\psi\rangle_{\text{sep}}^{(b)}$ with a ratio of $|A_{ab}|^2 : (1-|A_{ab}|^2)$. We then calculate the various expectation values of $\hat{M}_k = |\Pi_k\rangle\langle\Pi_i|$ (see section 8.11 for the definition of the projectors $\hat{M}_k$ in the presence of imbalances $\{\alpha,\beta\}$ and losses $\{\eta\}$) as well as the variance $\tilde{\Delta}_b^{(1)} = \sum_k \text{Tr}(\hat{\rho}_{\text{sep}}^{(ab)}\delta M_k^2)$ for the randomly generated state $\hat{\rho}_{\text{sep}}^{(ab)}$ (specified by the random values A_{ab}, $\{\epsilon_1^{(a,b)},\epsilon_2^{(a,b)},\epsilon_3^{(a,b)},\epsilon_4^{(a,b)}\}$, and $\{\phi_1^{(a,b)},\phi_2^{(a,b)},\phi_3^{(a,b)},\phi_4^{(a,b)}\}$). The minimum value of $\tilde{\Delta}_b^{(1)}$ for all possible A_{ab}, $\{\epsilon_1^{(a,b)},\epsilon_2^{(a,b)},\epsilon_3^{(a,b)},\epsilon_4^{(a,b)}\}$, and $\{\phi_1^{(a,b)},\phi_2^{(a,b)},\phi_3^{(a,b)},\phi_4^{(a,b)}\}$ constrained by $\{p_1, y_c\}$ is what we denote by $\Delta_b^{(1)} = \min(\tilde{\Delta}_b^{(1)})$.

Similarly, we can construct $\Delta_b^{(2,3)} = \min(\tilde{\Delta}_b^{(2,3)})$ for biseparable states containing at most two-mode and three-mode entanglement. The only critical difference between the case of fully separable states and the case of (biseparable) entangled states is that we could also mix entangled states of different partitions for the latter case[e]. Realistically, the minimum uncertainties $\Delta_b^{(3,2,1)}$ for a given y_c will depend on the parameters $\{\alpha,\beta,\eta\}$ of the verification interferometer because of losses and imbalances in the verification setup. Due to the systematic uncertainties $\{\delta\alpha,\delta\beta,\delta\eta\}$ in our determinations of $\{\alpha,\beta,\eta\}$, $\Delta_b^{(3,2,1)}$ are convolved with the normal distributions of $\{\alpha,\beta,\eta\}$. This is a highly parallel computing problem of high concurrency, whereby we search for the minimum $\Delta_b^{(3,2,1)}$ for random quantum states (defined by *independent* variables A_{ab}, $\{\epsilon_1^{(a,b)},\epsilon_2^{(a,b)},\epsilon_3^{(a,b)},\epsilon_4^{(a,b)}\}$, and $\{\phi_1^{(a,b)},\phi_2^{(a,b)},\phi_3^{(a,b)},\phi_4^{(a,b)}\}$) convolved *independently* by the normal distributions of the parameters $\{\alpha,\beta,\eta\}$ which modify $\hat{M}_k$ (section 8.11).

In the matlab m-file, '`scan_batch.m`', we first run the 'GPUstart' command (see the open source CUDA project, 'GPUmat' for porting CUDA into Matlab) to initiate GPUmat package, and to check if the CUDA SDK is installed and if the GPU processors are CUDA compatible. The batch file then takes several inputs: constraints such as p_1 and y_c, numbers of states to generate and store in the GPU (or CPU) memory,

[e] e.g., (i) mixed state of a fully separable pure state and a biseparable entangled state containing two-mode entanglement, (ii) mixed state of bipartite entangled state for $(a|bcd)$ and $(abc|d)$, and etc.

numbers of states to wait until writing onto a temporary folder in a hard drive, and the parameters (α, β, η) describing the verification interferometer. Then, it loads and computes the functions, 'onemodescanner', 'twomodescanner', and 'threemodescanner', which are, respectively, defined in the codes '`onemodescanner.m`', '`twomodescanner.m`', and '`threemodescanner.m`'. Here, I list the Matlab code for the batch file.

```
%Scanner batch file for generating W-state bounds (K. S. Choi)
GPUstart
GPUmatSystemCheck
%This code assumes that that the GPU is compatible with NVIDIA?s CUDA SDK.

%Define phase uncertainty given by \Δ \phi=2\pi/phase_unc
%N_tot=Total number of states per each step of yc
%N_buff=Total number of states to store in the Ram before storing into hard
%drive
%yc_steps=number of equal steps for yc
phase_unc=1000;
p1=0.3;
N_tot=100000;
N_buff=50000;
yc_steps=20;

%Define the loss and imbalance parameters for the verification
%interferometer
betain=0.497;
betaout=0.484;
alphaAB=1-0.490;
alphaCD=0.487;
etaAout=0.948;
etaBin=0.958;
etaCin=0.899;
etaDout=0.932;
etaA=0.7*0.770;
etaB=0.7*0.776;
etaC=0.7*0.747;
etaD=0.7*0.718;
%err=fractional systematic error in the parameters above, following a
%normal distribution.
%stat_it=number of loss and imbalance parameters to
%generate per degenerate states (y_c) to create per each

err=0.05;
stat_it=250;
%load function XXXmodescanner() which initiate the Monte-Carlo sim and
```

```
%export into files
onemodescanner(phase_unc,p1,betain,betaout,alphaAB,alphaCD,etaAout,...
    etaBin,etaCin,etaDout,etaA,etaB,etaC,etaD,N_tot,N_buff,yc_steps,...
    2.19,100,err,stat_it);
twomodescanner(phase_unc,p1,betain,betaout,alphaAB,alphaCD,etaAout,...
    etaBin,etaCin,etaDout,etaA,etaB,etaC,etaD,N_tot,N_buff,yc_steps,...
    1.3175,1.4,err,stat_it);
threemodescanner(phase_unc,p1,betain,betaout,alphaAB,alphaCD,etaAout,...
    etaBin,etaCin,etaDout,etaA,etaB,etaC,etaD,N_tot,N_buff,yc_steps,...
    0.912,1,err,stat_it);
%end
%matlabpool close;
%check parity
 load -ascii 'one_mode_bound.mat'
 load -ascii 'two_mode_bound.mat'
 load -ascii 'three_mode_bound.mat'

plot(one_mode_bound(:,1),one_mode_bound(:,2),'r',one_mode_bound(:,1),...
    one_mode_bound(:,3),'--r',one_mode_bound(:,1),one_mode_bound(:,4),...
    '--r',two_mode_bound(:,1),two_mode_bound(:,2),'b',...
    two_mode_bound(:,1),two_mode_bound(:,3),'--b',two_mode_bound(:,1),...
    two_mode_bound(:,4),'--b',three_mode_bound(:,1),...
    three_mode_bound(:,2),'g',three_mode_bound(:,1),...
    three_mode_bound(:,3),'--g',three_mode_bound(:,1),...
    three_mode_bound(:,4),'--g')
xlabel('\it{y_{c}}')
ylabel('\Delta_{b}')
title('\Delta_{b} vs. \it{y_{c}}')
grid on
```

The actual computations for obtaining the minimum variances $\Delta_b^{(3,2,1)}$ for a given set of $\{y_c\}$ are run by the m-files, '`onemodescanner.m`', '`twomodescanner.m`', and '`threemodescanner.m`'. Here, the variance $\tilde{\Delta}_b^{(3,2,1)}$ for the given quantum state is computed by Matlab functions 'variance3m', 'variance2m', 'variance1m'. To avoid redundancy, here I only list the Matlab m-code for '`onemodescanner.m`', which generates the lower bound of $\Delta_b^{(1)}$ for fully separable states[f]. Note that 'GPUsingle' is used to load the parameters into the GPU memory, and we used standard GPU functions such as 'GPUmin' and 'GPUmax', as well as custom GPU functions such as 'variance1m'. Direct coding with CUDA C language would have required substantially more effort than to simply write the code with GPUmat, especially in terms of managements of

[f]Note that $\Delta_b^{(1)}$ for a given set of parameters of the quantum state (A_{ab}, $\{\epsilon_1^{(a,b)}, \epsilon_2^{(a,b)}, \epsilon_3^{(a,b)}, \epsilon_4^{(a,b)}\}$, and $\{\phi_1^{(a,b)}, \phi_2^{(a,b)}, \phi_3^{(a,b)}, \phi_4^{(a,b)}\}$), and the verification interferometer ($\{\alpha, \beta, \eta\}$ and $\{\beta_1, \beta_2, \beta_3\}$) is obtained through a compiled GPU function, 'variance1m.mex'. This function internally takes these GPU variables describing the quantum state and the verification interferometer, and then calculates $\tilde{\Delta}_b^{(1)}$ with single-precision. The GPU function 'variance1m' is a machine-specific. In practice, we analytically calculated the function $\tilde{\Delta}_b^{(1)}$ with Quantum Mathematica and converted to an m-file. This m-file is later precompiled in Matlab similar to the command 'emlmex' (for running embedded Matlab mex) before running the batch file in order to speed up the computation.

the data transfers between the CPU and GPU, concurrency, and their memory usages.

```
function onemodescanner(sigma,p1,betain,betaout,alphaAB,alphaCD,...
    etaAout,etaBin,etaCin,etaDout,etaA,etaB,etaC,etaD,Nloss,kj,resolve,...
    ycend,GPUmaxx,err,stat_it)
%GPUcompileStart(?onemodescanner?, ?-f?,
%sigma,p1,betain,betaout,alphaAB,alphaCD,etaAout,etaBin,etaCin,etaDout,
%etaA,etaB,etaC,etaD,Nloss,kj,resolve,ycend,GPUmaxx,err,stat_it)
%Here, we use GPUmat for GPU acceleration
iter=GPUsingle([0,0,0,0;0,0,0,1;0,0,1,0;0,0,1,1;0,1,0,0;0,1,0,1;0,1,1,0;0, ...
  1,1,1;1,0,0,0;1,0,0,1;1,0,1,0;1,0,1,1;1,1,0,0;1,1,0,1;1,1,1,1, ...
  0;1,1,1,1]);
time0=cputime;

% qc2s=(p1/GPUmaxx*rand(1,Nloss));
% qc4s=(p1/GPUmaxx*rand(1,Nloss));
et=GPUsingle(10^-4:ycend/resolve:ycend);
p2s=GPUsingle(3/8*et*p1^2);
prog_wait=waitbar(0,'1-mode boundary is being scanned. Please Wait ...');
betain_list=GPUsingle(random('norm',betain,betain*err,1,stat_it));
betaout_list=GPUsingle(random('norm',betaout,betaout*err,1,stat_it));
alphaAB_list=GPUsingle(random('norm',alphaAB,alphaAB*err,1,stat_it));
alphaCD_list=GPUsingle(random('norm',alphaCD,alphaCD*err,1,stat_it));
etaAout_list=GPUsingle(random('norm',etaAout,etaAout*0,1,stat_it));
etaBin_list=GPUsingle(random('norm',etaBin,etaBin*0,1,stat_it));
etaCin_list=GPUsingle(random('norm',etaCin,etaCin*0,1,stat_it));
etaDout_list=GPUsingle(random('norm',etaDout,etaDout*0,1,stat_it));
etaA_list=GPUsingle(random('norm',etaA,etaA*err,1,stat_it));
etaB_list=GPUsingle(random('norm',etaB,etaB*err,1,stat_it));
etaC_list=GPUsingle(random('norm',etaC,etaC*err,1,stat_it));
etaD_list=GPUsingle(random('norm',etaD,etaD*err,1,stat_it));
%std(random('norm',1,0.5,1,100))
%mean(random('norm',1,0.5,1,100))
init=20;
% GPUmaxten=GPUmaxx*((init-1)/ycend*(ycend-et)+1);
GPUmaxten=GPUsingle(GPUmaxx*((et./ycend).^(-1/init)-1)+1);
    clear et;
    %varri=zeros(1,Nloss);
    varianceout=GPUsingle(zeros(length(p2s),4));
    varianceout2=GPUsingle(zeros(length(p2s),stat_it));
    GPUfor iqq=GPUsingle(1:length(p2s))

        p2=p2s(iqq);
        varritemp=GPUsingle(zeros(1,floor(Nloss/kj+1)));
```

```
        let=1;

        vari_list=GPUsingle(zeros(1,stat_it));
        qc2s=GPUsingle(p1/GPUmaxten(iqq)*rand(1,Nloss));
        qc4s=GPUsingle(p1/GPUmaxten(iqq)*rand(1,Nloss));
        GPUfor stat_itr=GPUsingle(1:stat_it)
            waitbar((iqq+stat_itr/stat_it-1)/length(p2s));
            betain=GPUsingle(betain_list(stat_itr));
            betaout=GPUsingle(betaout_list(stat_itr));
            alphaAB=GPUsingle(alphaAB_list(stat_itr));
            alphaCD=GPUsingle(alphaCD_list(stat_itr));
            etaAout=GPUsingle(etaAout_list(stat_itr));
            etaBin=GPUsingle(etaBin_list(stat_itr));
            etaCin=GPUsingle(etaCin_list(stat_itr));
            etaDout=GPUsingle(etaDout_list(stat_itr));
            etaA=GPUsingle(etaA_list(stat_itr));
            etaB=GPUsingle(etaB_list(stat_itr));
            etaC=GPUsingle(etaC_list(stat_itr));
            etaD=GPUsingle(etaD_list(stat_itr));
            count=1;
            GPUfor itr = GPUsingle(1:2^4 )
                phi1s=GPUsingle(random('unif',-pi/sigma+...
                    pi*iter(itr,1),pi/sigma+...
                    pi*iter(itr,1),1,Nloss));
                phi2s=GPUsingle(random('unif',-pi/sigma+...
                    pi*iter(itr,2),pi/sigma+...
                    pi*iter(itr,2),1,Nloss));
                phi3s=GPUsingle(random('unif',-pi/sigma+...
                    pi*iter(itr,3),pi/sigma+...
                    pi*iter(itr,3),1,Nloss));
                phi4s=GPUsingle(random('unif',-pi/sigma+...
                    pi*iter(itr,4),pi/sigma+...
                    pi*iter(itr,4),1,Nloss));
                GPUfor cc=GPUsingle(1:kj:Nloss)
                    t0=GPUsingle(let);
                    i1=cc:GPUmin(cc+kj,Nloss);
                    qc2=qc2s(i1);
                    qc4=qc4s(i1);
                    phi1=phi1s(i1);
                    phi2=phi2s(i1);
                    phi3=phi3s(i1);
                    phi4=phi4s(i1);
                    hq1=GPUsingle((-1/2).*((-1)+p1+p2).^(-1).*(1+...
                        qc2).^(-1).*(1+qc4).^(-1).*(p1+(-1).*qc2+ ...
                    2.*p1.*qc2+p2.*qc2+(-1).*qc2.^2+p1.*qc2.^2+...
```

```
p2.*qc2.^2+(-1).*qc4+2.*p1.* ...
qc4+p2.*qc4+(-2).*qc2.*qc4+3.*p1.*qc2.*qc4+...
2.*p2.*qc2.*qc4+(-1).* ...
qc2.^2.*qc4+p1.*qc2.^2.*qc4+p2.*qc2.^2.*qc4+...
(-1).*qc4.^2+p1.*qc4.^2+p2.* ...
qc4.^2+(-1).*qc2.*qc4.^2+p1.*qc2.*qc4.^2+...
p2.*qc2.*qc4.^2+((1+qc2).*(1+ ...
qc4).*((-4).*((-1)+p1+p2).*((-1).*qc2.^2+...
(-1).*qc2.*qc4+(-1).*qc2.^2.* ...
qc4+(-1).*qc4.^2+(-1).*qc2.*qc4.^2+p2.*(1+...
qc2).*(1+qc4).*((-1)+qc2+qc4)+ ...
p1.*(1+qc2).*(1+qc4).*(qc2+qc4))+(1+qc2).*(1+...
qc4).*(((-1)+p2).*(qc2+qc4) ...
+p1.*(1+qc2+qc4)).^2)).^(1/2));
hq3=(-1/2).*((-1)+p1+p2).^(-1).*(1+...
    qc2).^(-1).*(1+qc4).^(-1).*(p1+(-1).*qc2+ ...
2.*p1.*qc2+p2.*qc2+(-1).*qc2.^2+p1.*qc2.^2+...
p2.*qc2.^2+(-1).*qc4+2.*p1.* ...
qc4+p2.*qc4+(-2).*qc2.*qc4+3.*p1.*qc2.*qc4+...
2.*p2.*qc2.*qc4+(-1).* ...
qc2.^2.*qc4+p1.*qc2.^2.*qc4+p2.*qc2.^2.*qc4+...
(-1).*qc4.^2+p1.*qc4.^2+p2.* ...
qc4.^2+(-1).*qc2.*qc4.^2+p1.*qc2.*qc4.^2+...
p2.*qc2.*qc4.^2+(-1).*((1+qc2) ...
.*(1+qc4).*((-4).*((-1)+p1+p2).*((-1).*qc2.^2+...
(-1).*qc2.*qc4+(-1).* ...
qc2.^2.*qc4+(-1).*qc4.^2+(-1).*qc2.*qc4.^2+...
p2.*(1+qc2).*(1+qc4).*((-1)+ ...
qc2+qc4)+p1.*(1+qc2).*(1+qc4).*(qc2+qc4))+...
(1+qc2).*(1+qc4).*(((-1)+p2).* ...
(qc2+qc4)+p1.*(1+qc2+qc4)).^2)).^(1/2)));
test=zeros(1,GPUmin(kj,Nloss-cc)+1);
GPUfor  kk=GPUsingle(1:GPUmin(kj,Nloss-cc)+1)
     if GPUabs(imag(hq1(kk)))<0.1 && GPUabs(...
             imag(hq3(kk)))...
             <0.1 && (0≤(hq1(kk))≤1) && ...
             (0≤(hq3(kk))≤1) && (0≤(qc2(kk))≤1)...
             && (0≤(qc4(kk))≤1)
         test(kk)=1;
     else
         test(kk)=0;
     end

GPUend
var_ind=find(test==1);
```

```
133
134                     varri = GPUmax(GPUabs(variance1m(p1,p2,qc2,qc4,...
135                         betain,betaout,alphaAB,alphaCD,etaAout,etaBin,...
136                         etaCin,etaDout,etaA,etaB,etaC,etaD,phi1,phi2,...
137                         phi3,phi4)),0);
138
139                 t1=GPUsingle(let+length(i1));
140                 vv=varri(var_ind);
141                 if isempty(var_ind)
142                     vv=0;
143                 end
144                 varritemp(count)=GPUmin(vv);
145                 count=count+1;
146                 clear varri
147             GPUend
148         GPUend
149         vari_list(stat_itr)=GPUmin(varritemp);
150     GPUend
151     yc=8/3*(p2*(1-p1-p2))/p1^2;
152     varianceout(iqq,1)=yc;
153     varianceout2(iqq,1)=yc;
154     hist(double(vari_list))
155     mean_data=mean(double(vari_list));
156     std_data=std (double(vari_list));
157     x=mean_data-5*std_data:std_data/5:mean_data+5*std_data;
158     y=histc (double(vari_list),x,2);
159     f = ezfit (x,y,'gauss2 (x) = norm*(exp (-(x-xc)^2/(2*...(tm1*...
160     heaviside (x-xc)+tm2*heaviside (-x+xc))^2)))',[stat_it/10 ...
161         std_data std_data mean_data]);
162     plot (x,y,'r*');
163     showfit (f);
164     % dispeqfit (f);
165     makevarfit (f);
166     tm1 = evalin ('base','tm1');
167     tm2 = evalin ('base','tm2');
168     xc = evalin ('base','xc');
169     Δc=[xc, tm1, tm2];
170     disp ('(Δc, +err, -err) = ');
171     disp (Δc);
172     vari_list=double(vari_list);
173     GPUfor lstr=1:stat_it
174     varianceout2(double(iqq),lstr)=vari_list(lstr);
175     GPUend
176      varianceout(double(iqq),2)=xc;
177      varianceout(double(iqq),3)=xc+tm1;
```

```
178           varianceout(double(iqq),4)=xc-tm2;
179          clear let
180      GPUend
181  close(prog_wait)
182  ploter = plot(varianceout(:,1),varianceout(:,2),varianceout(:,1),...
183      varianceout(:,3),'--',varianceout(:,1),varianceout(:,4),'--');
184  set(gca,'XTick',0:0.25:1.5)
185  xlabel('y_c')
186  ylabel('\Delta^{(1)}_b')
187  title('\Delta^{(1)}_b vs. y_c')
188  set(ploter,'Color','blue','LineWidth',.5)
189  time1=cputime-time0;
190  disp(['elapsed time (s)=',num2str(time1)]);
191  save one_mode_bound.mat -ascii varianceout;
192  save one_mode_bound2.mat -ascii varianceout2;
193
194  %GPUcompileStop
195  end
196
197  %%
```

Bibliography

1. Kimble, H. J. The quantum internet. *Nature* **453**, 1023–1030 (2008).

2. Preskill, J. P. Quantum computation. *Phys. 219 Lecture Notes* (1997).

3. Nielsen, M. A. & Chuang, I. L. *Quantum Computation and Quantum Information* (Cambridge University Press, Cambridge, 2000).

4. Duan, L.-M., Lukin, M. D., Cirac, J. I. & Zoller, P. Long-distance quantum communication with atomic ensembles and linear optics. *Nature* **414**, 413–418 (2001).

5. Lloyd, S. Universal quantum simulator. *Science* **273**, 1073–1078 (1996).

6. Acin, A., Cirac, J. I. & Lewenstein, M. Entanglement percolation in quantum networks. *Nature Phys.* **3**, 256–259 (2007).

7. Copsey, D. *et al.* Toward a scalable, silicon-based quantum computing architecture. *IEEE J. Sel. Top. Quant. Electron.* **9**, 1552–1569 (2003).

8. Cirac, J. I., Zoller, P., Kimble, H. J. & Mabuchi, H. Quantum state transfer and entanglement distribution among distant nodes in a quantum network. *Phys. Rev. Lett.* **78**, 3221–3224 (1997).

9. Briegel, H.-J., Dür, W., Cirac, J. I. & Zoller, P. Quantum repeaters: the role of imperfect local operations in quantum communication. *Phys. Rev. Lett.* **81**, 5932–5935 (1998).

10. Shor, P. W. Scheme for reducing decoherence in quantum computer memory. *Phys. Rev. A* **52**, 2493–2496 (1995).

11. Steane, A. Multiple particle interference and quantum error correction. *Proc. R. Soc. Lond. A* **452**, 2551–2577 (1996).

12. Shor, P. W. Fault-tolerant quantum computation. In *Proceedings of the 37th Symposium on the Foundations of Computer Science (FOCS)*, 56–65 (IEEE, Los Alamitos, California, 1996).

13. Aharonov, D. & Ben-Or, M. Fault-tolerant quantum computation with constant error. In *Proceedings of the 29th Annual ACM Symposium on the Theory of Computation (STOC)*, 176–188 (ACM Press, New York, New York, 1996).

14. Knill, E., Laflamme, R. & Zurek, W. H. Resilient quantum computation. *Science* **279**, 342–345 (1998).

15. Gottesman, D. A theory of fault-tolerant quantum computation. *Phys. Rev. A* **57**, 127–137 (1998).

16. Preskill, J. P. Reliable quantum computers. *Proc. R. Soc. Lond. A* **454**, 385–410 (1998).

17. Bennett, C. H. *et al.* Purification of noisy entanglement, and faithful teleportation via noisy channels. *Phys. Rev. Lett.* **76**, 722–725 (1996).

18. Duan, L. M., Giedke, G., Cirac, J. I. & Zoller, P. Entanglement purification of gaussian continuous variable quantum states. *Phys. Rev. Lett.* **84**, 4002–4005 (2000).

19. Bose, S., Vedral, V. & Knight, P. L. Purification via entanglement swapping and conserved entanglement. *Phys. Rev. A* **60**, 194–197 (1999).

20. Bennett, C. H. & Brassard, G. Quantum cryptography: Public key distribution and coin tossing. In *Proceedings of IEEE International Conference on Computers Systems and Signal Processing*, 175–179 (Bangalore, 1984).

21. Ekert, A. K. Quantum cryptography based on Bell's theorem. *Phys. Rev. Lett.* **67**, 661–664 (1991).

22. Bennett, C. H., Bessette, F., Brassard, G., Salvail, L. & Smolin, J. Experimental quantum cryptography. *Journal of Cryptology* **5**, 3–28 (1992).

23. Deutsch, D. *et al.* Quantum privacy amplification and the security of quantum cryptography over noisy channels. *Phys. Rev. Lett.* **77**, 2818–2821 (1996).

24. Cirac, J. I., Ekert, A. K., Huelga, S. F. & Macchiavello, C. Distributed quantum computation over noisy channels. *Phys. Rev. A* **59**, 4249–4254 (1999).

25. Gottesman, D. & Chuang, I. L. Demonstrating the viability of universal quantum computation using teleportation and single-qubit operations. *Nature* **402**, 390–393 (1999).

26. Preskill, J. P. Plug-in quantum software. *Nature* **402**, 357–358 (1999).

27. Chou, C. W. *et al.* Measurement-induced entanglement for excitation stored in remote atomic ensembles. *Nature* **438**, 828–832 (2005).

28. Moehring, D. L. *et al.* Entanglement of single-atom quantum bits at a distance. *Nature* **449**, 68–71 (2007).

29. Simon, J., Tanji, H., Ghosh, S. & Vuletić, V. Single-photon bus connecting spin-wave quantum memories. *Nature Phys.* **3**, 765–769 (2007).

30. Choi, K. S., Deng, H., Laurat, J. & Kimble, H. J. Mapping photonic entanglement into and out of a quantum memory. *Nature* **452**, 67–71 (2008).

31. Jost, J. D. *et al.* Entangled mechanical oscillators. *Nature* **459**, 683–685 (2009).

32. Weber, B. *et al.* Photon-photon entanglement with a single trapped atom. *Phys. Rev. Lett.* **102**, 030501 (2009).

33. Choi, K. S., Goban, A., Papp, S. B., van Enk, S. J. & Kimble, H. J. Entanglement of spin waves among four quantum memories. *Nature* **468**, 412–416 (2010).

34. Laurat, J., Choi, K. S., Deng, H., Chou, C. W. & Kimble, H. J. Heralded entanglement between atomic ensembles: Preparation, decoherence, and scaling. *Phys. Rev. Lett.* **99**, 180504 (2007).

35. Papp, S. B. *et al.* Characterization of multipartite entanglement for one photon shared among four optical modes. *Science* **324**, 764–768 (2009).

36. Chou, C.-W. *et al.* Functional quantum nodes for entanglement distribution over scalable quantum networks. *Science* **316**, 1316–1320 (2007).

37. Laurat, J. *et al.* Towards experimental entanglement connection with atomic ensembles in the single excitation regime. *New J. Phys.* **9**, 207–220 (2007).

38. Lougovski, P. *et al.* Verifying multipartite mode entanglement of W states. *New J. Phys.* **11**, 063029 (2009).

39. Amico, L., Fazio, R., Osterloh, A. & Vedral, V. Entanglement in many-body systems. *Rev. Mod. Phys.* **80**, 517–576 (2008).

40. Gühne, O. & Toth, G. Entanglement detection. *Phys. Rep.* **474**, 1–75 (2009).

41. Giovannetti, V., Lloyd, S. & Maccone, L. Quantum-enhanced measurements: Beating the standard quantum limit. *Science* **306**, 1330–1336 (2004).

42. Dicke, R. H. Coherence in spontaneous radiation processes. *Phys. Rev.* **93**, 99–110 (1954).

43. Zare, R. N. *Angular Momentum* (Wiley-Interscience, New York, 1988).

44. Gross, M. & Haroche, S. Superradiance: An essay on the theory of collective spontaneous emission. *Phys. Rep.* **93**, 301–396 (1982).

45. Black, A. T., Chan, H. W. & Vuletić, V. Observation of collective friction forces due to spatial self-organization of atoms: From rayleigh to bragg scattering. *Phys. Rev. Lett.* **91**, 203001 (2003).

46. Baumann, K., Guerlin, C., Brennecke, F. & Esslinger, T. Dicke quantum phase transition with a superfluid gas in an optical cavity. *Nature* **464**, 1301–1306 (2010).

47. Scully, M. O. & Svidzinsky, A. A. The Lamb shift–yesterday, today, and tomorrow. *Science* **328**, 1239–1241 (2010).

48. Hammerer, K., Sørensen, A. S. & Polzik, E. S. Quantum interface between light and atomic ensembles. *Rev. Mod. Phys.* **82**, 1041–1093 (2010).

49. Sangouard, N., Simon, C., de Riedmatten, H. & Gisin, N. Quantum repeaters based on atomic ensembles and linear optics. *Rev. Mod. Phys. (in press)* (2011).

50. Cerf, N. J., Leuchs, G. & Polzik, E. S. (eds.) *Quantum information with continuous variables* (World Scientific Publishing, New Jersey, 2007).

51. Kuzmich, A., Bigelow, N. P. & Mandel, L. Atomic quantum non-demolition measurements and squeezing. *Eur. Phys. Lett.* **42**, 481 (1998).

52. Kuzmich, A. *et al.* Quantum nondemolition measurements of collective atomic spin. *Phys. Rev. A* **60**, 2346 (1999).

53. Hald, J., Sørensen, J. L., Schori, C. & Polzik, E. S. Spin squeezed atoms: A macroscopic entangled ensemble created by light. *Phys. Rev. Lett.* **83**, 1319–1322 (1999).

54. Kuzmich, A., Mandel, L. & Bigelow, N. P. Generation of spin squeezing via continuous quantum nondemolition measurement. *Phys. Rev. Lett.* **85**, 1594–1597 (2000).

55. Duan, L.-M., Cirac, J. I., Zoller, P. & Polzik, E. S. Quantum communication between atomic ensembles using coherent light. *Phys. Rev. Lett.* **85**, 5643–5646 (2000).

56. Kuzmich, A. & Polzik, E. S. Atomic quantum state teleportation and swapping. *Phys. Rev. Lett.* **85**, 5639 (2000).

57. Sørensen, A. & Mølmer, K. Entanglement and extreme spin squeezing. *Phys. Rev. Lett.* **86**, 4431–4434 (2001).

58. Sørensen, A., Duan, L., Cirac, J. & Zoller, P. Many-particle entanglement with Bose-Einstein condensates. *Nature* **409**, 63–66 (2001).

59. Julsgaard, B., Kozhekin, A. & Polzik, E. S. Experimental long-lived entanglement of two macroscopic objects. *Nature* **413**, 400–403 (2001).

60. Sherson, J. F. *et al.* Quantum teleportation between light and matter. *Nature* **443**, 557–560 (2006).

61. Riedel, M. F. *et al.* Atom-chip-based generation of entanglement for quantum metrology. *Nature* **464**, 1170–1173 (2010).

62. Gross, C., Zibold, T., Nicklas, E., Estève, J. & Oberthaler, M. K. Nonlinear atom interferometer surpasses classical precision limit. *Nature* **464**, 1165–1169 (2010).

63. Krauter, H. *et al.* Entanglement generated by dissipation. *arXiv:1006.4344* (2011).

64. Gerbier, F., Folling, S., Widera, A., Mandel, O. & Bloch, I. Probing number squeezing of ultracold atoms across the superfluid-mott insulator transition. *Phys. Rev. Lett.* **96**, 090401 (2006).

65. Esteve, J., Gross, C., Weller, A., Giovanazzi, S. & Oberthaler, M. K. Squeezing and entanglement in a Bose-Einstein condensate. *Nature* **455**, 1216–1219 (2008).

66. Appel, J. *et al.* Mesoscopic atomic entanglement for precision measurements beyond the standard quantum limit. *Proc. Natl. Acad. Sci. U.S.A.* **106**, 10960–10965 (2009).

67. Wasilewski, W. *et al.* Quantum noise limited and entanglement-assisted magnetometry. *Phys. Rev. Lett.* **104**, 133601 (2010).

68. Leroux, I. D., Schleier-Smith, M. H. & Vuletić, V. Orientation-dependent entanglement lifetime in a squeezed atomic clock. *Phys. Rev. Lett.* **104**, 250801 (2010).

69. Leroux, I. D., Schleier-Smith, M. H. & Vuletić, V. Implementation of cavity squeezing of a collective atomic spin. *Phys. Rev. Lett.* **104**, 073602 (2010).

70. Raymer, M. G., Walmsley, I. A., Mostowski, J. & Sobolewska, B. Quantum theory of spatial and temporal coherence properties of stimulated Raman scattering. *Phys. Rev. A* **32**, 332–344 (1985).

71. Chou, C. W. *Towards a Quantum Network with Atomic Ensembles*. Ph.D. thesis, California Institute of Technology, Pasadena, CA (2006).

72. Kuzmich, A. *et al.* Generation of nonclassical photon pairs for scalable quantum communication with atomic ensembles. *Nature* **423**, 731–734 (2003).

73. van der Wal, C. H. *et al.* Atomic memory for correlated photon states. *Science* **301**, 196–200 (2003).

74. Chou, C. W., Polyakov, S. V., Kuzmich, A. & Kimble, H. J. Single-photon generation from stored excitation in an atomic ensemble. *Phys. Rev. Lett.* **92**, 213601 (2004).

75. Balic, V., Braje, D. A., Kolchin, P., Yin, G. Y. & Harris, S. E. Generation of paired photons with controllable waveforms. *Phys. Rev. Lett.* **94**, 183601 (2005).

76. Laurat, J. *et al.* Efficient retrieval of a single excitation stored in an atomic ensemble. *Opt. Express* **14**, 6912–6918 (2006).

77. Thompson, J. K., Simon, J., Loh, H. & Vuletić, V. A high-brightness source of narrowband, identical photon pairs. *Science* **313**, 74–77 (2006).

78. Felinto, D. *et al.* Conditional control of the quantum states of remote atomic memories for quantum networking. *Nature Phys.* **2**, 844–848 (2006).

79. Matsukevich, D. N. *et al.* Deterministic single photons via conditional quantum evolution. *Phys. Rev. Lett.* **97**, 013601 (2006).

80. Chen, S. *et al.* Deterministic and storable single-photon source based on a quantum memory. *Phys. Rev. Lett.* **97**, 173004 (2006).

81. Du, S., Kolchin, P., Belthangady, C., Yin, G. Y. & Harris, S. E. Subnatural linewidth biphotons with controllable temporal length. *Phys. Rev. Lett.* **100**, 183603 (2008).

82. Simon, J., Tanji, H., Thompson, J. K. & Vuletić, V. Interfacing collective atomic excitations and single photons. *Phys. Rev. Lett.* **98**, 183601 (2007).

83. Tanji, H., Ghosh, S., Simon, J., Bloom, B. & Vuletić, V. Heralded single-magnon quantum memory for photon polarization states. *Phys. Rev. Lett.* **103**, 043601 (2009).

84. Clauser, J. F., Horne, M., Shimony, A. & Holt, R. A. Proposed experiment to test local hidden-variable theories. *Phys. Rev. Lett.* **32**, 880–884 (1969).

85. Yuan, Z.-S. *et al.* Experimental demonstration of a bdcz quantum repeater node. *Nature* **454**, 1098–1101 (2008).

86. Fleischhauer, M. & Lukin, M. D. Dark-state polaritons in electromagnetically induced transparency. *Phys. Rev. Lett.* **84**, 5094–5097 (2000).

87. Fleischhauer, M. & Lukin, M. D. Quantum memory for photons: Dark-state polaritons. *Phys. Rev. A* **65**, 022314 (2002).

88. Hau, L. V., Harris, S. E., Dutton, Z. & Behroozi, C. H. Light speed reduction to 17 metres per second in an ultracold atomic gas. *Nature* **397**, 594–598 (1999).

89. Kash, M. M. *et al.* Ultraslow group velocity and enhanced nonlinear optical effects in a coherently driven hot atomic gas. *Phys. Rev. Lett.* **82**, 5229–5232 (1999).

90. Liu, C., Dutton, Z., Behroozi, C. H. & Hau, L. V. Observation of coherent optical information storage in an atomic medium using halted light pulses. *Nature* **409**, 490 (2001).

91. Phillips, D. F., Fleischhauer, A., Mair, A., Walsworth, R. L. & Lukin, M. D. Storage of light in atomic vapor. *Phys. Rev. Lett.* **86**, 783 (2001).

92. Eisaman, M. D. *et al.* Electromagnetically induced transparency with tunable single-photon pulses. *Nature* **438**, 837–841 (2005).

93. Chaneliere, T. *et al.* Storage and retrieval of single photons transmitted between remote quantum memories. *Nature* **438**, 833–836 (2005).

94. Harris, S. E. Electromagnetically induced transparency. *Phys. Today* **50**, 36–40 (1997).

95. Lukin, M. D. Colloquium: Trapping and manipulating photon states in atomic ensembles. *Rev. Mod. Phys.* **75**, 457 (2003).

96. Fleischhauer, M., Imamoglu, A. & Marangos, J. P. Electromagnetically induced transparency: Optics in coherent media. *Rev. Mod. Phys.* **77**, 633–641 (2005).

97. Appel, J., Figueroa, E., Korystov, D., Lobino, M. & Lvovsky, A. I. Quantum memory for squeezed light. *Phys. Rev. Lett.* **100**, 093602 (2008).

98. Honda, K. *et al.* Storage and retrieval of a squeezed vacuum. *Phys. Rev. Lett.* **100**, 093601 (2008).

99. Lettner, M. *et al.* Remote entanglement between a single atom and a Bose-Einstein condensate. *arXiv:1102.4285* (2011).

100. Moiseev, S. A. & Kröll, S. Complete reconstruction of the quantum state of a single-photon wave packet absorbed by a doppler-broadened transition. *Phys. Rev. Lett.* **87**, 173601 (2001).

101. Afzelius, M., Simon, C., de Riedmatten, H. & Gisin, N. Multimode quantum memory based on atomic frequency combs. *Phys. Rev. A* **79**, 052329 (2009).

102. Hétet, G. *et al.* Photon echoes generated by reversing magnetic field gradients in a rubidium vapor. *Opt. Lett.* **33**, 2323–2325 (2008).

103. Hétet, G., Longdell, J. J., Alexander, A. L., Lam, P. K. & Sellars, M. J. Electro-optic quantum memory for light using two-level atoms. *Phys. Rev. Lett.* **100**, 023601 (2008).

104. Lvovsky, A. I., Sanders, B. C. & Tittel, W. Optical quantum memory. *Nature Photon.* **3**, 706–714 (2009).

105. Nunn, J. *et al.* Multimode memories in atomic ensembles. *Phys. Rev. Lett.* **101**, 260502 (2008).

106. Hosseini, M. *et al.* Coherent optical pulse sequencer for quantum applications. *Nature* **461**, 241–245 (2009).

107. de Riedmatten, H., Afzelius, M., Staudt, M. U., Simon, C. & Gisin, N. A solid-state light-matter interface at the single-photon level. *Nature* **456**, 773–777 (2008).

108. Clausen, C. *et al.* Quantum storage of photonic entanglement in a crystal. *Nature* **469**, 508–511 (2011).

109. Saglamyurek, E. *et al.* Broadband waveguide quantum memory for entangled photons. *Nature* **469**, 512–515 (2011).

110. van Enk, S. J., Lutkenhaus, N. & Kimble, H. J. Experimental procedures for entanglement verification. *Phys. Rev. A* **75**, 052318 (2007).

111. Matsukevich, D. N. *et al.* Entanglement of remote atomic qubits. *Phys. Rev. Lett.* **96**, 030405 (2006).

112. Chen, Y.-A. *et al.* Memory-built-in quantum teleportation with photonic and atomic qubits. *Nature Phys.* **4**, 103–107 (2008).

113. Chen, Y.-A. *et al.* Heralded generation of an atomic noon state. *Phys. Rev. Lett.* **104**, 043601 (2010).

114. Zhao, B. *et al.* A millisecond quantum memory for scalable quantum networks. *Nature Phys.* **5**, 95–99 (2009).

115. Zhao, R. *et al.* Long-lived quantum memory. *Nature Phys.* **5**, 100–104 (2009).

116. Schnorrberger, U. *et al.* Electromagnetically induced transparency and light storage in an atomic mott insulator. *Phys. Rev. Lett.* **103**, 033003 (2009).

117. Zhang, R., Garner, S. R. & Hau, L. V. Creation of long-term coherent optical memory via controlled nonlinear interactions in Bose-Einstein condensates. *Phys. Rev. Lett.* **103**, 233602 (2009).

118. Longdell, J. J., Fraval, E., Sellars, M. J. & Manson, N. B. Stopped light with storage times greater than one second using electromagnetically induced transparency in a solid. *Phys. Rev. Lett.* **95**, 063601 (2005).

119. Jenkins, S. D., Matsukevich, D. N., Chanelière, T., Kuzmich, A. & Kennedy, T. A. B. Theory of dark-state polariton collapses and revivals. *Phys. Rev. A* **73**, 021803 (2006).

120. Matsukevich, D. N. *et al.* Observation of dark state polariton collapses and revivals. *Phys. Rev. Lett.* **96**, 033601 (2006).

121. Hofmann, H. F. & Takeuchi, S. Violation of local uncertainty relations as a signature of entanglement. *Phys. Rev. A* **68**, 032103 (2003).

122. Jiang, L., Taylor, J. M. & Lukin, M. D. Fast and robust approach to long-distance quantum communication with atomic ensembles. *Phys. Rev. A* **76**, 012301 (2007).

123. Zhao, B., Chen, Z. B., Chen, Y. A., Schmiedmayer, J. & Pan, J. W. Robust creation of entanglement between remote robust creation of entanglement between remote memory qubits. *Phys. Rev. Lett.* **98**, 240502 (2007).

124. Jiang, L., Taylor, J., Khaneja, N. & Lukin, M. Optimal approach to quantum communication algorithms using dynamics programming. *Proc. Natl. Acad. Sci. U.S.A.* **104**, 17291 (2007).

125. Sangouard, N. *et al.* Robust and efficient quantum repeaters with atomic ensembles and linear optics. *Phys. Rev. A* **77**, 062301 (2008).

126. Barrett, S. D., Rohde, P. P. & Stace, T. M. Scalable quantum computing with atomic ensembles. *New J. Phys.* **12**, 093032 (2010).

127. André, A. & Lukin, M. D. Manipulating light pulses via dynamically controlled photonic band gap. *Phys. Rev. Lett.* **89**, 143602 (2002).

128. André, A., Bajcsy, M., Zibrov, A. S. & Lukin, M. D. Nonlinear optics with stationary pulses of light. *Phys. Rev. Lett.* **94**, 063902 (2005).

129. Chang, D. E. *et al.* Crystallization of strongly interacting photons in a nonlinear optical fibre. *Nature Phys.* **4**, 884–889 (2008).

130. Gorshkov, A. V., Otterbach, J., Demler, E., Fleischhauer, M. & Lukin, M. D. Photonic phase gate via an exchange of fermionic spin waves in a spin chain. *Phys. Rev. Lett.* **105**, 060502 (2010).

131. Sangouard, N., Simon, C., Coudreau, T. & Gisin, N. Purification of single-photon entanglement with linear optics. *Phys. Rev. A* **78**, 050301 (2008).

132. Salart, D. *et al.* Purification of single-photon entanglement. *Phys. Rev. Lett.* **104**, 180504 (2010).

133. Colombe, Y. *et al.* Strong atom-field coupling for Bose-Einstein condensates in an optical cavity on a chip. *Nature* **450**, 272–276 (2007).

134. Brennecke, F. *et al.* Cavity QED with a Bose-Einstein condensate. *Nature* **450**, 268–271 (2007).

135. Herskind, P. F., Dantan, A., Marler, J. P., Albert, M. & Drewsen, M. Realization of collective strong coupling with ion coulomb crystals in an optical cavity. *Nature Phys.* **5**, 494–498 (2009).

136. Schuster, D. I. *et al.* High-cooperativity coupling of electron-spin ensembles to superconducting cavities. *Phys. Rev. Lett.* **105**, 140501 (2010).

137. Kubo, Y. *et al.* Strong coupling of a spin ensemble to a superconducting resonator. *Phys. Rev. Lett.* **105**, 140502 (2010).

138. Wu, H. *et al.* Storage of multiple coherent microwave excitations in an electron spin ensemble. *Phys. Rev. Lett.* **105**, 140503 (2010).

139. Eichenfield, M., Chan, J., Camacho, R. M., Vahala, K. J. & Painter, O. Optomechanical crystals. *Nature* **462**, 78–82 (2009).

140. Meiser, D. & Meystre, P. Superstrong coupling regime of cavity quantum electrodynamics. *Phys. Rev. A* **74**, 065801 (2006).

141. Nikoghosyan, G. & Fleischhauer, M. Photon-number selective group delay in cavity induced transparency. *Phys. Rev. Lett.* **105**, 013601 (2010).

142. Birnbaum, K. M. *Cavity QED with multilevel atoms*. Ph.D. thesis, California Institute of Technology, Pasadena, CA (2005).

143. Scully, M. O. & Zubairy, M. S. *Quantum Optics* (Cambridge University Press, Cambridge, 1997).

144. Westbrook, C. I. *et al.* Localization of atoms in a three-dimensional standing wave. *Phys. Rev. Lett.* **65**, 33 (1990).

145. Eichmann, U. *et al.* Young's interference experiment with light scattered from two atoms. *Phys. Rev. Lett.* **70**, 2359 (1993).

146. Grynberg, G., Lounis, B., Verkerk, P., Courtois, J. Y. & Salomon, C. Quantized motion of cold Cesium atoms in two- and three-dimensional optical potentials. *Phys. Rev. Lett.* **70**, 2249–2252 (1993).

147. Felinto, D., Chou, C. W., de Riedmatten, H., Polyakov, S. V. & Kimble, H. J. Control of decoherence in the generation of photon pairs from atomic ensembles. *Phys. Rev. A* **72**, 053809 (2005).

148. Scully, M. O., Fry, E. S., Ooi, C. H. R. & Wodkiewicz, K. Directed spontaneous emission from an extended ensemble of n atoms: Timing is everything. *Phys. Rev. Lett.* **96**, 010501 (2006).

149. Hong, C. K., Ou, Z. Y. & Mandel, L. Measurement of subpicosecond time intervals between two photons by interference. *Phys. Rev. Lett.* **59**, 2044–2046 (1987).

150. Legero, T., Wilk, T., Kuhn, A. & Rempe, G. Time-resolved two-photon quantum interference. *Appl. Phys. B* **77**, 797–802 (2003-12-01).

151. Gilowski, M. *et al.* Narrow bandwidth interference filter-stabilized diode laser systems for the manipulation of neutral atoms. *Opt. Comm.* **280**, 443–447 (2007).

152. Kogelnik, H. Coupled wave theory for thick hologram gratings. *Bell Syst. Tech. J.* **48**, 2909 (1969).

153. Alton, D. J. *et al.* Strong interactions of single atoms and photons near a dielectric boundary. *Nature Phys.* **7**, 159–165 (2011).

154. Dicke, R. H. *The Coherence Brightened Laser*, vol. 1, 35 (Columbia University Press, New York, 1964).

155. Arecchi, F. T. & Courtens, E. Cooperative phenomena in resonant electromagnetic propagation. *Phys. Rev. A* **2** (1970).

156. Skribanowitz, N., Herman, I. P., MacGillivray, J. C. & Feld, M. S. Observation of Dicke superradiance in optically pumped HF gas. *Phys. Rev. Lett.* **30**, 309–312 (1973).

157. Gross, M., Goy, P., Fabre, C., Haroche, S. & Raimond, J. M. Maser oscillation and microwave superradiance in small systems of rydberg atoms. *Phys. Rev. Lett.* **43**, 343–346 (1979).

158. Vrehen, Q. H. F., Hikspoors, H. M. J. & Gibbs, H. M. Quantum beats in superfluorescence in atomic Cesium. *Phys. Rev. Lett.* **38**, 764–767 (1977).

159. Gibbs, H. M., Vrehen, Q. H. F. & Hikspoors, H. M. J. Single-pulse superfluorescence in Cesium. *Phys. Rev. Lett.* **39**, 547–550 (1977).

160. Gross, M., Raimond, J. M. & Haroche, S. Doppler beats in superradiance. *Phys. Rev. Lett.* **40**, 1711–1714 (1978).

161. Inouye, S. *et al.* Superradiant Rayleigh scattering from a Bose-Einstein condensate. *Science* **285**, 571–574 (1999).

162. Zoller, P. *et al.* Quantum information processing and communication. *Eur. Phys. J. D* **36**, 203–228 (2005).

163. Friedberg, R., Hartman, S. R. & Manassah, J. T. Limited superradiant damping of small samples. *Phys. Lett. A* **40**, 365–366 (1972).

164. Carmichael, H. J. *Statistical Methods in Quantum Optics*, vol. I (Springer, Berlin, 1999).

165. Carmichael, H. J. *Statistical Methods in Quantum Optics*, vol. II (Springer, Berlin, 1999).

166. Gardiner, C. W. & Zoller, P. *Quantum Noise* (Springer, Berlin, 1999).

167. Rehler, N. E. & Eberly, J. H. Superradiance. *Phys. Rev. A* **3**, 1735–1751 (1971).

168. Ressayre, E. & Tallet, A. Markovian model for oscillatory superfluorescence. *Phys. Rev. A* **18**, 2196 –2203 (1978).

169. Raymer, M. G. & Walmsley, I. A. The quantum coherence properties of stimulated Raman scattering. In Wolf, E. (ed.) *Progress in Optics*, vol. 28, chap. 3, 181–270 (Elsevier, Amsterdam, 1990).

170. Mandel, O. & Wolf, E. *Optical Coherence and Quantum Optics* (Cambridge University Press, Cambridge, 1995).

171. Born, M. & Wolf, E. *Principles of Optics: Electromagnetic Theory of Propagation, Interference and Diffraction of Light* (Cambridge University Press, Cambridge, 1999).

172. Sørensen, M. W. & Sørensen, A. S. Three-dimensional theory for light-matter interaction. *Phys. Rev. A* **77**, 013826 (2008).

173. André, A., Duan, L. M. & Lukin, M. D. Coherent atom interactions mediated by dark-state polaritons. *Phys. Rev. Lett.* **88**, 243602 (2002).

174. Zeuthen, E., Grodecka-Grad, A. & Sørensen, A. S. Three-dimensional theory of quantum memories based on Lambda-type atomic ensembles. *arXiv:1105.2662v1* (2011).

175. Clauser, J. F. Experimental distinction between the quantum and classical field-theoretic predictions for the photoelectric effect. *Phys. Rev. D* **9**, 853–860 (1974).

176. Hong, C. K. & Mandel, L. Experimental realization of a localized one-photon state. *Phys. Rev. Lett.* **56**, 58–60 (1986).

177. Grangier, P., Roger, G. & Aspect, A. Experimental evidence for a photon anticorrelation effect on a beam splitter: A new light on single-photon interferences. *Europhys. Lett.* **1**, 173 (1986).

178. Wootters, W. K. Entanglement of formation of an arbitrary state of two qubits. *Phys. Rev. Lett.* **80**, 2245–2248 (1998).

179. Gray, H. R., Whitley, R. M. & Stroud, C. R., Jr. Coherent trapping of atomic populations. *Opt. Lett.* **3**, 218–220 (1978).

180. Kuklinski, J. R., Gaubatz, U., Hioe, F. T. & Bergmann, K. Adiabatic population transfer in a three-level system driven by delayed laser pulses. *Phys. Rev. A* **40**, 6741–6744 (1989).

181. Gaubatz, U., Rudecki, P., Schiemann, S. & Bergmann, K. Population transfer between molecular vibrational levels by stimulated raman scattering with partially overlapping laser fields. a new concept and experimental results. *J. Chem. Phys.* **92**, 5363 (1990).

182. Harris, S. E., Field, J. E. & Imamoglu, A. Nonlinear optical processes using electromagnetically induced transparency. *Phys. Rev. Lett.* **64**, 1107–1110 (1990).

183. Arimondo, E. Coherent population trapping in laser spectroscopy. In Wolf, E. (ed.) *Progress in Optics*, vol. 35, chap. 5, 257–354 (Elsevier, Amsterdam, 1996).

184. Vitanov, N. V., Fleischhauer, M., Shore, B. W. & Bergmann, K. Coherent manipulation of atoms and molecules by sequential pulses. *Adv. At. Mol. Opt. Phys.* **46**, 55–190 (2001).

185. Parkins, A. S., Marte, P., Zoller, P. & Kimble, H. J. Synthesis of arbitrary quantum states via adiabatic transfer of zeeman coherence. *Phys. Rev. Lett.* **71**, 3095 (1993).

186. Gorshkov, A. V., André, A., Fleischhauer, M., Sørensen, A. S. & Lukin, M. D. Universal approach to optimal photon storage in atomic media. *Phys. Rev. Lett.* **98**, 123601 (2007).

187. Gorshkov, A. V., André, A., Lukin, M. D. & Sørensen, A. S. Photon storage in Lambda-type optically dense atomic media. I. Cavity model. *Phys. Rev. A* **76**, 033804 (2007).

188. Gorshkov, A. V., André, A., Lukin, M. D. & Sørensen, A. S. Photon storage in Lambda-type optically dense atomic media. II. Free-space model. *Phys. Rev. A* **76**, 033805 (2007).

189. Gorshkov, A. V., André, A., Lukin, M. D. & Sørensen, A. S. Photon storage in Lambda-type optically dense atomic media. III. Effects of inhomogeneous broadening. *Phys. Rev. A* **76**, 033806 (2007).

190. Harris, S. E. & Yamamoto, Y. Photon switching by quantum interference. *Phys. Rev. Lett.* **81**, 3611–3614 (1998).

191. Harris, S. E. & Hau, L. V. Nonlinear optics at low light levels. *Phys. Rev. Lett.* **82**, 4611–4614 (1999).

192. Vitanov, N. V. & Stenholm, S. Population transfer via a decaying state. *Phys. Rev. A* **56**, 1463–1471 (1997).

193. Walls, D. F. & Milburn, G. J. *Quantum Optics* (Springer, Berlin, 2008), 2nd edn.

194. Matsko, A. B., Novikova, I., Scully, M. O. & Welch, G. R. Radiation trapping in coherent media. *Phys. Rev. Lett.* **87**, 133601 (2001).

195. Ringot, J., Szriftgiser, P. & Garreau, J. C. Subrecoil Raman spectroscopy of cold Cesium atoms. *Phys. Rev. A* **65**, 013403 (2001).

196. Radnaev, A. G. *et al.* A quantum memory with telecom-wavelength conversion. *Nature Phys.* **6**, 894–899 (2010).

197. Haffner, H. *et al.* Robust entanglement. *Appl. Phys. B* **81**, 151–153 (2005).

198. Langer, C. *et al.* Long-lived qubit memory using atomic ions. *Phys. Rev. Lett.* **95**, 060502 (2005).

199. Dicke, R. H. Interaction-free quantum measurements: A paradox? *Am. J. Phys.* **49**, 925 (1981).

200. Cabrillo, C., Cirac, J. I., García-Fernández, P. & Zoller, P. Creation of entangled states of distant atoms by interference. *Phys. Rev. A* **59**, 1025 (1999).

201. Bose, S., Knight, P. L., Plenio, M. B. & Vedral, V. Proposal for teleportation of an atomic state via cavity decay. *Phys. Rev. Lett.* **83**, 5158 (1999).

202. de Riedmatten, H. *et al.* Direct measurement of decoherence for entanglement between a photon and stored atomic excitation. *Phys. Rev. Lett.* **97**, 113603 (2006).

203. Chen, Z.-B., Zhao, B., Chen, Y.-A., Schmiedmayer, J. & Pan, J.-W. Fault-tolerant quantum repeater with atomic ensembles and linear optics. *Phys. Rev. A* **76**, 022329 (2007).

204. Matsukevich, D. N. & Kuzmich, A. Quantum state transfer between matter and light. *Science* **306**, 663–666 (2004).

205. Bennett, C. H., DiVincenzo, D. P., Smolin, J. A. & Wootters, W. K. Mixed-state entanglement and quantum error correction. *Phys. Rev. A* **54**, 3824 (1996).

206. Eisert, J., Simon, C. & Plenio, M. B. On the quantification of entanglement in infinite-dimensional quantum systems. *J. Phys. A* **35**, 3911–3923 (2002).

207. Laurat, J., Coudreau, T., Keller, G., Treps, N. & Fabre, C. Effects of mode coupling on the generation of quadrature Einstein-Podolsky-Rosen entanglement in a type-II optical parametric oscillator below threshold. *Phys. Rev. A* **71**, 022313 (2005).

208. Horodecki, R., Horodecki, P., Horodecki, M. & Horodecki, K. Quantum entanglement. *Rev. Mod. Phys.* **81**, 865–942 (2009).

209. Dür, W., Vidal, G. & Cirac, J. I. Three qubits can be entangled in two inequivalent ways. *Phys. Rev. A* **62**, 062314 (2000).

210. Verstraete, F., Dehaene, J., De Moor, B. & Verschelde, H. Four qubits can be entangled in nine different ways. *Phys. Rev. A* **65**, 052112 (2002).

211. Caves, C. M., Fuchs, C. A. & Schack, R. Unknown quantum states: The quantum de Finetti representation. *J. Math. Phys.* **42**, 4537 (2002).

212. Knill, E., Laflamme, R. & Milburn, G. J. A scheme for efficient quantum computation with linear optics. *Nature* **409**, 46–52 (2001).

213. Raussendorf, R. & Briegel, H. J. A one-way quantum computer. *Phys. Rev. Lett.* **86**, 5188 (2001).

214. Duan, L. M. & Kimble, H. J. Scalable photonic quantum computation through cavity-assisted interactions. *Phys. Rev. Lett.* **92**, 127902 (2004).

215. Blinov, B. B., Moehring, D. L., Duan, L.-M. & Monroe, C. Observation of entanglement between a single-trapped atom and a single photon. *Nature* **428**, 153–157 (2004).

216. Volz, J. *et al.* Observation of entanglement of a single photon with a trapped atom. *Phys. Rev. Lett.* **96**, 030404 (2006).

217. Beugnon, J. *et al.* Quantum interference between two single photons emitted by independently trapped atoms. *Nature* **440**, 779–782 (2006).

218. Boozer, A. D., Boca, A., Miller, R., Northup, T. E. & Kimble, H. J. Reversible state transfer between light and a single trapped atom. *Phys. Rev. Lett.* **98**, 193601 (2007).

219. Clauser, J. F. & Shimony, A. Bell's theorem. Experimental tests and implications. *Rep. Prog. Phys.* **41**, 1881–1927 (1978).

220. Fuchs, C. A., Gisin, N., Griffiths, R. B., Niu, C.-S. & Peres, A. Optimal eavesdropping in quantum cryptography. I. Information bound and optimal strategy. *Phys. Rev. A* **56**, 1163–1172 (1997).

221. Marcikic, I. *et al.* Distribution of time-bin entangled qubits over 50 km of optical fiber. *Phys. Rev. Lett.* **93**, 180502 (2004).

222. Pan, J.-W., Bouwmeester, D., Weinfurter, H. & Zeilinger, A. Experimental entanglement swapping: Entangling photons that never interacted. *Phys. Rev. Lett.* **80**, 3891 (1998).

223. Jia, X. *et al.* Experimental demonstration of unconditional entanglement swapping for continuous variables. *Phys. Rev. Lett.* **93**, 250503 (2004).

224. Takei, N., Yonezawa, H., Aoki, T. & Furusawa, A. High-fidelity teleportation beyond the no-cloning limit and entanglement swapping for continuous variables. *Phys. Rev. Lett.* **94**, 220502 (2005).

225. Turchette, Q. A. *et al.* Deterministic entanglement of two trapped ions. *Phys. Rev. Lett.* **81**, 3631 (1998).

226. Duan, L. M., Cirac, J. I. & Zoller, P. Three-dimensional theory for interaction between atomic ensembles and free-space light. *Phys. Rev. A* **66**, 023818 (2002).

227. Briegel, H.-J., van Enk, S. J., Cirac, J. & Zoller, P. *The Physics of Quantum Information*, 192 (Springer, New York, 2000).

228. Tan, S. M., Walls, D. F. & Collett, M. J. Nonlocality of a single photon. *Phys. Rev. Lett.* **66**, 252–255 (1991).

229. Hessmo, B., Usachev, P., Hoshang, H. & Gunner, B. Experimental demonstration of single photon nonlocality. *Phys. Rev. Lett.* **92**, 180401 (2004).

230. Jacques, V. *et al.* Experimental realization of Wheeler's delayed-choice gedanken experiment. *Science* **315**, 966–968 (2007).

231. Lounis, B. & Orrit, M. Single-photon sources. *Rep. Prog. Phys.* **68**, 1129–1179 (2005).

232. Sangouard, N. Long-distance entanglement distribution with single-photon sources. *Phys. Rev. A* **76**, 050301 (2007).

233. van Enk, S. J. Single-particle entanglement. *Phys. Rev. A* **72**, 064306 (2005).

234. Eisaman, M. D. *et al.* Shaping quantum pulses of light via coherent atomic memory. *Phys. Rev. Lett.* **93**, 233602 (2004).

235. Novikova, I. *et al.* Optimal control of light pulse storage and retrieval. *Phys. Rev. Lett.* **98**, 243602 (2007).

236. Gorshkov, A. V., André, A., Fleischhauer, M., Sørensen, A. S. & Lukin, M. D. Universal approach to optimal photon storage in atomic media. *Phys. Rev. Lett.* **98**, 123601 (2007).

237. Imamoglu, A. & Harris, S. E. Lasers without inversion: interference of dressed lifetime-broadened states. *Opt. Lett.* **14**, 1344–1346 (1989).

238. Boller, K. J., Imamolu, A. & Harris, S. E. Observation of electromagnetically induced transparency. *Phys. Rev. Lett.* **66**, 2593–2596 (1991).

239. Budker, D., Kimball, D. F., Rochester, S. M. & Yashchuk, V. V. Nonlinear magneto-optics and reduced group velocity of light in atomic vapor with slow ground state relaxation. *Phys. Rev. Lett.* **83**, 1767–1770 (1999).

240. Dalibard, J., Castin, Y. & Mølmer, K. Wave-function approach to dissipative processes in quantum optics. *Phys. Rev. Lett.* **68**, 580–583 (1992).

241. Gardiner, C. W., Parkins, A. S. & Zoller, P. Wave-function quantum stochastic differential equations and quantum-jump simulation methods. *Phys. Rev. A* **46**, 4363–4381 (1992).

242. Ketterle, W., Davis, K. B., Joffe, M. A., Martin, A. & Pritchard, D. E. High densities of cold atoms in a dark spontaneous-force optical trap. *Phys. Rev. Lett.* **70**, 2253–2256 (1993).

243. Petrich, W., Anderson, M. H., Ensher, J. R. & Cornell, E. A. Behavior of atoms in a compressed magneto-optical trap. *J. Opt. Soc. Am. B* **11**, 1332–1335 (1994).

244. Phillips, N. B., Gorshkov, A. V. & Novikova, I. Slow light propagation and amplification via electromagnetically induced transparency and four-wave mixing in an optically dense atomic vapor. *arXiv:0903.3937* (2009).

245. Gorshkov, A. V., Calarco, T., Lukin, M. D. & Sørensen, A. S. Photon storage in Lambda-type optically dense atomic media. IV. Optimal control using gradient ascent. *Phys. Rev. A* **77**, 043806 (2008).

246. Horodecki, M., Horodecki, P. & Horodecki, R. Separability of mixed states: necessary and sufficient condition. *Phys. Lett. A* **223**, 1 (1996).

247. Peres, A. Separability criterion for density matrices. *Phys. Rev. Lett.* **77**, 1413 (1996).

248. Miyake, A. & Verstraete, F. Multipartite entanglement in $2 \times 2 \times n$ quantum systems. *Phys. Rev. A* **69**, 012101 (2004).

249. Lamata, L., Leon, J., Salgado, D. & Solano, E. Inductive entanglement classification of four qubits under SLOCC. *Phys. Rev. A* **75**, 022318 (2007).

250. Paris, M. & Rehacek, J. (eds.) *Quantum State Estimation (Lecture Notes in Physics)*, vol. 649 (Springer, Berlin, Heidelberg, 2004).

251. Blume-Kohout, R. Optimal, reliable estimation of quantum states. *New J. Phys.* **12**, 043034 (2010).

252. Lvovsky, A. I. *et al.* Quantum state reconstruction of the single-photon fock state. *Phys. Rev. Lett.* **87**, 050402 (2001).

253. Björk, G., Jonsson, P. & Sanchez-Soto, L. L. Single-particle nonlocality and entanglement with the vacuum. *Phys. Rev. A* **64**, 042106 (2001).

254. Lombardi, E., Sciarrino, F., Popescu, S. & De Martini, F. Teleportation of a vacuum–one-photon qubit. *Phys. Rev. Lett.* **88**, 070402 (2002).

255. Lee, J.-W., Lee, E. K., Chung, Y. W., Lee, H.-W. & Kim, J. Quantum cryptography using single-particle entanglement. *Phys. Rev. A* **68**, 012324 (2003).

256. Zanardi, P. Quantum entanglement in fermionic lattices. *Phys. Rev. A* **65**, 042101 (2002).

257. Shi, Y. Quantum entanglement of identical particles. *Phys. Rev. A* **67**, 024301 (2003).

258. van Enk, S. J. Entanglement of electromagnetic fields. *Phys. Rev. A* **67**, 022303 (2003).

259. Nha, H. & Kim, J. W. Demonstrating multipartite entanglement of single-particle W states: Linear optical schemes. *Phys. Rev. A* **75**, 012326 (2007).

260. Nha, H. Linear optical scheme to demonstrate genuine multipartite entanglement for single-particle W states. *Phys. Rev. A* **77**, 062328 (2008).

261. van Loock, P. & Furusawa, A. Detecting genuine multipartite continuous-variable entanglement. *Phys. Rev. A* **67**, 052315 (2003).

262. Wang, Z.-W., Huang, Y.-F., Ren, X.-F., Zhang, Y.-S. & Guo, G.-C. Experimental entanglement verification and quantification via uncertainty relations. *Eur. Phys. Lett.* **78**, 40002 (2007).

263. Werner, R. F. Quantum states with Einstein-Podolsky-Rosen correlations admitting a hidden-variable model. *Phys. Rev. A* **40** (1989).

264. van Enk, S. & Kimble, H. J. Comment on 'quantum state transfer between matter and light'. *Science* **309**, 1187b (2005).

265. Oliver, B. & Stroud, C. Predictions of violations of Bell's inequality in an 8-port homodyne detector. *Phys. Lett. A* **135**, 407 (1989).

266. Hardy, L. Nonlocality of a single photon revisited. *Phys. Rev. Lett.* **73**, 2279 (1994).

267. Peres, A. Nonlocal effects in fock space. *Phys. Rev. Lett.* **74**, 4571 (1995).

268. Vaidman, L. Nonlocality of a single photon revisited again. *Phys. Rev. Lett.* **75**, 2063 (1995).

269. Greenberger, D. M., Horne, M. A. & Zeilinger, A. Nonlocality of a single photon? *Phys. Rev. Lett.* **75**, 2064 (1995).

270. Hardy, L. A reply to the comment by Lev Vaidman and D. M. Greenberger, M. A. Horne and A. Zeilinger. *Phys. Rev. Lett.* **75**, 2065 (1995).

271. Wildfeuer, C. F., Lund, A. P. & Dowling, J. P. Strong violations of Bell-type inequalities for path-entangled number states. *Phys. Rev. A* **76**, 052101 (2007).

272. Ashhab, S., Maruyama, K. & Nori, F. Detecting mode entanglement: The role of coherent states, superselection rules, and particle statistics. *Phys. Rev. A* **76**, 052113 (2007).

273. Aspect, A., Grangier, P. & Roger, G. Experimental tests of realistic local theories via Bell's theorem. *Phys. Rev. Lett.* **47**, 460–463 (1981).

274. Hillery, M., Buźek, V. & Berthiaume, A. Quantum secret sharing. *Phys. Rev. A* **59**, 1829 (1999).

275. Leibfried, D. *et al.* Creation of a six-atom Schrödinger cat state. *Nature* **438**, 639–642 (2005).

276. Haffner, H. *et al.* Scalable multiparticle entanglement of trapped ions. *Nature* **438**, 643–646 (2005).

277. Gao, W.-B. *et al.* Experimental demonstration of a hyper-entangled ten-qubit Schrödinger cat state. *Nature Phys.* **6**, 331–335 (2010).

278. Duan, L.-M., Giedke, G., Cirac, J. I. & Zoller, P. Inseparability criterion for continuous variable systems. *Phys. Rev. Lett.* **84**, 2722 (2000).

279. Simon, R. Peres-Horodecki separability criterion for continuous variable systems. *Phys. Rev. Lett.* **84** (2000).

280. Braunstein, S. L. & van Loock, P. Quantum information with continuous variables. *Rev. Mod. Phys.* **77**, 513 (2005).

281. Furusawa, A. *et al.* Unconditional quantum teleportation. *Science* **282**, 706–709 (1998).

282. Reck, M., Zeilinger, A., Bernstein, H. J. & Bertani, P. Experimental realization of any discrete unitary operator. *Phys. Rev. Lett.* **73**, 58 (1994).

283. Roos, C. F. *et al.* Control and measurement of three-qubit entangled states. *Science* **304**, 1478–1480 (2004).

284. de Gennes, P. G. *The physics of liquid crystals* (Oxford University Press, London, 1974).

285. Steffen, M. *et al.* Measurement of the entanglement of two superconducting qubits via state tomography. *Science* **313**, 1423–1425 (2006).

286. DiCarlo, L. *et al.* Demonstration of two-qubit algorithms with a superconducting quantum processor. *Nature* **460**, 240–244 (2009).

287. Aoki, T. Experimental creation of a fully inseparable tripartite continuous-variable state. *Phys. Rev. Lett.* **91**, 080404 (2003).

288. Su, X. *et al.* Experimental preparation of quadripartite cluster and Greenberger-Horne-Zeilinger entangled states for continuous variables. *Phys. Rev. Lett.* **98**, 070502 (2007).

289. Heaney, L. & Vedral, V. Natural mode entanglement as a resource for quantum communication. *Phys. Rev. Lett.* **103**, 200502 (2009).

290. Heaney, L., Cabello, A., Santos, M. F. & Vedral, V. Extreme nonlocality with one photon. *arXiv:0911.0770v2* (2010).

291. Vetsch, E. Optical interface created by laser-cooled atoms trapped in the evanescent field surrounding an optical nanofiber. *Phys. Rev. Lett.* **104**, 203603 (2010).

292. Deutsch, C. Spin self-rephasing and very long coherence times in a trapped atomic ensemble. *Phys. Rev. Lett.* **105**, 020401 (2010).

293. Ivanovic, I. D. How to differentiate between non-orthogonal states. *Phys. Lett. A* **123**, 257–259 (1987).

294. Dieks, D. Overlap and distinguishability of quantum states. *Phys. Lett. A* **126**, 303–306 (1988).

295. Peres, A. How to differentiate between non-orthogonal states. *Phys. Lett. A* **128**, 19 (1988).

296. Chefles, A. Unambiguous discrimination between linearly independent quantum states. *Phys. Lett. A* **239**, 339–347 (1998).

297. Gühne, O. & Tóth, G. Energy and multipartite entanglement in multidimensional and frustrated spin models. *Phys. Rev. A* **73**, 052319 (2006).

298. Lipkin, H. J., Meshkov, N. & Glick, A. J. Validity of many-body approximation methods for a solvable model. I. Exact solutions and perturbation theory. *Nucl. Phys.* **62**, 188–198 (1965).

299. Meshkov, N., Glick, A. J. & Lipkin, H. J. Validity of many-body approximation methods for a solvable model. II. Linearization procedures. *Nucl. Phys.* **62**, 199–210 (1965).

300. Glick, A. J., Lipkin, H. J. & Meshkov, N. Validity of many-body approximation methods for a solvable model. III. Diagram summations. *Nucl. Phys.* **62**, 211–224 (1965).

301. Stiebeiner, A., Garcia-Fernandez, R. & Rauschenbeutel, A. Design and optimization of broadband tapered optical fibers with a nanofiber waist. *Opt. Express* **18**, 22677–22685 (2010).

302. Vahala, K. J. Optical microcavities. *Nature* **424**, 839–846 (2003).

303. Renn, M. J. *et al.* Laser-guided atoms in hollow-core optical fibers. *Phys. Rev. Lett.* **75**, 3253–3256 (1995).

304. Ito, H. *et al.* Laser spectroscopy of atoms guided by evanescent waves in micron-sized hollow optical fibers. *Phys. Rev. Lett.* **76**, 4500–4503 (1996).

305. Christensen, C. A. *et al.* Trapping of ultracold atoms in a hollow-core photonic crystal fiber. *Phys. Rev. A* **78**, 033429 (2008).

306. Bajcsy, M. *et al.* Efficient all-optical switching using slow light within a hollow fiber. *Phys. Rev. Lett.* **102**, 203902 (2009).

307. Le Kien, F., Balykin, V. I. & Hakuta, K. Atom trap and waveguide using a two-color evanescent light field around a subwavelength-diameter optical fiber. *Phys. Rev. A* **70**, 063403 (2004).

308. Nayak, K. P. *et al.* Optical nanofiber as an efficient tool for manipulating and probing atomicfluorescence. *Opt. Express* **15**, 5431–5438 (2007).

309. Sagué, G., Vetsch, E., Alt, W., Meschede, D. & Rauschenbeutel, A. Cold-atom physics using ultrathin optical fibers: Light-induced dipole forces and surface interactions. *Phys. Rev. Lett.* **99**, 163602 (2007).

310. Balykin, V. I., Letokhov, V. S., Ovchinnikov, Y. B. & Sidorov, A. I. Quantum-state-selective mirror reflection of atoms by laser light. *Phys. Rev. Lett.* **60** (1988).

311. Metcalf, H. J. & van der Straten, P. *Laser cooling and trapping* (Springer-Verlag, New York, 1999).

312. Cronin, A. D., Schmiedmayer, J. & Pritchard, D. E. Optics and interferometry with atoms and molecules. *Rev. Mod. Phys.* **81**, 1051–1129 (2009).

313. Ovchinnikov, Y. B., Manek, I. & Grimm, R. Surface trap for Cs atoms based on evanescent-wave cooling. *Phys. Rev. Lett.* **79**, 2225–2228 (1997).

314. Rychtarik, D., Engeser, B., Nägerl, H. C. & Grimm, R. Two-dimensional Bose-Einstein condensate in an optical surface trap. *Phys. Rev. Lett.* **92**, 173003 (2004).

315. Bakr, W. S. *et al.* Probing the Superfluid-to-Mott insulator transition at the Single-Atom level. *Science* **329**, 547–550 (2010).

316. Aoki, T. *et al.* Observation of strong coupling between one atom and a monolithic microresonator. *Nature* **443**, 671–674 (2006).

317. Zoubi, H. & Ritsch, H. Hybrid quantum system of a nanofiber mode coupled to two chains of optically trapped atoms. *New J. Phys.* **12**, 103014 (2010).

318. Balykin, V. I., Hakuta, K., Le Kien, F., Liang, J. Q. & Morinaga, M. Atom trapping and guiding with a subwavelength-diameter optical fiber. *Phys. Rev. A* **70**, 011401 (2004).

319. In preparation (2011).

320. Brambilla, G. Optical fibre nanowires and microwires: a review. *J. Opt.* **12**, 043001 (2010).

321. Warken, F., Rauschenbeutel, A. & Bartholomaus, T. Fiber pulling profits from precise positioning. *Photon. Spectra* **42**, 73 (2008).

322. Love, J. *et al.* Tapered single-mode fibres and devices. I. Adiabaticity criteria. *IEE. Proc. J.* **138**, 343–354 (1991).

323. Black, R., Lacroix, S., Gonthier, F. & Love, J. Tapered single-mode fibres and devices. II. Experimental and theoretical quantification. *IEE. Proc. J.* **138**, 355–364 (1991).

324. Birks, T. & Li, Y. The shape of fiber tapers. *J. Lightwave Technol.* **10**, 432–438 (1992).

325. Pricking, S. & Giessen, H. Tapering fibers with complex shape. *Opt. Express* **18**, 3426–3437 (2010).

326. Horowitz, P. & Hill, W. *The Art of Electronics* (Cambridge University Press, Cambridge, 1989).

327. Zumbahlen, H. *Linear Circuit Design Handbook* (Newnes, Newton, 2008).

328. Baillard, X. *et al.* Interference-filter-stabilized external-cavity diode lasers. *Opt. Comm.* **266**, 609–613 (2006).

329. Libbrecht, K. G. & Hall, J. L. A low-noise high-speed diode laser current controller. *Rev. Sci. Instrum.* **64**, 2133 (1993).

330. Bradley, C. C., Chen, J. & Hulet, R. G. Instrumentation for the stable operation of laser diodes. *Rev. Sci. Instrum.* **61**, 2097 (1990).

331. Metropolis, N., Rosenbluth, A., Rosenbluth, M., Teller, A. & Teller, E. Equation of state calculations by fast computing machines. *J. Chem. Phys.* **21**, 1087–1092 (1953).

332. Kirkpatrick, S., Gelatt, C. D. & Vecchi, M. P. Optimization by simulated annealing. *Science* **220**, 671–680 (1983).

333. Cerny, V. Thermodynamical approach to the traveling salesman problem: An efficient simulation algorithm. *J. Opt. Theory Appl.,* **45**, 41–51 (1985).

334. Press, W. H., Teukolsky, S. A., Vetterling, W. T. & Flannery, B. P. *Numerical Recipes* (Cambridge University Press, Cambridge, 1992).

335. Ghosh, G. *Handbook of thermo-optic coefficients of optical materials with applications* (Academic Press, New York, 1997).

336. Kien, F. L., Liang, J. Q., Hakuta, K. & Balykin, V. I. Field intensity distributions and polarization orientations in a vacuum-clad subwavelength-diameter optical fiber. *Opt. Comm.* **242**, 445–455 (2004).

337. Savard, T. A., O'Hara, K. M. & Thomas, J. E. Laser-noise-induced heating in far-off resonance optical traps. *Phys. Rev. A* **56**, R1095 (1997).

338. Barnett, A. H. *et al.* Substrate-based atom waveguide using guided two-color evanescent light fields. *Phys. Rev. A* **61**, 023608 (2000).

339. Ovchinnikov, Y. B., Shulga, S. V. & Balykin, V. I. An atomic trap based on evanescent light waves. *J. Phys. B: At. Mol. Opt. Phys.* **24**, 3173 (1991).

340. Dowling, J. P., Gea-Banacloche, J., Bederson, B. & Walther, H. *Evanescent Light-Wave Atom Mirrors, Resonators, Waveguides, and Traps*, vol. 37, 1–94 (Academic Press, 1996).

341. Boustimi, M., Baudon, J., Candori, P. & Robert, J. van der Waals interaction between an atom and a metallic nanowire. *Phys. Rev. B* **65**, 155402 (2002).

342. Dupont-roc, J., Polonsky, N., Cohen-Tannoudji, C. & Kastler, A. Lifting of a Zeeman degeneracy by interaction with a light beam. *Phys. Lett.* **25A**, 87–88 (1967).

343. McKeever, J. *et al.* State-insensitive cooling and trapping of single atoms in an optical cavity. *Phys. Rev. Lett.* **90**, 133602 (2003).

344. Katori, H., Takamoto, M., Palchikov, V. G. & Ovsiannikov, V. D. Ultrastable optical clock with neutral atoms in an engineered light shift trap. *Phys. Rev. Lett.* **91**, 173005 (2003).

345. Ye, J., Kimble, H. J. & Katori, H. Quantum state engineering and precision metrology using state-insensitive light traps. *Science* **320**, 1734–1738 (2008).

346. Kaplan, A., Andersen, M. F. & Davidson, N. Suppression of inhomogeneous broadening in rf spectroscopy of optically trapped atoms. *Phys. Rev. A* **66**, 045401 (2002).

347. Kien, F. L., Balykin, V. I. & Hakuta, K. State-insensitive trapping and guiding of Cesium atoms using a two-color evanescent field around a subwavelength-diameter fiber. *J. Phys. Soc. Jpn.* **74**, 910–917 (2005).

348. Deutsch, I. H. & Jessen, P. S. Quantum-state control in optical lattices. *Phys. Rev. A* **57**, 1972–1986 (1998).

349. Deutsch, I. H. & Jessen, P. S. Quantum control and measurement of atomic spins in polarization spectroscopy. *Opt. Comm.* **283**, 681–694 (2010).

350. Happer, W. & Mathur, B. S. Effective operator formalism in optical pumping. *Phys. Rev.* **163**, 12–25 (1967).

351. Schmieder, R. W. Matrix elements of the quadratic stark effect on atoms with hyperfine structure. *Am. J. Phys.* **40**, 297 (1972).

352. Casimir, H. B. G. & Polder, D. The influence of retardation on the London-van der Waals forces. *Phys. Rev.* **73**, 360–372 (1948).

353. Blagov, E. V., Klimchitskaya, G. L. & Mostepanenko, V. M. van der Waals interaction between microparticle and uniaxial crystal with application to hydrogen atoms and multiwall carbon nanotubes. *Phys. Rev. B* **71**, 235401 (2005).

354. Stern, N. P., Alton, D. J. & Kimble, H. J. Simulations of atomic trajectories near a dielectric surface. *submitted to New J. Phys.* (2011).

355. Lennard-Jones, J. E. Processes of adsorption and diffusion on solid surfaces. *Trans. Faraday Soc.* **27**, 333–359 (1932).

356. Lifshitz, E. M. & Pitaevskii, L. P. *Statistical Physics, Part II* (Pergamon Press, Oxford, 1980).

357. Gorza, M. P. & Ducloy, M. van der Waals interactions between atoms and dispersive surfaces at finite temperature. *Eur. Phys. J. D* **40**, 343–356 (2006).